ENERGY AND CHEMICAL ENGINEERING - OUTCOMES FROM THE EFCE ENERGY SECTION IN THE 12TH EUROPEAN CONGRESS ON CHEMICAL ENGINEERING (ECCE12)

EDITED BY: Francois M. A. Marechal, Fabrizio Bezzo and Theodoros Damartzis
PUBLISHED IN: Frontiers in Energy Research and Frontiers in Chemical Engineering

frontiers Research Topics

ISSN 1664-8714
ISBN 978-2-88971-059-1
DOI 10.3389/978-2-88971-059-1

About Frontiers

Frontiers is more than just an open-access publisher of scholarly articles: it is a pioneering approach to the world of academia, radically improving the way scholarly research is managed. The grand vision of Frontiers is a world where all people have an equal opportunity to seek, share and generate knowledge. Frontiers provides immediate and permanent online open access to all its publications, but this alone is not enough to realize our grand goals.

Frontiers Journal Series

The Frontiers Journal Series is a multi-tier and interdisciplinary set of open-access, online journals, promising a paradigm shift from the current review, selection and dissemination processes in academic publishing. All Frontiers journals are driven by researchers for researchers; therefore, they constitute a service to the scholarly community. At the same time, the Frontiers Journal Series operates on a revolutionary invention, the tiered publishing system, initially addressing specific communities of scholars, and gradually climbing up to broader public understanding, thus serving the interests of the lay society, too.

Dedication to Quality

Each Frontiers article is a landmark of the highest quality, thanks to genuinely collaborative interactions between authors and review editors, who include some of the world's best academicians. Research must be certified by peers before entering a stream of knowledge that may eventually reach the public - and shape society; therefore, Frontiers only applies the most rigorous and unbiased reviews.
Frontiers revolutionizes research publishing by freely delivering the most outstanding research, evaluated with no bias from both the academic and social point of view. By applying the most advanced information technologies, Frontiers is catapulting scholarly publishing into a new generation.

What are Frontiers Research Topics?

Frontiers Research Topics are very popular trademarks of the Frontiers Journals Series: they are collections of at least ten articles, all centered on a particular subject. With their unique mix of varied contributions from Original Research to Review Articles, Frontiers Research Topics unify the most influential researchers, the latest key findings and historical advances in a hot research area! Find out more on how to host your own Frontiers Research Topic or contribute to one as an author by contacting the Frontiers Editorial Office: frontiersin.org/about/contact

ENERGY AND CHEMICAL ENGINEERING - OUTCOMES FROM THE EFCE ENERGY SECTION IN THE 12TH EUROPEAN CONGRESS ON CHEMICAL ENGINEERING (ECCE12)

Topic Editors:
Francois M. A. Marechal, École Polytechnique Fédérale de Lausanne, Switzerland
Fabrizio Bezzo, University of Padua, Italy
Theodoros Damartzis, École Polytechnique Fédérale de Lausanne, Switzerland

Citation: Marechal, F. M. A., Bezzo, F., Damartzis, T., eds. (2021). Energy and Chemical Engineering - Outcomes from the EFCE Energy Section in the 12th European Congress on Chemical Engineering (ECCE12). Lausanne: Frontiers Media SA. doi: 10.3389/978-2-88971-059-1

Table of Contents

frontiers in Energy Research

ORIGINAL RESEARCH
published: 06 March 2020
doi: 10.3389/fenrg.2020.00032

Engineering Method for Calculating of an Axial Valve Separator With an External Location of the Locking Part

Anna Kapranova[1]*, *Sergey Neklyudov*[2], *Anton Lebedev*[1], *Alexander Meltser*[2] and *Dmitriy Voronin*[2]

[1] Department of Theoretical Mechanics and Resistance of Materials, Faculty of Mechanical Engineering, Yaroslavl State Technical University, Yaroslavl, Russia, [2] JSC Regulator, Yaroslavl, Russia

The purpose of the work is to develop an analytical method for calculating the effective ranges of structural parameters of the throttle part of the axial valve with the external location of the locking shell based on the proposed stochastic models of bubble formation at the initial stage of hydrodynamic cavitation. In contrast to the well-known engineering methods for choosing the conditional bore diameter for the designed control device constructed using the Pi-Buckingham theorem, this calculation method relies not only on gyrodynamic similarity criteria, but also on functional dependences for the laws of distribution of cavitation bubbles according to various characteristics (specific size bubbles, the degree of opening of the node "separator-external locking shell"). This takes into account a wide range of design and operating parameters, including the required valve capacity, as well as the physical and mechanical characteristics of the working medium. A block diagram of the calculation of the node "separator-external locking shell" for the specified axial valve is proposed. The influence of a set of design parameters for the "separator-external locking shell" assembly from the rational ranges of their variation obtained using the proposed analytical calculation algorithm on the size of cavitation bubbles is investigated. It has been established that when using the latest results in comparison with the values of parameters from irrational ranges of change, there is a tendency to reduce the ensemble average value of the diameter of the cavitation bubble by 1.95 times, when switching to a mode from 20% of the degree of separation of the separator to 80% of the opening of the throttle holes, the nominal valve capacity increases by 10.7 times. The results obtained illustrate the possibility of preventing an increase in the intensity of formation of cavities in the flow part of the control device already at the initial stage of the occurrence of cavitation.

Keywords: valve, separator, hydrodynamic cavitation, engineering method, parameter, stochastic model

OPEN ACCESS

Edited by:
Theodoros Damartzis, Federal Institute of Technology in Lausanne, Switzerland

Reviewed by:
Hadi Taghavifar, Malayer University, Iran
Xuewen Cao, China University of Petroleum, China

***Correspondence:**
Anna Kapranova
kapranova_anna@mail.ru

Specialty section:
This article was submitted to Process and Energy Systems Engineering, a section of the journal Frontiers in Energy Research

Received: *05 December 2019*
Accepted: *19 February 2020*
Published: *06 March 2020*

Citation:
Kapranova A, Neklyudov S, Lebedev A, Meltser A and Voronin D (2020) Engineering Method for Calculating of an Axial Valve Separator With an External Location of the Locking Part. Front. Energy Res. 8:32. doi: 10.3389/fenrg.2020.00032

INTRODUCTION

Improving engineering methods for calculating valves is a pressing issue in the field of pipeline fittings design. The use of valves (Emerson, 2020; Flowserve, 2020; Mokveld, 2020; Rust, 2020; Talis, 2020) in various branches of the chemical and oil and gas industry continues to expand. At the same time, the requirements for the main indicators of fluid transportation, such as throughput and expenditure characteristic of the valve, are constantly becoming tougher. The task of reducing the intensity of cavitation effects (Knapp et al., 1970; Franc and Michel, 2005; Xu et al., 2015) in the

flow part of the valve can be successfully solved by throttling fluid flows in designs (Emerson, 2020; Flowserve, 2020; Mokveld, 2020; Rust, 2020; Talis, 2020), which differ, for example, according to a number of characteristics: the shape of the throttle body, the number of throttle stages, the shape of throttle openings, the type of throttle channels, etc. Axial valves (Weevers, 1982; Peterman and Keithahn, 1987; Esveldt, 2012; Preston, 2018; Canjuga, 2019; Ziegler, 2019) provide a straight-line flow of fluid with minimal resistance when opened. Note that this type of valve is actively used in controlling flows, both liquid (Weevers, 1982; Peterman and Keithahn, 1987; Esveldt, 2012; Preston, 2018; Canjuga, 2019; Ziegler, 2019; Emerson, 2020; Flowserve, 2020; Mokveld, 2020; Rust, 2020; Talis, 2020) and gaseous media (Bian et al., 2019a,b; Cao and Bian, 2019; Emerson, 2020; Flowserve, 2020; Mokveld, 2020; Rust, 2020; Talis, 2020). Moreover, the system "perforated separator—internal piston" (Weevers, 1982; Peterman and Keithahn, 1987; Esveldt, 2012; Preston, 2018; Canjuga, 2019), in particular, with one (Peterman and Keithahn, 1987; Esveldt, 2012; Preston, 2018; Canjuga, 2019) or several throttle stages (Weevers, 1982) of throttling, when the internal piston, as a rule, is most widely used as a locking and regulating element. driven by rack and pinion (Preston, 2018; Canjuga, 2019) or crank mechanism. On the one hand, the shut-off and control system in the indicated design (Weevers, 1982; Peterman and Keithahn, 1987; Esveldt, 2012; Preston, 2018; Canjuga, 2019) allows separation of the fluid flows due to the formation of radial jets in the direction of the central axis of the valve, which contributes to the radial displacement of the cavitation bubbles formed in the central part of the separator and their accelerated removal from him. Thus, in the central part of the separator with one (Peterman and Keithahn, 1987; Esveldt, 2012; Preston, 2018; Canjuga, 2019) or several stages (Weevers, 1982) of throttling, the region of the working medium is displaced, which is subsequently subjected to the developed stage of cavitation, which prevents the collapse of bubbles near the inner surface of the cylindrical separator, and, consequently, its erosion. However, on the other hand, the internal arrangement of the locking element, in particular in the form of a piston (Weevers, 1982; Peterman and Keithahn, 1987; Esveldt, 2012; Preston, 2018; Canjuga, 2019), complicates the design of the sealing assembly, increases the energy costs of the drive and contributes to additional turbulization of the medium flow due to the location of the piston rod and spacers in the cavitation area. In Weevers (1982), another design version of the locking and regulating system in the form of a hollow cylindrical sleeve covering the separator was used. However, this design (Weevers, 1982) turned out to be quite complex and did not solve the problem of cavitation at small stages of valve opening. Note that the active use of various nozzle designs and the principle of swirling the working fluid flow are observed in Mokveld products (Mokveld, 2020), and similar technical solutions are used for gas liquefaction (Bian et al., 2019a,b; Cao and Bian, 2019). In particular, the analysis of design features of axial valves was performed in Lebedev et al. (2016, 2017a).

Regarding the methods for calculating the effective ranges of the design parameters of control valves, two approaches are most widespread: analytical estimation (Arzumanov, 1971, 1985; Blagov, 1990) using the Pi-Buckingham theorem (Buckingham, 1915; Misic et al., 2010) or numerical modeling for gaseous (Bian et al., 2019a,b; Cao and Bian, 2019) and liquid (Qu et al., 2015; Hou et al., 2017; Rudolf et al., 2017; Qiu et al., 2019; Tang et al., 2019) environments using ready-made software products (Ansys Inc, 2013, 2017). Moreover, the first approach requires a wide experimental base, and the second requires a long adaptation of the software product to the main factors influencing the course of the studied processes, including cavitation (Knapp et al., 1970; Franc and Michel, 2005; Xu et al., 2015), in a specific design. The formation of the theoretical base for the development of an engineering methodology for the analytical calculation of the desired parameters of control valves in this work is carried out on the basis of the stochastic approach by the energy method (Klimontovich, 2014). This choice (Kapranova et al., 2016c) from a variety of methods for describing the cavitation phenomenon, which include deterministic (Besant, 1859; Baron Rayleigh, 1911–1919; Plesset and Chapman, 1971; Chahine, 1994), stochastic (Volmer and Weber, 1926; Frenkel, 1946; Hsu, 1962; Lienhard and Karimi, 1981; Shin and Jones, 1993; Kwak and Kim, 1998; Ellas and Chambre, 2000) and combined Sokolichin et al., 1997; Koch et al., 2012; Seung and Kwak, 2017 approaches, is explained by the possibility of modeling differential functions of the distribution of the number of cavitation bubbles according to the characteristic features of the studied process (specific size of the bubbles, the degree of opening of the valve) depending on the structural, operational parameters of the regulating device and the physico-mechanical properties of the working medium (Weevers, 1982).

Usually the stochastic approach (Volmer and Weber, 1926; Frenkel, 1946; Hsu, 1962; Lienhard and Karimi, 1981; Shin and Jones, 1993; Kwak and Kim, 1998; Ellas and Chambre, 2000) [as models of homogeneous nucleation (Volmer and Weber, 1926; Frenkel, 1946; Lienhard and Karimi, 1981), their modifications with the introduction of the heterogeneity factor (Kwak and Kim, 1998; Ellas and Chambre, 2000), or heterogeneous nucleation (Hsu, 1962; Shin and Jones, 1993)] and combined one (Sokolichin et al., 1997; Koch et al., 2012; Seung and Kwak, 2017) suggest the use of the postulation of the differential distribution functions of cavitation nuclei by their size based on experimental dependences. Note that the deterministic approach (Besant, 1859; Baron Rayleigh, 1911–1919; Plesset and Chapman, 1971; Chahine, 1994) is usually implemented either when describing the behavior of a single bubble of variable radius, or in modified models taking into account additional factors of inertial, thermal, and diffusion nature. However, the latter approach is most relevant when applied to the estimation of the velocity regimes of growth of cavitation bubbles near the wall, including during numerical simulation (Qian et al., 2016).

The team of authors analyzed the design features of direct-flow type control valves (Lebedev et al., 2016, 2017a,b), methods for modeling the cavitation phenomenon (Kapranova et al., 2016c) and calculation of the main indicators of this process (Kapranova et al., 2016d,e), and also performed theoretical (Kapranova et al., 2016a,b, 2017, 2018a,b; Kapranova, 2018; Kapranova and Miadonye, 2019) and experimental (Esveldt, 2012; Lebedev et al., 2017a,b; Preston, 2018) studies of the initial

stage of hydrodynamic cavitation with axisymmetric throttling of fluid flows, which made it possible to obtain a theoretical justification and experimental confirmation (Kapranova and Miadonye, 2019) of the possibility of reducing the intensity of formation of cavitation bubbles and the use of external locking shell. As a result of these studies, the authors proposed the design of an axial valve (Arzumanov, 1985; Lebedev et al., 2018) with a locking and regulating system "perforated separator—external locking cylinder-conical shell." The specified design (Arzumanov, 1985; Lebedev et al., 2018) involves a coaxial arrangement of the separator and the movable external locking member, which has the form of hollow cylindrical shell (**Figure 1**). Thus, the throttle round holes of the fixed separator overlap when the cylindrical shell obeys along its outer cylinder-conical surface. This shell can be set in motion as a rack and a crank mechanism.

Thus, after solving a number of problems in developing stochastic models for the formation of cavitation bubbles in an axial valve separator by their size (Kapranova et al., 2016a, 2017, 2018a) and the degree of its opening (Kapranova, 2018; Kapranova et al., 2018b; Kapranova and Miadonye, 2019), after performing a series of comparative analysis (Kapranova and Miadonye, 2019) of the theoretical (Kapranova et al., 2016a, 2017, 2018a,b; Kapranova, 2018; Kapranova and Miadonye, 2019) and experimental results (Lebedev et al., 2017a,b) the next goal of studies of axisymmetric throttling of fluid flows is the development of engineering methods for calculating operational and design parameters of the separator-locking shell assembly.

METHODS

To ensure the effective operation of an axial valve with an external position of the locking member, an engineering procedure has been proposed for calculating a separator with round throttle holes. The purpose of the work is to develop a scientifically based method for calculating the effective ranges of the design parameters of the throttle part of the axial valve. Currently, the design of equipment (Hou et al., 2017; Qiu et al., 2019) subject to the effect of cavitation, as a rule, is based on the active use of ready-made software products (Tang et al., 2019), and as a result, has a numerical representation of the results (Rudolf et al., 2017) of their application in graphical or tabular form. Visualization of the studied process (Qu et al., 2015), performed by this method, has a high degree of visibility for a particular device, however, this requires the preliminary implementation of labor-intensive experimental validation (Qu et al., 2015). Such an approach often puts the designer in a dependent position on the level of development of numerical methods, on the completeness of taking into account in the finished software package the main factors of influence on the studied physical phenomena, requires a long adaptation of this software package to the specific regulatory requirements of the customer of control valves. In this presentation, preference is given to constructing an engineering methodology for calculating the main assembly of the valve using estimated analytical dependencies that allow us to analyze the mechanics of the behavior of the system of forming bubbles in the process of throttling the fluid flow. The theoretical basis for this calculation is stochastic modeling of the bubble formation process in the separator at the initial stage of hydrodynamic cavitation (Klimontovich, 2014; Kapranova et al., 2016a,b). Earlier, the authors used the stochastic approach with the equilibrium representation of the states of the energetically closed macrosystem (Klimontovich, 2014; Tang et al., 2019) within the framework of the Ornstein-Uhlenbeck random process (Kapranova et al., 2016b) to form the model of this process the bubble formation process in the separator at the initial stage of hydrodynamic cavitation. The proposed stochastic models (Kapranova et al., 2016a, 2017, 2018a,b; Kapranova, 2018; Kapranova and Miadonye, 2019) allowed us to obtain differential distribution functions of the number of cavitation bubbles formed during the initial stage of the evolution of hydrodynamic cavitation, according to their size (Kapranova et al., 2016a, 2017, 2018a) and the degree of opening of the axial valve (Arzumanov, 1971; Lebedev et al., 2017a,b). The performed experimental studies (Lebedev et al., 2017a,b) confirmed the possibility of reducing the intensity of hydrodynamic cavitation at its initial stage when using the modernized part of "separator-locking shell" of axial valve. In this case, a comparative analysis (Kapranova and Miadonye, 2019) of the obtained theoretical (Kapranova et al., 2016a, 2017, 2018a,b; Kapranova, 2018; Kapranova and Miadonye, 2019) and experimental (Lebedev et al., 2017a,b) results for the dependence of the differential distribution function of the number of bubbles $f_z(z)$ at the initial stage of hydrodynamic cavitation with a separator with round holes depending on the degree of their opening with using an external locking shell showed satisfactory convergence with a relative error not exceeding 13%. Note that the value of z is determined by the ratio of the given position z' for the movable shutter (external locking shell) along its axis to the conditional position L corresponding to the length of the perforated part of the separator. The well-known classical method for calculating some rational parameters of a control valve (Arzumanov, 1971, 1985), which is actively used in various interpretations, including numerical ones, does not imply the use of functional dependencies for the laws of distribution of cavitation bubbles according to various characteristics, but it contains a reliable algorithm for the designer's actions when choosing the type regulatory device, depending on the regulatory data of the customer. In this case, the basis of the calculation is a set of empirical dependences for the diameter of the nominal bore, the valve throughput on a number of operating parameters characterizing the movement of the fluid flow (maximum achievable fluid flow, pressure drop, etc.) and the main hydrodynamic similarity criterion (critical Reynolds number). An empirical analysis of the conditions for achieving a critical value of the cavitation coefficient as a doubled criterion of Euler similarity plays a decisive role in the choice of type of control device (Knapp et al., 1970; Franc and Michel, 2005; Xu et al., 2015; Kapranova et al., 2016e). The last operation is performed according to the critical value of the hydraulic resistance coefficient using graphical experimental material (Arzumanov, 1971, 1985; Blagov, 1990) at the stage of estimating the maximum value of the valve throughput in comparison

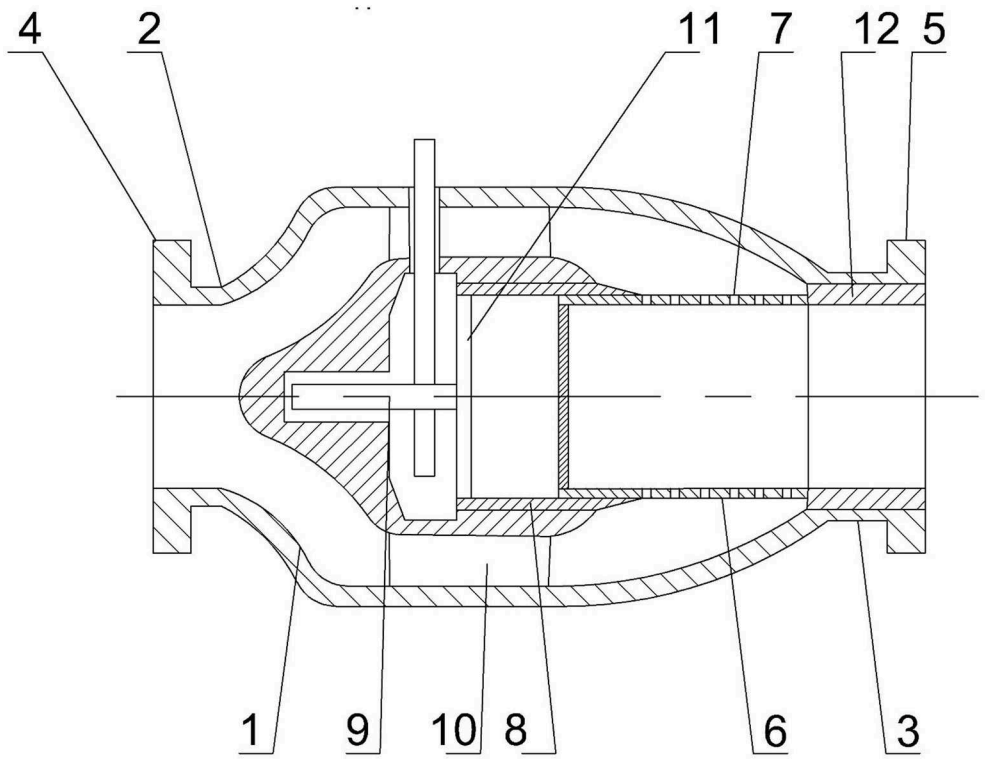

FIGURE 1 | Schematic diagram of an axial valve with an external positioning of the locking member: 1–outer case, 2 and 3–inlet and outlet nozzles, 4 and 5–flanges, 6–separator, 7–throttle holes, 8–cylindrical conical (external locking shell), 9–rack and pinion mechanism, 10–cavity of the inner housing, 11–radial partitions, 12–expansion sleeve.

with the routine. Thus, the application of the classical method for choosing the type of control device is associated with the application of the Pi-Buckingham theorem (Buckingham, 1915; Misic et al., 2010) in solving the scaling problem and reducing the number of constant parameters describing the process under study. As a result of the model (Kapranova et al., 2016a,b), the integral characteristics of the cavitation bubble were calculated. The expression obtained using model (Kapranova et al., 2016a) for calculating the average over the ensemble of the diameter D_{cb} for the macrosystem of cavitation bubbles (Kapranova et al., 2017; Kapranova, 2018) takes into account the physical and mechanical properties of the working medium, as well as the main design and operating parameters of the axial valve. In particular, the analysis of graphic material for the functional dependence of $D_{cb} = D_{cb}(D_y, K_{vy})$ on the conditional diameter D_y and the corresponding throughput ability of the K_{vy} valve is presented in Kapranova A. B. et al. (2019). Another model (Kapranova, 2018; Kapranova et al., 2018b; Kapranova and Miadonye, 2019) made it possible to establish a connection between the critical value of the Reynolds number Re_{cr} in the case of a complete opening of the valve and its design parameters. So, these expressions for D_{cb} (Kapranova et al., 2017, 2018a) and Re_{cr} based on (Kapranova, 2018; Kapranova et al., 2018b; Kapranova and Miadonye, 2019), as well as the obtained expressions for the energy parameter of the stochastic model (Kapranova et al., 2018b) and the hydraulic resistance coefficient (Kapranova et al., 2018c) are used in the proposed engineering method for calculating the separator and constitute the main difference from the known approach (Arzumanov, 1971, 1985). Note that in practice, the identification of the cavitation region in the flow part of the control device is associated with the analysis of the dependence of the hydraulic resistance coefficient for the conditional flow area on the cavitation number k_C, which is also reflected in this work.

RESULTS AND DISCUSSION

Selection of the Main Parameters of the Liquid Throttling Process in an Axial Valve With an External Locking Shell

We divide the whole set of parameters of the studied process of throttling the fluid flow into several sets: for design parameters q, for mode parameters τ, for additional φ. In particular, the main structural parameters of the axial valve with the design of an external movable locking device (Lebedev et al., 2018) (**Figure 1**) include: $q = \left\{q_{k_1} = const\right\}$, $k_1 = \overline{1, \rho_1}$ for the separator, external shells and corresponding parts of the housing: the diameter of the round throttle holes d_0, the arc distance between the holes in the same row $S_{\varphi 1}$, the distance between the rows of these holes l_0, the thickness of the separator h, the number of holes for one row u_1, the number of these rows u_2, respectively, the inner and outer diameters separator D_{out} and D_c, the length of

its perforator of the left part L, the bevel angle for the cylindrical part of the shell α, the inner diameter for the cylindrical part of the outer casing D_{cas2}, the outer diameter of the inner valve body D_{ch2}, the wall thickness of the inner and outer casing δ_2. Thus, the explicit representation of the set $\{q_{k_2} = const\}$ has the form

$$q = \{d_0, S_{\varphi 1}, l_0, h, u_1, u_2, D_{out}, D_c, L, \alpha, D_{cas2}, D_{ch2}, \delta_2\}, \quad k_1 = 13. \quad (1)$$

Set (1) is conveniently divided into three subsets for the main parameters of the separator $q_{11} = \{q_{k_{11}} = const\}$, $k_{11} = \overline{1, \rho_{11}}$, for the outer locking shell $q_{12} = \{q_{k_{12}} = const\}$, $k_{12} = \overline{1, \rho_{12}}$, and for the body $q_{13} = \{q_{k_{13}} = const\}$, $k_{13} = \overline{1, \rho_{13}}$

$$q_{11} = \{d_0, S_\varphi, l_0, h, u_1, u_2, D_{out}, D_c, L\}, \quad k_{11} = 9, \quad (2)$$

$$q_{12} = \{\alpha\}, \quad k_{12} = 1, \quad (3)$$

$$q_{13} = \{D_{cas2}, D_{ch2}, \delta_2\}, \quad k_{13} = 3, \quad (4)$$

Specified operating parameters $\tau = \{\tau_{k_2} = const\}$, $k_2 = \overline{1, \rho_2}$ are the maximum attainable expenditure Q_{1max} (m^3/h) of the liquid through the regulating device at a given value of the medium temperature t_1 (°C), the minimum pressure drop ΔP_{min}, the maximum pressure in the center of the bubble P_{max}, which corresponds to the minimum value of its radius r_{min}, the saturated vapor pressure of the medium p_s, the velocity of the fluid in the pipeline w then for $\{\tau_{k_2} = const\}$ we have

$$\tau = \{Q_{1max}, t_1, \Delta p_{min}, P_{max}, r_{min}, p_s, w\}, \quad k_2 = 7. \quad (5)$$

The following additional parameters are taken into account: $\varphi = \{q_{k_3} = const\}$, $k_3 = \overline{1, \rho_3}$

$$\varphi = \{\rho_L, \rho_g, \rho_s, \nu_1, \sigma, \gamma, k\}, \quad k_3 = 7. \quad (6)$$

describing the physical and mechanical properties of the medium: respectively, the density of the liquid ρ_L, gas ρ_g and vapor ρ_s; kinematic viscosity of the liquid ν_1 at a given value of its temperature t_1 (°C), surface tension coefficient σ, volumetric weight of the medium γ, adiabatic exponent k.

We make a selection of input $x_1 = \{x_{1,\,k_4}\}$, $k_4 = \overline{1, \rho_4}$ and output $x_2 = \{x_{2,\,k_5}\}$, $k_5 = \overline{1, \rho_5}$ parameters for the process of regulating fluid flows in the flow part of the axial valve

$$x_1 = \{Q_{1max}, \delta^{min}_{\Delta p_{min}}, \delta^{max}_{\Delta p_{min}}, t_1, w\}, \quad k_4 = 5, \quad (7)$$

$$x_2 = \{K'_{vy}\}, \quad k_5 = 1. \quad (8)$$

where the set x_1 is a subset of the operational parameters τ from (2); $\delta^{min}_{\Delta p_{min}}$, $\delta^{max}_{\Delta p_{min}}$ are limits for Δp_{min}; K'_{vy} is required valve throughput.

When describing the block diagram (**Figures 2**, **3**) for calculating the design parameters of the "separator-external locking shell" assembly of the axial valve, from the listed sets (2)–(8), it is necessary to select the following parameters:

- for input data input: sets φ, x_1, x_2, respectively, from (6) to (8); the set of initial values of a number of parameters from the subset $q_0 = \{q_{k_0} = const\}$, $k_0 = \overline{1, \rho_0}$ for the set $q_0 = \{q_{k_0} = const\}$, $k_0 = \overline{1, \rho_0}$ from (1)

$$q_0 = \{h^{(0)}, D^{(0)}_{out}, D^{(0)}_c, L^{(0)}, \alpha^{(0)}, D^{(0)}_{cas2}, D^{(0)}_{ch2}\}, \quad k_0 = 7, \quad (9)$$

as well as the subset $\tau_1 = \{q_{k_{21}} = const\}$, $k_{21} = \overline{1, \rho_{21}}$ for the set of regime parameters τ from (5)

$$\tau_1 = \{r_{min}, p_s, w\}, \quad k_{21} = 3, \quad (10)$$

- to search for the limits of change of parameters from q-set (1) in the form of the set of desired design parameters $q^* = \{q^*_{k_1} = const\}$, $k_1 = \overline{1, \rho_1}$ for the designed axial valve elements (**Figure 1**) according to sets (2)–(4): for the separator $q^*_{11} = \{q^*_{k_{11}} = const\}$, $k_{11} = \overline{1, \rho_{11}}$, for the external locking shell $q^*_{12} = \{q^*_{k_{12}} = const\}$, $k_{12} = \overline{1, \rho_{12}}$ and for the body $q^*_{13} = \{q^*_{k_{13}} = const\}$, $k_{13} = \overline{1, \rho_{13}}$.

The proposed block diagram (Kapranova et al., 2019b) (**Figures 2**, **3**) consists of 25 main blocks for calculating 13 effective values of the design parameters of the axial valve separator tested in calculating the example in Kapranova et al. (2020).

Description of the Work Flowchart of the Engineering Methodology for Calculating the Parameters of These System of the Separator-External Locking Shell

Block 1 (**Figure 2**) includes the introduction of the parameters listed above: regime $\tau = \{\tau_{k_2} = const\}$, $k_2 = \overline{1, \rho_2}$ from (5), including the input set x_1-set from (7); additional characteristics reflecting the physicomechanical properties of the working medium and the gas-vapor system inside the bubble $\varphi = \{q_{k_3} = const\}$, $k_3 = \overline{1, \rho_3}$ from (6); weekend x_2 from (8). In particular, according to the x_1-set from (7), the variation limits $\delta^{min}_{\Delta p_{min}}$ and $\delta^{max}_{\Delta p_{min}}$ are set for the minimum pressure drop Δp_{min} from (7) for a fixed value of the medium temperature t_1 (°C)

$$\delta^{min}_{\Delta p_{min}} \le \Delta p_{min} \le \delta^{max}_{\Delta p_{min}} \quad (11)$$

Block 2 (**Figure 2**) calculates the interval of variation in the maximum flow capacity of the valve $K^{(1)}_{vmax} \in [\delta^{min}_{K_{vy1}}; \delta^{max}_{K_{vy1}}]$ for given values of $\delta^{min}_{\Delta p_{min}}$ and $\delta^{max}_{\Delta p_{min}}$ from (11) taking into account the dependence $K_{vmax}(\Delta p_{min})$ (Arzumanov, 1971), also used in (Kapranova et al., 2020)

$$\delta^{min}_{K_{vy1}} = \eta_1 Q_{1max} \left(\frac{\gamma}{1,02 \times 10^{-5} \delta^{max}_{\Delta p_{min}}} \right)^{1/2},$$

$$\delta^{max}_{K_{vy1}} = \eta_2 Q_{1max} \left(\frac{\gamma}{1,02 \times 10^{-5} \delta^{min}_{\Delta p_{min}}} \right)^{1/2}, \quad (12)$$

where Q_{1max} (m^3/h) is the maximum attainable flow rate of the fluid through the valve; γ (g×c/cm^3) is the bulk density of

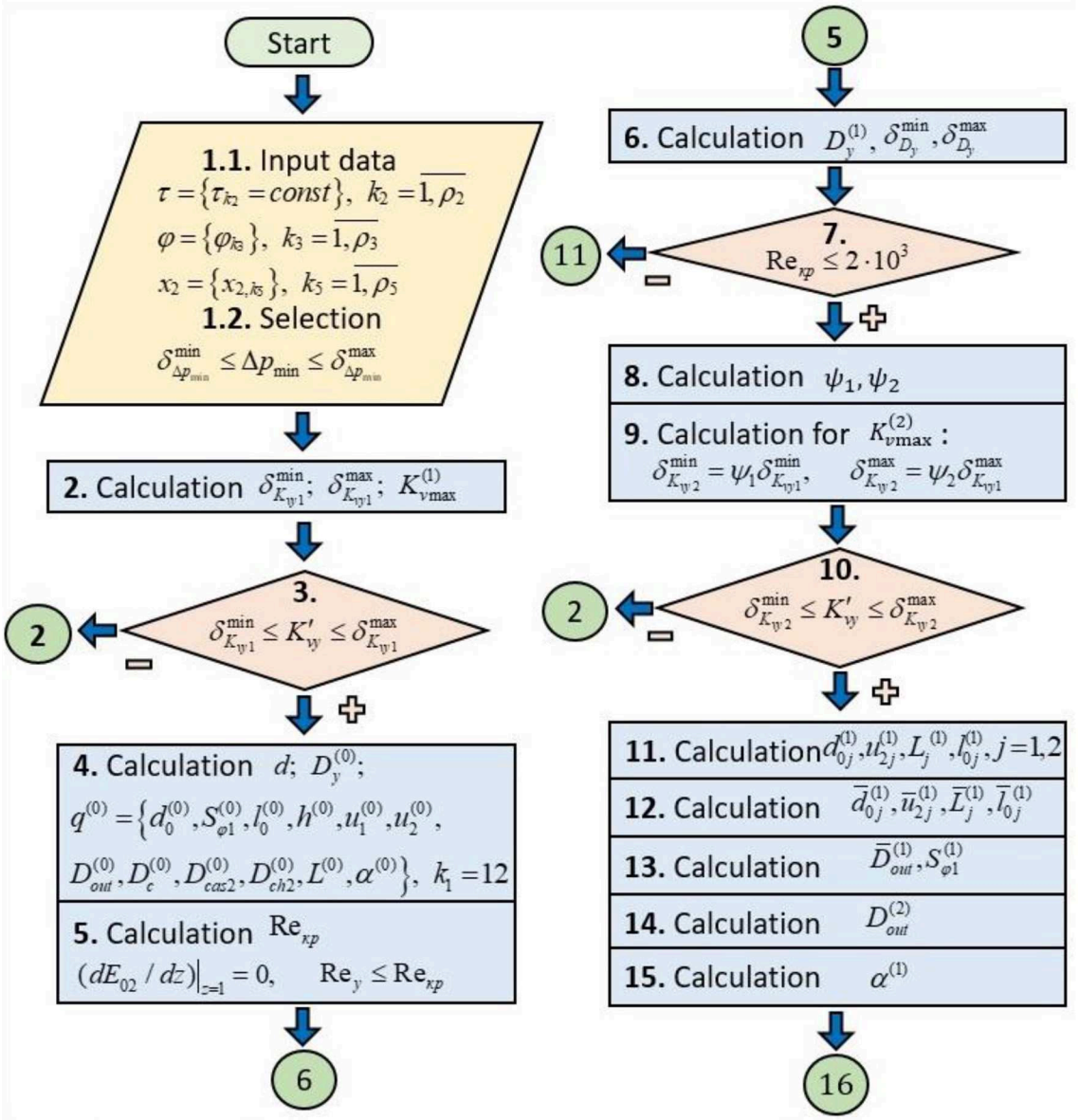

FIGURE 2 | Conventional block diagram of the calculation of the design parameters of the axial valve separator with the external location of the locking member (Part 1).

the liquid; η_1 and η_2 are safety factors in the range of at least 10–20% of the calculated value for the maximum throughput K_{vmax} according to Arzumanov (1971), for example, $\eta_1 = 1.1$ and $\eta_2 = 1.2$ (Kapranova et al., 2020); dimension for $\delta^{min}_{\Delta p_{min}}$ and $\delta^{min}_{\Delta p_{min}}$ is Pa.

Using *conditional block 3* (**Figure 2**), the condition of belonging of the required value of throughput K'_{vy} for the valve to the obtained range of values is checked

$$\delta^{min}_{K_{vy1}} \le K'_{vy} \le \delta^{max}_{K_{vy1}}. \tag{13}$$

If inequality (13) is satisfied, the transition to *block 4* follows; otherwise, it returns to *block 2* (**Figure 2**) with the change of the safety factors η_1 and η_2 by 10–20%, respectively.

In *block 4* (**Figure 2**) initial values are set:

- diameter of conditional passage $D^{(0)}_y$ (m), as the nearest integer to the larger side $\lceil d \rceil$ ("ceiling" d)

$$D^{(0)}_y = \lceil d \rceil, \tag{14}$$

- for the diameter of the pipeline d (m) according to Bian et al. (2019a)

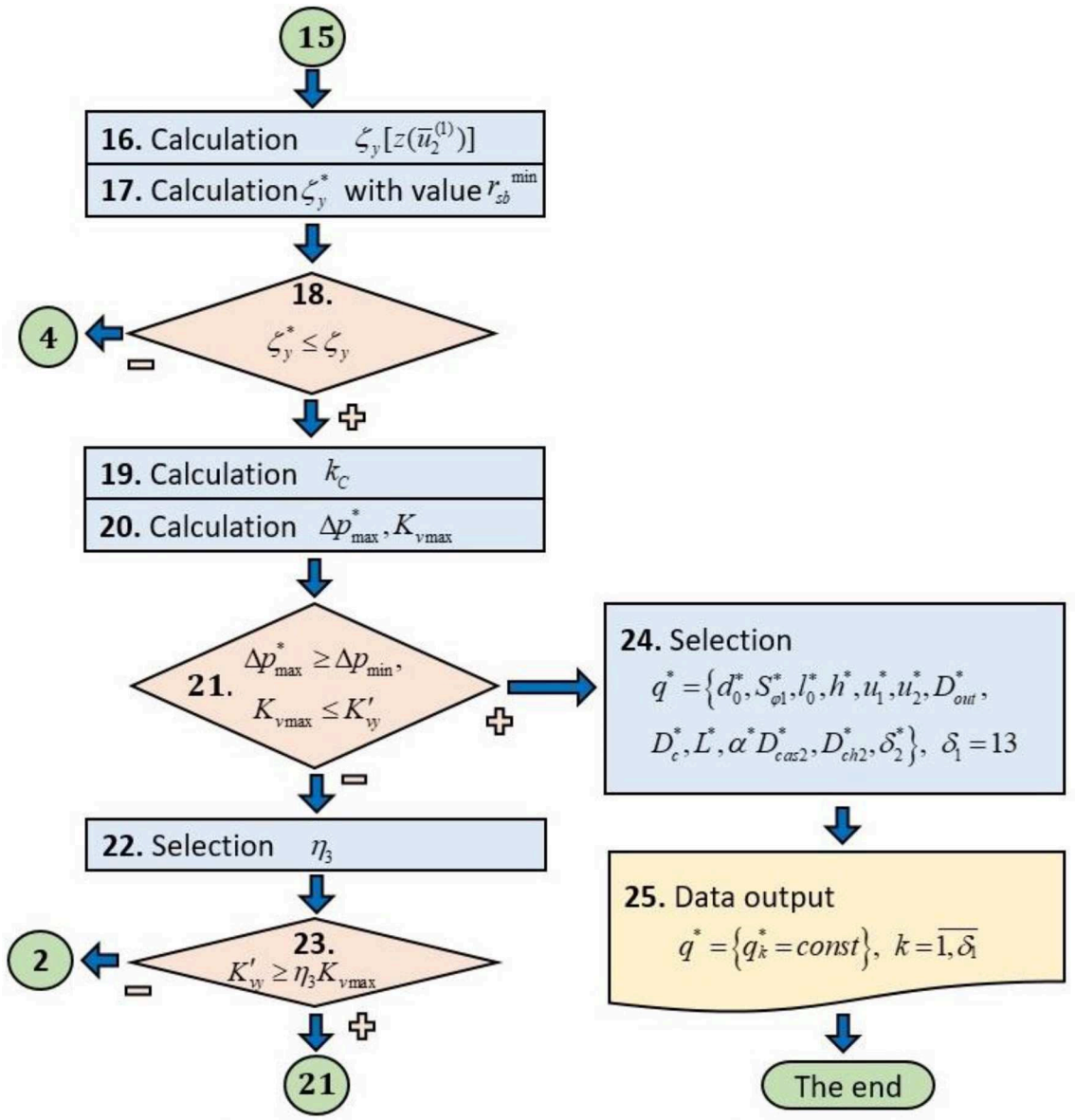

FIGURE 3 | Conventional block diagram of the calculation of the design parameters of the axial valve separator with the external location of the locking member (Part 2).

$$d = 1.88 \times 10^{-2}(Q_{1max}/w)^{1/2}, \tag{15}$$

where the fluid velocity w, for example, is usually taken for a water supply system $w = 1.0$ m/s, when supplied to a centrifugal pump $w = 2.0$ m/s, during transportation $w = 3.0$ m/s;

- for the design parameters described in sets (1), (9)

$$q_{01} = \left\{d_0^{(0)}, S_\varphi^{(0)}, l_0^{(0)}, u_1^{(0)}, u_2^{(0)}, h^{(0)}, D_{out}^{(0)}, D_c^{(0)}, L^{(0)}, \alpha^{(0)}, D_{cas2}^{(0)}, D_{ch2}^{(0)}\right\},$$
$$k_{01} = 12 \tag{16}$$

using the following expressions (Kapranova, 2018; Kapranova et al., 2020): $\delta_2^{(0)} = 0.1D_y^{(0)}$; $h^{(0)} = \delta_2^{(0)}/2$; $D_{out}^{(0)} = 1.1D_y^{(0)}$; $L^{(0)} = 2.2D_{out}^{(0)}$; $d_0^{(0)} = 0.14D_{out}^{(0)}$; $S_{\varphi 1}^{(0)} = d_0^{(0)}$; $l_0^{(0)} = \left[3(d_0^{(0)} + S_{\varphi 1}^{(0)}\right) - d_0^{(0)}]/3$; $u_2^{(0)} = \pi D_{out}^{(0)}/(2d_0^{(0)})$; $u_1^{(0)} = (L^{(0)} - l_0^{(0)})/(l_0^{(0)} + d_0^{(0)})$; $D_c^{(0)} = D_{out}^{(0)} + h^{(0)}$; $D_{ch2}^{(0)} = 3D_{out}^{(0)}/2$; $D_{cas2}^{(0)} = 2D_{out}^{(0)}$; $\alpha^{(0)} = \pi/4$ taking into account the value of the conditional diameter $D_y^{(0)}$ from (14) and the condition $h = D_c - D_{out}$ with a checkerboard arrangement of the throttle holes of the cylindrical separator. Note that when determining the values $u_1^{(0)}$, $u_2^{(0)}$, the right-hand sides of the corresponding

expressions contain the integer parts of the indicated relations of quantities.

In *block 5* (**Figure 2**), the critical value of the Reynolds number Re_{cr} is determined when, when the inequality

$$\mathrm{Re}_y \le \mathrm{Re}_{cr}, \tag{17}$$

cavitation-free flow of liquid in the valve is observed at a conditional value of the Reynolds number Re_y. In this case, the extremum condition is used

$$\left(dE_{02}dz \right)\big|_{z=1} = 0, \tag{18}$$

for the energy parameter $E_{02}(z)$ with the value of the phase variable $z\,(u_2) = 1$, i.e., with full valve opening for a stochastic model of bubble formation at an early stage of hydrodynamic cavitation (Kapranova, 2018; Kapranova et al., 2018b; Kapranova and Miadonye, 2019). Here z is the phase variable corresponding to the number of the throttle bore of the separator $n_2 = \overline{0, u_2}$. The parameter $E_{02}(z)$ is determined by the expression for the energy $E_{02}(\xi, \eta, z)$ of the cavitation bubble at the moment of its stochastization (when the trajectories of the formed bubbles acquire a random character), where ξ and , η are the conditional values of the diameter of the cavitacin bubble and the velocity of its center of mass. Condition (18) implies the approximation

$$(r_m/\{\psi_{10}[u_2(z)]\})^{1/2}\,\mathrm{erf}\left[\nu_L\,(r_m/\{\psi_{10}[u_2(z)]\})^{-1/2}\right] = 0, \tag{19}$$

which can be used as an algebraic equation for the value Re_{cr} from (Kapranova, 2018; Kapranova et al., 2020)

$$\mathrm{Re}_{cr} = \frac{32\rho_L k_{\zeta 1} h_0^{(0)} u_1^{(0)} \left(D_y^{(0)}\right)^2 \left[2\left(L^{(0)} - l_0^{(0)}\right) - s_0^{(0)}\right]}{\left[\rho_L k_{\zeta 1}\left(B_1 + s_2^{(0)}\right) + 4a_1 r_{min}^4\right] s_0^{(0)} \left(d_0^{(0)}\right)^3}. \tag{20}$$

Condition (19) contains the error function erf(μ) with argument μ. In the expressions (19), (20) it is indicated: r_m, ν_L are the characteristic values of the radius of the bubble and the velocity of the fluid, respectively; $\psi_{10}(z) = r_m[\tau_{11}(1) + \varsigma_{12}(z)\tau_{12}(1)]$ according to Kapranova and Miadonye (2019); $\varsigma_{12}(z)$ is the dependence of the hydraulic resistance coefficient on the phase variable z for the transition region of the fluid flow ($10 < \mathrm{Re} < 10^4$), obtained in (Kapranova et al., 2018c)

$$\varsigma_{12}(z) = s_1\left(\frac{Lz}{s_0} - \frac{1}{2}\right) + s_2 + s_4\left[\frac{s_0 s_3 (s_0 + s_6 z)}{2(Lz - l_0)\varepsilon(z)} - 1\right]^2, \tag{21}$$

In (21) it is indicated: $\varepsilon(z)$ is the modified compression ratio of the jet from Kapranova et al. (2016a) with parameters $U_0 = 0.57$; $U_1 = 0.043$; $U_0 = 1.1$ from Arzumanov (1971); the coefficients $\tau_{11}(1), \tau_{12}(1)$, s_0, s_3, s_6, $s_0^{(0)}, s_2^{(0)}, B_1, k_{\zeta 1}, a_1$ due to Kapranova et al. (2018c) depend on the design parameters of the valve and the characteristics of the liquid-gas-vapor system, in particular $a_1 = 2\pi(\alpha_g\rho_g + \alpha_s\rho_s)/3$ Using expressions (14), (21) and the values described in *block 4* (**Figure 2**) for the initial approximations of the design parameters for the set q_{01} from (19), the following expression of the relationship between the design parameters is accepted

$$s_0^{(0)} \equiv l_0^{(0)} + d_0^{(0)},$$

$$s_2^{(0)} \equiv u_1^{(0)}\frac{\alpha^{(0)}}{90}\frac{\left(D_y^{(0)}\right)^4}{\left[\left(D_{cas2}^{(0)} - 2\delta_2^{(0)}\right) - \left(D_{ch2}^{(0)}\right)^2\right]^2},$$

$$s_3^{(0)} \equiv \frac{4D_{out}^{(0)}}{\pi u_1^{(0)}\left(d_0^{(0)}\right)^2}, \tag{22}$$

$$s_1^{(0)} \equiv \frac{64 u_1^{(0)} h^{(0)}\left(D_y^{(0)}\right)^2}{\mathrm{Re}_{cr}\left(d_0^{(0)}\right)^3},$$

$$s_4^{(0)} \equiv \frac{2\left[\left(D_{cas2}^{(0)} - 2\delta_2^{(0)}\right) - \left(D_{ch2}^{(0)}\right)^2\right]^2}{\left(D_y^{(0)}\right)^4},$$

$$s_5^{(0)} \equiv \frac{4u_2^{(0)}\left(S_{\varphi 1}^{(0)} + d_0^{(0)}\right)}{\pi\left(d_0^{(0)}\right)^2},\quad s_6^{(0)} \equiv \frac{7}{2}L^{(0)}, \tag{23}$$

$$s_7^{(0)} \equiv \frac{u_1^{(0)}}{90}\frac{S_{\varphi 1}^{(0)} h^{(0)}\left(1 + D_{out}^{(0)}/D_c^{(0)}\right)^4}{\left[\left(D_{cas2}^{(0)} - 2\delta_2^{(0)}\right) - \left(D_{out}^{(0)}\right)^2\right]^2},$$

$$B_1 \equiv s_4^{(0)}\left[\frac{s_0^{(0)} s_3^{(0)}\left(s_0^{(0)} + s_6^{(0)}\right)}{2\left(L^{(0)} - l_0^{(0)}\right)\varepsilon[z\left(u_2^{(0)}\right)]} - 1\right]^2, \tag{24}$$

$$k_{\zeta 1} \equiv 8\pi r_m^4(\alpha_s\rho_s + \alpha_s\rho_s)/\left\{3\rho_L\,\varsigma_{12}^{(0)}\left[z\left(u_2^{(0)}\right)\right]\right\}, \tag{25}$$

$$\varepsilon\left[z\left(u_2^{(0)}\right)\right] \equiv U_0 + U_1/\left\{U_2 - \left[s_7^{(0)} - s_5^{(0)}\left(s_0^{(0)} + s_6^{(0)}\right)\right]/2\right\}, \tag{26}$$

$$\varsigma_{12}^{(0)}\left[z\left(u_2^{(0)}\right)\right] \equiv s_1^{(0)}\left[\left(L^{(0)} - l_0^{(0)}\right)/s_0^{(0)} - 1/2\right] + s_2^{(0)} + B_1, \tag{27}$$

The physical and mechanical characteristics of the working medium ρ_L, ρ_g, ρ_s from (25) correspond to the set $\varphi = \{q_{k_3} = const\}$, $k_3 = \overline{1, \rho_3}$ from (6). Expression (27) corresponds to the initial approximation for the hydraulic resistance function $\varsigma_{12}(z)$ on the phase variable z from (21) (Kapranova et al., 2018c), taking into account the dependence of the degree of valve opening $z(u_2)$ on parameter u_2 with the equality of argument $u_2 = u_2^{(0)}$ according to the accepted value $u_2^{(0)}$ in *block 4*.

Block 6 (**Figure 2**) sets the 1st approximation for the conditional diameter $D_y^{(1)}$ (m) using the empirical formula from (Arzumanov, 1971)

$$D_y^{(1)} = (3.53\,Q_{1max})/(\nu_1 \mathrm{Re}_{cr}), \tag{28}$$

where the values of Q_{1max} (m^3/h) and ν_1 (cm^2/c) are determined by the set (5); Re_{cr} is the critical value of the Reynolds number from (20). The limits of change for the value $\delta_{D_y}^{min}, \delta_{D_y}^{max}$ of $D_y^{(1)}$ (m) from (28)

$$\delta_{D_y}^{min} \le D_y^{(1)} \le \delta_{D_y}^{max}, \tag{29}$$

are established taking into account (12) for $\delta^{min}_{K_{vy1}}$, $\delta^{max}_{K_{vy1}}$, in the form

$$\delta^{min}_{D_y} = \left(\frac{4\delta^{min}_{K_{vy1}} \varsigma^{(0)}_{12}\left[z\left(u^{(0)}_2\right)\right]}{10^4 \pi m_0} \right)^{1/2},$$
$$\delta^{max}_{D_y} = \left(\frac{4\delta^{max}_{K_{vy1}} \varsigma^{(0)}_{12}\left[z\left(u^{(0)}_2\right)\right]}{10^4 \pi m_0} \right)^{1/2}, \quad (30)$$

where the value $\varsigma^{(0)}_{12}\left[z\left(u^{(0)}_2\right)\right]$ is calculated using (27). The expressions in (30) were obtained using the well-known empirical relationship between the coefficients of the transmission capacity of the regulating device and hydraulic resistance (Arzumanov, 1985; Blagov, 1990) at the value of the coefficient $m_0 = 5.04$.

Service *block 7* (**Figure 2**) compares the calculated critical value of the Reynolds number Re_{cr} from (20) with the characteristic value of this criterion for liquid flow in cavitation-free mode according to the recommendations from Arzumanov (1971) (if which is not met, go to *block 11*, **Figure 2**) $\mathrm{Re}_{cr} \le 2\times10^3$. If this inequality is true, in *block 8* (**Figure 2**), correction coefficients ψ_1, ψ_2 for the viscosity of the working medium are calculated similarly to the recommendations from Arzumanov (1971) for the limits of the valve throughput $K^{(2)}_{vmax} \in \left[\delta^{min}_{K_{vy2}}; \delta^{max}_{K_{vy2}}\right]$ taking into account (12), (28), (20) for the values $\delta^{min}_{K_{vy2}}; \delta^{max}_{K_{vy2}}$, Re_{cr}, as well as the values of initial approximations adopted in *block 4* (**Figure 2**) for the design parameters $D^{(1)}_y$, $d^{(0)}_0$, $u^{(0)}_2$, in the form

$$\psi_1 = 1.07\times10^{-2} \frac{\delta^{min}_{K_{vy1}}}{\omega_y\left[z\left(u^{(0)}_1\right)\right]} \left[\frac{\pi\left(D^{(1)}_y + d^{(0)}_0\right)}{\mathrm{Re}_{cr} D^{(1)}_y}\right]^{1/2},$$
$$\psi_2 = 1.07\times10^{-2} \frac{\delta^{max}_{K_{vy1}}}{\omega_y\left[z\left(u^{(0)}_1\right)\right]} \left[\frac{\pi\left(D^{(1)}_y + d^{(0)}_0\right)}{\mathrm{Re}_{cr} D^{(1)}_y}\right]^{1/2}, \quad (31)$$

The expressions in (31) contain the value of the conditional section area $\omega_y\left[z\left(u^{(0)}_1\right)\right] = \pi u^{(0)}_1 u^{(0)}_2 \left(d^{(0)}_0\right)^2 z\left(u^{(0)}_1\right)/4$ (m^2) depending on the degree of valve opening z according to the parameter values $d^{(0)}_0, u^{(0)}_1, u^{(0)}_2$ accepted in block 4 (**Figure 2**). Therefore, in *block 9* (**Figure 2**), taking into account (12), (31), a new range of variation in the valve throughput can be determined $\delta^{min}_{K_{vy2}} = \psi_1 \delta^{min}_{K_{vy1}}, \delta^{max}_{K_{vy2}} = \psi_2 \delta^{max}_{K_{vy1}}$.

The conditional block 10 (**Figure 2**) checks the condition that the required valve throughput K'_{vy} belongs to a new range of values $\delta^{min}_{K_{vy2}}; \delta^{max}_{K_{vy2}}$ using the following inequality $\delta^{min}_{K_{vy2}} \le K'_{vy} \le \delta^{max}_{K_{vy2}}$ similar to (13). If the last inequality is true, the transition to the *block 11* (**Figure 2**) is carried out, in case of its injustice—return to block 2 with a change in the values n_1 and n_2 of the safety factors and, accordingly, by 10–20%.

In *block 11* (**Figure 2**), the values of the first approximations are estimated $d^{(1)}_{0j}, u^{(1)}_{2j}, L^{(1)}_j, l^{(1)}_{0j}$, $j = 1, 2$ for the limits of variation of the following design parameters of the separator $d^{(1)}_0, u^{(1)}_2, L^{(1)}, l^{(1)}_0$ according to the inequalities: $d^{(1)}_{01} \le d^{(1)}_0 \le d^{(1)}_{02}, u^{(1)}_{21} \le u^{(1)}_2 \le u^{(1)}_{22}, L^{(1)}_1 \le L^{(1)} \le L^{(1)}_2, l^{(1)}_{01} \le l^{(1)}_0 \le l^{(1)}_{02}$ using a system of equations including:

- the expression $\varsigma_y[z(u_2)]/\varsigma_y[z(n_2)] = 1$, which reflects the condition for linear profiling of the dependence $\sigma(z)$ of the throughput characteristic of the control device on the degree of its opening according to the definition of $\sigma[z(n_2)] = K_{vy}[z(n_2)]/K_{vy}[z(u_2)]$, $n_2 = \overline{0, u_2}$;
- extremum condition for the hydraulic resistance coefficient $\varsigma_{12}(z)$ from (21) with respect to the parameter $u^{(1)}_2$ when the valve is fully open when the condition $z(u_2) = 1$ is satisfied, in the form

$$\left(d\varsigma_{12} du_2\right)\big|_{z(u_2)=1} = 0, \quad (32)$$

- two geometric relations between the sought parameters $d^{(1)}_0, u^{(1)}_1, l^{(1)}_0, L^{(1)}$ taking into account the checkerboard arrangement of the throttle holes on cylindrical surface of the separator

$$L^{(1)} = u^{(1)}_2\left(l^{(1)}_0 + d^{(1)}_0\right) + l^{(1)}_0, \quad l^{(1)}_0 = \left[3^{1/2}\left(d^{(1)}_0 + S^{(0)}_{\varphi 1}\right) - d^{(1)}_0\right]/2, \quad (33)$$

The solution of system (32), (33) is accompanied by the expansion of the first two equations from those listed in the Maclaurin series with respect to unknowns corresponding to the parameter values u_2, d_0 to terms of order $O(u_2^2)$, $O(d_0^2)$, then the values $u^{(1)}_{2j}, d^{(1)}_{0j}$ take

$$u^{(1)}_{2j} = \left[2\left(l^{(0)}_{0j}/\left(L^{(0)}_j - l^{(0)}_{0j}\right)\right)^2\right], \quad j = 1, 2, \quad (34)$$

$$d^{(1)}_{0j} = 2^{1/2}\left(\frac{2}{9}\right)^2 \frac{l^{(0)}_{0j}\left[9\pi l^{(0)}_{0j} S^{(0)}_{\varphi 1}\left(2N_2 - s^{(0)}_{7j}\right)/\left[2\left(L^{(0)}_j - l^{(0)}_{0j}\right)\right]\right]^{1/2}}{\pi\left(L^{(0)}_j - l^{(0)}_{0j}\right)\left(2N_2 - s^{(0)}_{7j}\right)}, \quad j = 1, 2, \quad (35)$$

$$l^{(1)}_{0j} = \left[3^{1/2}\left(d^{(1)}_{0j} + S^{(0)}_{\varphi 1}\right) - d^{(1)}_{0j}\right]/2, \; L^{(1)}_j = u^{(1)}_{2j}\left(l^{(1)}_{0j} + d^{(1)}_{0j}\right) + l^{(1)}_{0j}, \quad j = 1, 2, \quad (36)$$

where $s^{(0)}_{7j}$ correspond to the formula (24); parameters $d^{(0)}_{0j}, L^{(0)}_j, l^{(0)}_{0j}, S^{(0)}_{\varphi 1j}$–to the expressions adopted in *block 4* (**Figure 2**), taking into account $\delta^{min}_{D_y}, \delta^{max}_{D_y}$–the limits of change of the value $D^{(1)}_y$ (m) from (29). Note that the right-hand side of (34) contains an integer value from the corresponding relation.

In the next *block 12* (**Figure 2**), the calculation $\overline{u}_2{}^{(1)}$, $\overline{d}^{(1)}_0$, $\overline{L}^{(1)}$, $\overline{l}^{(1)}_0$ is carried out of the required parameters

d_0, u_2, L, l_0 as averaged values $d_{0j}^{(1)}, u_{2j}^{(1)}$, $L_j^{(1)}, l_{0j}^{(1)}$ from the obtained boundary expressions (34)–(36):

$$\overline{u}_2^{(1)} = \left[\frac{u_{21}^{(1)} + u_{22}^{(1)}}{2}\right], \overline{d}_0^{(1)} = \frac{d_{01}^{(1)} + d_{02}^{(1)}}{2},$$
$$\overline{L}^{(1)} = \frac{L_1^{(0)} + L_2^{(0)}}{2}, \overline{l}_0^{(1)} = \frac{l_{01}^{(1)} + l_{02}^{(1)}}{2}, \quad (37)$$

Note that in (37) for $\overline{u}_2^{(1)}$ only the integer value of the obtained right-hand side is also taken.

Block 13 (**Figure 2**) is designed to estimate the value of the first approximation of the parameter $S_{\varphi 1j}^{(1)}$ using the formula $S_{\varphi 1j}^{(1)} = \pi \overline{D}_{out}^{(1)}/\overline{u}_1^{(0)} - \overline{d}_0^{(1)}$, where the inner diameter $\overline{D}_{out}^{(1)}$ of the separator according to (35) and the accepted approximations in *blocks 4, 6* (**Figure 2**) is determined by the limits of change $\delta_{D_y}^{min}$, $\delta_{D_y}^{max}$ for the value $D_y^{(1)}$, then $\overline{D}_{out}^{(1)} = 1.1(\delta_{D_y}^{min} + \delta_{D_y}^{max})/2$.

Block 14 (**Figure 2**) includes the calculation of the second approximation for the inner diameter of the separator $D_{out}^{(2)}$ using the corollary from the extremum condition (18) for the energy parameter $E_{02}(z)$ from the stochastic model of bubble formation at an early stage of hydrodynamic cavitation (Kapranova et al., 2016b, 2018a) in the form

$$\left\{\frac{d}{dz}\left[\frac{\nu_L}{\pi^{1/2}}\exp\left(\frac{\psi_{10}(z)}{r_m}\right) - \frac{1}{2}\left\{\left(\frac{r_m}{\psi_{10}(z)}\right)^{1/2} \operatorname{erf}\left[\nu_L\left(\frac{\psi_{10}(z)}{r_m}\right)^{1/2}\right]\right\}\right]\right\}\Bigg|_{z=1} = 0, \quad (38)$$

Given the form of the function $\psi_{10}(z)$ described in *block 5* (**Figure 2**), for the desired parameter value, condition (38) yields the value of the desired structural parameter

$$D_{out}^{(2)} = \frac{3\left[B_3 + B_2(B_4 + s_4^{(1)})\right]}{4B_2B_5\ s_4^{(1)}}\left(\overline{L}^{(1)} - l_0^{(2)}\right)\left\{N_0 + \frac{N_1}{B_6 - B_7/\left[2\left(D_{cas2}^{(0)} - 2\delta_2^{(0)}\right)^2\right]}\right\}, \quad (39)$$

where according to the expressions adopted in *blocks 4, 5, 12* (**Figure 2**) for $D_c^{(0)}, D_{cas2}^{(0)}, \delta_2^{(0)}, D_{ch2}^{(0)}, \alpha^{(0)}, l_0^{(0)}, a_1$ as well as the expressions (33), (36), (37) for $\overline{d}_0^{(1)}$, $\overline{u}_1^{(1)}$, $\overline{L}^{(1)}, \overline{D}_y^{(1)}, \overline{u}_2^{(1)}$, $\overline{S}_{\varphi 1}^{(1)}$ are indicated: $\overline{D}_y^{(1)} = (\delta_{D_y}^{\min} + \delta_{D_y}^{\max})/2$, $B_3 \equiv \exp(\nu_L{}^2 a_1 r_m^3)$, $B_4 \equiv s_2{}^{(0)} + s_1{}^{(0)}[(\overline{L}^{(1)} - 1)/s_0{}^{(1)} - 1/2]$, $B_5 \equiv 2s_0^{(1)}(s_0^{(1)} + s_6^{(1)})/[\pi \overline{u}_1^{(1)}(\overline{d}_0^{(1)})^2]$, $B_6 \equiv N_2 - s_5^{(1)}(s_0^{(1)} + s_6^{(1)})/4$, $B_7 \equiv S_{\phi 1}^{(1)} h^{(0)} \overline{u}_1^{(1)}/90$, $s_0^{(1)} \equiv \overline{l}_0^{(1)} + \overline{d}_0^{(1)}$, $s_6^{(1)} \equiv 7\,\overline{L}^{(1)}/2$,

$$s_1{}^{(0)} \equiv \frac{64}{\mathrm{Re}_{ykr}}\frac{\overline{u}_1^{(1)} h^{(0)} (\overline{D}_y^{(1)})^2}{(\overline{d}_0^{(1)})^3},$$

$$s_2^{(1)} \equiv \overline{u}_1^{(1)}\frac{\alpha^{(0)}}{90^0}\frac{(\overline{D}_y^{(1)})^4}{[(D_{cas2}^{(0)} - 2\delta_2^{(0)})^2 - (D_{ch2}^{(0)})^2]^2}, \quad (40)$$

$$s_3^{(1)} \equiv \frac{4D_{out}^{(1)}}{\pi \overline{u}_1^{(1)}(\overline{d}_0^{(1)})^2}, s_4^{(1)} \equiv \frac{2[(D_{cas2}^{(0)} - 2\delta_2^{(0)})^2 - (D_c^{(0)})^2]^2}{(\overline{D}_y^{(1)})^4},$$
$$s_5^{(1)} \equiv \frac{4u_2^{(1)}(S_{\phi 1}^{(1)} + \overline{d}_0^{(1)})}{\pi(\overline{d}_0^{(1)})^2}. \quad (41)$$

In *block 15* (**Figure 2**), to determine the first approximation of the bevel angle for the cylindrical part of the shell $\alpha^{(1)}$, we also apply the corollary from the extremum condition (18) for $E_{02}(z)$ from the stochastic model of bubble formation at an early stage of hydrodynamic cavitation (Kapranova, 2018; Kapranova et al., 2018b; Kapranova and Miadonye, 2019) in form

$$\left[\frac{\nu_L}{\pi^{1/2}}\exp\left(-\frac{\psi_{10}(z)}{r_m}\right) - \frac{1}{2}\left(\left[\frac{r_m}{\psi_{10}(z)}\right]^{1/2} \operatorname{erf}\left\{\nu_L\left[\frac{\psi_{10}(z)}{r_m}\right]^{1/2}\right\}\right)\right]\Bigg|_{z=1} = 0. \quad (42)$$

Therefore, according to (42), the value of the desired structural parameter is determined by the expression $\alpha^{(1)} = \left\{s_1^{(1)}\left[s_0^{(1)} - 2\left(\overline{L}^{(1)} - l_0^{(2)}\right)\right] + 2s_0^{(1)}[\theta_1 - \theta_4]\right\}/(2s_0^{(1)}\theta_2)$, where they $s_0^{(1)}$, $s_1^{(1)}$, $\overline{L}^{(1)}$, $l_0^{(2)}$ are calculated according to the expressions adopted in *blocks 12, 14* (**Figure 2**), taking into account the notation

$$\theta_1 \equiv s_4^{(1)}\left[\frac{s_0^{(1)} s_3^{(1)}(s_0^{(1)} + s_6^{(1)})}{2\theta_2\theta_3(\overline{L}^{(1)} - l_0^{(2)})} - 1\right]^2,$$
$$\theta_2 \equiv \frac{\overline{u}_1^{(1)}}{90^0}\frac{(\overline{D}_y^{(1)})^4}{[(D_{cas2}^{(0)} - 2\delta_2^{(0)})^2 - (D_{ch2}^{(0)})^2]^2}, \quad (43)$$
$$\theta_3 = U_0 + \frac{U_1}{U_2 + s_7^{(1)}/2 - [s_5^{(1)} s_0^{(1)} + s_6^{(1)}]/4},$$
$$\theta_4 \equiv 12\frac{a_1 r_m^4}{k_{\zeta 2}\rho_L}, \quad (44)$$
$$k_{\zeta 2} \equiv 8\pi r_m^4 \frac{(\alpha_g \rho_g + \alpha_s \rho_s)}{\rho_L \zeta_{12}^{(0)}[z(u_2^{(1)})]},$$
$$s_7^{(1)} \equiv \frac{\overline{u}_1^{(1)}}{90^0}\frac{S_{\phi 1}^{(1)} h^{(0)}(1 + D_{out}^{(2)}/D_c^{(0)})}{[(D_{cas2}^{(0)} - 2\delta_2^{(0)})^2 - (D_{out}^{(2)})^2]}, \quad (45)$$

To calculate the values $s_5^{(1)}$, $s_6^{(1)}$, $D_{cas2}^{(0)}, a_1, \delta_2^{(0)}$, $\varsigma_{12}^{(0)}$, $\overline{u}_1^{(1)}$, $\overline{S}_{\varphi 1}^{(1)}$, $h^{(0)}, D_{out}^{(2)}, D_c^{(0)}$ in (43)–(45), the formulas are used, which are contained in *blocks 4, 5* (**Figure 2**), as well as expressions (27), (40), (41). In conclusion, we determine the first approximation of the following parameters: $\delta_2^{(1)} = 0.1 D_y^{(1)}$, $h^{(1)} = \delta_2^{(1)}/2$, $D_c^{(1)} = h^{(1)} + D_{out}^{(2)}$, $D_{ch2}^{(1)} = 3\,D_{out}^{(2)}/2$, $D_{cas2}^{(1)} = 2\,D_{out}^{(2)}$.

In *block 16* (**Figure 3**), the value for the hydraulic resistance coefficient is calculated according to (21) and the formulas from (Kapranova et al., 2018c)

$$\zeta_y[z(\overline{u}_2^{(1)})] = s_1^{(0)}\left(\frac{Lz(\overline{u}_2^{(1)})-\overline{l}_0^{(1)}}{s_0^{(1)}}-\frac{1}{2}\right)+s_2^{(1)} + s_4^{(1)}\left\{\frac{s_0^{(1)}s_3^{(1)}[s_0^{(1)}+s_6^{(1)}z(\overline{u}_2^{(1)})]}{2[Lz(\overline{u}_2^{(1)})-\overline{l}_0^{(1)}]\varepsilon[z(\overline{u}_2^{(1)})]}-1\right\}^2, \quad (46)$$

where the compression ratio of the jet, in contrast to (26), is equal to

$$\varepsilon[z(\overline{u}_2^{(1)})] = U_0 + U_1/(U_2-\{s_7^{(1)} - s_5^{(1)}[s_0^{(1)} + s_6^{(1)}z(\overline{u}_2^{(1)})]/2\}/2), \quad (47)$$

and the constants $s_j^{(0)}$, $j=\overline{1,7}$ correspond to the expressions from *block 14* (**Figure 2**).

In *block 17* (**Figure 3**) calculates the critical value for the coefficient of hydraulic resistance ζ_y^* from the condition of achieving the minimum value for the ensemble average diameter of the cavitation bubble D_{cb} according to Kapranova et al. (2017, 2018a,c), Kapranova A. B. et al. (2019), which corresponds to the following condition

$$\frac{\nu_L}{\pi^{1/2}}\exp\left(-\frac{C_4{}^{1/2}}{E_{01}r_m}\right)-\frac{1}{2}\left[\frac{E_{01}}{\tau_1(1)}\right]^{1/2}\operatorname{erf}\left\{\nu_L\left[\frac{\tau_1(1)}{E_{01}}\right]^{1/2}\right\} = 0. \quad (48)$$

In condition (48), the coefficients $E_{01}, C_4, \tau_{11}(1)$ from the stochastic model (Kapranova et al., 2016a), which describes the process of formation of a bubble system at the initial stage of hydrodynamic cavitation in a control device, depend on the physical and mechanical properties of the working medium (including the density of the liquid, gas and vapor, and kinematic viscosity fluid at a given value of its temperature, surface tension coefficient, volumetric weight of the medium, adiabatic index) and the desired value ζ_y^*, then where indicated: $\zeta_y^* = 2r_m\{\theta_9/2+a_1r_m^3[(32r_m^3/k_1)-4/3]\}/(3k_{\zeta 2}\rho_L)$, $\theta_9 \equiv \{\theta_6/\theta_5-[\theta_7 + k_{\zeta 2}\rho_L\theta_8/m_0]\}^{1/3}$, $\theta_7 \equiv 512a_1^3r_m^9$, $\theta_6 \equiv 108y_0a_1r_m(k_\zeta\rho_L)^2$, $\theta_8 \equiv 12\sqrt{3}\{E_{01}a_1y_0[27y_0(k_\zeta\rho_L)^2-25a_1\theta_7r_m{}^8\theta_5]/r_m\}^{1/2}$, $\theta_5 \equiv m_0(a_1r_m{}^3/E_{01})^{1/2}$, $m_0 \equiv 5.04$, $y_0 \equiv [\pi^{1/2}\operatorname{erf}(1) - 6\exp(-1)]/[4\exp(-1)]$.

In *conditional block 18* (**Figure 3**), a possible manifestation of a cavitation effect in the flow part of the valve is checked. Fulfillment of the following condition $\zeta_y^* \le \zeta_y$ leads to a graphical estimation of the cavitation coefficient k_C in block 19 (**Figure 3**) from empirical reference data (Arzumanov, 1971) for the critical value of the coefficient of hydraulic resistance ζ_y^* obtained in *block 17* (**Figure 3**). Otherwise, when the inequality $\zeta_y^* > \zeta_y$ holds, it returns to *block 4* (**Figure 2**), associated with setting the critical value of the Reynolds number Re_{cr} and changing the value of $D_y^{(0)}$ in (14).

In the next *block 20* (**Figure 3**), the calculation is performed:

- critical (maximum permissible) pressure drop $\Delta p_{max}^* = k_{C.max}(p_1 - p_{H1})$ during the regime of fluid movement with a critical value of k_{Cmax} for the cavitation coefficient k_C, where p_1 (kgf/cm^2) is the absolute fluid pressure to the control valve at its maximum flow rate; p_{H1} (kgf/cm^2) is absolute pressure of saturated steam at temperature t_1 (°C);
- valve capacity in cavitation operation according to the well-known formula (Arzumanov, 1971, 1985) $K_{vmax} = \eta_{12}Q_{1max}(\gamma/\Delta p_{max}^*)^{1/2}$ with a safety factor of η_{12};

Conditional block 21 (**Figure 3**) checks one of two inequalities:

- for differential pressure $\Delta p_{max}^* \ge \Delta p_{min}$;
- for valve capacity K_{vmax} and the required value K'_{vy} when $K_{vmax} \le K'_{vy}$.

If these inequalities are true, the calculation can be completed with the transition to *blocks 24* and *25* (**Figure 3**) to select and display the desired parameters of the separator. Otherwise, it is required to select a value in the subsequent *block 22* (**Figure 3**) in order to n_3 fulfill the condition for the conditional throughput from *block 23* (**Figure 3**) according to the inequality $K'_{vy} \ge \eta_3 K_{vmax}$, where n_3 is the safety factor within at least 10–20% of maximum value, i.e., in the range (1.1–1.2) units, and then return to *block 2* (**Figure 2**).

Thus, in *block 25* (**Figure 3**), the desired structural parameters of the designed axial valve separator are output in the form of the set $q^* = \{q_k^* = const\}, k = \overline{1, \delta_1}$ according to the set $q = \{q_{k_1} = const\}$, $k_1 = \overline{1, \rho_1}$, from (1) when choosing the desired parameters, performed in *block 24* (**Figure 3**)

$$q^* = \{\, d_0^*, S_\varphi^*, l_0^*, h^*, u_1^*, u_2^*, D_{out}^*, D_c^*, L^*, \alpha^*, D_{cas2}^*, D_{ch2}^*, \delta_2^* \,\}, \quad \delta_1 = 13, \quad (49)$$

Moreover, in the set (49) the following approximations are used: $d_0^* = \overline{d}_0^{(1)}$, $S_\varphi^* = \overline{S}_{\varphi 1}^{(1)}$, $l_0^* = l_0^{(2)}$, $u_1^* = \overline{u}_1^{(1)}$, $u_2^* = \overline{u}_2^{(1)}$, $D_{out}^* = D_{out}^{(2)}$, $D_c^* = D_c^{(0)}$, $L^* = \overline{L}^{(1)}$, $\alpha^* = \alpha^{(1)}$, $D_{cas2}^* = D_{cas2}^{(1)}$, $D_{ch2}^* = D_{ch2}^{(1)}$, $\delta_2^* = \delta_2^{(2)}$ then

$$q^* = \left\{\overline{d}_0^{(1)}, \overline{S}_{\varphi 1}^{(1)}, l_0^{(2)}, \overline{u}_1^{(1)}, \overline{u}_2^{(1)}, D_{out}^{(2)}, D_c^{(0)}, \overline{L}^{(1)}, \alpha^{(1)}, D_{cas2}^{(1)}, D_{ch2}^{(1)}, \delta_2^{(2)}\right\}, \quad \delta_1 = 13, \quad (50)$$

for the diameter of the radial throttle holes; the diameter of the round throttle holes d_0, the arc distance between the holes in the same row S_φ, the distance between the rows of these holes l_0, the thickness of the separator h, the number of holes for one row u_1, the number of these rows u_2, respectively, the inner and outer diameters separator D_{out} and D_c, the length of its perforator of the left part L, the bevel angle for the cylindrical part of the shell α, the inner diameter for the cylindrical part of the outer casing D_{cas2}, the outer diameter of the inner valve body D_{ch2}, the wall thickness of the inner and outer casing δ_2.

The Influence of a Set of Design Parameters From the Rational Ranges of Their Change for the Node "Separator-Locking Shell" on the Size of Cavitation Bubbles

From a practical point of view, of particular interest is the analysis of the influence of the desired set of design

parameters from rational ranges of their change for the "separator-external locking shell" unit on the size of cavitation bubbles, as a reflection of the result of an engineering calculation on the nature of the course of the initial stage of hydrodynamic cavitation in the flow part of the designed control device.

The described engineering methodology from sections Selection of the Main Parameters of the Liquid Throttling Process in an Axial Valve With an External Locking Shell, Description of the Work Flowchart of the Engineering Methodology for Calculating the Parameters of These System of the Separator-External Locking Shell was tested in Kapranova et al. (2020) using the example of the calculation of the "separator-external locking shell" assembly of an axial valve with a regulated value of the valve throughput $K'_{vy} = 6$ m^3/h when choosing water as the working medium and the following parameters of the throttling process: $Q_{1max} = 0.5$ m^3/h; $\Delta p_{min} = 0.90$ kPa; $\rho_L = 10^3$ kg/m^3; $t_1 = 30^\circ C$; $\nu_1 = 0.81\times10^{-2}$ cm^2/s; $\sigma = 7.28\times10^{-4}$ H/m; $w = 0.43$ m/s; $r_{min} = 10^{-3}$ m; $p_{max} = 1.3\times10^5$ кПа; $p_s = 10^{-3}$ Pa; $\rho_g = 1.205$ kg/m^3; $\rho_s = 1.44\times10^{-2}$ kg/m^3 and adiabatic index $k = 1.3$. According to the calculation example performed in Kapranova et al. (2020) based on the engineering method (Kapranova et al., 2019b) described in this paper, with $K'_{vy} = 6$ m^3/h; $\mathrm{Re}_{cr} = 5209,58$; $\zeta_y^* = 0.119$ obtained rational ranges of changes of the desired parameters, in particular, the average value of d_0 from the specified range is $\overline{d}_0^{(1)} = 5.05\times10^{-3}$ m with a separator outlet diameter of $D_{out}^{(2)} = 4.19\times10^{-2}$ m and the length of its perforated part $\overline{L}^{(1)} = 8.21\times10^{-2}$ m with the number of rows of throttle holes $\overline{u}_2^{(1)} = 7$ for $\overline{u}_1^{(0)} = 12$ pieces in each and the distance between these rows $\overline{l}_0^{(1)} = 5.84\times10^{-3}$ m. Moreover, additional design parameters of the separator-external locking shell assembly correspond to the following effective values: separator thickness $h^{(1)} = 2.11\times10^{-3}$ m; its outer diameter $D_c^{(1)} = 4.55\times10^{-2}$ m; inner diameter for the cylindrical part of the outer casing $D_{cas2} = 8.69\times10^{-2}$ m; the outer diameter of the inner valve body $D_{ch2} = 6.25\times10^{-2}$ m; wall thickness of the inner and outer shell $\delta_2 = 4.22\times10^{-3}$ m; bevel angle for the cylindrical part of the shell $\alpha^{(1)} = 44,84^0$. The indicated values for the set of sought-for structural parameters $q^* = \left\{q_k^* = const\right\}, k = \overline{1,\delta_1}$ from expressions (49) and (50) allow, by analogy with the approach from Kapranova A. B. et al. (2019), based on (Kapranova et al., 2017, 2018a) to analyze the dependence $D_{cb} = D_{cb}(D_y,\ K_{vy})$ between the ensemble average value of the diameter D_{cb} for the macro-system of cavitation bubbles, the conditional diameter D_y and the corresponding throughput of the K_{vy} valve for its opening degree z (**Figures 4A,B**).

The values of $D_{cbj},\ j = \overline{1,4}$ for the ensemble-average diameter of cavitation bubbles for various indicators of the degree of opening of the separator $z = \{0.2;0.5;0.8;1.0\}$ are determined by the position of the end points of the lines for graphs *1–4* according to **Figure 4A**. Additionally, as a more comprehensive three-dimensional illustration, the dependence $D_{cb}(D_y,\ K_{vy})$ in **Figure 4B** is presented. An analysis of the results showed that the transition from mode 1 of the separator with a degree of opening of 20% to mode 3 with 80% opening of the throttle openings is accompanied by an increase in the conditional throughput of the K_{vy} valve by 10.7 times (as the ratio K_{vy3}/K_{vy1}), and in the case of the transition from mode 3 to full opening (mode 4), the ratio $K_{vy4}/K_{vy3} = 1,\ 4$. For comparison, we note that the case considered in Kapranova A. B. et al. (2019) for other values of the design parameters of the separator-external locking shell assembly that are not related to the rational ranges of their changes leads to the following relations $K_{vy3}/K_{vy1} = 2.1$ and $K_{vy4}/K_{vy3} = 1.4$. In addition, according to **Figure 4A**, a decrease in the size of the resulting bubbles is noted in $D_{cb1}/D_{cb4} = 1.35$ times from the range of the ensemble average diameter of the cavitation bubble $D_{cb} = (0.74 - 1.0)\times10^{-3}$ m against the case from Kapranova A. B. et al. (2019), when $D_{cb1}/D_{cb4} = 1.12$ from the range $D_{cb} = (1.6 - 1.8)\times10^{-3}$ m. Moreover, a comparison of the results presented in **Figure 4A** and in Kapranova A. B. et al. (2019) showed that there is a tendency to decrease the D_{cb} value by 1.95 times when taking into account the rational ranges of changes in the desired design parameters $q^* = \left\{q_k^* = const\right\}, k = \overline{1,\delta_1}$ obtained in this article.

KEY FINDINGS AND RESULTS

The proposed block diagram consists of 25 main blocks for calculating 13 effective values of the design parameters of an axial valve separator. For example, the required parameters include: diameter of round throttle holes d_0, arc distance between the holes in one row, distance between rows of these holes, separator thickness, number of holes for one row, number of these rows, diameter of the outlet of the separator, its perforated part length, bevel angle for the cylindrical part of the shell, etc. Specified operating parameters are the maximum attainable fluid flow through the regulating device at a given value of the medium temperature, the minimum pressure drop, the maximum pressure in the center of the bubble, which corresponds to the minimum value of its radius, the saturated vapor pressure of the medium, the velocity of the fluid in the pipeline. The input parameters for the calculation are the maximum attainable flow rate of the medium, the temperature of the medium, the limits of variation of the minimum pressure drop and the velocity of the fluid in the pipeline. The output parameter is the required valve capacity K'_{vy}. The block diagram (**Figures 2**, **3**) proposes a phased calculation of various approximations of the desired design parameters depending on the selected intervals for changing the maximum value of the valve capacity. The indicated intervals are refined three times when taking into account the required value of K'_{vy} throughput with the choice of safety factors. The first time this is done at specified intervals for changing the minimum pressure drop, the second after calculating Re_{cr} based on (Kapranova, 2018; Kapranova et al., 2018b; Kapranova and Miadonye, 2019) to determine the correction factors for the viscosity of the medium, the third after evaluating the hydraulic resistance coefficient ζ_y^* (Kapranova et al., 2018c) from the minimum condition values of D_{cb} (Kapranova et al., 2017, 2018a, 2019a). Note that the

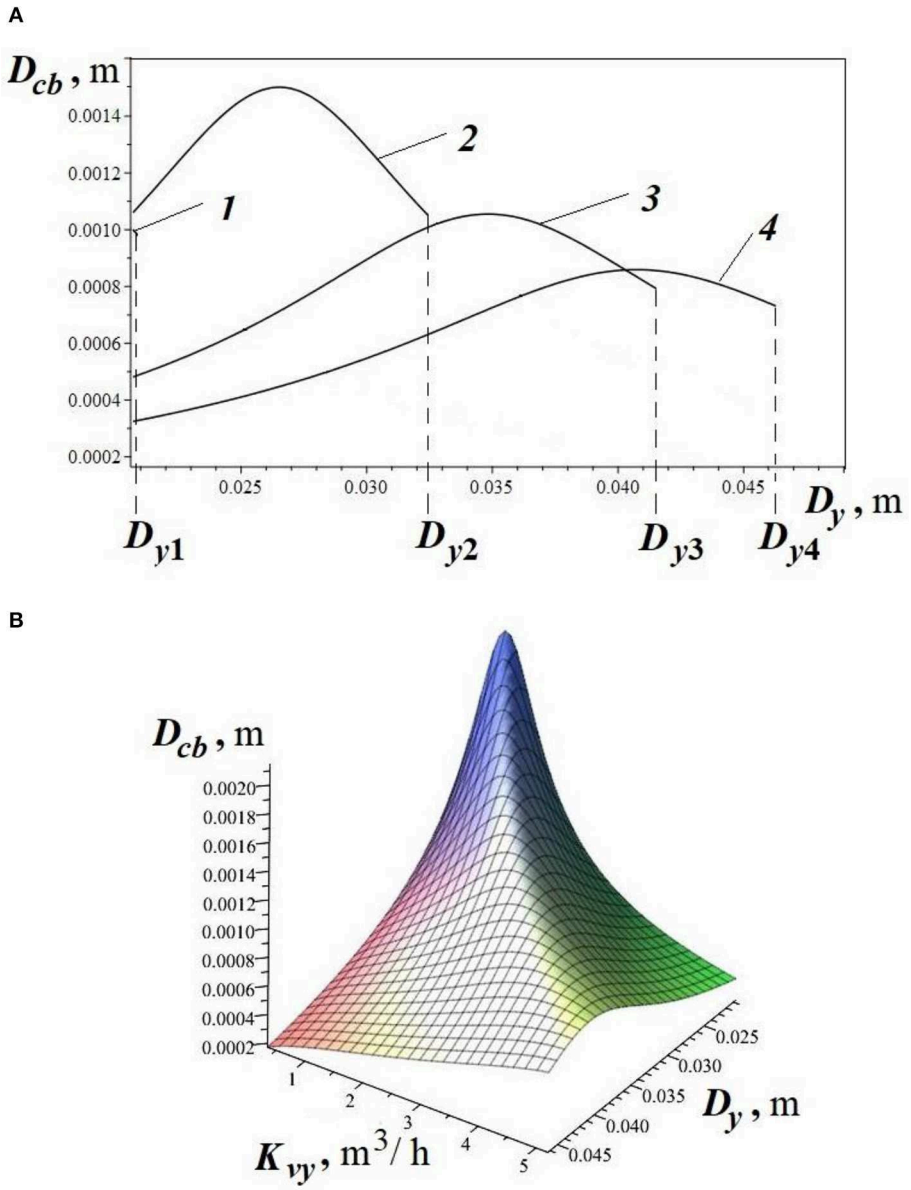

FIGURE 4 | The influence of the main indicators of the process of throttling the working medium in the node "separator-external locking shell" on the value of the ensemble average diameter of the cavitation bubble by the example of the dependencies: **(A)** $D_{cb}(D_y)$; *1* – $z = 0.2$; $D_{y1} = 8.44\times10^{-3}$ m; $K_{vy1} = 3.553\times10^{-1}$ m^3/h; *2* – $z = 0.5$; $D_{y2} = 2.11\times10^{-2}$ m; $K_{vy2} = 2.200$ m^3/h; *3* – $z = 0.8$; $D_{y3} = 3.38\times10^{-2}$ m; $K_{vy3} = 3.799$ m^3/h; *4* – $z = 1.0$; $D_{y4} = 4.22\times10^{-2}$ m; $K_{vy4} = 5, 205$ m^3/h; **(B)** $D_{cb}(D_y, K_{vy})$.

calculation of the conditional flow area for the control valve separator depends on the configuration of the throttle holes, which significantly affects the application of the expressions proposed in the method according to the models (Kapranova et al., 2018a,b,c; Kapranova and Miadonye, 2019). For example, this is reflected when using expressions (20)–(28) in *blocks 5, 6* (**Figure 2**) for the critical value of the Reynolds number Re_{cr}, when choosing the first approximation for the conditional diameter $D_y^{(1)}$, and therefore, when calculating the value of the hydraulic resistance coefficient, including the critical ζ_y^* (*blocks 17* and *18*, **Figure 3**), etc. An analysis of the obtained critical value of the Reynolds number in comparison with the characteristic value from Kapranova et al. (2020) allows us to assess the need for additional consideration of the viscosity of the working medium using correction factors and to clarify the limits of change of the device throughput coefficient when setting the next approximation of the valve design parameters to ensure its effective operation according to the regulatory value K'_{vy}. The work of the proposed engineering calculation method (sections Selection of the Main Parameters of the Liquid Throttling Process in an Axial Valve With an External Locking Shell, Description of the Work Flowchart of the Engineering

Methodology for Calculating the Parameters of These System of the Separator-External Locking Shell) is illustrated by the example of comparative analysis (section The Influence of a Set of Design Parameters From the Rational Ranges of Their Change for the Node "Separator-Locking Shell" on the Size of Cavitation Bubbles) for the ensemble average diameter of the cavitation bubbles formed in the "separator-external locking shell" assembly with the external arrangement of the latter in the design of the control valve, depending on taking into account the values of design parameters from rational and irrational ranges of their change.

Thus, summarizing the results of this study leads to the following main conclusions and results:

- In the presented engineering method for calculating the main structural parameters (sections Selection of the Main Parameters of the Liquid Throttling Process in an Axial Valve With an External Locking Shell, Description of the Work Flowchart of the Engineering Methodology for Calculating the Parameters of These System of the Separator-External Locking Shell) for the direct-flow type apparatus (Lebedev et al., 2018), the following facts received their practical application:

  (1) Analysis of the design features of direct-flow type control valves (Lebedev et al., 2016, 2017a,b), methods for modeling the cavitation phenomenon (Kapranova et al., 2016c) and calculation of the main indicators of this process (Kapranova et al., 2016d,e);
  (2) Stochastic models (Kapranova et al., 2016a,b, 2017, 2018a,b; Kapranova, 2018; Kapranova A. B. et al., 2019; Kapranova and Miadonye, 2019) for the process of bubble formation in the initial stage of hydrodynamic cavitation, the results of which are in satisfactory agreement (Kapranova and Miadonye, 2019) with the experimental data (Lebedev et al., 2017a,b) and justify the possibility of reducing the cavitation intensity in the node "separator-external locking shell."

- The proposed engineering methodology for calculating the main structural parameters of the node "separator-external locking shell" uses two approaches:

  (1) Application of the Pi-Buckingham theorem (Buckingham, 1915; Misic et al., 2010) in solving the problem of scaling and lowering the number of constant parameters describing the process under study, within the framework of the well-known classical algorithm for choosing the type of control device (Arzumanov, 1971, 1985) based on the experimental relationships between the main process indicators (*blocks 2* and *6*, expressions (12) and (30), section Description of the Work Flowchart of the Engineering Methodology for Calculating the Parameters of These System of the Separator-External Locking Shell), as well as an empirical analysis of the conditions for attaining critical values of hydrodynamic similarity criteria: a) the Reynolds number (*block 6*, expression (28), section Description of the Work Flowchart of the Engineering Methodology for Calculating the Parameters of These System of the Separator-External Locking Shell); b) the cavitation coefficient as a doubled Euler number (Knapp et al., 1970; Franc and Michel, 2005; Xu et al., 2015; Kapranova et al., 2016e) (*blocks 18* and *20*, section Description of the Work Flowchart of the Engineering Methodology for Calculating the Parameters of These System of the Separator-External Locking Shell);
  (2) Using for calculating the set of sought-for structural parameters $q^* = \left\{q_k^* = const\right\}, k = \overline{1, \delta_1}$ functional dependencies obtained from models (Kapranova et al., 2016a,b, 2017, 2018a,b; Kapranova, 2018; Kapranova and Miadonye, 2019) and reflecting the conditions for the minimum size of the cavitation bubbles formed (*block 17*, expression (48), section Description of the Work Flowchart of the Engineering Methodology for Calculating the Parameters of These System of the Separator-External Locking Shell), hydraulic resistance (*blocks 11* and *16*, expressions (32) and (46), section Description of the Work Flowchart of the Engineering Methodology for Calculating the Parameters of These System of the Separator-External Locking Shell), energy parameters of the cavitation bubble system (*blocks 14* and *15*, expressions (38) and (42), section Description of the Work Flowchart of the Engineering Methodology for Calculating the Parameters of These System of the Separator-External Locking Shell), etc.

- When assessing the impact of the design parameters of the separator-external locking shell assembly on the nature of cavitation bubble formation, a comparative analysis (section The Influence of a Set of Design Parameters From the Rational Ranges of Their Change for the Node "Separator-Locking Shell" on the Size of Cavitation Bubbles) of the application of parameters from rational (Kapranova et al., 2020 according to the present methodology) and irrational (Kapranova A. B. et al., 2019) ranges of their change which showed that when using the results of Kapranova et al. (2020), there is a tendency to reduce the value between the ensemble average diameter value D_{cb} by 1.95 times, while the transition from a mode from 20% for the degree of the opening of the separator to 80% for the opening of it's throttle openings and the last operation is accompanied by an increase in the value of the conditional throughput of the K_{vy} valve by 10.7 times.

Let us briefly dwell on the main directions of further improvement of the proposed engineering methodology for calculating the parameters of the separator-external locking shell unit, as an object of research of various nature (hydrodynamic, vibro-acoustic, managerial, etc.) that go beyond the scope of the tasks posed in this work. As already noted in section Methods, the relative error of theoretical calculations (Kapranova, 2018; Kapranova et al., 2018b; Kapranova and Miadonye, 2019) in comparison with experimental data (Lebedev et al., 2017a,b) in estimating the distribution of bubbles by the degree of opening of the axial valve with an external locking shell did not exceed 13% according to Kapranova and Miadonye (2019). This fact is reflected in the results of applying the engineering methodology described in section Results and Discussion, due to the use of

the results of stochastic models (Kapranova, 2018; Kapranova et al., 2018b; Kapranova A. B. et al., 2019; Kapranova and Miadonye, 2019) for the process of bubble formation in the initial stage of hydrodynamic cavitation. However, these models do not take into account the consequences of the evolution of the cavitation phenomenon in the flow part of the valve, for example, the possible process of combining bubbles, the growth of their diameters and subsequent collapse. The emphasis in the proposed models and the corresponding engineering methodology for calculating the design parameters of the designed unit "separator-external locking shell" is made on the possibility of preventing an increase in the intensity of formation of cavities in the flow part of the regulating device already at the initial stage of the occurrence of cavitation. In addition, there are a number of difficulties that a designer may encounter in practice when implementing the described methodology. Additionally, it should be investigated: the conditions for reducing noise effects during the implementation of high-speed flow regimes of the working medium, and, therefore, vibro-acoustic characteristics; force factors in the movable elements of the device in order to calculate the hydrodynamic balance of the control valve; quality issues of the process of managing the static and dynamic characteristics of this unit, etc.

CONCLUSIONS

An analytical method has been developed for calculating the effective ranges of the structural parameters of the locking-regulating system "perforated separator—external locking cylinder-conical shell" based on the proposed stochastic models of bubble formation at the initial stage of hydrodynamic cavitation. In particular, in addition to the gyrodynamic similarity criteria, the following were used: differential distribution functions of the bubble distribution density at the initial stage of hydrodynamic cavitation in two phase variables—the conditional diameter of the cavitation bubble (Kapranova et al., 2018a) and the degree of valve opening (Kapranova and Miadonye, 2019). In addition, the proposed block diagram of the calculation of the node "separator-external locking shell" uses estimated analytical expressions: for the value of the coefficient of hydraulic resistance (Kapranova et al., 2018c); for the average ensemble diameter of the cavitation bubble from the indicated works (Kapranova et al., 2016c); for the critical value of the Reynolds criterion depending on the desired design parameters (Kapranova, 2018).

When studying the influence of a set of design parameters for the "separator-external locking shell" assembly from certain rational ranges of their change, a tendency is found to reduce the ensemble average value of the diameter of the cavitation bubble by almost 2 times compared with the values of the parameters from irrational limits. It is shown that for these comparative cases, a change in the degree of opening of the throttle holes of the separator from 20 to 80% is able to change the valve throughput by more than 10 times.

The proposed methodology for the engineering calculation of the design parameters of an axial valve with an external location of the locking body is of interest to designers of control valves in the chemical and oil refining industries, and can be expanded when designing axial valves of other structures on a theoretical basis using a stochastic approach (Kapranova et al., 2019a).

DATA AVAILABILITY STATEMENT

All datasets generated for this study are included in the article/supplementary material.

AUTHOR CONTRIBUTIONS

All authors listed have made a substantial, direct and intellectual contribution to the work, and approved it for publication.

FUNDING

This work was supported by JSC Regulator (Yaroslavl, Russia). The funder was not involved in the study design, collection, analysis, and interpretation of data, the writing of the article or the decision to submit for publication.

REFERENCES

Ansys Inc (2013). *ANSYS Fluent UDF Manual*. Available online at: http://www.pmt.usp.br/academic/martoran/NotasModelosGrad/ANSYS%20Fluent%20UDF%20Manual.pdf (accessed February 13, 2020).

Ansys Inc (2017). *ANSYS Fluent User's Guide*. Available online at: https://archive.org/details/ANSYSFluentUsersGuide/mode/2up (accessed February 13, 2020).

Arzumanov, E. S. (1971). *Calculation and Selection of the Regulatory Bodies of Automatic Systems*. Moscow: Energy.

Arzumanov, E. S. (1985). *Hydraulic Regulatory Bodies of Automated Control Systems. [Gidravlicheskiye reguliruyushchiye organy sistem avtomatizirovannogo upravleniya]*. Moscow: Engineering [Mashinostroyeniye].

Baron Rayleigh, J. W. S. (1911–1919). *Scientific Papers*, Vol. 6: 1911–1919. Cambridge: Cambridge University Press, 1899–1920.

Besant, W. H. (1859). *Hydrostatics and Hydrodynamics*. London: Cambridge University Press.

Bian, J., Cao, X., Teng, L., Sun, Yu., and Gao, S. (2019a). Effects of inlet parameters on the supersonic condensation and swirling characteristics of binary natural gas mixture. *Energy* 188:116082. doi: 10.1016/j.energy.2019.116082

Bian, J., Cao, X., Yang, W., Song, X., Xiang, C., and Gao, S. (2019b). Condensation characteristics of natural gas in the supersonic liquefaction process. *Energy* 168, 99–110. doi: 10.1016/j.energy.2018.11.102

Blagov, E. E. (1990). *Throttle and Control Valves of Thermal Power Plants and Nuclear Power Plants. [Drossel'no-reguliruyushchaya armatura TES i AES]*. Moscow: Energoatomizdat. [Energoatomizdat].

Buckingham, E. (1915). The principle of similitude. *Nature* 96, 396–397. doi: 10.1038/096396d0

Canjuga, S. (2019). *Axial Valve of the Modular Concept of Construction*. Patent WO2019220153A2, F16K 37/00, F16K 27/02. Zagreb: World Intellectual Property Organization (WIPO).

Cao, X., and Bian, J. (2019). Supersonic separation technology for natural gas processing: a review. *Chem. Eng. Process.* 136, 138–151. doi: 10.1016/j.cep.2019.01.007

Chahine, G. L. (1994). *Strong Interactions Bubble/Bubble and Bubble/Flow*. Dordrecht: Kluwer Academic Publishers; Springer. 195–206. doi: 10.1007/978-94-011-0938-3_18

Ellas, E., and Chambre, P. L. (2000). Bubble transport in flashing flow. *Int J. Multiphase Flow* 26, 191–206. doi: 10.1016/S0301-9322(99)00011-7

Emerson, F. (2020). Available online at: https://www.emerson.com/en-us/automation/fisher (accessed January 26, 2020).

Esveldt, V. (2012). *Throttle Valve*. Patent US8297315B2. F16K 47/08. Werkendam: United States Patent and Trademark Office (USPTO).

Flowserve (2020). *Linear Control Valves*. Available online at: https://www.flowserve.com/en/products/valves/linear-control-valves (accessed January 26, 2020).

Franc, J.-P., and Michel, J.-M. (2005). "Fluid mechanics and its applications," in *Fundamentals of Cavitation*, Vol. 76 (Springer Science + Business Media), 306. doi: 10.1007/1-4020-2233-6

Frenkel, J. (1946). *Kinetic Theory of Liquids. International Series of Monographs on Physics*. London: Oxford University Press.

Hou, C.-W., Qian, J., Chen, F., Jiang, W., and Jin, Z. (2017). Parametric analysis on throttling components of multi-stage high pressure reducing valve. *Appl. Thermal Eng.* 128, 1238–1248. doi: 10.1016/j.applthermaleng.2017.09.081

Hsu, Y. Y. (1962). On the size range of active nucleation cavities on a heating surface. *J. Heat Transf.* 94, 207–212. doi: 10.1115/1.3684339

Kapranova, A. (2018). On the influence of the degree of opening of the regulator valve separator on the process of formation of cavitation bubbles. *J. Chem. Eng. Process Technol.* 9:36. doi: 10.4172/2157-7048-C3-016

Kapranova, A., Lebedev, A., and Meltser, A. (2017). The definition of the integral characteristics of the process of formation of cavitation bubbles when operating the control valve. *J. Chem. Eng. Process Technol.* 8:58. doi: 10.4172/2157-7048-C1-009

Kapranova, A., Lebedev, A., Meltser, A., and Neklyudov, S. (2018a). Determination of the average parameters of cavitation bubbles in the flowing part of the control valves. *Int. J. Mech. Eng. Technol.* 9, 25–31.

Kapranova, A., and Miadonye, A. (2019). Stochastic simulation of cavitation bubbles formation in the axial valve separator influenced by degree of opening. *J Oil Gas Petrochem. Sci.* 2, 70–75. doi: 10.30881/jogps.00026

Kapranova, A., Miadonye, A., Lebedev, A. E., and Meltser, A. M. (2019a). "Formation of a general approach to stochastic modeling of the initial stage of hydrodynamic cavitation in a control valve," in *Proceedings of the International Conference on Innovative Applied Energy–IAPE'19* (Oxford), 38. Available online at: http://www.iape-conference.org/Downloads~/Proceedings/Proceedings%20of%20IAPE'19.pdf

Kapranova, A., Neklyudov, S., Lebedev, A., and Meltser, A. (2018b). Investigation of the energy of the stochastic motion of cavitation bubbles in the separator of the axial valve, depending on the degree of its opening. *Int. J. Mech. Eng. Technol.* 9, 160–166.

Kapranova, A., Neklyudov, S., Lebedev, A., and Meltser, A. (2018c). Qualitative evaluation of the coefficient of hydraulic resistance in the area of the divider of the fluid flow of the axial valve. *Int. J. Mech. Eng. Technol.* 9, 153–159.

Kapranova, A., Neklyudov, S., Lebedev, A., Meltser, A., and Voronin, D. (2019b). "Engineering method for calculating of an axial valve separator with an external location of the locking part," in *Bridging Science With Technology: 12th European Congress of Chemical Engineering/5th European Congress of Applied Biotechnology–ECCE12/ECAB5* (Florence), 660–663.

Kapranova, A. B., Lebedev, A. E., Meltser, A. M., and Neklyudov, S. V. (2016a). Stochastic model of process of formation of cavitation bubbles in the flow path of control valve. *Vestn. IGEY Her IGEY*. 4, 24–29. doi: 10.17588/2072-2672.2016.4.024-029

Kapranova, A. B., Lebedev, A. E., Meltser, A. M., and Neklyudov, S. V. (2019). The ensemble-averaged characteristics of the bubble system during cavitation in the separator. *E3s Web Conf.* 140:06005. doi: 10.1051/e3sconf/201914006005

Kapranova, A. B., Lebedev, A. E., Meltser, A. M., and Neklyudov, S. V. (2020). "About formation of elements of a cyber-physical system for efficient throttling of fluid in an axial valve," in *Cyber-Physical Systems: Advances in Design & Modelling. Studies in Systems, Decision and Control*, Vol. 259, eds A. Kravets, A. Bolshakov, and M. Shcherbakov (Cham: Springer), 109–119. doi: 10.1007/978-3-030-32579-4_9

Kapranova, A. B., Lebedev, A. E., Meltser, A. M., and Solopov, S. A. (2016b). The application process of the Ornstein-Ulenbek to the formation of cavitation bubbles. *Czas. Tech. Mech.* 113, 136–144. doi: 10.4467/2353737XCT.16.101.5500

Kapranova, A. B., Lebedev, A. E., Meltser, A. M., Solopov, S. A., and Neklyudov, S. V. (2016d). About methods for calculating hydraulic resistance regulatory authorities during transportation single component media. *Fundam. Res.* 4, 52–60.

Kapranova, A. B., Lebedev, A. E., Meltser, A. M., Solopov, S. A., and Serov, E. M. (2016c). Methods of modeling the developmental stages of hydrodynamic cavitation. *Fundam. Res.* 3, 268–273.

Kapranova, A. B., Lebedev, A. E., Meltser, A. M., Solopov, S. A., and Serov, E. M. (2016e). On the way to assess critical parameters cavitation in transport regulators in the working environment. *Fundam. Res.* 3, 488–494.

Klimontovich, Y. L. (2014). *Turbulent Motion and Chaos Structure: A New Approach to the Statistical Theory of Open Systems*. Moscow: LENAND.

Knapp, R. T., Daily, J. W., and Hammitt, F. G. (1970). *Cavitation*. New York, NY: McGraw-Hill.

Koch, S., Garen, W., Hegedus, F., Neu, W., Reuter, R., and Teubner, U. (2012). Time-resolved measurements of shock induced cavitation bubbles in liquids. *Appl. Phys.* 108, 345–351. doi: 10.1007/s00340-012-5070-1

Kwak, H.-Y., and Kim, Y. W. (1998). Homogeneous nucleation and macroscopic growth of gas bubble in organic solutions. *Int. J. Heat Mass Transf.* 41, 757–767. doi: 10.1016/S0017-9310(97)00182-8

Lebedev, A. E., Kapranova, A. B., Meltser, A. M., Neklyudov, S. V., Serov, E. M., and Voronin, D. V. (2017a). *Design Features of the New Control Valves Direct-Flow Type*. Rostov-on-Don: Engineering Herald of Don (Inzhenernyy vestnik Dona). Available online at: http://www.ivdon.ru/uploads/article/pdf/IVD_31_lebedevN.pdf_64daa310a4.pdf (accessed February 28, 2020).

Lebedev, A. E., Kapranova, A. B., Meltser, A. M., Neklyudov, S. V., Serov, E. M., and Voronin, D. V. (2017b). Development of the design of a direct-flow control valve with an upper position of the locking organ. *Mod. High Tech.* 9, 48–52.

Lebedev, A. E., Kapranova, A. B., Meltser, A. M., Solopov, S. A., and Neklyudov, S. V. (2016). Analysis of devices for reducing pressure in control valves. *Mod. High Techn.* 8, 68–71.

Lebedev, A. E., Kapranova, A. B., Meltser, A. M., Solopov, S. A., Voronin, D. V., and Neklyudov, S. V. (2018). *Direct-Acting Control Valve*. Patent on the model 175446 Russian Federation, IPC F16K 1/12, F16K 47/14, F16K 3/24. Yaroslavl: Federal Service for Intellectual Property (Rospatent).

Lienhard, J. H., and Karimi, A. (1981). Homogeneous nucleation and the spinodal line. *J. Heat Transf.* 103, 61–64. doi: 10.1115/1.3244431

Misic, T., Najdanovic-Lukic, M., and Nesic, L. (2010). Dimensional analysis in physics and the Buckingham theorem. *Eur. J. Phys.* 31, 893–906. doi: 10.1088/0143-0807/31/4/019

Mokveld (2020). *Axial Flow Valves*. Available online at: https://mokveld.com/en/home (accessed January 26, 2020).

Peterman, C. P., and Keithahn, J. D. (1987). *Flow Control Apparatus*. Patent US 4635678. F16K 3/00, F16K 31/528, F16K 31/52, F16K 3/26, F16K 001/36; F16K 031/528. Houston, TX: United States Patent and Trademark Office (USPTO).

Plesset, M. S., and Chapman, R. B. (1971). Collapse of an initially spherical vapour cavity in the neighbourhood of a solid boundary. *J. Fluid Mech.* 47, 283–290. doi: 10.1017/S0022112071001058

Preston, T. J. (2018). *Valve*. KR20180055897A, F16K 3/26, F16K 3/26, F16K 3/314. Staffordshire: Korea Intellectual Property Office (KR).

Qian, J., Liu, B., Jin, Z., Zhang, H., and Lu, A. (2016). Numerical analysis of flow and cavitation characteristics in a pilot-control globe valve with different valve core displacements. *J. Zhejiang Univ. Sci. A* 17, 54–64. doi: 10.1631/jzus.A1500228

Qiu, C., Jiang, C.-H., Zhang, H., Wu, J.-Y., and Jin, Z. (2019). Pressure drop and cavitation analysis on sleeve regulating valve. *Processes* 7:829. doi: 10.3390/pr7110829

Qu, W., Tan, L., Cao, S., Xu, Y., Huang, J., and Xu, Q. (2015). Experiment and numerical simulation of cavitation performance on a pressure-regulating valve with different openings. *IOP Conf. Ser. Mater. Sci. Eng.* 4:72. doi: 10.1088/1757-899X/72/4/042035

Rudolf, P., Kubina, D., Kozák, J., Hudec, M., and Pochylý, F. (2017). Dynamics of the cavitating flow downstream of the orifice plate. *AIP Conf. Proc.* 1:1889. doi: 10.1063/1.5004367

Rust (2020). *Axial Valves*. Available online at: http://www.roost.ru/katalog/klapany/osevie_klapan/ (accessed January 26, 2020).

Seung, S., and Kwak, HY. (2017). Shock wave propagation in bubbly liquids at small gas volume fractions. *J. Mech. Sci. Technol.* 31, 1223–1231. doi: 10.1007/s12206-017-0221-2

Shin, T. S., and Jones, O. C. (1993). Nucleation and flashing in nozzles-1. A distributed nucleation model. *Int. J. Multiphase Flow* 19, 943–964. doi: 10.1016/0301-9322(93)90071-2

Sokolichin, A., Eigenberger, G., Lapin, A., and Lubbert, A. (1997). Dynamic numerical simulation of gas-liquid two-phase flows: Euler/Eler versus Euler/Lagrange. *Chem. Eng. Sci.* 52, 611–626. doi: 10.1016/S0009-2509(96)00425-3

Talis, E. (2020). Available at: https://www.talis-group.com/brands/erhard.html (accessed January 26, 2020).

Tang, T. F., Gao, L., Li, B., Liao, L., Xi, Y., and Yang, G. (2019). Cavitation optimization of a throttle orifice plate based on three-dimensional genetic algorithm and topology optimization. *Struct. Multidiscipl. Optimiz.* 60, 1227–1244. doi: 10.1007/s00158-019-02249-z

Volmer, V., and Weber, A. (1926). Keimbildung in uebersaetigen Daempfen. *Z. Phys. Chem.* 119, 277–301. doi: 10.1515/zpch-1926-11927

Weevers, H. H. (1982). *Control Valve*. Patent US4327757. F16K 47/14. Gouda: United States Patent and Trademark Office (USPTO).

Xu, S., Qiao, Y., Liu, X., Church, C. C., and Wan, M. (2015). "Fundamentals of cavitation," in *Cavitation in Biomedicine*, eds M. Wan, Y. Feng, and G. Haar (Dordrecht: Springer). doi: 10.1007/978-94-017-7255-6_1

Ziegler, F. (2019). *Piston Valve Controlled by Own Medium [Eigenmedium gesteuertes Ringkolbenventil]*. Patent DE102013108940B4 Germany, F16K 1/126. Mannheim: Patent and Trademark Office.

Conflict of Interest: SN, AM, and DV were employed by the company JSC Regulator (Yaroslavl, Russia).

The remaining authors declare that the research was conducted in the absence of any commercial or financial relationships that could be construed as a potential conflict of interest.

frontiers in Chemical Engineering

ORIGINAL RESEARCH
published: 07 April 2020
doi: 10.3389/fceng.2020.00002

Three Dimensional CFD Studies of a Solar Chimney: Effect of Geometrical Parameters and Diurnal Variations on Power Generated

Arijit A. Ganguli[1,2]* *and Sagar Deshpande*[2]

[1] School of Engineering and Applied Sciences, Ahmedabad University, Ahmedabad, India, [2] Department of Chemical Engineering, Institute of Chemical Technology, Mumbai, India

Solar power has gained particular importance in the current era due to a need of harnessing the biggest and cleanest source of energy, i. e., solar energy. One of the most innovative as well as simple technique to generate solar power is using a solar chimney. Solar chimney power plant, however, requires high investment costs and traditionally have been of very low efficiency. Mathematical and CFD models pose a good way to optimize performance of such kind of chimneys. Several factors affect the power generation from a solar chimney including geometric factors (like collector diameter, chimney height) and diurnal temperature variations. The challenge however lies in diurnal variation of temperatures and hence unstable power generation. In the present work, a pilot scale CFD model of solar chimney (of prototype of Manzanares Chimney, Spain, Haaf, 1984) was built and validated with experimental data and analytical models from the literature (∼ <10% deviation from experimental data). Subsequently, flow patterns were studied and a parametric study was carried out for the chimney for the key parameters, namely, chimney height, and collector diameter. For the first time effect of diurnal variations on the power generated was studied. With consideration of diurnal variations, power generation during night was found to be a linear function of chimney height and collector diameter; while, during day time, the power-generated increased exponentially with variation in collector diameter and chimney height.

Keywords: solar chimney, CFD, heat transfer, energy efficiency, mathematical modeling

OPEN ACCESS

Edited by:
José María Ponce-Ortega, Michoacana University of San Nicolás de Hidalgo, Mexico

Reviewed by:
Fabricio Nápoles, Michoacana University of San Nicolás de Hidalgo, Mexico
Carlos Rubio-Maya, Michoacana University of San Nicolás de Hidalgo, Mexico
Luis Fabián Fuentes-Cortés, Technological Institute of Celaya, Mexico

***Correspondence:**
Arijit A. Ganguli
ganguliarijit@gmail.com

Specialty section:
This article was submitted to Computational Methods in Chemical Engineering, a section of the journal Frontiers in Chemical Engineering

Received: *04 December 2019*
Accepted: *10 March 2020*
Published: *07 April 2020*

Citation:
Ganguli AA and Deshpande S (2020) Three Dimensional CFD Studies of a Solar Chimney: Effect of Geometrical Parameters and Diurnal Variations on Power Generated. Front. Chem. Eng. 2:2. doi: 10.3389/fceng.2020.00002

INTRODUCTION

Energy is one of the most important needs for the mankind. With conventional energy sources steadily depleting, economic and environmentally safe sustainable energy source needs to be found. The main sources of energy have been tabulated in **Table 1**. Clean energy in terms of electricity can be generated by using renewable sources like solar, biomass, wind etc. Solar energy is one of the untapped energy sources in countries (South East Asian countries like India, European countries like Spain, African countries etc.), which have enough amount of sunlight throughout the year and enough land to receive sunlight. India has been harnessing solar power extensively in the recent years. Many devices to harness the power of solar energy, such as, photovoltaic cells, concentrated troughs etc., have been used to tap the solar energy. Implementation of these devices, however,

TABLE 1 | Market share of various energy sources in India and their environmental significance.

Energy sources	Location	Market share (%)	Environmental significance
Coal power	Central India	59.8	Health hazards like lung diseases
Nuclear power	Western and Southern India	1.8	Waste handling, accident prone
Oil and gas	Western India	8	Emissions of SO_x, NO_x, particulates in mercury, greenhouse gases, contributions to regional haze
Hydropower	Northen, Eastern, and Southern India	14	High Initial Investments
Wind power	Western and Central India	9.2	High transmission costs
Biomass	Rural areas in India	2.6	Availability of biomass
Solar sources PV cells, troughs etc.	Rural areas in Eastern India	2.9	Low efficiency
Other sources	All over India	1.7	Lack of awareness

demands large amounts of land to be occupied. This means the land would be particularly barren land. A viable option is in which energy can be utilized along with cultivation occurring on the land. Such an objective can be to certain extend can be fulfilled by harnessing the concept of a solar chimney.

Schematic of a typical solar chimney is shown in **Figure 1**. Solar Chimney Power Plant works on the principle of natural convection based on the temperature gradient in the atmosphere and the chimney top. Also at the bottom of the chimney, solar collector absorbs solar radiations and stores the heat on natural ground. The radiation from the sun falls on the transparent cover (1). The cover is inclined and forms a cover on the natural ground (2) The air enclosed in the space (3) between (1) and (2) heats up with time. At the center of the cover lies a vertical cylindrical chimney (4) of height H and diameter D1. As temperature of the air enclosed in (3) increases, density difference between the air outside the cover (ambient air) also increases and the air enclosed in (3) and cold air gets sucked through (5). Hot air moves upward through the chimney causing an up-draft. While moving, air rotates the turbine (6) placed at the joint between the cover (2) and chimney (4). Turbine generates electricity by converting mechanical energy into electrical energy.

Due to large capital involved in building the solar chimney, experimental pilot set ups have limited scope. On the other hand, advanced CFD simulations can be proved to be better tool to optimize the performance of the existing solar chimneys as well as designing improved configurations. Moreover, with cost of computation coming down and computation power going up, advanced CFD simulations can be used for detailed studies. Nonetheless, experimental validation of these simulations are essential to ensure that required physics is captured in the model. This has been our motivation for the present work.

The present paper is described as follows: Section Literature Review covers the literature overview which includes experimental as well as theoretical attempts in this field. The objective of the present work is summarized in section Objective of Present Work in order to extend limitations from the previous models. Sections Mathematical modeling and Model Equations of Theoretical Models From Literature cover governing equations used for the CFD simulations. Results are illustrated in section Results and Discussion which incorporate, model validations as well as sensitivity studies for Indian conditions. Finally, we conclude the findings in section Conclusions.

LITERATURE REVIEW

Researchers over the last many years have worked on analysis of solar chimney for an effective source of power generation. Significant work has been done during the past 3 decades on the effectivity of solar chimney as a power generation source. We present only a few of them here in the context and alignment of the present work. **Table 2** presents some of the prominent experimental, analytical and CFD works. Research work has been done using experimental methods (Haaf, 1984; Zhou et al., 2007; Shahreza and Imani, 2015), analytical models (Padki and Sherif, 1989a,b, 1999; Pasumarthi and Sherif, 1998a,b; Bernardes et al., 2003; Dai et al., 2003; Pretorius and Kroger, 2006; Tingzhen et al., 2006; Koonsrisuk and Chitsomboon, 2009; Panse et al., 2011) and Computational Fluid dynamics (CFD) analysis (Ming et al., 2008; Fasel et al., 2012; Filkoski et al., 2013; Gholamalizadeh and Kim, 2014; Hassan et al., 2018).

The experimental work majorly refers to the solar chimney power plant in the Manzanares desert in Spain (capacity to generate power of 50 kW), which was built as a joint effort between German ministry and a Spanish utility company. Schlaich (1995) described the concept of solar chimney power plant. (Haaf, 1984) discussed the principle and construction of the power plant. Haaf (1984) also reported the design criteria and cost analysis of the Manzanares plant as well as experimental data of preliminary test results. Another important experimental work on a pilot plant was conducted by Zhou et al. (2007). Though the pilot plant was much smaller in size (capacity to generate power of 5W), objective was to study the temperature field across the entire plant. The authors tried to find the diurnal variation of temperature across the solar collector. Their experiments could provide key data on following two parameters: 1. Maximum temperature difference in the center of the solar collector and the air outside the solar collector. 2. Criteria for obtaining a steady power generation based on identification of a span in a day when steady air flow can be obtained (without any temperature inversion). Recently, Shahreza and Imani (2015) performed experimental and numerical simulations on a small scale model of solar chimney (Diameter of chimney = 16 cm and height = 150 cm while collector diameter = 92 cm. Authors used intensifiers to intensify the heat radiated from the sun. They also used air tanks to absorb the heat radiation reflected by the intensifiers to store the heat from radiations. Authors claimed to have obtained velocities of the order of

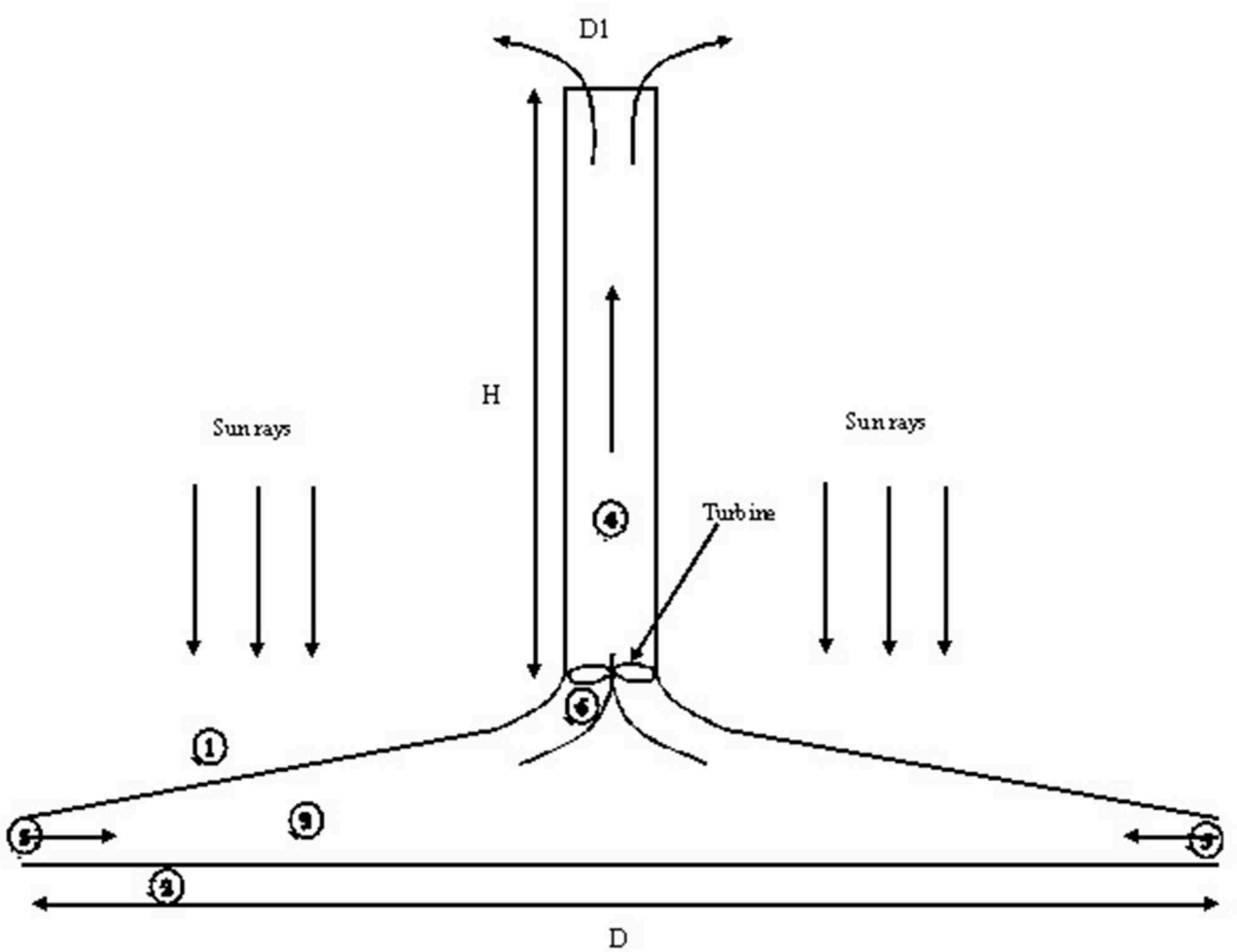

FIGURE 1 | Schematic of a typical solar Chimney.

5.12 m/s. Further, the authors performed CFD simulations for this experimental model and found good agreement with experimental results.

Padki and Sherif (1989a,b) developed one dimensional models to find thermodynamic aspects of solar chimney power plants. They also presented a mathematical model and validated the model with experimental results of Manzanares plant. Chitsomboon (2001) presented an analytical model for frictionless one dimensional flow using conservation equations of mass and energy integrated with ideal gas relations. Author also developed a two dimensional CFD code using implicit finite volume methodology. The results of analytical model and CFD model were compared for power predictions (both qualitative and quantitative) and good agreement was observed. The analytical model of Chitsomboon (2001) determined both flow and temperature at different parts of the solar power plant. Dai et al. (2003) performed a simple energy balance to find the efficiency of the solar collector as well as the overall efficiency of the solar chimney. They used the model to predict effect of parameters, like, solar irradiance, chimney height and collector diameter on power generation. They also carried out study on the yearly variation of power for three different regions in the northwestern region of China. Koonsrisuk and Chitsomboon (2013) developed an iterative mathematical model to predict the temperatures and pressures at different points across key points in the solar chimney. Model was used by the authors to predict pressure ratio (ratio of pressure drop between inlet and outlet of air from the chimney to the pressure drop at the turbine). Model was validated with the experimental results of Manzanares prototype Spain and sensitivity studies was performed using this model for power output as a function of mass flow rate variation, pressure ratio variation, for different heights, irradiances and collector diameters. Authors found that for the system with a constant driving pressure, optimum pressure ratio was 2/3, while for a non-constant driving force, the pressure ratio is a function of plant size and solar heat flux. Hence, they claimed that their model can suggest an appropriate plant size for serving

TABLE 2 | Literature review of the most prominent experimental, analytical and CFD research works.

References	Chimney Dimensions				Type of study	CFD details					Parametric studied	Assumptions	Limitations	Findings
	Collector diameter (m)	Height from ground (m)	Chimeny Diameter (m)	Chimney height (m)	Analyical/ Experimental/ CFD simulation	Turbulence model	Dimension (2D or 3D)	Grid details	Radiation model	Fluid properties constant or function of temperature				
Haaf (1984)	244	1.85	10	195	Experimental	NA	NA	NA	NA	Constant properties	Temperature distribution across the chimney and space between collector and ground		1	1
Dai et al. (2003)	500	2.5	10	200	Analytical	NA	NA	NA	NA	Constant properties	Chimney height, collector diameter and solar irradiance on power generation	1, 2, 3, 4, 5	2	2,3
Zhou et al. (2007)	10	0.8	0.3	8	Experimental	NA	NA	NA	NA	Constant properties	Temperature distribution across the chimney and space between collector and ground		3	4,5
Ming et al. (2008)	244	2	10	200	CFD analysis	Standard k-ε model	Two dimensional axisymmetric	Not provided	Not considered	Constant properties	Temperature, pressure and velocity distribution from ground layer to chiney inlet	1, 2, 3, 4	4	6, 7, 8
Koonsrisuk and Chitsomboon (2009)	100	2	4	100	CFD and analytical model	None	5 degree of 360 degree section (3D domain)	Tetrahedral grid, grid elements: $5x10^4$ to $2.5x10^5$	Details not provided	Buoyncy considered	Effect of chimney height and chimney radius on power generated	1, 2, 3, 4, 5	5, 6, 7	9
Fasel et al. (2012)	244	2	10	198	CFD simulations	Reynolds Stress Model	Axisymmetric 2D simulations	No details provided	Details not provided	Constant	Effect of chimney gap on power, nusselt number predictions,	1, 2, 3, 4, 5	8	10, 11, 12, 13

(Continued)

TABLE 2 | Continued

References	Chimney Dimensions				Type of study	CFD details					Parametric studied	Assumptions	Limitations	Findings
	Collector diameter (m)	Height from ground (m)	Chimeny Diameter (m)	Chimney height (m)	Analyical/ Experimental/ CFD simulation	Turbulence model	Dimension (2D or 3D)	Grid details	Radiation model	Fluid properties constant or function of temperature				
Filkoski et al. (2013)	100	2	top radius = 8.75 m; bottom = 6.25 m	100	CFD simulations	Realizable k-ε model	Three dimensional (3D)	276000 cells hexahedral mesh	Discrete ordinates (DO) model	Density, viscosity, specific heat and thermal conductivity as function of temperature	Effect of solar irradiation on power generated	1, 2, 3, 4, 5	9, 10	14
(Gholamalizadeh and Kim, 2014)	244	1.85	10	195	CFD simulations	Realizable k-ε model	Three dimensional (3D)	Intermediate Mesh with 0.9% deviation in velocity from fine mesh chosen	Discrete ordinates (DO) model	Constant properties	Effect of solar irradiation on temperature, velocity and pressure distribution	1, 2, 3, 4	11	15, 16, 17
Shahreza and Imani (2015)	92	110	16	150	Experimental and CFD simulations	Realizable k-ε model	3D simulation	382113 elements out of four hexahedral mesh	Not considered	Constant properties		1, 2, 3, 4, 5	12, 13	18, 19, 20, 21
Hassan et al. (2018)	244	Collector = 2 m; Chimney base =6	10	195	CFD simulations	Realizable k-ε model	3D simulation	Intermediate mesh in three mesh sizes	Discrete ordinates (DO) model	Constant properties	Effect of Chimney diverging angle and collecctor slope variation on chimney performance	1, 2, 3, 4, 5	14	22, 23

Findings: ***1.*** *First ever comprehensive experimental data for a prototype which has helped to predict theoretical models and CFD simulations for the last 3 decades.* ***2.*** *Development of an analytical model which can predict the performance of a solar power plant over the entire year.* ***3.*** *Case studies for different villages in China where the power plant can be implemented and provide uninterrupted cheap power supply.* ***4.*** *Transient temperature variation across the solar chimney from morning to evening in a day.* ***5.*** *The temperature difference is lowest in the morning (∼7K) due to temperature inversion and remains around 15 to 20 K during the rest of the day.* ***6.*** *Analysis of flow and heat transfer including energy storage layer.* ***7.*** *Radiation heat transfer is integrated in the boundary conditions for heat transfer.* ***8.*** *Storage of heat in energy storage layer increases with increase in radiation flux.* ***9.*** *Compared 5 theoretical models for predictions of power for variation in collector radius, distance of collector above the ground, chimney diameter and chimney height with CFD predictions was found to be the most reliable among all models* ***10.*** *CFD simulations for different scaled versions of Manzaranes prototype were made starting from scaling down to labscale model (1:250) and scaled up model version (5:1).* ***11.*** *Number of versions considered were 8 (1:250; 1:30; 1:10; 1:5; 1:2; 1:1; 2:1; 5:1).* ***12.*** *RSM model is considered for turbulence which is the best as compared to other turbulence models except Large eddy simulations and Direct numerical simulations.* ***13.*** *Temperature distributions have been evaluated for all scales for particular locations of chimney.* ***14.*** *Recommends to include heat accumulation strategies on the ground to increase overall plant efficiency.* ***15.*** *Comparison between one band and two band radiation models were performed and it was shown that the greenhouse effect has an important role in predicting characteristics of flow and temperature.* ***16.*** *The model predictions of velocity at the chimney inlet as well as the temperatures at the chimney inlet show good agreement with the Manzaranes plant data.* ***17.*** *The energy storage in the ground has been modeled extremely well.* ***18.*** *Use of intensifiers to intensify the heat radiation received from Sun.* ***19.*** *The authors have managed to get velocities at the inlet of 5.12 m/s in a small lab scale set-up which is remarkable* ***20.*** *The authors have also used heat storage material which helps in increase in performance of the model.* ***21.*** *The experimental model is supplemented by CFD simulations.* ***22.*** *Both velocity and temperature increases with increasing collector's slope due to enhanced heat transfer and mass flow rate.* ***23.*** *Higher collector slopes also deteriorate the smooth air flow by developing vortices and recirculation of air, which obstructs the air flow and may reduce the overall performance.*

Limitations: ***1.*** *No modeling effort has been suggested eg. Empirical correlation using the modeling data* ***2.*** *Temperature distribution inside the chimney predicted by the model is 20-25 K under-predicted than the experimental results of prototype of Manzaranes solar power plant.* ***3.*** *The model does not consider the contribution of energy storage to temperature distribution across the chimney* ***4.*** *Does not provide data on power generated during the day from the experimental facility.* ***5.*** *Turbulence models and radiation models have not been specified for CFD simulations.* ***6.*** *The CFD simulations are made for only 50 geometry instead of a full scale geometry.* ***7.*** *The models are compared with CFD predictions and not with experimental data.* ***8.*** *Axisymmetric simulations have been performed instead of full scale simulations.* ***9.*** *The article is limited to sensitivity of solar irradiance and does not speak on effect of chimney height, chimney diameter, angle of slope from ground or variation of diameter from top to bottom.* ***10.*** *No model for Storage of heat in energy storage layer is present* ***11.*** *The work is limited to model predictions for temperature and velocity distributions but not for effect of chimney height, chimney collector etc is not shown.* ***12.*** *Sensitivity analysis with respect to height of chimney and diameter of the collector has not been performed in the work.* ***13.*** *Gap from the ground is much higher than the tranditional solar chimneys and needs extensive amount of more studies on how it can be effectively utilized.* ***14.*** *Sensitivity analysis with respect to height of chimney and diameter of the collector has not been performed in the work.*

Assumptions: ***1.*** *The temperature of heat absorption layer (earth surface) is equal to the average air temperature in the solar collector.* ***2.*** *The air temperature increases along the flow direction (toward the center radially inward).* ***3.*** *Air follows the ideal gas law.* ***4.*** *The properties of air like density, specific heat are constant for the temperature difference considered in this work.* ***5.*** *B3Ground is at a certain temperature T1 and ambient temperature T2.*

electricity to each village, which would be feasible for the local government.

Several authors have performed CFD studies for solar chimney power plants mostly for the geometrical dimensions of Manzanares power plant and validated their model with experimental data of the plant. Ming et al. (2008) performed CFD simulations to understand flow and heat transfer across the solar chimney. Authors, however, considered ground as an energy storage layer. They presented conjugate numerical simulations of the energy storage layer, collector and chimney. They used the standard k-ε model for solving turbulence equations. Main focus of the study was on importance of energy storage layer in predicting the overall prediction of temperature distribution and performance of the plant. Sangi et al. (2011) also performed CFD simulations with energy storage layer and validated with plant data of Manzaranes plant. They tried to predict temperature pressure and velocity distributions with their models. Fasel et al. (2012) carried out CFD simulations to study the effect of distance of the collector from the ground on power input. They carried out extensive simulation work to understand the effect of scale (with reference to Manzanares pilot plant) on temperature distributions between ground and temperature cover, on the collector near to the chimney and on the ground. The scales ranged from scaling down 250 times the Manzanares plant to scaling up 5 times the Manzanares plant. They found that power varied very differently in case of smaller and larger scales and hence an optimum height for optimum power generated could not be obtained. They used 2D axisymmetric simulations using unsteady Reynolds Averaged Navier-Stokes Equations (RANS) to solve the turbulence. They also compared three different turbulence models like k-ε, k-ω, and RANS and found that RANS gave the best predictions. Deviations in the prediction of power output were attributed to the fluid dynamics in between the collector and ground. Filkoski et al. (2013) performed 3D CFD simulations for a solar chimney of collector radius of 100 m and height of 100 m, with the chimney radius increasing along its height the base being 6.25 to 10.5 m. The realizable k-ε model was chosen for turbulence formulation, while discrete ordinates (DO) model was considered for accounting for thermal radiations. Authors showed predictions of velocity and temperature patterns and recommended CFD as a powerful tool for analysis of solar chimney studies. They also stressed on a need to include heat accumulation methods, like, water pipes, water bags etc., on the ground so that considerable heat can be stored in the ground to enhance the temperature gradients at night. Authors, however, did not study the effect of diurnal variations on power generated. Gholamalizadeh and Kim (2014) performed CFD simulations for the Manzaranes prototype using the realizable k-ε model for turbulence parameters and DO model for radiation heat transfer. They captured the temperature profile of the ground, thermal efficiency of the collector and power generated and validated their model with experimental results of Manzaranes prototype. They also performed detailed analysis of the green-house effect causing depth of heat penetration in the ground and increase in mean ground temperature. This increase in mean ground temperature influenced the predicted heat storage of the ground. Authors were able to provide better predictions for temperature distributions than previous researchers and could also match the Manzanares experimental data very well. Hassan et al. (2018) performed 3D CFD simulations with energy storage layer of the ground. Authors varied the chimney diverging angle from 1 to 3° and collector slope 4 to 10°. They found that the diverging angle of 1° raises the velocity from 9.1 m/s to a remarkable value of 11.6 m/s, which is good for improving the performance of the chimney.

OBJECTIVE OF PRESENT WORK

The review of the current literature has shown that there are only a few experimental works for raw data. Most researchers have built analytical models and tried to validate their models with the help of the available experimental data. Further, the most used experimental data is the one of Haaf (1984) to validate the models. Several analytical and CFD studies have been also undertaken, the major focus however being the effect of the geometric parameters (like the angle of the slope of collector, diverging angle of the chimney from base to top, the height of the chimney and diameter of the collector) on the performance of the chimney. Some numerical studies have been performed on the energy storage methodologies to simulate ground as an energy storage and excellent results have been obtained. There has been considerable focus on understanding the temperature distribution from the ground to the collector which is extremely important. However, once the model is robust, there seems to be a need for doing sensitivity of variation of power to cover the diurnal variations. This is a challenging task since the ground temperature, the temperature distribution across the collector, the mean velocities at the chimney inlet, the temperature difference between ground and the collector, radiation intensity all are interconnected. Further, no CFD studies have been carried out for understanding the effect of diurnal variations on the power generated.

We present a Computational Fluid Dynamics (CFD) model to study the potential of Solar Chimney as a provider of clean energy source. The CFD model is validated with the experimental data of Haaf (1984), theoretical models of Dai et al. (2003) and Panse et al. (2011). The present work illustrates a comprehensive approach to carry out simulations for understanding the effect of geometric parameters as well as diurnal variations on the power generated. The major contributions are as follows:

1. The study of diurnal variations provides the entire research fraternity with having an insight on further studies to be carried out on how to operate the plant during the entire day/month/year for having a sustained power supply to the power grid.
2. An effort has been made to simulate full scale geometry, with optimized grid, not compromising on the near wall mesh and turbulence model selection.
3. The CFD model has been validated with experimental data as well as with analytical models before carrying out the sensitivity study. The present work provides us with a robust model which can be used to further optimize

TABLE 3 | Governing equations.

Continuity	$\frac{\partial \rho}{\partial t} + \nabla \cdot (\rho \langle u_k \rangle) = 0$
Momentum	$\frac{\partial (\rho \langle u_k \rangle)}{\partial t} + \nabla \cdot (\rho \langle u_k \rangle \langle u_k \rangle) = -\nabla \langle p \rangle + \nabla \cdot \bar{\tau}_k + \rho \vec{g}$ $\bar{\tau}_k = \mu_{eff} \left(\nabla \langle u_k \rangle + (\nabla \langle u_k \rangle)^T - \frac{2}{3} \mu_{eff} \nabla \cdot \langle u_k \rangle I \right)$
Turbulent kinetic energy	$\frac{\partial (\rho k)}{\partial t} + \nabla \cdot (\langle u_i \rangle \rho k) = \nabla \left[\left(\mu + \frac{\mu_t}{\sigma_k} \right) \nabla k \right] + G_k + G_b - Y_k$ Turbulent kinetic energy $G_k = \nu_t \left\| \overline{S} \right\|^2$ where $\left\| \overline{S} \right\| = \sqrt{2 \overline{S_{ijk} S_{ijk}}}$ and $\left\| \overline{S_{ijk}} \right\| = \frac{1}{2} \left(\frac{\partial u_r}{\partial z} + \frac{\partial u_z}{\partial r} + \frac{\partial u_\theta}{\partial z} + \frac{\partial u_z}{\partial \theta} + \frac{\partial u_r}{\partial \theta} \right)$ Generation of turbulence due to buoyancy $G_b = -\beta g \frac{\nu_t}{\sigma_t} \frac{\partial \langle T \rangle}{\partial z}$ Dissipation of this turbulence kinetic energy, $Y_k = \epsilon \rho_L \beta^*_\infty f_{\beta^*} k\omega$ where $\beta^*_\infty = 0.09$, $f_{\beta^*} = \begin{cases} 1, & \chi_k \leq 0 \\ \left[\frac{1+680\chi_k^2}{1+400\chi_k^2} \right], & \chi_k > 0 \end{cases}$ and $\chi_k = \frac{1}{\omega^3} \frac{\partial k}{\partial z} \frac{\partial \omega}{\partial z}$
Energy dissipation rate equation	$\frac{\partial (\rho \omega)}{\partial t} + \nabla \cdot (\langle u_i \rangle \rho \omega) = \nabla \left[\left(\mu + \frac{\mu_t}{\sigma_\omega} \right) \nabla \omega \right] + G_\omega - Y_\omega$ Production of ω, $G_\omega = \frac{\alpha_\infty}{\nu_t} G_k$ where $\alpha_{\infty,1}$ and $\alpha_{\infty,2}$ are constants. $\alpha_{\infty,1} = 1$, $\alpha_{\infty,2} = 0.52$ and $Y_\omega = \rho \beta_r \omega^2$
Energy	$\frac{\partial (\rho T)}{\partial t} + \nabla \cdot (\rho \langle u_i \rangle T) = \nabla \cdot \left(\frac{k_{eff}}{C_p} \left(\nabla \cdot \langle u_k T \rangle + (\nabla \cdot \langle u_k T \rangle)^T \right) \right)$

the chimney geometry for (a) effect of energy storage on power generated diurnally, (b) monthly/yearly variations by carrying out rigorous simulations with different temperature boundary conditions, (c) understanding the physics of flow and structures during the operation of the plant at steady and unsteady state conditions.

MATHEMATICAL MODELING

In this section, we describe the methodology used for the CFD simulations including assumptions considered, governing equations solved, turbulence model selected and convergence criteria set. The grid sensitivity study is also exemplified in this section.

Assumptions

1. The temperature of heat absorption layer (earth surface) is equal to the average air temperature in the solar collector.
2. The air temperature increases along the flow direction (toward the center radially inward).
3. Air follows the ideal gas law.
4. The properties of air like density, specific heat are constant for the temperature difference considered in this work.
5. Ground is at a certain temperature T1 and ambient temperature T2.

Governing Equations, Turbulence Models, and Boundary Conditions

The governing equations used for the computational domain are given in **Table 3**. Boundary conditions are as follows: The inlet was kept as pressure inlet with ambient temperature conditions. The walls of the collector were given radiation conditions using the Rosseland model. The other parameters were listed in **Table 3**. The outflow boundary condition was given for the outlet of the chimney. The vertical chimney walls were kept at ambient wall temperatures. The ground was assumed to be constant temperature boundary condition.

Grid Sensitivity

In the present work, the cylindrical chimney geometry was considered, and full scale geometry was used for grid generation. The hexahedral mesh was generated for the entire geometry with fine mesh near the walls. We managed to keep the cells to a lower value to improve the computational time to perform number of simulations. Therefore, the total computational time was reduced. Top and front view of the 3D mesh is depicted in **Figures 2A,B**. Grid independence was investigated by considering three different grid cases: (a) 710,000, (b) 750,000, and (c) 850,000 as shown in **Figure 3**. A non-uniform hexahedral grid was used with a finer grid near the duct (where turbine is placed) where high velocity gradients were more important as compared to other zones. Approximately 60% of the nodes were located in this region, and 40% were located in the rest of the region where (according to the experimental results) the fluid was essentially quiescent and the temperature varied linearly along the length i.e., radius of the collector circle. The Y+ near the walls were kept <30 so that any effect of turbulence near wall could be captured.

For these three cases, we compared the results of mean quantities at different positions. All the chosen grids predicted mean flow patterns effectively, but for further simulations a grid size of 750,000 cells were used. Minor differences were observed between 750,000 and 850,000. However, these were found to be within the (5% average error).

Method of Solution

The continuity, momentum, energy, and turbulence equations described in **Table 3** (specify equation no.) were solved using commercial flow simulation software ANSYS FLUENT 17[1]. The SST k-ω turbulence model was used for the turbulence associated with the flow. The convergence criteria for sum of normalized residues was set to 1×10^{-4} for continuity as well as for momentum, 1×10^{-6} for energy equations, while 1×10^{-5} for turbulence equations. The under-relaxation

[1] ANSYS FLUENT 17.0 Theory Guide. ANSYS, Inc.

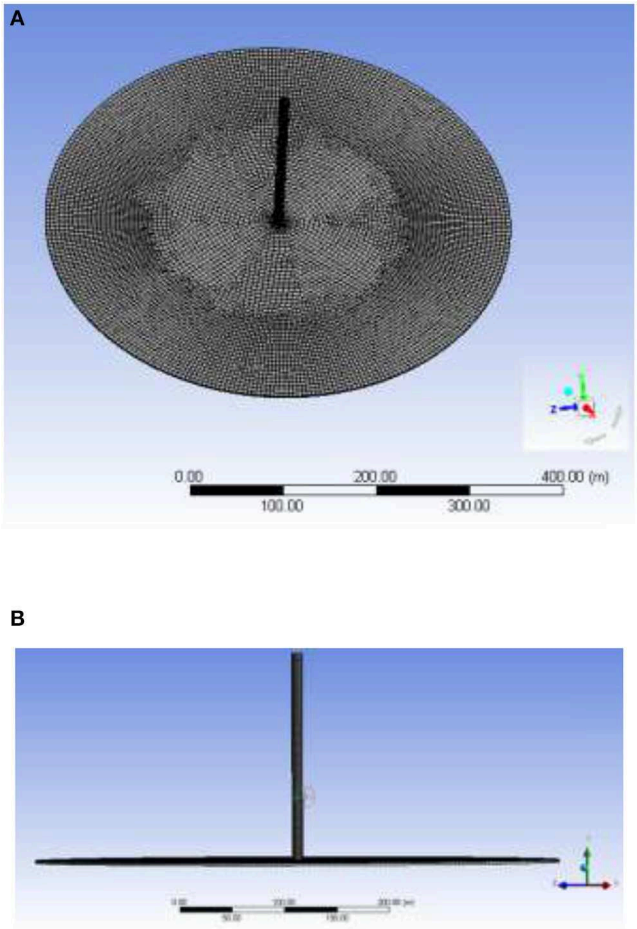

FIGURE 2 | Mesh used for the 3D geometry **(A)** Top view and **(B)** Front view.

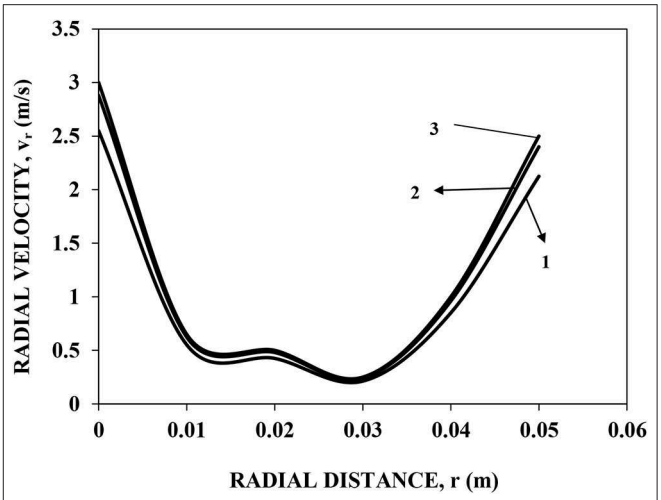

FIGURE 3 | Grid sensitivity 1. 701000 nodes, 2. 750000 nodes, and 3. 850000 nodes.

parameters were set to 0.3 for pressure, 1 each for density, energy and body forces, 0.7 for momentum equations, 0.8 for turbulence equations and 0.7 for energy equations. In this study, a segregated solver was employed for obtaining the solution of momentum equations. The momentum, energy and turbulence equations were discretized using the Second-Order Upwind Scheme (SOUS) and for pressure equation, PRESTO scheme was used. Note that SOUS scheme in the commercial software Ansys FLUENT 17[1] prevents numerical diffusion while taking care of the fact that it does not dampen the disturbances which cause the instability. Thus, this scheme ensured spatial accuracy in the simulations.

Turbulence Model Selection

The turbulence equations were solved using the SST k-ω model. The present problem under consideration has adverse pressure gradients at the node where there is an updraft of air. Due to adverse pressure gradients, the resolution at the near wall and the selection of turbulence model would be crucial for the energy dissipation predictions. Further, flow separation occurs since there is sudden expansion and recirculation is seen at the central portion. RNG k-ε has been used widely in literature for turbulence. Though RNG k-ε model is good for separated flows the near wall predictions for adverse pressure gradients needs attention in the problem at hand. We performed a study for comparing the performance of the two turbulence models for radial distribution of centerline velocities (As shown in **Figure 4C** to see centerline position). **Figure 4A** shows the variation of radial velocity for both turbulence models. A zoomed version of the near wall velocity is shown in **Figure 4B**. Clearly, there is slight deviation (∼2–3%) between velocities predicted by RNG k-ε and SST k-ω models.

MODEL EQUATIONS OF THEORETICAL MODELS FROM LITERATURE

Theoretical Model of Dai et al. (2003)

The Equations 1 to 5 have been reproduced from Dai et al. (2003). The efficiency of solar collector was calculated using the formulation of Dai et al. (2003):

$$\eta_{coll} = (\tau\alpha) - \frac{\beta \Delta T_{\alpha}}{G} \tag{1}$$

The mechanical power taken up by the turbine is given by

$$P_{mech} = \frac{2}{3}\eta_{coll}\frac{g}{C_p T_0} H A_{coll} G \tag{2}$$

The electrical energy is given by

$$P_{mech} = \frac{2}{3}\eta_{coll}\eta_{mech}\frac{g}{C_p T_0} H A_{coll} G \tag{3}$$

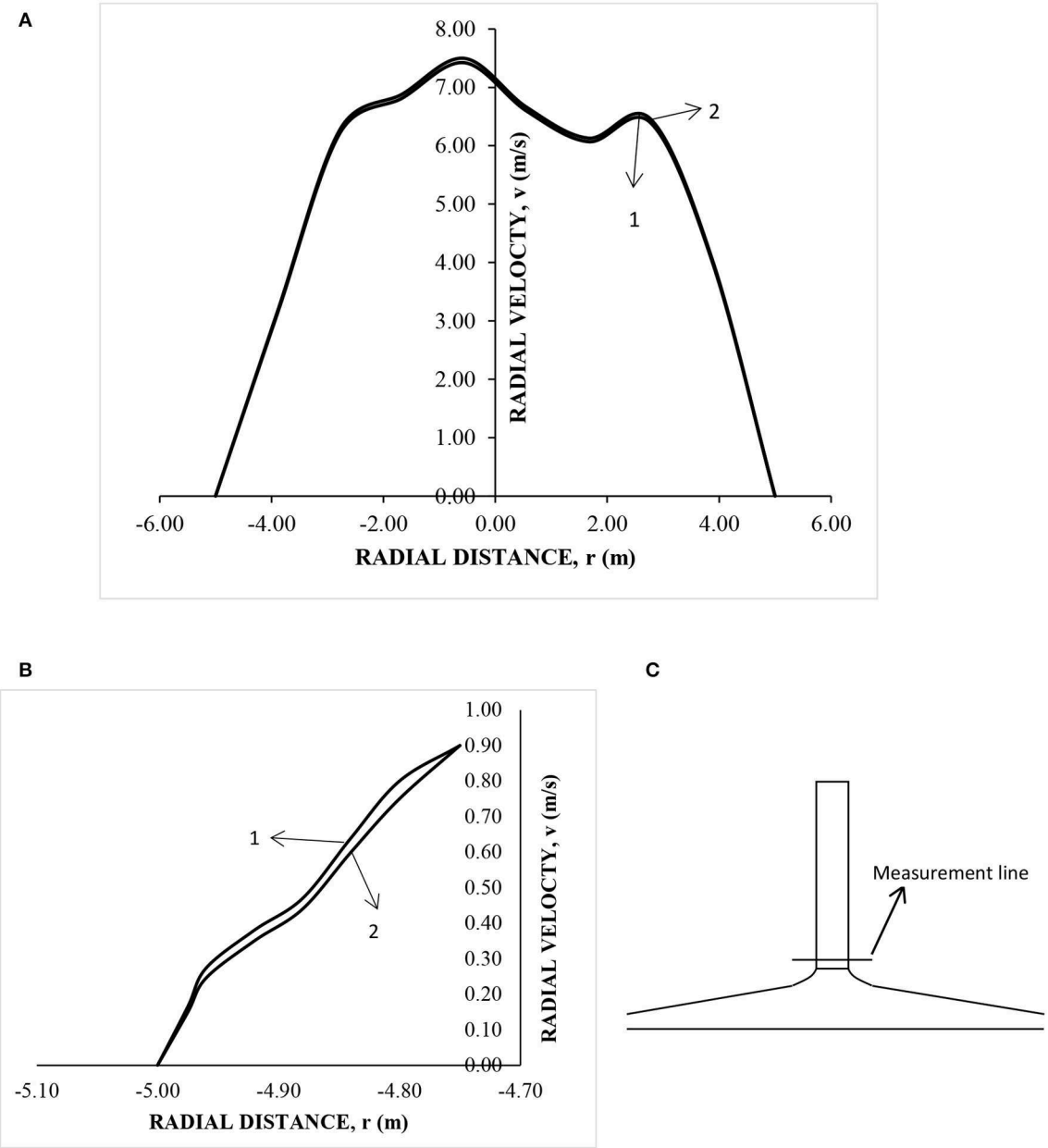

FIGURE 4 | Comparison of velocity for selection of turbulence model **(A)** Velocity profiles over the measurement line, **(B)** Near wall velocity profiles, and **(C)** Position of line selected for velocity profile (1) SST k-ω model (2) RNG k-ε model.

The total power contained in the flow is given by

$$P_t = \frac{gH}{T_0} V_c \Delta T A_c \tag{4}$$

$$where\ V_c = \frac{(\tau\alpha)\, A_{coll} G - \beta \Delta T_\alpha A_{coll}}{\rho_{coll} A_c C_P \Delta T} \tag{5}$$

Temperature difference is the one between ground and the collector.

Theoretical Model of Panse et al. (2011)

Panse et al. (2011) have considered the equation of complete energy balance to find the kinetic power of the emerging air draft. The energy balance given by them is given by:

Amount of solar energy absorbed = Change in enthalpy of air + Heat losses to the surroundings + Frictional energy loss + change in pressure energy + change in potential energy + change in kinetic energy.

Since the solar chimney is inclined, the area of the solar collector considered by Panse et al. (2011) has been mapped as

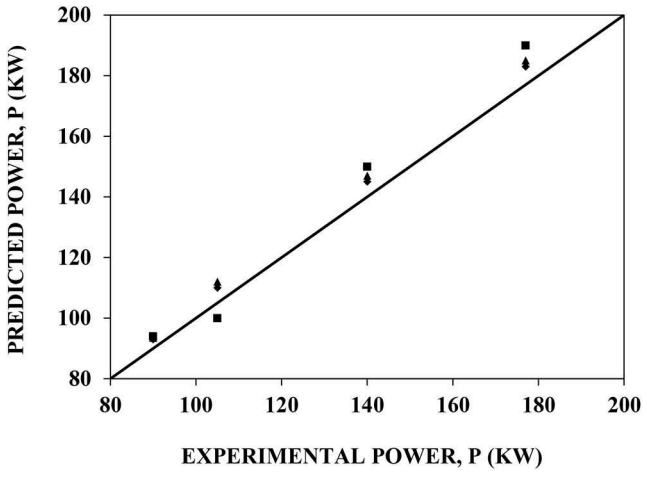

FIGURE 5 | Parity plot of predicted power with experimental power. ■ CFD ▲ Theoretical model by Dai et al. (2003) ♦ Theoretical model by Panse et al. (2011).

TABLE 4 | Dimensions and parametric specifications of the Solar Chimney for Manzaranes plant and present model.

Parameters	Dimensions
(A) Collector specifications for model of Dai et al. (2003)	
Collector diameter	244 m
Chimney height	195 m
Chimney diameter	10 m
Distance from ground to cover	2.5 m
Collector efficiency factor	0.8
Heat loss coefficient	10
Transmittance	0.65
Absorptivity	0.2
(B) Chimney specifications for present model	
Chimney height	200 m
Chimney diameter	10 m
Collector diameter	500 m
Annular gap (Distance from ground to cover)	2.5 m

per Manzanares collector area. The collector area of Panse et al. (2011) is 50,000 m^2, whereas collector area of Manzanares is 45,216 m^2. Further, the overall deviation of Panse et al. (2011) from that of experimental data of Manzanares was around 5% (under-prediction) (**Figure 5**) based on power output ($P = 47.5$ kW as compared to 50 kW as per experimental data).

RESULTS AND DISCUSSION

In this section, the results of the CFD predictions are presented. The CFD model was first validated with the experimental results of Haaf (1984) as well as was compared with findings of the theoretical models (Dai et al., 2003 and Panse et al., 2011). The predictions were further illustrated in the form of Flow patterns (velocity and temperature contours) of the solar chimney. For prediction of temperature and flow patterns a lower irradiance of 200 W/m^2 was selected. The study was further extended to analyze the sensitivity of key parameters namely, height, and diameter of the chimney. For sensitivity with height and diameter, we envisage the areas in India with higher irradiance and hence, 1,000 W/m^2 was selected. The study also involved validation of model taking into account the diurnal variation of power. For diurnal variations, temperature difference between collector and ground was given as boundary condition to predict velocities at the chimney. This consideration was found to be a better way to predict diurnal variations since variation of solar irradiance over 24 h might be difficult to assume.

Model Validation

A parity plot is presented in **Figure 5**, which shows the predictions of maximum and minimum power using CFD and the theoretical models (Dai et al., 2003 and Panse et al., 2011) against the experimental results of Haaf (1984). The CFD model shows around 7% deviation from the experimental results, while the theoretical model by Panse et al. (2011) shows around 5% deviation and the theoretical model of Dai et al. (2003) also shows around 7% deviation. The theoretical models as well as CFD simulations have shown comparable predictions of power. However, theoretical models have a limitation that they do not capture asymmetric effects. As a results, reliability of predictions over diverse conditions as well as different scales of operations would be limited in the case of theoretical models. CFD simulations, on the other hand, captures these dynamics in to their governing equations. Turbulence generated in the central core, where turbine is placed, become more and more critical as size of the Chimney increases and this aspect is captured effectively in the CFD models. Additionally, detailed flow as well as turbulence information is required for designing light weight turbines, essential for optimum translation of kenetic energy into electrical energy.

Flow Patterns

Domain selected for performing the CFD simulations was of Dai et al. (2003). The domain chosen is that as specified in **Table 4**. The collector diameter is twice that of Manzaranes prototype. The irradiance for the simulations was selected to be 200 W/m^2. In **Figure 6**, we show velocity contours in the domain under consideration. As observed in the figure, velocities at the far end of the chimney diameter (the entry of air) are higher. As the air moves inside horizontally toward the vertical pipe (chimney) the air velocity is lower than the entry air. It is evident that there is expansion along the collector diameter across the horizontal distance. Due to this, the pressure increases and velocities are lower as expected from Bernoulli's equation. Subsequently, as the air approaches near the central zone, velocities increase as the overall area starts converging. When air reaches the node (where the turbine is placed), there is a sudden decrease in pressure resulting in sharp increase in velocity to a maximum. The air moves up with these velocities outwards in the vertical direction. Maximum velocities of the order of 13 m/s were observed. **Figures 6A–C** denote

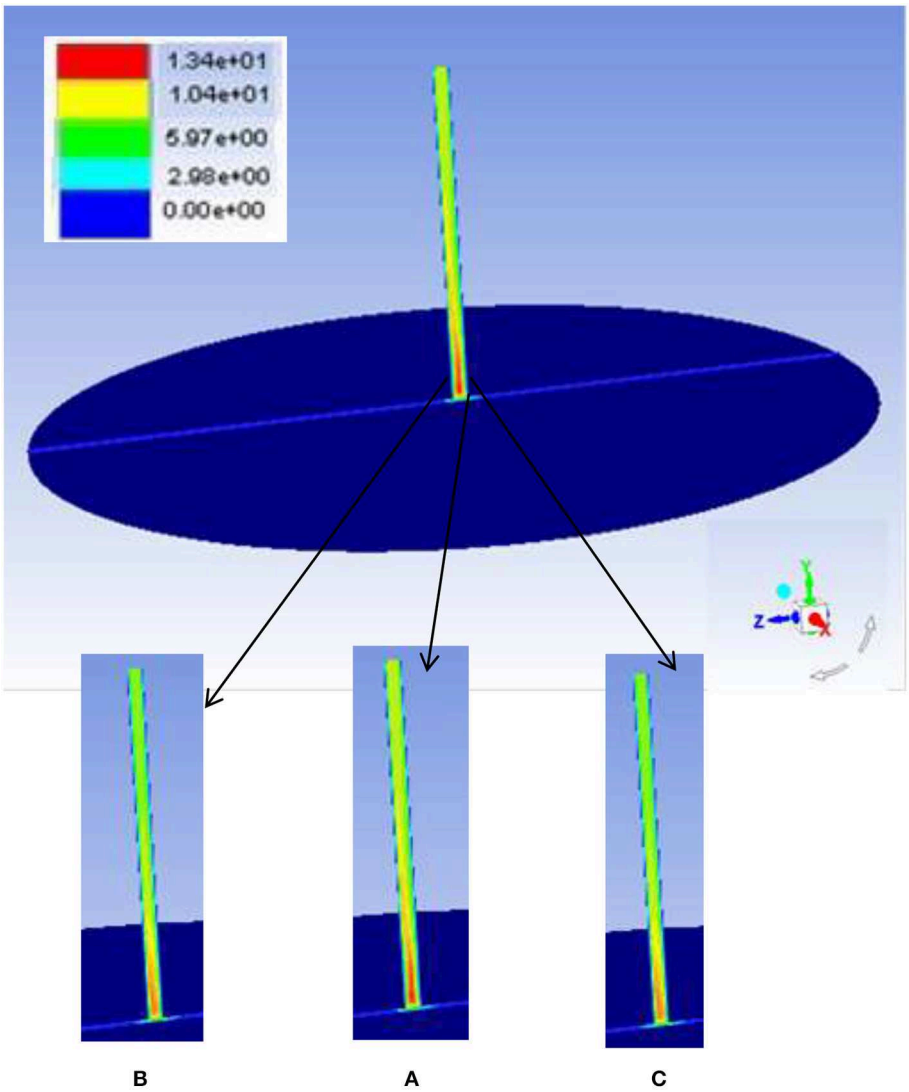

FIGURE 6 | Velocity contours for the solar chimney considered as per Manzaranes geometry **(A)** Central plane, **(B)** $r = 4$ m, and **(C)** $r = -4$ m.

the 3-dimensional effect of the chimney. **Figure 6A** shows the velocities at the centerline (r = 0) of the chimney and are the highest (∼12 m/s), while **Figures 6B, C** are r = 4 m and r = −4 m, respectively. The maximum velocities are found to decrease to around 11.25 m/s and 12.5 m/s, respectively. This trend also highlights the importance of full scale 3D simulations instead of sectionized simulations or axisymmetric simulations. Mean average velocities across the plane are around 12 m/s.

Figure 7 shows temperature contours of the entire collector surface, and also depicts the vertical centerline temperatures (which includes the temperatures of the space between ground and glass surface as well as the chimney). Clearly, the temperatures increase from 296 to 310 K as we reach the chimney inlet (as can be seen in the zoomed in figure).

The predicted results of both velocity and temperature were in good agreement with Ming et al. (2008) ($v = 10$ m/s; $\Delta T = 4.5$ K), which they have predicted for an irradiance of 200 W/m^2 and for a chimney whose collector is half as than that of the current chimney. The temperature difference is found to be around 10 K while mean velocities were found to be around 12 m/s. Higher temperature differences and velocities as compared to Ming et al. (2008) obtained in the present simulation is attributed to the larger collector area.

Effect of Chimney Height and Collector Diameter on Power Generated

To study the effect of height and collector diameter on the performance of the chimney in terms of power generated two cases have been considered namely (a) constant collector

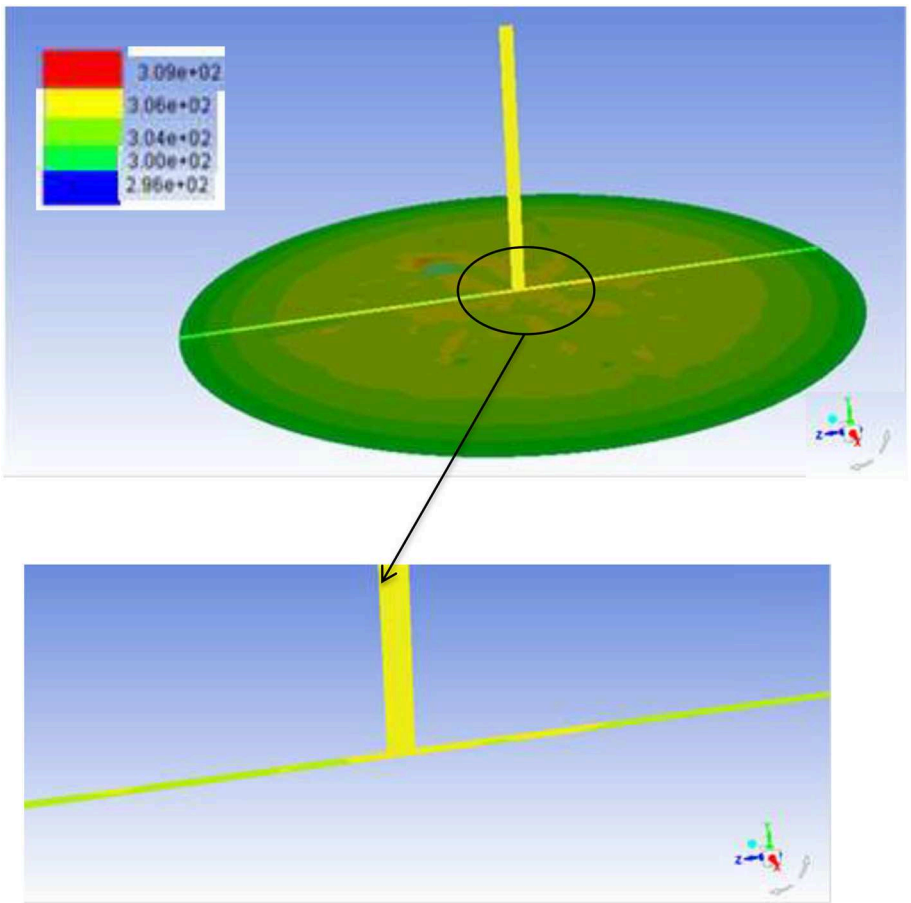

FIGURE 7 | Temperature contours for the solar chimney considered as per Manzaranes geometry.

diameter D = 500 m with variation in height from 50 to 200 m; (b) constant height H = 200 m with variation in diameter from D = 150 m to 500 m. The irradiance for the simulations was selected to be 1,000 W/m^2. CFD simulations were carried out to understand the effect of chimney height on the generated power. The collector area was considered constant (D = 500 m) for these simulations. As observed, the power generated increased exponentially with chimney height (**Figure 8**). Simulations were carried for the height up to 200 m. The predicted power for a height of 200 m was 370 KW. Further, the power generated was also dependant on the collector area. **Figure 9** shows that the predicted power increases as the collector area increases in an exponential manner. The trends were similar to studies of Koonsrisuk and Chitsomboon (2009). A maximum power up to 450 KW can be obtained with a collector diameter of 500 m. The exponential increase in power was seen for both increase in chimney height with constant collector diameter as well as increase in collector diameter with increasing chimney height. This increase could be attributed to the increase in central velocity at the node for both the cases. From Equation 4, total power was observed to be directly proportional to the velocity and since the velocity increases exponentially the power also increases exponentially. The values of power generated were much higher due to the high temperature differences considered and therefore, higher velocities at chimney inlet were predicted. It was evident from the predictions that solar irradiation during the day was much higher for such power generation to occur.

Diurnal Variations of Power Generated

In countries which receive considerable sunlight throughout the year, the maximum and minimum temperatures throughout 24 h may fluctuate within 25°C. Hence, CFD simulations were performed with temperature of 45°C during the day and 20°C during the night. The temperatures were chosen in close resemblance to places in India, which receive the most sun radiations across the year (Deccan Plateau). The solar irradiance was chosen as 1,000 W/m^2 during the day. Though the ambient temperature during night might be low, the stored heat of the ground would keep a surface temperature higher than the ambient temperature. Hence, suitable temperature difference has been taken accordingly. Parameters chosen for the variation are the chimney height and the total collector diameter. A trend of the predictions were similar to those described in the previous section (**Figures 10**, **11**) especially during the day time. This trend indicates that the power generated increases exponentially with

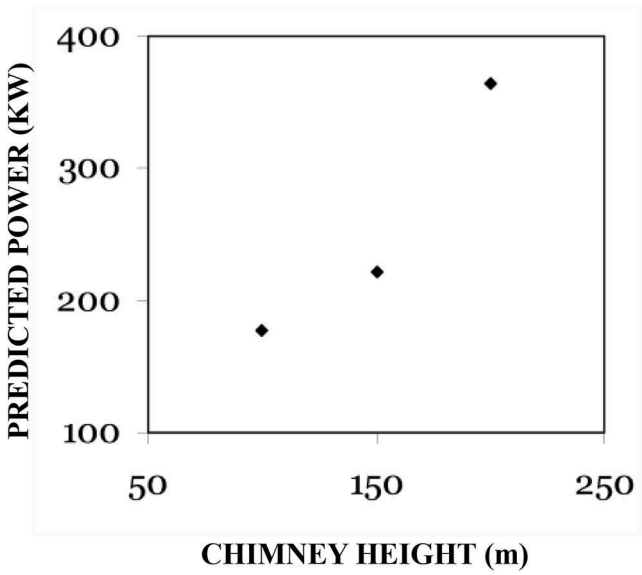

FIGURE 8 | Variation of predicted power with Chimney height.

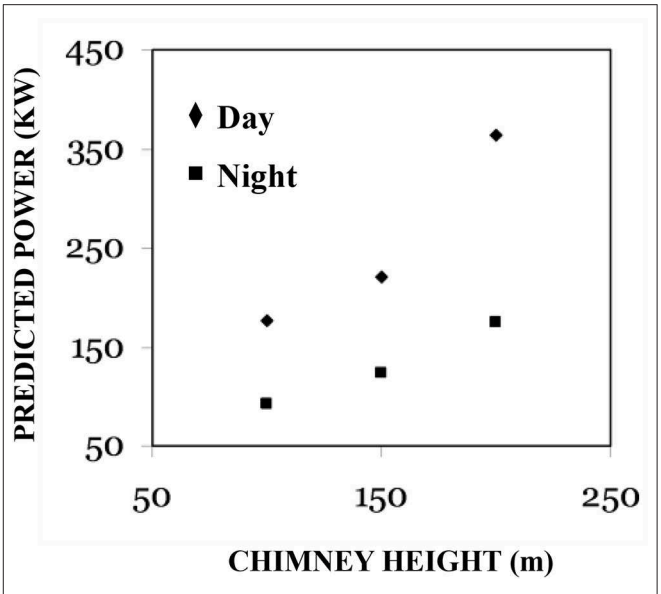

FIGURE 10 | Diurnal variation of predicted power with Chimney height.

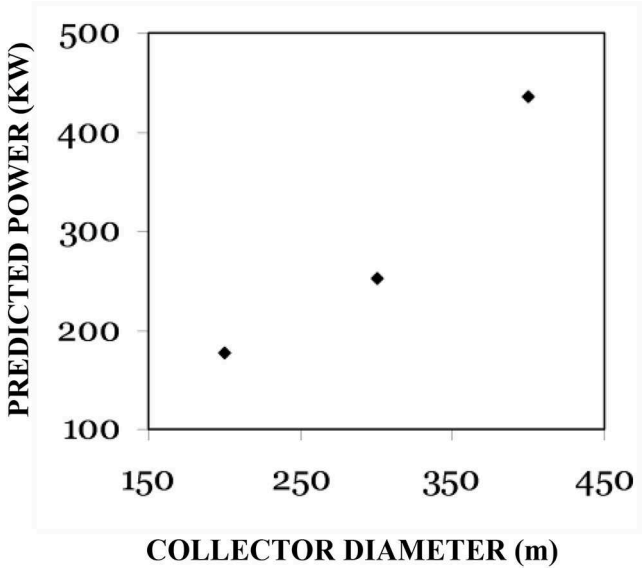

FIGURE 9 | Variation of predicted power with Collector diameter.

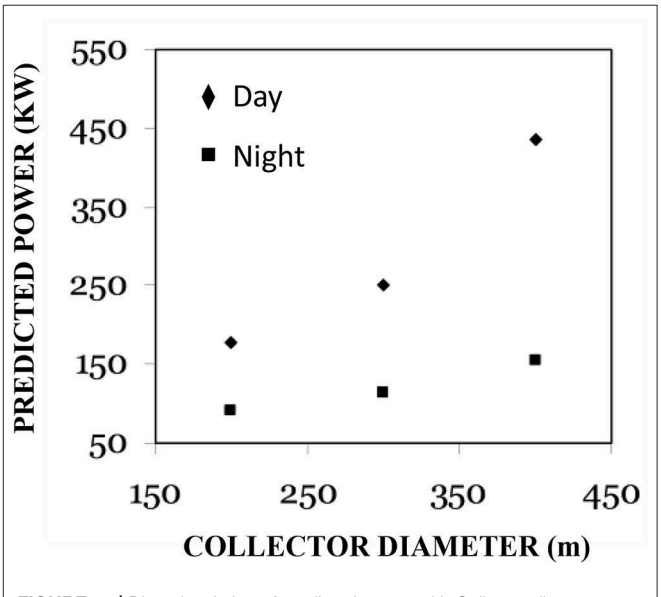

FIGURE 11 | Diurnal variation of predicted power with Collector diameter.

increase in chimney height and collector diameter. However, during the night, increase in the predicted power is marginal with an increase in either the collector diameter or chimney height. Interestingly, the increase in power generated for increase in height during night time is better than the increase in collector diameter.

CONCLUSIONS

Solar Chimney is one of the unexplored areas in the possible option in the field of renewable solar energy utilization. CFD can prove to be a useful tool to build confidence in the design and implementation of a solar chimney. Hence, a CFD model has been developed for a case in the literature. The model was validated with the experimental data in the literature and a good agreement was found. Flow patterns in the solar chimney suggested that peak velocities up to 11 m/s can be obtained for the temperature and dimensions of the chimney under consideration. A parametric study was performed for the solar chimney to assess overall power generated for two combinations, (a) by varying the height of the chimney ($H = 50$ to 200 m) at a constant collector diameter of 500 m and (b) by varying the collector diameter from 150 to 500 m for a constant height of

200 m. It was observed that for both cases the power increases exponentially as the collector diameter increases. This can be attributed to increase in central velocity at the chimney inlet where an updraft is experienced.

Another important aspect regarding prediction of power during the diurnal variations was attributed in the present paper. An important conclusion from the predicted results can be drawn that the increase in power in the night is marginal when collector diameter is increased for a fixed height. Variation of height for a fixed collector diameter gives a better trend of increase in power. The overall conclusion would be to increase the height keeping a standard collector diameter. Secondly, ways and means to find materials to store heat during the day time for the night time would help maintain the consistency in power generation over entire 24 h cycle and reduce uncertainty. As seen in literature, survey researchers have been trying to use heat storage materials and perform simulations for day time and improve the power generation. The present work actually also emphasizes that conditions during the night needs to be emphasized to see the effect of heat storage materials on the performance of power generated during night time.

DATA AVAILABILITY STATEMENT

The datasets generated for this study are available on request to the corresponding author.

AUTHOR CONTRIBUTIONS

AG: conceptualization, methodology, data curation, investigation, writing original draft, writing, review, and editing. SD: conceptualization, investigation, and review.

ACKNOWLEDGMENTS

The authors would like to acknowledge the inputs provided by Professor A. B. Pandit during this work.

REFERENCES

Bernardes, M. A., dos, S., and Weinrebe, A., Voß, G. (2003). Thermal and technical analyses of solar chimneys. *Solar Energy* 75, 511–524. doi: 10.1016/j.solener.2003.09.012

Chitsomboon, T. (2001). A validated analytical model for flow in solar chimney. *Int. J. Renew. Energy Eng.* 3, 339–346.

Dai, Y. J., Huang, H. B., and Wang, R. Z. (2003). Case study of solar chimney power plants in Northwestern regions of China. *Renew. Energy* 28, 1295–1304. doi: 10.1016/S0960-1481(02)00227-6

Fasel, H., Shams, E., and Gross, A. (2012). "CFD analysis for solar chimney power plants," in *9th International conference on Heat Transfer Fluid Mechanics and Thermodynamics* (Malta).

Filkoski, R. V., Stojkovski, F., and Stojkovski, V. (2013). "A CFD study of a solar chimney power plant operation," in *Proceedings of SEEP 2013* (Maribor).

Gholamalizadeh, E., and Kim, M.-H. (2014). Three-dimensional CFD analysis for simulating the greenhouse effect in solar chimney power plants using a two-band radiation model. *Renew. Energy* 63, 498–506. doi: 10.1016/j.renene.2013.10.011

Haaf, W. (1984). Solar chimneys, Part II: Preliminary test results from the Manzanares pilot plant. *Int. J. Solar Ener.* 2, 141–161. doi: 10.1080/01425918408909921

Hassan, A., Ali, M., and Waqas, A. (2018). Numerical investigation on performance of solar chimney power plant by varying collector slope and chimney diverging angle. *Energy* 142, 411–425. doi: 10.1016/j.energy.2017.10.047

Koonsrisuk, A., and Chitsomboon, T. (2009). Partial geometric similarity for solar chimney power plant modeling. *Solar Energy* 83, 1611–1618. doi: 10.1016/j.solener.2009.05.011

Koonsrisuk, A., and Chitsomboon, T. (2013). Mathematical modeling of solar chimney power plants. *Energy* 51, 314–322. doi: 10.1016/j.energy.2012.10.038

Ming, T. Z., Liu, W., Pan, Y., and Xu, G. L. (2008). Numerical analysis of flow and heat transfer characteristics in solar chimney power plants with energy storage layer. *Energy Conver. Mange.* 49, 2872–2879. doi: 10.1016/j.enconman.2008.03.004

Padki, M. M., and Sherif, S. A. (1989a). "Solar chimney for medium-to-large scale power generation," in *Proceedings of the Manila International Symposium on the Development and Management of Energy Resources,* Vol. 1 (Manila), 423–437.

Padki, M. M., and Sherif, S. A. (1989b). "Solar chimney for power generation in rural areas," in *Seminar on Energy Conservation and Generation through Renewable Resources* (Ranchi), 91–96.

Padki, M. M., and Sherif, S. A. (1999). On a simple analytical model for solar chimneys. *Int. J. Energy Res.* 23, 345–349. doi: 10.1002/(SICI)1099-114X(19990325)23:4<345::AID-ER485>3.0.CO;2-Z

Panse, S. V., Jadhav, A. S., Gudekar, A. S., and Joshi, J. B. (2011). Inclined solar chimney for power production. *Energy Conver. Manage.* 52, 3096–3102. doi: 10.1016/j.enconman.2011.05.001

Pasumarthi, N., and Sherif, S. A. (1998a). Experimental and theoretical performance of a demonstration solar chimney model - part I: mathematical model development. *Int. J. Energy Res.* 22 277–288. doi: 10.1002/(SICI)1099-114X(19980310)22:3<277::AID-ER380>3.0.CO;2-R

Pasumarthi, N., and Sherif, S. A. (1998b). Experimental and theoretical performance of a demonstration solar chimney model - part II: experimental and theoretical results and economic analysis. *Int. J. Energy Res.* 22 443–461. doi: 10.1002/(SICI)1099-114X(199804)22:5<443::AID-ER381>3.0.CO;2-V

Pretorius, J. P., and Kroger, D. G. (2006). Solar chimney power plant performance. *J Solar Energy Engg.* 128, 302–311. doi: 10.1115/1.2210491

Sangi, R., Amidpour, M., and Hosseinizadeh, B. (2011). Modeling and numerical simulation of solar chimney power plants. *Solar Energy* 85, 829–838. doi: 10.1016/j.solener.2011.01.011

Schlaich, J. (1995). *The Solar Chimney: Electricity From the Sun*. Geislingen: Axel Menges.

Shahreza, A. R., and Imani, H. (2015). Experimental and numerical investigation on an innovative solar chimney. *Energy Conserv. Manage.* 95, 446–452. doi: 10.1016/j.enconman.2014.10.051

Tingzhen, M., Wei, L., and Guoliang, X. (2006). Analytical and numerical investigation of the solar chimney power plant systems. *Int J. Energy Res.* 30, 861–873. doi: 10.1002/er.1191

Zhou, X., Yang, J., Xiao, B., and Hou, G. (2007). Experimental study of temperature field in a solar chimney power setup. *Appl. Ther. Eng.* 27, 2044–2050. doi: 10.1016/j.applthermaleng.2006.12.007

Conflict of Interest: The authors declare that the research was conducted in the absence of any commercial or financial relationships that could be construed as a potential conflict of interest.

NOMENCLATURE

A_{coll}	Solar collector area (m^2)
C_P	Specific heat of fluid (kJ m^{-2})
D	Collector Diameter (m)
D1	Chimney diameter (m)
f_β	Constant as in **Table 3**
G	Solar irradiance (W/m^2)
G_b	Generation of turbulence due to buoyancy (m^4 s^{-1})
G_k	Generation of turbulence kinetic energy due to mean velocity gradients ($kg.m^{-1}s^3$)
G_ω	Production of ω ($kgm^{-1}s^3$)
g	Gravitational constant (m s^{-2})
H	height of the chimney (m)
P_t	Total power or useful energy contained in the flow (W)
A_c	Cross sectional area of the solar chimney (m^2)
T_0	Ambient temperature (K)
I	Turbulence intensity (%)
k	Turbulent kinetic energy per unit mass (m^2 s^{-2})
k_{eff}	Effective thermal conductivity (W m^{-1} K^{-1})
l_i	Integral length scale (m)
$\dot{m}$	Mass flow rate of hot air passing through the solar chimney(kg s^{-1})
P_{mech}	Mechanical power of the turbine (W)
$\lvert\overline{S}\rvert$	Mean strain rate (s^{-1})
$\overline{S_{ij}}$	Strain rate (s^{-1})
T	Temperature (K)
ΔT	Temperature rise between collector inflow and outflow
ΔT_a	Temperature difference between the heat absorption layer and the ambient air
$\langle \Delta T \rangle$	Average temperature driving force (K)
t	Time (s)
u	Velocity component (m s^{-1})
u_r	Mean radial velocity, (m s^{-1})
u_z	Mean axial velocity, (m s^{-1})
$\langle u \rangle$	Time averaged of velocity (m s^{-1})
u_θ	Mean annular velocity, (m s^{-1})
v_c	Central velocity used in Equation 5 (m s^{-1})
V	Mean axial velocity (m s^{-1})
Y_k	Dissipation of turbulent kinetic energy (s^{-1})
Y_ω	Dissipation of turbulent kinetic energy in ω equation
z	Any distance along the length of rectangular tank (m)
Greek symbols	
$\alpha_{\infty,1}$	Constant in Energy dissipation rate equation for production of ω
$\alpha_{\omega,2}$	Constant in Energy dissipation rate equation for production of ω
α_ω	Constant in Energy dissipation rate equation for production of ω
β	Thermal expansion coefficient (K^{-1})
β_r	Constant as in **Table 3**
β^*_∞	Constant as in **Table 3**
η_{coll}	Solar collector efficiency
η_{mech}	Mechanical efficiency of turbine
$\tau\alpha$	Effective product of transmittance and absorbance
ρ	Density of fluid (kg m^{-3})
Δ	Difference in a quantity e.g., Temperature
ε	Turbulent energy dissipation rate per unit mass (m^2 s^{-3})
λ	Latent heat of vaporization (J kg^{-1})
μ	Dynamic viscosity (Pa s)
μ_{eff}	Effective viscosity of fluid (Pa s)
v_t	Turbulent viscosity (m^2 s^{-1})
ω	Specific dissipation rate (s^{-1})
χ_k	Constant as in **Table 3**
σ_k	Turbulent prandtl number for turbulent kinetic energy equation

frontiers in Energy Research

ORIGINAL RESEARCH
published: 02 July 2020
doi: 10.3389/fenrg.2020.00146

Advanced Packed-Bed Ca-Cu Looping Process for the CO_2 Capture From Steel Mill Off-Gases

José Ramón Fernández[1], Vincenzo Spallina[2] and Juan Carlos Abanades[1]*

[1] Spanish Research Council, Instituto Nacional de Ciencia y Tecnología del Carbono (INCAR-CSIC), Oviedo, Spain,
[2] Department of Chemical Engineering and Analytical Science, University of Manchester, Manchester, United Kingdom

A novel configuration of the Ca-Cu looping process based on dynamically operated packed-bed reactors is proposed to convert blast furnace gas (BFG) into H_2/N_2 and highly concentrated CO_2, accompanied by a large amount of high-temperature heat. Preliminary energy and mass balances of the process reveal that around 30% of the BFG can be upgraded via calcium assisted water gas shift (WGS) if only BFG is used as reducing gas in the reduction/calcination stage. A higher amount of H_2/N_2 can be produced by using other steel mill off gases, such as coke oven gas (COG) or basic oxygen furnace gas (BOFG), or natural gas in the regeneration of the CO_2 sorbent. This decarbonized fuel gas could be used for onsite power generation or to obtain sponge iron by a Direct Reduced Iron (DRI) process, increasing the overall capacity of the steel plant. Energy efficiencies higher than 75% have been calculated, reaching maximum values around 88% in case of using natural as fuel gas for the sorbent regeneration stage. Low values for the specific energy consumption of around 1.5 MJ_{LHV}/kg_{CO2} and CO_2 capture efficiencies higher than 95% support the further development of the proposed Ca-Cu looping process.

Keywords: CO_2 capture, hydrogen, steel mill, chemical looping combustion, calcium looping, energy efficiency

OPEN ACCESS

Edited by:
Theodoros Damartzis, École Polytechnique Fédérale de Lausanne, Switzerland

Reviewed by:
Lunbo Duan, Southeast University, China
Edward Anthony, University of Ottawa, Canada

****Correspondence:***
José Ramón Fernández
jramon@incar.csic.es

Specialty section:
This article was submitted to Process and Energy Systems Engineering, a section of the journal Frontiers in Energy Research

Received: *04 April 2020*
Accepted: *15 June 2020*
Published: *02 July 2020*

Citation:
Fernández JR, Spallina V and Abanades JC (2020) Advanced Packed-Bed Ca-Cu Looping Process for the CO_2 Capture From Steel Mill Off-Gases. Front. Energy Res. 8:146. doi: 10.3389/fenrg.2020.00146

INTRODUCTION

Iron and steel production is a very energy-intensive industry (i.e., around 20 GJ are demanded for the production of 1 ton of steel) and accounts for around 7% of total CO_2 emissions (Cavaliere, 2019). Nowadays, more than 1700 million tons of crude steel are annually produced and the demand for steel will continue growing for the next decades until it approaches 2600 million t/year by 2050 (ArcelorMittal, 2019). The steel sector faces the need for dramatically reducing carbon emissions (i.e., 50% reduction by 2050 and reach net zero CO_2 emissions by 2100) to comply with the challenging climate change mitigation targets agreed after COP21, which are aimed at limiting the increase in global temperature to 1.5°C (IPCC, 2018).

About 70% of steel produced worldwide is obtained through the Blast Furnace-Basic Oxygen Furnace (BF-BOF) process, which generates around 1.8 tons of CO_2 per ton of crude steel (IEA Report, 2017). Another option is to produce steel from scrap via Electric Arc Furnace (EAF), where the solid iron is melted by electric power. This alternative allows a reduction of above 50% in the energy demand, but the process is limited by the availability of scrap and the quality requirements of the steel (IEAGHG, 2013; ZEP, 2015). Finally, the Direct Reduced Iron (DRI) can reduce the carbon footprint by 25% compared to conventional blast furnaces (IEA Report, 2019). In the

commercialized varieties of this technology (i.e., Midrex and Hylsa), natural gas is converted into a syngas that acts as reductant agent instead of coke. Iron ore is reduced to metal iron in the shaft furnace and subsequently fed into an electric arc furnace to produce steel (Ho et al., 2013; Bechara et al., 2018).

In this context, CO_2 Capture and Storage (CCS) must play a decisive role in decarbonizing the steel production far beyond the current levels achieved with existing technologies (IPCC, 2018). The post-combustion technologies that use aqueous solutions with amines can be applied in principle to remove the CO_2 from steel mill off-gases. However, the relatively high energy requirements for amine regeneration and the limited chemical stability showed in the long term have hampered so far the deployment of this technology in steel plants (Arasto et al., 2013; Tsupari et al., 2013). During the VALORCO project, the investigations were focused on the development of advanced amine-based sorbents that showed high CO_2 sorption capacity (four times higher than aqueous monoethanolamine, MEA) and negligible degradation after a large number of cycles (Dreillard et al., 2017). The demonstration of this technology in operational environment at pre-commercial scale (i.e., at Technological Readiness Level 7, TRL7) is the goal of the ongoing 3D Project (Lacroix et al., 2019). The first large-scale CO_2 capture plant installed in a steel industry operates since 2016 in Abu Dhabi with a capture capacity of 0.8 $MtCO_2$/year. This facility treats the shaft off-gas obtained in a DRI process and the separation of CO_2 is carried out by MDEA absorption (Sakaria, 2017).

During the Ultra-Low CO_2 Steelmaking project (ULCOS), Top Gas Recycling (TGR) was shown to be the most promising technology tested, which consists in injecting almost pure oxygen into the furnace instead of air. In these conditions, the high partial pressure of CO_2 in the product gas facilitates its subsequent separation downstream (typically by pressure swing adsorption). The gas free of CO_2, which mainly contains CO and H_2, is partially recirculated to the furnace to reduce the iron ore, thereby lowering significantly the need for coke in the process (IEAGHG, 2013; van der Stel et al., 2013; Jin et al., 2015). The COURSE50 programme has been focused on investigating the potential of H_2-rich gases, such as coke oven gas (COG), as reducing agents in the blast furnace instead of coke. In this line, novel chemical and physical adsorption methods have been developed to capture first the CO_2 from the blast furnace gas (BFG) and then use waste heat available in the steel plant for the regeneration of the sorbents (Tonomura, 2013; Nishioka et al., 2016).

Pre-combustion technologies to decarbonize the blast furnace gas (typically containing around 45%vol. of CO and CO_2) are attractive alternatives to significantly reduce the carbon footprint of the steelmaking process as the BFG contains more than 60% of the total CO_2 emitted by the plant. By means of a sorption enhanced water-gas-shift (SEWGS) process, the BFG is converted into a H_2-enriched gas (>30%vol H_2), whereas the CO_2 generated in the reactor is removed *in situ* due to the presence of a high-temperature sorbent (typically a hydrotalcite-based solid that is also water-gas-shift catalyst at temperatures between 300 and500°C) (Ji et al., 2018). The demonstration of this technology up to TRL6-7 has been carried out during the consecutive EU programmes CACHET, CAESAR, and STEPWISE (van Selow et al., 2009; Boon et al., 2015; Gazzani et al., 2015). It has been observed that the main challenge for the scaling-up of the SEWGS process is the high cost for the sorbent regeneration and the low inherent CO_2 sorption capacity of the sorbent (best carrying capacities of promoted hydrotalcites have been measured at up to 8 wt.%).

CaO-based materials have been widely proposed as CO_2-sorbents in other pre-combustion applications (Harrison, 2008; Blamey et al., 2010; Martavaltzi et al., 2010), since they exhibit much larger CO_2 carrying capacities [ranging from 30 to 45%wt in newly developed CaO materials (Valverde, 2013; Erans et al., 2016)], very high theoretical energy recovery and they can be obtained from abundant and inexpensive natural sources. However, these processes have traditionally faced a major obstacle as CO_2 capture concept because they require high temperatures (around 900°C) to carry out the regeneration of the sorbent by $CaCO_3$ calcination in rich atmospheres of CO_2. Supplying a large thermal power input for regeneration [calcination requires a minimum of 3.9 MJ/kg of CO_2 evolved from calcination (Hills, 1967)] is a major engineering challenge, even if this energy can be effectively recovered during carbonation and heat recovery stages. One option is to combine the sorption enhanced reactions with chemical looping combustion, so that the large amount of energy needed for the calcination is supplied by the oxidation of Ni- (Antzara et al., 2015) or Fe-based oxygen carriers (Tian et al., 2016). Although these configurations avoid the need for large heat-transfer surfaces at very high temperature, they still require an air separation unit (ASU) to obtain a CO_2-rich gas during the decomposition $CaCO_3$ to CaO. In the Ca-Cu looping process, the exothermic reduction of CuO to Cu using a gaseous fuel (e.g., CH_4, CO, or H_2) supplies the necessary heat to carry out simultaneously the calcination of the carbonated sorbent producing exclusively CO_2 and H_2O without the presence of an ASU in the process (Fernández et al., 2012). A substantial progress has been made during the EU ASCENT project on dynamic reactor modeling (Martini et al., 2016, 2017; Fernández and Abanades, 2017a), development of Ca-Cu materials (Kazi et al., 2017), process integration (Riva et al., 2018; Martínez et al., 2019b), and experimental validation from small reactors to packed beds at TRL5 (Fernández and Abanades, 2017b; Grasa et al., 2017; Díez-Martín et al., 2018; Martínez et al., 2019a). Some recent works have proposed the use of the Ca-Cu based process to convert the BFG into valuable products, such H_2/N_2 and pure CO_2, using a combination of several interconnected fluidized beds operating in continuous mode (Fernández et al., 2017; Martínez et al., 2018). This configuration facilitates the heat management during the highly exothermic redox stages but it is limited in the operating pressure (only atmospheric) and requires a challenging solids segregation unit to separate the CaO- from the Cu-based materials once the sorbent has been regenerated.

We propose in this work a novel Ca-Cu looping configuration based on packed-bed reactors, that is able to operate at high pressure to transform blast furnace gas into a H_2-rich gas with higher LHV as well as a large amount of high-temperature heat. This decarbonized fuel gas can be used for onsite power generation or to obtain sponge iron by a

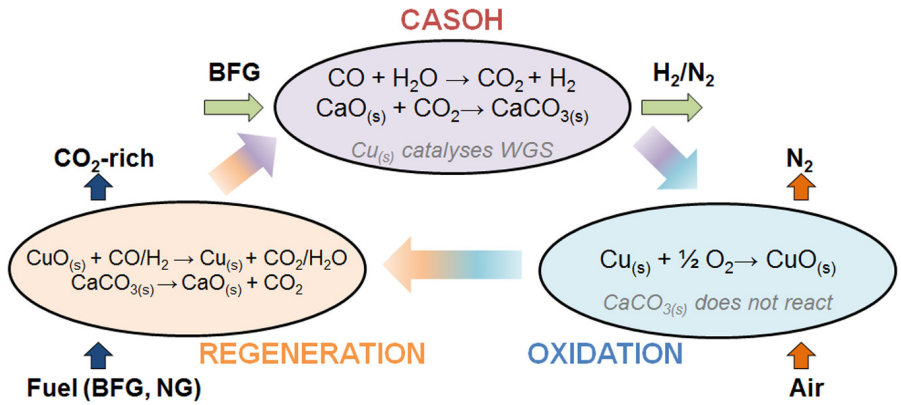

FIGURE 1 | Scheme of the Ca-Cu chemical looping process for the production of H_2-rich gas from BFG and CO_2 ready for storage or reutilization.

DRI process, increasing the overall capacity of the plant. The arrangement of several packed-bed reactor will perform in a sequence of three main reaction stages (i.e., BFG upgrading, Cu oxidation and CO_2 sorbent regeneration) following well established principles of dynamic operation as for other commercial PSA/TSA processes and regenerative heat-transfer processes (see simplified scheme in **Figure 1**). Four different configurations are considered here in terms of process operating conditions and fuel utilization. The performance obtained for the different Ca-Cu integrated plants will be compared in terms of primary energy consumption, product yields, CO_2 purity and potential CO_2 capture rate to demonstrate the theoretical viability of the process.

PROCESS DESCRIPTION

The Ca-Cu looping process allows great flexibility in the feedstock and a modular reactor configuration (i.e., in size and number of parallel units) is feasible. The main fuel off-gases of the steel mill (see characteristics in **Table 1**) can be decarbonized with this technology depending on the level of integration of the Ca-Cu process, giving rise to a wide variety of products and uses (see **Figure 2**). The characteristics of the steel mill off-gases are listed in **Table 1** (Santos, 2013).

TABLE 1 | Composition of the steel mill off-gases used for the calculations (Santos, 2013).

	Blast furnace gas (BFG)	Coke oven gas (COG)	Basic oxygen furnace gas (BOFG)
	Composition (%vol)		
CH_4	–	25	–
CO	23	7	57
CO_2	23	3	15
H_2	4.5	60	2
H_2O	–	–	12
N_2	49.5	5	14
O_2	–	–	–
Flowrate (Nm^3/t of steel)	1630	164	70

Apart from the BFG, which can be converted into a H_2/N_2 gas by means of an enhanced WGS process (explained above), the basic oxygen furnace gas (BOFG) (with around 60%vol. of CO) can also be valorized following the same procedure to produce separately a H_2-enriched gas (>75% purity), N_2 and pure CO_2. Moreover, the COG (with about 25 and 60%vol. of CH_4 and H_2, respectively) can be fed into a Ca-Cu chemical loop combined with sorption enhanced reforming (in a similar way to the process schemes reviewed in Martínez et al., 2019a) to obtain almost pure H_2 and N_2 useful for power generation o chemical synthesis (e.g., ammonia) (Martínez et al., 2017). Any possible combination of BFG, COG, and BOFG can be considered by tuning the Ca/Cu ratio in the reactors (Alarcón and Fernández, 2015) to obtain the desired products and the CO_2 capture rate that can range from 10 to 95%.

Among all the aforementioned possibilities, this work is focused on the valorization of the BFG, as it is by far the main off-gas emitted by a steelmaking plant. **Figure 3** shows the process scheme of the proposed Ca-Cu looping process for BFG, which is composed of several packed-bed reactors dynamically operated in parallel with alternating temperature and pressure to accommodate the conditions of every solids bed. The main stage of the process involves the production of a H_2/N_2 fuel gas (stream 4) through the water-gas-shift reaction of the CO contained in the BFG (around 23%vol.). In this stage, called Calcium Assisted Steel-mill Off-gas Hydrogen (CASOH) production, Cu-based particles act as WGS catalyst and the presence of CaO allows a substantial part of the CO_2 to be removed from the reacting atmosphere as soon as it is produced. The continuous elimination of CO_2 by the carbonation of the CaO-based sorbent shifts the WGS equilibrium toward a higher production of H_2, so that a very high conversion of the inlet CO is feasible at temperatures between 500 and 700°C. The resulting gas contains more than 30%vol of H_2 diluted with N_2 and very low amounts of CO and CO_2.

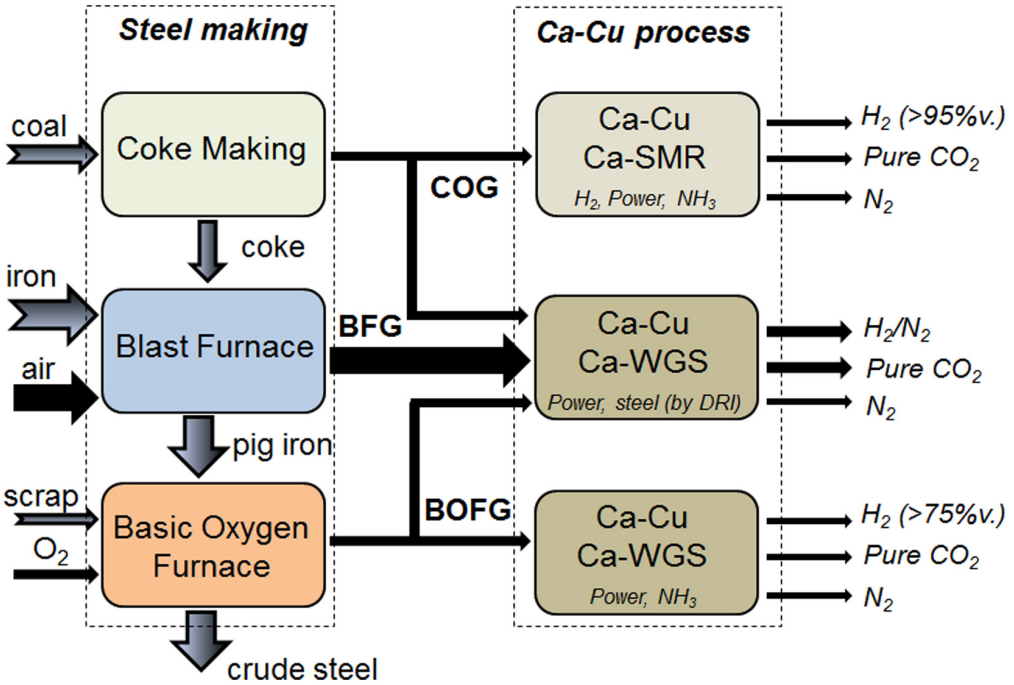

FIGURE 2 | Possible levels of integration of the Ca-Cu looping process in a steel mill (thicker arrows are used to highlight the main mass flow rates).

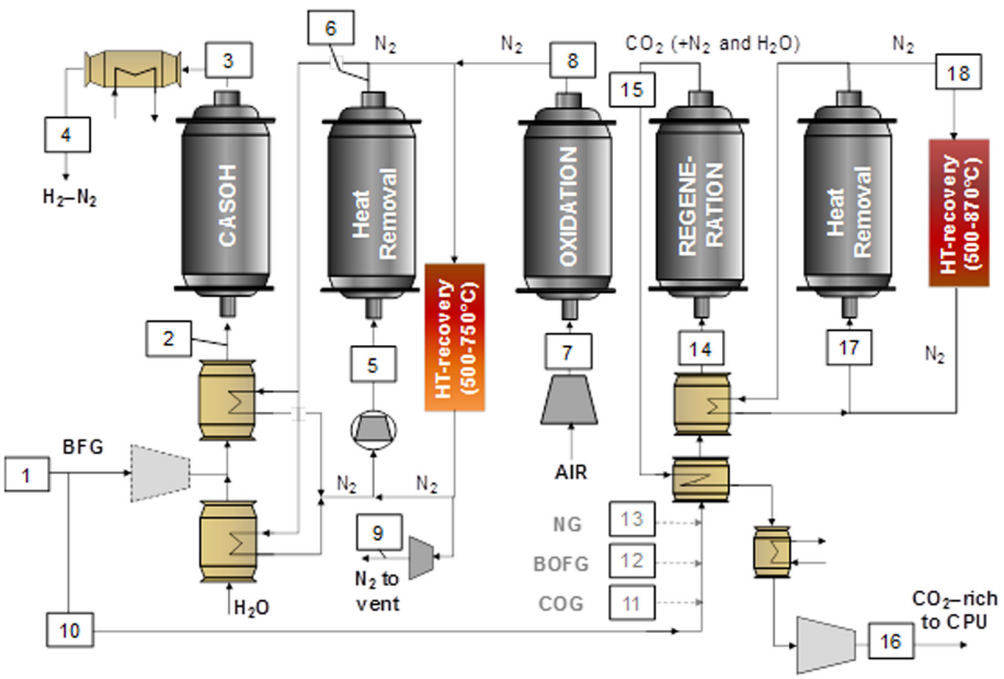

FIGURE 3 | Illustration of the CASOH scheme reaction network using BFG for both H_2/N_2 production and sorbent regeneration (other low N_2-content fuel gases can also be used in the regeneration stage to further increase the CO_2 purity in the product gas).

Figure 4A shows the important role of the CaO sorbent in the thermodynamics of the WGS process. In conventional WGS, a maximum concentration of 40%vol. H_2 (on a N_2-free and dry basis) can be achieved at 550°C, at atmospheric pressure and with a steam-to-carbon molar ratio of 1. At higher temperatures, the concentration of H_2 is progressively reduced at the expense

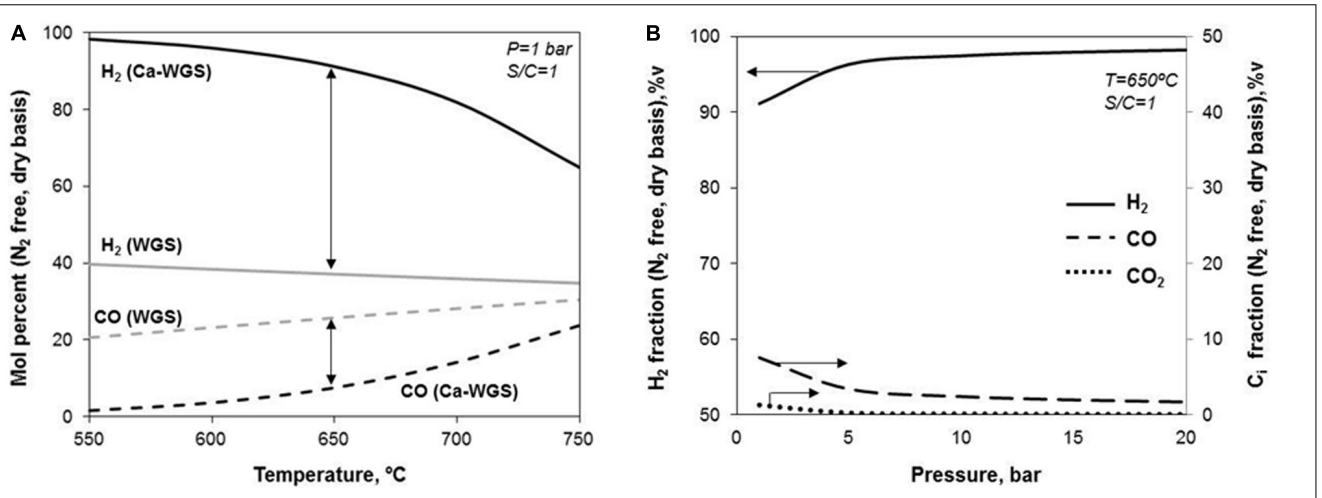

FIGURE 4 | (A) Equilibrium of WGS reaction as a function of the temperature with and without CaO-based sorbent; **(B)** effect of pressure on Calcium assisted WGS reaction.

of an increase in the concentration of CO in the product gas from 20%vol. at 550°C to 30%vol. at 750°C. In contrast, when CO_2 is removed from the gas phase by the carbonation of CaO, almost pure H_2 (above 98%vol.) with only 1%vol. of CO (on a dry basis) can be produced at 550°C. The advantages of the Calcium assisted WGS decrease at higher temperatures giving rise to lower concentrations of H_2. At temperatures above 750°C (and at atmospheric pressure), the carbonation of CaO is less favored thermodynamically, and as a result of that, the performance of the Calcium assisted WGS approaches that of standard WGS without CO_2 capture. Taking into account the high content of CO and CO_2 in the BFG and the exothermic nature of both WGS and CaO carbonation reactions ($\Delta H_{298\ K}$ = -41 and -179 kJ/mol, respectively), a great proportion of inert solids (i.e., the materials on which the active CaO and Cu phases are supported) is required in the bed in order to avoid a solid temperature increase and the generation of hot spots during the CASOH stage, that would impede high H_2 yields.

With respect to the effect of the pressure on the Calcium assisted WGS, the production of H_2 is promoted at increasing pressures due to the reduction in the number of gaseous moles associated to the overall reaction (WGS + CaO carbonation). As can be seen in **Figure 4B**, around 90%vol. of H_2 and 8%vol. of CO (on a dry basis) can be achieved working at 650°C, at atmospheric pressure and with a S/C molar ratio of 1 in the feed. However, it is possible to obtain a product gas with a H_2 content of 97%vol., around 3%vol. of CO and a negligible amount of CO_2 performing at 10 bar while maintaining the rest of operating conditions. Since the compression of BFG may be costly, operating the CASOH stage at high pressure may be particularly interesting if part of the energy recovered from the process is used for power generation (i.e., burning the H_2/N_2 gas or producing high-pressure steam) or if the process downstream requires high pressure (i.e., ammonia production). Finally, other important parameter in the Calcium assisted WGS operation is the S/C molar ratio in the feed. As explained in a previous work (Fernández et al., 2017), almost pure H_2 (on a dry basis) is feasible with moderate steam consumption (i.e., with S/C molar ratios of around 1).

Once the CaO-based particles approach total carbonation with CO_2, the maximum conversion of BFG to H_2/N_2 achieved during the CASOH stage is no longer feasible and the reactor would perform as a stationary WGS unit. It is therefore necessary to add reaction stages to regenerate the sorbent while producing a concentrated stream of CO_2. As can be seen in **Figure 1**, such process requires first a reaction stage in which the Cu-based particles are oxidized to CuO, as their subsequent reduction with a fuel gas will supply the heat needed for the regeneration of the carbonated sorbent. However, by the end of the CASOH operation, the solids bed is left at temperatures up to 700–800°C, which are excessively high to directly initiate the highly exothermic Cu oxidation stage ($\Delta H_{298\ K}$ = -312 kJ/mol O_2). For this reason, an intermediate heat removal stage at high pressure to avoid $CaCO_3$ calcination is included in the process scheme to extract the excess of heat from the solids by flowing through the reactor (stream 6 in **Figure 3**) an inert gas (typically N_2), which also acts as purge for the subsequent oxidation and it can be operated in a semi-closed loop fed into at an appropriate temperature (around 500°C) to start safely with the oxidation of the Cu-based particles.

During the Cu oxidation stage, a flow of air (stream 8 in **Figure 3**) progressively reacts with the metal-based particles and the heat released rapidly increases the temperature of the bed until a maximum value is achieved in the oxidation front. Temperatures close to 800°C allow a fast and complete conversion of O_2 giving as a result a product gas mainly composed of N_2 (stream 9) during the pre-breakthrough period (Alarcón et al., 2017). Moreover, this operation must be carried out preferably at high pressure (i.e., around 10 bar) to minimize the partial calcination of $CaCO_3$ that, would lead to CO_2 slip during this stage. In these mild oxidation conditions, the

chemical stability of the metal oxide is ensured in the long term after successive redox cycles (Adanez et al., 2012) and the raise in temperature required in the next sorbent regeneration stage to achieve values of around 900°C is moderate, which permits reasonable Cu/Ca ratios in the composition of the solids bed.

In the following stage, the CaO-based sorbent is regenerated by *in situ* calcination of $CaCO_3$ ($\Delta H_{298\ K}$ = 171 kJ/mol) when burning a fuel gas containing CO, H_2, and/or CH_4 with the oxygen contained in CuO ($\Delta H_{298\ K}$ = -126.9 kJ/mol CO, $\Delta H_{298\ K}$ = -85.8 kJ/mol H_2, $\Delta H_{298\ K}$ = -178 kJ/mol CH_4). This is equivalent to the operation carried out in typical fuel reactors of chemical looping combustion systems. This stage must be performed at atmospheric pressure to moderate the temperature required for the calcination of $CaCO_3$, according to the $CaO/CaCO_3$ equilibrium (i.e., between 850 and 900°C depending on the concentration of CO_2 in the product gas). Different fuel gases can be used, such as BFG, COG, BOFG, or external natural gas (mostly CH_4), which determines the Cu/Ca ratio required in the bed to sustain the reduction/calcination stage. The use of exclusively BFG as reducing gas avoids the consumption of valuable gases with higher calorific value. However, this option restricts the amount of H_2/N_2 produced through the CASOH operation, as will be explained in the next section. Moreover, CO_2 diluted with N_2 (around 60%vol. CO_2 on a dry basis) is obtained as gaseous product (BFG typically contains concentrations of N_2 close to 50 vol.%), which makes necessary a larger compression and separation unit (CPU) downstream to finally dispatch pure CO_2 for permanent storage or chemical synthesis. The use of COG and BOFG in the regeneration stage allows a higher amount of BFG to be upgraded in the CASOH reactor, and a great decarbonization (about 95%) in the steel plant can be achieved, as these gases end up as highly pure CO_2 and H_2O during the reduction/calcination reactions. However, the availability of COG and BOFG in the plant is limited, thus BFG or external CH_4 must be supplied in this case to accomplish the calcination of the CO_2 sorbent. The use of exclusively CH_4 in the reduction/calcination operation allows all the BFG to be processed in the CASOH stage and simplifies the purification of the CO_2-rich gas obtained in the process, as only CO_2 and H_2O would be produced in the reduction/calcination operation (i.e., only a minimum CO_2 conditioning other than water condensation before compression would be needed). However, this option would involve a great external energy input to the system, so a thorough economical evaluation is required to determine the feasibility of this option.

Once both calcium- and copper-based particles have been totally converted, a large fraction of the solids bed is left at temperatures around 870°C, which are excessively high to carry out an optimal performance of the CASOH stage in a subsequent cycle. Therefore, the heat accumulated in the packed-bed reactor is blown out by flowing through the bed a pressurized stream of recycled inert gas (typically N_2) that enters at a suitable temperature (around 500°C) to begin afterward with the CASOH stage. The gas (stream 18 in **Figure 3**) is discharged at around 870°C, cooled to 500°C and recirculated back to the reactor operated in a closed loop or it can be expanded in a gas turbine for power generation. The exhaust N_2 will be re-compressed and recirculated to the heat removal stages in a similar operation to that carried out in packed-bed chemical looping combustion (CLC) systems (Spallina et al., 2014) or in post-combustion applications where the flue gas is recirculated to increase the CO_2 content in the gas, thereby facilitating the CO_2 capture (Jonshagen et al., 2010).

RESULTS

Reactor Operation

The dynamic performance of the packed-bed reactors in every stage of the proposed process is described in this work by means of a relatively simple reactor model, in which ideal regenerative heat exchange between gas and solids is assumed as well as plug flow without axial dispersion and solid-gas reactions taking place in sharp reaction fronts. These suppositions have been used in previous works to approximate the operation of fixed-bed reactors in CLC (Noorman et al., 2007; Fernández et al., 2012) and catalytic processes (Kolios et al., 2000). Moreover, numerous studies have demonstrated experimentally the veracity of this approach (Kumar et al., 2000; Dupont et al., 2008; Noorman et al., 2010; Spallina et al., 2017).

When the resistance to mass and heat transfer is negligible, the velocity at which the reaction front moves through an adiabatic bed (u_{rf}) can be calculated as follows:

$$u_{rf} = \frac{\rho_{gas} u_{gas} x_{gi} M_{sj}}{\varepsilon \rho_s x_{sj} M_{gi} \varphi} \quad (1)$$

TABLE 2 | Operating conditions of every stage of the Ca-Cu looping process for the reference case.

Conditions	Value
Solids properties	
Active content in CaO-based solid, %wt.	10
Active content in Cu-based solid, %wt.	30
CASOH stage	
Initial bed temperature, °C	500
Pressure, bar	10
S/C molar ratio	1.2
Inlet gas temperature, °C	500
Cu oxidation stage	
Initial bed temperature, °C	500
Pressure, bar	10
Inlet gas temperature, °C	500
Reduction/calcination stage	
Initial bed temperature, °C	763/500
Pressure, bar	1
Feed temperature, °C	800
Calcination temperature, °C	870
Heat removal stages	
Initial bed temperature (HR1), °C	754/523
Initial bed temperature (HR2), °C	870/800
Pressure, bar	10
Inlet temperature (HR1), °C	523
Inlet temperature (HR2), °C	500

where u_g is the velocity of the gas, ρ_{gas} and ρ_s denote the density of the gas and the solid, respectively, x_{gi} and x_{sj} represent the mass fraction of the reacting component i in the gas and component j in the solid, respectively, M_i is the molecular weight of reacting phases, ε is the bed porosity and φ is the stoichiometric coefficient of the solid/gas reaction. Likewise, the velocity of the heat exchange fronts (u_{he}) advancing along the reactor can be obtained as follows:

$$u_{he} = \frac{\rho_{gas} u_{gas} c_{p,gas}}{\rho_s c_{p,s}} \quad (2)$$

The maximum temperature change caused by the exothermic or endothermic reactions can be calculated by means of an energy balance assuming adiabatic conditions, according to Eq. (3) and Eq. (4).

$$\Delta T = \frac{\Delta H_r}{\frac{c_{ps} M_{sj}}{x_{sj}\phi} - \frac{c_{pgas} M_{gi}}{x_{gi}}} \quad \text{if } u_{rf} > u_{he} \quad (3)$$

$$\Delta T = \frac{\Delta H_r}{\frac{c_{pgas} M_{gi}}{x_{gi}} - \frac{c_{ps} M_{sj}}{x_{sj}\phi}} \quad \text{if } u_{rf} < u_{he} \quad (4)$$

A reference case has been studied in detail to demonstrate the feasibility of the process, in which a fraction of the BFG produced in the steel mill is upgraded to H_2/N_2, whereas the rest of this gas is used as sole reducing agent in the sorbent regeneration stage. Both mass and energy balances have been solved for every stage of the process assuming adiabatic reactors. A set of operating conditions and a heat management strategy (explained below) have been adopted to ensure a suitable performance of the reactors. The input of operating conditions adopted in this case are listed in **Table 2**. **Figure 5** shows the evolution of the temperature profiles during the operation in every stage of the process for the conditions assumed in the reference case.

To produce 1 million tons of steel per year, approximately 51.7 Nm^3/s of BFG are emitted (Santos, 2013). In the reference case, about 30% of the BFG is directed to the CASOH stage mixed with 4.5 Nm^3/s of steam to obtain a steam-to-CO molar ratio of 1.2 in the feed (stream 2 in **Figure 3**). Meanwhile, the remaining 70% of the BFG (stream 10 in **Figure 3**) is used in the sorbent regeneration stage, as explained below. The energy balance in the reduction/calcination stage for the conditions listed in **Table 2** when only BFG is used as fuel imposes a $CuO/CaCO_3$ molar ratio in the bed of 1.4 to ensure that the heat released by the reduction of CuO to Cu is enough to drive the decomposition of $CaCO_3$ to CaO. **Table 3** includes the flow rates, temperatures and compositions of the gaseous streams calculated for this case.

In these conditions, when the CASOH stage starts the bed will contain 66%wt of Ca-based material (with 7%wt of active CaO, according to the solids properties listed in **Table 2**) and 34%wt of Cu-based particles (i.e., 10%wt of Cu supported over 24 wt% of SiO_2). To carry out the CASOH stage, the mixture of BFG and steam is compressed up to 10 bar and subsequently preheated up to approximately 500°C. Moreover, the solids in the bed are initially at 500°C as a result of a previous heat removal stage. This temperature should allow a very fast reaction of CO with H_2O to form CO_2 and H_2 catalyzed by the Cu-based particles. According to the reactor model explained above, a slight increase in the solids temperature of 23°C is produced due to the modest exothermicity of the WGS reaction. At 523°C, 10 bar and a S/C molar ratio of 1.2, the WGS equilibrium predicts a CO conversion of around 80%. CO_2 is assumed to be removed as soon as the product gas contacts with active calcium oxide, which increases the conversion of CO. Thus, a carbonation front is formed and moves ahead at a velocity (u_{rf}) that can be calculated by means of Eq. (1). Considering the composition of both reacting gas and solids, the carbonation front advances near 6 times faster than the resulting heat exchange front (i.e., $u_{rf} > u_{he}$) and leaves behind carbonated solids (and Cu-based particles) heated by the carbonation reaction. For the conditions of the reference case, a maximum temperature of 754°C (Eq. 3) is achieved in the heat plateau developed between both reaction and heat exchange fronts. At this temperature, it is possible to obtain a product gas (stream 3) with 32% H_2, 60% N_2 and less than 2% of CO and CO_2 (see **Table 3**).

Because of the rapid heat transfer between the gas and solids, the product gas acquires the temperature of the unconverted solids downstream and it is delivered at 500°C during the entire CASOH stage. A flow of 13.5 Nm^3/s of decarbonized H_2/N_2 gas is obtained, which can be used to cover energy requirements of the steel mill (as happens with BFG and other off-gases in conventional plants without CO_2 capture), to generate power or to produce additional steel by means of a DRI process avoiding carbon emissions. The integration of these uses of the H_2/N_2 stream is beyond the scope of this work. Assuming that the H_2 contained in stream 3 (i.e., 4.32 Nm^3/s) was able to fully reduce iron ore (Fe_2O_3) in a parallel DRI process, about 0.23 Mt/year of steel would be produced additionally in the steel plant (i.e., 23% of increased production).

When the carbonation front approaches the reactor exit, all the active CaO (i.e., 10%wt of the calcium-based material) has been carbonated and the CASOH stage concludes. At this point, near 80% of the solids are ideally left at 754°C and the rest of the bed at 523°C, as a result of the advance of the heat exchange front resulting from the carbonation reaction (see **Figure 4**).

Once the CASOH stage has finished, the fact that a large fraction of the reactor is left at around 750°C makes it necessary the addition of a heat removal stage to eliminate the excess of heat absorbed in the bed before starting the highly exothermic copper oxidation stage. An inlet flow of 157 Nm^3/s of N_2 (stream 5 in **Figure 3**) allows this operation to be carried out in the same cycle time than the CASOH stage. This stream comes recirculated and re-compressed from a high-temperature recovery system (see **Figure 3**) and it is fed at 523°C through the part of the reactor at lower temperature. As the N_2 goes through the bed, the heat exchange front located in the transition between the zones at 523/754°C gradually moves toward the reactor exit, whereas the outlet gas (stream 6 in **Figure 3**) is released at 754°C. The heat recovered from the exit gas can be used to supply heat to other unit of the steelwork (e.g., partly pre-heating a reheating oven) or it can be recovered to produce HP steam for additional power generation. In this way, N_2 is operated in

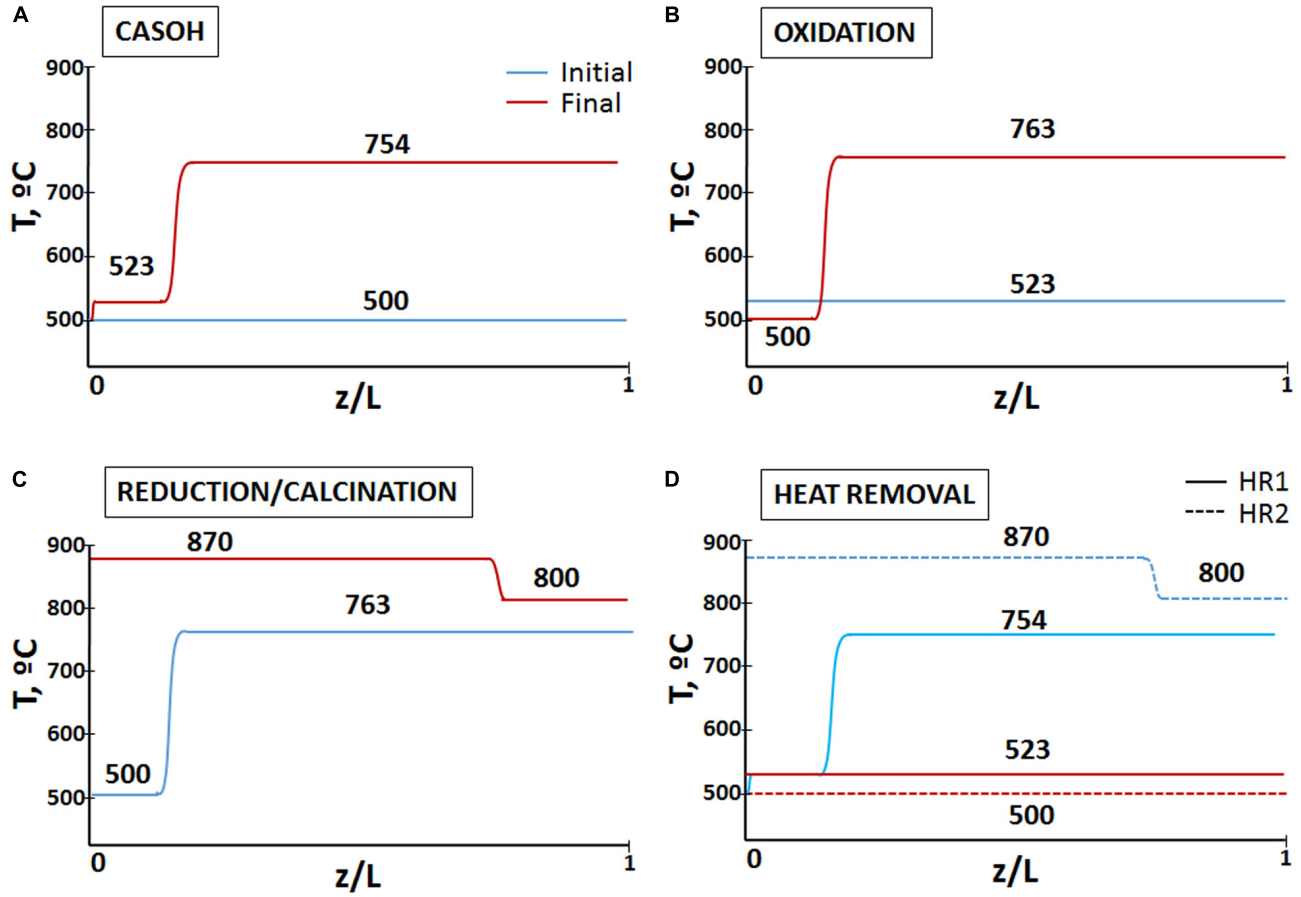

FIGURE 5 | Temperature profiles at initial and final conditions in every stage of the Ca-Cu looping process for the conditions assumed in the reference case (plug flow without axial dispersion, ideal heat exchange between gas and solids, and reactions taking place in sharp reaction fronts are assumed). **(A)** CASOH stage, **(B)** oxidation stage, **(C)** redcution/calcination stage, and **(D)** heat removal stages.

TABLE 3 | Main characteristics of the gaseous streams of the Ca-Cu looping process (see **Figure 3**) obtained by solving the mass and energy balances in the reference case.

Stream	**1**	**2**	**3**	**4**	**5**	**6**	**7**	**8**	**9**	**14**	**15**	**16**	**17**	**18**
Flow, Nm^3/s	51.7	20.7	13.5	12.7	156.9	156.9	23.3	18.6	18.6	35.5	42.5	40.9	179.3	179.3
Flow, kmol/s	2.3	0.9	0.6	0.6	7.0	7.0	1.0	0.8	0.8	1.6	1.9	1.8	8.0	8.0
Flow, kg/s	70.4	25.7	11.6	10.9	196.1	196.1	30.0	23.4	23.4	48.4	69.1	67.8	224.1	224.1
T, °C	25.0	488.1	500.0	25.0	523.0	754.0	500.0	523.0	116.0	800.0	500.0	30.0	500.0	851.5*
							Composition, %vol.							
CH_4	–	–	–	–	–	–	–	–	–	–	–	–	–	–
CO	23	18	1	1	–	–	–	–	–	23	–	–	–	–
H_2	4.5	3.5	32.1	34	–	–	–	–	–	4.5	–	–	–	–
CO_2	23	18	1	1	–	–	–	1.1	1.1	23	54.9	57.1	–	–
H_2O	–	21.6	6.5	–	–	–	–	–	–	–	3.8	–	–	–
O_2	–	–	–	–	–	–	21	–	–	–	–	–	–	–
N_2	49.5	38.9	59.5	64.0	100	100	79	98.9	98.9	49.5	41.3	42.9	100.0	100.0

**Average temperature during the duration of the stage.*

a closed loop cycle in which only a small make up is required to account for the amount of gas used as purge gas. This stage ends when all the heat stored at 754°C is blown out of the bed. At this point, the solids bed is left at a uniform and sufficiently high temperature (i.e., 523°C) to initiate the subsequent Cu oxidation operation.

During the Cu oxidation, a flow of air of 23.3 Nm^3/s (stream 7 in **Figure 3**) is required to adapt the duration of this stage to the previous ones. The inlet gas is supplied at 10 bar and 500°C. According to the solid compositions listed in **Table 2**, the reactor contains 10%wt of Cu at the beginning of the Cu oxidation stage. In these conditions, the oxidation front goes through the bed around 9 times faster than the corresponding heat exchange front, according to Eq. (1) and Eq. (2), and the maximum increase in temperature in the oxidation front is 240°C, calculated by means of Eq. (3).

The rapid advance of the oxidation front facilitates that the solids bed reaches a maximum temperature of 763°C. An operating pressure of 10 bar ensures a very low leakage of CO_2 caused by partial calcination of $CaCO_3$ ($P_{CO2,eq}$ at 763°C is 0.11 bar). The high temperature achieved in the oxidation front permits the complete conversion of the oxygen, giving as a result an outlet flow of 18.6 Nm^3/s basically composed of N_2 (with only 1.1%vol of CO_2), which is discharged at 523°C. Once the Cu present in the reactor has been totally oxidized, the bed is divided into two zones at different temperature as a consequence of the advance of both oxidation and heat exchange fronts at different velocities. A small fraction of the solids located close to the reactor inlet (around 10% of the solids bed) remains at 500°C (i.e., the temperature of inlet air) and the remaining 90% of the reactor is left at 763°C.

As mentioned above, for the conditions of the reference case, about 70% of the BFG is needed to regenerate the CO_2 sorbent carbonated in the CASOH stage. Moreover, the pressure must be reduced close to atmospheric conditions to favor the calcination reaction at temperatures below 900°C. In this case, the operation is carried out with a flow of 35.5 Nm^3/s of BFG°C, which enters preheated at 800°C (stream 14 in **Figure 3**). This high temperature allows the fast reduction of CuO with the CO and H_2 contained in the BFG and avoids the re-carbonation of the calcium-based particles left behind the heat exchange front generated by the reduction/calcination reactions (see **Figure 5C**). Under these circumstances, the temperature of the solids in the reduction front rapidly increases until a value of 870°C is achieved. The composition of both solids bed and BFG makes the reduction front move through the reactor around 4 times faster than the resulting heat exchange front leaving behind a heat plateau at 870°C. This temperature should be sufficient to ensure the complete calcination of the sorbent ($P_{CO2eq,\ 870^\circ C}$ = 0.65), taking into account that the maximum concentration of CO_2 expected in the product gas is 55%vol, assuming total oxidation of the BFG. Downstream of the reduction front, the product gas rapidly reaches the temperature of the unconverted solids and it is discharged at 500°C. The concentrated stream of CO_2 (stream 16 in **Figure 3**) needs an additional purification step before being ready for use or storage, but the analysis of such purification options (physical absorption, cryogenic distillation, membrane separation, adsorption, etc.) is outside the scope of this work. As mentioned above, fuel gases without N_2 would be preferable to minimize the footprint of such purification stage.

Once the reduction/calcination operation has finished, around 75% of the bed remains at 870°C and the rest of the reactor is left at 800°C. As explained above, the CASOH stage requires much lower temperatures, so the excess of heat stored in the bed is recovered by feeding into N_2 at high pressure in a similar manner to the previous heat removal stage. Therefore, a flow of 179.3 Nm^3/s of N_2 at 10 bar and 500°C (stream 17 in **Figure 3**) enters the reactor and the exit gas containing high-temperature heat can be used to cover energy demand in other part of the plant or used to produce high-pressure steam for the generation of power in a steam turbine. During approximately 75% of the duration of the heat removal operation, the N_2 stream is emitted at 870°C and the rest of the time it is discharged at 800°C (i.e., an average temperature of the exit gas of 852°C). This stage culminates when the bed is left at 500°C (i.e., the temperature chosen to start the CASOH stage in a subsequent cycle).

There are other alternatives to increase the amount of H_2/N_2 obtained from BFG through the Ca-Cu looping process. If the COG and BOFG are also used as reducing gases to regenerate the Ca-based sorbent (together with BFG to cover the energy requirements of the operation), a higher proportion of BFG can be converted into H_2-enriched gas in the CASOH stage (Case 2 in **Table 4**). In this particular configuration, around 45% of the BFG available from the steel mill can be upgraded (i.e., 22.9 Nm^3/s and around 40% of additional H_2-rich stream compared to the previous case) via the Calcium assisted WGS process described above. With this option, almost the complete decarbonization of the steel plant is feasible, as most of the carbon present in the steel mill off-gases is finally emitted in the CO_2-rich gas produced in the reduction/calcination stage. Moreover, the purification of the CO_2 is facilitated as the product gas resulting from the regeneration stage contains a higher concentration of CO_2 (i.e., 64%vol. on a dry basis).

If CH_4 is used as fuel in the reduction/calcination stage, all the BFG produced during the steelmaking process can be directed to the CASOH stage (Case 3 in **Table 4**), thereby maximizing the production of H_2/N_2 (i.e., 42.3 Nm^3/s). In these conditions, the purification of CO_2 is greatly simplified because only CO_2 and $H_2O_{(v)}$ are produced during the regeneration. However, this option demands a large energy input to the Ca-Cu looping process (i.e., 20.3 Nm^3/s of CH_4 equivalent to 594 MW_{th}) to decarbonize all the BFG (i.e., with a calorific value of around 181 MW_{th}, assuming LHV_{BFG} = 2.6 MJ/kg). Moreover, the lower enthalpy of the reduction reaction with CH_4 imposes a larger Cu/Ca molar ratio in the bed (i.e., a value of 4.2 in this specific case), which results in significantly larger reactors to treat the same flow of BFG. The higher proportion of Cu in the bed (15%wt in this case) shoots up the temperature in the oxidation front until 870°C, which highly increases the loss of CO_2 by partial calcination of $CaCO_3$ in this stage (even operating at 15 bar as in Case 4 of **Table 4**), and consequently, the CO_2 capture efficiency of the process decreases to around 85%.

Integration in the Steel Mill

The overall process performance of the cases discussed above are summarized in this section. The preliminary energy analysis is based on the following assumptions:

TABLE 4 | Main performance results of different configurations of the Ca-Cu process fueled with steel mill off-gases.

		Case 1 Only BFG	Case 2 BFG/COG/BOF	Case 3 BFG/NG	Case 4 BFG/NG
CASOH operating P	Bar	10	10	10	15
Thermal input, BFG	$MW_{LHV,BFG}$	175.07	175.07	175.07	175.07
Flowrate, BFG	kmol/s	2.31	2.31	2.31	2.31
Thermal input, COG	$MW_{LHV,COG}$	–	84.80	–	–
Flowrate, COG	kmol/s	–	0.23	–	–
Thermal input, BOFG	$MW_{LHV,BOF}$	–	16.44	–	–
Flowrate, BOFG	kmol/s	–	0.10	–	–
Thermal input, NG	$MW_{LHV,NG}$	–	–	594.0	594.0
Flowrate, NG (100% CH_4)	kmol/s	–	–	0.74	0.74
Thermal output, H_2/N_2	$MW_{LHV,H2-rich}$	48.44	68.14	153.64	153.62
Flowrate, dry	kmol/s	0.57	0.80	1.79	1.79
Composition, dry	$H_2/N_2/CO_x$	34/64/2	34/64/2	35/64/1	35/64/1
CO_2 purity, dry (before CPU)	%	57.0%	64.1%	99.8%	99.9%
CO_2 emitted	%	2.0%	4.2%	20.4%	15.9%
Cold gas efficiency	%	27.7%	24.7%	20.0%	20.0%
Electric utilities	MW_{el}	48.3	55.7	82.7	95.8
Heat recovery (500–200°C)	MW_{th}	18.5	20.2	22.9	24.1
Heat recovery (870–500°C)	MW_{th}	98.5	176.2	577.3	583.4
Energy efficiency	%	74.1%	79.7%	88.5%	88.0%
Primary energy efficiency	%	69.8%	77.6%	90.5%	89.2%
Specific energy consumption for CO_2 removed	MJ_{LHV}/kg_{CO2}	1.68	1.62	1.37	1.50

Heat Recovery

Two different heat recovery units are considered to distinguish the quality of the heat. The high-temperature heat (i.e., in the range from 500 to 870°C) can be used to supply heat directly in some point of the steel mill, thereby reducing the energy demand of the integrated steelworks, as well as for the production of high-pressure steam for power generation. Moreover, part of this heat is also needed to preheat the fuel fed into the regeneration stage up to 800°C. On the other hand, the intermediate-temperature heat (i.e., between 200 and 500°C), which is mainly obtained from the cooling of product gases, can be used to preheat gaseous feedstock, to produce the steam required in the CASOH process and to produce additional intermediate-pressure (IP) steam for thermal and electricity generation.

Electric Utilities

If the power generation from burning the H_2/N_2 obtained during CASOH is not considered, the Ca-Cu looping process has some electricity demand to operate the compressors of the plant, in particular those needed to feed BFG for CASOH, air for the Cu oxidation and the CO_2-rich stream obtained in the regeneration stage that must be sent (compressed up to 80 bar) to the CO_2 Purification Unit (CPU). However, a small fraction of electricity is recovered by expanding the flue gas from the oxidation stage to the atmosphere.

CO_2 Emissions

Most of the CO_2 emitted to the atmosphere is produced by partial calcination of $CaCO_3$ during the oxidation stage. This number can increase depending on the separation efficiency of the CO_2 purification unit (likely > 90%) except for the cases 3 and 4, where virtually pure CO_2 is directly obtained (after H_2O_v condensation) from the regeneration reactor. The efficiency of the separation also depends on the CO_2 purity at the regeneration step.

Table 4 summarizes the thermodynamic performance of all the proposed Ca-Cu looping configurations. The energy content of the H_2/N_2 fuel production is calculated with the cold gas efficiency (CGE) by means of Eq. (5):

$$CGE = \frac{\dot{m}_{H_2\ rich} LHV_{H_2\ rich}}{\sum \dot{m}_i LHV_i};\ i: BFG,\ COG,\ BOFG,\ NG \quad (5)$$

where i can be BFG, COG, BOFG, NG, m is the mass flow rate and LHV the corresponding low heating value of the fuels. The overall energy efficiency (η_E) is obtained assuming for the inlet and outlet energy streams of the process the same quality as follows:

$$\eta_E = \frac{\dot{m}_{H_2\ rich} LHV_{H_2\ rich} + H_{>500°C} + H_{>200°C}}{\sum \dot{m}_i LHV_i + E_{el}} \quad (6)$$

The primary energy efficiency (η_{PE}) is calculated by means of Eq. (7) assuming that the energy conversion in a boiler has an efficiency of 0.9 and the electricity generated in a combined cycle shows an efficiency of 0.6.

$$\eta_{PE} = \frac{\dot{m}_{H_2\ rich} LHV_{H_2\ rich} + \frac{H_{>500°C} + H_{>200°C}}{0.9}}{\sum \dot{m}_i LHV_i + \frac{E_{el}}{0.6}} \quad (7)$$

Finally, it has been calculated the specific energy consumption for CO_2 removed (λ_{CO2}), which measures the primary energy consumption related to CO_2 captured. This coefficient is

conceptually similar to the SPECCA (Specific Primary Energy Consumption for CO_2 Avoided) coefficient conventionally used to compare different CO_2 capture technologies with respect to a benchmark process (Spallina et al., 2017), and it provides valuable quantitative information about the feasibility of the separation process according to Eq. (8).

$$\lambda_{CO_2}\left[\frac{MJ_{\mathrm{LHV}}}{kg_{CO_2}}\right] = \frac{\sum \dot{m}_i LHV_i + \frac{E_{el}}{0.6} - \dot{m}_{H_2\ rich} LHV_{H_2\ rich} - \frac{H_{>500°C} + H_{>200°C}}{0.9}}{\dot{m}_{\mathrm{CO_2,\ equivalent\ in}} - \dot{m}_{\mathrm{CO_2,\ emitted}}} \quad (8)$$

The results indicate that the capacity to convert BFG into H_2/N_2 is limited to around 30% due to the high fuel requirement during the regeneration stage, which is no longer available as chemical energy. However, the high-temperature heat available results very promising since the quality and accessibility can be exploited in several other application including internal uses within the steelworks. In general, the energy efficiency (η_E) is higher than 75%, reaching maximum values around 88% in case of using natural as fuel gas for regeneration. Low values for the specific energy consumption of around 1.5 MJ_{LHV}/kg_{CO2} demonstrates that the proposed process offers great CO_2 capture rates with moderate energy penalty. The main difference between cases 1–2 and cases 3–4 is the purity at which the CO_2 is delivered after the regeneration stage. The significantly lower N_2 content in the CO_2-rich gas in cases 3 and 4 also decreases the cost of compression (up to 80 bar) to feed the CPU, resulting in higher energy efficiencies and reduced specific consumption for the separation of CO_2. Depending on the CO_2 purification route used in case 1 and case 2, the electric and thermal duty may vary significantly. Despite the overall higher energy performance obtained in the case 3 and case 4, this options are penalized in terms of CGE and higher CO_2 leakage (i.e., hot spots generated during the oxidation stage in beds loaded with higher content of Cu), which may result relevant in terms of economic performance and CO_2 capture efficiency.

CONCLUSION

A process design has determined the operating windows for a Ca-Cu looping process designed to obtain H_2-rich gas from BFG with CO_2 capture. The resulting decarbonized fuel gas can be used for onsite power generation or to obtain sponge iron by a DRI process, increasing the overall capacity of the plant. A large amount of high-temperature heat (up to 870°C) is also produced, which is suitable for covering heat demand of the steel mill or for power generation. Several configurations of the Ca-Cu looping process involving different fuel gases for the regeneration stage are technically viable in terms of process operating conditions and fuel utilization. The performance for every case has been compared in terms of primary energy consumption, product yields, CO_2 purity and potential CO_2 capture rate. Preliminary energy and mass balances of the process indicate that around 30% of the BFG can be upgraded via calcium assisted WGS if only BFG is used as reducing gas in the reduction/calcination stage. The maximum temperature achieved during the Cu oxidation stage can be maintained below 760°C, resulting in a negligible calcination of the $CaCO_3$ present in the bed. The regeneration stage carried out with the remaining 70% of the BFG gives as a result a product gas with 55%v. of CO_2 diluted in N_2, which needs a subsequent CO_2 purification step in a CPU. An energy efficiency of 74% for this option has been calculated together with a CO_2 capture efficiency of 98%. When the COG and BOFG available in the steel mill are used as reducing gases (together with BFG to cover the energy requirements of the operation), about 45% of the BFG can be upgraded giving as a result around 40% of additional H_2-rich stream compared to the previous case. An energy efficiency of 80% for this case is obtained together with a CO_2 capture efficiency of 95%. CO_2 purification is less demanding as the product gas from the regeneration stage contains a higher concentration of CO_2 (i.e., 64%vol. on a dry basis). When natural gas is used as fuel for sorbent regeneration, all the BFG can be directed to the CASOH stage, thereby maximizing the production of H_2/N_2. In these conditions, the purification of CO_2 is much easier as only CO_2 and $H_2O_{(v)}$ are produced during the regeneration stage. This option demands a large energy input to decarbonize all the BFG (i.e., around 600 MW_{th} of methane to upgrade 180 MW_{th} of BFG). However, most of the energy can be recovered as high-temperature heat resulting an energy efficiency for this option around 90%. The lower reduction enthalpy of CuO with CH_4 imposes higher copper content in the bed, which causes high temperatures during Cu oxidation, and therefore, higher CO_2 leakage resulting in a lower CO_2 capture efficiency of 80%. A higher pressure of 15 bar during Cu oxidation allows an improved CO_2 capture efficiency of 85%. In general, low values for the specific energy consumption between 1.4 and 1.7 MJ_{LHV}/kg_{CO2} have been calculated, which demonstrates the potential of this process to obtain H_2/N_2 gas and pure CO_2 from BFG with moderate energy penalty.

DATA AVAILABILITY STATEMENT

The raw data supporting the conclusions of this article will be made available by the authors, without undue reservation, to any qualified researcher.

AUTHOR CONTRIBUTIONS

JF carried out the process design and developed the basic reactor modeling. VS carried out the integration of the different Ca-Cu configurations in the steel mill. JA contributed to the process design, the discussion of the results, and revised the manuscript. All authors contributed to the article and approved the submitted version.

FUNDING

The authors acknowledge the financial support from the EPSRC BREINSTORM project, EP/S030654/1.

REFERENCES

Adanez, J., Abad, A., Garcia-Labiano, F., Gayan, P., and de Diego, L. F. (2012). Progress in chemical looping combustion and reforming technologies. *Prog Energy Combust.* 38, 215–282. doi: 10.1016/j.pecs.2011.09.001

Alarcón, J. M., and Fernández, J. R. (2015). CaCO3 calcination by the simultaneous reduction of CuO in a Ca/Cu chemical looping process. *Chem Eng Sci.* 137, 254–267. doi: 10.1016/j.ces.2015.06.030

Alarcón, J. M., Fernández, J. R., and Abanades, J. C. (2017). Study of a Cu-CuO chemical loop for the calcination of CaCO3 in a fixed bed reactor. *Chem. Eng. J.* 325, 208–220. doi: 10.1016/j.cej.2017.05.070

Antzara, A., Herecleous, E., Bukur, D. B., and Lemonidou, A. A. (2015). Thermodynamic analysis of hydrogen production via chemical looping steam methane reforming coupled with in situ CO2 capture. *Int. J. Greenh. Gas Con.* 32, 115–128. doi: 10.1016/j.ijggc.2014.11.010

Arasto, A., Tsupari, E., Karki, J., Pisila, E., and Sorsamaki, L. (2013). Post-combustion capture of CO2 at an integrated steel mill – Part I: technical concept analysis. *Int. J. Greenh. Gas. Con.* 16, 271–277. doi: 10.1016/j.ijggc.2012.08.018

ArcelorMittal (2019). *Climate Action Report 1, Luxembourg*. Available at: https://corporate.arcelormittal.com/media/press-releases/arcelormittal-publishes-first-climate-action-report (accessed February 18, 2020).

Bechara, R., Hamadeh, H., Mirgaux, O., and Patisson, F. (2018). Optimization of the iron ore direct reduction process through multiscale process modeling. *Materials* 11, 1094–1112.

Blamey, J., Anthony, E. J., Wang, J., and Fennell, P. S. (2010). The calcium looping cycle for large-scale CO2 capture. *Prog. Energ. Combus. Sci.* 36, 260–279. doi: 10.1016/j.pecs.2009.10.001

Boon, J., Cobden, P. D., van Dijk, H. A. J., and van Sint Annaland, M. (2015). High-temperature pressure swing adsorption cycle design for sorption-enhanced water-gas shift. *Chem. Eng. Sci.* 122, 219–231. doi: 10.1016/j.ces.2014.09.034

Cavaliere, P. (2019). *Clean Ironmaking and Steelmaking Processes Efficient Technologies for Greenhouse Emissions Abatement*. Switzerland: Springer Nature.

Díez-Martín, L., López, J. M., Fernández, J. R., Martínez, I., Grasa, G., and Murillo, R. (2018). Complete Ca/Cu cycle for H2 production via CH4 sorption enhanced reforming in a lab-scale fixed bed reactor. *Chem. Eng. J.* 350, 1010–1021. doi: 10.1016/j.cej.2018.06.049

Dreillard, M., Broutin, P., Briot, P., Huard, T., and Lettat, A. (2017). Application of the DMX CO2 capture process in steel industry. *Energy Procedia* 114, 2573–2589. doi: 10.1016/j.egypro.2017.03.1415

Dupont, V., Ross, A. B., Knight, E., Hanley, I., and Twigg, M. V. (2008). Production of hydrogen by unmixed steam reforming of methane. *Chem. Eng. Sci.* 63, 2966–2979. doi: 10.1016/j.ces.2008.02.015

Erans, M., Manovic, V., and Anthony, E. J. (2016). Calcium looping sorbents for CO2 capture. *Appl. Energ.* 180, 722–742. doi: 10.1016/j.apenergy.2016.07.074

Fernández, J. R., and Abanades, J. C. (2017a). Optimized design and operation strategy of a Ca- Cu chemical looping process for hydrogen production. *Chem. Eng. Sci.* 166, 144–160. doi: 10.1016/j.ces.2017.03.039

Fernández, J. R., and Abanades, J. C. (2017b). Overview of the Ca–Cu looping process for hydrogen production and/or power generation. *Curr. Opin. Chem. Eng.* 17, 1–8. doi: 10.1016/j.coche.2017.04.010

Fernández, J. R., Abanades, J. C., Murillo, R., and Grasa, G. (2012). Conceptual design of a hydrogen production process from natural gas with CO2 capture using a Ca–Cu chemical loop. *Int. J. Greenh. Gas Con.* 6, 126–141. doi: 10.1016/j.ijggc.2011.11.014

Fernández, J. R., Martínez, I., Abanades, J. C., and Romano, M. C. (2017). Conceptual design of a Ca–Cu chemical looping process for hydrogen production in integrated steelworks. *Int. J. Hydrogen Energ.* 42, 11023–11037. doi: 10.1016/j.ijhydene.2017.02.141

Gazzani, M., Romano, M. C., and Manzolini, G. (2015). CO2 capture in integrated steelworks by commercial-ready technologies and SEWGS process. *Int. J. Greenh Gas. Contr.* 41, 249–267. doi: 10.1016/j.ijggc.2015.07.012

Grasa, G., Navarro, M. V., Lopez, J. M., Diez-Martin, L., Fernandez, J. R., and Murillo, R. (2017). Validation of the H2 production stage via SER under relevant conditions for the Ca/Cu reforming process practical application. *Chem. Eng. J.* 324, 266–278. doi: 10.1016/j.cej.2017.04.134

Harrison, D. P. (2008). Sorption-enhanced hydrogen production: a review. *Ind. Eng. Chem. Res.* 47, 6486–6501. doi: 10.1021/ie800298z

Hills, A. W. D. (1967). Equilibrium decomposition pressure of calcium carbonate between 700 and 900 °C. *Bull. Inst. Min. Met.* 76C, 241–245.

Ho, M. T., Bustamante, A., and Wiley, D. E. (2013). Comparison of CO2 capture economics for iron and steel mills. *Int. J. Greenh. Gas. Contr.* 19, 145–159. doi: 10.1016/j.ijggc.2013.08.003

IEA Report (2017). *Energy Technology Perspectives: Catalysing Energy Technology Transformations*. Paris: International Energy Agency.

IEA Report (2019). *The Future of Hydrogen: Seizing today's opportunities*. France: International Energy Agency.

IEAGHG (2013). *Overview of the Current State and Development of CO2 Capture Technologies in the Ironmaking Process, 2013/TR3*. Cheltenham: IEAGHG.

IPCC (2018). *Global Warming of 1.5°C. An IPCC Special Report on the Impacts of Global Warming of 1.5°C Above Pre-Industrial Levels and Related Global Greenhouse Gas Emission Pathways, in the Context of Strengthening the Global Response to the Threat of Climate Change, sustainable Development, and Efforts to Eradicate Poverty*. Geneva: IPCC.

Ji, G., Yao, J. G., Clough, P. T., Diniz da Costa, J. C., Anthony, E. J., Fennell, P. S., et al. (2018). Enhanced hydrogen production from thermochemical processes. *Energ. Env. Sci.* 11, 2647–2672.

Jin, P., Jiang, Z., Bao, C., Hao, S., and Zhang, X. (2015). The energy consumption and carbon emission of the integrated steel mill with oxygen blast furnace. *Resour. Conserv. Recycl.* 117, 58–65. doi: 10.1016/j.resconrec.2015.07.008

Jonshagen, K., Sipocz, N., and Genrup, M. (2010). A novel approach of retrofitting a combined cycle with post combustion CO2 capture. *J. Eng. Gas Turbines Power* 133, 011703–011710.

Kazi, S. S., Aranda, A., di Felice, L., Meyer, J., Murillo, R., and Grasa, G. (2017). Development of Cost effective and high performance composite for CO2 Capture in Ca-Cu looping process. *Energy Procedia* 114, 211–219. doi: 10.1016/j.egypro.2017.03.1163

Kolios, G., Frauhammer, J., and Eigenberger, G. (2000). Autothermal fixed-bed reactor concepts. *Chem. Eng. Sci.* 55, 5945–5967. doi: 10.1016/s0009-2509(00)00183-4

Kumar, R. V., Lyon, R. K., and Cole, J. A. (2000). "Unmixed reforming: a novel authothermal cycling steam reforming process," in *Advances in Hydrogen Energy*, eds C. E. Gregoire Pedro and F. W. Laurent (Higham, MA: Kluwer Academic Publishers).

Lacroix, M., Broutin, P., Lethier, S., Nevicato, D., Petetin, B., De Coninck, E., et al. (2019). "DMX demonstration in dunkirk: 3D projects granted by H2020: scope and objectives," in *TCCS-10 Conference, Trondheim*, Norway.

Martavaltzi, C. S., Pampaka, E. P., Korkakaki, E. S., and Lemonidou, A. A. (2010). Hydrogen Production via steam reforming of methane with simultaneous CO2 capture over CaO-Ca12Al14O33. *Energy Fuels* 24, 2589–2595. doi: 10.1021/ef9014058

Martínez, I., Armaroli, D., Gazzani, M., and Romano, M. C. (2017). Integration of the Ca–Cu process in ammonia production plants. *Ind. Eng. Chem. Res.* 56, 2526–2539. doi: 10.1021/acs.iecr.6b04615

Martínez, I., Fernández, J. R., Abanades, J. C., and Romano, M. C. (2018). Integration of a fluidized bed Ca–Cu chemical looping process in a steel mill. *Energy* 163, 570–584. doi: 10.1016/j.energy.2018.08.123

Martínez, I., Fernandez, J. R., Martini, M., Gallucci, F., van Sint Annaland, M., Romano, M. C., et al. (2019a). Recent progress of the Ca-Cu technology for decarbonisation of power plants and carbon intensive industries. *Int. J. Greenh. Gas Con.* 85, 71–85. doi: 10.1016/j.ijggc.2019.03.026

Martínez, I., Martini, M., Riva, L., Gallucci, F., Van Sint Annaland, M., and Romano, M. C. (2019b). Techno-economic analysis of a natural gas combined cycle integrated with a Ca-Cu looping process for low CO2 emission power production. *Int. J. Greenh. Gas. Con.* 81, 216–239. doi: 10.1016/j.ijggc.2018.12.026

Martini, M., Martinez, I., Romano, M. C., Chiesa, P., Gallucci, F., and van Sint Annaland, M. (2017). Increasing the carbon capture efficiency of the Ca/Cu looping process for power production with advanced process schemes. *Chem. Eng. J.* 328, 304–319. doi: 10.1016/j.cej.2017.07.048

Martini, M., van den Berg, A., Gallucci, F., and van Sint Annaland, M. (2016). Investigation of the process operability windows for Ca-Cu looping for hydrogen production with CO2 capture. *Chem. Eng. J.* 303, 73–88. doi: 10.1016/j.cej.2016.05.135

Nishioka, K., Ujisawa, Y., Tonomura, S., Ishiwata, N., and Sikstrom, P. (2016). Sustainable aspects of CO2 ultimate reduction in the steelmaking process

(COURSE50 Project), part 1: hydrogen reduction in the blast furnace. *J. Sustain Metall.* 2, 200–208. doi: 10.1007/s40831-016-0061-9

Noorman, S., Gallucci, F., van Sint Annaland, M., and Kuipers, H. (2010). Experimental investigation of a CuO/Al2O3 oxygen carrier for chemical-looping combustion. *Ind. Eng. Chem. Res.* 49, 9720–9728.

Noorman, S., van Sint Annaland, M., and Kuipers, H. (2007). Packed bed reactor technology for chemical-looping combustion. *Ind. Eng. Chem. Res.* 46, 4212–4220. doi: 10.1021/ie061178i

Riva, L., Martínez, I., Martini, M., Gallucci, F., van Sint Annaland, M., and Romano, M. C. (2018). Techno-economic analysis of the Ca-Cu process integrated in hydrogen plants with CO2 capture. *Int. J. Hydrogen Energ.* 43, 15720–15738. doi: 10.1016/j.ijhydene.2018.07.002

Sakaria, D. (2017). "Case Study: Al Reyadah CCUS Project," in *Carbon Sequestration Leadership Forum*, (United Arab Emirates: Abu Dhabi Carbon Capture Company - Al Reyadah).

Santos, S. (2013). *Overview of the Current State and Development of CO2 Capture Technologies In the Ironmaking Process*. Cheltenham: IEA Publications.

Spallina, V., Marinello, B., Gallucci, F., Romano, M. C., and van Sint Annaland, M. (2017). Chemical looping reforming in packed-bed reactors: Modelling, experimental validation and large-scale reactor design. *Fuel Proces. Technol.* 156, 156–170. doi: 10.1016/j.fuproc.2016.10.014

Spallina, V., Romano, M. C., Chiesa, P., Gallucci, F., van Sint Annaland, M., and Lozza, G. (2014). Integration of coal gasification and packed bed CLC for high efficiency and near-zero emission power generation. *Int. J. Greenh. Ga.s Con.* 27, 28–41. doi: 10.1016/j.ijggc.2014.04.029

Tian, S., Li, K., Jiang, J., Chen, X., and Yan, F. (2016). CO2 abatement from the iron and steel industry using a combined Ca-Fe chemical loop. *Appl. Energ.* 170, 345–352. doi: 10.1016/j.apenergy.2016.02.120

Tonomura, S. (2013). Outline of Course 50. *Energy Procedia* 37, 7160–7167. doi: 10.1016/j.egypro.2013.06.653

Tsupari, E., Karki, J., Arasto, A., and Pisila, E. (2013). Post-combustion capture of CO2 at an integrated steel mill – part II: economic feasibility. *Int. J. Greenh. Gas. Con.* 16, 278–286. doi: 10.1016/j.ijggc.2012.08.017

Valverde, J. M. (2013). Ca-based synthetic materials with enhanced CO2 capture efficiency. *J. Mater. Chem. A* 1, 447–468. doi: 10.1039/c2ta00096b

van der Stel, J., Louwerse, G., Sert, D., Hirch, A., Eklund, N., and Pettersson, M. (2013). Top gas recycling blast furnace developments for 'green' and sustainable steelmaking. *Ironmak. Steelmak.* 40, 483–489. doi: 10.1179/0301923313z.000000000221

van Selow, E. R., Cobden, P. D., Verbraeken, P. A., Hufton, J. R., and van den Brink, R. W. (2009). Carbon capture by sorption-enhanced Water-Gas shift reaction process using hydrotalcite-based material. *Ind. Eng. Chem. Res.* 48, 4184–4193. doi: 10.1021/ie801713a

ZEP (2015). *CCS for Industry: Modelling the Lowest-Cost Route for Decarbonizing Europe*. Atlanta, GA: ZEP.

Conflict of Interest: The authors declare that the research was conducted in the absence of any commercial or financial relationships that could be construed as a potential conflict of interest.

frontiers in Energy Research

ORIGINAL RESEARCH
published: 03 July 2020
doi: 10.3389/fenrg.2020.00134

Energy-Efficient Distillation Processes by Additional Heat Transfer Derived From the FluxMax Approach

Dominik Schack[1], *Alexander Jastram*[1], *Georg Liesche*[1] *and Kai Sundmacher*[1,2]*

[1] Department Process Systems Engineering, Max Planck Institute for Dynamics of Complex Technical Systems, Magdeburg, Germany, [2] Department Process Systems Engineering, Otto-von-Guericke-University Magdeburg, Magdeburg, Germany

Distillation processes are an essential component of any chemical plant for the separation and purification of condensable mixtures. However, distillation columns account for the largest contribution to the total energy consumption of chemical processes due to their high heat demands. Consequently, there is a strong need for energy efficient column designs to reduce drastically the carbon dioxide emissions and thus to reach the settled climate goals of the chemical industry. In this paper, the FluxMax approach is used to identify energy optimal column designs. The representation of the distillation process by the elementary processes mixing, heating/cooling and phase separation leads to increased degrees of freedom of optimization compared to classical column modeling approaches. In this way, a non-conventional design with minimal energy consumption is identified. The energy-optimized configuration is a column with improved heat transfer between vapor and liquid streams. MESH equations are used for the validation of the FluxMax design, as they are state-of-the-art in process modeling tools. While the new design reduces the energy demand by up to 64% compared to the classical design, additional heat exchange area is required to exploit the energy reduction potential. A multi-objective optimization—energy duty vs. heat exchanger area—is carried out to identify the optimal trade-off between energy demand and heat exchanger area related capital cost. The highly energy-efficient designs identified by the FluxMax approach may be realized in practice by horizontal columns or modularized container solutions.

Keywords: process design, distillation columns, energy-efficiency, heat exchange, heat integration, methanol

OPEN ACCESS

Edited by:
Francois M. A. Marechal, École Polytechnique Fédérale de Lausanne, Switzerland

Reviewed by:
Massimiliano Errico, University of Southern Denmark, Denmark
Rajagopalan Srinivasan, Indian Institute of Technology Madras, India

***Correspondence:**
Kai Sundmacher
sundmacher@mpi-magdeburg.mpg.de

Specialty section:
This article was submitted to Process and Energy Systems Engineering, a section of the journal Frontiers in Energy Research

Received: *26 March 2020*
Accepted: *02 June 2020*
Published: *03 July 2020*

Citation:
Schack D, Jastram A, Liesche G and Sundmacher K (2020) Energy-Efficient Distillation Processes by Additional Heat Transfer Derived From the FluxMax Approach. Front. Energy Res. 8:134. doi: 10.3389/fenrg.2020.00134

1. INTRODUCTION

In order to achieve the ambitious goal of greenhouse gas emission neutrality within the European Union by 2050, the chemical industry is required to reduce drastically carbon dioxide emissions (European Commission, 2018). In addition to the substitution of raw materials by renewable resources, an increase in material and energy efficiency would reduce greenhouse gas emissions. A critical aspect for the resource efficiency of chemical processes is product purification due to the high energy demand and low energy efficiency of distillation columns (de Koeijer and Kjelstrup, 2000). Especially the backmixing of already separated streams within the column and large temperature differences in reboiler and condenser lead to large energy losses (Halvorsen and Skogestad, 2011). As a consequence, many papers were published in recent years that aim

to identify energy optimal distillation column designs. Most of these publications are based either on shortcut methods such as the Fenske-Underwood-Gilliland method (Fenske, 1932; Gilliland, 1940; Underwood, 1949) or on rigorous tray-by-tray model formulations (Biegler et al., 1997). Bausa et al. (1996) introduced a shortcut method using a new energy efficiency criterion by determining the pinch points of both column sections. In this way the minimum energy demand of non-ideal multi-component mixtures can be estimated efficiently. Another shortcut method was proposed by Adiche and Vogelpohl (2011), which allows the design of distillation columns for the separation of azeotropic mixtures. Caballero and Grossmann (2014) provided a broad overview of the optimization of both individual distillation columns and distillation processes. Halvorsen and Skogestad (2011) focused on energy-efficient distillation arrangements such as thermally coupled divided wall columns or multi-effect columns with additional heat transfer by pressure adjustment, which are particularly suitable for the modernization of existing plants. Ledezma-Martinez et al. (2018) investigated crude oil distillation plants and showed that a preflash unit can reduce the heat demand. Jiang et al. (2018b) compared different process intensification strategies for multi-component distillation and investigated the possibility of using synergy effects to design distillation systems that are both energy and economically efficient. In particular, the reduction potential by thermal coupling and simultaneous heat and mass integration is emphasized (Jiang et al., 2018a). An overview of heat integrated distillation columns (HIDiC) is given by Nakaiwa et al. (2003). HIDiCs are a special configuration of multi-effect columns that allow internal heat transfer from the rectification section to the stripping section. In combination with the use of heat pumps this leads to significant energy savings (Agrawal and Yee, 1994). The use of heat pumps is also the focus of the selection scheme proposed by Kiss et al. (2012). The scheme identifies the most promising technologies for a given separation task. Similarly, an enumeration-based framework of Cui et al. (2019) evaluates a variety of multi-effect processes, using shortcut methods to enable quick decision making (Cui et al., 2016). In the literature there are further surrogate models that try to overcome challenges posed by dynamic operations (Schäfer et al., 2019) or the need for global optimization (Keßler et al., 2019). In contrast, Waltermann and Skiborowski (2019) proposed a superstructure approach based on rigorous modeling to identify economically attractive distillation processes. In addition to the strong need for methods that allow a fast and efficient selection of different alternatives, there is also a necessity for process synthesis approaches to generate promising process alternatives. Papalexandri and Pistikopoulos (1996) introduced a modular representation framework using a mass and heat exchange superstructure for process synthesis, which was also applied to distillation processes (Ismail et al., 1999). Shah and Kokossis (2002) invented a synthesis framework that replaced the superstructure with a supertask representation. Since these methods are often only valid for ideal mixtures, Brüggemann and Wolfgang (2004) proposed a rapid screening approach for non-ideal mixtures, in which the distillation alternatives are ordered according to a suitable measure, such as energy consumption. A graph-theoretical approach that represents a chemical process as a network of nodes and edges leading to a mixed-integer optimization problem was presented by Friedler et al. (1992). In another work, this concept was used to solve separation network synthesis problems (Heckl et al., 2010). In contrast, Holiastos and Manousiouthakis (2004) used an infinite dimensional linear programming approach to identify globally optimal distillation network designs. The recently introduced FluxMax approach (Liesche et al., 2019; Schack et al., 2020) enables the optimization of chemical processes across different length scales while avoiding binary decision variables. The main features of FluxMax are simultaneous process design and heat integration as well as effective decoupling of process-based non-linearities by discretization of the thermodynamic state space. The proof-of-concept for application to separation processes was demonstrated in a recent publication (Schack et al., 2019). It was shown that each individual column tray can be represented by the elementary processes mixing, heating, cooling, and phase separation, as shown in **Figure 1**. In this paper it is shown that the FluxMax approach not only allows the design of classical distillation columns, but also the identification of novel designs with minimum energy consumption by using additional degrees of freedom due to the FluxMax formulation.

Binary methanol-water separation is selected as case study because of exceptional relevance of methanol (CH_3OH) in the context of Renewable-to-Chemicals. Methanol is very often regarded as a key molecule for the storage of electrical surplus energy (Surya Prakash et al., 2011; Räuchle et al., 2016; Moioli et al., 2019). The main reasons are: Methanol (i) is already an important platform chemical, (ii) can be used as direct gasoline substitute or can be further processed as Diesel substitute to DME or OME, (iii) is liquid at ambient conditions and thus has beneficial storage properties, and (iv) can be synthesized in a one step reaction from carbon dioxide (CO_2) and hydrogen (H_2). Furthermore, it was shown that an economically competitive production process can be designed even when using renewable energies (Schack et al., 2018) and under uncertain market situations (Adams et al., 2018).

After an introduction to the FluxMax approach and its formulation for distillation processes in section 2, the case study of the methanol-water separation is introduced in section 3. In addition to the objective functions for identifying the most energy efficient design as well as the stage minimal configuration, an extension of the classical modeling approach based on the MESH equations is derived. This serves as a benchmark of the results obtained by the FluxMax formulation. Finally, the designs obtained with the FluxMax approach and based on the MESH equations are compared in section 4. It is shown that the novel FluxMax design has a signifcantly lower energy demand than distillation column designs based on the regular MESH equations.

2. FLUXMAX APPROACH FOR DISTILLATION PROCESSES

The key idea of the FluxMax approach is to decouple process-based non-linearities from the subsequent flow optimization problem by discretization of the thermodynamic state space.

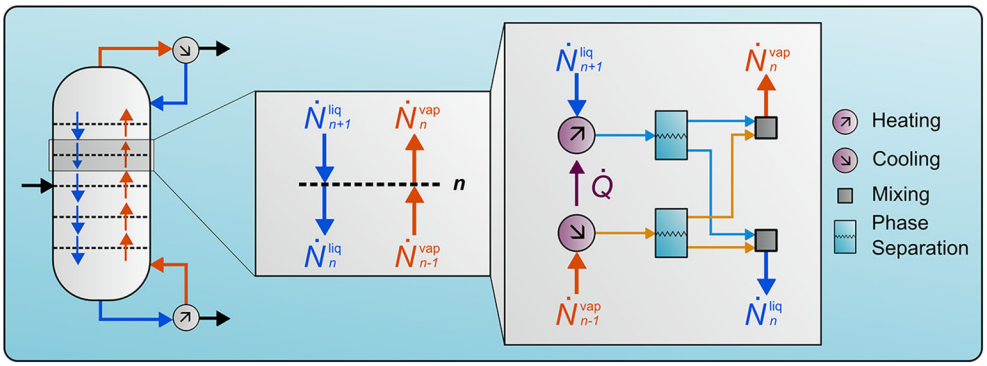

FIGURE 1 | Representation of the overall distillation process as a sequence of elementary processes mixing (gray), heating/cooling (magenta), and phase separation (cyan) as well as single tray fluxes. Adapted from Schack et al. (2019).

Therefore, the chemical process has to be represented by elementary processes. **Figure 1** shows the reprensentation of the distillation process by the elementary processes mixing, heating, cooling and phase separation. In a distillation column the mixing of hot vapor and cold liquid stream results in a distinct mixing temperature of each tray n that enables the phase separation. The FluxMax approach considers each flux separately: The hot vapor stream $\dot{N}_{n-1}^{\mathrm{vap}}$ has to be cooled to meet the tray temperature, and the cold liquid stream $\dot{N}_{n+1}^{\mathrm{liq}}$ has to be heated accordingly. Then, the phase separation of both streams takes place and the new vapor and liquid fractions are mixed together accordingly. The resulting liquid $\dot{N}_{n}^{\mathrm{liq}}$ and vapor $\dot{N}_{n}^{\mathrm{vap}}$ streams leave tray n and enter the neighboring trays.

The introduction of nodes and edges allows the representation of a chemical process as a directed graph. The FluxMax approach can be divided into three steps as shown in **Figure 2**: (i) discretization of the thermodynamic state space, (ii) modeling of the transitions between discrete state points, and (iii) simultaneous flow optimization and heat integration. The following introduction of the FluxMax formulation for separation processes is based on a prior contribution (Schack et al., 2019). However, the heat integration section is extended to enable not only the representation of classical column designs but also exploiting additional degrees of freedom due to the consideration of additional heat transfer options. A more comprehensive description of the FluxMax approach can be found in Schack et al. (2020) and Liesche et al. (2019).

2.1. Directed Graph Representation of Distillation Processes

In case of an isobaric distillation process, the thermodynamic state space is characterized by the thermodynamic coordinates temperature T and molar compositions x_α of the components $\alpha \in \mathcal{A}$, where $\mathcal{A}$ is the set of all pure substances. Three types of nodes are introduced: Thermodynamic substance nodes (TSN) $\mathrm{M}_i \in \mathcal{M}$, elementary process nodes (EPN) $\mathrm{E}_j \in \mathcal{E}$, and utility nodes (UN) $\mathrm{U}_l \in \mathcal{U}$, where $\mathcal{M}$, $\mathcal{E}$ and $\mathcal{U}$ denote the sets of all TSNs, EPNs, and UNs, respectively. A TSN is a discrete state point in the thermodynamic state space $(T, \mathbf{x})$ and thus corresponds to a specific chemical mixture at distinct temperature and composition. The transition from one TSN M_i to another M_{i+1} indicates a change of at least one thermodynamic coordinate, which is facilitated by the EPN E_j. For each EPN, a stoichiometric equation with generalized stoichiometric coefficients $\chi_{(\mathrm{E}_j)}^{(\mathrm{M}_i)}$ is introduced, which expresses the molar change of M_i during its transition through E_j. According to **Figure 2**, two types of EPN are required, corresponding to the elementary processes of heating/cooling and phase separation. It is important to mention that no unique EPN is required for the mixing process as only mixtures with identical thermodynamic coordinates are mixed. Thus the TSNs themselves can be interpreted as mixers. The stoichiometric coefficients for heating and cooling equal unity and minus unity ($\mathrm{M}_1 \longrightarrow \mathrm{M}_2$), respectively, as the number of moles remains constant. The stoichiometric equation for each elementary phase separation process S_j is given as follows:

$$\mathrm{M}_1 \rightarrow \chi_{(\mathrm{S}_j)}^{(\mathrm{M}_2)}\mathrm{M}_2 + \chi_{(\mathrm{S}_j)}^{(\mathrm{M}_3)}\mathrm{M}_3 \quad \forall\, \mathrm{S}_j \in \mathcal{E} \tag{1}$$

The stoichiometric coefficients $\chi_{(\mathrm{S}_j)}^{(\mathrm{M}_i)}$ are determined by the following equation system, where $x_{\alpha,\mathrm{F}}$ denotes the molar composition of component α of the flash inlet flux, and $x_{\alpha,\mathrm{B}}$, $x_{\alpha,\mathrm{D}}$ denote the corresponding compositions at the boiling (B) and dew (D) point curves at flash temperature:

$$x_{\alpha,\mathrm{F}} = \chi_{(\mathrm{S}_j)}^{(\mathrm{M}_2)} x_{\alpha,\mathrm{B}} + \chi_{(\mathrm{S}_j)}^{(\mathrm{M}_3)} x_{\alpha,\mathrm{D}} \tag{2}$$

$$1 = \chi_{(\mathrm{S}_j)}^{(\mathrm{M}_2)} + \chi_{(\mathrm{S}_j)}^{(\mathrm{M}_3)} \tag{3}$$

Here, it is assumed that the flash outlet is described by the vapor-liquid equilibrium. In general, non-ideal effects corresponding to efficiency losses or degradation effects could also be included, e.g., by introducing efficiency factors. In addition to the stoichiometric coefficients, a generalized process extent number (PEN) $\dot{\Gamma}_{(\mathrm{E}_j)}$ is introduced for each EPN that measures the

process extent. Since $\dot{\Gamma}_{(\mathrm{E}_j)}$ equals zero if E_j is inactive, the PEN also determines active EPNs in the subsequent optimization problem. The third class of nodes, the UNs U_l, are introduced for two reasons. First, the UNs provide the external heating and cooling duties at predefined temperature levels. Secondly, the UNs enable the indirect heat integration as an integral part of the optimization problem by introducing additional inequality constraints as described in section 2.3.

2.2. Conservation Laws of the Distillation Process

Steady state behavior is assumed, which results in no accumulation of mass and/or energy within the nodes. **Table 1** shows the mass- and energy balances for the three nodes introduced above.

The TSNs distribute mixtures with the same thermodynamic state within the chemical process network. Consequently, a TSN is connected by internal mass fluxes $\dot{N}^{(\mathrm{M}_i)}_{(\mathrm{E}_j)}$ corresponding to the input or output fluxes of EPNs, and by external fluxes that correspond to initially provided reactants $\dot{N}^{(\mathrm{M}_i)}_{\mathrm{ext,\,in}}$ or the final product $\dot{N}^{(\mathrm{M}_i)}_{\mathrm{ext,\,out}}$. No energy balances are required for TSNs as the thermodynamic state of all fluxes interacting with M_i is identical by definition, i.e., a mixture of the same composition but different temperature results in different TSNs. The chemical transition within the thermodynamic state space takes place via the EPNs. As a result, energy balances are formulated in addition to mass balances. The molar ratio of outlet and inlet fluxes is determined by the generalized stoichiometric coefficient $\chi^{(\mathrm{M}_i)}_{(\mathrm{E}_j)}$. The heat fluxes $\dot{Q}^{(\mathrm{U}_l)}_{(\mathrm{E}_j)}$ and $\dot{Q}^{(\mathrm{E}_j)}_{(\mathrm{U}_l)}$ connect an EPN to an UN and are dependent on the specific heating $\varphi^{\mathrm{in}}_{(\mathrm{E}_j)}$ or $\varphi^{\mathrm{out}}_{(\mathrm{E}_j)}$ cooling duty. These specific duties are calculated a priori, e.g., by non-linear equations of state. In addition, $\dot{Q}^{(\mathrm{E}_i)}_{(\mathrm{E}_j)}$ and $\dot{Q}^{(\mathrm{E}_j)}_{(\mathrm{E}_i)}$ correspond to internal heat fluxes that directly link two EPNs E_j and E_i. The direct heat transfer between EPNs is only considered in case of direct heat integration as introduced in the following section. While the superscripts of the fluxes denote the origin node, the subscript denotes the destination node. The utility nodes do not interact with mass fluxes, but only with heat fluxes. Besides the internal fluxes connecting EPNs and UNs, external heat fluxes are introduced, corresponding to the external heating $\dot{Q}^{\mathrm{ext,in}}_{(\mathrm{U}_l)}$ and cooling fluxes $\dot{Q}^{\mathrm{ext,out}}_{(\mathrm{U}_l)}$ of the utility node U_l.

2.3. Heat Integration Model

In this work the heat integration model introduced by Schack et al. (2020) is used. There, two distinct approaches—direct and indirect heat integration—were proposed. Indirect heat integration refers to the use of UNs at a predefined temperature that provide the internal heat transfer. In contrast, the direct approach considers the direct coupling of hot and cold streams as illustrated in **Figure 3**. Two inequalities are introduced to limit the heat fluxes transferred from hot streams to the cold stream or the cold utility, respectively, (Equation 4a) or from hot the utility/stream toward the cold streams (Equation 4b), respectively. Here, $T^{(\mathrm{E}_j)}_{\mathrm{in}}$, and $T^{(\mathrm{E}_j)}_{\mathrm{out}}$ denote the inlet and outlet temperatures of the corresponding cold or hot streams, and $\Delta T_{\min}$ the minimum temperature difference between both streams. The utilities are assumed to be heating or cooling reservoirs at a constant temperature. As a consequence, the in- and outlet temperature of i-th utility is set to the same utility temperature T^{util}_i. In addition, $\mathcal{K}^{\mathrm{H}}_m$ and $\mathcal{K}^{\mathrm{C}}_m$ denote the m-th row of the set of all possible permutations $\mathcal{K}^{\mathrm{H}}$ and $\mathcal{K}^{\mathrm{C}}$, respectively. These sets contain all possible combinations of interacting hot and cold streams for which heat transfer constraints must be formulated as derived in Schack et al. (2020).

$$0 \leq \frac{\mathrm{T}^{\max}_{\mathrm{H,in}} - T_{\mathrm{C,in},(\mathrm{E}_j)} - \Delta T_{\min}}{T_{\mathrm{C,out},(\mathrm{E}_j)} - T_{\mathrm{C,in},(\mathrm{E}_j)}} \varphi^{\mathrm{in}}_{(\mathrm{E}_j)} \dot{\Gamma}_{(\mathrm{E}_j)} - \sum_{k^{\mathrm{H}}_{mj} \in \mathcal{K}^{\mathrm{H}}_m} \dot{Q}^{(k^{\mathrm{H}}_{mj})}_{(\mathrm{E}_j)} \qquad \forall \dot{Q}^{(k^{\mathrm{H}}_{mj})}_{(\mathrm{E}_j)} \in \mathcal{K}^{\mathrm{H}}_m \tag{4a}$$

$$0 \leq \frac{T_{\mathrm{H,in},(\mathrm{E}_j)} - T^{\min}_{\mathrm{C,in}} - \Delta T_{\min}}{T_{\mathrm{H,in},(\mathrm{E}_j)} - T_{\mathrm{H,out},(\mathrm{E}_j)}} \varphi^{\mathrm{out}}_{(\mathrm{E}_j)} \dot{\Gamma}_{(\mathrm{E}_j)} - \sum_{k^{\mathrm{C}}_{mj} \in \mathcal{K}^{\mathrm{C}}_m} \dot{Q}^{(\mathrm{E}_j)}_{(k^{\mathrm{C}}_{mj})} \qquad \forall \dot{Q}^{(\mathrm{E}_j)}_{(\mathrm{k}^{\mathrm{C}}_{mj})} \in \mathcal{K}^{\mathrm{C}}_m \tag{4b}$$

The inequalities introduced in Equation (4) do not take into account in which order a hot stream transfers its heat to distinct cold streams if more than one partner stream is possible. Likewise applies to cold streams that are connected to more than one hot stream. It becomes obvious that the available heat that can be transferred to the second cold stream is lower than to the first cold stream since the energetic content of the hot stream is steadily decreasing. Therefore, two additional inequalities are introduced to account for the actual energy content.

$$0 \leq \frac{T_{k,\mathrm{in}} - T_{\mathrm{C,in},(\mathrm{E}_j)} - \Delta T_{\min}}{T_{\mathrm{C,out},(\mathrm{E}_j)} - T_{\mathrm{C,in},(\mathrm{E}_j)}} \left(\varphi^{\mathrm{in}}_{(\mathrm{E}_j)} \dot{\Gamma}_{(\mathrm{E}_j)} - \sum_{\substack{l \in \mathcal{K}^{\mathrm{H}} \\ l \neq k}} \dot{Q}^{(l)}_{(\mathrm{E}_j)} - \dot{Q}^{\mathrm{ext,\,in}}_{(\mathrm{E}_j)} \right) - \dot{Q}^{(k)}_{(\mathrm{E}_j)} \qquad \forall k \in \mathcal{K}^{\mathrm{H}} \tag{5a}$$

$$0 \leq \frac{T_{\mathrm{H,in},(\mathrm{E}_j)} - T_{k,\mathrm{in}} - \Delta T_{\min}}{T_{\mathrm{H,in},(\mathrm{E}_j)} - T_{\mathrm{H,out},(\mathrm{E}_j)}} \left(\varphi^{\mathrm{out}}_{(\mathrm{E}_j)} \dot{\Gamma}_{(\mathrm{E}_j)} - \sum_{\substack{l \in \mathcal{K}^{\mathrm{C}} \\ l \neq k}} \dot{Q}^{(\mathrm{E}_j)}_{(l)} - \dot{Q}^{\mathrm{ext,\,out}}_{(\mathrm{E}_j)} \right) - \dot{Q}^{(\mathrm{E}_j)}_{(\mathrm{k})} \qquad \forall k \in \mathcal{K}^{\mathrm{C}} \tag{5b}$$

The choice of the heat integration approach—direct or indirect—as well as the number of utilities affect the degrees of freedom of the subsequent optimization. In Schack et al. (2019), it was demonstrated how the FluxMax approach enables the design of classic distillation columns by introducing one dedicated UN for each discrete flash temperature. For an assumed minimum temperature driving force of $\Delta T_{\min} = 0$, a single column tray is represented as illustrated in **Figure 3A**. The magenta arrows in **Figure 3A** indicate the internal heat transfer from hot vapor stream (red arrow) toward cold liquid stream (blue arrow) via the corresponding UN.

Figure 3B shows how the consideration of additional utilities—with predefined temperatures between tray

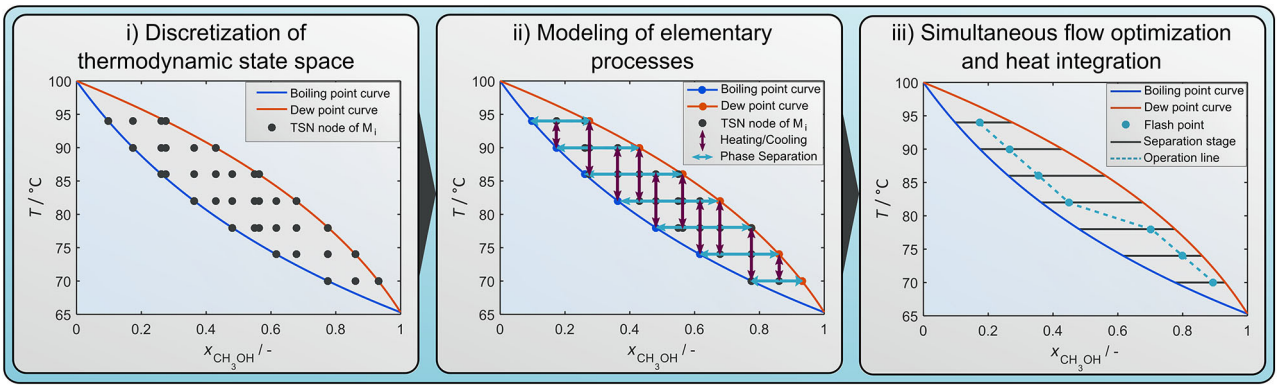

FIGURE 2 | Schematic procedure of the FluxMax approach for distillation column design. Adapted from Schack et al. (2019).

TABLE 1 | Conservation laws for introduced nodes.

Node	Mass balances	Energy balances
TSN $\forall\, M_i \in \mathcal{M}$	$0 = \sum_{E_j \in \mathcal{E}} \operatorname{sgn}\left(\chi_{(E_j)}^{(M_i)}\right) \dot{N}_{(E_j)}^{(M_i)} + \dot{N}_{\text{ext, in}}^{(M_i)} - \dot{N}_{\text{ext, out}}^{(M_i)}$	-
EPN $\forall\, E_j \in \mathcal{E}$ $\forall\, M_i \in \mathcal{M}$	$0 = -\operatorname{sgn}\left(\chi_{(E_j)}^{(M_i)}\right) \dot{N}_{(E_j)}^{(M_i)} + \chi_{(E_j)}^{(M_i)} \dot{\Gamma}_{(E_j)}$	$0 = \sum_{U_l \in \mathcal{U}} \left(\dot{Q}_{(E_j)}^{(U_l)} - \dot{Q}_{(U_l)}^{(E_j)}\right) + \left(\varphi_{(E_j)}^{\text{out}} - \varphi_{(E_j)}^{\text{in}}\right) \dot{\Gamma}_{(E_j)} + \sum_{E_i \in \mathcal{E}} \left(\dot{Q}_{(E_j)}^{(E_i)} - \dot{Q}_{(E_i)}^{(E_j)}\right)$
UN $\forall\, U_l \in \mathcal{U}$	-	$0 = \sum_{E_j \in \mathcal{E}} \left(\dot{Q}_{(U_l)}^{(E_j)} - \dot{Q}_{(E_j)}^{(U_l)}\right) + \dot{Q}_{(U_l)}^{\text{ext,in}} - \dot{Q}_{(U_l)}^{\text{ext,out}}$

temperatures—increases the heat transfer options and thus the degrees of freedom. The additional UNs enable the heat transfer between vapor and liquid flows entering and leaving the same two trays n and $n+1$ as well as the classical transfer between vapor and liquid flow entering the same tray n. The consideration of an infinite number of utilities is equivalent to the direct heat integration approach, where the hot vapor stream can transfer its heat directly to the cold liquid stream as illustrated in **Figure 3C**. While the direct approach leads to an increased computational effort, the calculation of the heat integration potential corresponds to the reduction potential obtained by pinch analysis—and thus to the maximum thermodynamically achievable—as shown in Schack et al. (2020). In contrast, the indirect approach limits the computational complexity, but is only an approximation of the thermodynamically possible energy reduction potential.

3. CASE STUDY

In this section the case study—the methanol-water separation—is introduced, followed by the derivation of the resulting optimization problems for both the FluxMax as well as the MESH formulation.

3.1. Methanol-Water Separation

Equation (6) shows the reaction equation of direct synthesis from carbon dioxide and water, which can be regarded as a combination of the reverse water-gas-shift reaction and the carbon monoxide synthesis process (Ott et al., 2012).

$$CO_2 + 3\,H_2 \longrightarrow CH_3OH + H_2O \tag{6}$$

While the obvious advantage lies in the direct use of the greenhouse gas CO_2, the coupled by-production of water (H_2O) is an unavoidable shortcoming that requires a downstream separation of the reactor output stream, even if all other possible side reactions—such as the production of higher alcohols or ethers (Ott et al., 2012)—are neglected. The unconverted gaseous reactants can be easily separated and recycled by cooling the reactor output stream and condensing the methanol-water mixture. However, a 50/50 mixture of methanol and water is fixed by the chemistry and must be further separated.

This separation task constitutes the case study of the present work. Whereas previous work (Schack et al., 2019) emphasized the feasibility and applicability of the FluxMax approach to the distillation design problem, the focus of this publication is the identification of non-conventional distillation designs with increased energy efficiency. The additional degrees of freedom provided by the consideration of additional heat integration possibilities introduced in section 2.3 are used.

The specifications of the scenario under consideration are listed in **Table 2**, assuming that the products are saturated liquid or vapor streams.

Following the three step procedure of the FluxMax approach introduced in section 2 the thermodynamic state space is

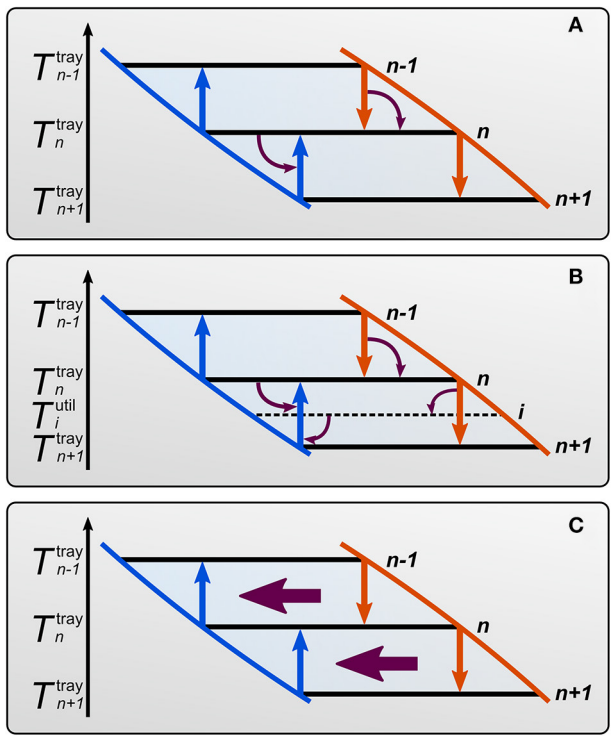

FIGURE 3 | Schematic illustration of the heat integration model: For classic distillation columns by consideration of one utility for each tray **(A)**, and for the exploitation of additional degrees of freedom: Applying indirect heat integration **(B)**, and direct heat integration **(C)**.

TABLE 2 | Definition of scenario.

Parameter	Symbol	Unit	Value
Operation pressure	p	bar	1
Feed temperature	T^{feed}	°C	80
Bottom temperature	T^{bot}	°C	93.52
Top temperature	T^{top}	°C	67.83
Feed composition	$x^{\text{feed}}_{CH_3OH}$	-	0.50
Bottom composition	$x^{\text{bot}}_{CH_3OH}$	-	0.10
Top composition	$x^{\text{top}}_{CH_3OH}$	-	0.95

discretized. The relevant thermodynamic state space for the isobaric binary separation of methanol and water is defined by the temperature T and the molar fractions of methanol x_{CH_3OH} and water x_{H_2O}. In addition, the entire thermodynamic state space is further limited by the vapor-liquid equilibrium which determines the attainable region. Assuming ideal conditions in both liquid and vapor phase, the boiling point curve which bounds the attainable region is computed as follows:

$$p = \sum_{\alpha \in \mathcal{A}} x_\alpha p_\alpha^{\text{sat}} \tag{7}$$

where p is the operation pressure and p_α^{sat} the saturation pressure of component α. The corresponding dew point curve

TABLE 3 | Antoine parameters for pure water and methanol for the relevant temperature range.

α	A_α	B_α	C_α	T_{low}/K	T_{up}/K	References
Water	4.6543	1435.264	-64.848	255.9	373	Stull, 1947
Methanol	5.20409	1581.341	-33.50	288.1	356.83	Ambrose and Sprake, 1970

is calculated by the equilibrium condition (Equation 8) and the definition of the equilibrium constant $K_\alpha := y_\alpha / x_\alpha$.

$$K_\alpha = \frac{p_\alpha^{\text{sat}}}{p} \tag{8}$$

The saturation pressure depends on the temperature and can be expressed by the semi-empirical Antoine equation:

$$\log_{10} p_\alpha^{\text{sat}} = \text{A}_\alpha - \frac{\text{B}_\alpha}{T + \text{C}_\alpha} \tag{9}$$

The Antoine parameters A_α, B_α, and C_α for pure water and methanol are listed in **Table 3**. They are valid if the pressure is given in bar and the temperatures in K.

3.2. Formulation of Optimization Problems

Based on the model derived in the previous chapter, the optimization problem is derived in this section. In addition, the design optimization problem based on the MESH equations is introduced for validation purposes.

3.2.1. FluxMax Formulation

The FluxMax formulation results in a linear feasible region due to the discretization of the thermodynamic state space (Liesche et al., 2019; Schack et al., 2020). If the objective function is also linear in terms of the fluxes (decision variables), the problem can be solved as a purely linear optimization problem (LP). The LP is given in Equation (10).

$$\begin{aligned} \min_{\boldsymbol{\varphi}} \; & f(\boldsymbol{\varphi}) \\ \text{s.t. } & \mathbf{A}_{\text{eq}}\boldsymbol{\varphi} = \mathbf{b}_{\text{eq}} \\ & \mathbf{A}_{\text{iq}}\boldsymbol{\varphi} \leq \mathbf{b}_{\text{iq}} \\ & \boldsymbol{\varphi}_{\text{lb}} \leq \boldsymbol{\varphi} \leq \boldsymbol{\varphi}_{\text{ub}} \end{aligned} \tag{10}$$

The vector of decision variables $\boldsymbol{\varphi} = (\dot{\mathbf{N}}, \dot{\boldsymbol{\Gamma}}, \dot{\mathbf{Q}})^\top$ contains all fluxes, namely mass fluxes $\dot{\mathbf{N}}$, heat fluxes $\dot{\mathbf{Q}}$, and the generalized process extent numbers $\dot{\boldsymbol{\Gamma}}$.

The mass and energy balances of TSNs, EPNs, and UNs (see **Table 1**) act as equality constraints and are expressed by the coefficient matrix $\mathbf{A}_{\text{eq}}$ and the vector of right-hand sides $\mathbf{b}_{\text{eq}}$. To limit the maximum amount of heat internally transferred, Equations (4) and (5) provide the inequality constraints, that are expressed by the coefficient matrix of inequalities $\mathbf{A}_{\text{iq}}$ and corresponding right hand sides $\mathbf{b}_{\text{iq}}$. In addition, the lower $\boldsymbol{\varphi}_{\text{lb}}$ and upper bounds $\boldsymbol{\varphi}_{\text{ub}}$ correspond to non-negativity constraints as well as external feed and product specifications according to the case study introduced in section 3.1.

The FluxMax approach is applied to two different objective functions: (i) minimization of number of separation trays (f^{I}), and (ii) minimization of the total energy duties (f^{II}). The number of trays is minimal if the liquid reflux stream from the condenser to the top tray is maximized. According to the FluxMax formulation, this liquid reflux stream corresponds to the sum of all liquid fluxes $\dot{N}^{\mathrm{liq,top}}_{(\mathrm{D}_j)}$ that are heated at the lowest tray temperature under consideration by means of the heater $\mathrm{D}_j \in \mathcal{E}$.

$$f^{\mathrm{I}}(\boldsymbol{\varphi}) = -\sum_{\mathrm{D}_j \in \mathcal{E}} \dot{N}^{\mathrm{liq,top}}_{(\mathrm{D}_j)} \tag{11}$$

The second objective function f^{II} seeks to identify the most energy efficient column design and can be written as sum of external heating $\dot{Q}^{\mathrm{ext,in}}_{(\mathrm{U}_l)}$ and cooling duties $\dot{Q}^{\mathrm{ext,out}}_{(\mathrm{U}_l)}$, which are desired to be minimized:

$$f^{\mathrm{II}}(\boldsymbol{\varphi}) = \sum_{\mathrm{U}_l \in \mathcal{U}} \dot{Q}^{\mathrm{ext,in}}_{(\mathrm{U}_l)} + \sum_{\mathrm{U}_l \in \mathcal{U}} \dot{Q}^{\mathrm{ext,out}}_{(\mathrm{U}_l)} \tag{12}$$

A key parameter of distillation columns is the reflux ratio r,which is defined as ratio between liquid reflux stream from the condenser and the total top product stream $\dot{N}_{\mathrm{top}}$:

$$r = \sum_{\mathrm{D}_j \in \mathcal{E}} \frac{\dot{N}^{\mathrm{liq,top}}_{(\mathrm{D}_j)}}{\dot{N}_{\mathrm{top}}} \tag{13}$$

3.2.2. MESH Formulation

The results that are obtained from the FluxMax formulation of the column design problem are benchmarked with results that are obtained from the solution of the MESH equations. With the MESH equations, the distillation column design is addressed using a tray-by-tray formulation (Biegler et al., 1997). The characteristic of the MESH equations is the solution of mass (M), equilibrium (E), summation (S), and energy balance in its enthalpy form (H) for each tray. Each tray is considered an equilibrium tray, which means that vapor and liquid flows leave a tray at thermodynamic equilibrium. **Figure 4A** illustrates the flows interacting with trays n and $n+1$. An overall distillation column for a binary mixture with reboiler and condenser duties has five degrees of freedom that are typically fixed using the feed condition as well as top and bottom product specifications. If heating and cooling duties can be theoretically provided at each tray, the degrees of freedom are increased by $n_{\mathrm{tray}} - 2$ where n_{tray} is the total number of trays including reboiler and condenser trays. Thus the tray temperatures can be set to any desired values.

Optimizing the tray temperature for a given feed and top/bottom product specification leads to the optimization problem in Equation (15) where all mass fluxes between trays, tray duties and tray temperatures are decision variables that are contained in the vector $\boldsymbol{\varphi} = (\dot{\mathbf{N}}^{\mathrm{feed}}, \dot{\mathbf{N}}^{\mathrm{liq}}, \dot{\mathbf{N}}^{\mathrm{vap}}, \dot{\mathbf{Q}}^{\mathrm{ext}}_n, \dot{\mathbf{Q}}^{\mathrm{out}}_n, \mathbf{T}_n)^{\top}$. $\dot{\mathbf{N}}^{\mathrm{feed}}$ is the vector of feed mass fluxes that is not illustrated in **Figure 4**. The objective function is the sum of external heating

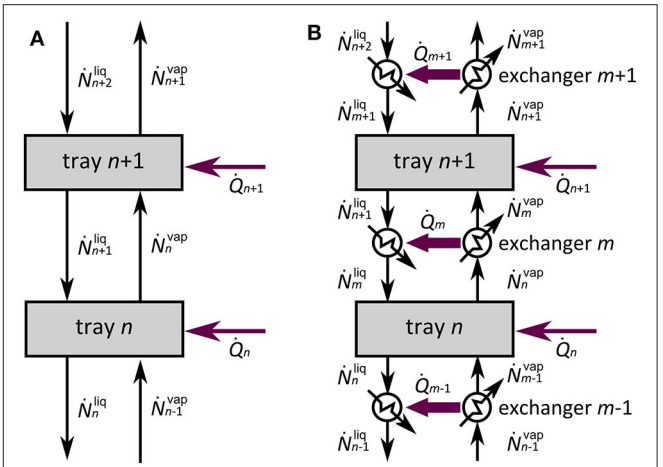

FIGURE 4 | Schematic illustration of tray n and neighboring tray $n+1$ for the regular formulation of MESH equations **(A)** and for the case where intermediate heat exchangers $m-1$, m and $m+1$ are considered **(B)**.

$\dot{Q}^{\mathrm{ext}}_n$ and cooling $\dot{Q}^{\mathrm{out}}_n$ requirements (Equation 14) of all trays n which is a linear objective function.

$$f(\boldsymbol{\varphi}) = \sum_{n=1}^{n_{\mathrm{tray}}} \dot{Q}^{\mathrm{ext}}_n + \sum_{n=1}^{n_{\mathrm{tray}}} \dot{Q}^{\mathrm{out}}_n \tag{14}$$

However, the equality constraints that contain the tray models are non-linear equations as derived in the **Supplementary Material** of this contribution. The resulting non-linear programming problem (NLP) is given as:

$$\begin{aligned} \min_{\boldsymbol{\varphi}} \; & f(\boldsymbol{\varphi}) \\ \text{s.t. } & h(\boldsymbol{\varphi}) = \mathbf{0} \\ & \boldsymbol{\varphi}_{\mathrm{lb}} \leq \boldsymbol{\varphi} \leq \boldsymbol{\varphi}_{\mathrm{ub}} \end{aligned} \tag{15}$$

The system of the MESH modeling equations is contained in $h(\boldsymbol{\varphi})$ and the lower and upper bounds correspond to non-negativity constraints and external feed and product specifications.

As an additional benchmark for the FluxMax results, the MESH equations are extended with $n_{\mathrm{HX}} = n_{\mathrm{tray}} - 1$ heat exchangers in order to enable heat exchange between vapor and liquid fluxes between trays as depicted in **Figure 4B** and derived in the **Supplementary Material**. Mass and energy balances for the heat exchangers are added to the system of modeling equations $h(\boldsymbol{\varphi})$ and the heat flows $\dot{Q}_m$ of the heat exchangers are added as new decision variables. Furthermore, feasibility constraints for the inter-tray heat exchange must be fulfilled:

$$T^{\mathrm{vap}}_n \geq T^{\mathrm{liq}}_m + \Delta T_{\mathrm{min}} \qquad m = 1, \ldots, n_{\mathrm{HX}} \tag{16a}$$

$$T^{\mathrm{vap}}_m \geq T^{\mathrm{liq}}_{n+1} + \Delta T_{\mathrm{min}} \qquad m = 1, \ldots, n_{\mathrm{HX}} \tag{16b}$$

These feasibility constraints are added to the optimization problem as inequality constraints $g(\boldsymbol{\varphi})$. They ensure that the

temperature from the bottom to the top of the column is decreasing monotonically.

4. RESULTS

The presented results are divided into three parts. The first part is the application of the FluxMax approach to classical distillation design tasks. Particularly the influence of the selected discretization is analyzed. In contrast, the second part emphasizes the exploitation of additional degrees of freedom by the FluxMax formulation. It is shown that an improved heat transfer between vapor and liquid streams drastically reduces the energy demand. Since the exploitation of the energy reduction potential requires an improved heat transfer, the third part evaluates implementation of the additional heat transfer and the influence of the minimum driving force of the heat transfer on the required heat exchange area.

4.1. Application to Conventional Distillation Design Tasks

4.1.1. Optimal Design of Distillation Processes

Figure 5 depicts the equilibrium diagram as temperature T vs. molar fraction x_{CH_3OH} of the low boiler methanol for a temperature discretization of 17 stages. The heat integration model for identifying classical distillation columns according to **Figure 3A** is used. The vapor-liquid area between boiling and dew curve is the attainable region (gray area) of the thermodynamic state space for the column design: All EPNs/TSNs are located in this region. The molar fraction $x_{H_2O} = 1 - x_{CH_3OH}$ of the missing component water can easily be calculated. The attainable region is enclosed by the boiling point curve (blue) and the dew point curve (red). In addition, the inlet and desired product specifications are marked as magenta and green dots. The black dots in **Figure 5** correspond to the TSNs and thus to the discrete points in the thermodynamic state space, which are connected by the elementary processes heating or cooling in vertical direction and phase separation in horizontal direction (see also **Figure 2**). The left-hand side of **Figure 5** shows the actual state space representation of the optimal pathways according to the considered objective function. The active elementary processes along the different TSNs from the feed TSN—magenta point—to the lower and upper product TSNs—green points—are indicated by the cyan lines.

Once the optimal solution has been found, all liquid and vapor flows entering or leaving a particular tray and the corresponding molar composition are known. This allows the calculation of the actual mixing points (**Figures 5B,D** cyan points) at each tray. The resulting operation lines (dashed cyan line) are shown on the right-hand side of **Figure 5**. In addition, the corresponding liquid (red line) and vapor (blue line) flows are shown.

The two upper diagrams (**Figures 5A,B**) show the optimal results for the first objective: Minimizing the number of trays (Equation 11). The optimization algorithm reveals that the separation task in this scenario (**Table 2**) requires at least five separation trays. In order to achieve the desired product purification with the minimum number of trays, stages with as different temperatures as possible are selected. The resulting operation line has the shape of a zigzag curve, with the slopes between the first two or the last two trays being as steep as possible. While the number of trays is minimal, the energy duty (534.0 kW/mol_{feed}) and the reflux ratio (7.83) are very high. The beginning of each distillation column design is the calculation of the minimum number of stages. This is typically achieved using the Fenske equation (Fenske, 1932), but the results in **Figure 5A** show, that the FluxMax approach returns the same minimum number of trays.

The lower two plots (**Figures 5C,D**) correspond to the most energy efficient column design. As expected, the optimal path is found when phase separation occurs at all possible discrete temperature levels. It can be seen that starting from the TSN of the feed, the mixture is split into the corresponding saturated equilibrium states, which are then cooled or heated to the next possible temperature considered, which represents a different column tray. The resulting operation line in **Figure 5D** is located in the stripping section of the column near the boiling point curve and in the rectifying section near the dew point curve. The total energy demand is 36.0 kW/mol_{feed} and the reflux ratio is 0.25.

Both results are consistent with the expectation that the total energy demand is inversely proportional to the number of trays. In the following, the FluxMax approach is utilized using additional degrees of freedom. It is shown that improved heat exchange leads to the same energy reduction as an increase in the number of stages. To illustrate the effect for a different number of stages, it is necessary to force the optimizer to select a certain number of trays. However, unlike the MESH equations, FluxMax formulations are based on a flux optimization on a predefined temperature grid. There the energy minimum is always found for the maximum number of stages, which corresponds to temperature discretization as can be seen in **Figure 5C**. In order to be able to use the same discretization—which guarantees the comparability of the results—and still force the optimization algorithm to select only a limited number of trays, integer variables y_n are introduced below for each tray. In this way, the actual number of selected trays n_{tray} is limited by the following inequality:

$$\sum_{n=1}^{n_{tray}} y_n \leq n_{tray} \tag{17}$$

Although the remaining FluxMax formulation remains the same, it is important to note that the following figures are based on a mixed integer linear program (MILP) solved with the efficient MILP solver SCIP (Gleixner et al., 2018).

Figure 6 illustrates again the operation lines for the most energy efficient design identified for a discretization of 17 temperature levels. However, unlike **Figure 5**, the newly added constraints limit the selectable levels to 9 (**Figure 6A**), and 11 (**Figure 6B**), respectively. Interestingly, the optimization algorithm selects the stages so that more trays are active near the feed point and only a few in the remaining stripping and rectifying section. By selecting trays with smaller temperature differences in the feed section of the column, a better

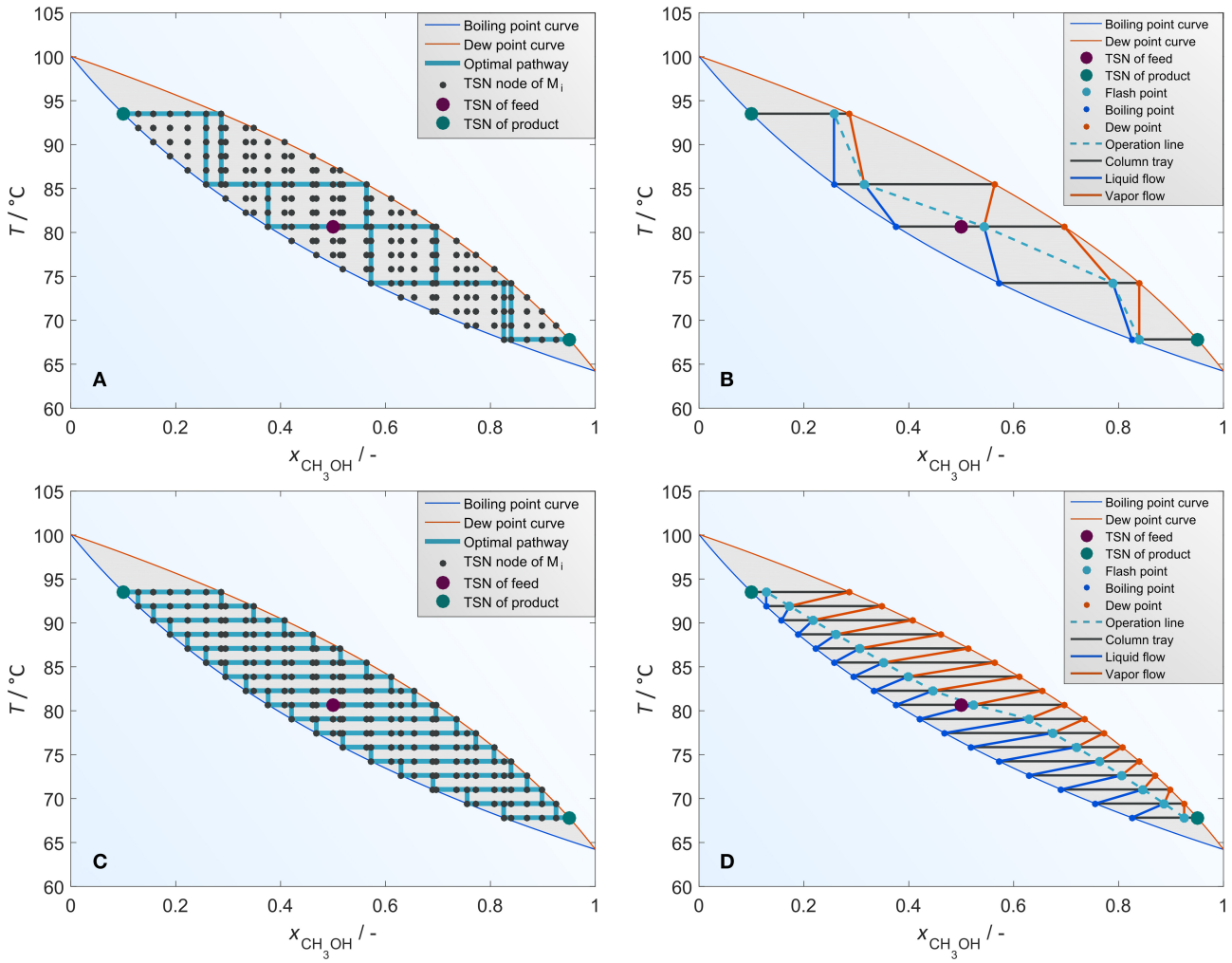

FIGURE 5 | Optimal pathway within the thermodynamic state space for the two objective functions (Equations 11, 12; left-hand sides), and corresponding operation line for a temperature discretization of 17 (right-hand sides); minimization of number of trays **(A,B)**, and total energy minimization **(C,D)**.

approximation to the optimal operating line for the unlimited case is achieved (**Figure 5D**). Again, the calculated results correspond well with the known temperature profiles of classical distillation columns (Biegler et al., 1997).

4.1.2. Influence of the Temperature Discretization

While the benefit of the FluxMax formulation is the decoupling of the non-linearities from the optimization step by discretization of the thermodynamic state space, the disadvantage is the grid dependence of the obtained results. Therefore, in the following the energy demand is analyzed as a function of different temperature discretizations, corresponding to the maximum number of trays. **Figure 7** shows the influence of the selected temperature discretization on the energy demand for the classical column design task as shown in **Figure 3A**. For each discretization—5, 9, 17, 33—the temperatures are distributed equidistantly between the desired top and bottom product temperatures. This ensures two prerequisites: i) a separate tray is always considered at the assumed feed temperature, and ii) for each finer discretization, the same temperatures of the coarser grids are considered in addition to the newly added temperatures. While the first condition ensures that no pre-heating or pre-cooling of the feed is required, the second condition allows a fair comparison of the different cases. In addition to the results obtained by the FluxMax formulation, the energy duties calculated by classical MESH equations are shown in **Figure 7**.

As expected, **Figure 7** shows that the calculated total energy demand depends strongly on the discretization. The finer the grid, the more the calculated energy duties correspond to the MESH results. In case of the coarsest discretization of only 5 temperature steps, the calculated energy demand does not depend on the limitation of the selectable stages, because the maximum number of trays is only 5. In the other cases, however, the grid dependency decreases with increasing number of actually selected trays. Even with a discretization of 9 temperature levels, the FluxMax results are quite close to the

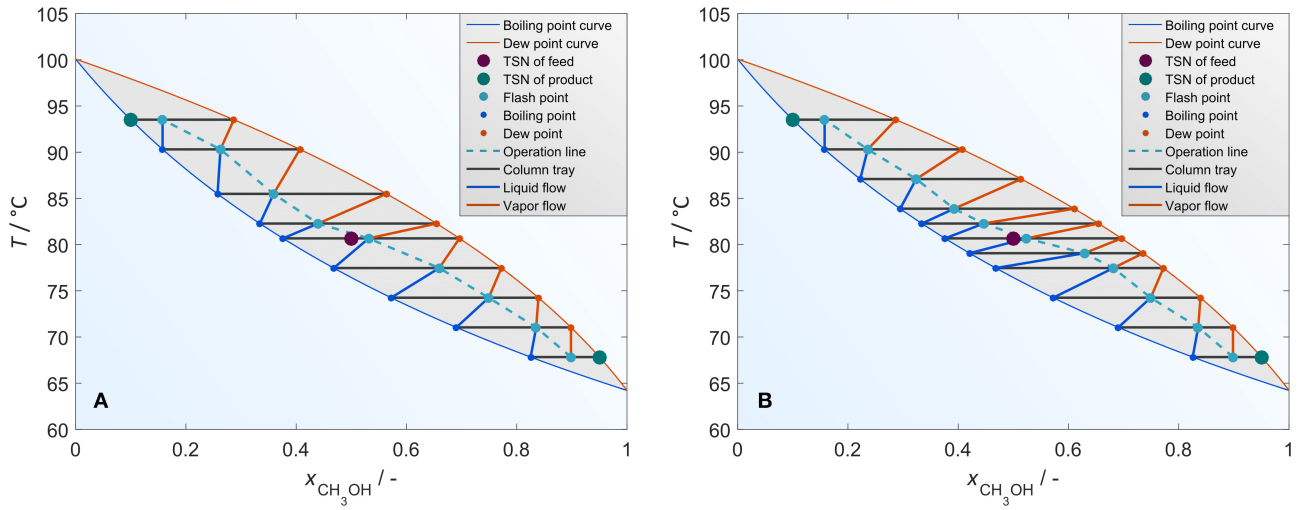

FIGURE 6 | Operation line for a temperature discretization of 17 if the number of selectable tray stages is limited to 9 **(A)**, and 11 **(B)**.

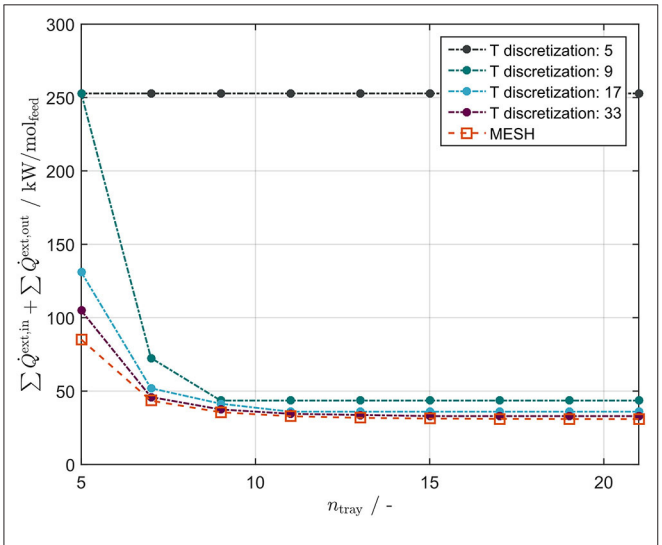

FIGURE 7 | Influence of number of separation stages on the total energy duty if no additional heat transfer is considered. Illustrated are the results of the FluxMax formulation considering different temperature discretizations (5, 9, 17, and 33 temperature levels) as well as of the classical MESH formulation.

MESH results if the number of selected trays is bigger than 7. In contrast, the selection of an appropriate grid is crucial if the number of trays is low. However, it is important to note that the accuracy of the FluxMax formulation can be improved not only by finer grids, but also by the selected temperatures. Both formulations have the same energy requirement when the actual tray temperatures calculated with the MESH equations are used as input for the FluxMax formulation. The discretization procedure with adding new temperature levels is bound to this example. Separation tasks with for example azeotropic points or other non-ideal behavior may require different discretization schemes.

4.2. Energy Efficient Designs by Additional Heat Transfer

After presenting the general applicability of the FluxMax approach to separation tasks, the following shows the influence of the additional heat transfer options as shown in **Figures 3B,C**. Within the FluxMax approach, each mass and heat flux is modeled separately. The formulation thus allows the identification of non-conventional configurations. In the case of the distillation column, the consideration of improved heat transfer between liquid and vapor streams—enabled either by direct or indirect heat integration—results in a lower energy consumption compared to classical column design. **Figure 8** illustrates the energy requirements for the configurations with improved heat integration. A minimum temperature difference of $\Delta T_{min} = 0$ K is assumed. In this way, the theoretically maximum amount of heat that can be transferred is evaluated. Later, the influence of different minimum driving forces will be examined in more detail. Furthermore, the energy requirements calculated with the MESH equations are presented as a benchmark. For indirect heat integration, the discretization, which corresponds to the number of utility nodes, plays a role: An additional utility node is introduced at the intermediate temperature of two neighboring separation stages. Thus, the more auxiliary nodes are considered, the more additional heat transfer options are available, resulting in lower energy requirements. In any case the energy demand is lower compared to non-heat integrated columns (see **Figure 7**). Compared to the benchmark case, the largest energy saving potential is observed when the maximum number of stages is small ($\leq$ 9). In this range, even rather coarse discretizations lead to more energy efficient configurations: Even a temperature discretization of 9—corresponding to 17 utility levels—result in a lower energy consumption as the classical MESH design. For a larger number of stages, however, the optimizer cannot find better configurations because the discretization is limited.

However, if direct heat integration is considered, which corresponds to an infinite number of utility nodes, the calculated results are independent of the temperature discretization. For any number of stages, the same theoretically feasible minimum energy requirement is calculated at 30.7 kW for each mole of feed flux, resulting in energy savings of up to 64% compared to classical MESH designs. The calculated heat integration potential has also been validated using the extended MESH equations, which result in the same results as the direct heat integration approach. Since the energy demand of standard columns decreases rapidly with an increasing number of stages, the potential for columns with improved heat transfer decreases with each additional tray.

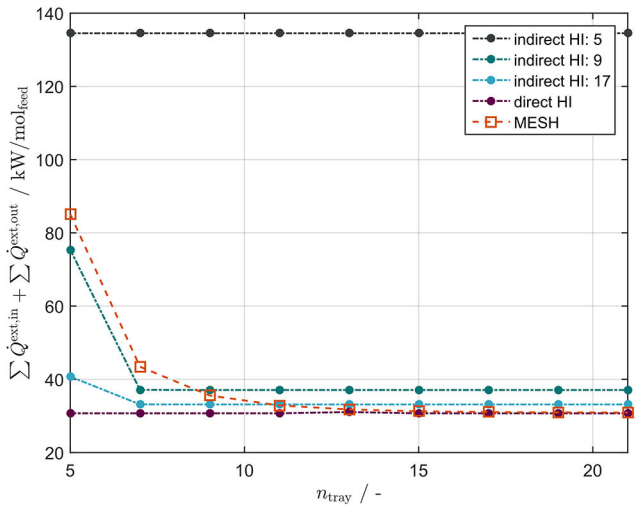

FIGURE 8 | Influence of number of separation stages on the total energy duty if additional heat transfer is considered. Illustrated are the results of the FluxMax formulation considering different temperature discretizations (5, 9, and 17 temperature levels) as well as of the classical and extended MESH formulations as a benchmark.

If the direct heat integration result is taken as the minimum energy requirement and thus the most energy efficient configuration, it is evident that an improved heat transfer (with $\Delta T_{\text{min}} = 0$ K) corresponds to a classical column design with an infinite number of trays. Consequently, there is a trade-off between additional separation stages—corresponding to the column area—and additional heat transfer area. Before discussing the influence of considering different minimum driving forces ΔT_{min} on the required heat transfer area, **Figure 9A** shows the additional heat transfer within the column schematically. A two-phase heat exchanger transfers the heat provided by the hot vapor stream flowing between two stages to the cold liquid stream flowing in the opposite direction. The practical realization of two-phase heat exchangers is beyond the scope of this work, therefore the interested reader is referred to adequate literature (Bejan and Kraus, 2003; Kuznetsov, 2018). In contrast to the MESH formulation, the FluxMax formulation is not associated to a particular design. As a consequence, besides the representation as classic distillation column (**Figure 9A**), the resulting configuration can also be interpreted as a series of heat integrated flash drums with intermediate heat exchange (**Figure 9B**). The interpretation as flash drums allows a simpler

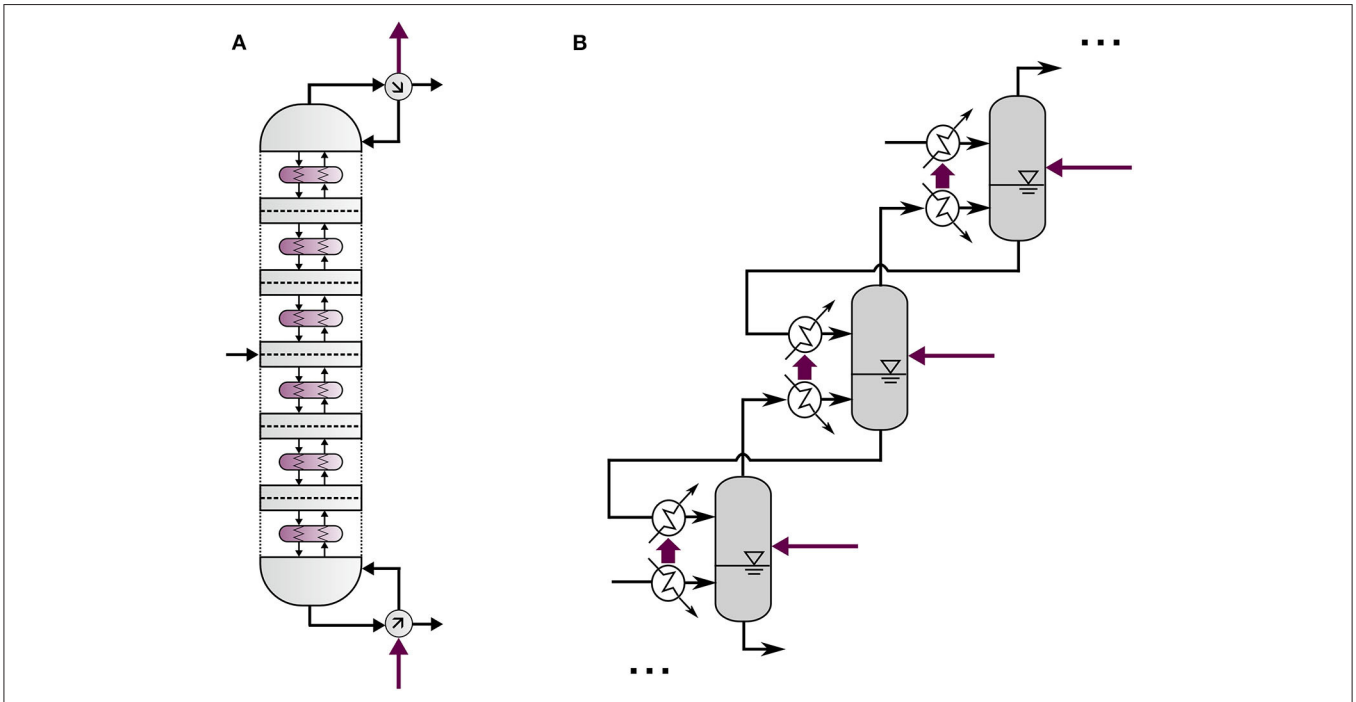

FIGURE 9 | Schematic illustration of a column with intermediate heat exchangers **(A)**, and corresponding interpretation as a series of heat integrated flash drums **(B)**.

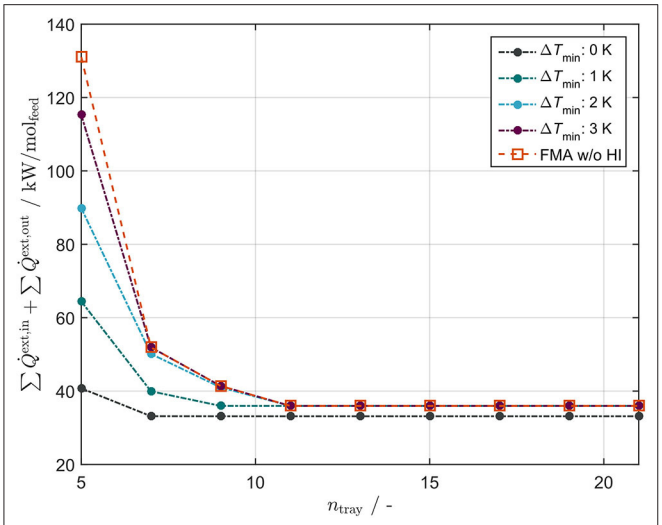

FIGURE 10 | Influence of the selected minimum temperature difference ΔT_{min} of the additional heat transfer. Illustrated are the heat integrated results for $\Delta T_{min} = 0, 1, 2, 3$ K as well as the non-integrated result as a benchmark for discretization of 17 temperature stages.

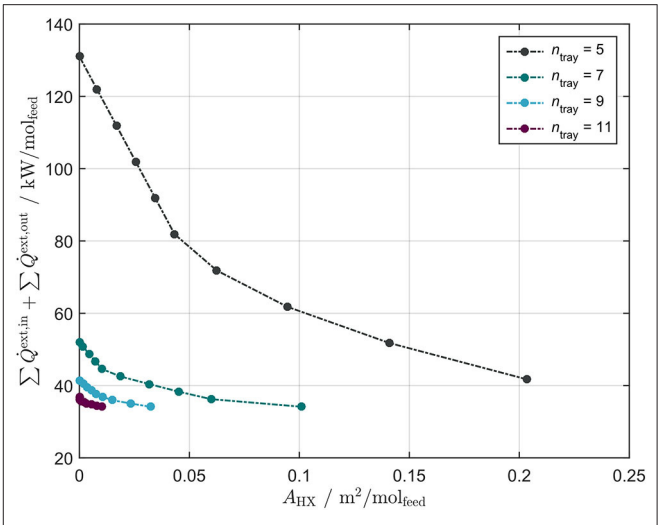

FIGURE 11 | Pareto curve of the two competing objectives illustrating the trade-off between minimization of total energy duty and minimization of additional heat transfer area for different number of separation stages: 5, 7, 9, and 11 stages.

technical implementation as well as the modular design of the separation system. The latter is particularly interesting in the context of Power-to-X, where smaller decentralized plants can be built to make efficient use of excess electrical energy. According to **Figure 8**, a sequence of a minimum number of flash drums is sufficient to reduce the total energy demand drastically.

4.3. Implementation of the Improved Heat Transfer

4.3.1. Influence of the Minimum Driving Force ΔT_{min}

In all calculations up to this point, a minimum driving force of $\Delta T_{min} = 0$ K is assumed, which is technically not possible, since it would require an infinitely large heat exchange area. To obtain finite areas, a minimum driving force $\Delta T_{min} > 0$ K must be present. **Figure 10** illustrates the influence of the assumed minimum temperature difference ΔT_{min} on the actual energy demand. In addition to the results obtained by considering four different minimum driving forces ($\Delta T_{min} = 0, 1, 2, 3$ K), the non-heat integrated case is presented as a benchmark. All results are based on a discretization of 17 temperature levels.

The black curve ($\Delta T_{min} = 0$ K) and the red benchmark curve (non-heat integrated case) are the same as the corresponding curves in **Figures 7**, **8**. They correspond to both the best and worst case scenarios for a given temperature discretization. Two observations can be made: (i) the bigger the minimum driving force becomes, the bigger the energy duties become and the closer the curve becomes to the benchmark curve, and (ii) for a certain number of stages there is no heat integration potential for $\Delta T_{min} > 0$ K. Both observations indicate for the case study under consideration that, on the one hand, there is an enormous energy saving potential for a small number of stages, but that this potential can only be used for very small driving forces. Even at very small minimum temperature differences of $\Delta T_{min} = 3$ K, which are already very small compared to the usually technically applied minimum driving forces of $\Delta T_{min} > 10$ K, the potential almost disappears. However, there may be technical solutions that can exploit the identified energy saving potential. A possible realization of the calculated design could be the concept of horizontal columns, where the contact time between vapor and liquid streams is increased and adjusted by the angle of the column (Kim et al., 2013; Jang and Kim, 2015).

4.3.2. Evaluation of the Required Heat Exchanger Area

The previously presented results show that improved heat transfer reduces drastically the energy demand of distillation columns. However, the heat has to be transferred across very small temperature differences, which results in a low driving force for the heat transfer and thus large heat exchange areas. The heat exchange area $A^{HX}_{(E_j)}$ that is required for each EPN E_j depends on the sum of received heat fluxes and the corresponding mean logarithmic temperature differences $\Delta T^{(E_i)}_{m,(E_j)}$ and $\Delta T^{(U_l)}_{m,(E_j)}$ of the internal heat transfers between EPNs E_i as well as UNs U_l toward E_j. Furthermore, the transfer area is inversely proportional to the heat transfer coefficient k^{HX}:

$$A^{HX}_{(E_j)} = \frac{1}{k^{HX}} \left(\sum_{E_i \in \mathcal{E}} \frac{\dot{Q}^{(E_i)}_{(E_j)}}{\Delta T^{(E_i)}_{m,(E_j)}} + \sum_{U_l \in \mathcal{U}} \frac{\dot{Q}^{(U_l)}_{(E_j)}}{\Delta T^{(E_i)}_{m,(E_j)}} \right) \quad (18)$$

The heat transfer coefficient k^{HX} depends on the fluids and the type of heat exchanger. A constant value of 3000 W/m^{2}K is assumed for the two-phase heat exchange, which corresponds to a vapor-liquid heat transfer in a spiral plate heat exchanger (Roetzel and Spang, 2010). It is evident that there is a trade-off between

an increase in internal heat flows—corresponding to a reduction in operating costs—and more heat transfer area corresponding to an increase in capital costs. A multi-objective optimization is performed by applying the ϵ-constraint method (Miettinen, 1998). Therefore, one of the competing targets (Equation 18) is added as an additional constraint to the optimization problem. As a result, the Pareto-optimal point of the second objective (Equation 12) is calculated. By systematic variation of the heat exchanger area, the Pareto curves for distinct number of stages and a minimum driving force $\Delta T_{\min} = 0$ are generated and plotted in **Figure 11**.

The Pareto curves denote the limits at which an improvement of one objective is only possible if the second objective is simultaneously worsened. According to **Figure 8**, it can be seen that the energy saving potential decreases with an increasing number of stages. Interestingly, the slope of the curves is steepest for small heat exchanger areas. This means that a rather small heat exchanger area leads to a rather large energy saving potential, especially for small columns with a small number of stages. After the first steep decline, the curves become flatter, which corresponds only to a small energy reduction. Consequently, the required area is very high if the full integration potential is to be exploited at the minimum number of stages. The heat transfer area required to save a separation tray also becomes smaller for larger columns. While a heat exchange area of almost 0.14 m^2/mol_{feed} is needed to achieve the same energy demand for 5 stages compared to a column with 7 stages, only 0.025 m^2/mol_{feed} is sufficient to save two additional trays.

Figure 11 also summarizes the main results of this paper. The results show that an improved heat exchange reduces the energy demand up to 64% compared to classic distillation columns, and thus can contribute to the reduction of carbon dioxide emissions. For the case study under consideration, however, heat transfer across very small temperature differences is required, which result in additional heat exchanger areas up to 0.21 m^2 per mole feed stream. Nevertheless, the separation of different mixtures—with more distant boiling points—could have a greater potential for larger temperature differences and thus less heat exchange area.

5. CONCLUSION

This paper proposes an approach to design distillation columns with significantly reduced energy requirements. In order to achieve optimal designs, the FluxMax approach decouples process-based non-linearities from the optimization problem by discretizing the thermodynamic state space and representing the distillation process by three elementary processes: Mixing, heating/cooling and phase separation. The versatility of the FluxMax approach is demonstrated by applying two different objective functions: Minimizing (i) the number of trays, and (ii) the energy demand. As a consequence of the simultaneous consideration of heat integration by introducing inequality constraints, the design space is increased compared to classical design methods based on the MESH equations. The case study under consideration is the methanol-water separation, which is a key step of the methanol production process that is of high interest in the context of Renewables-to-Chemicals. A non-conventional design has been identified that outperforms classical distillation column designs based on the MESH equations. It is shown that an improved heat transfer between hot vapor streams and cold liquid streams—with the consequence of additional heat exchange area—reduces the energy consumption in the same way as additional separation stages of classical columns. In this way, the optimized design based on the FluxMax formulation reduces the energy consumption by up to 64% compared to conventional designs. The trade-off between the reduction in energy demand—corresponding to lower operating costs—and the increase in heat exchange area—corresponding to higher capital costs—is analyzed through multi-objective optimization. The MESH equations are extended and used to validate the FluxMax design and prove that the achieved results are thermodynamically consistent. The results underline the strength of the FluxMax approach to design distillation processes with increased degrees of freedom, which allows the identification of highly energy efficient designs.

However, the presented results show that heat must be transferred across very small temperature differences to fully exploit the identified energy reduction potential. Nevertheless, it is possible that separation tasks of other mixtures—with more different boiling points of the pure components—also have a high potential for higher temperature differences, which would lead to a lower requirement for heat exchange area. The practical implementation of the highly energy-efficient designs by using horizontal columns is also possible, which reduces the surface area by improving the heat transfer by extending the contact time of vapor and liquid streams. The identified energy potential is of particular interest for applications with a limited number of trays, e.g., decentralized or modularized container systems, as the FluxMax design can be represented as a cascade of heat-integrated flash drums with internal heat exchange.

DATA AVAILABILITY STATEMENT

The original contributions presented in the study are included in the article/**Supplementary Material**, further inquiries can be directed to the corresponding author/s.

AUTHOR CONTRIBUTIONS

DS and GL developed the design methodology. DS extended the methodology to distillation processes, performed the main calculations, and wrote the manuscript. AJ supported the calculations. GL contributed to the calculations and supported the writing of the manuscript. KS supervised the project. All authors contributed to the article and approved the submitted version.

SUPPLEMENTARY MATERIAL

The Supplementary Material for this article can be found online at: https://www.frontiersin.org/articles/10.3389/fenrg.2020.00134/full#supplementary-material

REFERENCES

Adams, T. A. II, Thatho, T., Le Feuvre, M. C., and Swartz, C. L. E. (2018). The optimal design of a distillation system for the flexible polygeneration of dimethyl ether and methanol under uncertainty. *Front. Energy Res.* 6:41. doi: 10.3389/fenrg.2018.00041

Adiche, C., and Vogelpohl, A. (2011). Short-cut methods for the optimal design of simple and complex distillation columns. *Chem. Eng. Res. Design* 89, 1321–1332. doi: 10.1016/j.cherd.2011.02.014

Agrawal, R., and Yee, T. F. (1994). Heat-pumps for thermally linked distillation-columns - an exercise for argon production from air. *Indus. Eng. Chem. Res.* 33, 2717–2730. doi: 10.1021/ie00035a023

Ambrose, D., and Sprake, C. H. S. (1970). Thermodynamic properties of organic oxygen compounds XXV. Vapour pressures and normal boiling temperatures of aliphatic alcohols. *J. Chem. Thermodyn.* 2, 631–645. doi: 10.1016/0021-9614(70)90038-8

Bausa, J., Watzdorf, R. v., and Marquardt, W. (1996). Minimum energy demand for nonideal multicomponent distillations in complex columns. *Comput. Chem. Eng.* 20, S55–S60. doi: 10.1016/0098-1354(96)00020-8

Bejan, A., and Kraus, A. D. (2003). *Heat Transfer Handbook*. Hoboken, NJ: Wiley.

Biegler, L. T., Grossmann, I. E., and Westerberg, A. W. (1997). *Systematic Methods of Chemical Process Design*. Upper Saddle River, NJ: Prentice Hall.

Brüggemann, S., and Wolfgang, M. (2004). Rapid screening of design alternatives for nonideal multiproduct distillation processes. *Comput. Chem. Eng.* 29, 165–179. doi: 10.1016/j.compchemeng.2004.07.009

Caballero, J. A., and Grossmann, I. E. (2014). *Optimization of Distillation Processes*. Boston, MA: Academic Press. doi: 10.1016/B978-0-12-386547-2.00011-9

Cui, C., Xi, Z., Liu, S., and Sun, J. (2019). An enumeration-based synthesis framework for multi-effect distillation processes. *Chem. Eng. Res. Design* 144, 216–227. doi: 10.1016/j.cherd.2019.02.018

Cui, C., Yin, H., Yang, J., Wei, D., Sun, J., and Guo, C. (2016). Selecting suitable energy-saving distillation schemes: Making quick decisions. *Chem. Eng. Process. Process Intensif.* 107, 138–150. doi: 10.1016/j.cep.2016.05.009

de Koeijer, G. M., and Kjelstrup, S. (2000). Minimizing entropy production rate in binary tray distillation. *Int. J. Thermodyn.* 3, 105–110.

European Commission (2018). *A Clean Planet for all A European Strategic Long-Term Vision for a Prosperous, Modern, Competitive and Climate Neutral Economy*. Report.

Fenske, M. R. (1932). Fractionation of straight-run Pennsylvania gasoline. *Indus. Eng. Chem.* 24, 482–485. doi: 10.1021/ie50269a003

Friedler, F., Tarjan, K., Huang, Y. W., and Fan, L. T. (1992). Graph-theoretic approach to process synthesis - axioms and theorems. *Chem. Eng. Sci.* 47, 1973–1988. doi: 10.1016/0009-2509(92)80315-4

Gilliland, E. R. (1940). Multicomponent rectification estimation of the number of theoretical plates as a function of the reflux ratio. *Indus. Eng. Chem.* 32, 1220–1223. doi: 10.1021/ie50369a035

Gleixner, A., Bastubbe, M., Eifler, L., Gally, T., Gamrath, G., Gottwald, R. L., et al. (2018). *The SCIP Optimization Suite 6.0*. Report, Optimization Online.

Halvorsen, I. J., and Skogestad, S. (2011). Energy efficient distillation. *J. Nat. Gas Sci. Eng.* 3, 571–580. doi: 10.1016/j.jngse.2011.06.002

Heckl, I., Friedler, F., and Fan, L. T. (2010). Solution of separation-network synthesis problems by the P-graph methodology. *Comput. Chem. Eng.* 34, 700–706. doi: 10.1016/j.compchemeng.2010.01.019

Holiastos, K., and Manousiouthakis, V. (2004). Infinite-dimensional state-space (IDEAS) approach to globally optimal design of distillation networks featuring heat and power integration. *Indus. Eng. Chem. Res.* 43, 7826–7842. doi: 10.1021/ie010434i

Ismail, S. R., Pistikopoulos, E. N., and Papalexandri, K. P. (1999). Modular representation synthesis framework for homogeneous azeotropic separation. *AIChE J.* 45, 1701–1720. doi: 10.1002/aic.690450809

Jang, D. J., and Kim, Y. H. (2015). A new horizontal distillation for energy saving with a diabatic rectangular column. *Korean J. Chem. Eng.* 32, 2181–2186. doi: 10.1007/s11814-015-0048-4

Jiang, Z., Madenoor Ramapriya, G., Tawarmalani, M., and Agrawal, R. (2018a). Minimum energy of multicomponent distillation systems using minimum additional heat and mass integration sections. *AIChE J.* 64, 3410–3418. doi: 10.1002/aic.16189

Jiang, Z., Ramapriya, G. M., Tawarmalani, M., and Agrawal, R. (2018b). Process intensification in multicomponent distillation. *Chem. Eng. Trans.* 69, 841–846. doi: 10.3303/CET1869141

Keßler, T., Kunde, C., McBride, K., Mertens, N., Michaels, D., Sundmacher, K., et al. (2019). Global optimization of distillation columns using explicit and implicit surrogate models. *Chem. Eng. Sci.* 197, 235–245. doi: 10.1016/j.ces.2018.12.002

Kim, B. C., Chun, H. H., and Kim, Y. H. (2013). Energy-efficient diabatic distillation using a horizontal distillation column. *Indus. Eng. Chem. Res.* 52, 14927–14935. doi: 10.1021/ie4013997

Kiss, A. A., Flores Landaeta, S. J., and Infante Ferreira, C. A. (2012). Towards energy efficient distillation technologies-making the right choice. *Energy* 47, 531–542. doi: 10.1016/j.energy.2012.09.038

Kuznetsov, V. V. (2018). *Two-Phase Heat Exchangers*. Cham: Springer International Publishing. doi: 10.1007/978-3-319-26695-4_20

Ledezma-Martinez, M., Jobson, M., and Smith, R. (2018). Simulation-optimization-based design of crude oil distillation systems with preflash units. *Indus. Eng. Chem. Res.* 57, 9821–9830. doi: 10.1021/acs.iecr.7b05252

Liesche, G., Schack, D., and Sundmacher, K. (2019). The FluxMax approach for simultaneous process synthesis and heat integration: production of hydrogen cyanide. *AIChE J.* 65:e16554. doi: 10.1002/aic.16554

Miettinen, K. (1998). *Nonlinear Multiobjective Optimization, 1st Edn*. New York, NY: Springer US. doi: 10.1007/978-1-4615-5563-6

Moioli, E., Mutschler, R., and Züttel, A. (2019). Renewable energy storage via CO2 and H2 conversion to methane and methanol: assessment for small scale applications. *Renew. Sustain. Energy Rev.* 107, 497–506. doi: 10.1016/j.rser.2019.03.022

Nakaiwa, M., Huang, K., Endo, A., Ohmori, T., Akiya, T., and Takamatsu, T. (2003). Internally heat-integrated distillation columns: a review. *Chem. Eng. Res. Design* 81, 162–177. doi: 10.1205/026387603321158320

Ott, J., Gronemann, V., Pontzen, F., Fiedler, E., Grossmann, G., Kersebohm, D. B., et al. (2012). *Methanol*. Weinheim: Wiley-VCH Verlag GmbH & Co; KGaA. doi: 10.1002/14356007.a16_465.pub3

Papalexandri, K. P., and Pistikopoulos, E. N. (1996). Generalized modular representation framework for process synthesis. *AIChE J.* 42, 1010–1032. doi: 10.1002/aic.690420413

Räuchle, K., Plass, L., Wernicke, H. J., and Bertau, M. (2016). Methanol for renewable energy storage and utilization. *Energy Technol.* 4, 193–200. doi: 10.1002/ente.201500322

Roetzel, W., and Spang, B. (2010). *C3 Typical Values of Overall Heat Transfer Coefficients*. Berlin; Heidelberg: Springer. doi: 10.1007/978-3-540-77877-6_6

Schack, D., Liesche, G., and Sundmacher, K. (2019). Simultaneous heat and mass flow optimization of a distillation column applying the FluxMax approach. *Chem. Eng. Trans.* 76, 337–342. doi: 10.3303/CET1976057

Schack, D., Liesche, G., and Sundmacher, K. (2020). The FluxMax approach: simultaneous flux optimization and heat integration by discretization of thermodynamic state space illustrated on methanol synthesis process. *Chem. Eng. Sci.* 215:115382. doi: 10.1016/j.ces.2019.115382

Schack, D., Rihko-Struckmann, L., and Sundmacher, K. (2018). Linear programming approach for structure optimization of renewable-to-chemicals (R2Chem) production networks. *Indus. Eng. Chem. Res.* 57, 9889–9902. doi: 10.1021/acs.iecr.7b05305

Schäfer, P., Caspari, A., Kleinhans, K., Mhamdi, A., and Mitsos, A. (2019). Reduced dynamic modeling approach for rectification columns based on compartmentalization and artificial neural networks. *AIChE J.* 65:e16568. doi: 10.1002/aic.16568

Shah, P. B., and Kokossis, A. C. (2002). New synthesis framework for the optimization of complex distillation systems. *AIChE J.* 48, 527–550. doi: 10.1002/aic.690480311

Stull, D. R. (1947). Vapor pressure of pure substances. organic and inorganic compounds. *Indus. Eng. Chem.* 39, 517–540. doi: 10.1021/ie50448a022

Surya Prakash, G. K., Olah, G. A., and Goeppert, A. (2011). "Beyond oil and gas: the methanol economy, in *ECS Transactions*, Vol. 35, eds S. Creager, I. Fritsch, and N. Sridhar (Montreal, QC), 31–40. doi: 10.1149/1.3645178

Underwood, A. J. V. (1949). Fractional distillation of multicomponent mixtures. *Indus. Eng. Chem.* 41, 2844–2847. doi: 10.1021/ie50480a044

Waltermann, T., and Skiborowski, M. (2019). Efficient optimization-based design of energy-integrated distillation processes. *Comput. Chem. Eng.* 129:106520. doi: 10.1016/j.compchemeng.2019.106520

Conflict of Interest: The authors declare that the research was conducted in the absence of any commercial or financial relationships that could be construed as a potential conflict of interest.

frontiers in Energy Research

ORIGINAL RESEARCH
published: 31 July 2020
doi: 10.3389/fenrg.2020.00189

Ethylene Glycol/Ethanol Anolyte for High Capacity Alkaline Aluminum-Air Battery With Dual-Electrolyte Configuration

*Tanawat Phusittananan[1], Wathanyu Kao-ian[1], Mai Thanh Nguyen[2], Tetsu Yonezawa[2,3], Rojana Pornprasertsuk[4,5,6], Ahmad Azmin Mohamad[7] and Soorathep Kheawhom[1,5]**

[1] Department of Chemical Engineering, Faculty of Engineering, Chulalongkorn University, Bangkok, Thailand, [2] Division of Materials Science and Engineering, Faculty of Engineering, Hokkaido University, Sapporo, Japan, [3] Institute for the Promotion of Business-Regional Collaboration, Hokkaido University, Sapporo, Japan, [4] Department of Materials Science, Faculty of Science, Chulalongkorn University, Bangkok, Thailand, [5] Research Unit of Advanced Materials for Energy Storage, Chulalongkorn University, Bangkok, Thailand, [6] Center of Excellence on Petrochemical and Materials Technology, Chulalongkorn University, Bangkok, Thailand, [7] School of Materials and Mineral Resources Engineering, Universiti of Sains Malaysia, Nibong Tebal, Malaysia

OPEN ACCESS

Edited by:
Francois M. A. Marechal,
École Polytechnique Fédérale de Lausanne, Switzerland

Reviewed by:
Hadi Taghavifar,
Malayer University, Iran
Sagir Alva,
Mercu Buana University, Indonesia
Anming Hu,
The University of Tennessee, Knoxville, United States

***Correspondence:**
Soorathep Kheawhom
soorathep.k@chula.ac.th

Specialty section:
This article was submitted to Process and Energy Systems Engineering, a section of the journal Frontiers in Energy Research

Received: 04 February 2020
Accepted: 15 July 2020
Published: 31 July 2020

Citation:
Phusittananan T, Kao-ian W, Nguyen MT, Yonezawa T, Pornprasertsuk R, Mohamad AA and Kheawhom S (2020) Ethylene Glycol/Ethanol Anolyte for High Capacity Alkaline Aluminum-Air Battery With Dual-Electrolyte Configuration. Front. Energy Res. 8:189. doi: 10.3389/fenrg.2020.00189

Aluminum-air batteries (AABs), due to their low cost and high specific capacity, receive much attention nowadays. Nonetheless, a vital problem curbing wide application of AABs is corrosion of the aluminum (Al) anode, which is triggered by hydrogen evolution reaction (HER). Therefore, this work tackles the problem of anode corrosion in an alkaline Al-air flow battery (AAFB) by implementing a dual-electrolyte system. The battery configuration consists of an Al anode | anolyte | anion exchange membrane | catholyte | air cathode. The anolytes in this work are ethylene glycol/ethanol solutions (0, 5, 10, 20, and 30%) v/v containing 3 M potassium hydroxide (KOH). A polymer gel electrolyte (Carbopol® 940) is employed as the catholyte. The corrosion of an Al electrode in the anolytes is duly examined. It is significant that when the ratio of ethylene glycol exceeds 5% v/v, this negatively affects the dissolution process and suppresses Al corrosion. Furthermore, the battery using the anolyte with 5% v/v ethylene glycol, at a discharge current density of 5 mA/cm^2, demonstrates peak power of 3.75 mW/cm^2. The battery also exhibits the highest specific discharge capacity of 2,100 mAh/g_{Al} (70% utilization of Al) at a discharge current density of 2.5 mA/cm^2. In general, the dual-electrolyte system affirms its effectiveness in controlling anodic corrosion, quelling passivation of the Al surface in the alkaline AABs and boosting discharge capacity. KOH in ethylene glycol/ethanol solution is a promising anolyte being more environmentally friendly, less toxic and providing favorable electrochemical performance.

Keywords: aluminum-air battery, corrosion, dual-electrolyte, flow battery, specific capacity, ethanol, ethylene glycol

INTRODUCTION

Metal–air batteries (MABs) are among the lightest and highest energy density batteries. Traditionally, MABs use a metal anode and an air cathode consuming oxygen directly from ambient air (Li and Lu, 2017; Liu et al., 2017; Lao-Atiman et al., 2019). Several types of MABs have been developed e.g., lithium–air (Nomura et al., 2017; Yoo et al., 2017), sodium–air (Dilimon et al., 2017), zinc–air (Hosseini et al., 2018b, 2019; Abbasi et al., 2019), magnesium–air (Li et al., 2017;

Shrestha et al., 2019), and aluminum–air (Hong and Lu, 2017; Mori, 2017). During discharge, oxidation of the metal anode arises, whilst oxygen reduction reaction (ORR) takes place at the air cathode. The air cathode consists of an ORR catalyst layer and gas diffusion layer having a porous membrane that allows oxygen diffusion from ambient air (Li et al., 2019; Poolnapol et al., 2020).

Aluminum-air batteries (AABs) are specifically intriguing for different reasons. They have been developed as range extenders for electric vehicles supplementing integrated rechargeable batteries. Likewise, AABs have been used in military applications where their high capacity and light weight are of huge advantage. It is noted that aluminum (Al) is low in cost, safe and abundant. Moreover, dissolution of an Al anode involves a three-electron transfer. The Al anode is exceptionally light, and as the active cathode material is oxygen from ambient air, the whole package can be much lighter than many other battery types. The low atomic weight and trivalent state of the Al anode offers a high specific capacity (2.98 Ah/g_{Al}) and high energy density (theoretically 8.1 Wh/g_{Al}), which are greater than those of current lithium-ion batteries (LIBs) (Mori, 2019).

During discharge, the Al anode converts into aluminum hydroxide [$Al(OH)_3$] and aluminum oxide (Al_2O_3). It is evident that these oxide/hydroxide species tend to accumulate at both the anode and cathode and retard electrochemical reactions (Mori, 2019). Importantly, conversion of $Al(OH)_3$ and Al_2O_3 back to Al is rather difficult. Thus far, AABs have just been suitable for non-rechargeable batteries. Work is underway to develop mechanically replaceable Al anodes so that entire battery packs or the Al anode could be swapped promptly at refilling stations.

The overall reaction of an Al-air system is described as follows: $Al + 3/4O_2 + 3/2H_2O \rightarrow Al(OH)_3$ with a theoretical cell voltage of 2.70 V (Chen et al., 2015). In an alkaline aqueous electrolyte, half-reactions at the anode are shown, as in Eqs. (1 and 2):

$$Al + 3OH^- \rightarrow Al(OH)_3 + 3e^- E^0 = -2.30\ V \quad (1)$$

$$Al + 4OH^- \rightarrow Al(OH)_4{}^- + 3e^- E^0 = -2.31\ V \quad (2)$$

During discharge, the cathodic ORR is represented as in Eq. 3:

$$1/2O_2 + H_2O + 2e^- \rightarrow 2OH^- E^0 = 0.40\ V \quad (3)$$

Parasitic water reduction is shown, as in Eq. 4, where both HER and Al oxidation, occurring at the Al surface, take place:

$$H_2O + e^- \rightarrow OH^- + 1/2H_2 E^0 = -0.83\ V \quad (4)$$

The shortcoming of AABs rests on their high rate of self-discharge. This deficiency is on account of the severe corrosion of the Al anode caused by the parasitic HER. Though AABs can be stored for an extended period in their unused condition, once discharge begins, they start to degrade extremely quickly. In a month of storage, AABs can lose eighty percent of their capacity. Corrosion of an Al anode leads to unacceptably low Al utilization efficiency (Hopkins et al., 2018). Besides, it results in the production and build-up of hydrogen gas in the cell.

Numerous techniques have been developed to mitigate the corrosion of an Al anode: namely, (1) introducing additives to the electrolyte (Abdel-Gaber et al., 2010; Liu et al., 2016), (2) using gel electrolytes (Mohamad, 2008), (3) using non-aqueous electrolytes (Gelman et al., 2014), (4) using Al alloys (Abedin and Endres, 2004; Rashvand et al., 2013; Wang et al., 2015a), (5) coating the Al anode with ceramics (Mori, 2014, 2015), and (6) operating at low temperature (Zuo et al., 2019). Nevertheless, these efforts have proved inadequate and have often made the battery system more intricate.

The mechanisms behind AABs involve Al dissolution at the anode and ORR at the cathode. In traditional AABs, anodic self-corrosion is the major challenge. The Al corrosion issue can be effectively handled by restricting Al dissolution in a non-aqueous electrolyte. However, in such an electrolyte, ORR is kinetically sluggish. Thus, a dual-electrolyte AAB having an anion exchange membrane separating the organic anolyte and aqueous catholyte was developed (Wang et al., 2014). This configuration conferred flexibility in implementing a very distinctive anolyte and catholyte. By implementing an apposite anolyte, the corrosion of the Al anode can be considerably suppressed, and a high-performance battery can be achieved.

Methanol offers excellent corrosion inhibition in an alkaline solution (Wang et al., 2007, 2009). Earlier, methanol was applied as an anolyte in dual-electrolyte AABs (Wang et al., 2014; Teabnamang et al., 2020). Results showed that very high discharge capacity could be attained. However, methanol is flammable and volatile. Moreover, it is also toxic when inhaled. Other anolytes, therefore, having lower vapor pressure, being less toxic and more eco-friendly are preferred. Corrosion of an Al (AA5052) anode in ethylene glycol solution containing 4 M sodium hydroxide (NaOH) was studied in AABs (Wang et al., 2015b). In an alkaline ethylene glycol solution, it was found that dicarboxylic acid additives enhanced electrochemical activity and discharge performance of AA5052 Al alloy. The corrosion of Al and Al alloy in ethylene glycol-water solution with different additives was also investigated. Further, a protective effect of sebacic acid was reported (Zaharieva et al., 2009). The corrosion mechanisms of Al alloys in ethylene glycol solution were studied (Weon and Woo, 2013). It is noted that precipitation and thickening of aluminum hydroxides are major phenomena affecting the corrosion behavior of Al alloys. In different solutions, the mechanisms of Al dissolution are different. In an alkaline aqueous solution, Al dissolution involves repetitive formation and destruction of thin Al_2O_3 layers over the Al surface; dissolution of Al is controlled via the through-film dissolution process (Koroleva et al., 1999).

Teabnamang et al. (2020) studied Al corrosion in 3 M KOH methanol solutions containing different ratios of water. It was reported that in 3 M KOH anhydrous methanol solution, the resultant oxide film on the Al surface was compact and smooth. By introducing water to the solution, the properties of the oxide film altered. The existence of water in the methanol solutions led to a loose and porous oxide film. The porous structure thus accelerated the transfer of the reactive species between the Al surface and the electrolyte.

Another crucial concern of AABs is passivation of the Al anode arising from the build-up of discharged products on the surface of the Al anode. The passivation problem can be solved by employing a circulation of electrolytes. By supplying electrolytes regularly to minimize the concentration gradient of the discharge products, anode passivation can be reduced (Hosseini et al., 2018a; Ryu et al., 2018).

This work sets out to resolve the problem of anode corrosion in an alkaline AAFB by implementing a dual-electrolyte system having a configuration of an Al anode | anolyte | anion exchange membrane | catholyte | air cathode. 3 M KOH in ethylene glycol/ethanol solutions (0, 5, 10, 20, and 30%) v/v are examined as the anolytes. The corrosion behavior and electrochemical characteristics of an Al electrode in the anolytes are investigated via hydrogen evolution test (gasometric method), potentiodynamic polarization (Tafel polarization) and electrochemical impedance spectroscopy (EIS). Subsequently, performance of the batteries using different anolytes are investigated.

MATERIALS AND METHODS

Materials

The cathode current collector was made of nickel (Ni) foam (99.97%, 100 pore per inch, 1 mm thick, Qijing Trading Co., Ltd., China). Aluminum (Al) plates (99.99% Qijing Trading Co., Ltd., China) were employed as working electrodes in the corrosion test and anodes in the AAFB. An anion-exchange membrane (AMI-7001S, Membrane International Inc., United States) was applied to separate the anolyte and the catholyte. The electrolyte of the half-cell test and the anolyte of the battery was made from ethanol (99.8%), ethylene glycol (99%), and potassium hydroxide pellets (KOH, 99%), purchased from QRëC, New Zealand. The cathode was prepared using polytetrafluoroethylene (PTFE powder, 1 μm, Sigma-Aldrich, Singapore), carbon black (Vulcan® BP2000 and XC-72, Cabot Corporation, United States), manganese (IV) oxide (MnO_2, 5 μm, 99.99%, Sigma-Aldrich, Singapore), poly(styrene-co- butadiene) (Sigma-Aldrich, Singapore) and toluene (99.5%, Loba Chemie Pvt Ltd., India). Carbopol® 940 polymer (CBP940, Lubrizol Corporation, United States) was used to prepare the polymer gel catholyte. All chemicals were used as received, without any additional refinement.

Battery Fabrication

Figure 1 depicts a schematic illustration of the dual-electrolyte AAFB. The anode electrode was (30 mm× 50 mm× 0.19 mm) and weighed 0.8 g. The ethylene glycol/ethanol solutions (0, 5, 10, 20, and 30%) v/v containing 3 M KOH were used as anolytes. The catholyte is a polymer gel electrolyte prepared by mixing CBP940 1.2 wt.% in 3 M KOH aqueous solution. The gel electrolyte significantly reduced electrolyte loss due to evaporation during

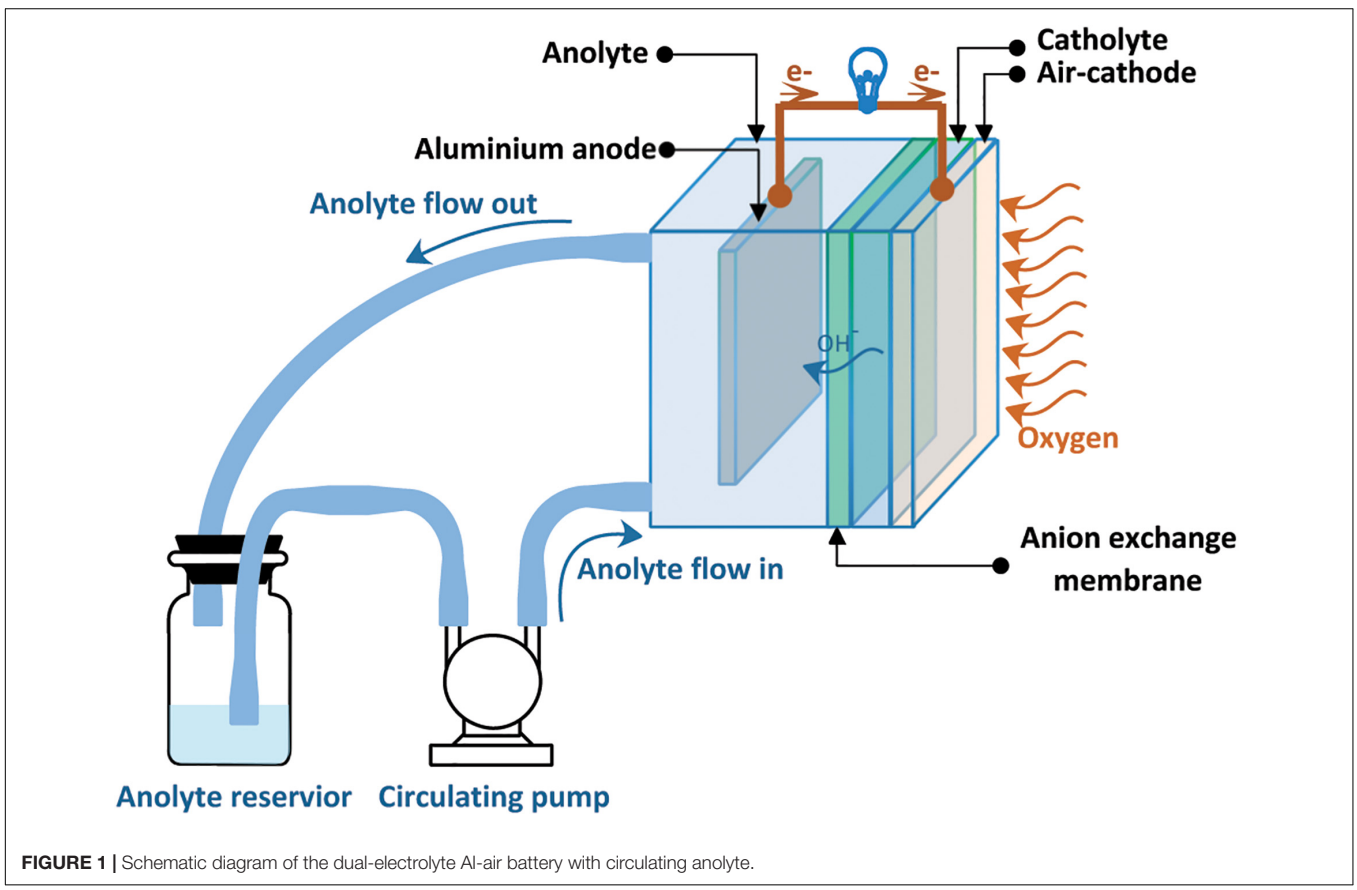

FIGURE 1 | Schematic diagram of the dual-electrolyte Al-air battery with circulating anolyte.

battery operation. An anion-exchange membrane (3 cm× 3 cm) was used, as separator, to separate the catholyte and the anolyte. Before the test, the anion-exchange membrane was activated by soaking in an aqueous solution of 5 M sodium chloride (NaCl) at 30°C for 24 h.

The air cathode is composed of three layers: the catalyst layer (inner side), the cathode current collector and the gas diffusion layer (outer side). The catalyst layer is in contact with the catholyte. The active area of the cathode reaction is 4 cm^2. The cathode was fabricated as a double-sided, coated electrode where the middle layer is the current collector, made of Ni foam. As for the gas diffusion layer, the outer surface of the air cathode was prepared by coating a mixture of carbon (XC-72), D-glucose, and PTFE binder in 10 ml ethanol having a ratio of (40:40:20) wt.%, respectively. The well-dispersed paste was applied onto the Ni foam and then pressed using a manual hot press at 350°C for 15 min. The gas diffusion layer showed hydrophobicity and helped to prevent leakage of the electrolyte whilst enabling oxygen gas to permeate the cell. To prepare the inner side, both MnO_2 0.3 g, as the catalyst, and carbon BP2000 0.7 g were mixed and dispersed in 8.5 mL of toluene and stirred for 60 min. Subsequently, 1.5 ml of 7.5 wt.% poly(styrene-co-butadiene) in toluene solution was introduced. The mixture was stirred for another 60 min. and the prepared paste was coated two times onto the other side of the Ni foam. Finally, the coated Ni foam was pressed at 150°C for 10 min. using a manual hot press.

Figure 2 illustrates the cell design consisting of an aluminum anode, a chamber for the anolyte, an anion exchange membrane (acting as separator), a chamber for the catholyte as well as the air cathode. The distance between the anode and cathode is 18 mm,

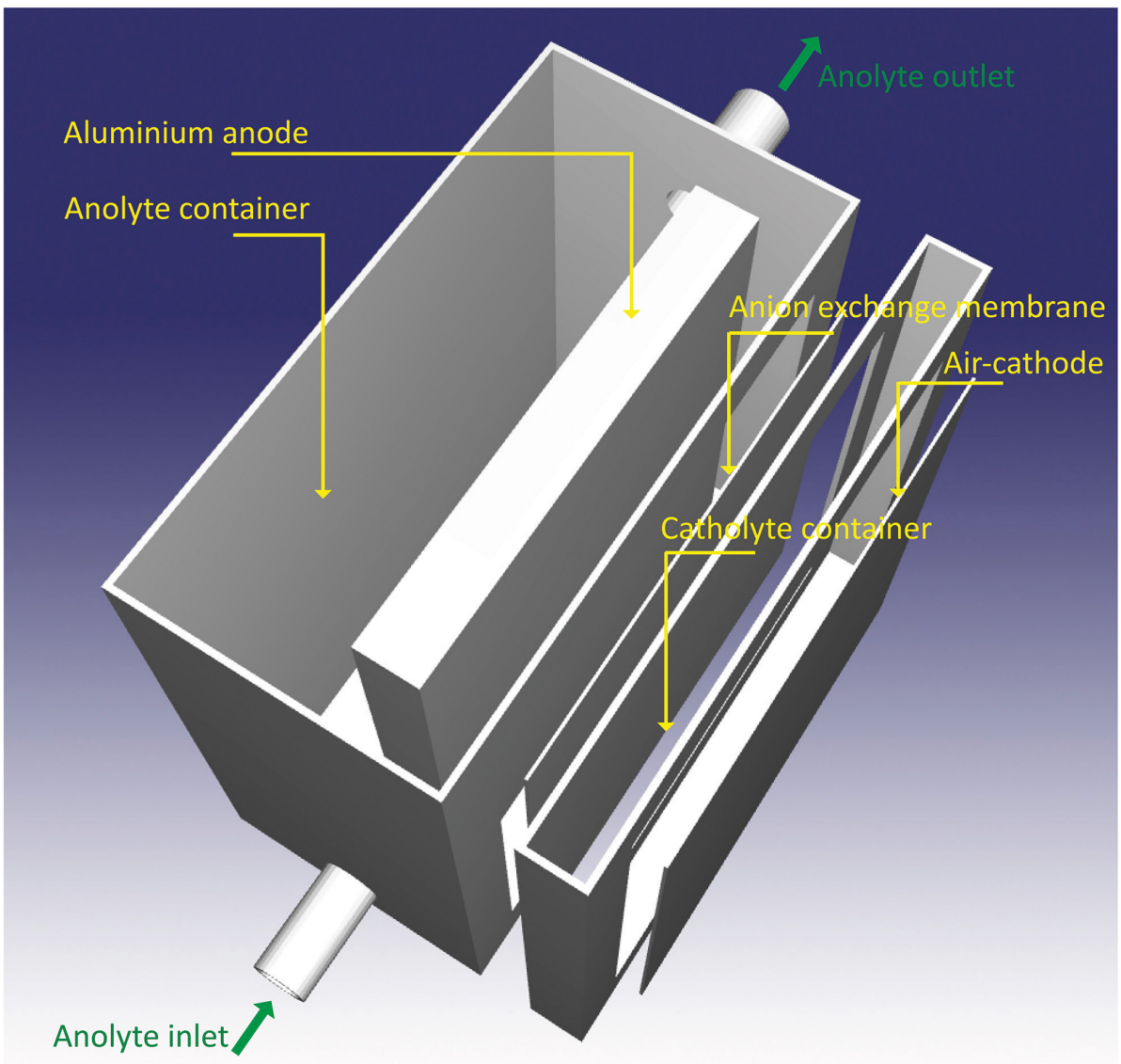

FIGURE 2 | Design of the dual-electrolyte Al-air battery.

and the distance between the anode to the separator is 14 mm. The distance determines the ohmic resistance of the cell as well as the pressure drop of pump. As the distance increases, the ohmic resistance increases proportionally. However, the pressure drop decreases inversely to the distance.

Corrosion of the Al Anode and Battery Testing

Figure 3 demonstrates an experimental setup for the hydrogen evolution test (Moghadam et al., 2017). The tests were performed at 30°C during 60 min. of immersion in ethylene glycol/ethanol solutions (0, 5, 10, 20, and 30%) v/v containing 3 M KOH. Prior to the test, Al samples (1 × 1 cm^2) were rinsed with acetone five times repeatedly. Then, each Al sample was immersed into a beaker containing 50 ml of the solution. Then, a funnel was placed over the sample, making sure that all the hydrogen gas generated from corrosion of the sample is accumulated. Next, a burette was installed over the funnel and was initially filled with the solution. The hydrogen which was in the funnel entered the burette and gradually displaced the solution. The burette allowed the volume of generated hydrogen gas to be determined as a function of time. Each test was repeated five times. Reaction rates

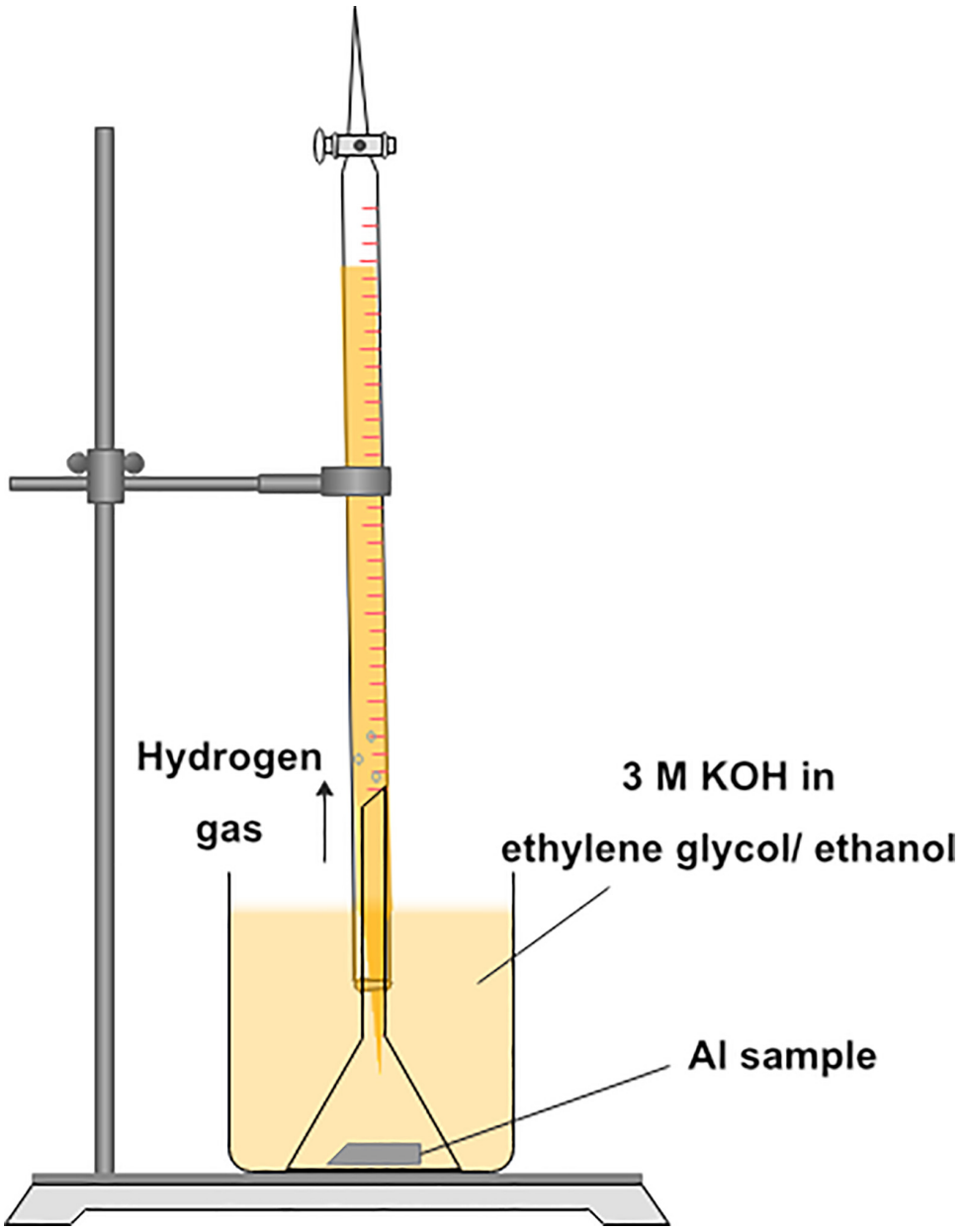

FIGURE 3 | Experimental set up for hydrogen evolution measurement.

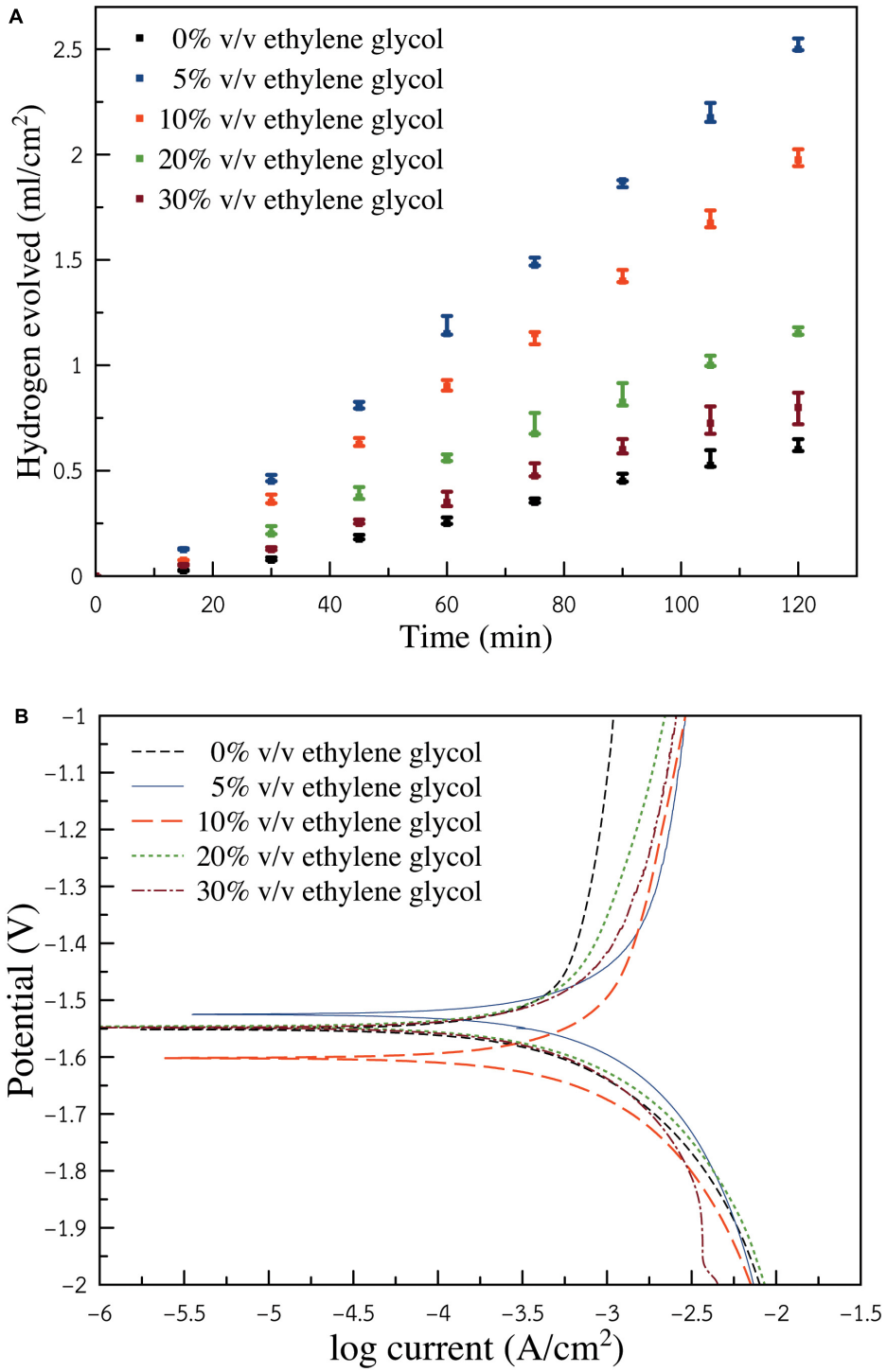

FIGURE 4 | (A) Hydrogen gas evolved from Al sample in ethylene glycol/ethanol solutions (0, 5, 10, 20, and 30%) v/v containing 3 M KOH **(B)** Potentiodynamic polarization (Tafel polarization) of Al electrode in ethylene glycol/ethanol solutions (0, 5, 10, 20, and 30%) v/v containing 3 M KOH.

were identified by the slope of the straight lines in the gasometry plots.

A three-electrode configuration was employed to study the electrochemical characteristics of the Al anode in ethylene glycol/ethanol solutions (0, 5, 10, 20, and 30%) v/v containing 3 M KOH. The three-electrode cell consisted of: a platinum (Pt) counter electrode (1 × 1) cm^2, Ag/AgCl reference electrode and an Al plate working electrode (1 cm× 1 cm). The

Al working electrode was rinsed three times with acetone prior to the test at 30°C. A potentiostat/galvanostat (PAR VersaSTAT 3, Ametek Inc., United States) was used to examine electrochemical impedance spectroscopy (EIS) and potentiodynamic polarization. Potentiodynamic polarization was carried out using a scan rate of 5 mV/s in the potential region cover (−1.0 to −2.0) V vs. Ag/AgCl. Besides, EIS was carried out at a frequency range of 200 kHz–0.2 Hz and voltage excitation 5 mV at open circuit voltage (OCV). Further, both battery discharge capacity and voltage-current polarization curve were analyzed by battery testing system (Neware, China). The operation of the battery was carried out at 25°C.

RESULTS AND DISCUSSION

Generally, in alkaline aqueous solutions, Al exhibits severe self-corrosion without passivation effect (Pyun and Moon, 2000). Thus, an oxide film, which is a discharge product, is electrochemically formed by the incorporation of hydroxide ions (OH^-) into the film and the migration of OH^- through the film toward the Al/film interface. Corresponding corrosion reactions are shown, as in Eq. 5:

$$Al + 3OH^- \rightarrow Al(OH)_3 + 3e^- \quad (5)$$

Subsequently, the film is dissolved chemically by the attacking of OH^- at the film/electrolyte interface, as shown below in Eq. 6. In addition, the electrons produced by Eq. 5 are consumed instantly by the water reduction reaction, as shown accordingly in Eq. 7:

$$Al(OH)_3 + OH^- \rightarrow Al(OH)_4{}^- \quad (6)$$

$$3H_2O + 3e^- \rightarrow 3OH^- + 3/2H_2 \quad (7)$$

In Eq. 7, the oxide films, which are produced, are loose and porous. The films cannot protect the underlying Al surface. It is seen that the Al dissolution herein is controlled by the through-film dissolution process (Koroleva et al., 1999).

Self-corrosion of Al can also take place in the case of anhydrous ethanol or ethylene glycol alkaline solutions. However, the mechanisms of Al corrosion in alkaline ethanol and ethylene glycol are different from that of alkaline aqueous solutions. Oxide films of Al-ethanol [Al(CH_3CH2O)3] and Al-ethylene glycol [Al(HOCH2CH2O)3], which show an inhibition effect on the Al corrosion process, are formed in these solutions. These films can suppress further anodic dissolution of Al (Zhang et al., 2008). For instance, the Al dissolution was controlled by the precipitation and thickening of the oxide films (Weon and Woo, 2013).

Figure 4A presents the relationship between hydrogen gas generated as a function of time. The linear variation for the volume of hydrogen gas progressed according to the time for each condition. The volume of hydrogen can speculate how much Al consumed itself through HER. It is seen that the electrolyte without ethylene glycol exhibited the lowest hydrogen evolution rate of 0.005 ml cm^{-2} min^{-1}. By introducing ethylene glycol to the solution, the hydrogen evolution rate increased. Consequently, the condition of 5% v/v ethylene glycol exhibited the highest hydrogen evolution rate of 0.022 ml cm^{-2} min^{-1}. Yet, further increasing the ratio of ethylene glycol resulted in the decrease of HER. The condition of (10, 20, and 30%) v/v ethylene glycol showed hydrogen evolution rates of (0.017, 0.010, and 0.007 ml cm^{-2} min^{-1}), respectively. However, it is reported that in both ethanol and ethylene glycol, the oxide films produced can retard Al dissolution kinetics. As for the ethylene glycol/ethanol solution, the surface of Al was concealed by mixed Al-ethanol and Al-ethylene glycol oxide films. The mixed films provided less protection than the films generated from the alkaline ethanol solution. The presence of ethylene glycol was seen to accelerate HER. The corrosion rate of Al also increased.

Figure 4B depicts the potentiodynamic polarization of an Al electrode in ethylene glycol/ethanol solutions (0, 5, 10, 20, and 30%) v/v containing 3 M KOH. Corrosion potential of the electrolyte containing 0% v/v ethylene glycol was detected at −1.53 V. As ethylene glycol was introduced, the corrosion potential of the electrolytes showed a negative shift. The negative shift indicated a higher tendency of Al corrosion. Nonetheless, as the ratio of ethylene glycol increased, corrosion potential shifted positively. This indicated that at a higher content of ethylene glycol, Al exhibited lower corrosion tendency, which was in agreement with the result of gasometry of hydrogen evolution. Polarization resistance and other related properties were determined using Butler-Volmer and Stern-Geary equations (Abdel-Gaber et al., 2008; Shinagawa et al., 2015), as shown in Eqs. (8 and 9):

$$I = I_{\text{corr}}\left(e^{\frac{2.303(E-E_{\text{corr}})}{\beta_a}} - e^{\frac{2.303(E-E_{\text{corr}})}{\beta_c}}\right) \quad (8)$$

$$R_p = \frac{\beta_a|\beta_c|}{2.303I_{\text{corr}}(\beta_a + |\beta_c|)} \quad (9)$$

where, E is the electrode potential. E_{corr} is the corrosion potential. I is the measured current density. I_{corr} is the corrosion current density. βa and βc represent the anodic and cathodic Tafel slopes, respectively. By estimating the Tafel slopes as a straight line, polarization resistance (R_p), representing the transition resistance between the electrode and the electrolyte, can be estimated.

Table 1 shows electrochemical polarization parameters viz. corrosion potential (E_{corr}), corrosion current density (I_{corr}), anodic slope (β_a), cathodic slope (β_c), and polarization resistance (R_p). Corrosion rate is proportionally related to

TABLE 1 | Electrochemical polarization parameters of an Al electrode in ethylene glycol/ethanol solutions (0, 5, 10, 20, and 30%) v/v containing 3 M KOH.

% ethylene glycol	E_{corr} (V vs. Ag/AgCl)	I_{corr} (mA cm^{-2})	β_a (V dec^{-1})	β_c (V dec^{-1})	R_p (Ω)
0%	−1.53	0.57	1.52	−0.27	177.24
5%	−1.59	1.35	1.08	−0.52	112.12
10%	−1.55	1.12	1.24	−0.42	121.52
20%	1.55	0.84	1.25	−0.34	138.65
30%	−1.55	0.82	1.31	−0.38	155.97

polarization resistance. Higher polarization resistance shows lower corrosion current. Greater polarization resistance indicates greater corrosion inhibition property. It is seen that the lowest polarization resistance was attained when the electrolyte having 5% v/v ethylene glycol was used. Nonetheless, as the ratio of ethylene glycol increased further, polarization resistance gradually increased. The anodic slope shows the corrosion tendency of the anode. The smallest anodic slope (1.08 V/dec) and smallest polarization resistance (112.12 Ω) was obtained via the electrolyte containing 5% v/v ethylene glycol, indicating the greatest corrosion propensity of the Al electrode. The corrosion current density of the electrolyte containing 5% v/v ethylene glycol was 1.35 mA/cm^2. The greatest anodic Tafel slope (1.52 V/dec) occurred in the electrolyte without ethylene glycol. The corrosion current density of the electrolyte without ethylene glycol was found to be 0.57 mA/cm^2 while polarization resistance was 177.24 Ω. The Tafel slope suggests how large overpotential is required to increase the reaction rate. The lesser anodic slope suggests higher Al corrosion tendency. The greater anodic slope and larger polarization show a definitive advantage in the corrosion inhibition of Al. However, it has unfavorable effects on battery performance, as Al dissolution requires a greater overpotential.

Electrochemical impedance spectroscopy technique was used to examine the characteristics of the Al dissolution process. **Figure 5A** displays Nyquist plots of Al electrode in ethylene glycol/ethanol solutions (0, 5, 10, 20, and 30%) v/v containing 3 M KOH. All cases exhibited similar characteristics. Similar results were also reported for Al in alkaline aqueous solutions (Abdel-Gaber et al., 2008). The impedance spectra contain a small capacitive loop at a low frequency, a small inductive loop at a middle frequency, and a large capacitive loop at high frequency. The capacitive semicircle at high frequency is ascribed to the redox reaction of Al $\leftrightarrow$ Al^+ which was noted as being the rate-determining step in the dissolution process (Moghadam et al., 2017). The inductive loop at middle frequency arose from an adsorption of intermediates on the Al surface. The other capacitive loop at low frequency is attributed to $Al^+ \leftrightarrow Al^{3+}$ redox reaction (Verma et al., 2015). In an alkaline aqueous solution, Al dissolution involves the repeated formation and dissolution of thin Al_2O_3 films over the Al surface (Koroleva et al., 1999). Thus, Al^{3+} ions, formed by the oxidation of Al at the Al_2O_3 film/Al interface, migrated across the films to the electrolyte. Instantaneously, OH^- ions migrated across the films to the Al surface. Therefore, the anodic dissolution of Al is controlled via the through-film dissolution mechanism.

As for ethanol or ethylene glycol electrolytes, the films of Al-ethanol and Al-ethylene glycol are involved. These films exhibited a lower migration rate of Al^{3+} and OH^- than that of an alkaline aqueous electrolyte. Consequently, they can suppress the dissolution process of Al (Zhang et al., 2008).

It is significant that the 3 M KOH ethanol electrolyte, without ethylene glycol, displayed the highest diameter of capacitive and inductive loops. However, when ethylene glycol was introduced, this led to a decrease in the diameter size of the capacitive semicircle. The presence of ethylene glycol was seen to reduce charge transfer resistance as well as bulk resistance. Hence, the corrosion rate of Al increased. Results revealed that the ethanol electrolyte, without ethylene glycol, had the highest charge transfer resistance, indicating that the surface of Al was occupied by the Al-ethanol film, which had the smallest migration rate of Al^{3+} and OH^-. In the case of the electrolyte containing ethylene glycol, the surface of Al was covered by the heterogeneous films consisting of Al-ethanol and Al-ethylene glycol species. The mixed films showed a higher migration rate of Al^{3+} and OH^-. Consequently, they exhibited faster Al dissolution kinetics.

The electrolyte containing 5% v/v ethylene glycol showed the smallest diameter of capacitive and inductive loops, indicating

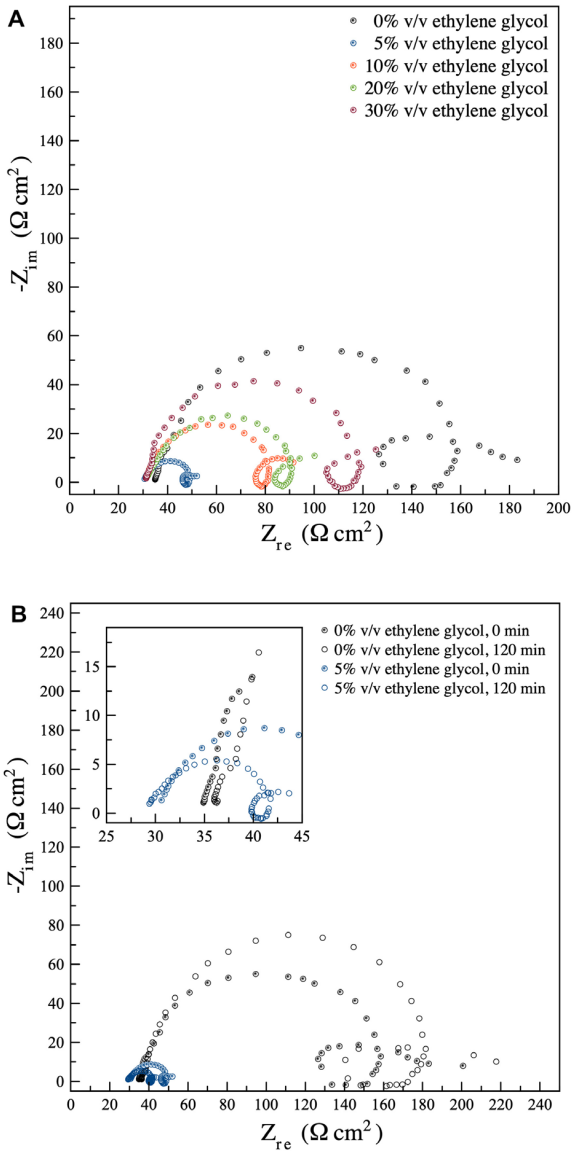

FIGURE 5 | Nyquist plots of EIS, performed at the potential 0 V (vs. OCV) in the frequency range 200 kHz to 0.2 Hz with AC amplitude of 5 mV: **(A)** An Al electrode in ethylene glycol/ethanol solutions (0, 5, 10, 20, and 30%) v/v containing 3 M KOH **(B)** An Al electrode in ethylene glycol/ethanol solutions (0 and 5%) v/v containing 3 M KOH at different immersion times (0 and 120 min).

the fast kinetics of charge transfer reactions associated with the redox process. However, when the ratio of ethylene glycol was increased, the diameter of capacitive and inductive loops gradually increased. In other words, the charge transfer resistance of the dissolution process became larger as the ratio of ethylene glycol increased. In effect, the dissolution process turned

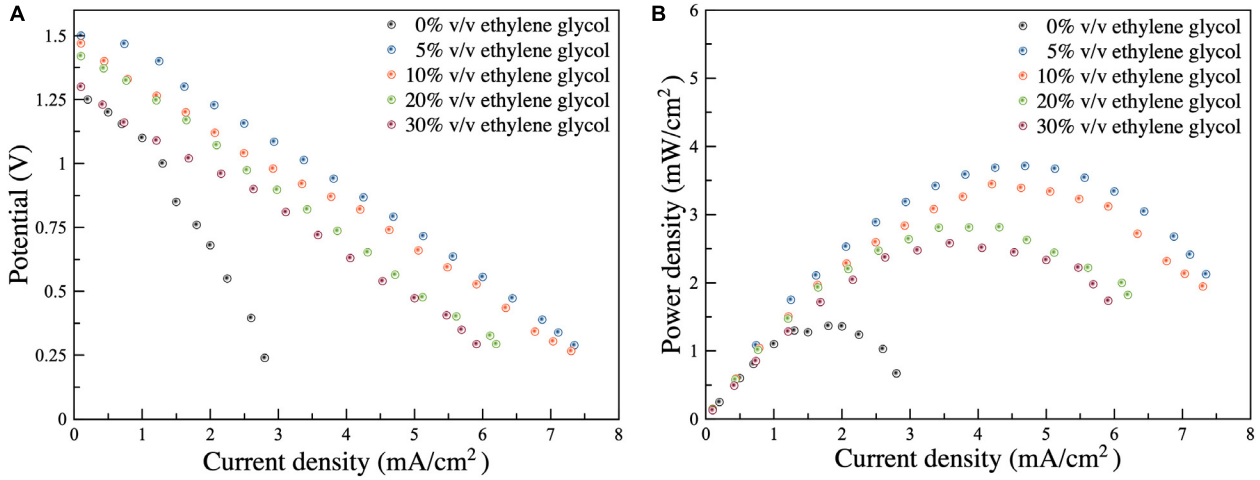

FIGURE 6 | (A) Polarization characteristics of the dual-electrolyte Al-air battery using an anolyte of ethylene glycol/ethanol solutions (0, 5, 10, 20, and 30%) v/v containing 3 M KOH **(B)** Power density as a function of current density for the dual-electrolyte Al-air battery using an anolyte of ethylene glycol/ethanol solutions (0, 5, 10, 20, and 30%) v/v containing 3 M KOH.

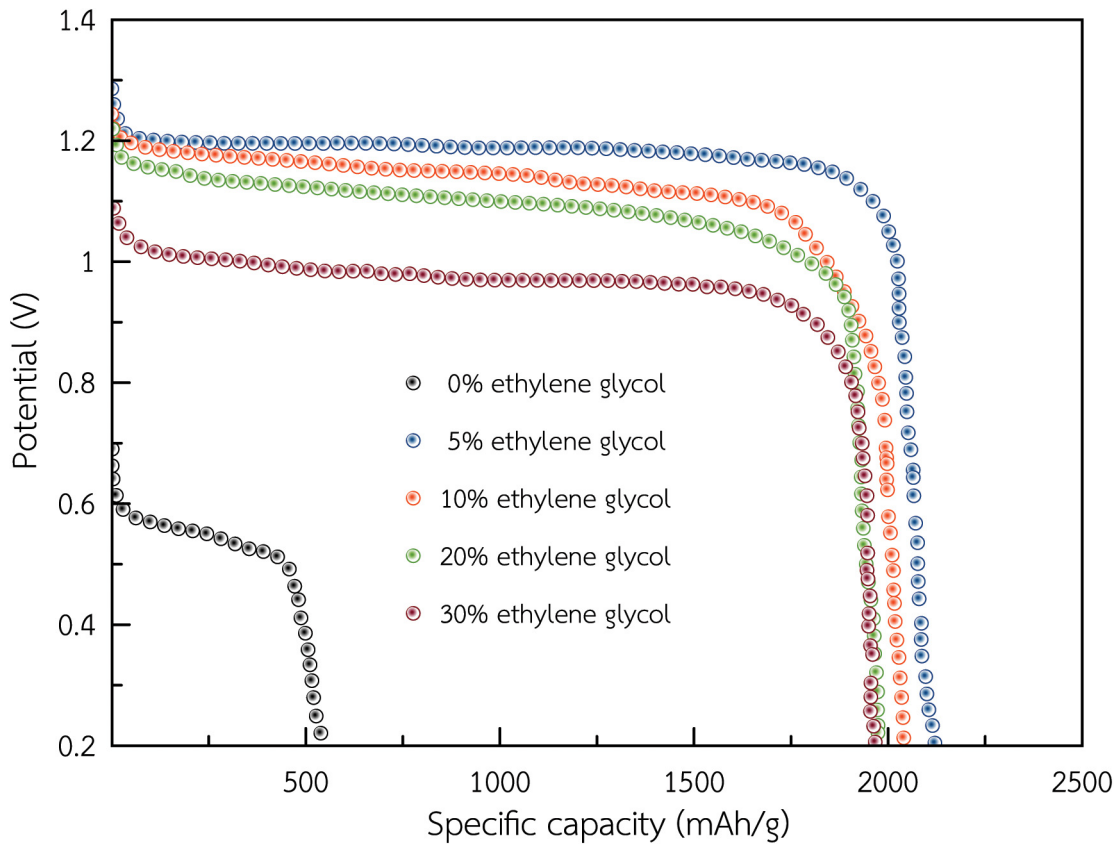

FIGURE 7 | Discharge profiles of the dual-electrolyte Al-air battery using an anolyte of ethylene glycol/ethanol solutions (0, 5, 10, 20, and 30%) v/v containing 3 M KOH at a discharge current density of 2.5 mA/cm^2.

out to be more sluggish; and the system showed enhanced corrosion inhibition.

Figure 5B presents the Nyquist plots of Al electrode in ethylene glycol/ethanol solutions (0 and 5%) v/v containing 3 M KOH at immediate immersion of Al and after 120 min. Thus, it was found that the diameters of the capacitive and inductive loops, regarding the 3 M KOH ethanol electrolyte, without ethylene glycol, increased after 120 min. immersion. At the beginning, the anode was fresh and showed the highest anodic activity (the lowest charge transfer resistance). Then, the charge transfer resistance increased through time. This indicated that the formation of the Al-ethanol films acted as a passivation layer and suppressed Al dissolution. In comparison, when ethylene glycol was introduced to the electrolyte, the width of the capacitive semicircle decreased with time. That is, the charge transfer resistance decreased, as immersion time increased, signifying that the films produced, consisting of Al-ethanol and Al-ethylene glycol species, exhibited no passivation.

Following the examination of Al corrosion and dissolution, performance of the dual-electrolyte AAFB was studied. Before the test, the cell was fabricated, and the anolyte was circulated for one hour without the Al anode. Then, the effects of ethylene glycol/ethanol solution anolytes were studied, at a circulation rate of anolyte 10 ml/min. In **Figure 6**, the polarization characteristics of the battery are presented. It was observed that the limiting current density increased when ethylene glycol was introduced as follows: (2.80, 7.45, 7.40, 6.30, and 6.00 mA/cm^2) using (0, 5, 10, 20, and 30%) v/v ethylene glycol electrolytes, respectively. Maximum power density was calculated via current density and discharge voltage providing: (1.25, 3.75, 3.50, 2.75, and 2.50 mW/cm^2), respectively. It was found, therefore, that the presence of ethylene glycol enhanced the performance of the battery because of its higher activity and lower charge transfer resistance; and thereby promoted Al dissolution.

The dual-electrolyte AAFB exhibited linear polarization characteristics. The OCV of 3 M KOH ethanol electrolyte, without ethylene glycol, was 1.25 V. When ethylene glycol was added (5, 10, 20, and 30%) v/v, the OCVs were (1.50, 1.45, 1.40, and 1.35 V), respectively. It was evident, therefore, that by introducing ethylene glycol, the OCV of the battery was enhanced. However, when ethylene glycol content further increased, the OCV of the battery gradually dropped.

Figure 7 displays discharge profiles of the dual-electrolyte Al-air battery using an anolyte of ethylene glycol/ethanol solutions (0, 5, 10, 20, and 30%) v/v containing 3 M KOH at a discharge current density of 2.5 mA/cm^2. At discharge current density of 2.5 mA/cm^2, the battery having 5% v/v ethylene glycol achieved the highest specific capacity of 2,100 mAh/g_{Al} bringing about 70% utilization efficiency. Moreover, the battery could discharge continuously for more than 24 h. When the ratio of ethylene glycol increased, specific capacity of the battery decreased slightly (2053, 1980, and 1965 mAh/g_{Al}) at the condition of (10, 20, and 30%), respectively. Simultaneously, when the ethylene glycol ratio increased, the average discharge voltage decreased along with Al utilization percentage. This proved that the AAFB could exhibit a significant higher coulombic efficiency using the electrolyte 3 M KOH ethanol containing 5% v/v ethylene glycol.

Table 2 presents a comparison of the dual-electrolyte AAFB proposed in this work with other AABs previously reported. Results can vary depending on different parameters, such as cell configuration, ORR catalyst, electrolyte and conditions of the experiment. The dual-electrolyte AAFB exhibited higher specific discharge capacity. Though the dual-electrolyte AAFB using a methanol anolyte showed the highest discharge capacity (Teabnamang et al., 2020), methanol is flammable and volatile. Thus, using the methanol anolyte in an AAFB can pose a safety risk in battery operation. Moreover, methanol has adverse health effects on humans. In contrast, ethylene glycol/ethanol anolyte offers greater safety and is more environmentally friendly, less toxic with trade-off electrochemical performance and discharge capacity. The dual-electrolyte AAFB having the ethylene glycol/ethanol anolyte demonstrated a significantly high discharge capacity. Nonetheless, power density of the dual-electrolyte AAFB must be further improved. Power density depends on numerous factors i.e., ORR catalyst, catholyte, and the structure of a gas diffusion layer. More sophisticated ORR catalysts and different air cathode structure can be applied to improve power density.

TABLE 2 | Comparison of the dual AAFB proposed in this work with other AABs previously reported.

Configuration	Electrolyte and air cathode	Maximum power density (mW/cm^2)	Discharge capacity (mAh/g_{Al})	References
Dual electrolyte AAFB	5% v/v ethylene glycol/ethanol with 3 M KOH, MnO_2/C catalyst	3.75	2,100	This work
Dual electrolyte AAFB	Methanol with 3 M KOH, MnO_2/C catalyst	7.5	2,328	Teabnamang et al., 2020
Dual electrolyte AAB	Methanol with 3 M KOH, Pt/C catalyst	28	1,810	Wang et al., 2014
Rechargeable single electrolyte AAB	Solid state/($AlCl_3$, urea, carboxymethyl cellulose, glycerin), TiN catalyst	N/A	35.8	Mori, 2019
Single electrolyte AAB	4 M NaOH aqueous solution, CoO catalyst	48	770.34	Park et al., 2017
Single electrolyte AAB	5 M NaOH aqueous solution with 25 mM thiourea	N/A	1,282	Moghadam et al., 2017
Paper-based solid electrolyte AAB	Gel polymer electrolyte containing NaOH, Ag/C catalyst	3.8	900.8	Wang et al., 2019
Solid electrolyte AAB	Gel polymer electrolyte (2 M KOH), Pt/C catalyst	N/A	239	Yu et al., 2018

CONCLUSION

In this work, self-corrosion of an Al electrode in an alkaline dual-electrolyte AAFB was investigated. It is evident that 3 M KOH ethanol solution, without ethylene glycol, exhibited excellent corrosion inhibition. However, sluggish Al dissolution kinetics resulted in lower battery performance. Further, the introduction of ethylene glycol to the 3 M KOH ethanol solution led to enhanced Al dissolution kinetics. Moreover, both Tafel polarization and EIS confirmed that 3 M KOH ethanol solution, having 5% v/v ethylene glycol, showed the smallest polarization resistance and the smallest charge transfer resistance. Overall, results demonstrated that the dual-electrolyte AAFB proved to be an effective approach to control anodic corrosion and passivation. It is noted that the dual-electrolyte AAFB performed sufficiently well and provided excellent discharge capacity.

DATA AVAILABILITY STATEMENT

All datasets generated for this study are included in the article/supplementary material.

AUTHOR CONTRIBUTIONS

SK conceived the research project and wrote the first draft. TP and WK conducted the experiments. TP analyzed the data with consultation from SK. SK, RP, AM, MN, and TY contributed to the subsequent drafts. All authors reviewed the manuscript.

FUNDING

This research was funded by the Thailand Research Fund (RSA6180008) and Rachadapisek Sompote Fund of Chulalongkorn University.

ACKNOWLEDGMENTS

The Energy Storage Cluster of Chulalongkorn University was acknowledged.

REFERENCES

Abbasi, A., Hosseini, S., Somwangthanaroj, A., Mohamad, A. A., and Kheawhom, S. (2019). Poly(2,6-Dimethyl-1,4-Phenylene Oxide)-based hydroxide exchange separator membranes for zinc–air battery. *Int. J. Mol. Sci.* 20:3678. doi: 10.3390/ijms20153678

Abdel-Gaber, A. M., Khamis, E., Abo-Eldahab, H., and Adeel, S. (2008). Inhibition of aluminium corrosion in alkaline solutions using natural compound. *Mater. Chem. Phys.* 109, 297–305. doi: 10.1016/j.matchemphys.2007.11.038

Abdel-Gaber, A. M., Khamis, E., Abo-Eldahab, H., and Adeel, S. (2010). Novel package for inhibition of aluminium corrosion in alkaline solutions. *Mater. Chem. Phys.* 124, 773–779. doi: 10.1016/j.matchemphys.2010.07.059

Abedin, S. Z. E., and Endres, F. (2004). Electrochemical behaviour of Al, Al-In and Al-Ga-in alloys in chloride solutions containing zinc ions. *J. Appl. Electrochem.* 34, 1071–1080. doi: 10.1023/b:jach.0000042672.23588.df

Chen, L. D., Nørskov, J. K., and Luntz, A. C. (2015). Al–air batteries: fundamental thermodynamic limitations from first-principles theory. *J. Phys. Chem. Lett.* 6, 175–179. doi: 10.1021/jz502422v

Dilimon, V. S., Hwang, C., Cho, Y.-G., Yang, J., Lim, H.-D., Kang, K., et al. (2017). Superoxide stability for reversible Na-O2 electrochemistry. *Sci. Rep.* 7:17635.

Gelman, D., Shvartsev, B., and Ein-Eli, Y. (2014). Aluminum–air battery based on an ionic liquid electrolyte. *J. Mater. Chem. A* 2, 20237–20242. doi: 10.1039/c4ta04721d

Hong, Q., and Lu, H. (2017). In-situ electrodeposition of highly active silver catalyst on carbon fiber papers as binder free cathodes for aluminum-air battery. *Sci. Rep.* 7:3378.

Hopkins, B. J., Shao-Horn, Y., and Hart, D. P. (2018). Suppressing corrosion in primary aluminum–air batteries via oil displacement. *Science* 362:658. doi: 10.1126/science.aat9149

Hosseini, S., Abbasi, A., Uginet, L.-O., Haustraete, N., Praserthdam, S., Yonezawa, T., et al. (2019). The influence of dimethyl sulfoxide as electrolyte additive on anodic dissolution of alkaline zinc-air flow battery. *Sci. Rep.* 9:14958.

Hosseini, S., Han, S. J., Arponwichanop, A., Yonezawa, T., and Kheawhom, S. (2018a). Ethanol as an electrolyte additive for alkaline zinc-air flow batteries. *Sci. Rep.* 8:11273.

Hosseini, S., Lao-Atiman, W., Han, S. J., Arpornwichanop, A., Yonezawa, T., and Kheawhom, S. (2018b). Discharge performance of zinc-air flow batteries under the effects of sodium dodecyl sulfate and pluronic F-127. *Sci. Rep.* 8:14909.

Koroleva, E. V., Thompson, G. E., Hollrigl, G., and Bloeck, M. (1999). Surface morphological changes of aluminium alloys in alkaline solution:: effect of second phase material. *Corros. Sci.* 41, 1475–1495. doi: 10.1016/s0010-938x(98)00188-7

Lao-Atiman, W., Bumroongsil, K., Arpornwichanop, A., Bumroongsakulsawat, P., Olaru, S., and Kheawhom, S. (2019). Model-based analysis of an integrated zinc-air flow battery/zinc electrolyzer system. *Front. Energy Res.* 7:15.

Li, C.-S., Sun, Y., Gebert, F., and Chou, S.-L. (2017). Current progress on rechargeable magnesium–air battery. *Adv. Energy Mater.* 7:1700869. doi: 10.1002/aenm.201700869

Li, Y., Li, Q., Wang, H., Zhang, L., Wilkinson, D. P., and Zhang, J. (2019). Recent progresses in oxygen reduction reaction electrocatalysts for electrochemical energy applications. *Electrochem. Energy Rev.* 2, 518–538. doi: 10.1007/s41918-019-00052-4

Li, Y., and Lu, J. (2017). Metal–air batteries: will they be the future electrochemical energy storage device of choice? *ACS Energy Lett.* 2, 1370–1377. doi: 10.1021/acsenergylett.7b00119

Liu, J., Wang, D., Zhang, D., Gao, L., and Lin, T. (2016). Synergistic effects of carboxymethyl cellulose and ZnO as alkaline electrolyte additives for aluminium anodes with a view towards Al-air batteries. *J. Power Sour.* 335, 1–11. doi: 10.1016/j.jpowsour.2016.09.060

Liu, Y., Sun, Q., Li, W., Adair, K. R., Li, J., and Sun, X. (2017). A comprehensive review on recent progress in aluminum–air batteries. *Green Energy Environ.* 2, 246–277. doi: 10.1016/j.gee.2017.06.006

Moghadam, Z., Shabani-Nooshabadi, M., and Behpour, M. (2017). Electrochemical performance of aluminium alloy in strong alkaline media by urea and thiourea as inhibitor for aluminium-air batteries. *J. Mol. Liquid.* 242, 971–978. doi: 10.1016/j.molliq.2017.07.119

Mohamad, A. A. (2008). Electrochemical properties of aluminum anodes in gel electrolyte-based aluminum-air batteries. *Corros. Sci.* 50, 3475–3479. doi: 10.1016/j.corsci.2008.09.001

Mori, R. (2014). A novel aluminium–Air rechargeable battery with Al2O3 as the buffer to suppress byproduct accumulation directly onto an aluminium anode and air cathode. *RSC Adv.* 4, 30346–30351. doi: 10.1039/c4ra02165g

Mori, R. (2015). Addition of ceramic barriers to aluminum–air batteries to suppress by-product formation on electrodes. *J. Electrochem. Soc.* 162, A288–A294.

Mori, R. (2017). Rechargeable aluminum–air battery using various air-cathode materials and suppression of byproducts formation on both anode and air cathode. *ECS Transact.* 80, 377–393. doi: 10.1149/08010.0377ecst

Mori, R. (2019). All solid state rechargeable aluminum–air battery with deep eutectic solvent based electrolyte and suppression of byproducts formation. *RSC Adv.* 9, 22220–22226. doi: 10.1039/c9ra04567h

Nomura, A., Ito, K., and Kubo, Y. (2017). CNT sheet air electrode for the development of ultra-high cell capacity in lithium-air batteries. *Sci. Rep.* 7:45596.

Park, I.-J., Choi, S.-R., and Kim, J.-G. (2017). Aluminum anode for aluminum-air battery – Part II: Influence of In addition on the electrochemical characteristics of Al-Zn alloy in alkaline solution. *J. Power Sour.* 357, 47–55. doi: 10.1016/j.jpowsour.2017.04.097

Poolnapol, L., Kao-Ian, W., Somwangthanaroj, A., Mahlendorf, F., Nguyen, M. T., Yonezawa, T., et al. (2020). Silver decorated reduced graphene oxide as electrocatalyst for zinc–air batteries. *Energies* 13:462. doi: 10.3390/en13020462

Pyun, S.-I., and Moon, S.-M. (2000). Corrosion mechanism of pure aluminium in aqueous alkaline solution. *J. Solid State Electrochem.* 4, 267–272. doi: 10.1007/s100080050203

Rashvand, A. M., Jafarian, M., Moghanni, B. O. H., Gobal, F., Hosseini, S. M., et al. (2013). Study of the alloying additives and alkaline zincate solution effects on the commercial aluminum as galvanic anode for use in alkaline batteries. *Mater. Chem. Phys.* 143, 133–142. doi: 10.1016/j.matchemphys.2013.08.035

Ryu, J., Jang, H., Park, J., Yoo, Y., Park, M., and Cho, J. (2018). Seed-mediated atomic-scale reconstruction of silver manganate nanoplates for oxygen reduction towards high-energy aluminum-air flow batteries. *Nat. Commun.* 9:3715.

Shinagawa, T., Garcia-Esparza, A. T., and Takanabe, K. (2015). Insight on Tafel slopes from a microkinetic analysis of aqueous electrocatalysis for energy conversion. *Sci. Rep.* 5:13801.

Shrestha, N., Raja, K. S., and Utgikar, V. (2019). Mg-RE alloy anode materials for mg-air battery application. *J. Electrochem. Soc.* 166, A3139–A3153.

Teabnamang, P., Kao-Ian, W., Nguyen, M. T., Yonezawa, T., Cheacharoen, R., and Kheawhom, S. (2020). High-capacity dual-electrolyte aluminum–air battery with circulating methanol anolyte. *Energies* 13:2275.

Verma, C., Singh, P., Bahadur, I., Ebenso, E. E., and Quraishi, M. A. (2015). Electrochemical, thermodynamic, surface and theoretical investigation of 2-aminobenzene-1,3-dicarbonitriles as green corrosion inhibitor for aluminum in 0.5M NaOH. *J. Mol. Liquid.* 209, 767–778. doi: 10.1016/j.molliq.2015.06.039

Wang, D., Li, H., Liu, J., Zhang, D., Gao, L., and Tong, L. (2015a). Evaluation of AA5052 alloy anode in alkaline electrolyte with organic rare-earth complex additives for aluminium-air batteries. *J. Power Sour.* 293, 484–491. doi: 10.1016/j.jpowsour.2015.05.104

Wang, D., Zhang, D., Lee, K., and Gao, L. (2015b). Performance of AA5052 alloy anode in alkaline ethylene glycol electrolyte with dicarboxylic acids additives for aluminium-air batteries. *J. Power Sour.* 297, 464–471. doi: 10.1016/j.jpowsour.2015.08.033

Wang, J. B., Wang, J. M., Shao, H. B., Chang, X. T., Wang, L., Zhang, J. Q., et al. (2009). The corrosion and electrochemical behavior of pure aluminum in additive-containing alkaline methanol–water mixed solutions. *Mater. Corros.* 60, 269–273. doi: 10.1002/maco.200805074

Wang, J.-B., Wang, J.-M., Shao, H.-B., Zhang, J.-Q., and Cao, C.-N. (2007). The corrosion and electrochemical behaviour of pure aluminium in alkaline methanol solutions. *J. Appl. Electrochem.* 37, 753–758. doi: 10.1007/s10800-007-9310-8

Wang, L., Liu, F., Wang, W., Yang, G., Zheng, D., Wu, Z., et al. (2014). A high-capacity dual-electrolyte aluminum/air electrochemical cell. *RSC Adv.* 4, 30857–30863. doi: 10.1039/c4ra05222f

Wang, Y., Pan, W., Kwok, H., Lu, X., and Leung, D. Y. C. (2019). Low-cost Al-air batteries with paper-based solid electrolyte. *Energy Proc.* 158, 522–527. doi: 10.1016/j.egypro.2019.01.146

Weon, J.-I., and Woo, H.-S. (2013). Corrosion mechanism of aluminum alloy by ethylene glycol-based solution. *Mater. Corros.* 64, 50–59. doi: 10.1002/maco.201106222

Yoo, K., Banerjee, S., Kim, J., and Dutta, P. (2017). A review of lithium-air battery modeling studies. *Energies* 10:1748. doi: 10.3390/en10111748

Yu, Y., Chen, M., Wang, S., Hill, C., Joshi, P., Kuruganti, T., et al. (2018). Laser sintering of printed anodes for al-air batteries. *J. Electrochem. Soc.* 165, A584–A592.

Zaharieva, J., Milanova, M., Mitov, M., Lutov, L., Manev, S., and Todorovsky, D. (2009). Corrosion of aluminium and aluminium alloy in ethylene glycol–water mixtures. *J. Alloys Comp.* 470, 397–403.

Zhang, G. A., Xu, L. Y., and Cheng, Y. F. (2008). Mechanistic aspects of electrochemical corrosion of aluminum alloy in ethylene glycol–water solution. *Electrochim. Acta* 53, 8245–8252.

Zuo, Y., Yu, Y., Zuo, C., Ning, C., Liu, H., Gu, Z., et al. (2019). Low-temperature performance of Al-air batteries. *Energies* 12:612.

Conflict of Interest: The authors declare that the research was conducted in the absence of any commercial or financial relationships that could be construed as a potential conflict of interest.

frontiers in Energy Research

BRIEF RESEARCH REPORT
published: 31 July 2020
doi: 10.3389/fenrg.2020.00179

Artificial Intelligence Assisted Dynamic Control of Environmental Emissions From Hybrid Energy Process Plants (HEPP)

U. Tuzun[1,2,3]*

[1] Churchill College, University of Cambridge, Cambridge, United Kingdom, [2] International Process Engineering Consultant, Weybridge, United Kingdom, [3] U.K. Delegate, European Federation of Chemical Engineering (EFCE) Energy Section, EFCE Working Party on Mechanics of Particulate Solids, Paris, France

A model digital data processing platform is proposed based on "deep-learning" methodology that can be used to identify the emissions patterns from process plants with hybrid energy recovery and energy generation facilities. The non-invasive dynamic monitoring and correlation of particulate, VOCs and other greenhouse gas emissions from semi-batch and continuous process plants is demonstrated with use of neural encoding and pattern recognition using a multi-layer perceptron and multi-stack encoder configuration. A multi-layer environmental perceptron (MLEP) is developed based on the above analyses that aims to detect patterns of emission types, rates and concentrations as a function of variation of plant operational conditions and process variables. Four different task algorithms are constructed and are currently trained for use in (i) In-Plant Product Quality Control Domain and (ii) In-Plant Process Efficiency Target Control Domain. As a further consequence, environmental impact assessment is considered within the hazards and process safety frameworks that conventionally issue sanctions and penalize non-compliance with imposition of environmental levy scales rather than offering process improvement incentives. The latter is demonstrated to be possible by facilitating dynamic corrective action and hazard prevention using MLEP platforms should emission ceilings be frequently and/or periodically exceeded in 24/7 continuous plant operations. Potential applications of the MLEP (MLEP) are illustrated in the context of dynamic emissions control and abatement in hybrid energy process plants (HEPP) and combined power plants using process-integrated CO_2 capture and storage schemes.

Keywords: digital platforms, network analysis, environmental sensors, emissions control, HEPP

OPEN ACCESS

Edited by:
Theodoros Damartzis, École Polytechnique Fédérale de Lausanne, Switzerland

Reviewed by:
Limei Shen, Huazhong University of Science and Technology, China
Dimitrios Ipsakis, Technical University of Crete, Greece

***Correspondence:**
U. Tuzun
prof.ugur.tuzun@cantab.net

Specialty section:
This article was submitted to Process and Energy Systems Engineering, a section of the journal Frontiers in Energy Research

Received: *04 May 2020*
Accepted: *09 July 2020*
Published: *31 July 2020*

Citation:
Tuzun U (2020) Artificial Intelligence Assisted Dynamic Control of Environmental Emissions From Hybrid Energy Process Plants (HEPP). Front. Energy Res. 8:179. doi: 10.3389/fenrg.2020.00179

INTRODUCTION

Industrial process emissions of greenhouse gases, VOCs and particulates are shown to represent some 20–30% of all environmental emissions in industrialized economies (see for example, Erickson and Brase, 2019). Furthermore, the International Energy Agency [IEA] (2018) estimates that urban areas currently account for over 67% of energy-related global emissions, which are expected to rise to 74% by 2030; see IEA Report (2018). It is also expected that 89% of the

increase in CO2 emissions from energy use will be from developing economies by 2030. Hence, reducing greenhouse gas emissions and improving air quality are two interrelated challenges for world economies in combatting climate change and degradation of natural habitats; refer to Erickson and Brase (2019). 7th Environment Action Programme (7th EAP) mandated by EU aims to develop by 2018 "strategy for non-toxic environment that is conducive to innovation and the development of sustainable substitutes including non-chemical solutions"; refer also to European Environment Agency [EEA] (2016) National Emissions Ceilings Directive (2016/2284/EU) and the Clean Air Programme.

Figure 1 shows a schematic summarizing the three main categories of operations where adverse environmental impacts are to be minimized: (1) Abatement and/or capture of atmospheric emissions of fine particulates, volatile organic compounds, and other greenhouse gases during recovery of heat losses, and re-use and re-generation of power;. (2) further treatment of byproducts to yield value-added products and recycle and re-use of process waste in energy generation and/or raw material provision to other industry sectors; and (3) use of recyclable and/or bio-degradable packaging materials of commercial products.

All three categories of these activities combined now constitute essential parts of industrial plant design and operation to achieve best possible compliance with environmental regulations (see for example European Environment Agency [EEA], 2016). Best Available Techniques (BATs) advocated for Large Combustion Plants (L) with total rated thermal input equal to or greater than 50 MW of electrical power and heat production. Clearly, once a plant is operational, it also becomes imperative to monitor environmental emissions regularly to minimize atmospheric pollution as well as monitoring possible accumulation over time of pollutants ejected to environmental land and water with a view to re-process waste streams containing pollutants of high toxicity detrimental to natural habitat and human health.

Many of the classical chemical process plant control algorithms are established to provide feed-back loops and differential and integral control of set-points of process variables evaluated from the process control parameters such as recycle rates, flow rates, concentrations and phase distributions of materials; followed by "pinch" techniques used to achieve final product purity whilst providing maximum heat recovery (see for example Smith, 2005) for a comprehensive account of industrial energy systems integration. However, these steady-state process control algorithms often lack transient response analyses required to monitor and control environmental emissions largely due to the existence of "hidden layers" of interaction of process variables affecting the values of the "visible" measurements recorded by digital environmental sensors.

A rather more sophisticated type of operator control is therefore needed based on "deep-learning" methodology which makes use of supervised and unsupervised neural network algorithms aimed at establishing multivariate pattern recognition with varying numbers of hidden layers of process variables, operational conditions and material properties (see Tuzun, 2017, 2018). Application of emissions bubble concept for emissions monitoring and control is illustrated more recently by Tuzun (2020b) using a case study from a multi-feed option fuel production plant which also incorporates the integration of CAPEX and OPEX minimization whilst meeting regulatory emission targets set for the emissions bubble.

MONITORING ATMOSPHERIC EMISSIONS AND PATTERN RECOGNITION

Little process data is reported in the open literature on VOCs, particulate and other greenhouse gas emissions from individual process and power generation plants due to the regulatory implications discussed in the introduction. However, an analogy is established in terms of the process time between data reported on emissions from animal feedstock and agricultural waste storage silos of methane and the higher weight alcohols such as ethanol, and acetic acid and acetaldehydes and esters (see Wenda-Piesik et al., 2010; Hafner et al., 2013) for reported data sets. These data sets show high atmospheric release rates (typically, 0.5–5 g m^{-2} hr^{-1} with an air velocity of 0.5 m s^{-1}) of more volatile compounds which feature significantly in the relatively short exposure times (typically 10–30 min) of the field sensors. In contrast, much higher accumulated emission results are revealed for heavier organics over time periods of the order of several hours. Furthermore, the VOCs emissions produced by bacteria and yeasts during and post-anaerobic processes are strongly affected by high temperatures and humidity (see Wenda-Piesik et al., 2010).

Bent (2015) and Yue et al. (2017) provide an in-depth analysis of the sources of agricultural greenhouse gas emissions from farm production to food consumption. Bent (2015) provides links to literature on chemical routes to eliminate methane and NO_x by nitrification/de-nitrification (NO to NO_2/NO_3 and ammonification (NH_3). Yue et al. (2017) present extensive statistics indicating that Carbon footprint from food supply side to be almost threefold of those on the food consumption side. Greatest source of methane emissions are noted to be from farming of crops and fertilizer applications as well as from the use of crops as feed to livestock. These confirm the previous observations of Bent (2015).

Greenhouse gas emissions such as CO_2 and NOx and Methane feature more heavily in power generating plants and those process plants which run combined cycle gas turbines and waste heat recovery (see for example Zare and Mahmoudi, 2015; Zhang et al., 2019). Furthermore, large combustion plants and waste incinerators can generate as much as 46% CO_2 and 18% NOx by volume in process flue gases; refer to European Environment Agency [EEA] (2016) and IEA-GHG (2019). With greenhouse gas emissions, the atmospheric release rate is fast whilst the accumulated emission readings are influenced by the advance and expansion of plumes as a function of the stack heights of the burner units (see Markiewicz, 2006) for details of mathematical modeling.

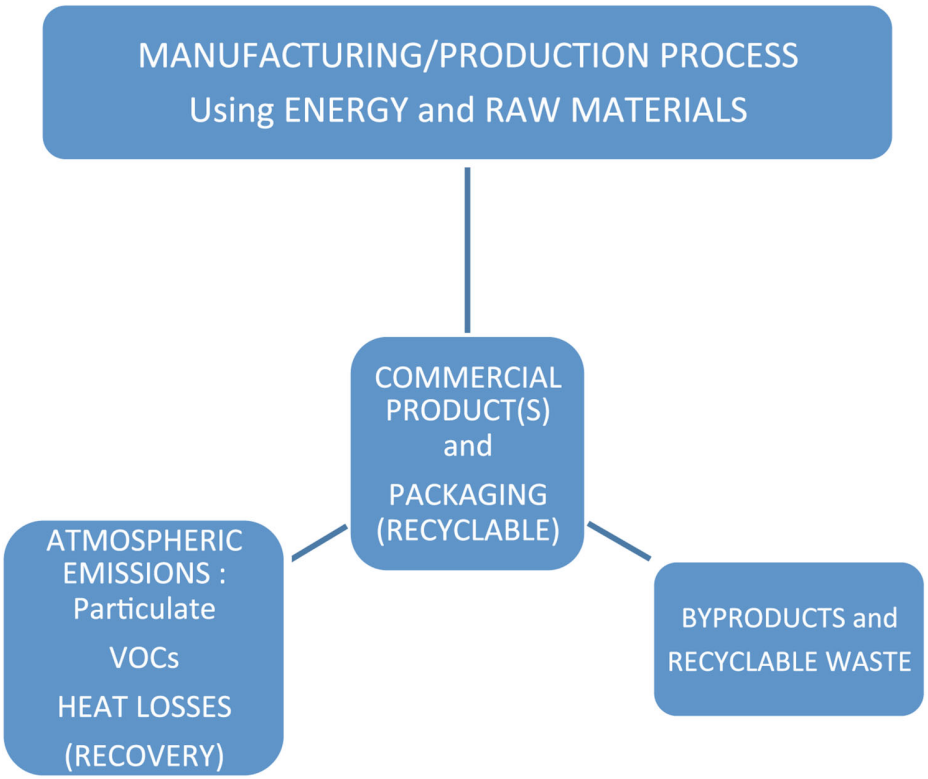

FIGURE 1 | Green process/production/manufacturing: recovery, and reuse of materials and energy and minimizing atmospheric emissions.

Particulate emissions with (PM-2.5) and (PM-10) micron limits are measured through online sampling around the particulate matter storage, handling and processing units (see for example, Kulp and Ponte, 2000). These emissions are shown to periodically peak and gradually disperse over time as a function of the operations performed by the batch, semi-batch and continuous operational units of the process plants.

Hence, in reliable monitoring of all three categories of emissions; VOCs, greenhouse gases and particulate matter, digital data gathering by multiple and integrated sensor systems become necessary; those that can self-correlate emission release rates, concentration profiles with simultaneous measurements of process temperature and relative humidity at the very least; refer to **Figure 2** below for a schematic of environmental sensor platform used by Sensirion AG Switzerland. Such an integrated sensor and parallel emissions field data gathering platform could be used in the construction of the logistical (i) selection, (ii) identification, and (iii) data recording functions for a given HEPP application; refer to **Figure 2**.

Such an integrated environmental sensing platform is the essential pre-requisite for (i) demonstrating compliance with environmental health and safety regulations and emissions ceilings discussed above as well as (ii) facilitating the use of neural network analyses for time-series pattern recognition of atmospheric emissions from spatially distributed emission sources within and immediately adjacent to the combined process and energy cycle plants.

DIGITAL PLATFORM CONSTRUCTION FOR MULTIVARIATE PROCESS AND ENVIRONMENTAL DATA SETS

Environmental field sensors (refer to **Figure 2**) can be placed at different locations within potentially high-emitting plant sections or throughout the entire plant layout at specific spatial intervals. These sensors can be tuned to record data at set frequencies over varying time intervals and/or only when at levels above the non-compliance thresholds set by the operator. The dynamic process values measured of these process environmental variables are affected by each other. Accordingly, the fluctuations measured of one set of environmental sensing variable will/may affect the dynamic variations in the other environmental data sets. The interdependency of the dynamics of these environmental variables will reveal patterns in time-series and in spatially distributed data sets collected simultaneously from sensors placed at different locations within a process plant or indeed at different locations within a single large process unit/section.

Trellis Diagram Construction

In parallel to the environmental emissions data gathering, the process operator system will have (i) set point and acceptable limit specifications of a range of product stream quality parameters and (ii) process efficiency determinants of the process

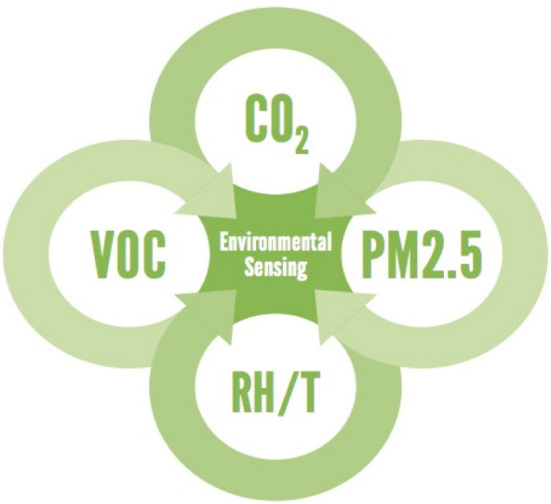

1. SELECTION: Sensor Type Location & Population via Emission Bubble(s) Identification within HEPP sub-sections

2. IDENTIFICATION: Hybrid Energy Input & Output Flows through successive unit operations and intermediate material storage and handling stages

3. DATA RECORDING: Spatial and Temporal Sampling Frequency in sync with process operating parameters and online quality control

FIGURE 2 | Environmental sensing platform required for multiple detection and measurement.

unit operations. To connect the environmental sensor data to the process control data above, a **Trellis Diagram** of the pathways of possible connectivity between the "hidden" layers/units and the observed operator symbols can be generated based on the sequential and parallel stages of the process flowsheet (see Tuzun, 2018) for the demonstration of studies involving two and three hidden layer applications in cereal processing plants (Kulp and Ponte, 2000) and pharmaceutical process plants (see also Fujiwara et al., 2005). These will also be published in detail.

Operator Tuning of "Preferred" States

The use of input and output data convolutions produce large time-series data sets that can be correlated either by defining **contrastive divergence or convergence** to and from preferred states; e.g., future emissions targets. Alternatively, or even concurrently, it is also possible to make use of different permutations of connectivity of the hidden process layers to arrive at convergent and divergent patterns of causality of the spatial data sets connecting different process units and plant sections. This method of operative tuning would then also allow for the recognition of "peak events" and anomalies in time-series data. Consequently, connected process variable re-adjustment is made possible by direct operator intervention using environmental sensor data rather than using environmental sensor data purely as process safety alarms.

Figure 3 shows a conceptual schematic of an operator driven platform for environmental emissions minimization whilst maintaining appropriate operator thresholds of variability of process unit operations to achieve optimal process efficiency and product quality.

Multiple Input/Multiple Output (MIMO) Multiplex Digital Platform Construction

Environmental compliance of hybrid process and energy plants (HEPP) is best served by a multiplex platform for regular and simultaneous data transfer to enable the analysis of environmental impact on a continuous and operator interactive basis. Such dynamic statistical data processing is also potentially relevant to a significant number of other on-site operational efficiency assessments including (i) energy use and recovery; (ii) supply chain efficiency of raw materials and energy inputs; (iii) byproducts recovery; (iv) regeneration and reuse of process water. Hence, as well as providing the means for an efficient dynamic environmental impact control, such digital platforms can also be used effectively to decide and execute dynamic process improvements through corrective and preventive actions to be tried and tested by the interactive operator control. This could in turn lead to significant potential energy and material resource savings and waste minimization paving the way for green processing and clean technology applications commensurate with circular economy targets (see for example, Mendoza et al., 2017; Tisserant et al., 2017).

A tailor-made development and utilization of a Multiple Input/Multiple Output (MIMO) system and method are necessary that could facilitate environmental sensor data acquisition via a Multiplex Digital Platform. MIMO system and method are patented for use in wireless LAN and broadband data reception and transmission (see for example Jia and Julian, 2014; Sun et al., 2015).

MIMO system includes steps comprising (i) multiple sensor input streams, (ii) control value checks and noise pruning/elimination and data matrix inversion followed by

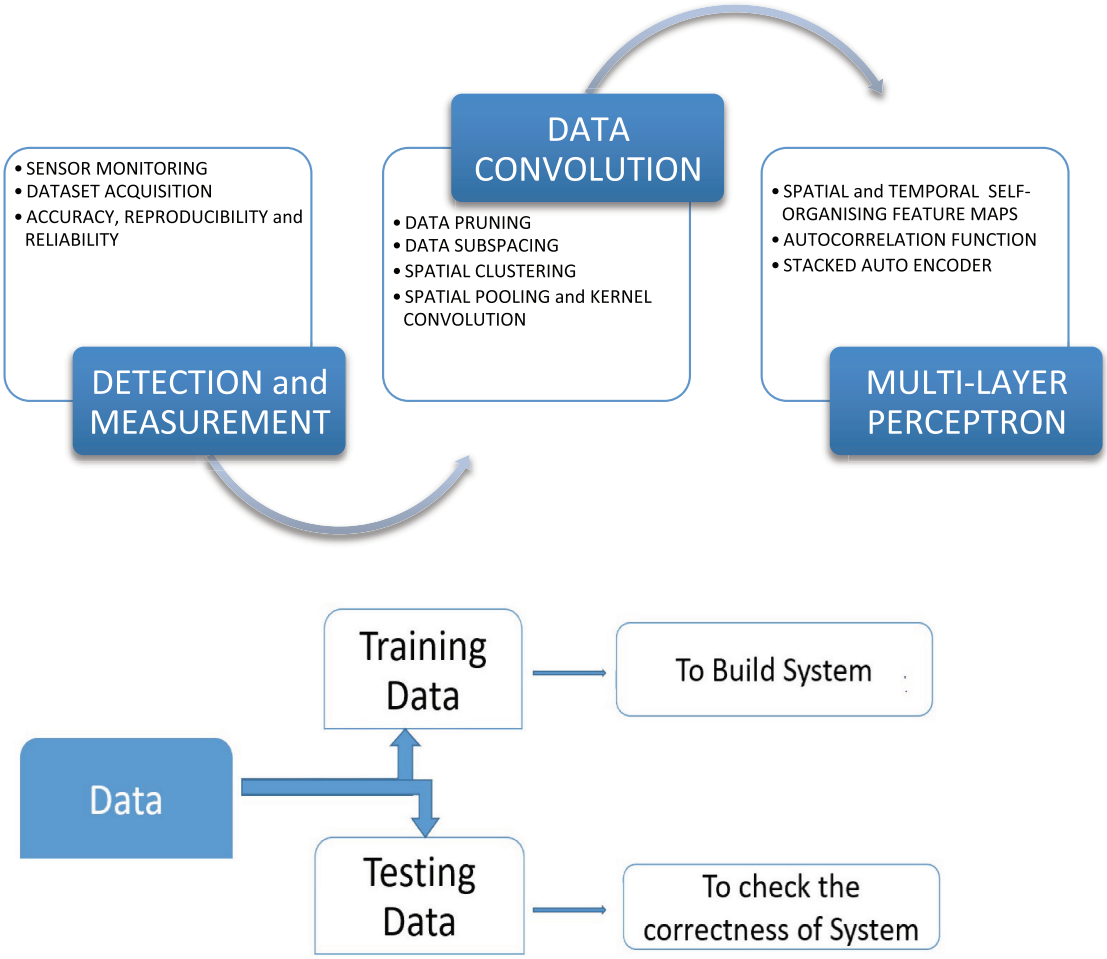

FIGURE 3 | (A) Construction of a digital platform for environmental data analysis: (i) multiple parallel sensor data gathering, (ii) spatial and Temporal Trend Evaluation through input and output data convolutions, and (iii) pattern recognition by unsupervised and supervised deep-learning. **(B)** Application and installation of the digital platform for environmental data analysis (i) **Training:** 4 × task algorithm development in 2 × test domains (ii) **Testing:** (i) emissions bubble(s), (ii) hybrid energy input and output energy flows. A digital platform for environmental data analysis: build-train-test methodology.

(iii) data stream splitting/data selection adding associated service descriptors (process plant topographic labeling); (iv) multiplex **ENCODING** of split and selected data sets for error correction in reconstructed data sets; and (v) digitization of the data sets for inter-leaver and modulator functions enabling the use of the **VITERBI** algorithm (see for example Lou, 1995; Wu, 2006). The use of the said algorithm allows the recognition of patterns by identifying and selecting the most likely sequence of "hidden states/layers" of process operational data which result in a given pattern of observed states/events; e.g., recorded time-series of air-borne emissions data sets at different plant sections.

The operations involving the use of the Viterbi algorithm are also referred to as **DECODING** the connectivity of the "hidden" operational layers of the process plant. Mathematical construction procedures of a Convolutional Neural Network (CNN) to enable output data decoding is described briefly below (see Haykin, 2008) for more details.

NEURAL NETWORK ANALYSES OF MULTIVARIATE PROCESS DATA

There are two types of mathematical approach to neural network applications known as unsupervised and supervised "Deep-Learning" techniques; they can be used separately, independently or simultaneously: (i) **Unsupervised Deep-Learning** using iterative construction of self-organizing maps (SOM) of environmental sensor data clusters by producing affine transformations of spatial and temporal neighborhood sub-spaces of data of high similarity generated with customized distance metrics (see for example Langkvist et al., 2014; Antoniades and Took, 2016); (ii) **Supervised Deep-Learning** achieved through calculation of contrastive convergence and divergence of data from targeted outputs using connectivity of hidden layers (units/neurons) of a multi-layer perceptron (MLP); refer to section "Digital Platform Construction for

Multivariate Process and Environmental Data Sets" and (see Haykin, 2008) for details.

In unsupervised deep learning, the mathematical model constructs input vectors that correspond to the "preferred state" of all sensors and controls. The convergence and divergence to and from the time-series patterns displayed with the spatial SOM grid of the "preferred state" can then be monitored by operator tuning of the process control parameters; refer to **Figure 3**. Iterative visual superimposition of real-life data sets on the SOM grid representing the preferred state of all sensors and process controls allows process control tuning in a manner, rather like using a virtual kaleidoscope.

Previous Developments With CNN Applications

It is also important to establish the extent of previous developments of the CNN algorithm construction and application in other diverse environmental process related fields of study. Here, by way of related examples, we will contrast the Multi-Layer Environmental Perceptron (MLEP) proposed here for monitoring and control of industrial plant emissions; with the works in computer-assisted electrical tomography for imaging building structures to monitor impacts of extreme weathering (see Rymarczyk et al., 2018); mapping scalp detectors activity to intracranial EEG for monitoring causality of epilepsy and aiding with clinical diagnosis (see Antoniades et al., 2018) and speech/speaker recognition in long temporal acoustic signal convolution contexts to model phonetic information; refer to Snyder et al. (2015). All these studies make use of the Convoluted Neural Network analysis based on the construction and training of algorithms on hidden-layers of connectivity as well as unsupervised pattern recognition techniques based on data pooling and sub-space mapping techniques; refer to Haykin (2008).

The above examples are cited because of their use of algorithm constructions with increasing order of sophistication. Long-time averaged spatial image construction with electrical tomography (Rymarczyk et al., 2018) relies on 2-D planar data filtered re-constructions from simultaneous voltage and capacitance readings from multiple sensors whilst the clinical data analysis with intracranial EEG analyses time series of data in individual channels and thus uses only 1-D filtered data sets; refer to Antoniades et al. (2018). In acoustic recognition algorithms, speaker recognition is established using i-vector mapping and Gaussian Mixture Models (GMM) (2-D) voice recognition with additional CNN algorithm addition *a posteriori* for alignment of phonetic content in tied 3-D states or senones used to define phonetic sub-space similarity against a trained reference state for advanced speaker identification with content; refer to Snyder et al. (2015).

It is clear from the examples provided above that the MLEP proposed for industrial emissions monitoring and abatement could use both spatial mapping and time-series re-construction analyses of environmental sensor data sets based on unsupervised mapping and supervised convolution techniques; refer to **Figure 3**. The MLEP is constructed to connect dynamically the three successive stages of dynamic process data analysis and process abatement: (i) detection and measurement, (ii) data convolution, and (iii) deep-learning for pattern recognition; refer to **Figure 3A**.

Finally, the supervised deep learning by CNN construction requires *a priori* training to be achieved with repeated modulation at different frequencies (i.e., different input data sampling intervals) of the hidden-layer algorithms using randomly generated field sensor data sets. This helps to establish the reference states; expressed as channel-labeled waveforms in a multi-channel data analyzer; for comparison with real-life data sets to enable operator fine-tuning of the process parameters affecting the environmental sensor readings. There is ample textbook literature and dedicated on-line sites for independent learning such as (adeveloperdiary.com) which also provide illustrations of sample software and case study demonstration packages.

Novel Kaleidoscope Model of Process Environmental Compliance Control

A novel **KALEIDOSCOPE MODEL** of a MLEP is currently being developed to facilitate pattern recognition with supervised deep learning. This is achieved by auto-correlation of data using alternate sequences of "hidden layers" and increasing the hierarchy of hidden layers by placing additional specs of variables in each layer. The early results indicate that it is possible to build up increased layers of multivariate and multi-stack encoder operation (refer to section "Operator Tuning of "Preferred" States" above). This will allow for greater degrees of freedom of operator control in fine-tuning of data acquisition by the digital environmental field sensors by continuous monitoring of the process dynamics; refer to **Figure 2**.

Further progress with successful implementation of the MLEP is likely to reduce the need for routine large-scale uncorrelated raw data storage and handling currently necessitated by the conventional "*in situ*" process measurements. This is expected to allow the plant operators to focus predominantly on the product quality and process efficiency targets.

Furthermore, the operational records produced by the MLEP enabling green process applications can in turn be used to design novel integrated environmental sensors that can collect and auto-correlate data directly, targeting environmental compliance performance of a hybrid energy process plant.

Figure 4 shows a conceptual schematic of the MLEP digital data processing platform comprising the two simultaneous machine learning cycles of input and output data convolutions and construction of SOMs, spatial clustering and time-series pattern recognition in reconstructed data. The operator interface will then be used to (i) reset noise filter parameters, (ii) refresh digital sensor output frequency thresholds, and (iii) re-adjust process parameter values to comply with the environmental emission ceilings on a dynamic basis. **Figure 4** also illustrates the dynamic operator interface functions synced with the MLEP to recover and maintain the "preferred state" control of environmental emissions. It is expected that specific process applications will/may require multiple sets of hardware for

operational control of different plant sections established to be potential high-emitters. This is believed to be in accordance with the "emissions bubble" concept approved by the European Environment Agency (EEA) Directives (2016-2284). This considers the weighted average of emissions of all emitters within the "bubble" for approval of regulatory compliance.

Real-Life Training and Plant Trials With MLEP

Generic training of the MLEP with different deep-learning algorithms such as Recurrent Neural Network (RNN) and Time-Delay Neural Network (TDNN) is designed and tested by producing simultaneous input and output data convolutions (see for example Haykin, 2008). It is possible to design information pathways connecting multiple "hidden layers" with operator observed data sets by selecting functional connectivity between the time series of key material sample properties and process variables for each unit operation in the process plant starting with the Trellis diagram constructions described in section "Trellis Diagram Construction." This is procedure is known as defining the **learning rules** which allows the neural network to maintain a sort of "state" facilitating such tasks as **a sequence prediction**. Training of the constructed pathways of connectivity with specific deep-learning algorithms is affected using plant operator and environmental emissions data sets.

The operational data training (as seen in **Figure 3B**) using the digital platform is affected by the development of 4 task algorithms: (i) estimation of **variability** of material flow rates, (ii) estimation of **variability** of emissions of different kinds, (iii) estimation of **operational disruption** rates and (iv) re-current anomaly detection and **Environmental Neural Switch** when spatial variability takes precedence over temporal variability and vice versa. Here, issues such as noise elimination, input-output signal time drift, and cumulative time-series pattern recognition indexed to sample reference states are computed to build up a reference library of the "**known states**" of the process plant operation.

In real-life plant operation, the **contrastive convergence and divergence** to and from the "known states" is recognized when the measured parameters and sequence-predicted values from the NN algorithms are kept within certain pre-set safe operating limits. When environmental emissions values rise significantly above the "**preferred state,**" then this would allow HAZOP procedures to kick in at different levels of pre-set perceived risk levels. To date, a real-life demonstration of the automated linking of HAZOP and MLEP-based harmful emissions data predictions based on environmental sensor inputs is yet to be pioneered. The additional challenge is imposed by the difficulty of **smart guessing** as to the likely duration of the "**harmful state**" and the optimal path to recovery to the "**preferred state.**" To be able to perform these additional functions effectively, the MLEP needs to have capability for "**evaluative decision-making**" which requires the higher level of cognitive recognition and assessment typically observed with human brain activity subjected to a **situate metacognitive learning** environment (see for example Tuzun, 2020a).

DISCUSSION OF POTENTIAL HYBRID ENERGY PROCESS PLANT APPLICATIONS WITH MLEP

It is appropriate to consider the potential use of the MLEP with industrial plants engaged in (i) synthetic chemicals/materials production, (ii) bio-chemicals/biomaterials extraction from natural and agricultural products, and (iii) gas and liquid fuels production. Clearly, a hybrid energy process plant in the first two categories will also have options to exercise with regards to combined cycle electrical power generation using heat recovery cycles whereas the plants engaged primarily in fuel production will increasingly want to exercise options to produce hybrid fuel mixes by dilution of high carbon content of fossil fuels with bio-extracted organics, synthetic organic byproducts and hydrogen (see for example Holm-Nielsen and Ehimen, 2014; Staffell et al., 2019). Furthermore, processes involving anaerobic digestion of agricultural waste (see Dooms et al., 2018) are also in compliance with the requirements to eliminate waste through regeneration and re-use; refer to **Figure 1** for green process applications. Hence, with both strategies of hybrid energy process applications, the aim is to provide reduced greenhouse gas emissions such as CO_2 and NO_x whilst also reducing atmospheric pollutants such as VOCs and particulate emissions.

It is possible that the HEPP plants will able to use their own process waste as fuel if not entirely on their own but with integration into hybrid processes that will generate energy as well as energy recovery and material products from waste (see for example Al-Atta et al., 2018).

MLEP applications (refer to section "Previous Developments with CNN Applications"), within this environmental compliance background, can be utilized to demonstrate two primary routes for environmental impact Correction and Prevention (CAPA) (see Corrective Preventive Actions [CAPA] Guidelines, 2012): (1) "In-plant" Environmental Compliance Monitoring and Control of Emission Levels; and (2) "In-process" Abatement of Harmful Emissions. It can be argued that both strategies can be used simultaneously whilst the abatement schemes can be also factored into new plan designs and retrofits based on the experience gained with dynamic compliance monitoring and control of harmful emissions.

Potential Role of MLEP With Integrated Carbon Capture and Storage (CCS) Schemes

Capture and storage of CO_2 in industrial plants is advocated to be a much needed principal technology development to combat climate change by reducing drastically the atmospheric emissions of CO_2 that are shown scientifically to be responsible for global warming and its associated adverse environmental impacts (see for example Mc Sweeney et al., 2009; IPCC, 2014). This mandate has led to the development of power production integrated with CO_2 capture. Recent examples of new technology developments include chemical looping combustion (CLC) with dual circulating fluidized beds (see Arnaiz del Pozo et al., 2019) and internally circulating fluid bed reactor (ICR) which

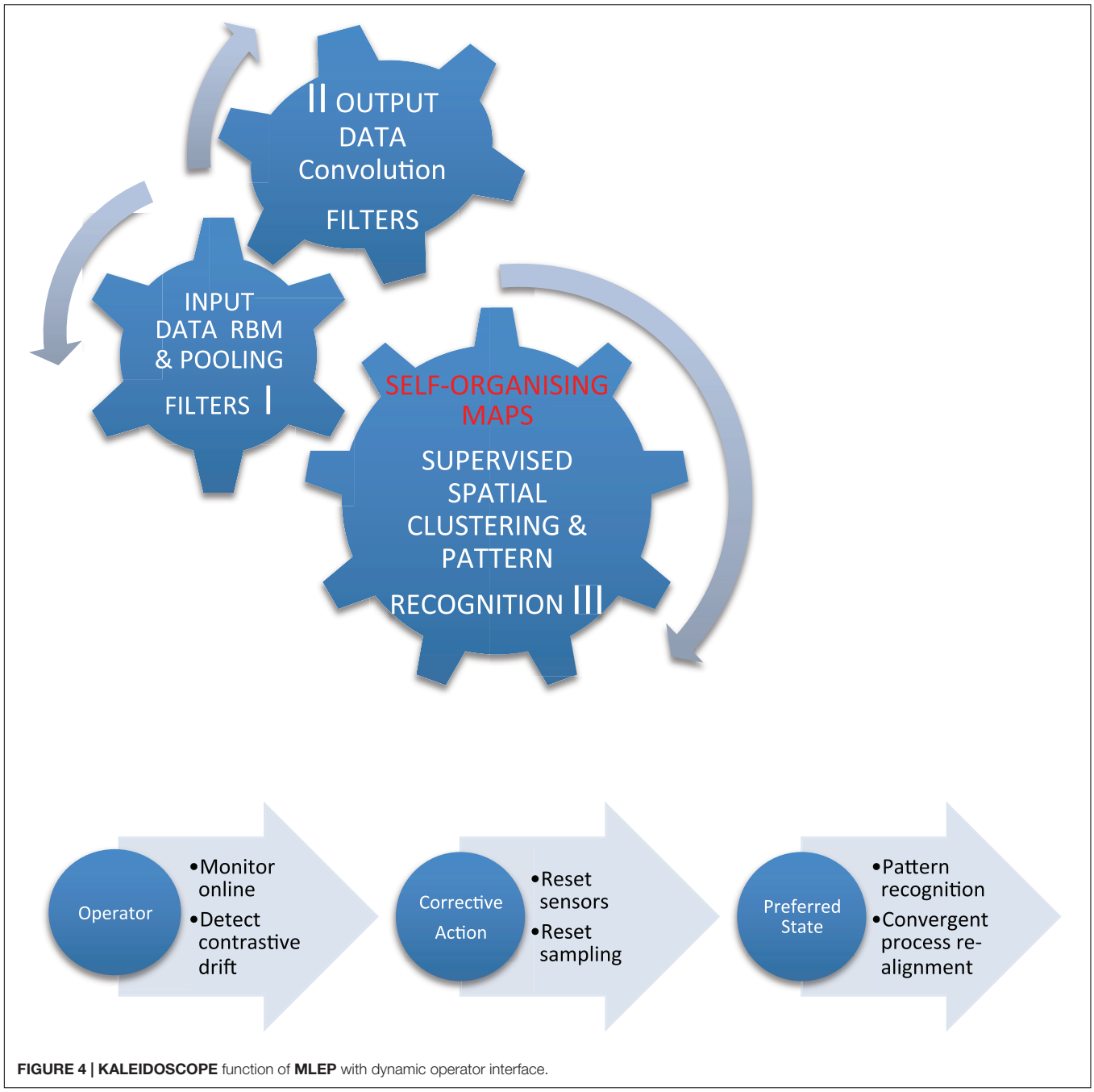

FIGURE 4 | KALEIDOSCOPE function of **MLEP** with dynamic operator interface.

combine natural gas reduction by air with particulate oxygen carrier (typically NiO particles supported on Al_2O_3) circulation to achieve conversion to CO_2 (see Cloete et al., 2019). Common to these recent technology developments, is the desire to minimize the additional energy penalty of CO_2 capture and storage, by integrating it fully within the combined power generation of the natural gas combined cycle (NGCC) plants.

IEA Sustainable Development Scenario (see International Energy Agency [IEA], 2018) assumes CO_2 prices of $63 per ton in 2025 and $140 per ton in 2040. It is expected that the above hybrid energy technology developments will bring the price down to $50 and below by avoiding separate energy intensive carbon capture process "add-on" s to existing power plants. However, the successful implementation of these most recent technologies depends on the ability to avoid CO_2 leaks from the fuel section to the air section; reducing the CO_2 capture efficiency of the reactor unit, while also avoiding N_2 leaks from the air section to the fuel section; reducing the purity of the CO_2 captured.

Furthermore, recent studies also show that scale up of a single ICR reactor unit even by 20% by size can exasperate the above leaks sufficiently to reduce the purity of captured CO_2 from 96 to 93% (see Cloete et al., 2019). There is also the increased cost

of handling elutriated solids with the increased reactor size (see Argyle and Bartholomew, 2015). The most important criteria for designing and operating the ICR units is therefore to minimize the amount of gas leakage between the reactor sections whilst maintaining an optimal rate of oxygen carrying solids circulation to ensure that the fuel is completely converted.

With both the CLC and ICR technology developments, it is imperative that the process efficiency and product purity is optimized through the use of a multiplex digital platform that can produce dynamic corrective action by periodic readjustment of the process parameters that will minimize contaminating gas leaks during gas switch and excessive solids elutriation. Here, it may be possible to develop supervised deep-learning strategies that will facilitate pattern recognition in time-series of multiple sensor data sets. This will in turn, allow for the operator fine-tuning, to achieve the "preferred state" that will maximize both the captured CO_2 purity and the percentage of CO_2 captured. It is believed that the wider implementation of these technologies depends greatly in their ability to utilize multivariate dynamic process control with fast convolutional neural network techniques described above so that significant fluctuations of captured CO_2 purity and capture efficiency could be avoided. Due to the highly cyclic nature of the gas switch and solids circulation operations, the conventional steady-state set point process control techniques will prove inadequate to achieve the marginal process gains required with increased plant capacity.

CONCLUSION

The current studies relating to the use of field sensors and temporal and spatial data gathering for environmental compliance purposes in chemical and material processing plants are found to yield large and complex data sets. These can be analyzed effectively using "deep-learning" methods and systems of statistical analysis similar to those already developed for applications as diverse as tomographic imaging, medical sensor signal trace analysis and automatic speech recognition to name but a few.

The significance threshold of cross-correlations are established and ranked by first pre-pruning of data for bias and random error using statistical regression. Harvested data sets are subsequently analyzed using a digital processor platform that comprises as a multi-layer auto-encoder and a convolutional neural network decoder. Once operator defined "preferred state" is established for the process inputs and outputs, then process monitoring is carried out within a digital framework that calculates significance of divergence and convergence to and from the preferred-state in pre-selected temporal sequences for different spatial neighborhoods (emission bubbles) as a measure of the environmental compliance of the process operations.

A MLEP model considered can facilitate automated machine-learning; using a novel kaleidoscopic procedure for synchronizing input and output data convolution cycles, pattern recognition algorithms and a dynamic operator interface. Current R&D program in progress has so far constructed model MLEPs for two and three hidden-layer connectivity applications of solids handling and processing applications in a cereal processing plant (see Tuzun, 2018) and a research paper is underway to present the initial results. A similar project is being kick-started with a pharmaceutical process application based on the previous work of Fujiwara et al. (2005). Alongside the development of neural network algorithms for process plant applications, an interactive matrix of [4,2] operating task algorithms are constructed to facilitate data training in 4 different **variability modes** within two different "in-plant" **operation domains**; refer to section "Real-Life Training and Plant Trials with MLEP" and **Figure 3B**.

The potential use of a digital MLEP multiplex platform is demonstrated to be ideally suited for the operations of hybrid energy process plants (HEPP) for chemicals and materials production; specifically for "in-plant" monitoring of environmental emissions and "in-process" control and abatement. Similar opportunities are illustrated in the operation of CO_2 capture and storage schemes wholly integrated into process operations of combined cycle power generation plants. Further work will focus on the application of trained algorithms for environmental process monitoring and control using "real-life" plant data sets.

DATA AVAILABILITY STATEMENT

All datasets generated for this study are included in the article/supplementary material, further inquiries can be directed to the corresponding author.

AUTHOR CONTRIBUTIONS

The author is the sole contributor to the manuscript unless otherwise stated in the text.

FUNDING

Partial travel funding (2017–2018) was provided by the IChemE, United Kingdom; and EFCE Working Party for Mechanics of Particulate Solids for attendance at EFCE meetings and international conferences. Further conference attendance funding was received from University of Edinburgh (2017) and Oxford University (2016), United Kingdom. The R&D activity is also supported by a non-commercial feasibility study (2019–) in California, United States.

ACKNOWLEDGMENTS

We would like to acknowledge preliminary discussions (2015–2016) with staff of Xenesis Ltd. at Surrey Technology Centre, Surrey Research Park, Guildford, Surrey, United Kingdom. Further discussions with and input from colleagues at IChemE UK Energy Centre (2018–2019) and EFCE Energy Section are also gratefully acknowledged.

REFERENCES

Al-Atta, A., Huddle, T., Rodriguez, Y. G., Mato, F., Garcia-Serna, J., Cocero, M. J., et al. (2018). A techno-economic assessment of the potential for combining supercritical water oxidation with "in-situ" hydrothermal synthesis of nano-catalysts using a counter-current mixing reactor. *Chem. Eng. J.* 344, 431–440. doi: 10.1016/j.cej.2018.03.058

Antoniades, A., Spyrou, L., Martin-Lopez, D., Valentin, A., Alarcon, G., Sanei, S., et al. (2018). Deep neural architectures for mapping scalp to intracranial EEG. *Int. J. Neural Syst.* 28:1850009. doi: 10.1142/s0129065718500090

Antoniades, A., and Took, C. C. (2016). "Speeding up feature selection: a deep-inspired network pruning algorithm, (2016)," in *International Joint Conference on Neural Networks (IJCNN), 24-29 July 2016, Vancouver*, British Columbia, doi: 10.1109/IJCNN.2016.7727221

Argyle, M. D., and Bartholomew, C. H. (2015). Heterogeneous catalyst activation and regeneration: a review. *Catalysts* 5, 145–269. doi: 10.3390/catal5010145

Arnaiz, del Pozo, C., Cloete, S., Cloete, J. H., Jimenez-Alvaro, A., and Amini, S. (2019). The potential of chemical looping combustion using the gas switching concept to eliminate the energy penalty of CO2 capture. *Int. Greenhouse Gas Control* 83, 265–281. doi: 10.1016/j.ijggc.2019.01.018

Bent, E. (2015). *The Ground Exhales: Reducing Agriculture's Greenhouse Gas*. Guelph, ON: University of Guelph. Available online at: www.theconversation.com

Cloete, J. H., Khan, M. N., Cloete, S., and Amini, S. (2019). Simulation-based design and economic evaluation of a novel internally circulating fluidised for power production with CO2 capture. *Processes* 7:723. doi: 10.3390/pr7100723

Corrective and Preventive Actions (Capa) Guidelines, (2012). *Corrective and Preventive Actions (CAPA) Guidelines*. Available at: www.rmbimedical.com/RegulatoryAffairs/capaguidelines.pdf.

Dooms, M., Benbelkacem, H., and Buffiere, P. (2018). High solid temperature phased anaerobic digestion from agricultural wastes: putting several reactors in sequence. *Biochem. Eng. J.* 130, 21–28. doi: 10.1016/j.bej.2017.11.011

Erickson, L. E., and Brase, G. (2019). *Reducing Greenhouse Gas Emissions and Improving Air Quality – Two Interrelated Global Challenges*. CRC Press: Taylor & Francis.

European Environment Agency [EEA] (2016). "National emissions ceilings directive," in *Clean Air Programme*, Directive (EU) 2016/2284 [Copenhagen: European Environment Agency (EEA)].

Fujiwara, M., Zoltan, N. K., Chew, J. W., and Braatz, R. D. (2005). First principles and direct design approaches for the control of pharmaceutical crystallization. *J. Process Control* 15, 493–504. doi: 10.1016/j.jprocont.2004.08.003

Hafner, S. D., Howard, C., Muck, R. E., Roberta, B. F., Montes, F., Green, G. G., et al. (2013). Emission of volatile organic compounds from silage: compounds, sources, implications. *Atmospheric Environ.* 77, 827–839. doi: 10.1016/j.atmosenv.2013.04.076

Haykin, S. O. (2008). *Neural Networks and Learning Machines: A Comprehensive Foundation*, 3rd Edn. Mississauga, ON: Pearson International.

Holm-Nielsen, J. B., and Ehimen, E. A. (2014). "4-biorefinery plant design, engineering and process optimization," in *Advances in Biorefineries: Biomass and Waste Supply Chain Exploitation*, ed. K. Waldron, (Sawston: Woodhead Publ), 89–111. doi: 10.1533/9780857097385.1.89

IEAGHG, (2019). *CCS in Climate Change Scenarios*. Cheltenham: IEA Greenhouse Gas R&D Programme.

International Energy Agency [IEA], (2018). *World Energy Outlook*. Paris: IEA.

IPCC, (2014). *Fifth Assessment Report: "Mitigation of Climate Change"*. Cambridge: Intergovernmental Panel on Climate Change.

Jia, Z., and Julian, D. J. (2014). *Synchronization of Signals for Multiple Data Sinks. United States Patent 9877130*

Kulp, K., and Ponte, J. G. Jr. (eds) (2000). *Handbook of Cereal Science and Technology*, 2nd Edt. Edn. Boca Raton, FL: CRC Press.

Langkvist, M., Karlsson, L., and Loutfi, A. (2014). A review of unsupervised feature learning and deep learning for time-series Modeling. *Pattern Recognit. Lett.* 42, 11–24. doi: 10.1016/j.patrec.2014.01.008

Lou, H. L. (1995). Implementing the viterbi algorithm. *IEEE Signal Process.* 12, 42–52. doi: 10.1109/79.410439

Markiewicz, M. T. (2006). "Mathematical modeling of the heavy gas dispersion," in *Models and Techniques for Health and Environmental Hazard Assessment Part 2: Air Quality Modeling*, ed. M. Borysiewicz, (Otwock-Swierk: Institute of Atomic Energy), 279–302.

Mc Sweeney, C., New, M., and Lizcano, G. (2009). *Climate Change Country Profiles-UK*. Oxford: Oxford University, School of Geography and Environment, Tyndall Centre for Climate Change Research, Report Commissioned by British Council, RMetS and RGS-IBG.

Mendoza, J. M. F., Sharmina, M., Gallego-Schmid, A., Heyes, G., and Azapagic, A. (2017). Integrating backcasting and eco-design for the circular economy: the BECE framework. *J. Indus. Ecol.* 21, 526–544. doi: 10.1111/jiec.12590

Rymarczyk, T., Klosowski, G., and Kozlowski, E. (2018). A non-destructive system based on electrical tomography and machine-learning to analyze moisture of buildings. *Sensors* 18:2285. doi: 10.3390/s18072285

Smith, R. (2005). *Chemical Process: Design and Integration*. Hoboken, NJ: John Wiley & Sons Ltd.

Snyder, D., Garcia-Romero, D., and Povey, D. (2015). "Time delay deep neural network-based universal background models for speaker recognition," in *IEEE Transactions, IEEE Workshop on Automatic Speech Recognition and Understanding (ASRU)* (New York, NY: IEEE).

Staffell, I., Scamman, D., Velazquez-Abad, A., Balcombe, P., Dodds, P. E., Ekins, P., et al. (2019). The role of hydrogen and fuel cells in the global energy system. *Energy Environ. Sci.* 12, 463–491.

Sun, Q., Choi, W.-J., Jeffrey, M. G., and Tehrani, A. M. (2015). *MIMO System and Method, US-Patent: US8989294 B2 (March 2015)*. San Diego, CA: Qualcomm Inc.

Tisserant, A., Pauliuk, S., Merciai, S., Schmidt, J., Fry, J., Wood, R., et al. (2017). Solid waste and the circular economy: a global analysis of waste treatment and waste footprints. *J. Indus. Ecol.* 21, 628–640. doi: 10.1111/jiec.12562

Tuzun, U. (2017). "Quality monitoring and control in breakfast cereal processes using neural network convolution of dynamic process data," in *International Conference on Processing, Handling and Characterization of Particulate Materials (PARMAT 2017)*, Barcelona, 2476.

Tuzun, U. (2018). "Quality monitoring and control of air-borne particulates and VOCs emissions using neural network convolution of dynamic process data," in *Proceedings of the 6th International Conference on Green Process Engineering, 3-6 June 2018*, Toulouse, 76.

Tuzun, U. (2020a). Introduction to systems engineering and sustainability part i: student-centred learning for chemical and biological engineers. *Educ. Chem. Eng.* 31, 85–93. doi: 10.1016/j.ece.2020.04.004

Tuzun, U. (2020b). Introduction to systems engineering and sustainability part ii: interactive teaching of sustainability modeling by systems integration design for chemical and biological engineers. *Educ. Chem. Eng.* 31, 94–104. doi: 10.1016/j.ece.2020.04.005

Wenda-Piesik, A., Piesik, Ligor, T., and Buszewski, B. (2010). VOCs from cereal plants infested with crown rot: their identity and their capacity for inducing production of VOCs in uninfested plants, PEST. *Int. J. Pest Manage.* 56, 377–383. doi: 10.1080/09670874.2010.505668

Wu, Y. (2006). "A trellis connectivity analysis of random linear network coding with buffering," in *Proceedings of the 2006 IEEE International Symposium on Information Theory*, Seattle, WA, 768–772.

Yue, Q., Xu, X., Hillier, K., Cheng, K., and Pan, G. (2017). Mitigating greenhouse gas emissions in agriculture: from farm production to food consumption. *J. Clean. Product.* 149, 1011–1019. doi: 10.1016/j.jclepro.2017.02.172

Zare, V., and Mahmoudi, S. M. S. (2015). A thermodynamic comparison between organic rankine and kalina cycles for waste heat recovery from the gas turbine modular helium reactor. *Energy* 79, 398–406. doi: 10.1016/j.energy.2014.11.026

Zhang, H., Zao, H., Li, Z., and Hu, E. (2019). Optimization potentials for the waste heat recovery of a gas-steam combined cycle power plant based on absorption heat pump. *J. Therm. Sci.* 28, 283–293. doi: 10.1007/s11630-018-1055-7

Conflict of Interest: The author declares that the research was conducted in the absence of any commercial or financial relationships that could be construed as a potential conflict of interest.

frontiers in Energy Research

ORIGINAL RESEARCH
published: 07 August 2020
doi: 10.3389/fenrg.2020.00135

To the Calculation of the Average Value of the Volume Fraction of the Key Bulk Component at the Intermediate Stage of Mixing With an Inclined Bump

Anna Kapranova, Ivan Verloka, Daria Bahaeva, Mikhail Tarshis and Sergey Cherpitsky*

Department of Theoretical Mechanics and Resistance of Materials, Faculty of Mechanical Engineering, Yaroslavl State Technical University, Yaroslavl, Russia

OPEN ACCESS

Edited by:
Theodoros Damartzis, École Polytechnique Fédérale de Lausanne, Switzerland

Reviewed by:
Vadim Mizonov, Ivanovo State Power University, Russia
Henryk Otwinowski, Czestochowa University of Technology, Poland

***Correspondence:**
Anna Kapranova
kapranova_anna@mail.ru

Specialty section:
This article was submitted to Process and Energy Systems Engineering, a section of the journal Frontiers in Energy Research

Received: *01 February 2020*
Accepted: *02 June 2020*
Published: *07 August 2020*

Citation:
Kapranova A, Verloka I, Bahaeva D, Tarshis M and Cherpitsky S (2020) To the Calculation of the Average Value of the Volume Fraction of the Key Bulk Component at the Intermediate Stage of Mixing With an Inclined Bump. Front. Energy Res. 8:135. doi: 10.3389/fenrg.2020.00135

The aim of this work is to develop a stochastic method for calculating the average value of the volume fraction of a key bulk component at an intermediate stage of mixing with an inclined bump based on the energy method. The specified characteristic is used to assess the quality of the granular mixture when choosing a criterion in the form of a heterogeneity coefficient of the product obtained at the corresponding stage of operation of the gravitational apparatus. This equipment is designed to produce a mixture of solid dispersed components in a ratio of 1/10 or more. At the same time, at each stage of mixing, two types of mixing devices (brush elements and inclined bump surfaces) work. A distinctive feature of the application of the energy method is to obtain an analytical relationship for the desired characteristics of the process of mixing bulk materials, taking into account their physical and mechanical properties and a set of structural and operational parameters of the apparatus. The calculation of the increment angles of reflection of rarefied flows of bulk components after interaction with the bump surface is proposed. The differential distribution functions of the number of particles of these components over the states of macrosystems are taken into account. The basis is the results of stochastic modeling of mixing of flowing media with brushes. The effectiveness of the intermediate stage of mixing with the bump using the coefficient of heterogeneity of the granular mixture is analyzed. The influence of the most significant design parameters of the gravitational apparatus and its operating modes on the quality of the intermediate mixture in comparison with the results for the initial and final steps is investigated. It has been established that this class of parameters includes the angular velocity of rotation of the drum, the angle of inclination of the bump to the horizontal, the pitch of screw winding, and a comprehensive indicator of the deformation of the brush elements. For example, an increase in the last complex indicator by 0.05 units leads

to a decrease in the inhomogeneity coefficient by (0.15–0.80%) in the studied range of the angular velocity of rotation of the drums. In addition, the consequence of this is a decrease of 0.5 s^{-1} for the value of the angular velocity of the mixing drum, which corresponds to the minimum value for the specified quality criterion of the mixture. The latter fact allows under the selected conditions ensuring a reduction in energy costs for the expended power drives of the mixing drums. The results of the work, confirmed by experimental studies, predict rational ranges of change of significant process parameters using the criteria for the best mixing of components proposed by the authors earlier.

Keywords: stochastic modeling, mixing, parameter, brushes, bump, increment angles

INTRODUCTION

The urgency of the problem of mixing loose components is explained by the diversity of the purpose of the mixtures obtained for the needs of various industries and the agroindustrial complex. At the same time, the tasks of obtaining homogeneous composites, whose properties are imposed by strict regulated consumer requirements in the field of thermal and nuclear energy, are of particular relevance. In addition, the heterogeneity of the mixture of solid dispersed media, intended further for the production of rubber products, glass, porcelain, asphalt concrete, and so on, significantly reduces the quality of the finished product and affects the overall production indicators of energy and resource efficiency. Factors such as humidity and especially pronounced adhesive properties of the components being mixed make it difficult to solve this problem and lead to additional costs in processing these materials. The development of methods for mixing bulk components in a regulatory ratio of 1:10 or more, in particular, actively used in glass and foundry, requires the designers of the appropriate equipment to perform a system–structural analysis of this process.

The basis of this analysis is a theoretical prediction of the efficiency of the mixing process at each stage. The gravitational method for obtaining a free-flowing mixture with the specified ratio of components in the finished product proposed in Zaitzev et al. (2016) implies the presence of three mixing stages on trays with two steps in each. In this case, the first step involves the use of additional mixing elements in the form of brushes, and the second, fender surfaces.

The aim of the work is to develop a method for calculating the average value for the volume fraction of the key bulk component at the intermediate stage of gravity mixing using an inclined bump stop surface. This characteristic of the mixing process is necessary in assessing the quality of the mixture with a regulatory ratio of 1:10 components, as an indicator of the effectiveness of the intermediate stage of the process under study. The proposed expression for the desired characteristic of the key component was obtained on the basis of the stochastic approach (Klimontovich, 2014; Kapranova et al., 2016), taking into account the results of modeling the formation of rarefied streams of solid dispersed materials. The stochastic modeling of the studied process of mixing bulk solids in rarefied flows is based on the energy method (Klimontovich, 2014), tested by the authors when describing the kinetics of a non-equilibrium energetically open macrosystem (Kapranova et al., 2016). This method allows one to build the distribution of particle density of each mixed component according to the characteristic parameter of the studied technological operation. In this case, the particle sizes, the densities of their substances, and dissipative effects when interacting with the mixing elements of the apparatus, its design parameters, and the regulatory parameters of the finished mixture are taken into account. Various variations of stochastic modeling methods are known (Johnson et al., 1962; Kendall and Stuart, 1967; Mizonov et al., 2016; Rosato et al., 2016; Zhuang et al., 2016; Alsayyad et al., 2018), in particular, cell-based (Mizonov et al., 2016) in the framework of the theory of the AA Markov process, time series (Johnson et al., 1962; Kendall and Stuart, 1967), cybernetic, and so on. In contrast to them, the method proposed for use (Klimontovich, 2014) allows one to obtain an analytical representation of the result, which is essential when constructing an engineering methodology for calculating the designed mixer of bulk materials.

At the same time, at the first step for the stage of intermediate mixing, it is supposed to use brush elements on a rotating drum (Kapranova et al., 2015, 2016; Kapranova and Verloka, 2018a). At the second step, a fencing surface is used (Kapranova and Verloka, 2016, 2017; Kapranova et al., 2018a; Verloka et al., 2018) for impact interaction with rarefied flows of mixed materials formed after scattering by brushes. The indicated expression uses the function for the volume fraction of the key component, depending on the reflection angles of each of the two bulk materials from the baffle surface (Verloka et al., 2018). In addition, the latter function takes into account the previously proposed method for calculating volume fractions (Kapranova and Verloka, 2018b; Kapranova et al., 2018b; Kapranova A. B. et al., 2020) for mixed portions of components that correspond to the intermediate stage of this process (Kapranova et al., 2019a). Note that a convenient criterion for assessing the quality of a mixture in this case is its heterogeneity coefficient, which is determined by the traditional one and is estimated on the basis of the proposed models of the authors (Kapranova and Verloka, 2018b; Kapranova et al., 2018b; Kapranova A. B. et al., 2020) at various stages of mixing: the first (Verloka et al., 2018), intermediate (Kapranova and Verloka, 2017; Kapranova et al., 2019a), and final (Kapranova et al., 2019b).

THEORY

Description of the Gravitational Principle of Mixing Bulk Components by Additional Mixing Elements

Let the gravitational apparatus require a loose mixture of two components ($i = 1,2$) with the ratio of their volumes $\Omega_{1,n_\vartheta}/\Omega_{2,n_\vartheta} = \alpha_{1,n_\vartheta}/\alpha_{2,n_\vartheta}$, where $\Omega_{i\tau}$ and $\alpha_{i\tau}$ are, respectively, the volume and volume fraction of component i at stage τ for $\tau = \overline{1,n_\vartheta}$. Moreover, the notation for the subscript i is as follows: "**1**" is the transporting component; "**2**" is the key, then let the condition $\alpha_{1,n_\vartheta} \ll \alpha_{2,n_\vartheta}$ be fulfilled. The gravitational principle of mixing bulk components is implemented using a set of inclined trays located at an angle μ_ϑ when it is counted from the vertical wall of the apparatus body to the bottom surface of the tray. The alternate location of the trays on opposite sides of the vertical walls of the apparatus at different levels provides a transition from one mixing stage to another. A feature of the proposed method of mixing in a gravitational apparatus is the use at the intermediate stage (**Figures 1A–C**) of auxiliary mixing elements, which allow us to divide the process of intermediate mixing of bulk components into two steps. Schematic diagrams of these steps are shown in **Figure 1A**. The first step of mixing at its intermediate stage involves spreading from tray 5 layers of granular materials with the help of brush elements 8 ($j = \overline{1,n_b}$), mounted on the cylindrical drum 7 along counter-propagating helical lines of constant pitch $k = 1,2$ (**Figures 1B,C**). The second step is the impact interaction with the inclined baffle surface 9 formed in the first step of the torches of bulk components. Note that further modeling takes into account the discharge of loose components $i = 1,2$ from each of the deformed brush elements 8 ($j = \overline{1,n_b}$), fixed on the cylindrical surface of drum 7 along oncoming helical lines $k = 1,2$.

It is assumed that at the intermediate stage ϑ for $\tau = 1,\ldots,\vartheta-1,\vartheta,\vartheta+1,\ldots,n_\vartheta$ for gravitational mixing (**Figure 1A**), two streams 2 and 4 are fed vertically to the inclined tray into the gap between drum 7 with brush element 8 and the specified tray 5. One stream 2 is a loose mixture obtained in the previous stage at $\tau = \vartheta - 1$ for the gravitational mixing process and has a preliminary composition with two components ($i = 1,2$) in the ratio of their volumes $\Omega_{1,\vartheta-1}/\Omega_{2,\vartheta-1} = \alpha_{1,\vartheta-1}/\alpha_{2,\vartheta-1}$. Another stream 4 is supplied to the indicated inclined tray 5 and consists of only one (key) component $i = 2$. The volume of this stream 4 is equal to the difference in volumes $\Omega_{2,\vartheta} - \Omega_{2,\vartheta-1}$ and corresponds to the increment of the fraction of this component $\Delta\alpha_{2,\vartheta} = \alpha_{2,\vartheta} - \alpha_{2,\vartheta-1}$ at the stage ϑ. To calculate the value of $\Delta\alpha_{2,\vartheta}$, we use the recurrence relation proposed by the authors of Kapranova and Verloka (2016) and tested in Kapranova and Verloka (2018b), Kapranova et al. (2018b), and Kapranova A. B. et al. (2020). In this calculation, the principle of mixing equal volumes at stage ϑ is taken into account when $\Omega_{1,\vartheta-1} + \Omega_{2,\vartheta-1} = \Omega_{2,\vartheta}$. Let a particle of granular material i have a spherical shape, diameter $D_{Si} = n_{di}^{-1}\sum_{g=1}^{n_{di}} d_{ig}$ averaged over fractions, and substance density ρ_{Si}. Here it is indicated that $d_{ig} = \left(d_{ig,\max} + d_{ig,\min}\right)/2$ is the average particle diameter of the fraction фракции $= \overline{1,n_{di}}$; n_{di} is the number of fractions for the material component i; $d_{ig,\max}$ and $d_{ig,\min}$ are the maximum and minimum values of the particle diameters in each selected fraction g.

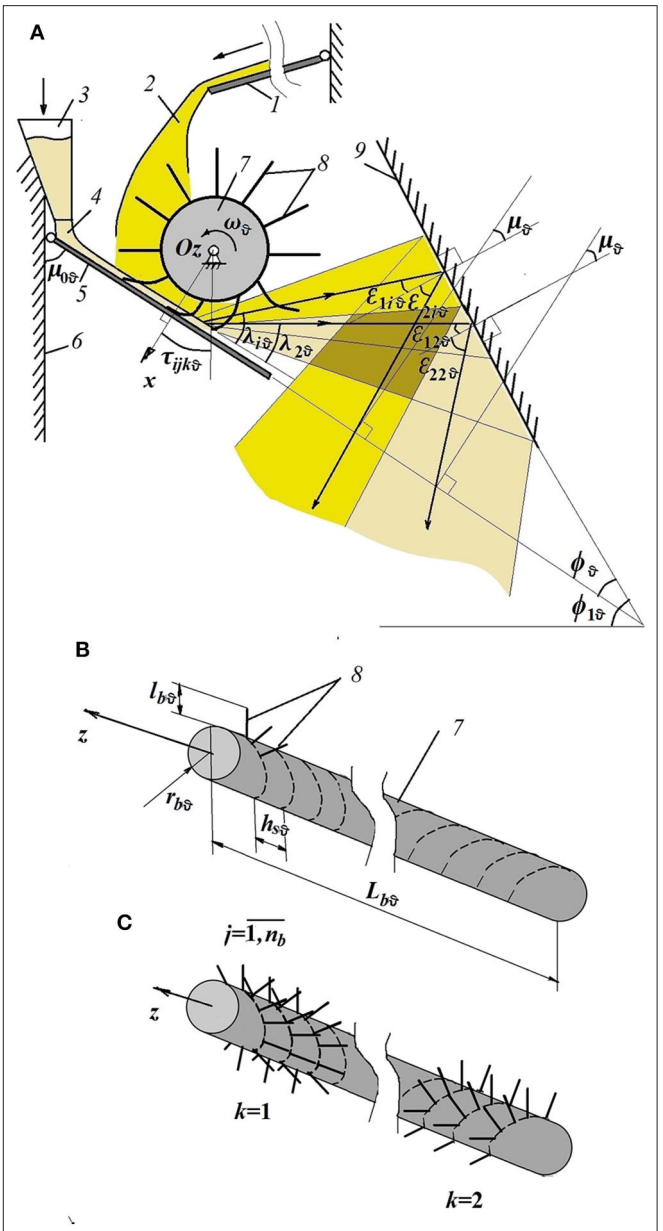

FIGURE 1 | Conditional schemes: **(A)** for the intermediate stage of mixing ($\tau = \vartheta$) of bulk components ($i = 1,2$) in the gravitational apparatus when their flows interact with the brush elements $j = \overline{1,n_b}$ (step 1) and the bump surface (step 2): 1—inclined tray; 2—the flow of the granular mixture after the stage $\tau = \vartheta - 1$ with the preliminary composition of two components ($i = 1,2$) in the ratio of their volumes $\Omega_{1,\vartheta-1}/\Omega_{2,\vartheta-1} = \alpha_{1,\vartheta-1}/\alpha_{2,\vartheta-1}$; 3—hopper dispenser; 4—the flow of the key loose component ($i = 2$) with the volume ($\Omega_{2,\vartheta} - \Omega_{2,\vartheta-1}$) corresponding to the increment of the fraction of this component $\Delta\alpha_{2,\vartheta} = \alpha_{2,\vartheta} - \alpha_{2,\vartheta-1}$; 5—inclined tray; 6—wall of the housing; 7—drum; 8—brush elements; 9—bump surface; **(B)** for drum 7; **(C)** for drum 7 and brush elements 8. The copyright holder of the patents referenced here is Yaroslavl State Technical University, Yaroslavl, Russia.

The Main Features of Modeling the Process of Formation of Rarefied Flows of Loose Components by Brush Elements

Initially, we consider the process of formation of rarefied flows of bulk components ($i = 1,2$, **Figure 1A**) after their discharge by deformed brush elements 8 ($j = \overline{1,n_b}$), mounted on rotating drum 7 along oncoming helical lines $k = 1,2$ (**Figure 1C**). The application of the stochastic approach in the framework of the energy method (Klimontovich, 2014) to simulate a random process of mixing granular media at the indicated first step (Kapranova and Verloka, 2018a; Kapranova A. B. et al., 2020) involves considering the motion of a spherical particle of material i in a phase volume with the element $d\Phi_{ijk\vartheta} = dv_{xijk\vartheta}\, dv_{yijk\vartheta}$ at the intermediate stage ϑ.

Here, the Hamilton parameters are chosen as phase variables as the components of the velocity ($v_{xijk\vartheta}$, $v_{yijk\vartheta}$) for the center of mass of the indicated particle in the Cartesian coordinate plane Oxy perpendicular to the axis of rotation of the drum Oz (**Figures 1A–C**).

Then, the transition to polar coordinates ($r_{ijk\vartheta}$, $\theta_{ijk\vartheta}$) when the angular coordinate θ_{ij} is counted from the abscissa axis Ox leads to the next change in the representation phase volume element $d\Phi_{ijk\vartheta} = -\omega_\vartheta{}^2 r_{ijk\vartheta}\, dr_{ijk\vartheta}\, d\theta_{ijk\vartheta}$. The specified axis Ox is perpendicular to the surface of tray 5, along which the layers of granular components slide into the gap between tray 5 and drum 7 with brush elements 8.

It is believed that particle collisions after interacting with brush elements 8 of counter-helical lines $k = 1,2$ are significant and can be considered as large-scale fluctuations in the state of the particle macrosystem of each bulk component $i = 1,2$. This fact suggests that the indicated macrosystem i has an influx of energy from the outside, that is, energetically open (Kapranova and Verloka, 2018a). The states of such systems are described according to approach (Klimontovich, 2014) using the Fokker–Planck-type kinetic equation with a random Langevin source when choosing the ordering criterion for these states in the form of the Lyapunov S-theorem of the function (Klimontovich, 2014). Using the energy representation of the kinetic equation of the Fokker–Planck type with respect to the distribution function for the states of the macrosystem of particles ($i = 1,2$), we restrict ourselves to the stationary solution of this equation obtained at the time of stochasticization of the macrosystem i similarly (Kapranova and Verloka, 2018a; Verloka et al., 2018).

In the case of the energy openness of this macrosystem i, the general form of the obtained stationary solution can be represented depending on the energy of a single particle $E_{ijk\vartheta}$. In this case, two types of energy parameters are introduced with the introduction of two types of energy parameters: $E_{0ijk\vartheta}$ and $E_{fijk\vartheta}$ are, respectively, the energy of the macrosystem at the indicated time and the loss of this energy due to interparticle collisions, as large-scale fluctuations states. Then we have

$$h_{ijk\vartheta} = A_{ijk\vartheta} \exp\left[\frac{-E_{ijk\vartheta}}{E_{0ijk\vartheta}} + E^2_{fijk\vartheta}/(2E_{ijk\vartheta})^2\right]. \quad (1)$$

Note that in Kapranova and Verloka (2018a), based on Klimontovich (2014), an analysis was made of possible stationary solutions of the Fokker–Planck-type kinetic equation in the energy representation from the standpoint of dividing the parameters of the random process of mixing bulk components into optimizing and control ones. In expression (1), the constant $A_{ijk\vartheta}$, taking into account the form Φ_{ijk}, is determined by the normalization equation of the form

$$\int_{\Phi_{ijk\vartheta}} h_{ijk\vartheta}\, d\Phi_{ijk\vartheta} = 1. \quad (2)$$

The dependence of the energy $E_{ijk\vartheta}(r_{ijk\vartheta}, \theta_{ijk\vartheta})$ for the motion of a spherical particle of material **i** in the phase volume with the element $d\Phi_{ijk\vartheta}$ is constructed by analogy with Kapranova and Verloka (2018a) in the form

$$E_{ijk\vartheta}\left(r_{ijk\vartheta}, \theta_{ijk\vartheta}\right) = \mu_{1\vartheta}\theta^2_{ijk\vartheta} + \mu_{2ijk\vartheta}(\theta_{ijk\vartheta}) r^2_{ijk\vartheta}. \quad (3)$$

Here, the values of the coefficient $\mu_{1\vartheta}$ and the functions $\mu_{2ijk\vartheta}(\theta_{ijk\vartheta})$ are determined by the physicomechanical properties of the mixed components and brush elements, as well as by the set of design and operating parameters of the gravity mixer, the choice of which is described in Kapranova A. B. et al. (2020).

The main structural parameters include the following (**Figures 1A,B**): $r_{b\vartheta}$ and $L_{b\vartheta}$ are radius and length of the drum; $l_{b\vartheta}$ and $h_{s\vartheta}$ are the length of the brush elements and the pitch of their screw winding; the following parameters are included in the operating parameters: ω_ϑ is angular velocity of rotation of the drum; $h_{0\vartheta}$ is the height of the gap between tray 5 and the surface of drum 7. Expression (3) takes into account the nature of free motion for particles of material i, provided that they have random angular momenta at the moment of elastic interaction with the brush element j for screw winding k at the intermediate mixing stage ϑ. Then, according to (1), an analytical expression can be obtained for the differential distribution function $h_{ijk\vartheta}(\tau_{ijk\vartheta})$ for the number of particles of material i over the spread angle $\tau_{ijk\vartheta}$ by the brush element j for screw winding k in accordance with the definition:

$$h_{ijk\vartheta}\left(\tau_{ijk\vartheta}\right) \equiv N^{-1}_{ijk\vartheta}\, dN_{ijk\vartheta}/d\tau_{ijk\vartheta}. \quad (4)$$

In this case, the search for the explicit form of the energy parameters $E_{0ijk\vartheta}$ and $E_{fijk\vartheta}$ for the random process of mixing bulk components is determined by solving the system of equations. This system includes equations: energy balance (Kapranova et al., 2015, 2018a; Kapranova and Verloka, 2018a) and conservation of flows (Kapranova and Verloka, 2018a), taking into account large-scale fluctuations of states of macrosystem i, when the collisions of particles of various materials are most significant after scattering with a brush element j corresponding to the opposite screw windings at $k = 1$ and $k = 2$.

It follows from expressions (1) to (4) that the general form of the desired function $h_{ijk\vartheta}\left(\tau_{ijk\vartheta}\right)$ for the formation of sparse

flows of loose components ($i = 1,2$) after they are dumped by deformed brush elements ($j = \overline{1,n_b}$) fixed on rotating drums along oncoming helical lines $k = 1,2$ can be represented in the form:

$$h_{ijk\vartheta}\left(\tau_{ijk\vartheta}\right) = b_{0ijk\vartheta}\left(\mathrm{erf}\left\{b_{1ijk\vartheta}\left[1+b_{2ijk\vartheta}\left(\tau_{ijk\vartheta}-\varphi_{ijk\vartheta}\right)^2\right]\right\}\right) - \mathrm{erf}\left(\left(b_{1ijk\vartheta}\right)\right) \times \exp\left[b_{3ijk\vartheta}\left(\tau_{ijk\vartheta}-\varphi_{ijk\vartheta}\right)^2\right]. \quad (5)$$

The coefficients $b_{lijk\vartheta}$, $l = 0,1,2,3$ from expression (5) depend on the design and operating parameters of the gravity mixer, as well as the physicomechanical characteristics of the mixed materials and brush elements; $\varphi_{ijk\vartheta}$ is the characteristic angle determined by the bending geometry of the deformed brushes.

The Main Features of Modeling the Mixing of Granular Materials After Impact Interaction With an Inclined Bump Surface

At the second step of the intermediate stage ϑ for mixing granular materials (Kapranova and Verloka, 2016, 2018b), it is proposed to use bump surface 9 (**Figures 1A–C**) installed so that the formed rarefied flows of bulk components ($i = 1,2$) after discharge by deformed brush elements 8 ($j = \overline{1,n_b}$) from oncoming helical lines $k = 1,2$ of the rotating drum 7 experienced impact interaction with bump surface 9. After this impact interaction, new rarefied flows of granular components are formed having corresponding reflection angles $\gamma_{ijk\vartheta}$, which are measured from the normal to bump surface 9. These new rarefied flows have intersection areas in which additional mixing of loose components takes place. The bulk mixture obtained at the intermediate stage falls onto the lower inclined tray located on the opposite side of the body of the gravitational apparatus and slides along it, proceeding to the next mixing stage $\tau = \vartheta+1$. The general form of the differential distribution function $H_{ijk\vartheta}(\gamma_{ijk\vartheta})$ for the number of particles of material i according to the angle of reflection $\gamma_{ijk\vartheta}$ from the chipper according to the results of Kapranova and Verloka (2016, 2018b) depends on the representation (5) for the function $h_{ijk\vartheta}(\tau_{ijk\vartheta})$

$$H_{ijk\vartheta}(\gamma_{ijk\vartheta}) = B_{0ijk\vartheta}\left(\mathrm{erf}\left\{B_{1ijk\vartheta}\left[1 + B_{2ijk\vartheta}B_{4ijk\vartheta}\left(\gamma_{ijk\vartheta}\right)\right]\right\}\right) - \mathrm{erf}\left(\left(B_{1ijk\vartheta}\right)\right) \times \exp\left[B_{3ijk\vartheta}B_{4ijk\vartheta}\left(\gamma_{ijk\vartheta}\right)\right]. \quad (6)$$

The coefficients $B_{lijk\vartheta}$, $l = 0,1,2,3$ from expression (6) are also determined by the designing and operating parameters of the studied process and physicomechanical properties for the mixed components and brush elements. The functional dependence $B_{4ijk\vartheta}\left(\gamma_{ijk\vartheta}\right)$ is defined by the geometric relation from Kapranova and Verloka (2018b) between the characteristic angles $\tau_{ijk\vartheta}$ and $\gamma_{ijk\vartheta}$.

Having made the transition to the averaged values for the angles of incidence $\varepsilon_{1ik\vartheta}$ on the bump suface 9 of rarefied flows, which are described using the function $h_{ijk\vartheta}\left(\tau_{ijk\vartheta}\right)$, and the reflection angles $\varepsilon_{2ik\vartheta} = n_b^{-1}\sum_{j=1}^{n_b}\gamma_{ijk\vartheta}$ from this bump element 9 in terms of the number of deformed brush elements j for each component i mixed, we obtain from (6) the following representation for the desired function $W_{ijk\vartheta}(\varepsilon_{2ik\vartheta})$.

We pass to the averaged values for the angles of incidence $\varepsilon_{1ik\vartheta}$ on the bump suface 9 of rarefied flows, which are described using the function $h_{ijk\vartheta}\left(\tau_{ijk\vartheta}\right)$, and the reflection angles $\varepsilon_{2ik\vartheta} = n_b^{-1}\sum_{j=1}^{n_b}\gamma_{ijk\vartheta}$ from this bump element 9 in terms of the number of deformed brush elements j for each component i mixed. We obtain from (6) the following representation for the desired function $W_{ijk\vartheta}(\varepsilon_{2ik\vartheta})$:

$$W_{ijk\vartheta}(\varepsilon_{2ik\vartheta}) = B_{0ijk\vartheta}\left(\mathrm{erf}\left\{B_{1ijk\vartheta}\left[1 + B_{2ijk\vartheta}\beta_{4ijk\vartheta}\left(\varepsilon_{2ik\vartheta}\right)\right]\right\}\right) - \mathrm{erf}\left(\left(B_{1ijk\vartheta}\right)\right) \times \exp\left[B_{3ijk\vartheta}\beta_{4ijk\vartheta}\left(\varepsilon_{2ik\vartheta}\right)\right] \quad (7)$$

where the functional dependence $\beta_{4ijk\vartheta}(\varepsilon_{2ik\vartheta})$, in contrast to $B_{4ijk\vartheta}\left(\gamma_{ijk\vartheta}\right)$ from (6), is also determined by the recovery coefficients for particles of the mixed components i. Additionally, the assumption is made that the values $\varepsilon_{2i1\vartheta} = \varepsilon_{2i2\vartheta} \equiv \varepsilon_{2i\vartheta}$ are equal due to the symmetrical arrangement of the screw windings of the brush elements 8 on the surface of the mixing drum 7 (**Figure 1A**). This assumption allows us to further omit the subscript k in the notation $\varepsilon_{2i\vartheta}$ for the reflection angles of the particles of material i. The preservation of the indicated index k when designating the function $W_{ijk\vartheta}(\varepsilon_{2ik\vartheta}) \equiv W_{ijk\vartheta}(\varepsilon_{2i\vartheta})$ is explained by taking into account when it calculates particle collisions from rarefied flows of mixed components formed when interacting with brush elements from symmetric screw windings.

Therefore, taking into account (7), the complete non-equilibrium distribution functions $R_{ik\vartheta}(\varepsilon_{2i\vartheta})$ for the number of particles of component i, depending on the described reflection angles $\varepsilon_{2i\vartheta}$, take the form

$$R_{ik\vartheta}\left(\varepsilon_{2i\vartheta}\right) = \prod_{j=1}^{n_b} W_{ijk\vartheta}\left(\varepsilon_{2i\vartheta}\right). \quad (8)$$

Using expression (8), the function $\Psi_\vartheta(\varepsilon_{21\vartheta},\varepsilon_{22\vartheta})$ is determined for the volume fraction of the key component ($i = 2$) obtained at the intermediate stage ($\tau = \vartheta$) for the process of mixing bulk materials after averaging over the number of symmetrical screw windings k for brush elements

$$\Psi_\vartheta\left(\varepsilon_{21\vartheta},\varepsilon_{22\vartheta}\right) = \frac{1}{2}\sum_{k=1}^{2}\frac{\rho_{S1}R_{1k\vartheta}\left(\varepsilon_{21\vartheta}\right) + \rho_{S2}\sum_{\tau=1}^{\vartheta-1}\alpha_{2,\tau}R_{2k\vartheta}\left(\varepsilon_{22\vartheta}\right)}{\rho_{S1}R_{1k\vartheta}\left(\varepsilon_{21\vartheta}\right) + \rho_{S2}\sum_{\tau=1}^{\vartheta}\alpha_{2,\tau}R_{2k\vartheta}\left(\varepsilon_{22\vartheta}\right)}. \quad (9)$$

Here, according to the recurrence relation proposed by the authors of Kapranova and Verloka (2016), the value of the volume fraction of the key component $\alpha_{2,\tau}$ at an arbitrary mixing stage τ depends on the ratio of the volume fractions of bulk components at the final stage $\alpha_{1,n_\vartheta}/\alpha_{2,n_\vartheta}$

$$\alpha_{2,\tau} = \alpha_{1,1}\{(\tau - 1)[\left(\alpha_{2,n_\vartheta}-1\right)/2+1]-1\}. \quad (10)$$

Note that in formula (10) it is assumed that the volume fractions of the transporting component ($i = 1$) are equal at the initial

($\tau = 1$) and final ($\tau = \mathbf{n}_\vartheta$) mixing stages $\alpha_{1,1} = \alpha_{1,n_\vartheta}$. In addition, expression (9) contains values for the densities of substances ρ_{Si} corresponding to each component i.

Assessment of the Quality of a Mixture of Bulk Components After an Intermediate Stage of Their Gravitational Mixing

It is proposed to evaluate the quality of the bulk mixture obtained at the intermediate stage ($\tau = \vartheta$) using the criterion in the form of the inhomogeneity coefficient $K_{C\vartheta}$, %, which is calculated using expression (9) for the function $\Psi_\vartheta\,(\varepsilon_{21\vartheta}, \varepsilon_{22\vartheta})$, according to the following formula:

$$K_{C\vartheta} = 100\left(\frac{\langle \Psi_\vartheta{}^2\rangle}{\langle \Psi_\vartheta\rangle^2} - 1\right)^{1/2} \tag{11}$$

where $\langle \Psi_\vartheta\rangle$ and $\langle \Psi_\vartheta{}^2\rangle$ are the values, respectively, for the average of the fraction of the key component ($i = 2$) and the average of the square of the specified fraction from (9)

$$\langle \Psi_\vartheta\rangle = \prod_{i=1}^{2}(2\varepsilon_{2i\vartheta} + \Delta\varepsilon_{2i\vartheta}/2)^{-1}\int_{\varepsilon_{22\vartheta}}^{\varepsilon_{22\vartheta}+\Delta\varepsilon_{22\vartheta}/2} d\varepsilon_{22\vartheta}\int_{\varepsilon_{21\vartheta}}^{\Delta\varepsilon_{21\vartheta}+\Delta\varepsilon_{21\vartheta}/2}\Psi_\vartheta\,(\varepsilon_{21\vartheta}, \varepsilon_{22\vartheta})d\varepsilon_{21\vartheta}, \tag{12}$$

$$\langle \Psi_\vartheta{}^2\rangle = \prod_{i=1}^{2}(2\varepsilon_{2i\vartheta} + \Delta\varepsilon_{2i\vartheta}/2)^{-1}\times\int_{\varepsilon_{22\vartheta}}^{\varepsilon_{22\vartheta}+\Delta\varepsilon_{22\vartheta}/2} d\varepsilon_{22\vartheta}\int_{\varepsilon_{21\vartheta}}^{\Delta\varepsilon_{21\vartheta}+\Delta\varepsilon_{21\vartheta}/2}[\Psi_\vartheta\,(\varepsilon_{21\vartheta}, \varepsilon_{22\vartheta})]^2 d\varepsilon_{21\vartheta}. \tag{13}$$

In expressions (12) and (13), the calculation of the maximum values for the reflection angles $\varepsilon_{2i\vartheta}$ of each of the bulk components ($i = 1, 2$) from bump surface 9 (**Figure 1A**) at the studied intermediate stage ($\tau = \vartheta$) of their mixing is carried out, taking into account their increments $\varepsilon_{2i\vartheta}$. The increment data $\varepsilon_{2i\vartheta}$ is calculated using the geometric relationship for the relationship between the reflection angles $\varepsilon_{2i\vartheta}$, the scattering $\lambda_{i\vartheta}$, and the spread $\tau_{ijk\vartheta}$

$$\Delta\varepsilon_{2i\vartheta} = 2\left\{\left[u_{1\vartheta}\left(\phi_{1\vartheta}\right) - \lambda_{i\vartheta}\right]u_{4i\vartheta}\left(\phi_{1\vartheta}\right)tg\left(\frac{\Delta\lambda_{i\vartheta}}{2}\right)\frac{1 + tg\,(\lambda_{i\vartheta})\,tg\left(\frac{\Delta\lambda_{i\vartheta}}{2}\right)}{1 - tg\,(\lambda_{i\vartheta})\,tg\left(\frac{\Delta\lambda_{i\vartheta}}{2}\right)} - \frac{\Delta\lambda_{i\vartheta}\,u_{4i\vartheta}\,(\phi_{1\vartheta})}{2}\right\} \tag{14}$$

where $u_{1\vartheta}\,(\phi_{1\vartheta}) = \phi - \phi_{1\vartheta} - \mu_0$; $u_{2\vartheta}\left(\phi_{1\vartheta}\right) = u_{1\vartheta}\left(\phi_{1\vartheta}\right) + \phi/2$; $u_{3\vartheta}\left(\phi_{1\vartheta}\right) = \phi_{1\vartheta} + \mu_{0\vartheta}$; $u_{4i\vartheta}\left(\phi_{1\vartheta}\right) = p_{1i\vartheta}\left(\phi_{1\vartheta}\right)u_{2\vartheta}\left(\phi_{1\vartheta}\right)\sin\left(\mu_\vartheta\right)$; $u_{5i\vartheta}\left(\phi_{1\vartheta}\right) = L_i/h_i - ctg[u_{3\vartheta}\left(\phi_{1\vartheta}\right) - \pi/2]$; $p_{1i\vartheta}\left(\phi_{1\vartheta}\right) = \{[1 - u_{2\vartheta}\left(\phi_{1\vartheta}\right)]u_{5\vartheta}\,(\phi_{1\vartheta})\}/\{2u_{5\vartheta}\,(\phi_{1\vartheta})\,[1 - u_{5\vartheta}\left(\phi_{1\vartheta}\right)]\}$; $p_{2i\vartheta}\left(\phi_{1\vartheta}\right) = [u_{5i\vartheta}\left(\phi_{1\vartheta}\right) + u_{2\vartheta}\,(\phi_{1\vartheta})]/\cos(u_{3\vartheta}\left(\phi_{1\vartheta}\right) - \pi/2)$; where $\mu_{0\vartheta}$ is the angle of inclination of tray 5 to the vertical. At the same time, for the intermediate mixing stage ϑ, we used the functional relationship $k_{vi\vartheta} = k_{vi\vartheta}(\phi_{1\vartheta}, \mu_\vartheta, L_{i\vartheta}, h_{i\vartheta})$ between the recovery coefficient $k_{vi\vartheta} \equiv \sin\varepsilon_{2i\vartheta}/\sin\varepsilon_{1i\vartheta}$ and geometric parameters. The following notation is used here for which the following notation is used: $\phi_{1\vartheta}$ is the angle of inclination of bump surface 9 to the horizontal planes; μ_ϑ is the characteristic angle between the perpendiculars to bump surface 9 and tray 5; $L_{i\vartheta}$ is the width of the dispersion of particles of component i along tray 5; $h_{i\vartheta}$ is the height between this tray 5 and bump surface 9 at the point of impact interaction of the averaged flow of component i.

Thus, when describing the relationship between the scattering angle $\tau_{ijk\vartheta}$ from the brushes 8 and the reflection angle $\varepsilon_{2i\vartheta}$ from bump surface 9 (Kapranova and Verloka, 2016; Verloka et al., 2018), the recovery coefficient $k_{vi\vartheta}$ is used, which characterizes the directions of the averaged velocities of rarefied flows of each component ($i = 1, 2$) at impact on bump surface 9 and when they are reflected from it.

In expression (14), the averaged values $\lambda_{i\vartheta} = (2n_b)^{-1}\sum_{k=1}^{2}\sum_{j=1}^{n_b}\lambda_{ijk\vartheta}$ by the number of deformed brush elements j for scattering angles $\lambda_{ijk\vartheta}$ for particles of components ($i = 1, 2$) from the surface of tray 5 under the mixing drum 7 in their rarefied flows (**Figures 1A,C**) formed after scattering by the indicated brush elements 8 ($j = \overline{1, n_b}$) screw winding k. In this case, the following approximation is taken when calculating the increments for the scattering angles $\Delta\lambda_{i\vartheta} = (2n_b)^{-1}\sum_{k=1}^{2}\sum_{j=1}^{n_b}\Delta\tau_{ijk\vartheta}$. Here, the increments of the scattering angles $\tau_{ijk\vartheta}$ are determined from the equations of equality of flows of loose components i with the number of particles N_{ik} at the entrance to the gap between tray 5 and drum 7 for interaction with the brush elements 8 of the screw winding k for $N_i = \sum_{k=1}^{2}N_{ik}$ as follows:

$$\sum_{i=1}^{2}N_{ik} = (2\tau_{ijk\vartheta} + \Delta\tau_{ijk\vartheta}/2)^{-1}\sum_{i=1}^{2}\int_{\tau_{ijk\vartheta}}^{\tau_{ijk\vartheta}+\Delta\tau_{ijk\vartheta}/2}\prod_{j=1}^{n_b}h_{ijk\vartheta}\left(\tau_{ijk\vartheta}\right)d\tau_{ijk\vartheta}, \tag{15}$$

So, both quantities $\langle \Psi_\vartheta\rangle$, $\langle \Psi_\vartheta{}^2\rangle$ from expressions (11–13) are calculated using the differential distribution functions $R_{ik\vartheta}\,(\varepsilon_{2i\vartheta})$ for the number of particles of each component i after interacting with bump surface 9 (Kapranova and Verloka, 2016) by angle of reflection $\varepsilon_{2i\vartheta}$ for the direction of the average particle velocity i. In this case, the results of the stochastic model of the formation of rarefied flows by brush elements (Kapranova and Verloka, 2018a; Verloka et al., 2018) are used for the differential distribution functions $h_{ijk\vartheta}(\tau_{ijk\vartheta})$ for the number of particles of component i after they are scattered by each brush element j over the spread angle $\tau_{ijk\vartheta}$. Note that when calculating the integrals on the right-hand sides of expressions (12), (13), we used the Maclaurin expansion of the following function $f_{i\vartheta}\,(\varepsilon_{2i\vartheta}) = 1/\{\beta_{0i\vartheta} + \beta_{1i\vartheta}\exp[\sum_{j=1}^{n_b}\beta_{2i\vartheta}(\beta_{3i\vartheta} + \beta_{4i\vartheta}\varepsilon_{2i\vartheta})^2]\}$ in their integrands up to terms of order $O(\varepsilon_{2i\vartheta}{}^2)$, where the coefficients $\beta_{ri\vartheta}; r = \overline{1,4}$ depend on the design parameters and the physical mechanical properties of bulk materials.

RESULTS AND DISCUSSION

Thus, we have proposed a method for calculating the dependence Ψ_{ϑ} ($\varepsilon_{21\vartheta}$,$\varepsilon_{22\vartheta}$) for the volume fraction of the key component ($i = 2$) obtained at the intermediate stage ($\tau = \vartheta$) for the process of mixing bulk materials after averaging over the number of symmetrical screw winding k for brush elements 8 (**Figures 1A–C**) according to expression (9). This technique allows us to describe the dependence of the heterogeneity coefficient of the resulting mixture $K_{C\vartheta}$, % at the indicated intermediate stage in various ranges of changes for the main process parameters in accordance with expression (11).

Let us trace this dependence by the example of mixing two loose components (semolina GOST 7022-97 for $i = 1$ and natural sand GOST 8736-93 for $i = 2$) with comparable values of particle diameters averaged over fractions D_{Si} and true densities of the substance ρ_{Si}, a mixture of which imitates toxic compounds used in various chemical industries (D_{S1}=4.0×10^{-4} m; D_{S2}=1.5×10^{-4} m; $\rho_{S1} = 1.44\times10^{3}$ kg/m^3; $\rho_{S1} = 1.525\times10^{3}$ kg/m^3). In an experimental study of the particle size distribution of the mixed components according to the GOST 4403-91 methodology, two sets of sieves with nominal hole sizes were used: (1) 6.7×10^{-4} m; 5.0×10^{-4} m; 3.5×10^{-4} m; 2.5×10^{-4} m; (2) 5.0×10^{-4} m; 3.5×10^{-4} m; 2.5×10^{-4} m; 5.6×10^{-5} m. The percentage of particles was found from the total mass of component i, taking into account the particle size distribution for semolina GOST 7022-97 ($i = 1$): 81.0%—fractions with a diameter $d_{11} = (3.5 - 6.7) \times 10^{-4}$ m; 19.0%—$d_{12} = (2.5 - 3.5)\times10^{-4}$ m; for natural sand GOST 8736-93 ($i = 2$): 0.8%—$d_{21} = (3.5 - 5.0)\times10^{-4}$ m; 8.7%—$d_{22} = (2.5 - 3.5)\times10^{-4}$ m; 87.5%—$d_{23} = (0.56 - 2.5)\times10^{-4}$ m and 3%—for the diameter $d_{24} < 5.6\times10^{-5}$ m. When calculating the average diameter of the bulk component, only fractions whose content in the mixture exceeded 10% were taken into account.

The values of the additional characteristics of the physicomechanical properties of the working materials and brush elements are, respectively, equal to $k_{v1\vartheta} = 0.1587$; $k_{v2\vartheta} = 0.1853$ for the recovery coefficients when the particles hit the bump; $k_u = 5.0\times10^{-4}$ kg × m/rad for the angular stiffness of brushes 8 (**Figures 1A–C**). In this case, the regulatory ratio for the proportions of components i after performing the final mixing stage $\tau = n_{\vartheta}$ should be $\alpha_{1,n_{\vartheta}}/\alpha_{2,n_{\vartheta}} = 1/10$. Note that the above values for the recovery coefficients $k_{v\vartheta}$ upon impact of particles on the bump were determined by the method proposed by the authors (Kapranova et al., 2013). The established functional dependence is applied between the sought coefficient, the average experimental value for the angle of reflection of the particle flux from the bump surface, the given angle of inclination of the bump, and some geometric parameters of the model unit.

Preliminary studies of the authors (Kapranova and Verloka, 2018b; Kapranova A. B. et al., 2020) showed that the following characteristics are of particular interest in choosing the most rational ranges for changing the parameters of the studied process at the intermediate stage ($\tau = \vartheta$): angular velocity of rotation ω_{ϑ} for drum 7; the angle of inclination of bump surface 9 to the horizontal plane $\phi_{1\vartheta}$; the pitch of the screw winding $h_{s\vartheta}$ of the brush elements 8 on the surface of drum 7; and complex indicator $\Delta_{\vartheta} = l_{b\vartheta}/h_{0\vartheta}$. The last parameter Δ_{ϑ} reflects the degree of deformation of the brush elements of length $l_{b\vartheta}$ in the gap height $h_{0\vartheta}$ between drum 7 and tray 5.

In addition, according to Verloka and Kapranova (2018), Kapranova and Verloka (2018b), and Kapranova et al. (2019b), it is sufficient to achieve the specified regulatory ratio 1/10 to perform three stages of mixing (initial τ=1, intermediate $\tau = \vartheta = 2$ and final $\tau = n_{\vartheta} = 3$), because an increase in the number of stages to n_{ϑ}=10 does not lead to a significant difference in the quality indicators of the mixture. Note that the preliminary selection of the variation limits for the described basic parameters from the set $\{\omega_{\vartheta}, \phi_{1\vartheta}, \Delta_{\vartheta}, h_{s\vartheta}\}$ is determined by the analysis of the comparative simulation results of the differential distribution function $h_{ijk\vartheta}(\tau_{ijk\vartheta})$ for the number of particles of material **i** by the spread angle $\tau_{ijk\vartheta}$ by brush element j for screw winding k from the expression (4). In particular, according to (Kapranova and Verloka, 2018a; Kapranova A. B. et al., 2020), the criterion for the best mixing of the components is the condition for the approximation of characteristic angles $\sigma^{ex}_{ik\vartheta}$ for the maxima of the total differential distribution functions $F_{ik\vartheta}(\sigma_{ik\vartheta}) = \prod_{j=1}^{n_b} h_{ijk\vartheta}(\tau_{ijk\vartheta})$ for the number of particles of both components ($i = 1,2$) over the average scattering angle $\sigma ik\vartheta$, as well as the shape of the curves for the indicated functions $F_{ik\vartheta}(\sigma_{ik\vartheta})$. When using this condition in the form $\sigma^{ex}_{1k\vartheta}$=$\sigma^{ex}_{2k\vartheta}$ for the following values of the design parameters for the mixing process under study ($r_{b2} = 3.0\times10^{-2}$ m; $l_{b2} = 4.5\times10^{-2}$ m; $L_{b2} = 1.85\times10^{-1}$ m; μ_{02}=1.3083 rad) and its additional characteristics ($L_{12} = 2.8\times10^{-1}$ m; $L_{22} = 2.4\times10^{-1}$ m; h_{12}=8.0×10^{-2} m; $h_{22} = 6.0\times10^{-2}$ m; $\mu_2 = 0.7071$ rad), the preliminary limits of variation of the main characteristic parameters in experimental studies are chosen as $\omega_{\vartheta} = (44 - 51)$ s^{-1}; $\phi_{1\vartheta}$= (0.87 − 1.04) rad; $\Delta_{\vartheta} = (1.49 - 1.62)$; $h_{s\vartheta} = (1.59 - 1.61)\times10^{-2}$ m, taking into account the deformation of the brush elements ($j = \overline{1,n_b}$) with a total number $n_b = 3$ with rotation of the drum by an angle $\pi/2$ rad. It is indicated here: $r_{b\vartheta}$ and $L_{b\vartheta}$ are radius and length of the drum; $l_{b\vartheta}$ and $h_{s\vartheta}$ are the length of the brush elements and the pitch of their helical winding.

When performing the experimental part of the research (Verloka and Kapranova, 2018), a patented method was used to assess the quality of the granular mixture based on pixel analysis of photographs of experimental samples by calculating the position of the "threshold hue" (Zaisev et al., 2017) based on Petrov et al. (2012) using an open access software product Mixan (2015). In particular, according to Zaisev et al. (2017), the experimental value of the inhomogeneity coefficient for the mixing stage ϑ was calculated using the formula

$$K_{C\vartheta,\,ex} = \left(\frac{100}{C_{\vartheta}}\right)\left((n_{q\vartheta}-1)^{-1}\sum_{q=1}^{n_{q\vartheta}}(C_{2\vartheta q} - C_{\vartheta})^2\right)^{\frac{1}{2}}. \quad (16)$$

Formula (16) contains the notation: C_{ϑ} and $C_{2\vartheta q}$ values, respectively, for the "ideal" fraction of the key component ($i = 2$) in the mixture and the proportion of this component in the

selected sample; $n_{q\vartheta}$ is the number of samples. The $C_{2\vartheta q}$ fraction data are determined by the ratio of the number of pixels of a certain shade of gray for the key component in the sample to the total number of pixels for this material. Values $C_{2\vartheta q}$ are sorted in a histogram on a scale for shades of gray within (0–255) units. Based on the coordinates of the centers of gravity for the areas of the histograms corresponding to the components of the resulting granular mixture, the abscissa of the middle of the segment between the indicated centers is calculated. The coordinate set in this way on the scale of shades of gray corresponds to the "threshold hue" (Zaisev et al., 2017).

Comparison of theoretical and experimental (Verloka and Kapranova, 2018) results at the intermediate stage of mixing ($\tau = \vartheta = 2$) for the dependence of the heterogeneity coefficient $K_{C2}(\omega_2)$, % for mixture of the semolina GOST 7022-97, and natural sand GOST 8736-93 in the ratio of their volume fractions $\alpha_{1,n_\vartheta}/\alpha_{2,n_\vartheta} = 1/10$ are shown, respectively, in **Figures 2A–C** for various values of the complex exponent $\Delta_\vartheta = \Delta_2$ and the following choice of $\phi_{12} = 0.96$ rad; $h_{s2} = 1.6\times10^{-2}$ m.

Moreover, the relative error of the data of theory and experiment (Verloka and Kapranova, 2018) does not exceed (5–7%). We note that the best convergence of the indicated results is noted at $\Delta_2 = 1.5$ (**Figure 2B**, graph 2 and experimental points 2″) under conditions of obtaining the highest quality mixture ($K_{C2} = 9.8$% for theory and $K_{C2,ex} = 10.1$% for experiment) when the angular velocity is reached, a drum with brush elements equal to $\omega_2 = 47$ s^{-1}. Note that the analysis of the dependence $K_{Cn_\vartheta}(\Delta_{n_\vartheta})$, performed in Kapranova et al. (2019b), confirms the obtained result of achieving the highest quality mixture (**Figure 2B**, graph 2 and experimental points 2″) at $\omega_2 = 47$ s^{-1}, if the value $\Delta_2 = \Delta_{n_\vartheta} = (1.49 - 1.52)$. Additionally, **Figure 2D** shows the theoretical results for $K_{C\tau}(\omega_\tau)$, % at all mixing stages ($\tau = 1,2,3$) according to the data for the initial (Kapranova and Verloka, 2018b) and final (Kapranova et al., 2019b) stages of obtaining this mixture with $\Delta_2 = 1.6$.

An increase in Δ_τ for every 0.05 unit leads to a shift of the graph families $K_{C\tau}(\omega_\tau)$ to the left along the abscissa axis (**Figure 2D**, graphs 1–3) with a decrease not only in the minimum values of the inhomogeneity coefficients $K_{C1,\min} > K_{C2,\min} > K_{C3,\min}$ in the range $(5.9 - 12.9)$%, but also in the corresponding values of $\omega_1 < \omega_2 < \omega_3$ within $(45.6 - 45.8)$ s^{-1}. The latter fact makes it possible under these conditions to guarantee a reduction in energy costs for the expended capacities of the mixing drum drives 7 (**Figures 1A–C**).

KEY FINDINGS AND RESULTS

Here are the main conclusions and results of this study

- A generalization of the results of stochastic modeling of the formation of rarefied flows of bulk components in the case of an intermediate stage ($\tau = \vartheta$) of their gravitational mixing in the given ratios of 1/10 or more is carried out, taking into account the method of dosing for the key ($i = 2$) and transporting ($i = 1$) components according to Kapranova and Verloka (2016) [expression (10), section Assessment of the Quality of a Mixture of Bulk Components After an

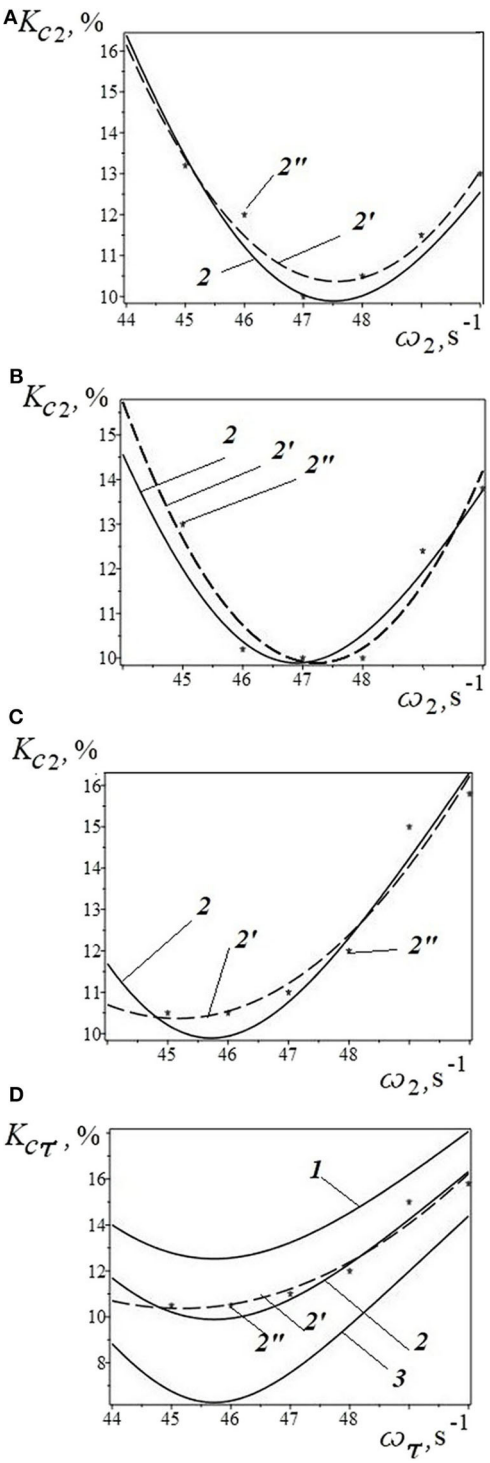

FIGURE 2 | The dependence of the heterogeneity coefficient $K_{C\tau}(\omega_\tau)$ (%) for a mixture of semolina GOST 7022-97 and natural sand GOST 8736-93 in the ratio of their volume fractions $\alpha_{1,n_\vartheta}/\alpha_{2,n_\vartheta} = 1/10$: **(A–C)** $K_{C2}(\omega_2)$ (%) for the intermediate mixing stage ($\tau = \vartheta = 2$); **(D)** for three stages of mixing ($\tau = 1, 2, 3$), **(A)** $\Delta_2 = 1.45$; **(B)** $\Delta_2 = 1.5$; **(C,D)** $\Delta_2 = \Delta_\tau = 1.6$; *1*—$\tau = 1$; *2*—$\tau = 2$; *3*—$\tau = 3$; *2*—theory, *2′*—regression curves **(A)**: $K_{C2}(\omega_2) = 1040 - 43.3\omega_2 + 0.46\omega_2^2$; **(B)**: $K_{C2}(\omega_2) = 1261 - 53\omega_2 + 0.56\omega_2^2$; **(C,D)**: $K_{C2}(\omega_2) = 520 - 22.5\omega_2 + 0.25\omega_2^2$, *2″* are the experimental points for $K_{C2,ex}$ (Verloka and Kapranova, 2018); $\phi_{12} = 0.96$ rad; $h_{s2} = 1.6\times10^{-2}$ m.

Intermediate Stage of Their Gravitational Mixing] for the implementing in two steps:

1) with the help of brush elements ($\boldsymbol{j = \overline{1,n_b}}$) (Kapranova and Verloka, 2018a; Verloka et al., 2018; Kapranova A. B. et al., 2020) provided that the latter are fixed on oncoming helical lines ($\boldsymbol{k = 1, 2}$), a cylindrical mixing drum [expression (5), section The Main Features of Modeling the Process of Formation of Rarefied Flows of Loose Components by Brush Elements];
2) after impact interaction with an inclined baffle surface (Kapranova and Verloka, 2016, 2018b) [expressions (7), (8), section The Main Features of Modeling the Mixing of Granular Materials After Impact Interaction With an Inclined Bump Surface].

- A method for calculating the volume fraction of the key component ($\boldsymbol{i = 2}$) obtained at the intermediate stage ($\tau = \boldsymbol{\vartheta}$) for the process of mixing bulk materials [expression (9), section 2.3]. In particular, the calculation method is based on the specified generalization of the results of stochastic modeling (Kapranova and Verloka, 2016, 2018a,b; Verloka et al., 2018; Kapranova A. B. et al., 2020) taking into account the method of dispensing the key ($\boldsymbol{i = 2}$) and transporting [($\boldsymbol{i = 1}$) components according to Kapranova and Verloka (2016); expression (10), section Assessment of the Quality of a Mixture of Bulk Components After an Intermediate Stage of Their Gravitational Mixing].
- Expressions (12) and (13) are obtained for calculating the values, respectively, for the average of the fraction of the key component ($\boldsymbol{i = 2}$) and the average of the square of the specified fraction. These expressions allow, in the case of an intermediate stage ($\tau = \boldsymbol{\vartheta}$), gravitational mixing of bulk materials in the given ratios **1/10** or more. These expressions allow a quality assessment of the mixture according to the criterion of heterogeneity (11) (section 2.4). In this case, the basis for the calculation is the indicated generalization of the results of the authors' models, taking into account the scattering angles from deformed brush elements and the scattering angles of the flows of granular components in and angles of reflection from an inclined baffle.
- These generalizations of the results of the authors' models make it possible

1) to identify the most significant parameters of the structure and its operation modes (angular velocity of rotation of the drum, angle of inclination of the chipper to the horizontal, pitch of screw winding, and a comprehensive indicator of the deformation of brush elements; section Assessment of the Quality of a Mixture of Bulk Components After an Intermediate Stage of Their Gravitational Mixing);
2) to predict rational ranges of their changes (section Assessment of the Quality of a Mixture of Bulk Components After an Intermediate Stage of Their Gravitational Mixing) due to the previously proposed criterion for the best mixing of components (Kapranova and Verloka, 2018a; Kapranova A. B. et al., 2020) in the analysis of the total differential distribution functions for the number of particles of both components on average scattering and reflection angles.

- An example is the process of mixing of two components (semolina GOST 7022-97 and natural sand GOST 8736-93 in a ratio of 1/10) after an intermediate stage ($\tau = \boldsymbol{\vartheta} = \boldsymbol{2}$, section 2.4) of gravitational mixing with the implementation of two steps (using brushes and an inclined bump surface). These bulk materials mimic the toxic composition for the needs of the chemical industry. The article analyzes the influence of the most significant design parameters and its operation modes on the value of the inhomogeneity coefficient in comparison with the results for the initial ($\tau = \boldsymbol{1}$) (Kapranova and Verloka, 2018b) and final stages (τ=**3**) (Kapranova et al., 2019b). In particular, this analysis showed the possibility of reducing energy costs for the consumed power drives of mixing drums by varying the values of their angular speeds of rotation at various stages of the process under study. Moreover, the relative error of the theory data ($\boldsymbol{K_{C2} = 9.8\%}$) and experiment [$\boldsymbol{K_{C2,ex} = 10.1\%}$ (Verloka and Kapranova, 2018)] does not go beyond (**5-7%**).

CONCLUSIONS

An analytical method has been developed for assessing the quality of a granular mixture, taking into account physical, and mechanical properties and a set of structural and operational parameters of the apparatus based on the energy method in the framework of the stochastic approach. The differential functions of the distribution of the number of particles of these components over the states of the corresponding macrosystems were used. When studying the influence of the most significant parameters of the studied process of mixing solid dispersed materials, a set of relevant characteristics was established (the angular velocity of rotation of the drum, the angle of inclination of the bump to the horizontal, the pitch of the screw winding, a comprehensive indicator of the deformation of the brush elements). Using the example of model mixing of two non-humidified components, comparable in size and density (sand and semolina), the heterogeneity coefficient of the resulting mixture for the intermediate stage was calculated. For this stage, mixing is assumed in equal proportions between the resulting mixture after the initial stage and the new portion of the key component (sand). Note that the calculation of the volume fractions at each of the three stages of gravitational mixing is performed using a recurrent formula from Kapranova and Verloka (2016), so that the ratio of components in the finished product corresponds to the regulatory 1:10 or more. It is shown that an increase in the complex index of deformation of brush elements by 0.05 units leads to a decrease in the coefficient of heterogeneity by (0.15–0.80%) in the studied range of the angular velocity of rotation of the drums. At the same time, the minimum indices of the indicated coefficient correspond to the values of the angular velocity of the mixing drum, reduced by 0.5 s^{-1}. Thus, a reduction in the cost of expended power drives of the

mixing drums is achieved by reducing the values of their angular velocities without loss of quality of the resulting mixture. The distinctive features of the application of the obtained results, confirmed by experimental studies, include the possibility of predicting rational ranges of changes in significant parameters of the process under study.

The results of the work can be used in the formation of an engineering method for calculating a new gravity mixer of non-humidified bulk components in predetermined ratios of 1:10 or more with additional mixing elements (brushes and bump stops). In particular, the proposed dependences (14) for incrementing the reflection angles of rarefied flows were used in calculating the performance values of the gravitational apparatus at the corresponding stages of mixing bulk components (Kapranova A. et al., 2020).

DATA AVAILABILITY STATEMENT

All datasets generated for this study are included in the article.

AUTHOR CONTRIBUTIONS

All authors contributed to manuscript revision, read and approved the submitted version.

REFERENCES

Alsayyad, T., Pershin, V., Pasko, A., and Pasko, T. (2018). Virtual modeling of particles two-step feeding. *J. Phys*. 1084:012005. doi: 10.1088/1742-6596/1084/1/012005

Johnson, N., Kendall, M., and Stuart, A. (1962). Review: the advanced theory of statistics: Volume I (1958): Distribution Theory; The Advanced Theory of Statistics: Volume II (1961): Inference and Relationship. *J. R. Stat. Soc. Ser. D* 12, 138–142. doi: 10.2307/2987065

Kapranova, A., Verloka, I., and Bahaeva, D. (2020). "Factors of increasing the performance of the bulk material mixer of the gravity type," in *Proceedings of EECE 2019. EECE 2019. Lecture Notes in Civil Engineering,* Vol. 70, eds B. Anatolijs, V. Nikolai, and S. Vitalii (Cham: Springer), 337–347. doi: 10.1007/978-3-030-42351-3_30

Kapranova, A., Verloka, I., Bahaeva, D., Tarshis, M., and Cherpitsky, S. (2019a). "To the calculation of the average value of the volume fraction of the key bulk component at the intermediate stage of mixing with an inclined bump," in *Bridging Science with Technology: 12th European Congress of Chemical Engineering/5th European Congress of Applied Biotechnology – ECCE12/ECAB5* (Florence) 2015–2016.

Kapranova, A., Verloka, I., Bahaeva, D., Tarshis, M., Cherpitsky, S., and Sidorov, V. (2019b). "Investigation of the heterogeneity coefficient of the loose mixture at the final stage of mixing in a gravitational apparatus," in *Proceedings of the International Conference on Innovative Applied Energy - IAPE,19 14–15 March, 2019.* (Oxford). Available online at: http://www.iape-conference.org/Downloads/Proceedings/Proceedings%20of%20IAPE'19.pdf

Kapranova, A. B., Bakin, M. N., Lebedev, A. E., and Zaisev, A. I. (2013). Evaluation parameter recovery of shock interacting flows of solid dispersion media with a sloping baffle [Otsenka parametra vosstanovleniya udarno-vzaimodeystvuyuikh potokov tverdykh dispersnykh sred s naklonnym otboynikom] Russian Journal of Chemistry and Chemical Technology [Izvestiya vysshikh uchebnykh zavedeniy]. *Seriya* 56, 111–113. Available online at: https://www.elibrary.ru/item.asp?id=20160954

Kapranova, A. B., Bakin, M. N., and Verloka, I. I. (2018a). Simulation of the quality criterion of a mixture in a drum-belt apparatu. *Chem. Petrol. Eng.* 54, 287–297. doi: 10.1007/s10556-018-0477-0

Kapranova, A. B., Bakin, M. N.,Verloka, I. I., and Zaitzev, A. I. (2015). Methods for describing the motion of solid dispersed media in various planes for sections of a mixing drum. *[Sposoby opisaniya dvizheniya tverdykh dispersnykh sred v razlichnykh ploskostyakh dlya secheniy smesitel'nogo barabana]. Vestn. TGTY Her TGTY*. 58, 296–304. doi: 10.17277/vestnik.2015.02.pp.296-304

Kapranova, A. B., and Verloka, I. I. (2016). On the assessment of the content of the key component after shock dispersion of bulk materials at the initial stage of batch mixing. [Ob otsenke soderzhaniya klyuchevogo komponenta posle udarnogo rasseivaniya sypuchikh materialov na nachal'nom etape portsionnogo smeshivaniya]. *Vestn. IGEY Her IGEY*. 3, 78–83. doi: 10.17588/2072-2672.2016.3.078-083

Kapranova, A. B., and Verloka, I. I. (2017). The study of the volume fraction of key component in the second phase of the portion mixing by means of the device of gravity type. *J. Chem. Eng. Process Technol.* 8:59. doi: 10.4172/2157-7048-C1-009

Kapranova, A. B., and Verloka, I. I. (2018a). Stochastic description of the formation of flows of particulate components in apparatuses with brush elements. *Theor. Found. Chem. Eng.* 52, 1004–1018. doi: 10.1134/S0040579518050330

Kapranova, A. B., and Verloka, I. I. (2018b). On the features of estimating the coefficient of inhomogeneity of a loose mixture during the operation of a gravitational device. *J. Chem. Eng. Process Technol.* 9:53. doi: 10.4172/2157-7048-C3-018

Kapranova, A. B., Verloka, I. I., and Bahaeva, D. D. (2020). "About preparation of the analytical platform for creation of a cyber-physical system of industrial mixture of loose components," in *Cyber-Physical Systems: Advances in Design and Modelling. Studies in Systems, Decision and Control*, Vol. 259, eds A. Kravets, A. Bolshakov, and M. Shcherbakov (Cham: Springer), 81–91. doi: 10.1007/978-3-030-32579-4_7

Kapranova, A. B., Verloka, I. I., Lebedev, A. E., and Zaitzev, A. I. (2016). The model of dispersion of particles during their flow from chipping the surface. *Czas. Tech. Mech.* 113, 145–150. doi: 10.4467/2353737XCT.16.102.5501t

Kapranova, A. B., Verloka, I. I., Yakovlev, P. A., and Bahaeva, D. D. (2018b). Investigation of the quality of mixture at the first stage of work of the gravitational type apparatus. [Issledovaniye kachestva smesi na pervoy stadii raboty apparata gravitatsionnogo tipa]. *Rossiyskiy Khimicheskiy Zhurnal* 62, 48–50. Available online at: https://elibrary.ru/item.asp?id=36290375

Kendall, M. G., and Stuart, A. (1967). *The Advanced Theory of Statistics, Vol. 2. Inference and Relationship, 4th ed*, Hafner, 690.

Klimontovich, Y. L. (2014). *Turbulent Motion and Chaos Structure: A New Approach to the Statistical Theory of Open Systems*. LENAND, Moscow.

Mixan (2015). Available online at: https://pa2311.blogspot.com/2015/06/mixan-244.html (accessed May 29, 2020).

Mizonov, V., Balagurov, I., Berthiaux, H., and Gatumel, C. (2016). Gatumel Markov chain model of mixing kinetics for ternary mixture of dissimilar particulate solids. *Particuology* 31, 80–86. doi: 10.1016/j.partic.2016.05.006

Petrov, A. A., Lebedev, A. E., Zaisev, A. I., and Kapranova, A. B. (2012). Express-method for assessing the uniformity of mixtures of bulk materials [Ekspress-metod otsenki odnorodnosti smesey sypuchikh materialov] Russian Journal of Chemistry and Chemical Technology [Izvestiya vysshikh uchebnykh zavedeniy]. *Seriya* 55, 88–90. Available online at: https://www.elibrary.ru/item.asp?id=17858196

Rosato, A. D., Zuo, L., Blackmore, D., et al. (2016). Tapped granular column dynamics: simulations, experiments and modeling. *Comput. Particle Mech.* 3, 333–348. doi: 10.1007/s40571-015-0075-2

Verloka, I., and Kapranova, A. (2018). "Three-stage gravitational method for mixing bulk components. [Trekhstadiynyy gravitatsionnyy sposob smeshivaniya sypuchikh komponentov]," in *71st All-Russian. scientific and technical conf. Nuclear Technology University Students, Undergraduates and Graduate Students with International Participation (April 18, 2018): Sat Conf.: In 3 hours. Part 2 [Electronic resource]* (Yaroslavl), 27–29.

Verloka, I., Kapranova, A., Tarshis, M., and Cherpitsky, S. (2018). Stochastic modeling of bulk components batch mixing process in gravity apparatus. *Int.*

J. Mech. Eng. Technol. 9, 438–444. Available online at: http://www.iaeme.com/IJMET/issues.asp?JType=IJMET&VType=9&IType=2

Zaisev, A. I., Lebedev, A. E., Kapranova, A. B., Verloka, I. I., Badaev, N. V., Vatagin, A. A., et al. (2017). *A Method for Determining the Coefficient of Heterogeneity of a Mixture of Difficult to Separate Bulk Materials*. Patent 2620387 Russian Federation, G01N1/28. Bull. *N*. 15.

Zaitzev, A. I., Lebedev, A. E., Kapranova, A. B., and Verloka, I. I. (2016). *Gravity-Type Bulk Solids Mixer*. Patent 2586126 Russian Federation, IPC B01F3/18.

Zhuang, Y., Chen, X., and Liu, D. (2016). Stochastic bubble developing model combined with Markov process of particles for bubbling fluidized beds. *Chem. Eng. J*. 291, 206–214. doi: 10.1016/j.cej.2016.01.095

Conflict of Interest: The authors declare that the research was conducted in the absence of any commercial or financial relationships that could be construed as a potential conflict of interest.

frontiers in Energy Research

ORIGINAL RESEARCH
published: 11 August 2020
doi: 10.3389/fenrg.2020.00192

Bottom–Up Assessment Framework for Electrification Options in Energy-Intensive Process Industries

Holger Wiertzema[1], Elin Svensson[2] and Simon Harvey[1]*

[1] Division of Energy Technology, Department of Space, Earth and Environment, Chalmers University of Technology, Gothenburg, Sweden, [2] CIT Industriell Energi AB, Gothenburg, Sweden

Electrification of industrial processes is one of the frequently discussed options to reduce greenhouse gas emissions from energy-intensive industries. This paper presents a bottom–up framework to assess process electrification options for energy-intensive industrial process plants in terms of greenhouse gas emissions and energy costs. The framework is based upon pinch analysis energy targetting methods, and accounts for site-specific conditions, including the effects on heat recovery potential and overall mass and energy balances. Furthermore, interactions between the process site and the background energy system are considered and scenarios are introduced in order to assess the impact of electrification options under different possible future energy market conditions. The framework is illustrated by a case study for an existing chemical plant for which there is a broad variety of electrification options that affect the process in different ways. The option of replacing the natural gas based syngas production unit with electrified syngas and steam production is analysed in detail. The results indicate natural gas savings of 173 MW whereas the electricity demand increases by 267 MW, leading to a strong increase in energy costs but also avoided greenhouse gas emissions of 333 kt/a. For two selected energy market scenarios for 2030 and 2040, the energy costs increase by 59 and 50 M€/a, respectively. The framework can be used to compare electrification with other process greenhouse gas emission reduction measures and to support policy and industrial decision making.

Keywords: energy-intensive process industries, electrification, bottom–up assessment, chemical industry, techno-economic assessment, energy market scenarios

OPEN ACCESS

Edited by:
Theodoros Damartzis, École Polytechnique Fédérale de Lausanne, Switzerland

Reviewed by:
Martin Atkins, University of Waikato, New Zealand
Alessio Santecchia, École Polytechnique Fédérale de Lausanne, Switzerland

****Correspondence:***
Holger Wiertzema
holgerw@chalmers.se

Specialty section:
This article was submitted to Process and Energy Systems Engineering, a section of the journal Frontiers in Energy Research

Received: *06 May 2020*
Accepted: *20 July 2020*
Published: *11 August 2020*

Citation:
Wiertzema H, Svensson E and Harvey S (2020) Bottom–Up Assessment Framework for Electrification Options in Energy-Intensive Process Industries. Front. Energy Res. 8:192. doi: 10.3389/fenrg.2020.00192

INTRODUCTION

In 2014, the industrial sector accounted for 36% (154 EJ) of global final energy use and 24% (8.3 $GtCO_2$) of direct fossil CO_2 emissions. Five energy-intensive sectors, namely chemicals and petrochemicals, iron and steel, cement, pulp and paper as well as aluminium dominate in terms of industrial energy use with a share of 69% (International Energy Agency, 2017b).

In the light of the Paris agreement, the pressure on industry to contribute to substantial greenhouse gas emission reduction has increased. Electricity can be used to replace fossil fuels for direct process energy demand as well as to produce fuels and raw materials. This fuel switch in conjunction with the anticipated increasing amount of electricity from renewable sources can potentially lead to a significant reduction in greenhouse gas emissions at the plant but also at

the national and global energy systems level. As the production cost for renewable electricity is expected to decrease in the future, process electrification will become more economically feasible (International Energy Agency, 2017a). However, there is still a degree of uncertainty about who will bear the costs for the significant grid investments that are needed to achieve massive electrification of industry. Depending on the electricity generation mix, electrification can already today lead to a reduction of greenhouse gas emissions and cost. From a company's perspective, process electrification can be a measure not only to comply with emission limits but also to reduce the costs associated with emitting greenhouse gases (e.g., within EU ETS). This will become even more important in the future since the price for EU ETS emission allowances is expected to increase (European Roundtable on Climate Change and Sustainable Transition, 2019). Furthermore, electrification can enable participation in flexibility markets (e.g., by providing on demand load-shedding) which can lead to additional revenues.

Variety of Process Electrification Options

Electricity is a versatile energy carrier in industrial processes, and this leads to a comprehensive variety of electrification options. Electricity can be used directly in certain industrial process operations or indirectly via electro-fuels and electro-feedstock. It can be used for process heating purposes to drive heat pumps or electric steam generators. Advanced electro-thermal technologies such as electromagnetic radiation, plasma technologies and microwaves can be highly efficient and offer a high degree of controllability. In the future, high-temperature heat pumps will potentially be able to provide a much higher share of the industrial heat demand. Electricity can also provide the driving force for pressure-driven membrane separation processes or production of hydrogen through water electrolysis. This hydrogen can be used for process purposes (e.g., for hydrotreatment) or combined with CO or CO_2 to produce synthetic fuels or feedstock. Finally, innovative electro-chemistry concepts are expected to enable direct production of certain chemicals. Many of these technologies are (commercially) available today while others are still on the research level.

The large variety of electrification options poses a challenge for industrial decision-makers that need to make long-term investment decisions. Policymakers on the other hand are interested in the greenhouse reduction potentials of electrification and corresponding cost as a basis for policy design but also in how electrification of industrial processes will affect electricity demand and distribution infrastructure requirements.

Existing Studies Related to the Assessment of Process Electrification

Much research related to electrification of industrial processes has a strong focus on macro-economic top-down approaches and explorative studies. For example, Lechtenböhmer et al. (2016) estimated that complete electrification of the basic materials (steel, minerals and chemicals) industry in the EU would lead to an additional electricity demand of 1713 TWh/a in 2050, compared to the current level (2780 TWh/a) at the time of the study. Electrification is included in many roadmap studies conducted for specific sectors such as the chemical industry (DECHEMA, 2017), specific countries such as the Netherlands (Berenschot et al., 2017; Stork et al., 2018) or Sweden (Brolin et al., 2017), or specific sites such as the Port of Rotterdam (Samadi et al., 2016). A recent comprehensive review of publications related to decarbonisation pathways for the EU includes industrial electrification as an emissions reduction measure (Gerres et al., 2019).

However, top–down studies usually exclude detailed technological aspects and run the risk of neglecting the many challenges related to implementation in specific plants. Existing industrial process sites, even within the same sector, can be very different. In particular, the degree of integration can vary substantially between plants, i.e., how mass and energy flows between different process units are interconnected. As a result, it is difficult to estimate how introduction of electrification technologies will affect greenhouse gas emissions and costs without conducting site-specific studies.

The research literature related to process electrification also includes inventories of electrification technology options for different processes as well as information about the TRL. Some of these inventories are rather old (EPRI, 1989) and driven by the purpose of efficient use of electricity rather than greenhouse gas emissions reduction. More recent inventories such as (EPRI, 2009) are more extensive and some of them also include comparisons between conventional technologies and electricity-driven equivalents on the unit operation level (DECHEMA, 2017).

Studies based on the engineering bottom–up approach consider more detailed descriptions of the technologies and the impact on existing systems. In this paper, we consider that bottom–up assessment captures the impact of integrating electrification technologies into existing processes in terms of greenhouse gas emissions and cost, accounting for the specific characteristics of the existing process.

Many studies adopt a bottom–up approach to assess the impact of integrating new technologies into existing processes in order to decrease their carbon footprint. Examples are the integration of biomass-to-hydrogen options (Brau and Morandin, 2014) and Fischer-Tropsch fuels production from biomass (Johansson et al., 2014) in oil refineries, or biomass gasification-based syngas production into petrochemical processes (Arvidsson et al., 2014). For oil refining, there is also a techno-economic analysis of excess heat driven post combustion carbon capture and storage (Andersson et al., 2016). The common methodology of these studies is to develop new process designs, to perform process modelling and simulation to establish mass and energy balances and to extract data that is then used to estimate the potential for maximum process heat recovery using pinch analysis tools. The main performance indicators for the subsequent assessment are energy and exergy efficiency, greenhouse gas emission reduction potential, as well as total cost. In another study (Berghout et al., 2019), a bottom–up method for the assessment of technologies for greenhouse gas emission reductions in industrial plants was developed and applied in a case study for a complex oil refinery. Although

the method focuses on core processes of an industrial plant, it does not consider changes in terms of heat recovery potential when conventional unit operations are replaced. None of these studies focus on the integration of electrification technologies as new technology.

There are a number of bottom–up studies that focus on specific electrification technologies. Bühler et al. (2019) investigated options for electrification of process heat in milk powder production plants by implementing heat pumps and electric heaters in different configurations. Their study includes an energy, exergy, environmental and economic analysis, as well as different scenarios for future prices and emissions. Wallerand et al. (2018) developed a new method for optimal integration of heat pumps based on a superstructure optimisation model. However, the method was not applied to an existing plant and did not consider possible future changes of energy market conditions. Delikonstantis et al. (2019) evaluated a direct plasma-assisted methane-to-ethylene process and a hybrid plasma-catalytic methane-to-ethylene process. The authors state that further adaptions of the existing processes would be needed since the heat flows in the conventional process are highly integrated with the other processes of the plant. This means that heat demand for subsequent separation processes must be provided in another way. Pinch analysis was used to maximise heat integration of the plasma-assisted processes. Oluleye et al. (2016) developed a screening methodology to identify options to upgrade low grade excess heat with heat pumps. However, the focus of this work was to increase the degree of heat recovery and not to switch to using electricity to provide heat. Sandberg et al. (2019) used an optimisation model to assess the demand for electricity and biomass if energy-intensive processes in Sweden were to switch to these energy carriers to comply with a net zero emissions target.

There is a clear lack of techno-economic and greenhouse gas emission assessment studies for process electrification options from a bottom–up perspective that simultaneously address how electrification options affect different parts of an existing process in detail and that include future energy market scenarios. More specifically, no published study presents a consistent way of mapping relevant electrification options for a specific process plant, considering how core reactions, separation systems and utility systems, as well as utility demands and excess heat availability are affected. There is thus a lack of knowledge about how to adapt existing processes to electricity as energy carrier. Such knowledge is important not only to discard low-performing technologies at an early stage but also to identify conditions under which electrification options are viable.

Objective

The objective of this paper is to present a bottom-up assessment framework for the techno-economic and greenhouse gas assessment of electrification options for existing processes in energy-intensive industries. One novelty of the framework is that electrification options are clustered according to how they affect the plant processes, ranging from the utility system to the core reactions. Another novel contribution is that these effects are combined with an assessment of how electrification options affect the heat recovery potential on the process and plant level, as well as the fuel demand, co-generation potential and availability of excess heat. Pinch analysis is used to generate the data needed for the assessment. Furthermore, scenarios are introduced to assess electrification under possible future energy market conditions. The proposed assessment framework can be used to compare electrification with other greenhouse gas emission reduction measures in order to support industrial and policy decision-making.

The paper starts with a discussion about how electrification options impact an existing process on different process levels, as well as an overview of electrification options and their impacts for specific industrial sectors. Thereafter, the proposed bottom-up framework is presented and applied in a case study for an oxo-synthesis plant. The purpose of the case study is not only to illustrate the assessment framework for a specific plant, but also to identify challenges that are connected to the implementation of electrification technologies in that specific process.

IMPACT OF ELECTRIFICATION OPTIONS ON EXISTING INDUSTRIAL PROCESSES

Classification According to Impacts and Interaction With Surrounding Energy System

There is a wide range of electrification options and they affect existing industrial processes in different ways. One indirect electrification option is to replace fossil-fuel based raw materials and fuels by electricity-based equivalents which do not affect the plant itself. Direct electrification options (such as heat pumps) or indirect electrification options (in which intermediates are produced using electricity) affect the core process more since the existing process units are usually highly interconnected and optimised to reduce the external heating and cooling demand (although very few achieve maximum energy recovery). The impact of electrification on a process does not thus depend only on the electrification technology but also on the existing process configuration. For example, if a conventional unit operation that provides heat to another unit operation is replaced by an electricity-based technology, it is important to consider how the heat for the other unit operation can be provided instead.

Electrification options are often classified according to the direct/indirect electrification or the Power-to-X approaches. In this paper, this classification is extended and electrification options are classified according to the process design hierarchy and interactions model shown in **Figure 1**. This model was originally established for process design purposes (Gundersen, 2002). The left side of the figure shows the conventional process design procedure which starts from the core reactor, followed by design of the separation and recycling system, the heat recovery system, the heating and cooling system, as well as the water and effluent treatment system. It is thus important to identify which of these systems are affected by electrification. According to this view, introduction of electrification in one sub-system will only impact the sub-system as well as the systems in the

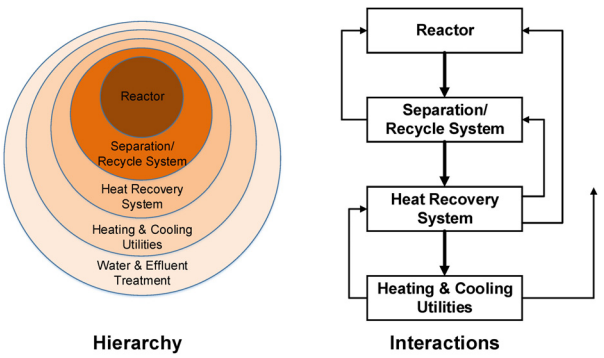

FIGURE 1 | Hierarchy and interactions of industrial process-related systems (adapted from Gundersen, 2002).

outer rings of the hierarchy diagram. However, as shown in the right side of the figure, the process sub-systems all interact with each other and it is important to consider upstream effects. For example, switching to electric steam production can lead to a surplus of internal residual gases that were previously combusted to provide process heat.

It is also important to consider the interaction of the process with the surrounding energy system. In particular, the carbon intensity of grid electricity production must be considered as well as the electricity price. Furthermore, it is important to include future prices for fossil fuels and costs for emitting greenhouse gases as they will have a strong impact on the economic feasibility of electrification options. These aspects again underline the importance of a co-evolution between increased electrification and a reduced carbon-intensity of the electricity system to achieve sustainable decarbonisation of industrial processes. Finally, electrification can impact the availability of excess heat that can be used for district heating or exported to nearby facilities.

Overview of Electrification Options for Specific Energy-Intensive Industries and Their Impacts on Existing Industrial Processes

An important initial part of the methodology is mapping and conducting a first evaluation of electrification options on the level of specific industrial sectors. **Table 1** shows a classification of electrification options in terms of process sub-systems affected for some major energy-intensive process industry sectors. The maturity level is included in this table by dividing the options into short-term and long-term.

Chemical and oil refining industries consist mainly of liquid and gaseous streams. Dominant processes in terms of energy demand include stream cracking and steam methane reforming (with natural gas as feedstock and fuel at the same time) in the petrochemical industry, and atmospheric distillation in oil refineries. In the chemical industry, steam is usually used for heating purposes. In general, temperatures range from low (<250°C) to medium (250–600°C). Otherwise, the range of processes and products varies strongly with different raw materials, fuels, and auxiliary materials (e.g., hydrogen for hydrotreatment). The same is true for process intermediates such as syngas. In oil refining, crude oil is separated into its components which are then purified, often by hydrotreating. Further downstream, cracking furnaces are used to reduce the length of hydrocarbon chains. Short-term electrification options are related to heat recovery and utilities whereas long-term options include a wide range of technologies that affect all levels of the process hierarchy.

In the pulp and paper industry, processing wood (by cooking, bleaching, separating etc.) requires large amounts of steam and hot water in the low temperature range (<250°C). Recovery boilers are used to combust the lignin-rich black liquor stream to produce steam to reduce the demand for external utilities. Biogenic resources are thus not only used as raw material but also as fuel so that fossil-related emissions are usually very low. The incentives to use electricity as energy carriers are thus lower compared to other industries. However, electrification options might be used to overcome production bottlenecks, to release biomass that can be used for other purposes (see Pettersson et al., 2020 for further discussion), or to diversify the plant's product portfolio.

In the cement and steel industry, solid materials are processed at high temperatures (>600°C). These processes require mainly reaction heat. Radical emission reduction will require breakthrough technologies which are only likely to be available in the long run.

ASSESSMENT FRAMEWORK FOR PROCESS ELECTRIFICATION OPTIONS

The steps involved in the proposed framework are presented below. The system boundaries for the individual steps are indicated in brackets. The framework can be used to assess individual electrification options but also combinations of electrification options. Illustrative examples for the different steps are shown in the case study in Section "Case Study: Assessment of Electrification Options for an Existing Oxo Synthesis Plant."

1. Definition of the existing process system and its unit operations (plant).
2. Identification of electrification options and the affected process levels (plant).
3. Modelling and simulation of the existing process to obtain data needed for process integration studies (plant).
4. Modelling and simulation of the electrified unit operation (unit operation).
5. Mass and heat integration studies of the reference process as well as the electrified process using pinch analysis tools (plant).
6. Inventory of all relevant changes in input and output flows of material and energy compared to the reference process (plant).
7. Techno-economic and greenhouse gas emission assessment (surrounding energy system).

TABLE 1 | Electrification options on different time scales for energy-intensive industries.

	Chemicals, petrochemicals and oil refining	Cement	Iron and steel	Pulp and paper
Special characteristics	(i) Many different products and processes at a wide range of temperatures (ii) High energy demand for steam cracking (850°C) and steam methane reforming (450–950°C) (iii) Large demand for hydrogen (for hydrotreatment, as well as ammonia and methanol production) (iv) Distillation for thermal separation widespread	High-temperature heat demand for kiln (1450°C). Large share of process-related emissions from calcination	High-temperature heat demand (1400°C)	(i) Low- to medium-temperature heat demand (ii) Black liquor residue (biogenic) is combusted for steam and power generation (iii) Drying and evaporation require a lot of energy (iv) Mainly biogenic greenhouse gas emissions
Short-term electrification options	(HR) Low temperature heat pumps (<100°C) (HR) Mechanical vapour recompression (U) Electric steam generation	(EF) Substitution of conventional fuels	(U) Electric arc furnaces	(HR) Low-temperature heat pumps (U) Electric steam generation (U) Electro-thermal processes (e.g., microwave) for drying (SR) Membrane separation
Long-term electrification options	(R) Production of chemicals via water electrolysis and synthesis steps, e.g., syngas (in combination with reverse water gas shift reaction), ammonia and methanol (R) Direct electro-catalytic processes (SR) Membrane separation (e.g., for olefins) (HR) High temperature heat pumps (U) High temperature furnaces (for steam cracking)	(U) Electrification of heat with high-temperature plasma kilns	(R) Electrowinning and hydrogen direct reduction for steel (U) Plasma heating and direct electric heating for minerals (NP) Production of electro-fuels from fossil CO_2	(R) Plasma-assisted calcination (NP) Production of electro-fuels from biogenic CO_2

*Process levels that are affected (see **Figure 1**): Reactor (R), Separation/recycle (SR), Heat recovery (HR), Utilities (U). Additionally: electro-fuels and electro-feedstock (EF), as well as new products (NP).*

The scope of the single steps of the approach may be adjusted to take into account the impacts of different electrification options. For example, if an electrification option such as electric steam generation affects the utility system only, it may be sufficient to model the utility system and to ignore the reaction, separation and heat recovery systems.

Definition of the Existing Process System and Its Unit Operations

The existing process system is first mapped at the plant level (core processes and process energy system) and the existing unit operations in the plant sub-processes are identified. This step is important not only as base for screening for electrification options that could replace existing unit operations but also to establish a reference case. In this step, information is collected about existing unit operations, their operating conditions, and how they are connected to each other. This also includes the identification of raw materials and intermediates since these could be produced by electricity-based processes as well. Furthermore, data about current greenhouse gas emissions, fuel types and demand, are collected. This information can come from flowsheets or data sets of measured values. Process simulation can be used to generate data that is not otherwise available (see section "Modelling and simulation of the electrified unit operation").

Identification of Electrification Options and the Affected Process Levels

Electrification options are identified by finding electricity-driven equivalents for the existing unit operations. This is an iterative process that starts by identifying technologies that are in principle suitable (e.g., electric steam generators to provide steam) before ensuring that specific electrification technologies can cope with the operating conditions in the existing system. Afterward, the electrification options are classified according to the model described in **Figure 1** to determine which levels of the process are affected, which has an impact on the modelling in the next step. Helpful tools for the identification of electrification options are technology inventories (such as EPRI, 2009) that list candidate electrification technologies that are suitable for specific industrial processes. Furthermore, technical data sheets for existing technologies (e.g., maximum outlet temperatures and temperature lifts for industrial heat pumps) can be used to assess whether these technologies can fulfil the requirements of the process.

Modelling and Simulation of the Existing Process to Obtain Data Needed for Process Integration Studies

In this step a model is created for the current process in order to generate data for all heat sources and heat sinks, as required

for pinch analysis purposes (see step "Mass and heat integration studies of the reference process as well as the electrified process using pinch analysis tools").

It should be noted that the extent of the model depends on the numbers of levels of the process that are affected according to the previous step. If only the utility system is affected, it may be sufficient to only model the utility system. The model should preferably be run for a number of representative operating conditions. Besides delivering information about the heat content of different streams in the process, the model should also provide information about the fuel demand and related greenhouse gas emissions.

Modelling and Simulation of the Electrified Unit Operation

In this step, a model for the electrified unit operation is created and used for simulation runs to obtain process stream data required for pinch analysis purposes, as described in the previous step. Is it important to adjust the model parameters to meet the specifications of the existing process, meaning that outlet flows must meet the same specifications as the corresponding flows in the conventional unit (flow rate, temperature, pressure and composition). The model also needs to give the electricity demand and related on-site greenhouse gas emissions (if any). The modelling takes place at the unit operation level of the electrification technology.

Mass and Heat Integration Studies of the Reference Process as Well as the Electrified Process Using Pinch Analysis Tools

The next step is to perform heat integration studies based on the stream data that was derived from the model runs in the two previous steps. This is done by applying pinch analysis tools to estimate heat recovery targets and thus the utility demand for a given temperature difference ΔT_{min}. For the reference process, a Grand Composite Curve (GCC) can be generated in order to establish the theoretical minimum hot and cold utility demands. Afterward, process streams that are related to the unit operation(s) to be replaced by the electrified unit operation are removed from the stream table. The remaining streams form the so-called background process. The process streams related to the electrified unit operation form the foreground process. Thereafter, the concept of split-GCC analysis is applied (Kemp, 2007), in which the GCCs for the foreground and background processes are plotted in the same figure in order to visualize how well the electrified unit operation can be heat integrated with the background process. An example for a split-GCC is shown in **Figure 6** in Section "Case Study: Assessment of Electrification Options for an Existing Oxo Synthesis Plant." In the ideal case, heat can be exchanged between the foreground and background processes, resulting in lower utility demands. It is assumed that the maximum energy recovery (MER) target is met both in the reference case and in the case with the electrified unit operation to allow a fair comparison.

Inventory of All Relevant Changes in Input and Output Flows of Material and Energy Compared to the Reference Process

In this step a full inventory is compiled for the following parameters for the two cases:

- Minimum heating and cooling demand (assuming maximum heat recovery).
- Electricity demand.
- Fuel balances (demand and fuel type).
- CHP opportunities.
- Excess heat availability.
- Direct process greenhouse gas emissions, as well as fuel-related greenhouse gas emissions.

This data constitutes the necessary input to the impact assessment.

Techno-Economic and Greenhouse Gas Emission Assessment

The final step is to perform a techno-economic and greenhouse gas emissions assessment. The assessment takes into account energy costs, as well as greenhouse gas emissions and associated costs. It is important to note that the system boundary is expanded in this step to include the surrounding energy system. In this manner, off-site greenhouse gas emissions are included in the assessment. The operating cost and the greenhouse gas emissions for the electrification technologies are highly dependent on the background energy system. The capital cost on the other hand depends on the estimated cost development for the individual technologies. The ultimate goal of this step is to calculate the possible reductions in greenhouse gas emissions versus the capital and variable cost compared to the reference case.

Background Energy System and Future Energy Market Scenarios

The integration of electrification options will normally lead to an increased electricity demand. Consequently, the change in greenhouse gas emissions depends on the electricity supply system. Since the potential for excess heat delivery (e.g., for district heating) can also be affected, it is important to take the corresponding change in revenues into account. Furthermore, selling new by-products that arise as a result of electrification can lead to additional revenue. To calculate the corresponding running cost (including revenues from excess heat and by-products) and the greenhouse gas emissions, information about the following parameters is required:

- Fossil fuel prices and emission factors.
- Electricity price and grid emission factors.
- Costs for greenhouse gas emissions (e.g., EU ETS, national tax systems and other relevant policy instruments).
- Income from export of excess heat and carbon intensity of the heat sink to which excess heat is exported.
- Sales prices and emission factors for new by-products.

For technologies with a high TRL that could be deployed already today, current values for these parameters can be used for an initial assessment. However, since electrification is one option for industry to comply with ambitious medium- and long-term national climate targets, the expected development of these parameters is of high interest. This is even more the case for electrification options with a low TRL which can only be considered for implementation in the medium- or long-term. This leads to a need for consistent future energy market scenarios in which the values of the aforementioned parameters are internally consistent. In this work, the ENPAC tool (Axelsson and Harvey, 2010) was used to generate consistent scenarios for energy prices and marginal greenhouse gas emissions associated with the use of energy for large-volume industrial customers based on forecasted prices for fossil fuels on the commodity market and costs associated with emitting greenhouse gases.

CASE STUDY: ASSESSMENT OF ELECTRIFICATION OPTIONS FOR AN EXISTING OXO SYNTHESIS PLANT

The assessment framework was applied in a case study of an existing oxo synthesis plant to identify process electrification options and to assess their impact on the processes. A more detailed assessment was performed for electrified syngas and steam production. The plant is part of a large chemical cluster on the west coast of Sweden.

Definition of the Existing Process System and Its Unit Operations

Figure 2 shows a simplified flowsheet of the main process units at the plant. In the oxo synthesis unit, olefins (mainly ethylene and propylene) react with syngas (CO and H_2) in the presence of a catalyst to form aldehydes. Part of the aldehydes are further processed to produce alcohols and acids. The olefins are purchased from a neighbouring site, whereas the syngas is produced on-site by non-catalytic partial oxidation (NC-POX) of natural gas. The oxygen is produced by an air separation unit. Fossil fuels are combusted for steam production. Low-pressure (LP) steam for oxo synthesis and further synthesis unit is produced in a gas boiler.

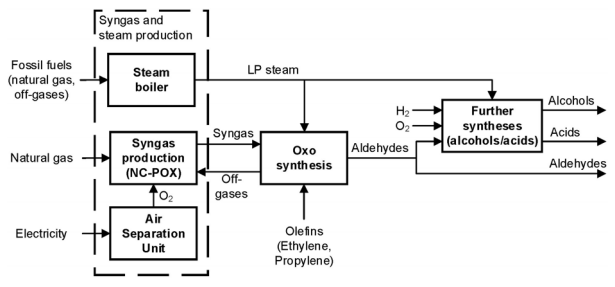

FIGURE 2 | Simplified flowsheet of the main process units at the oxo synthesis plant site including the main material flows. The units in the dashed box are related to the conventional syngas and steam production and used to establish the reference case for the detailed assessment.

The exothermic reaction in the oxo synthesis unit takes place in a stirred-tank reactor at 15–20 bar and temperatures between 85 and 115°C (Bahrmann and Bach, 2012). Cooling is required to remove reaction heat but also to condense the reaction products. After the separation of unreacted materials, the crude aldehyde passes a series of distillation columns for further product separation. These columns require heating and cooling for the reboilers and condensers, respectively.

In the syngas production unit, natural gas from the grid, oxygen from an air separation unit and off-gases from the oxo synthesis unit react in a non-catalytic partial oxidation unit to form syngas with a specific H_2/CO ratio and additional hydrogen. Syngas is an intermediate that is sent to the oxo synthesis unit. A more detailed description of the syngas unit can be found in Section "Modelling and simulation of the existing process to obtain data needed for process integration studies."

In smaller downstream process units, a fraction of the aldehydes from the oxo synthesis is processed further to produce alcohols and acids. Hydrogen is required for hydrogenation to produce the alcohols while oxygen is required for the acid production. The two reactions are highly exothermic. In both cases, distillation is used to separate by-products from the final product. These processes are not presented in detail but were included in the assessment.

Identification of Electrification Options and the Affected Process Levels

A technology inventory was conducted to identify different electrification options for parts of the oxo synthesis plant, see **Table 2**. The table also includes information about the technical maturity of the different options and indicates the process levels that are affected as described in the previous section. A low technical maturity corresponds to Technology Readiness Levels (TRL) of 1–4, medium to TRLs 5–7 and high to TRLs 8–9.

Electrification options 1–4 are options for indirect electrification to produce electro-feedstock while the processes units at the site are not affected. Since the chemical industry might be accountable for greenhouse gas emissions over the complete value chain in the future (similar to the motor fuel industry, see European Parliament, 2009), it is important to address emissions from fuels and feedstock as well as on-site emissions.

Options 5a-c could replace the current syngas production, although their technical maturity differs widely. They affect the existing process rather strongly since they replace the conventional syngas production (reaction and subsequent separation processes) completely. The elimination of process streams related to the conventional syngas production could induce strong changes on the internal heat recovery potentials since high temperatures are involved. Furthermore, large amounts of electricity as well as a source for CO_2 are needed to replace the natural gas demand since syngas is the main intermediate at the plant.

TABLE 2 | Detailed description of the process electrification options for the oxo synthesis plant including technical maturity and affected process levels (DECHEMA, 2017; Foit et al., 2017; Reller et al., 2017).

	Electrification option	Technical maturity	Affected process levels
1	Production of electro-methane to replace natural gas for the syngas production unit.	Medium	Electro-feedstock, no changes to the core process
2	Direct electro-catalytic production of ethylene (single-step electro-chemical reduction of CO_2 with a Cu-based catalyst.	Low	
3	Methanol-to-olefins with renewable methanol (methanol can be imported and processed on-site). Hydrogen from water electrolysis is combined with CO_2 in a methanol synthesis reaction to produce methanol. Methanol is then converted to ethylene and propylene.	High	
4	Water electrolysis to produce Hydrogen and oxygen for alcohol and acid synthesis	High	
5a	Syngas production by Reverse Water Gas Shift (RWGS) reaction coupled with water electrolysis.	Medium	Syngas production
5b	Syngas production by coupling carbon monoxide production from low-temperature electrolysis of CO_2 with hydrogen production from water electrolysis.	Low	
5c	High-temperature co-electrolysis of water and CO_2 with solid oxide electrolysis cells to produce syngas directly.	Low	
6	Electric steam generation to replace the combustion of fuel gas	High	Steam/utility system

The electrification options selected for the following in-depth assessment are highlighted.

Option 6 affects the utility system only. Subsequently, this electrification option has a lower impact on the existing process configuration according to the process design hierarchy. This technology is commercially available today. It was assumed that unit operations downstream from the syngas production are not affected by this option.

Higher levels of process electrification can be achieved by combining electrification options. For example, the whole oxo synthesis production process could be electrified by combining electrified syngas production (options 2a-c), electrified olefin production (option 4), production of hydrogen and oxygen for alcohol and acid syntheses by water electrolysis (option 5), as well as electrified steam production (option 6). This could lead to a strong reduction of on-site greenhouse gas emissions.

Selected Electrification Options

For the further illustration of the methodology, a combination of electrified syngas production by coupling a Reverse Water Gas Shift (RWGS) reaction with water electrolysis (option 2a) and electrified steam generation (option 6) was selected. This was motivated by the comparatively high technical maturity of the two options and the fact that they affect core parts of the existing process. Rather than replacing single unit operations, all unit operations connected to the conventional syngas production, as well as the conventional steam boiler, were replaced. Furthermore, syngas plays an important role in many chemical and petrochemical plants so that insights from this case study are relevant for other plants as well. RWGS in combination with water electrolysis has been discussed in other studies (Schwab et al., 2015).

Modelling and Simulation of the Existing Process to Obtain Data Needed for Process Integration Studies

Pinch data for the process units of the plant (see **Figure 2**) was mainly based on previous work (Hackl et al., 2011). However, a more detailed model developed by Arvidsson et al. (2014) was adopted for the conventional syngas production unit. The corresponding flowsheet is shown in **Figure 3**.

In the NC-POX reactor, natural gas, off-gases and oxygen react in the presence of steam to form a mixture of syngas (CO and H_2), CO_2, water and tail gas. After soot and CO_2 removal, a membrane is used to separate the syngas and pressure-swing absorption is used to separate hydrogen from the tail gas. Significant amounts of heat are released from cooling of the NC-POX reaction products from the reaction temperature of 1400°C down to 300°C. Further cooling is required before the CO_2 separation unit operations and for the final syngas product and the by-products. Heating is required to preheat the NC-POX reactor feed streams as well as preheating the feed stream into the active carbon bed and the ZnO bed that are used to remove impurities. The syngas production rate is 115 MW with a H_2/CO ratio of 1.1.

The stream data table generated for pinch analysis purposes can be found in **Supplementary Appendix A**. Since the conventional syngas production was replaced by electrified syngas production, the streams related to the conventional syngas production were removed from the stream data table that included streams related to the process units of the plant. The remaining streams constitute the background process for the following mass and heat integration studies. A stream table with these remaining streams can be found in **Supplementary Appendix B**.

Modelling and Simulation of the Electrified Unit Operation

Figure 4 shows an overview of the proposed electrified syngas and steam production process. The syngas production constitutes the foreground for the heat integration studies. To generate the required pinch stream data, a RWGS reaction model was coupled with a model for water electrolysis. In the RWGS reaction, carbon monoxide and water are produced from carbon dioxide and hydrogen. The required hydrogen is produced by electrolysis of water with oxygen as by-product. The hydrogen output from water electrolysis was adjusted to fulfil the demands of the RWGS

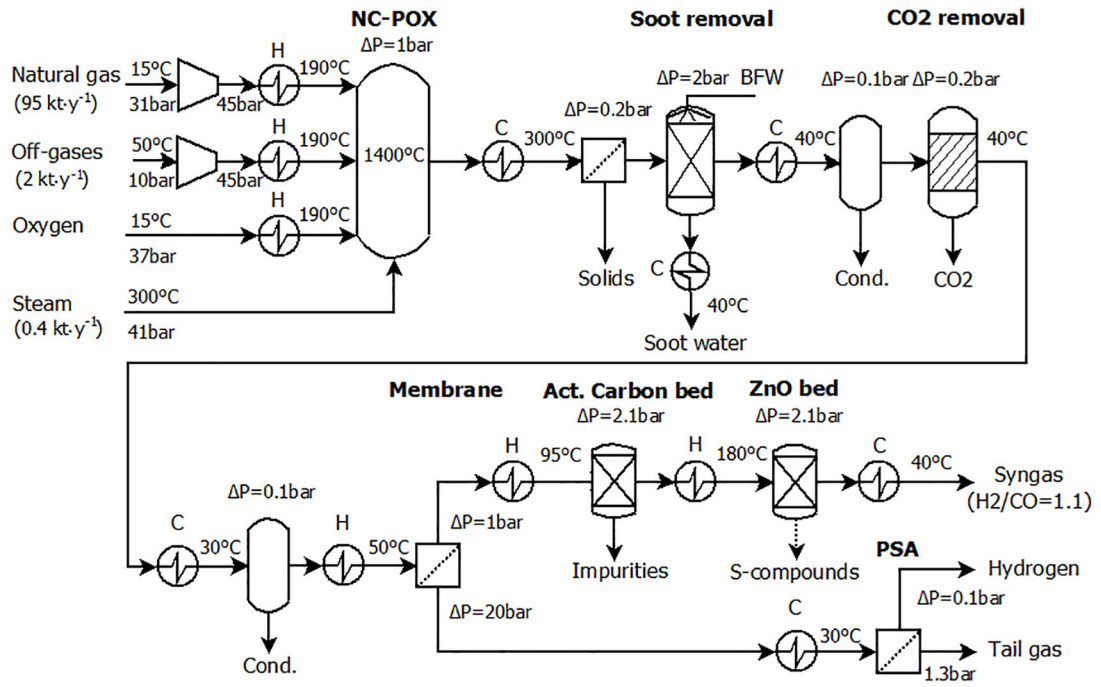

FIGURE 3 | Process scheme for the conventional syngas production. Reprinted with permission from Arvidsson et al. (2014). Copyright 2020 American Chemical Society.

reaction, to adjust the targetted H_2/CO ratio and to provide the hydrogen required by for downstream processes. The LP steam for the RWGS reaction unit and the units downstream from the syngas production are produced by an electric steam generator with an assumed thermal efficiency of 99%.

RWGS Reaction

For the RWGS reaction, an Aspen HYSYS model presented in Rezaei and Dzuryk (2019) for syngas production at 410 kPa was used and adjusted to meet the required syngas production rate, see **Figure 5**. At the core of the process is a fired heater in which CO_2 is hydrogenated at 900°C and 410 kPa. Flash drums are used to remove water from the process streams while unreacted CO_2 is captured by an MEA (monoethanolamine)-based absorption column. The MEA is regenerated in a regenerator column and led back to the absorption column while the CO_2 is recycled and mixed with the incoming feed. To increase the energy efficiency of the process, two feed-effluent heat exchangers are used to recover the reaction heat by preheating the reactor feed with the hot effluent stream. In addition, the feed to the regenerator column is preheated using the reboiler stream of the regeneration column. To run the process, low-pressure steam is needed for the regenerator column while electricity is required to drive pumps and compressors. Furthermore, natural gas is needed to provide the heat in the fired reactor since an electricity-driven equivalent for this high-temperature application is not available. Additionally, four coolers with cooling water and three compressors are required to adjust temperatures and pressure of the process streams.

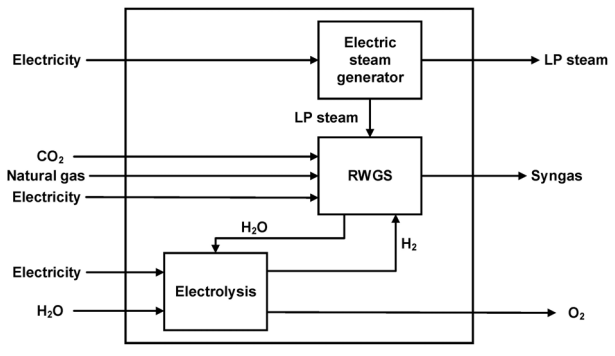

FIGURE 4 | Overview of the electrified syngas and steam production.

Water Electrolysis

It was assumed that hydrogen was produced from water electrolysis with alkaline electrolysis cells (AEC) since this technology is mature, commercially available and suitable for large-scale installations. The assumed operation parameters were based on Grahn and Jannasch (2018): operating temperature of 80°C, conversion efficiency of 0.65 $MW_{H2}(LHV)/MW_{el}$, excess heat release of 0.30 MW_{th}/MW_{el} at 70°C, water demand of 0.54 ton/MWh_{H2} and oxygen production of 0.24 ton/MWh_{H2}.

Stream Table for the Electrified Syngas Production

The stream data for both sub-processes of the electrified syngas production are shown in **Table 3**. It can be seen that the process

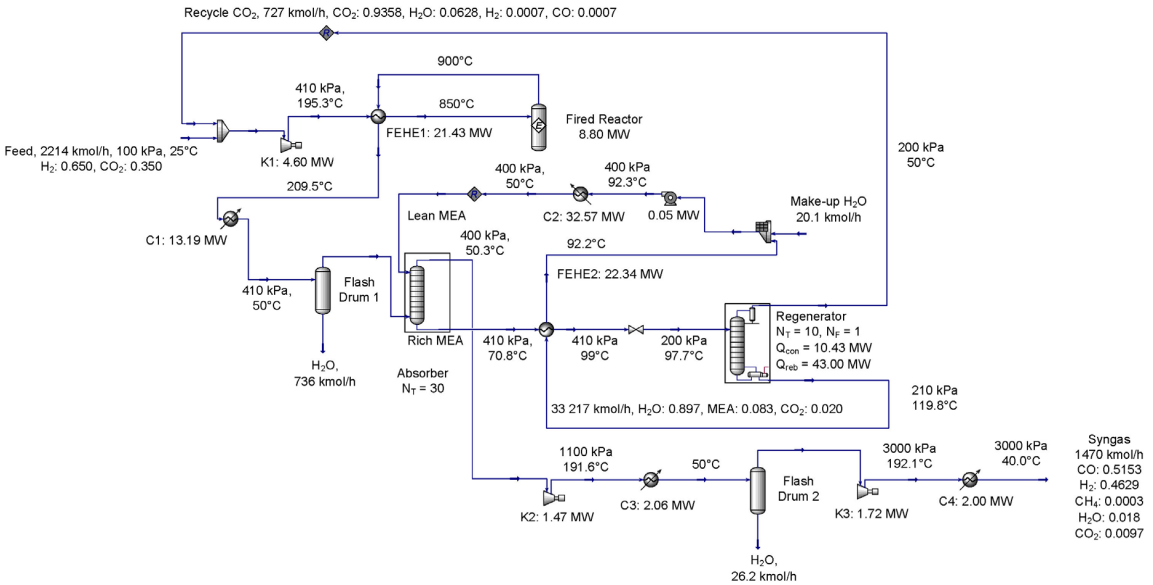

FIGURE 5 | The model used for the RWGS reaction based on Rezaei and Dzuryk (2019), adjusted to meet the requirements of the existing process. The flow compositions are on a molar basis.

has a high cooling demand, especially for the electrolyser, but also from two coolers and the condenser at the regenerator. The heating demand is mainly related to the reboiler of the regenerator. It should be noted that the internal heat exchanger FEHE1 (see **Figure 5**) was retained since the high driving force (logarithmic mean temperature difference of 30°C) and the small difference between the two temperature differences on the two sides (50 and 15°C) which indicate a good heat integration. Accordingly, the corresponding streams do not appear in the stream table.

Mass and Heat Integration Studies of the Reference Process as Well as the Electrified Process Using Pinch Analysis Tools

The following procedure was used to create the GCCs and split-GCCs for the heat integration studies:

1. A GCC for the reference case (current process configuration for the whole plant as shown in **Figure 2**) was created to identify minimum utility demands and district heating delivery potentials assuming maximum heat recovery.
2. A split-GCC for the reference case was constructed with the streams connected to conventional syngas production representing the foreground (see stream table in **Supplementary Appendix A**) and the remaining streams of the plant forming the background (see **Supplementary Appendix B**) to visualize potential heat flows between the foreground and the background.
3. A split-GCC with streams from the electrified syngas production in the foreground (see **Table 3**) and the remaining streams (see **Supplementary Appendix B**) was established to quantify the potential for heat integration.
4. A GCC for the oxo synthesis plant with electrified syngas production was established to derive utility demands and district heating potentials, assuming maximum heat recovery within the plant.

TABLE 3 | Stream table for the electrified syngas production consisting of RWGS reaction and AEC water electrolysis.

Sub-process	Type	Start temperature °C	Target temperature °C	Heat load MW
RWGS C1	Hot	210	50	13
RWGS C2	Hot	92	50	33
RWGS C3	Hot	192	50	2
RWGS C4	Hot	192	40	2
RWGS reboiler	Cold	120	120	43
RWGS condenser	Hot	50	50	11
Electrolyser	Hot	70	70	49

*C1–C4 are related to the coolers shown in **Figure 5**.*

The GCCs and split-GCCs were constructed assuming a global temperature difference for heat exchanging of 10°C. The curves were thereafter used to identify the heat integration potentials, energy targets and district heating delivery potentials.

Figure 6 shows the GCC and the split-GCC for the reference case based on **Figure 2** (including the downstream processing of syngas). The large heat pocket in the GCC decreases the minimum demand for hot utility which can be satisfied with LP steam (150°C). The district heating delivery potential was estimated for a supply and return temperature of 90°C and 55°C, respectively. The large cooling demand below the pinch temperature is mainly caused by the cooling requirements of

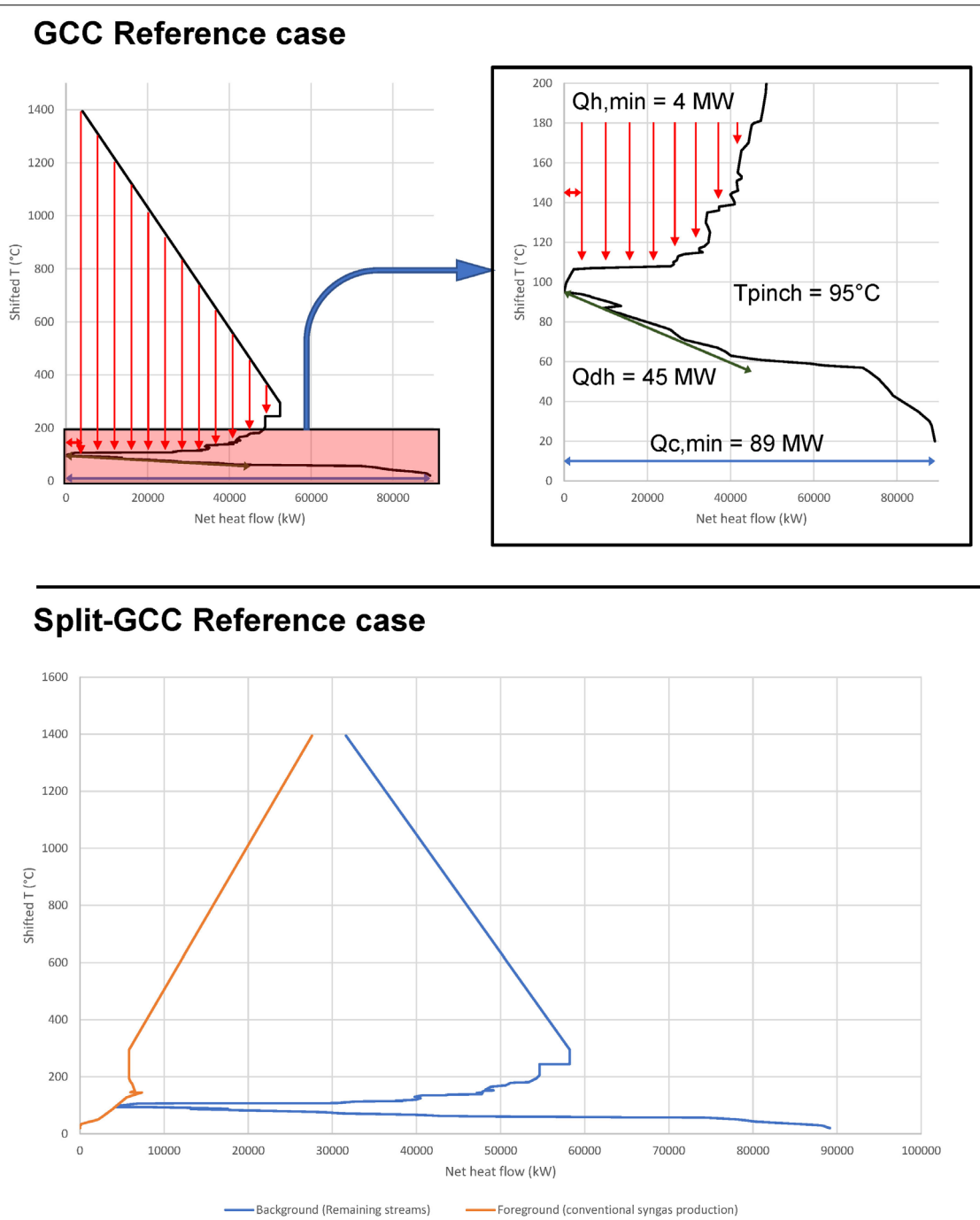

FIGURE 6 | GCC and split-GCC for the reference case. In the GCC, the minimum heating ($Q_{h,min}$) and cooling ($Q_{c,min}$) demands, as well as the district heating delivery potential (Q_{dh}) and the pinch temperature (T_{pinch}) are indicated. The red vertical arrows indicate heat flows within heat pockets.

the exothermic reactions related to the downstream processing of syngas. The split-GCC shows the source of the significant heat release from 1400°C to 300°C. One part can be seen in the foreground curve and stems from syngas cooling after the NC-POX reactor. The other part can be seen in the background process and is related to the combustion of process off-gases for steam generation, which was assumed to be unaffected by the proposed change of syngas production. The overlap of the foreground process in relation to the background process in the split-GCC shows clearly that surplus heat from conventional syngas production could be almost fully recovered to supply heat to other parts of the plant.

Figure 7 shows how the process is affected by electrifying the syngas production unit. The GCC shows that the heat

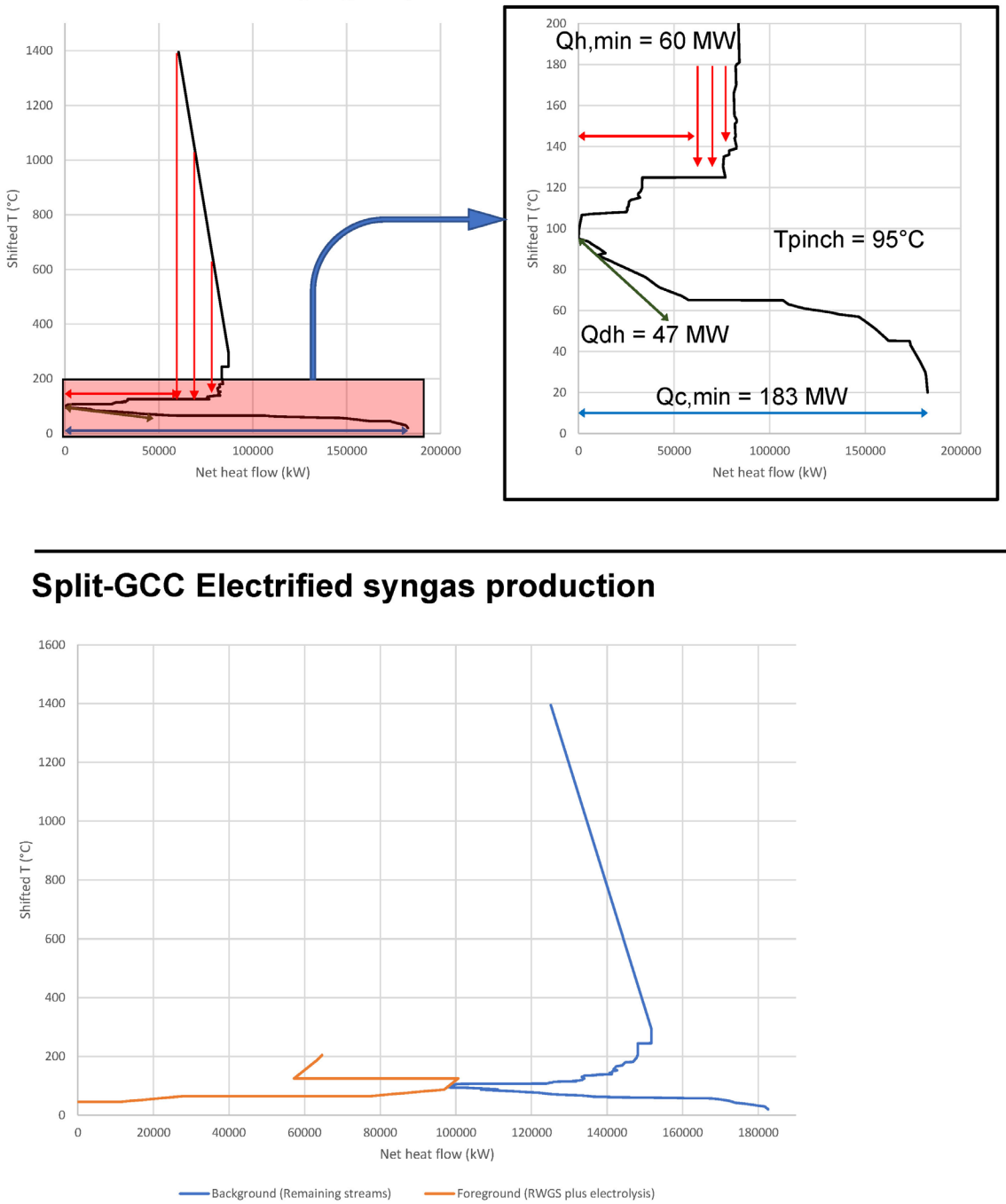

FIGURE 7 | GCC and split-GCC for the electrified syngas case. In the GCC, the minimum heating ($Q_{h,min}$) and cooling ($Q_{c,min}$) demands, as well as the district heating delivery potential (Q_{dh}) and the pinch temperature (T_{pinch}) are indicated. The red vertical arrows indicate the heat pocket.

pocket decreases while the minimum heating demand increases strongly. The split-GCC shows that this is because heat integration of the streams related to syngas production with the background process streams is basically not possible because of the low temperature level of the heat released in the foreground process. Rather than being able to provide heat to the background process, the electrified syngas production requires additional heat (mainly at 120°) for the reboiler in the RWGS process. In addition, the heating demand that could have been satisfied by surplus heat from conventional syngas production now has to be provided by external utility.

Figures 6, **7** show that the minimum hot utility demand, which in both cases can be satisfied by LP steam, increases by 56 MW while the cold utility demand increases by 94 MW when switching to electrified syngas production. It can also be seen that the district heating delivery potential varies only slightly between the two cases.

Inventory of All Relevant Changes in Input and Output Flows of Material and Energy Compared to the Reference Process

Table 4 shows a summary of mass and energy flows for the conventional and the electrified syngas production that are relevant for the techno-economic and greenhouse gas emission assessment. It was assumed that the fuel gas and off-gas demands can be handled as natural gas demands since this is the marginal fuel at the process site. The natural gas and electricity demands for LP steam production represent the demands that were identified from the heat integration studies. For the natural gas boiler, an efficiency of 90% was assumed. The results clearly highlight the consequences of switching from natural gas to electricity as main energy carrier when implementing electrified syngas production. It can also be seen that the electrified syngas production requires a large amount of CO_2 as feedstock while oxygen is generated as a new by-product. The energy demand for CO_2 separation was not considered since it was assumed that this is allocated to the source of CO_2 emissions. It can also be seen that the amount of tail gas is zero in the electrified syngas and steam production. This difference is not important since the tail gas is currently used to produce steam at the real plant that does not achieve maximum energy recovery. In the reference case with maximum heat integration, this amount of tail gas is not required.

TABLE 4 | Comparison of mass and energy flows for the conventional and the electrified syngas production.

Variable	Conventional syngas and steam production	Electrified syngas and steam production	Difference
Input	**MW**	**MW**	**MW**
Natural gas (total)	182	9	−173
• *NC-POX/RWGS*	*177*	*9*	
• *LP steam generation*	*5*	–	
Electricity (total)	11	278	+267
• *Air Separation Unit*	*11*	–	
• *Electrolysis*	–	*209*	
• *RWGS*	–	*8*	
• *LP steam generation*	–	*61*	
	t/h	**t/h**	**t/h**
Water	–	60	+60
CO_2 (feedstock)	–	34	+34
Output	**MW**	**MW**	**MW**
Syngas (H_2/CO ratio = 1.1)	115	115	0
Hydrogen	29	29	0
Tail gas	6.7	–	−6.7
District heating potential	45	47	+2.0
	t/h	**t/h**	**t/h**
Oxygen	–	33	+33

Techno-Economic and Greenhouse Gas Emission Assessment

Greenhouse Gas Emission Assessment

In the greenhouse gas emission assessment, on-site and off-site emissions were considered in terms of equivalent CO_2 emissions adopting a well-to-gate approach. The corresponding sources for greenhouse gas emissions are shown in **Figure 8**.

The on-site emissions from the conventional syngas production stem from combustion of natural gas to heat for the NC-POX reactor and produce utility steam. Off-site emissions arise from the production (extraction and preparation) and transport of natural gas and electricity (well-to-gate perspective).

For the electrified syngas production, the only on-site emissions are related to the combustion of natural gas to provide the high-temperature RWGS reaction heat. Off-site emissions stem from the production of natural gas and electricity (well-to-gate). In addition, the process is fed with CO_2 as feedstock that is assumed to be recovered from another process elsewhere. Since the assessment was a well-to-gate assessment, the emissions from the final products at the end of their lifetimes were not considered (since these were assumed to be the same for the reference and the electrified case), and the CO_2 feedstock was accounted as avoided emissions at the plant at which it was assumed to be captured. Emissions related to the production (e.g., by amine-based CO_2 capture which requires heat for the regenerator), and transport of the CO_2 feedstock were not considered since it was assumed that they were not allocated to the electrified syngas production plant. This is one of several approaches for handling CO_2 emissions in the context of carbon capture and utilisation (Tanzer and Ramírez, 2019).

The annual avoided greenhouse gas emissions (on-site and off-site), comparing the electrified with the conventional syngas production, were calculated as follows:

$$\Delta GHG = \left[P_{NG,NC-POX} * ghg_{NG,wtg+sg} - P_{NG,EL-Syngas} * ghg_{NG,wtg+comb} + (P_{EL,NC-POX} - P_{EL,EL-Syngas}) * ghg_{EL} + CO_{2,RWGS}\right] * t$$

with

- P_{NG}: natural gas demand in MW.
- P_{EL}: electricity demand in MW.
- ghg: corresponding greenhouse gas emission factors in CO_2eq/MWh (the abbreviation wtg stands for well-to-gate, comb stands for combustion while sg stands for syngas production).
- $CO_{2,RWGS}$: CO_2 feedstock demand for the RWGS reaction in kg/h.
- t: annual operating time in hours.

Based on Arvidsson et al. (2015), the greenhouse gas emissions from natural gas were assumed to be 53 kgCO_2eq/MWh for the sum of off-site emission and emissions related to the conventional syngas production ($ghg_{NG,wtg\ +\ sg}$) and 227 kgCO_2eq/MWh for

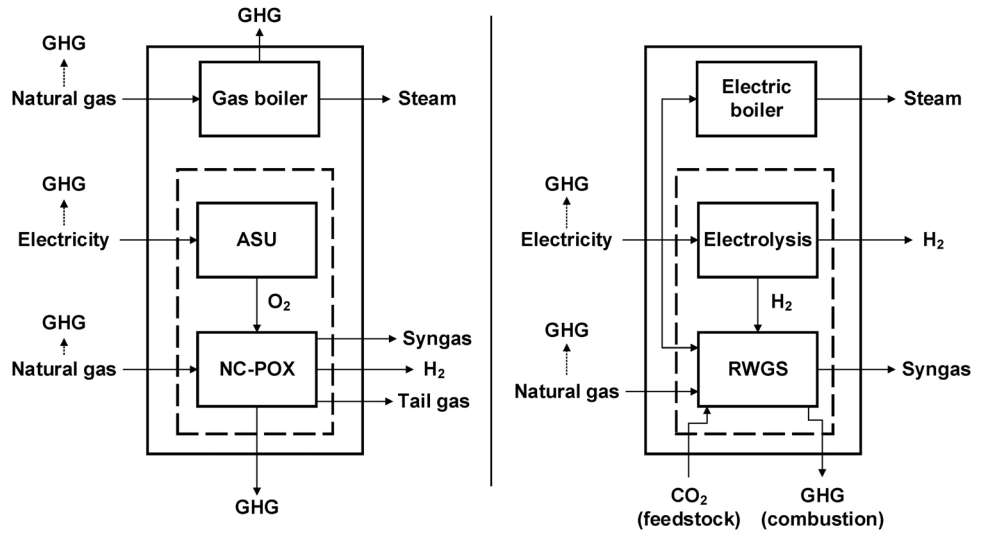

FIGURE 8 | On-site and off-site greenhouse gas (GHG) emissions for the conventional syngas production **(left)** and the electrified syngas production **(right)**. The dashed boxes represent the two syngas production technologies. Emissions crossing the solid-lines boxes are on-site emissions while emissions occurring outside of this box are off-site emissions.

the sum of off-site emissions and emissions from combustion ($ghg_{NG,wtg\ +\ comb}$). Furthermore, carbon-free power generation technologies such as wind and nuclear power were assumed as build margin power generation technology and the emission factor for electricity (ghg_{EL}) was set to zero. This assumption is based on the view that substantial electrification of industrial processes leads to a strong increase in electricity demand which in turn triggers investments in new electricity generation capacities. These new capacities must be essentially emission-free since large-scale electrification would otherwise not be acceptable. For wind and nuclear power, an emission factor of zero was assumed. This corresponds to emissions related to plant operation. Emissions related to plant construction and decommissioning are small over the lifetime of the plant. It should be noted that the greenhouse gas emissions related to electricity production are very low for Sweden already today (13 kg/MWh) due to the high share of hydro and nuclear power. Thus, the average emission factor of the electricity generation system is close to the marginal emission factors assumed in this study. The annual operating time was assumed to be 8000 h per year. Due to the small change in district heating delivery potential for the electrified syngas production (+2 MW), the district heating delivery was neglected in the emission assessment.

Techno-Economic Assessment

For the techno-economic assessment, the change in operating cost when switching to electrified syngas production was calculated as follows:

$$\Delta C = \left[(P_{NG,EL-Syngas} - P_{NG,NC-POX}) * c_{NG} + (P_{EL,EL-Syngas} - P_{EL,NC-POX}) * c_{EL} + CO_{2,RWGS} * c_{CO_2}\right] * t$$

with c as the corresponding cost factors.

The economic assessment was done for two energy market scenarios that were generated using the ENPAC tool (Axelsson and Harvey, 2010; Axelsson and Pettersson, 2014). Based on forecasted prices for fossil fuels on the commodity market and costs associated with emitting CO_2, the tool calculates energy prices, including natural gas and electricity prices, for large-volume customers. In this assessment, two scenarios based primarily on data from the "New policies" and the "Sustainable development" scenarios from IEA's World Energy Outlook 2018 (International Energy Agency, 2018) were generated, see Pettersson et al. (2020) for further details. The "New Policies" scenario is a predictive scenario that takes the impact of existing policy framework and today's announced policies into account. The "Sustainable Development" scenario on the other hand is a back-casting scenario in which energy-related CO_2 emissions peak in 2020 before they follow a trajectory that is fully aligned with the objectives of the Paris Agreement. The two scenarios were considered to study the effect of different ambition levels for greenhouse gas reduction. Scenario data for 2030 and 2040 was used to include a medium-term and a long-term perspective. In addition, it was assumed that the price for the CO_2 feedstock is zero as best-case scenario (see section "Discussion"). The corresponding cost factors are shown in **Table 5**. The cost for cold utility was not included in the assessment since cooling water is readily available in Sweden at a cost that is low compared to the cost connected to hot utility.

Overall Results

Table 6 summarises the resulting avoided greenhouse gas emissions and the changes in operating cost when comparing electrified syngas production and electric steam generation with conventional syngas production and fossil fuel-based steam generation for the two scenarios. The results indicate a large GHG emission savings potential, dominated by the CO_2 feedstock for

TABLE 5 | Cost factors generated with the ENPAC tool based on the two IEA World Energy Outlook 2018 scenarios "New Policies" and "Sustainable Development" (Pettersson et al., 2020).

Variable	Formula symbol	Unit	New Policies 2030	Sustainable Development 2040
CO_2 emission charge (general)	–	€/tCO_2	29	126
Natural gas price incl. CO_2 charge	c_{NG}	€/MWh	41	61
Electricity price incl. grid charge	c_{EL}	€/MWh	54	63
Build margin power generation technology	–	–	Wind power	Nuclear power
Price of CO_2 (feedstock)	c_{CO2}	€/tCO_2	0	0

TABLE 6 | Avoided GHG emissions and changes in operating cost for the two different scenarios.

Avoided GHG emissions	333 kt/a
• *Natural gas*	*77 kt/a*
• *Electricity*	*−16 kt/a*
• *CO_2 feedstock*	*272 kt/a*
Change in operating cost "New policies 2030"	+59 M€/a
• *Natural gas*	*−56 M€/a*
• *Electricity*	*+115 M€/a*
Change in operating cost "Sustainable Development 2040"	+50 M€/a
• *Natural gas*	*−85 M€/a*
• *Electricity*	*+135 M€/a*

the RWGS reaction. However, also the savings from the decreased use of natural gas are substantial. It should be noted that the greenhouse gas emission factors did not change between the scenarios. Both scenarios show a large increase in operating cost because of the strongly increased electricity demand. However, the increase is slightly smaller for the "Sustainable Development 2040" scenario in which the price difference between natural gas and electricity is very small. It should remember that no cost was assumed for the CO_2 feedstock.

DISCUSSION

The results from the case study underline the importance of accounting for heat integration opportunities at the site since the changes in heat recovery potential and utility demands when switching from conventional syngas and steam production to electrified syngas and steam production were not obvious. Process heat that from conventional syngas production process was no longer available to cover on-site heat demands and the electrification option further increased heat demands. This led not only to a high electricity demand for the electrification itself, but also to a significant increase in hot utility demand. The increased hot utility demand needs to be covered either by fuel combustion, which could partly outweigh the fossil feedstock avoided by the electrification or, as assumed in the case study, by heat production in an electric boiler, thus further increasing the site's electricity demand. The high electricity demand, in addition to a large demand for CO_2 feedstock, highlights two examples of challenges related to electrification. Furthermore, this highlights the importance of co-development of process electrification with decarbonisation of the electricity generation system.

The applicability and reliability of the bottom-up assessment framework depends strongly on the availability of detailed process data and models for existing unit operations and those that are connected to the process electrification option. Especially for new technologies, such data and models might not be available. Another integral and significant part of the assessment framework is the selection of system boundaries and energy market scenarios. The system boundaries must be selected carefully to allow a fair comparison with the reference cases but also with other options for greenhouse gas emission reduction. In the case study, the system boundary was extended to include off-site emission from natural gas and electricity production, as well the CO_2 uptake for the RWGS reaction to allow a holistic assessment. Especially for CO_2 feedstock, the system boundaries and the allocation of greenhouse gas emissions that are connected to the production of this CO_2 feedstock are not trivial. This is also the case for the assumptions about the prices of CO_2 feedstock and depends on the type of CO_2 (biogenic or fossil) and the capture process. In the case study, the CO_2 feedstock was treated as a free waste product from another plant. Although this approach can be found in other studies as well, it would also be possible to include greenhouse gas emissions connected to the production of CO_2 feedstock and to consider a certain price which could be based on the cost for capture. Furthermore, the choice of energy market scenarios has a strong impact on the greenhouse gas emission reduction potential and cost. It is important to include different scenarios based on different possible market developments since specific electrification options might perform well under one scenario but not for others. Such insights are crucial when it comes to the risk assessment of investments in electrification options. Costs related to upgrading the plant's grid connection capacity were not included since the focus of the methodology is to understand the impact of electrification on the existing processes itself and the resulting energy cost rather than the electric grid connection cost. However, this site-specific cost can potentially be large and cannot be neglected in the project planning if electrification options are to be implemented. It is also important to note that wide-spread electrification will require substantial investment in grid distribution capacity. These costs will ultimately be passed on to electricity users. Estimating such costs was not included in this study.

In the case study presented in this paper, off-site emissions related to the production and transport of natural gas and electricity were included. This is a good approach to get a more holistic picture of the overall emission consequences. However, specific plant owners might mainly be interested in greenhouse emissions that they can influence and that they are financially accountable for.

For the case study plant, it is suggested that this methodology is applied to other electrification options as well (single ones or in combinations) to also allow a comparison not only of electrification options versus the current situation (reference base) but also to allow a comparison among different

electrification options. The starting point is the inventory of electrification options for this plant. Results from these studies can also be used to allow a comparison with other decarbonisation options (e.g., increased use of biomass) to support industrial decision-making and guide the design of energy and environmental policies.

CONCLUSION

A bottom–up assessment framework for electrification options in energy intensive industrial process plants was presented and applied in a case study for an existing chemical plant. The broad variety of electrification options for industrial processes increases the necessity of such a systematic approach to identify promising options in terms of greenhouse gas emission reduction potential and energy costs. Since industrial process sites are often characterised by a high degree of process heat recovery, it is important to understand the interconnection between existing unit operations and the changes that result from introducing unit operations to increase process electrification on a detailed level.

The bottom–up assessment framework presented in this paper pays special regards to the on-site conditions of specific industrial plants and captures effects that are often overlooked in more general top–down studies that assume similar conditions for different industrial sites. A fundamental aspect of the framework is the inclusion of heat integration studies with pinch analysis tools to analyse how the heat surpluses or demands connected to electrification options change heat recovery potentials and utility demands. These effects can be substantial and complex and are usually not considered by top–down studies. However, they can be analysed using the proposed framework.

The framework also includes different energy market scenarios to investigate the performance for different future energy prices and costs related to greenhouse gas emissions. The careful selection of system boundaries and energy market scenarios is crucial to allow a fair comparison. The case study results as well as the fact that industrial process sites are usually very different suggest using the presented bottom–up approach to obtain a more accurate picture of the real greenhouse gas emission reduction potential and the cost for process electrification options.

The detailed assessment in the case when switching to electrified syngas and electrified steam production indicated natural gas savings of 173 MW while the electricity demand increased up to 267 MW, leading to a strong increase in energy costs but also avoided greenhouse gas emissions of 333 kt/a. For the two energy market scenarios for 2030 and 2040, the energy costs increase by 59M€/a and 50M€/a. Compared to the energy cost for the conventional syngas production, this equals an increase by 100% for the 2030 scenario and by 50% for the 2040 scenario.

The bottom-up assessment framework can be used to assess different electrification options and to compare them with a reference case or other greenhouse gas emission reduction measures and can complement top–down studies to get a more realistic picture of the greenhouse gas emission reduction potential and cost for process electrification.

DATA AVAILABILITY STATEMENT

All datasets presented in this study are included in the article/**Supplementary Material**.

AUTHOR CONTRIBUTIONS

All authors listed have made a substantial, direct and intellectual contribution to the work, and approved it for publication.

FUNDING

This work was conducted within the project "PROCEL Opportunities for decarbonisation of industrial processes through increased electrification" which was financed by the Swedish Energy Agency (project number P42221).

SUPPLEMENTARY MATERIAL

The Supplementary Material for this article can be found online at: https://www.frontiersin.org/articles/10.3389/fenrg.2020.00192/full#supplementary-material

REFERENCES

Andersson, V., Franck, P. -Å, and Berntsson, T. (2016). Techno-economic analysis of excess heat driven post-combustion CCS at an oil refinery. *Int. J. Greenh. Gas Control* 45, 130–138. doi: 10.1016/j.ijggc.2015.12.019

Arvidsson, M., Morandin, M., and Harvey, S. (2014). Biomass gasification-based syngas production for a conventional oxo synthesis plant - process modeling, integration opportunities, and thermodynamic performance. *Energy Fuels* 28, 4075–4087. doi: 10.1021/ef500366p

Arvidsson, M., Morandin, M., and Harvey, S. (2015). Biomass gasification-based syngas production for a conventional oxo synthesis plant - greenhouse gas emission balances and economic evaluation. *J. Clean. Prod.* 99, 192–205. doi: 10.1016/j.jclepro.2015.03.005

Axelsson, E., and Harvey, S. (2010). *Scenarios for Assessing Profitability and Carbon Balances of Energy Investments in Industry*. Report 2010:EU1Göteborg: AGS.

Axelsson, E., and Pettersson, K. (2014). *Energy Price and Carbon Balances Scenarios tool (ENPAC) – A Summary of Recent Updates*. Göteborg: Chalmers University of Technology.

Bahrmann, H., and Bach, H. (2012). *Oxo Synthesis. Ullmann's Encyclopedia of Industrial Chemistry*. Weinheim: Wiley-VCH.

Berenschot, C. E., Delft, Industrial Energy Experts Energy Matters, (2017). *Electrification in the Dutch Process Industry*. Available at: https://www.cedelft.eu/en/publications/download/2278 (accessed May 6, 2020).

Berghout, N., Meerman, H., van den Broek, M., and Faaij, A. (2019). Assessing deployment pathways for greenhouse gas emissions reductions in an industrial plant – A case study for a complex oil refinery. *App. Energy* 236, 354–378. doi: 10.1016/j.apenergy.2018.11.074

Brau, J.-F., and Morandin, M. (2014). Biomass-based hydrogen for oil refining: integration and performances of two gasification concepts. *Int. J. Hydrogen Energy* 39, 2531–2542. doi: 10.1016/j.ijhydene.2013.10.157

Brolin, M., Fahnestock, J., and Rootzén, J. (2017). *Industry's Electrification and Role in the Future Electricity System - A Strategic Innovation Agenda*. Available at: http://www.diva-portal.org/smash/get/diva2:1073841/FULLTEXT01.pdf (accessed May 6, 2020).

Bühler, F., Zühlsdorf, B., Nguyen, T.-V., and Elmegaard, B. (2019). A comparative assessment of electrification strategies for industrial sites: case of milk powder production. *Appl. Energy* 250, 1383–1401. doi: 10.1016/j.apenergy.2019.05.071

DECHEMA (2017). *Low Carbon Energy and Feedstock for the European Chemical Industry*. Available at: https://dechema.de/dechema_media/Downloads/Positionspapiere/Technology_study_Low_carbon_energy_and_feedstock_for_the_European_chemical_industry.pdf (Accessed May 6, 2020).

Delikonstantis, E., Scapinello, M., and Stefanidis, G. D. (2019). Process modeling and evaluation of plasma-assisted ethylene production from methane. *Processes* 7:68. doi: 10.3390/pr7020068

EPRI (1989). *Process Industries - Innovation through Electrotechnology*. Palo Alto, CA: EPRI.

EPRI (2009). *Program on Technology Innovation: Industrial Electrotechnology Development Opportunities*. Available at: https://www.epri.com/#/pages/product/1019416/ (accessed May 6, 2020).

European Parliament (2009). *Directive 2009/30/EC of the European Parliament and of the Council of 23 April 2009 amending Directive 98/70/EC as Regards the Specification of Petrol, Diesel and Gas-Oil and Introducing a Mechanism to Monitor and Reduce Greenhouse gas Emissions and Amending Council Directive 1999/32/EC as Regards the Specification of fuel Used by Inland Waterway vessels and Repealing Directive 93/12/EEC*. Available at: https://eur-lex.europa.eu/LexUriServ/LexUriServ.do?uri=OJ:L:2009:140:0088:0113:EN:PDF (accessed May 6, 2020).

European Roundtable on Climate Change and Sustainable Transition, (2019). *2019 State of the EU ETS Report*. Available at: https://ercst.org/wp-content/uploads/2019/05/2019-State-of-the-EU-ETS-Report.pdf (accessed May 6, 2020).

Foit, S. R., Vinke, I. C., de Haart, L. G. J., and Eichel, R.-A. (2017). Power-to-Syngas: an enabling technology for the transition of the energy system? *Angew. Chem. Int. Ed.* 56, 5402–5411. doi: 10.1002/anie.201607552

Gerres, T., Chaves, Ávila, J. P., Llamas, P. L., and San Román, T. G. (2019). A review of cross-sector decarbonisation potentials in the European energy intensive industry. *J. Clean. Prod.* 210, 585–601. doi: 10.1016/j.jclepro.2018.11.036

Grahn, M., and Jannasch, A.-K. (2018). *Electrolysis and Electro-Fuels in the Swedish Chemical and Biofuel Industry: a Comparison of Costs and Climate Benefits*. Sweden: f3 The Swedish Knowledge Centre for Renewable Transportation Fuels.

Gundersen, T. (2002). *A Process Integration Primer*. Available at: http://www.ivt.ntnu.no/ept/fag/tep4215/innhold/Retrofit-new.pdf (accessed May 6, 2020).

Hackl, R., Andersson, E., and Harvey, S. (2011). Targeting for energy efficiency and improved energy collaboration between different companies using total site analysis (TSA). *Energy* 36, 4609–4615. doi: 10.1016/j.energy.2011.03.023

International Energy Agency (2017a). *Renewable Energy for Industry - From Green Energy to Green Materials and Fuels*. Paris: International Energy Agency.

International Energy Agency (2017b). *Tracking Clean Energy Process 2017*. Paris: International Energy Agency.

International Energy Agency (2018). *World Energy Outlook 2018*. Paris: International Energy Agency.

Johansson, D., Berntsson, T., and Franck, P. -Å (2014). Integration of Fischer-Tropsch fuel production with a complex oil refinery. *Int. J. Environ. Sust. Dev.* 13, 50–73. doi: 10.1504/IJESD.2014.056413

Kemp, I. C. (2007). *Pinch Analysis and Process Integration*, 2nd Edn. Oxford: Butterworth-Heinemann.

Lechtenböhmer, S., Nilsson, L. J., Åhman, M., and Schneider, C. (2016). Decarbonising the energy intensive basic materials industry through electrification – Implications for future EU electricity demand. *Energy* 115, 1623–1631. doi: 10.1016/j.energy.2016.07.110

Oluleye, G., Smith, R., and Jobson, M. (2016). Modelling and screening heat pump options for the exploitation of low grade waste heat in process sites. *Appl. Energy* 169, 267–286. doi: 10.1016/j.apenergy.2016.02.015

Pettersson, K., Axelsson, E., Eriksson, L., Svensson, E., Berntsson, T., and Harvey, S. (2020). Holistic methodological framework for assessing the benefits of delivering industrial excess heat to a district heating network. *Int. J. Energy Res.* 2020, 2634–2651. doi: 10.1002/er.5005

Reller, C., Krause, R., Volkova, E., Schmid, B., Neubauer, S., Rucki, A., et al. (2017). Selective Electroreduction of CO2 toward ethylene on nano dendritic copper catalysts at high current density. *Adv. Energy Mater.* 7:1602114. doi: 10.1002/aenm.201602114

Rezaei, E., and Dzuryk, S. (2019). Techno-economic comparison of reverse water gas shift reaction to steam and dry methane reforming reactions for syngas production. *Chem. Eng. Res. Des.* 144, 354–369. doi: 10.1016/j.cherd.2019.02.005

Samadi, S., Lechtenböhmer, S., Schneider, C., Arnold, K., Fischedick, M., Schüwer, D., et al. (2016). *Decarbonization Pathways for the Industrial Cluster of the Port of Rotterdam*. Wuppertal: Wuppertal Institut.

Sandberg, E., Toffolo, A., and Krook-Riekkola, A. (2019). A bottom-up study of biomass and electricity use in a fossil free Swedish industry. *Energy* 167, 1019–1030. doi: 10.1016/j.energy.2018.11.065

Schwab, E., Milanov, A., Schunk, S. A., Behrens, A., and Schödel, N. (2015). Dry reforming and reverse water gas shift: alternatives for syngas production? *Chem. Ing. Tech.* 87, 347–353. doi: 10.1002/cite.201400111

Stork, M., de Beer, J., Lintmeijer, N., and den Ouden, B. (2018). *Chemistry for Climate: Acting on the need for speed - Roadmap for the Dutch Chemical Industry towards 2050*. Available at: https://www.vnci.nl/Content/Files/file/Downloads/VNCI_Routekaart-2050.pdf (accessed May 6, 2020).

Tanzer, S. E., and Ramírez, A. (2019). When are negative emissions negative emissions? *Energ. Environ. Sci.* 12, 1210–1218. doi: 10.1039/C8EE03338B

Wallerand, A. S., Kermani, M., Kantor, I., and Maréchal, F. (2018). Optimal heat pump integration in industrial processes. *Appl. Energy* 219, 68–92. doi: 10.1016/j.apenergy.2018.02.114

Conflict of Interest: ES was employed by the company CIT Industriell Energi AB.

The remaining authors declare that the research was conducted in the absence of any commercial or financial relationships that could be construed as a potential conflict of interest.

frontiers in Energy Research

ORIGINAL RESEARCH
published: 23 September 2020
doi: 10.3389/fenrg.2020.568465

System Design and Performance Evaluation of Wastewater Treatment Plants Coupled With Hydrothermal Liquefaction and Gasification

Rafael Castro-Amoedo, Theodoros Damartzis, Julia Granacher and François Maréchal*

Industrial Process and Energy Systems Engineering (IPESE), École Polytechnique Fédérale de Lausanne, Lausanne, Switzerland

Wastewater treatment and sludge disposal are responsible for considerable costs and emissions in a global scale. With population and urbanization growing, tackling the rational and efficient use of energy while fulfilling the desired effluent standards are imperative. In this work, a superstructure-based approach is designed to incorporate alternative treatments for wastewater. In particular, technologies like hydrothermal liquefaction and gasification, coupled with technologies for CO_2 conversion to value-added products are studied. Multi-objective optimization is applied as a way to generate multiple solutions that correspond to different system configurations. From a reference treatment cost of almost 0.16 $\$/m^3_{WW}$, an environmental impact of 0.5 $kgCO_2/m^3_{WW}$ and an energy efficiency of 5%, different configurations are able to transform a waste water treatment plant to a net profit unit, with a net environmental benefit and energy efficiency close to 65%. The investment in hydrothermal liquefaction producing biocrude coupled with catalytic hydrothermal gasification demonstrated to yield consistently better total costs and environmental impacts. Parametric analysis is performed in the inlet flow of wastewater to account for different sizes of waste water treatment plant, with smaller inlets achieving values closer to those of the state-of-the-art configuration.

Keywords: wastewater treatment plants, hydrothermal liquefaction, catalytic hydrothermal gasification, sustainability, efficiency

OPEN ACCESS

Edited by:
Antonio Espuña, Universitat Politecnica de Catalunya, Spain

Reviewed by:
Mariano Martín, University of Salamanca, Spain
Athanasios I. Papadopoulos, Centre for Research and Technology Hellas (CERTH), Greece

****Correspondence:***
Rafael Castro-Amoedo
rafael.amoedo@epfl.ch

Specialty section:
This article was submitted to Process and Energy Systems Engineering, a section of the journal Frontiers in Energy Research

Received: *01 June 2020*
Accepted: *19 August 2020*
Published: *23 September 2020*

Citation:
Castro-Amoedo R, Damartzis T, Granacher J and Maréchal F (2020) System Design and Performance Evaluation of Wastewater Treatment Plants Coupled With Hydrothermal Liquefaction and Gasification. Front. Energy Res. 8:568465. doi: 10.3389/fenrg.2020.568465

1. INTRODUCTION AND STATE OF THE ART

With increasing population growth, urbanization and industrialization, wastewater treatment plants (WWTPs) are of vital importance. Not only do they directly impact the aquatic ecosystem, but they also play a pivotal role in guaranteeing water security in a world scenario of hydric stress (OECD, 2012). Primarily focused on removing impurities from wastewater, practitioners used to pay little attention to both energy and environmental bill of their facilities. However, due to unavoidable legalization and even public perception, the water-energy nexus has become a key topic in the field (Gu et al., 2017), with the scientific community working to manage both, wastewater treatment quality and energy efficiency. WWTPs are generally the facilities with the highest energy bill in a municipality.

Abbreviations: WWTP, Wastewater treatment plant; WW, Wastewater; HTL, Hydrothermal liquefaction; CHTG, Catalytic hydrothermal gasification; TS, Total solids; VS, Volatile solids; OPEX, Operating expenditures; CAPEX, Capital expenditures; TC, Total cost; SNG, Synthetic natural gas; SOFC, Solid oxide fuel cell; SN, Steam network.

This refers up to 5% of the total electrical energy load (Chen and Chen, 2013), while the energy consumption is responsible for up to 40% (Panepinto et al., 2016) of the operating costs in such plants.

Low quality feedstocks are inherently difficult to valorize, one of the main reasons being typically the high amount of water they contain. Water can be removed by means of filtration and thermal drying, but that usually comes to a tremendous energetic (and economic) cost. Particular technologies have been developed to lead with this setback, profiting from the abundant availability of feedstocks as well as its price (typically free of charge).

In a study developed by Ang et al. (2019), the overall efficiency, costs, and impact are tackled, while introducing multiple input treatment options as well as several disposal scenarios. However, it does not consider different conversion pathways for wastewater, but it rather focuses on the conventional system configuration.

WWTP that rely only on biogas production and use it as heat and power source face a problem particularly difficult in summer and in southern latitudes. Indeed, with practically no storage of biogas being done industrially, biogas has to be burnt and the heat evacuated. This results in tremendous energetic losses as the demand in those periods is low. To this end, the production of biocrude and synthetic natural gas (SNG) as representative liquid and gaseous fuels, respectively, seems an interesting alternative. This is due to the fact that apart from the simultaneous production of fuels, it also offers storage options and thus is able to provide additional flexibility to the energy system.

Hydrothermal treatment coupled with WWTP has been already studied in the literature. Elliott (2020) considered the valorization of the plant's effluent for the production of biocrude using hydrothermal liquefaction (HTL). Similarly, Chen et al. (2014) focused their study on the feasibility of converting a mixed-culture algal biomass, and thus the exploitation of the contained carbon and the subsequent production of biocrude. On the other hand, hydrothermal gasification of sewage sludge has gained a prominent attention as well. Mainly focused in the production of SNG (Gassner et al., 2011), or even targeted in hydrogen (He et al., 2014), it offers an interesting alternative CO_2.

CO_2 removal from gaseous effluents and subsequent upgrading to value-added products has led to a growing number of publications in this field (Olajire, 2010). Indeed captured CO_2 can be transformed from a waste to a raw material and act as the building block molecule for the synthesis of organic compounds, with the primary focus of synthesizing biofuels but also biochemicals. A number of different processing routes have been proposed including the catalytic hydrogenation of CO_2 to methanol and olefins (Pérez-Fortes et al., 2016), SNG (Gorre et al., 2019), diesel (Dimitriou et al., 2015), and jet fuels (Willauer et al., 2012), to name a few. However, capturing CO_2 in industrial processes is responsible for around 75% of the overall cost of carbon capture and storage (Olajire, 2010).

Concerning mathematical approaches, a large majority of the publications focus either on environmental impact or economic implications of adopting a given configuration or treating a specific amount of wastewater. However, this approach is unable to capture the required trade-offs that decision-makers (DM) are looking for—solutions that are a compromise between sound environmental benefit and low to moderate economic costs. Sometimes DM look also for high efficiencies as objective, which might result to unbearable investment costs.

Indeed, most of the existing studies deal with the processing of the WWTP effluents in a straightforward rather than a systematic and explorative way. To the best of the authors' knowledge, there is no research addressing systematically the competition between the three main pathways, namely the benchmark system for biogas production, and the valorization through HTL and gasification for biocrude and SNG production respectively, exploring the synergies and opportunities of material, energy and economic integration.

The work developed in this publication utilizes system optimization as a solution generator. Thus costs, impacts and efficiencies of different system configurations of treatment options integrated in a WWTP are revealed. Consequently, system flexibility is increased to address challenging environmental regulations by means of multi-objective optimization (MOO) coupled with a superstructure-based approach.

The structure of this work is as follows: In Section 2, a superstructure-based approached is depicted and the main building blocks of the system are described; Section 3 shows the methodology followed as well as the key performance indicators (KPI) chosen to characterize the competing configurations. In Section 4, results are presented and discussed and finally in Section 5, conclusions are drawn and summarized.

2. PROCESS DESCRIPTION AND MODELING

A superstructure-based approach is the design methodology followed in this work to assess different wastewater thermochemical conversion routes, corresponding to the use and/or combination of different technologies. A similar approach has been proposed and used by several authors (Maronese et al., 2015; Santibañez-Aguilar et al., 2015). All process units are represented as black-box models, built by assessing the conversion features, either from extensive literature review or real, operating, units. Flowsheeting software (e.g., Belsim Vali) is used to describe the complex processes and is the base for the linearization of the mass and energy flows, based on a reference size (typically the inlet mass flow). The linear nature of the approach is kept by assuming linear operating and investment costs, as well as process efficiency. Flows entering and leaving a model boundaries allow connections between different technologies, granting a simple and fast integration and connection between them.

The superstructure proposed (**Figure 1**) tackles the challenge of wastewater treatment coupled with sludge handling, disposal and valorization.

The relevant units are described below, where only the most important assumptions will be discussed. All assumed

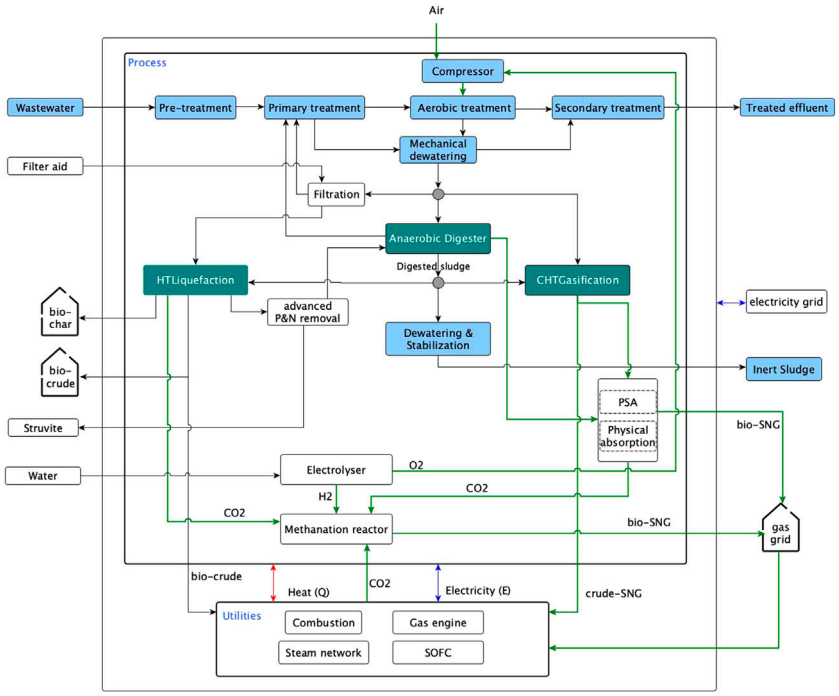

FIGURE 1 | Wastewater superstructure.

parameters, ranging from economic (**Tables 1** and **2**), environmental (**Table 3**) and thermodynamic/operating (**Table 4**) are to be found in the end of this section. For environmental considerations, only the most impactful units/flows were considered.

2.1. Wastewater Treatment Plant

WWTP are considered sources of CO_2, CH_4, and N_2O, due to the unavoidable leaks of biological processes taking place (aerobic and anaerobic treatments). According to Molinos-Senante et al. (2018) who modeled wastewater energy intensity for a large spectrum of facilities, WWTPs are energy intensity facilities. Average energy demand profiles were taken and incorporated in the model.

The light blue boxes (**Figure 1**) contain the backbone units of a classic, state-of-the-art WWTP. Wastewater is cleaned from contaminants and carbon-rich substances and leaves as a treated effluent that can be safely discharged in a receiving body. In the process, sludge is formed (primary and secondary), dewatered and sent to anaerobic digestion for biogas production, which is used to supply local energy needs. The remaining solid digestate is a major liability that needs drying and stabilization and imposes a cost for disposal in the overall WWTP system.

2.2. Hydrothermal Liquefaction

HTL is a thermochemical conversion process that makes use of water present in the feedstock to produce biocrude, a raw material for liquid transportation fuels, thus fully replacing crude oil. It mainly consists of a thermal degradation step to break down the large carbon chains contained in the biomass feedstock, the dissolution of useful materials in water and a recombination

TABLE 1 | Investment and operating costs for current and potential technologies.

Unit	c_u^{inv1} (***k***)	c_u^{inv2} (***k***/attribute)	Attribute	c_u^{op}	References
Waste water treatment plan	—	—	—	0.1 \$/m^3_{WW}	Gikas (2017)
P&N removal	—	—	—	350 \$/$ton_{Struvite}$	Huang et al. (2014)
Hydrothermal liquefaction	3,065	2,130	$dryton/h$	7.5 \$/dryton	Zhu et al. (2014), Snowden-Swan et al. (2016)
Hydrothermal liquefaction filter	324	1.8	m^2	—	Turton (2018)
Catalytic hydrothermal gasification	3,507	3,113	MW_{sludge}	94 \$/MWh_{sludge}	Gassner et al. (2011)
Solid oxide fuel cell	—	4.8	kW	—	Rubio-Maya et al. (2011)
Electrolyser	—	1.1	kW	—	Schmidt et al. (2017) and Hidalgo and Martín-Marroquín (2020)
Methanation	449	7.7	m^3_{CH4}/h	—	Turton (2018)
Engine	8.9	1.6	kW_{el}	—	Turton (2018)
Pressure swing adsorption	865	1.0	m^3/h	0.05 \$/m^3_{inlet}	Urban et al. (2009)
Steam network	1,390	1,700	MW_{el}	—	Turton (2018)

TABLE 2 | Reference environmental impacts of main activities.

Parameter	Description	Unit	Value	References
$k_{CO_2,WWTP}$	Impact of treating 1 $m^3$of wastewater (up to 4.7×10^{10}L/year)	kg_{CO_2}/m_3	290.4	Eco-invent 3.6
$k^-_{CO_2,biocrude}$	Impact of selling 1 kg of biocrude[1]	kg_{CO_2}/kg	−0.781	Eco-invent 3.6
$k^-_{CO_2,Struvite}$	Impact of replacing conventional phosphorus fertilizer by 1 kg of struvite	kg_{CO_2}/kg	−0.35	de Vries et al. (2016)
$k^+_{CO_2,gasgrid}$ $-k^-_{CO_2,gasgrid}$	Impact of buying/selling 1 MW h of natural gas from/to the grid (Europe)	kg_{CO_2}/MWh	149/−149	Eco-invent 3.6
$k_{CO_2,e}$	Impact of buying/selling 1 MW h of electricity from/to the grid (Europe)	kg_{CO_2}/MWh	356/−356	Kantor and Santecchia (2016)

[1]*Impact of replacing 66% of 1 kg of crude oil.*

(polymerization) step for the synthesis of the final products (Gollakota et al., 2018). As such, it is able to handle feedstocks with high moisture level (up to 90% content), avoiding the drying step that is needed for other kinds of technologies (Snowden-Swan et al., 2016). Wet wastes (like sludge) are usually readily available, thus dismissing preprocessing and preparation steps associated with lignocellulosic based feedstocks (He et al., 2014); Four products are obtained from HTL: i) biocrude, which is the main desirable product, ii) aqueous co-products (ACP) accounting for up to 75% of weight in product distribution, iii) biochar, which is a solid residue rich in carbon, retaining up to 45% of inlet carbon content, and iv) a gaseous stream, mainly constituted by CO_2 and H_20.

Albeit little attention has been given to the aqueous effluent, a great deal of carbon and other nutrients need treatment and valorization. A recent publication on the characterization of the aqueous stream compares several feedstocks with different operating conditions; in particular primary, secondary, and digested sludges are analyzed (Maddi et al., 2017). The authors conclude that higher lipid content results in increased biocrude yields, while more proteic substrates (present in high amounts in secondary sludge) are associated with higher (more than double) carbon amount in aqueous phase. For this reason it is suggested to use HTL either directly in digested sludge or in pre-digested sludge as a mixture of primary and secondary sludges. Bauer et al. (2018) also analyzed different feedstocks for HTL. They concluded that pre-digested as well as digested sludge show higher biocrude yields compared to other sources of waste. This study focuses also in evaluating the quantity and quality of the ACP. It is also reported that the ACP of liquefaction is far more noxious than common industrial wastewaters, requiring treatment before discharge. This might compromise the economic viability of stand-alone HTL units. It is, however, a decisive incentive to couple HTL in a WWTP, in order to benefit from process symbiosis.

HTL works at temperatures ranging from 250 up to 380°C and pressures up to 30 MPa, with residence times spanning from 5 to 60 min (Mørup et al., 2012). Oxygen removal is of critical importance, as lower concentrations allow higher heating values of bio-oil (around 35 MJ/kg). When compared with competing processes, like gasification and pyrolysis systems, HTL has a lower energy penalty as it avoids the water vaporization step.

Filtration followed by hydrothermal co-liquefaction has recently proved to be particularly efficient for wastewater sludge with different solids content (Biller et al., 2018; Anastasakis et al., 2018), and thus is included as an option for the superstructure. Indeed, higher performances are achieved, and operating costs are reduced, due to the avoided catalyst in the main reaction step. A schematic representation for a reference flow of 1,000 kg/h of inlet sludge is depicted in **Figure 2**. Different feedstocks compositions are handled by conversion to a generic layer, according to experimental results given by Snowden-Swan et al. (2016) and Bauer et al., (2018).

2.3. Catalytic Hydrothermal Gasification

Similarly to HTL, Catalytic hydrothermal gasification (CHTG) is able to valorize intrinsically difficult low quality feedstocks, being

TABLE 3 | Utilities operating costs and general economic assumptions.

Parameter	Description	Unit	Value	References
c^{op}_{disp}	Cost of disposing sludge per ton	$/ton	20	Snowden-Swan et al. (2016)
$c^+_{filteraid}$	Cost of buying 1 dry ton of filter aid	$/dryton	9.5	de Vries et al. (2016)
$c^+_{naturalgas}$	Cost of buying 1 MW h of natural gas from the grid	$/MWh	26	Main tables—Eurostat
c^+_e	Cost of buying 1 MW h of electricity from the grid	$/MWh	78	Main tables—Eurostat
c^+_{CW}	Cost of Cooling water (DT = 10°C)	$/MWh	5.2	Turton (2018)
$c^-_{struvite}$	Cost of selling 1 ton of struvite	$/ton	55	de Vries et al. (2016)
$c^-_{biocrude}$	Cost of selling 1 ton of biocrude	$/ton	220	—
$c^-_{bio-SNG}$	Cost of selling 1 MW h of bio-SNG	$/MWh	120	Gassner et al. (2011)
c^-_e	Cost of selling 1 MW h of electricity from the grid	$/MWh	180	Gassner et al. (2011)
$CEPCI_{2018}$	CEPCI index	—	603.1	—
n	Expected project lifetime	Years	20	—
i	Interest rate	—	0.08	—
t_{op}	Operating time	h/y	8,760	—

TABLE 4 | General assumptions and operating conditions.

Section	Operating conditions	Symbol	Unit	Default/value	References
Wastewater	Inlet flow	$\dot{m}^{+}_{WW}$	m^3/h	25,000	Snowden-Swan et al. (2016)
	Inlet solids fraction	–	g/kg	0.4	Biller et al. (2018)
	Wastewater heating value (wt)	Δh^{0}_{WW}	kJ/kg	16.8	Heidrich et al. (2011)
Primary sludge	Primary sludge composition (C, H, O, N)	—	wt% daf	47.8, 6.5, 6.6, 33.6	Maddi et al. (2017)
Secondary sludge	Secondary sludge composition (C, H, O, N)	—	wt% daf	43.6, 6.6, 7.9, 29.0	Maddi et al. (2017)
Digested sludge	Digested sludge composition (C, H, O, N)	—	wt% daf	38.7, 5.7, 4.5, 27.9	Maddi et al. (2017)
WWTP	Specific electricity need	e^{+}_{WWTP}	kWh/m^3_{WW}	0.6	Molinos-Senante et al. (2018)
	Primary sludge solids fraction (wt)	—	—	0.05	Biller et al. (2018)
	Secondary sludge solids fraction (wt)	—	—	0.017	Biller et al. (2018)
Aerobic reactor	O_2/VS ratio	O_2/VS	—	2.3	Andreoli et al. (2007)
	VS/TS ratio in secondary sludge	VS/TS	—	0.775	Andreoli et al. (2007)
	Volatile solids reduction	—	—	0.5	Andreoli et al. (2007)
	Oxygen transfer efficiency	r_{O_2}	—	0.1	Andreoli et al. (2007)
	Retention time	t_{ret}	Days	15	Andreoli et al. (2007)
Anaerobic digestor	Height to diameter ratio	H/D	—	3.5	Andreoli et al. (2007)
	Biogas yield per kg of VS	$Yield_{Biogas}$	m^3/kg	0.115	Andreoli et al. (2007)
	CH_4 Fraction in biogas	—	—	0.65	Andreoli et al. (2007)
	Inlet solids fraction (wt)	$Digestor_{solids}$	–	0.05	Andreoli et al. (2007)
	Reactor design parameter	—	kg_{vs}/m^3d	1.4	Andreoli et al. (2007)
	Temperature of digestor mesophilic regime	$T_{digestor}$	°C	35	Andreoli et al. (2007)
	External temperature	$T_{external}$	°C	20	—
	Temperature of inlet sludge	$T^{Digestor}_{Sludge}$	°C	20	—
	Heat transfer coefficient	$U_{digestor}$	$kWm^2°C$	0.0025	Andreoli et al. (2007)
Drying WWTP	Outlet solids fraction (wt)	$Dried_{solids}$	–	0.3	Andreoli et al. (2007)
	Heat requirements per kg of dry solids	$\dot{q}^{+}_{Drying}$	kWh/kg	0.61	Grobelak et al. (2019)
Struvite formation	Phosphorous and nitrogen recovery efficiency	—	—	0.9	Kataki et al. (2016)
	Struvite to wastewater ratio	—	—	0.0193	de Vries et al. (2016), Kataki et al. (2016)
HTL	Temperature of sludge feed	T^{HTL}_{sludge}	°C	25	–
	Temperature of HTL reactor	$T_{reactor}$	°C	340	Snowden-Swan et al. (2016)
	Temperature of biocrude exiting HTL	$T_{biocrude}$	°C	80	Tzanetis et al. (2017)
	Filter aid solids fraction (wt)	$filter_{solids}$	–	0.6	Snowden-Swan et al. (2016)
	Filter aid to sludge ratio (wt)	$ratio_{filter}$	–	0.25	Biller et al. (2018)
	Inlet solids fraction (wt)	HTL_{solids}	–	0.2	Biller et al. (2018)
	Biocrude yield (dry basis) per kg of solids entering	$Yield_{Biocrude}$	kg/kg_{solids}	0.44	Biller et al. (2018)
	Biocrude moisture content	$Moisture_{Biocrude}$	—	0.14	Anastasakis et al. (2018)
	Gas yield per kg of solids entering HTL	$Yield_{Gas}$	kg/kg_{solids}	0.19	Biller et al. (2018)
	Aqueous co-product yield per kg of solids entering HTL	$Yield_{ACP}$	kg/kg_{solids}	4.04	Biller et al. (2018)
	Bio-char yield per kg of solids entering HTL	$Yield_{bio-char}$	kg/kg_{solids}	0.33	Biller et al. (2018)
	Net heat requirement HTL	$\dot{q}^{+}_{HTL}$	kWh/kg_{inlet}	0.061	Biller et al. (2018)
	Filtration efficiency (wt)	$Eff_{Filtration}$	—	0.85	Biller et al. (2018)
	Reference area for HTL filter	$Area_{Filtration}$	m^2/m^3h	5.14	Daniel et al. (2009)
	Carbon partition in (biocrude, ACP, gas, biochar)	—	—	0.59, 0.25, 0.07, 0.09	Biller et al. (2018)
	Specific electricity need per kg of inlet sludge	e^{+}_{HTL}	kWh/kg	0.012	(Anastasakis et al., 2018)
	Lower heating value of biocrude	$\Delta h^{0}_{Biocrude}$	kJ/kg	37,800	Snowden-Swan et al. (2016)
	Lower heating value of filter aid	$\Delta h^{0}_{filter_{aid}}$	kJ/kg_{dry}	17,100	Biller et al. (2018)
	Biocrude density	Biocrude	kg/m^3	1,000	Snowden-Swan et al. (2016)

(Continued on following page)

TABLE 4 | (*Continued*) General assumptions and operating conditions.

Section	Operating conditions	Symbol	Unit	Default/value	References
CHTG	Inlet solids fraction (wt)	$CTHG_{solids}$		0.2	Gassner et al. (2011)
	Temperature of catalytic reactor	$T_{reactor}$	°C	350	Gassner et al. (2011)
	HTG process pressure	$P_{reactor}$	Bar	250	Mian et al. (2015)
	Net heat availability CHTG	$\dot{q}^{-}_{CHTG}$	kWh/kg_{inlet}	0.051	Gassner et al. (2011)
	Salt separation temperature	T_{salt}	°C	415	Gassner et al. (2011)
Gas upgrading	Water absorption pressure	$P_{absorption}$	Bar	250	Mian et al. (2015)
	Water absorption pressure stages	N_{stages}	—	5	Mian et al. (2015)
	Gas grid pressure	P_{grid}	Bar	70	Mian et al. (2015)
	Gas grid CH_4 quality	$Quality_{grid}$	—	0.98	Mian et al. (2015)
	Gas expander isentropic efficiency	Eff_{Gas}	—	0.8	Mian et al. (2015)
	Liquid expander isentropic efficiency	Eff_{Liquid}	—	0.82	Mian et al. (2015)
Pressure swing adsorption	Specific electricity needs	e^{+}_{PSA}	kWh/m^3	0.17	Urban et al. (2009)
	CH_4 recovery factor	$CH_{4recovery}$	—	0.98	Urban et al. (2009)
Engine	Thermal efficiency	$Eff_{thermal}$	—	0.55	Turton (2018)
	Electrical efficiency	$Eff_{electrical}$	—	0.31	Turton (2018)
	Heat availability temperature interval	T_{engine}	°C	[550–150]	–
Methanation	Specific electricity needs	$e^{+}_{Methanation}$	kWh/kg_{H2}	0.78	Wang et al. (2018)
	Available heat	$\dot{q}^{-}_{Methanation}$	kWh/kg_{H2}	9.1	Wang et al. (2018)
	Heat availability temperature interval	$T_{methanation}$	°C	[625–28]	Wang et al. (2018)
Solid oxide fuel cell	Specific electricity production	e^{-}_{SOFC}	kWh/kg_{CH4}	11.5	Facchinetti et al. (2011)
	Available heat	$\dot{q}^{-}_{SOFC}$	kWh/kg_{CH4}	3.2	Facchinetti et al. (2011)
	Heat availability temperature interval	T_{SOFC}	°C	[649–30]	Facchinetti et al. (2011)
Electrolysis	Specific electricity needs	$e^{+}_{Electrolysis}$	kWh/kg_{H_2O}	4.7	Wang et al. (2018)
	Available heat	$\dot{q}^{-}_{Electrolysis}$	kWh/kg_{H_2O}	0.2	Wang et al. (2018)
	Heat availability temperature interval	$T_{Electrolysis}$	°C	[91-27]	Wang et al. (2018)
Rankine cycle	Production level	—	—	50 bar (T_{sat} = 264°C), superheating of 100°C	—
	Utilization levels	—	—	5 bar (152°C) and 1.98 bar (120°C)	—
	Condensation level	—	—	0.1 bar (T = 46°C)	—
General assumptions	Lower heating value of SNG and Ngas	Δh^{0}_{SNG}	kJ/m^3	47,100	—
	Boiler thermal efficiency	Eff_{Boiler}	—	0.9	Turton (2018)
	Heat recovery minimum approach temperature	ΔT_{min}	°C	5	—
	Turbo-machinery efficiency (isentropic)	—	—	0.8	—

WWTP, wastewater treatment plant; HTL, hydrothermal liquefaction; CHTG, catalytic hydrothermal gasification.

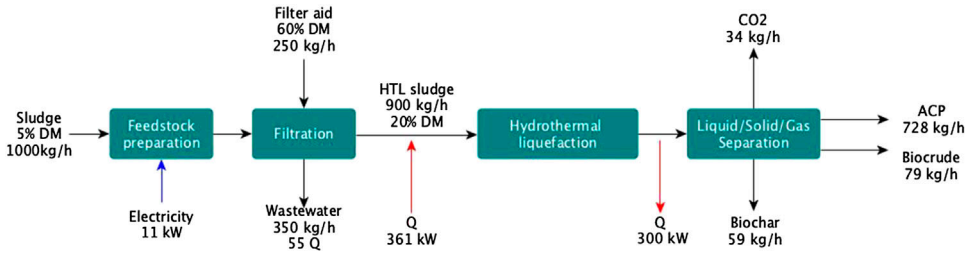

FIGURE 2 | Hydrothermal liquefaction schematic representation.

particularly suitable for those with more than 80% water content. The water evaporation step is by-passed as water is kept in the liquid phase under the imposed supercritical conditions, thus avoiding supplying the heat of vaporization. SNG or bio-SNG can be produced if upgraded from a methane rich gas leaving the catalytic reactor. The process diagram, **Figure 3**, shows the main steps including the upgrading, energy, and material needs.

Operating conditions and process description were the ones reported elsewhere (Gassner et al., 2011; Mian et al., 2015), using 20% solids content as input.

2.4. Phosporous and Nitrogen Recovery/ Struvite Formation

Besides Sun, water, and CO_2, minerals are a crucial nutrient for crops growth; in particular phosporous (P), nitrogen (N), and potassium (K) are the most relevant. Crop yields may be increased up to 100% by increasing the amount of nutrients in the soil, according to a recent report on struvite recovery (de Vries et al., 2016).

Mineral fertilisers (phosphate rock) are a non-renewable resource. Struvite ($MgNH_4PO_4{\cdot}6H_2O$) is a fertiliser that can be obtained from wastewater with high concentrations of both P and N; it can be precipitated by the addition of magnesium salts under basic conditions. Despite a lower solubility in water struvite is able to replace mineral fertilisers on a P_2O_5 basis (Degryse et al., 2017), including some cases where it performs statistically better (Li et al., 2019).

In a review of struvite from several feedstocks (Kataki et al., 2016), six different recovery technologies were described. Applied to municipal wastewater and with industrial applicability, only chemical precipitation is used. Fluidized bed reactors are the most deployed reactor for chemical precipitation (Li et al., 2019) and they were used as the modeling base in the present work. High P recovery (up to 90%) is reported, despite the addition of some P and/or NH_4 salts, that accounts for a large share (up to 90%) of operating costs (Ye et al., 2020).

In a recent review focusing on bottlenecks and challenges of struvite formation, Li et al. (2019) have shown that implementing struvite precipitation as a post-treatment technology (as implemented in **Figure 1**) for both P and N recovery helps reducing the burden associated with hydrothermal treatments. Furthermore, it reduces the volume that needs treatment in a WWTP.

From the cost perspective, several authors (Mayer et al., 2016; Kataki et al., 2016) agree on the non-profitability of recovering struvite by means of chemical precipitation, due to the low market value motivated by low market cost of rock phosphate. Struvite market prices are not consensual; 55 €/ton was taken as a reference (de Vries et al., 2016), which is the closest to commercial P fertilizers. Concerning operating costs, 350 €/ton of struvite were considered (Huang et al., 2014), coherent with the values reported in Mayer et al. (2016), and accounting for average values of chemical compounds added in a wastewater treatment environment. Complementary, Li et al. (2019) report that a selling price close to 430 $/ton of struvite would be enough to guarantee the investment on a plant in Belgium. The same reference asks for more research

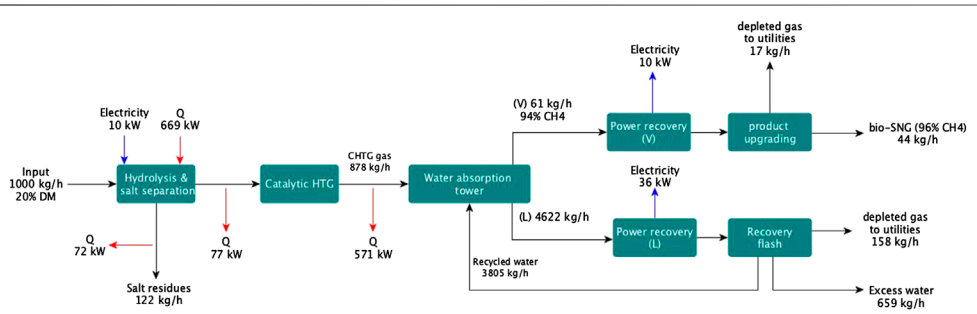

FIGURE 3 | Catalytic hydrothermal gasification schematic representation.

on the economics, with a focus on the reagents promoting struvite crystallization.

In addition, Rahimi et al. (2020) points economics as the major hinder to industrial deployment, mostly due to the need of magnesium salts to promote struvite precipitation. However, it sheds some light on the potential for magnesium oxide (MgO) as a cheap and abundant source of magnesium, that is expected to help changing the overall economics.

However, all of them agree on the lower environmental impact, as well as the need to reduce phosphorous discharges in receiving bodies. Thus, there is a direct environmental benefit of recovering struvite of 0.35 $kgCO_2-$ $eq/kg_{struvite}$.

2.5. CO_2 Removal and Upgrading

On the one hand, the positive impact of CO_2 removal from environment can be supported by economic incentives. On the other hand, if used and upgraded as a carbon source it can yield useful products, thus creating an economic off-set.

For moderate to high partial pressures (up to 40%), physical absorption processes might be used for CO_2 capture, as the gas is absorbed according to Henry's law (Olajire, 2010). Selexol process (Gassner et al., 2011) is implemented in CHTG to purify CH_4 up to gas grid quality. Pressure swing adsorption (PSA), a discontinuous process that removes CO_2 by cycles of adsorption and regeneration is also commonly used and implemented. For both processes, the mechanical power to be used has been estimated between 600 and 800 $kJ/kg_{crudegas}$. For PSA, temperature swing adsorption precedes to ensure drying over aluminium-oxide to ensure a dried feed (Gassner and Maréchal, 2009); the process consumes 11 MJ/kg_{H_2O} at a temperature between 160 and 190°C. Carbon dioxide removal models are thus developed based on overall efficiencies, performances, and energy intensity (Urban et al., 2009), as detailed simulation models are too complex and not designed for flowsheet calculations.

Both methanol and methane formation from CO_2 require expensive H_2 to work; the former has the advantage of consuming less H_2 and having an higher energy density (at standard conditions), being simultaneously easier to store. The latter has the main advantage of integration in the existing natural gas infrastructure. Miguel et al. (2015) have shown that from a thermodynamic point of view the valorization of CO_2 to methane (SNG) is easier and requires less harsh conditions. Methanation is also among the systems expected to contribute to a low-carbon economy, with chemical methanation showing the greatest potential to be implemented on large scale compared with the biological counterpart, not only due to economics but also to technical aspects (Hidalgo and Martín-Marroquín, 2020).

Conversion of CO_2 to valuable products is thus conditioned in this superstructure to SNG. The underlying principle is the Sabatier reaction, taking place in a (catalytic) methanation reactor and by making use of electrolysis as H_2 provider. The model is adapted from (Wang et al., 2018), making use of an alkaline electrolysis cell; high level of market maturity and utilization, coupled with the lowest investment costs among the electrolysis cells (Hidalgo and Martín-Marroquín, 2020), motivated the selection.

TABLE 5 | Key performance indicators.

Key performance indicators	Description
OPEX	Operating expenditure ($/$m^3_{WW}$)
CAPEX	Investment expenditure ($/$m^3_{WW}$)
TC	Total cost ($/$m^3_{WW}$)
Impact	Environmental impact ($kgCO_2/m^3_{ww}$)
ϵ	Global energy efficiency (–)
ϵ_m	Global energy intensity (kWh/m^3_{ww})
PBT	Pay-back time (years)

Hidalgo and Martín-Marroquín (2020) reviewed the current state of power-to-methane technologies with a forecast for the next 30 years, up to 2050. In the analysis, heavier deployment coupled with mass production are expected to drive both electrolysis and methanation prices down. The same reference points at hydrogen production as the major cost, with the range of current investment on alkaline electrolysis cell between 800 and 1,500 €/kW, in line with values from other sources (Schmidt et al., 2017).

2.6. Utilities

The utilities section consists of technologies used to close the thermal and energy balance of the process section. It includes a combustion unit, equivalent to a boiler, a gas engine, a steam network (SN), and a solid oxide fuel cell (SOFC). Operating conditions were not object of optimization. Efficiencies were taken as the most common values in the literature and steam temperature levels were chosen to fit the thermal profiles. The SOFC unit was modeled based on the work of (Facchinetti et al., 2011). SN investment cost was taken as the turbine cost.

3. METHODOLOGY

3.1. Key Performance Indicators

A number of KPI are used to compare different scenarios and to validate models taking into account an extensive literature review on the topic **Table 5**.

The thermodynamic performance of different system configurations is assessed based on the total conversion efficiency. This allows, besides characterizing chemical conversion, to evaluate the process integration quality based on both energy and mass efficiencies. Energy efficiency (**Eq. 1**) is defined as the ratio between the amount of energy leaving the system (either biocrude, SNG or biogas) and entering (besides wastewater, also electricity, natural gas, and filter aid biomass). For mass efficiency (**Eq. 2**) the ratio between the net energy input (defined as energy flows entering subtracted by flows leaving) and the total amount of wastewater entering the system is taken. When used, Δh^0_{WW} reports to the lower heating value of wastewater on a dry basis.

Environmental impact (**Eq. 3**) was calculated in terms of CO_2 emissions using the global warning potential 100a method, corresponding to the Intergovernmental Panel on Climate Change 2013 global warming potential impact method and considering a time-range of 100 years. It was

chosen due to its widespread use and easiness of comparison with other studies. It is computed as the ratio between the impact of operating the system (given as the impact sum of units, resources, and electricity) and the inlet flow of wastewater.

For both **Eqs 2** and **3** only one of the electricity flows is non-zero, which means that the system is either a net importer or exporter. Pay-back time is a metric targeting investment decisions and is defined as the ratio between the investment and the difference in operational expenditures accounted by the investment (**Eq. 4**).

$$\varepsilon = \frac{\Delta h^0_{\text{Biocrude}} \dot{m}^-_{\text{Biocrude,prod.}} + \Delta h^0_{\text{SNG}} \dot{m}^-_{\text{SNG,prod.}} + \Delta h^0_{\text{Biogas}} \dot{m}^-_{\text{Biogas}}}{\Delta h^0_{\text{WW}} \dot{m}^+_{\text{WW}} + \Delta h^0_{\text{filter}_{\text{aid}}} \dot{m}^+_{\text{filter}_{\text{aid}}} + \Delta h^0_{\text{Ngas}} \dot{m}^+_{\text{Ngas}} + \dot{E}^+} \quad (1)$$

$$\varepsilon_m = \frac{\begin{array}{c}\Delta h^0_{\text{Ngas}} \dot{m}^+_{\text{Ngas}} + \Delta h^0_{\text{filter}_{\text{aid}}} \dot{m}^+_{\text{filter}_{\text{aid}}} - \Delta h^0_{\text{Biocrude}} \dot{m}^-_{\text{Biocrude,sold}} \\ - \Delta h^0_{\text{SNG}} \dot{m}^-_{\text{SNG,sold}} + \left(\dot{E}^+ - \dot{E}^-\right)\end{array}}{\dot{m}^+_{\text{WW}}} \quad (2)$$

$$\text{Impact} = \frac{\left[\sum_u^U f_u k_{\text{CO}_2,u} + \sum_r^R m^+_r k^+_{\text{CO}_2,r} + \sum_r^R m^-_r k^-_{\text{CO}_2,r} + k_{\text{CO}_2,e}\left(\dot{E}^+ - \dot{E}^-\right)\right] t_{\text{op}}}{\dot{m}^+_{\text{WW}}} \quad (3)$$

$$\text{PBT} = \frac{\sum_u^U c^{\text{inv1}}_u y_u + c^{\text{inv2}}_u f_u}{\Delta\text{OPEX}} \quad (4)$$

3.2. Mathematical Formulation

The problem is formulated as a mixed-integer linear programming problem. The material and energy flow models contain relevant information concerning physical properties used to define both mass and energy requirements. The approach presented in Maréchal and Kalitventzeff (1998) is used to satisfy the minimum energy requirements. It combines heat cascade generation (**Eqs 9–11**) with pinch analysis to obtain the optimal utility network with respect to minimum cost, while satisfying both electricity (**Eq. 12**) and mass balances (**Eqs. 13–15**). Solutions are generated by considering a weighted sum of both objectives (**Eq. 5**), Operating expenditures (OPEX) (**Eq. 6**) and Capital expenditures (CAPEX) (**Eq. 7**). Constraints are also placed in the minimum and maximum capacity of each unit (**Eq. 8**).

$$\min_{f_u, y_u, \dot{E}^-, \dot{E}^+, \dot{m}^-_r, \dot{m}^+_r} (1-\alpha)\text{OPEX} + \alpha\ \text{CAPEX} \quad (5)$$

with:

$$\text{OPEX} = \left(\sum_r^R c^+_r \dot{m}^+_r + \sum_r^R c^-_r \dot{m}^-_r + \sum_u^U c^{\text{op}}_u f_u + c^+_e \dot{E}^+ - c^-_e \dot{E}^-\right) t_{\text{op}}\,[\$/\text{year}] \quad (6)$$

$$\text{CAPEX} = \sum_u^U \frac{i(1+i)^n}{(1+i)^n - 1}\left(c^{\text{inv1}}_u y_u + c^{\text{inv2}}_u f_u\right)[\$/\text{year}] \quad (7)$$

$$\text{f}^{\min}_u y_u \le f_u \le \text{f}^{\max}_u y_u \quad \forall u \in \mathbf{U} \quad (8)$$

Heat cascade: $\forall k \in \mathbf{K}$ **with** $T_{k+1} \ge T_k$

$$\sum_u^U \dot{\text{q}}_{u,k} f_u + \dot{R}_{k+1} - \dot{R}_k = 0 \quad (9)$$

$$\dot{R}_k \ge 0 \quad (10)$$

$$\dot{R}_0 = \dot{R}_{k+1} = 0 \quad (11)$$

Electricity balance:

$$\dot{E}^+ - \dot{E}^- + \sum_u^U f_u \dot{\text{e}}^-_u - \sum_u^U f_u \dot{\text{e}}^+_u = 0 \quad (12)$$

Resources mass balance: $\forall r \in$ R,

$$\dot{m}^+_r = \sum_u^U f_u \dot{\text{m}}^+_{r,u} \quad (13)$$

$$\dot{m}^-_r = \sum_u^U f_u \dot{\text{m}}^-_{r,u} \quad (14)$$

Units mass balance: $\forall u \in$ U,

$$\sum_r^R f_u \dot{\text{m}}^+_{r,u} = \sum_r^R f_u \dot{\text{m}}^-_{r,u} \quad (15)$$

The mixed-integer linear programming problem is written in AMPL (2013) and solved by IBM ILOG CPLEX Optimization Studio (Cplex, 2009). **Table 6** explain the Indices, sets, variables, and parameters used in the formulation.

3.3. Multi-Objective Optimization

Single objective optimization is often not enough for decision making, as there are typically conflicting objectives. MOO provides an efficient way of generating optimal solutions forming a Pareto front. A Pareto front represents a set of non-dominated solutions—meaning none of the objectives can be improved without degrading another one (Cui et al., 2017). MOO has been widely studied and applied in a multitude of research fields, among which biomass and waste conversion (Fazlollahi et al., 2012; Celebi et al., 2017). In this work, MOO is introduced in the objective function itself, by making use of a CAPEX weight factor (α in **Eq. 5**), that is allowed to change between 0 and 1. This guarantees the generation of a set of different solutions that in the end correspond to different system configurations. Steps of 0.005 were used.

4. RESULTS AND DISCUSSION

The optimization procedure yields a Pareto front (**Figure 4**) that can be translated into a set of different system configurations and optimal values for the decision variables (**Table 7**). Due to the nature of mathematical formulation used, the configuration and thus the set of decision variables is the same for different (albeit similar) values of CAPEX weight factor (α)—leading to overlapping solutions. Wastewater input corresponds to 25,000 ton/h which is translated to approximately 116 MW in the reference scenario. Sludge is anaerobically digested producing biogas, which is internally used to co-generate heat and electricity. Nevertheless, extra natural gas and electricity must

TABLE 6 | Index, sets, variables and parameters in the MILP formulation.

Index and set	Description
$u \in U$	Units U = {boiler, anaerobic digestor, HTL, HTG, ...}
$r \in R$	Resource R = {air, cooling water, natural gas, biocrude, ...}
$k \in K$	Temperature intervals K = $\{k_1 \ldots k_{n_k}\}$
Variable	**Description**
f_u	Sizing factor of unit u (–)
y_u	Binary variable to use or not unit u (–)
$\dot{E}^+$	Purchased electrical power (kW)
$\dot{E}^-$	Sold electrical power (kW)
$\dot{m}_r^+$	Mass flow of purchased/entering resource r (kg/h) or (m^3/h)
$\dot{m}_r^-$	Mass flow of sold/leaving resource r (kg/h) or (m^3/h)
$\dot{R}_k$	Residual heat in the temperature interval k (kW)
Parameter	**Description**
t^{op}	Total operating time per year (h/year)
f_u^{min}–f_u^{max}	Minimum/Maximum size of unit u (–)
c_r^+ /c_r^-	Specific cost of purchasing/selling resource r ($/kg)
c_e^+ /c_e^-	Price for purchased/sold electricity ($/kWh)
c_u^{inv1}–c_u^{inv2}	Fixed/Variable investment cost of unit u ($)
c_u^{op}	Operating specific cost of unit u per reference flow ($/Ref. flow)
I	Interest rate (–)
N	Expected project life time (years)
$k_{co_2,e}$	CO2 equivalent emissions of the electrical grid (kg_{co_2}/MWh)
$k_{co_2,u}$	CO2 equivalent emissions of using unit u (kg_{co_2}/Ref. flow)
$k_{co_2,r}^+$ /$k_{co_2,r}^-$	CO2 equivalent emissions of using/replacing resource r (kg_{co_2}/Ref. flow)
$\dot{m}_{r,u}^+$ –$\dot{m}_{r,u}^-$	Reference mass flow of resource r consumed/produced by unit u (kg/h) or (m^3/h)
$\dot{q}_u^+$ –$\dot{q}_u^-$	Reference heat load consumed/produced by unit u (kW)
$\dot{e}_u^+$ –$\dot{e}_u^-$	Reference electrical power consumed/produced by unit u (kW)
$\dot{q}_{u,k}$	Reference heat load of unit u in temperature interval k (kW)
A	CAPEX weight factor in the interval [0– 1] [–]

be supplied resulting in a global energy efficiency of almost 5% and an impact close to 0.50 $kgCO_2/m^3_{WW}$ (Ref. in **Table 7**). Sludge residuals which account for 10% of operating costs are disposed. Alongside with the potential for biogas upgrade, it was the main driving force for studying and proposing new ways of treating wastewater. It should be mentioned that biogas formation is not excluded from any configuration (**Table 7**). This is mainly due to the already installed anaerobic digester (no investment associated), but also to the potential of using PSA to upgrade biogas to gas grid level (SNG) and by making use of CO_2 as carbon source in the Sabatier reaction.

Generated solutions and in particular Pareto points, are able to provide an interesting trade-off not only between operating and investment costs, but also taking into consideration other KPI's, such as impact and efficiencies, as defined in **Table 5**. With increasing investment, the reduction of OPEX is mainly driven by increasing SNG and biocrude export and for some configurations, by electricity production.

From the reference cost of 0.1605 $\$/m^3_{WW}$, the total cost (TC) of the system is reduced for all the configurations, with savings ranging from 14 to 111%. The more modest reductions, up to 40% in TC (Pareto points between *a* and *f*), correspond to configurations where technologies are installed in small scale and the production of SNG is the main operating benefit. Sludge disposal is replaced by a mixture of nutrients recovery for struvite formation and either biocrude or SNG formation, in HTL or CTHG units respectively. Furthermore, biogas is preferably upgraded in a PSA unit. Environmental impact is reduced up to 23%, and energy efficiency goes as high as 40%, translating a better use of the intrinsic wastewater energetic content. Similarly, global energy intensity, which measures how much external energy is needed, is reduced up to 70%.

A second Pareto region corresponds from point *g* to *q*. It is mainly characterized by CO_2 recovery and upgrade to gas grid

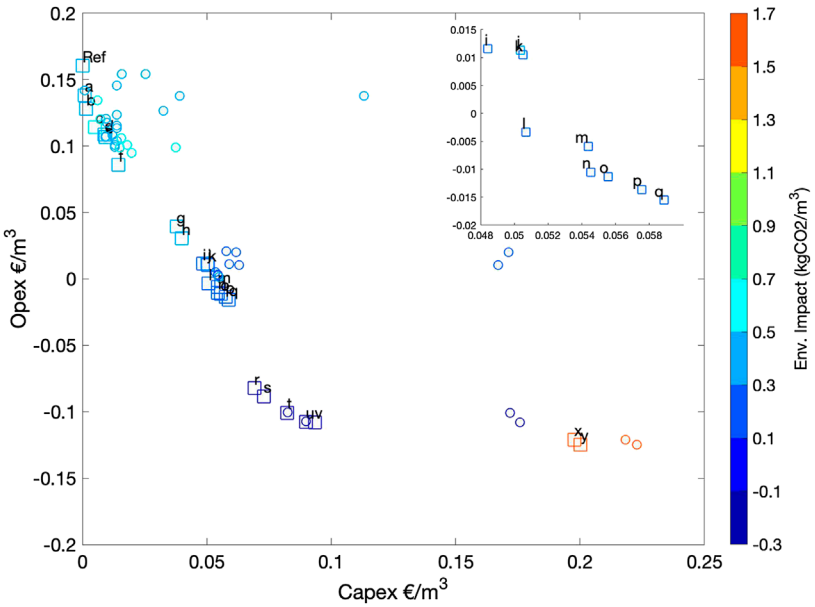

FIGURE 4 | Solution set (circles and squares); Pareto points are the ones represented by squares and contain the same reference as in **Table 7**. Color shows the interval gap of environmental impact. Subplot is a zoom for points between *i* and *q*.

TABLE 7 | Detailed energy, costs, sizes, and KPIs for Pareto points.

Section		Unit	Pareto points																								
			Ref.	*a*	*B*	*c*	*d*	*E*	*f*	*G*	*h*	*i*	*j*	*k*	*l*	*m*	*n*	*o*	*p*	*q*	*r*	*s*	*t*	*u*	*v*	*x*	*y*
Consumption	Wastewater	kW	116,667	116,667	116,667	116,667	116,667	116,667	116,667	116,667	116,667	116,667	116,667	116,667	116,667	116,667	116,667	116,667	116,667	116,667	116,667	116,667	116,667	116,667	116,667	116,667	116,667
	Filter aid	kW	–	–	–	–	6,560	–	7,490	71,250	71,250	96,666	71,250	142,500	142,500	142,500	142,500	142,500	142,500	142,500	142,500	142,500	142,500	142,500	142,500	142,500	142,500
	Electricity	kW	13,185	13,803	13,851	22,292	12,036	12,340	13,120	34,301	29,048	29,505	34,941	29,607	35,305	37,151	36,100	36,926	34,424	40,430	–	–	–	–	–	162,435	160,315
	CW	kW	–	–	–	405	–	1,771	3,527	52	1,445	759	6,081	191	54	409	61	64	214	3,392	82,282	83,058	83,713	84,685	84,658	121,789	122,205
	Natural gas	kW	2,628	–	–	–	–	–	–	–	–	–	–	–	–	–	–	–	–	–	–	–	2,629	2,629	2,629	–	–
Production	Electricity	kW	–	–	–	–	–	–	–	–	–	–	–	–	–	–	–	–	–	–	26,782	27,020	33,375	35,383	35,410	–	–
	SNG	kW	–	–	2,291	10,772	6,755	48,199	47,859	24,737	56,364	56,010	66,026	31,664	22,516	24,549	24,789	25,729	37,618	29,797	5,922	19,977	–	14,992	14,992	161,445	173,966
	SNG_{sold}	kW	–	–	2,291	10,772	6,755	10,729	15,932	24,736	26,668	26,913	36,329	16,671	22,514	24,547	24,788	25,727	25,889	29,795	5,922	8,250	–	–	–	161,432	162,225
	Biogas	kW	6,719	6,724	6,724	6,724	7,037	6,717	6,718	8,938	6,723	4,965	6,723	4,965	6,147	6,168	6,147	6,168	4,965	6,168	6,168	4,965	6,147	4,965	4,965	6,168	4,965
	Biocrude	kW	–	–	–	–	11,098	–	7,920	77,853	75,340	103,046	75,340	153,010	153,010	153,771	153,010	153,771	153,010	153,771	153,771	153,010	153,010	153,010	153,010	153,771	153,010
	$Biocrude_{sold}$	kW	–	–	–	–	–	–	–	73,457	73,620	100,303	64,320	154,815	150,779	150,336	149,246	149,157	149,666	144,771	–	–	–	–	–	52	–
	Biochar	ton/h	–	–	–	–	0.8	–	0.6	5.5	5.4	7.3	5.4	10.9	10.9	10.9	10.9	10.9	10.9	10.9	10.9	10.9	10.9	10.9	10.9	10.9	10.9
	Struvite	ton/h	–	2.6	2.6	2.6	0.1	–	–	0.6	–	–	–	1.1	1.6	1.1	1.6	1.1	0.8	1.1	1.1	0.8	1.6	1.1	1.1	1.1	0.8
Economics																											
CAPEX	PSA	k/y(m^3/h)	–	–	117	155	174	170	170	198	170	149	170	149	163	164	163	164	149	164	164	149	–	–	–	164 (726)	149 (585)
(Sizes)					(282)	(648)	(829)	(791)	(791)	(1,052)	(791)	(585)	(791)	(585)	(724)	(726)	(724)	(726)	(585)	(726)	(726)	(585)					
	Electrolysis	k/y(MW)	–	–	–	783	–	–	–	2,305	1,626	1,927	3,004	1,699	2,370	2,658	2,695	2,826	2,517	3,406	–	–	–	–	–	22,189	21,970
						(7.1)				(20.9)	(14.8)	(17.5)	(27.3)	(15.4)	(21.6)	(24.2)	(24.5)	(25.7)	(22.9)	(31.0)						(201.8)	(199.7)
	Methanation	k/y($m^3_{CH_4}$ /h)	–	–	–	180	–	–	–	441	325	376	561	337	452	502	508	531	478	630	–	–	–	–	–	3,853	3,815
						(174)				(513)	(362)	(429)	(669)	(378)	(528)	(592)	(600)	(629)	(560)	(759)						(4,944)	(4,895)
	SN	k/y(MW)	–	–	–	–	–	–	–	–	–	–	–	–	–	–	–	–	–	–	6,292	6,252	6,336	6,334	7,129	8,404	8,346
																					(39.4)	(39.2)	(39.7)	(39.7)	(44.4)	(52.0)	(51.7)
	HTL	k/y(dryton/h)	–	–	–	–	1,240	–	991 (3.2)	4,848	4,742	5,946	4,742	7,852	7,852	7,878	7,852	7,878	7,852	7,878	7,878	7,852	7,852	7,852	7,852	7,878	7,852
							(4.4)			(21.3)	(20.8)	(26.4)	(20.8)	(35.4)	(35.4)	(35.5)	(35.4)	(35.5)	(35.4)	(35.5)	(35.5)	(35.4)	(35.4)	(35.4)	(35.4)	(35.5)	(35.4)
	CHTG	k/y(MW_{sludge})	–	–	–	–	–	1,836	1,826	–	1,736	1,711	1,736	897 (1.8)	–	–	–	–	906 (1.8)	–	–	906 (1.8)	–	897 (1.8)	897 (1.8)	–	906 (1.8)
								(4.8)	(4.7)		(4.5)	(4.4)	(4.5)														
	SOFC	k/y(kW)	–	–	–	–	–	–	–	–	–	–	–	–	–	–	–	–	–	–	–	–	3,004	3,774	3,774	–	–
																							(6,257)	(7,863)	(7,863)		
	Engine	k/y(kW_{el})	–	216	216	–	545	–	175	492	157	499	813	130	245	711	725	770	704	813	813	813	813	813	813	813	813
				(1,346)	(1,346)		(3,402)		(1,085)	(3,072)	(973)	(3,112)	(5,073)	(806)	(1,527)	(4,440)	(4,525)	(4,806)	(4,395)	(5,073)	(5,073)	(5,073)	(5,073)	(5,073)	(5,073)	(5,073)	(5,073)
OPEX	WWTP	k/y	22,100	14,108	14,108	14,108	21,853	22,091	22,093	20,349	22,110	22,117	22,110	18,653	17,250	18,638	17,250	18,638	19,597	18,638	18,638	19,597	17,250	18,653	18,653	18,638	19,597
	Disposal	k/y	3,451	–	–	–	–	–	–	–	–	–	–	–	–	–	–	–	–	–	–	–	–	–	–	–	–
	HTL	k/y	–	–	–	–	284	–	252	2,435	2,396	3,264	2,396	4,828	4,828	4,840	4,828	4,840	4,828	4,840	4,840	4,828	4,828	4,828	4,828	4,840	4,828
	Struvite	k/y	–	8,008	8,008	8,008	252	–	–	1,769	–	–	–	3,476	4,884	3,494	4,884	3,494	2,533	3,494	3,494	2,533	4,884	3,476	3,476	3,494	2,533
	PSA	k/y	–	–	110	253	324	309	309	412	310	229	310	229	283	284	283	284	229	284	284	229	–	–	–	284	229
	CHTG	k/y	–	–	–	–	–	3,795	3,764	–	3,501	3,430	3,501	1,363	–	–	–	–	1,382	–	–	1,382	–	1,363	1,363	–	1,382
	Ngas	k/y	599	–	−2,408	−11,323	−7,101	−11,278	−16,748	−26,002	−28,034	−28,291	−38,189	−17,524	−23,667	−25,804	−26,057	−27,044	−27,214	−31,321	−6,225	−8,672	599	599	599	−16,9697	−17,0531
	Elec	k/y	9,009	9,431	9,464	15,232	8,224	8,432	8,965	23,437	19,848	20,160	23,874	20,230	24,123	25,384	24,666	25,231	23,521	27,625	−42,229	−42,606	−52,626	−55,792	−55,834	110,989	109,540
	CW	k/y	–	–	–	18	–	80	160	2	65	34	275	9	2	19	3	3	10	154	3,725	3,760	3,789	3,833	3,832	5,513	5,532
	$Struvite_{market}$	k/y	–	−1,259	−1,259	−1,259	−40	–	–	−278	–	–	–	−547	−768	−549	−768	−549	−398	−549	−549	−398	−768	−547	−547	−549	−398
	$Biocrude_{market}$	k/y	–	–	–	–	–	–	–	−13,483	−13,512	−18,410	−11,806	−28,415	−27,674	−27,593	−27,393	−27,377	−27,470	−26,572	–	–	–	–	–	−10	–
Impacts	WWTP	$kgCO_2/m^3_{WW}$	0.293	0.293	0.293	0.293	0.293	0.293	0.293	0.293	0.293	0.293	0.293	0.293	0.294	0.294	0.294	0.294	0.293	0.294	0.294	0.293	0.294	0.293	0.293	0.294	0.293
	$Struvite_{market}$	$kgCO_2/m^3_{WW}$	–	−0.037	−0.037	−0.037	−0.001	–	–	−0.008	–	–	–	−0.016	−0.022	−0.016	−0.022	−0.016	−0.012	−0.016	−0.016	−0.012	−0.022	−0.016	−0.016	−0.016	−0.012
	Ngas	$kgCO_2/m^3_{WW}$	0.016	–	−0.014	−0.064	−0.040	−0.064	−0.095	−0.147	−0.159	−0.160	−0.217	−0.099	−0.134	−0.146	−0.148	−0.153	−0.154	−0.178	−0.035	−0.049	0.016	0.016	0.016	−0.962	−0.967
	Elec	$kgCO_2/m^3_{WW}$	0.188	0.197	0.197	0.317	0.171	0.176	0.187	0.488	0.414	0.420	0.498	0.422	0.503	0.529	0.514	0.526	0.490	0.576	−0.381	−0.385	−0.475	−0.504	−0.504	2.313	2.283
	$Biocrude_{market}$	$kgCO_2/m^3_{WW}$	–	–	–	–	–	–	–	−0.219	−0.219	−0.298	−0.191	−0.461	−0.449	−0.447	−0.444	−0.444	−0.445	−0.431	–	–	–	–	–	−0.0002	–
KPI's	OPEX		0.1605	0.1383	0.1280	0.1143	0.1087	0.1070	0.0858	0.0395	0.0305	0.0116	0.0113	0.0105	−0.0034	−0.0059	−0.0105	−0.0113	−0.0136	−0.0156	−0.0823	−0.0883	−0.1007	−0.1077	−0.1079	−0.1210	−0.1246
	–		34.4	29.6	27.4	24.5	23.3	22.9	18.4	8.5	6.5	2.5	2.4	2.3	−0.7	−1.3	−2.3	−2.4	−2.9	−3.3	−17.6	−18.9	−21.6	−23.1	−23.1	−25.9	−26.7
	CAPEX		0.000	0.001	0.002	0.005	0.009	0.009	0.014	0.038	0.040	0.048	0.050	0.051	0.051	0.054	0.055	0.056	0.058	0.059	0.069	0.073	0.082	0.090	0.093	0.198	0.200
	–		0.0	0.2	0.3	1.1	1.9	2.0	3.1	8.1	8.6	10.4	10.8	10.8	10.9	11.7	11.7	11.9	12.3	12.6	14.8	15.6	17.6	19.2	20.0	42.4	42.9
	TC		0.161	0.139	0.129	0.119	0.118	0.116	0.100	0.077	0.071	0.060	0.062	0.061	0.047	0.049	0.044	0.044	0.044	0.043	−0.013	−0.015	−0.018	−0.018	−0.014	0.077	0.076
	–	/MWh_{WW}	34.4	29.8	27.7	25.6	25.2	24.9	21.5	16.6	15.1	12.9	13.2	13.1	10.1	10.4	9.4	9.5	9.4	9.3	−2.8	−3.3	−4.0	−3.8	−3.1	16.4	16.2
	Impact	$kgCO_2/m^3_{WW}$	0.497	0.453	0.440	0.510	0.423	0.405	0.385	0.408	0.329	0.255	0.383	0.139	0.191	0.213	0.193	0.206	0.172	0.245	−0.139	−0.152	−0.188	−0.211	−0.211	1.628	1.598
	–	$kgCO_2$/MWh	106	97	94	109	91	87	82	87	70	55	82	30	41	46	41	44	37	52	−30	−33	−40	−45	−45	349	342
	ϵ	–	0.051	0.052	0.052	0.088	0.134	0.376	0.408	0.463	0.608	0.656	0.636	0.640	0.597	0.603	0.603	0.607	0.650	0.614	0.617	0.668	0.608	0.661	0.661	0.748	0.780
	ϵ_m	kWh/m^3_{WW}	0.633	0.552	0.462	0.461	0.474	0.064	0.187	0.294	0.000	−0.042	0.222	0.025	0.180	0.191	0.183	0.182	0.055	0.335	4.392	4.289	4.470	4.390	4.389	5.738	5.624
	PBT	years	0	0.4	0.5	1.1	1.7	1.7	1.9	3.1	3.0	3.2	3.3	3.3	3.0	3.2	3.1	3.2	3.2	3.3	2.8	2.9	3.1	3.3	3.4	6.9	6.9

SNG, synthetic natural gas; PSA, pressure swing adsorption; SN, steam network; HTL, hydrothermal liquefaction; CHTG, catalytic hydrothermal gasification; SOFC, solid oxide fuel cell; WWTP, waste water treatment plant.

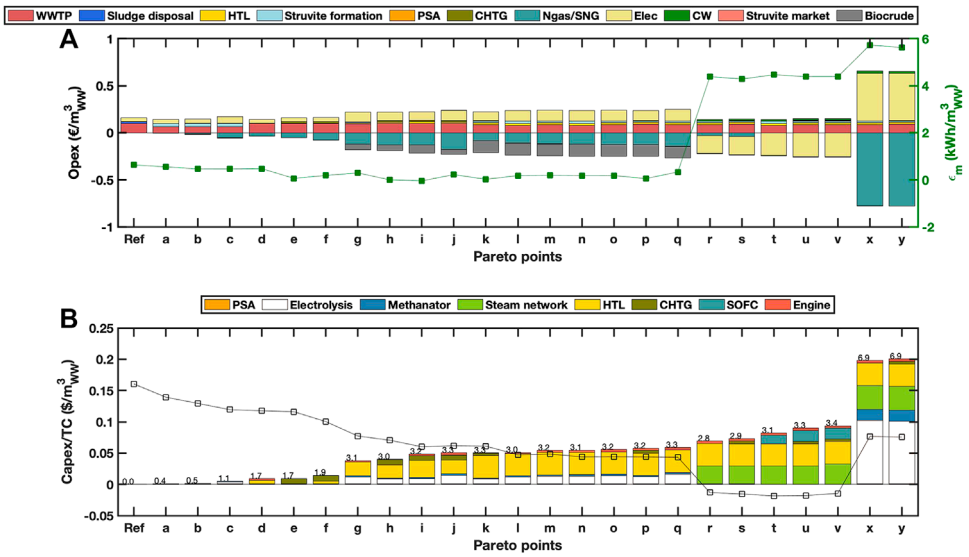

FIGURE 5 | Pareto optimal configuration; **(A)** stacked bars represent OPEX, line with markers represent ϵ_m, **(B)** stacked bars represent CAPEX, line with markers represent total cost (TC) and numbers above stacks show the PBT.

compatibility by investing in both electrolysis and methanation units. Together with CHTG, production and export of SNG are increased reaching values of 36 MW and economic benefits of 38 M$/y. At the same time, higher investment in HTL allows for biocrude injection in the market, yielding as well significant operating benefits (up to 28.4 M$/y). TC is reduced up to 73% and impact goes as low as 0.139 $kgCO_2/m^3_{ww}$, which is equivalent to a reduction of 72%. Energy efficiency goes as high as 65% and energy intensity records a negative value (point *i*), which translates to a net energy producer on a wastewater volume base.

A third Pareto section, from points *r* to *v*, provides a net economic benefit (negative TC), arising mainly from electricity production, complemented by an investment in the SN. At the same time biocrude is internally consumed, producing steam and electricity.The SNG production is reduced and for certain configurations reverted, meaning natural gas is imported from the grid. Electricity production is thus both an economic and environmental driving force. Indeed, the environmental impact is negative for all the section configurations which is equivalent to a net environmental benefit, with a global energy efficiency up to 66%. On the other hand, the need for importing natural gas and the internal use of biocrude justify energy intensities as high as seven times the reference case.

The last set of Pareto, corresponding to points *x* and *y* are the ones with the lowest OPEX but the highest investment. There is maximization of SNG export by means of CO_2 conversion to CH_4 through H_2 production *via* electrolysis, corresponding to heavy electricity consumption (up to 162 MW). Indeed, the incentive to

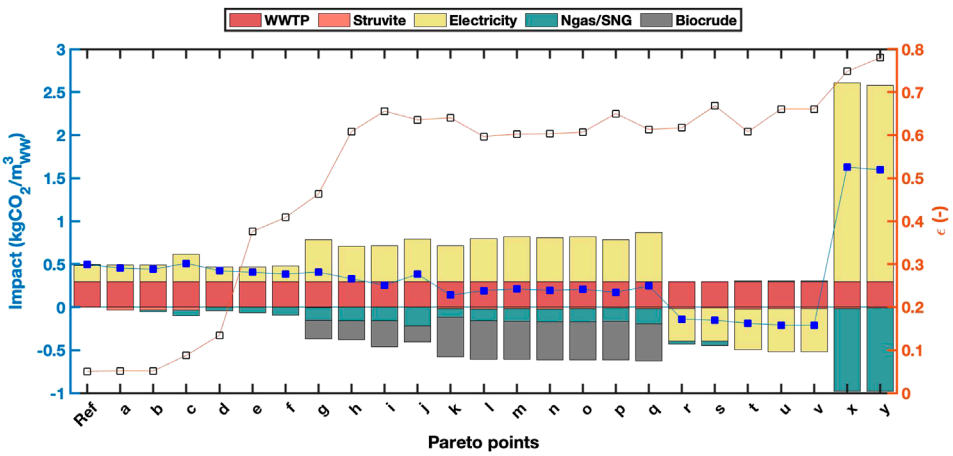

FIGURE 6 | Pareto optimal configuration with stacked bars corresponding to Impact partition, blue markers and line to the overall impact; orange line and axis correspond to ϵ.

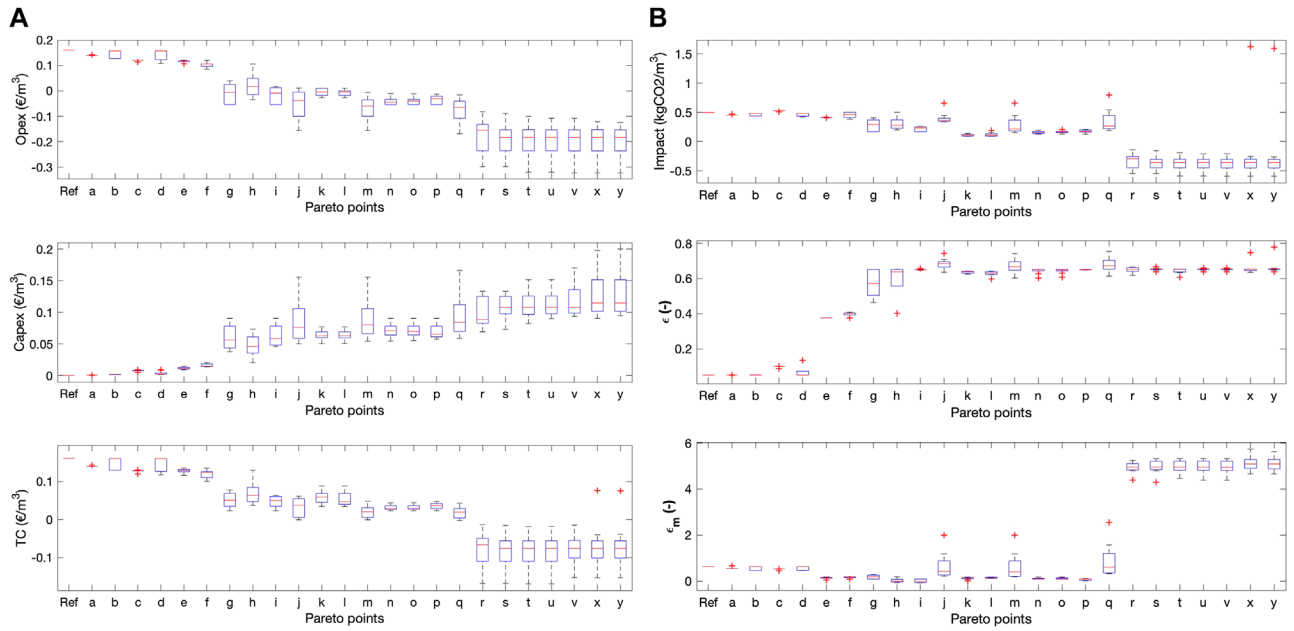

FIGURE 7 | Box plots for parametric analysis on inlet wastewater flow: **(A)** economic key performance indicators, **(B)** impact and efficiencies key performance indicators.

control investment is practically vanished in these cases and extremely expensive technologies are chosen even if the marginal operating benefit compared to the third Pareto region is small. However, both Pareto points present considerable environmental impact (three times the reference case) and a high energy intensity due to the need of importing electricity. In spite of it, TC is able to be reduced by 50% compared to the reference case. Lastly, the pay-back time, an important measure for investors, is close to 7 years which represents a liability due to the investment in technologies with reducing industrial implementation.

Figures 5A,B as well as **Figure 6** graphically represent the information contained in **Table 7** for all the Pareto front solutions. **Figure 5A** shows how biocrude and SNG are the major economic driving forces up to point *q*, after which electricity exports lead the economic benefit. Similarly, global energy intensity is reduced up to point *q*, after which by means of exporting electricity the export of biocrude is eliminated. This leads to energy intensity values up to seven times higher than the reference. **Figure 5B** graphically displays investment decisions as stacked bars, TC as a line and pay-back time as numbers above the stacks. For almost all the configurations HTL and PSA are chosen technologies as they are able to produce biocrude and SNG respectively. The use of electrolysis is also frequent as a way to produce H_2 for CO_2 upgrading. In the most expensive configurations the investment in electrolysis accounts for up to 50% of the total investment, leading inclusively to negative TCs as the production of electricity is maximized.

On the environmental impact and energy efficiency, **Figure 6** shows that up to the second Pareto region (point *q*) only a small to moderate reduction of the reference impact takes place. For the third region (from point *r* to *v*), exporting electricity and replacing an equivalent amount of CO_2 (the grid carbon intensity) renders those configurations negative equivalent emissions systems. The last two options (points *x* and *y*), which include maximizing electricity use to supply the production of SNG, show a considerable increase in impact. For all the configurations the energetic recovery of wastewater has drastically increased. However, as it is demonstrated it might not be a synonym of sound environmental performance. In particular, configurations x and y achieve the highest efficiencies despite a considerable increase in impact.

Total inlet wastewater (in weight or volume) is an important parameter that is likely to affect decision-making. In reality, although WWTPs tend to grow in area and equivalent people managed, the average wastewater in urban centers is rather small. To account for it a parametric analysis on the amount of inlet wastewater and thus the size of the facility was performed. It was changed between the reference amount of 25.000 ton/h, equivalent to 1.7 M inhabitants and 2.500 ton/h, corresponding to 0.17 M inhabitants, in steps of 2.500 ton/h. The results are shown in **Figure 7**. OPEX and CAPEX have a consistent decreasing and increasing tendency, respectively, regardless of the Pareto point or the inlet flow of wastewater. Concerning TC, the first points are more likely to be less competitive for small flows, which means a TC closer to the reference value.

In the first region, between points *a* and *f*, size plays a role with TC for some configurations being similar to the reference value. This aspect however, might hinder the feasibility of the configuration purposed. In the same way, impacts and both efficiencies have values that come close to that of the reference for low inlet flows.

For the second region, between points *g* and *q*, solutions provide consistently lower TC than the reference despite some extreme values in investment notably points *j*, *m*, and *q*. For those points, lower OPEX and negative TC are achieved. The consequence is immediate in terms of environmental impact, with values closer to those of the reference case. Similarly, the higher impact corresponds in this situation to a higher global energy intensity (ϵ_m).

The third region, between points *r* and *v*, shows the highest variability in TC. In this region, smaller flows achieve lower values compared to bigger ones due to an increasing investment in technology, but providing a considerably lower OPEX. By exploring new opportunities, the impact is also considerably reduced as export of both electricity and SNG are maximized. Nevertheless, the energy efficiency seems to be stable around 60%, and the energy intensity high regardless of the size, which is again due to the fact of internally using biocrude as an energy provider.

The fourth and last region, of points *x* and *y*, shows a curious behavior. The higher inlet flows corresponding to the main results shown (**Figure 5**) are outliers of the parametric analysis-observed in the TC box plot. Indeed the huge amount of wastewater and its intrinsic energetic content motivated the investment in technologies that make use of electricity to produce SNG (electrolysis and methanation units). However, with a reduced flow the system converges to a configuration very similar to those of the third region, amidst the corresponding reduction in global energy efficiencies. By changing system configuration the investment is reduced and TC shifts toward negative values, indicating a net economic profitable solution.

5. CONCLUSIONS

The production of biogas and its use for internal WWTP purposes is only able to explore 5% of the total intrinsic energetic content of wastewater. In order to minimize costs, technologies that allow handling and valorizing not only biogas, but also sludge (with variable water content) were studied. MOO was used to generate a set of competing solutions to be analyzed and discussed by DM.

HTL is chosen in almost all the configurations analyzed, which is the result of exploring system synergies for its aqueous by-product whose further treatment can be explored within a typical WWTP configuration. For investment costs of up to $0.10\,\$/m^3_{WW}$ an effective reduction of TC and environmental impact of up to 73% is achieved. At the same time, global energy efficiency goes as high as 60% and pay-back time around 3 years. For the same range of investment, capture and upgrading of CO_2 is also used, with electrolysis and methanation units adopted at low sizes. It is of interest to note that for some configurations the global energy efficiency substantially increases without a similar and comparable decrease in the environmental impact. For some solutions, CHTG is included in the optimal configuration. However, it is not heavily deployed for two reasons: biocrude from HTL seems to provide a better trade-off between OPEX and CAPEX and SNG can be obtained by investing in a PSA, which has lower economic barrier.

When higher investments are allowed, and because all economic results are extremely dependent on the economic assumptions, in particular electricity and (synthetic) natural gas prices as well as their ratio, investment in a SN coupled with a SOFC make use of the internally generated biocrude to maximize either electricity or SNG. In the end this provides substantial economic benefits. Actually, within the current assumptions framework the system's TC can go below 0, transforming it in a net economic profitable system. Simultaneously, environmental impact can also change to negative values as the electrical grid carbon intensity is considerably high. Obeying economic motivations, there are also two configurations that albeit reducing operating cost at the expense of higher investment have a considerable impact (three times higher the reference case) which hinders their application.

Parametric analysis was performed on the inlet wastewater flow, changing it between 10 and 100% of its nominal value. The results show that for lower investments, smaller flows endanger the conclusions, with TCs in line with the reference values. However, for higher investments the adopted configurations perform systematically better.

This work paves the way for cheaper and more sustainable wastewater industrial clusters, showing how well new conversion routes can be interconnected to generate new system configurations.

DATA AVAILABILITY STATEMENT

All datasets presented in this study are included in the article.

AUTHOR CONTRIBUTIONS

RA—Formulation and model developed, results generation, analysis, and discussion. TD—Literature review and manuscript review. JG—Catalytic hydrothermal gasification model adaption and manuscript review. FM—Supervision results and conclusions discussion. All authors contributed to the article and approved the submitted version.

FUNDING

This project has received funding from the European Union's Horizon 2020 research and innovation program under the Marie Skłodowska-Curie Grant Agreement No 754354 and under Grant Agreement No 818011.

REFERENCES

AMPL (2013). *Encyclopedia of operations research and management science*, Editors S. I. Gass and M. C. Fu (Boston, MA: Springer US), 52.

Anastasakis, K., Biller, P., Madsen, R., Glasius, M., and Johannsen, I. (2018). Continuous hydrothermal liquefaction of biomass in a novel pilot plant with heat recovery and hydraulic oscillation. *Energies* 11 (10), 2695. doi:10.3390/en11102695

Andreoli, V., von Sperling, M., and Fernandes, F. (Editors) (2007). "Sludge treatment and disposal," in *Biological wastewater treatment series*. London, UK: IWA Publication, Vol. 6.

Ang, M. S., Duyag, J., Tee, K. C., and Sy, C. L. (2019). A multi-period and multi-criterion optimization model integrating multiple input configurations, reuse, and disposal options for a wastewater treatment facility. *J. Clean. Prod.* 231, 1437–1449. doi:10.1016/j.jclepro.2019.05.246

Bauer, S. K., Reynolds, C. F., Peng, S., and Colosi, L. M. (2018). Evaluating the water quality impacts of hydrothermal liquefaction assessment of carbon, nitrogen, and energy recovery. *Bioresour. Technol. Rep.* 2, 115–110. doi:10.1016/j.biteb.2018.04.010

Biller, P., Johannsen, I., dos Passos, J. S., and Ottosen, L. D. M. (2018). Primary sewage sludge filtration using biomass filter aids and subsequent hydrothermal co-liquefaction. *Water Res.* 130, 58–68. doi:10.1016/j.watres.2017.11.048

Celebi, A. D., Ensinas, A. V., Sharma, S., and Maréchal, F. (2017). Early-stage decision making approach for the selection of optimally integrated biorefinery processes. *Energy* 137, 908–916. doi:10.1016/j.energy.2017.03.080

Chen, S., and Chen, B. (2013). Net energy production and emissions mitigation of domestic wastewater treatment system: a comparison of different biogas-sludge use alternatives. *Bioresour. Technol.* 144, 296–303. doi:10.1016/j.biortech.2013.06.128

Chen, W.-T., Zhang, Y., Zhang, J., Yu, G., Schideman, L. C., Zhang, P., et al. (2014). Hydrothermal liquefaction of mixed-culture algal biomass from wastewater treatment system into bio-crude oil. *Bioresour. Technol.* 152, 130–139. doi:10.1016/j.biortech.2013.10.111

CPLEX (2009). *IBM ILOG CPLEX V12.1: User's Manual for CPLEX*. Armonk, NY: International Business Machines Corporation.

Cui, Y., Geng, Z., Zhu, Q., and Han, Y. (2017). Review: multi-objective optimization methods and application in energy saving. *Energy* 125, 681–704. doi:10.1016/j.energy.2017.02.174

Daniel, R. C., Billing, J. M., Luna, M. L., Cantrell, K. J., Peterson, R. A., Bonebrake, M. L., et al. (2009). *Characterization of filtration scale-up performance. Tech. Rep. PNNL-1811*. Richland, WA: Pacific Northwest National Lab, Vol. 962841.

de Vries, S., Postma, R., van Scholl, L., Blom-Zandstra, G., Verhagen, J., and Harms, I. (2016). "Economic feasibility and climate benefits of using struvite from the Netherlands as a phosphate (P) fertilizer in West Africa," in *Plant production systems, PPO/PRI AGRO water-en biobased economy, PPO/PRI AGRO multifunctioneel landgebruik*. Wageningen, NL: Wageningen Plant Research.

Degryse, F., Baird, R., da Silva, R. C., and McLaughlin, M. J. (2017). Dissolution rate and agronomic effectiveness of struvite fertilizers-effect of soil pH, granulation and base excess. *Plant Soil.* 410 (1), 139–152. doi:10.1007/s11104-016-2990-2

Dimitriou, I., García-Gutiérrez, P., Elder, R. H., Cuéllar-Franca, R. M., Azapagic, A., and Allen, R. W. K. (2015). Carbon dioxide utilisation for production of transport fuels: process and economic analysis. *Energy Environ. Sci.* 8 (6), 1775–1789. doi:10.1039/c4ee04117h

Elliott, D. C. (2020). "Hydrothermal liquefaction of sludge and biomass residues," in *Wastewater treatment residues as resources for biorefinery products and biofuels*. New York, NY: Elsevier, 117–131.

Facchinetti, E., Favrat, D., and Marechal, F. (2011). Innovative hybrid cycle solid oxide fuel cell-inverted gas turbine with CO_2 separation. *Fuel Cells* 11 (4), 565–572. doi:10.1002/fuce.201000130

Fazlollahi, S., Mandel, P., Becker, G., and Maréchal, F. (2012). Methods for multi-objective investment and operating optimization of complex energy systems. *Energy* 45 (1), 12–22. doi:10.1016/j.energy.2012.02.046

Gassner, M., and Maréchal, F. (2009). Thermo-economic process model for thermochemical production of synthetic natural gas (SNG) from lignocellulosic biomass. *Biomass Bioenergy* 33 (11), 1587–1604. doi:10.1016/j.biombioe.2009.08.004

Gassner, M., Vogel, F., Heyen, G., and Maréchal, F. (2011). Optimal process design for the polygeneration of SNG, power and heat by hydrothermal gasification of waste biomass: thermo-economic process modelling and integration. *Energy Environ. Sci.* 4 (5), 1726. doi:10.1039/c0ee00629g

Gikas, P. (2017). Towards energy positive wastewater treatment plants. *J. Environ. Manag.* 203, 621–629. doi:10.1016/j.jenvman.2016.05.061

Gollakota, A., Kishore, N., and Gu, S. (2018). A review on hydrothermal liquefaction of biomass. *Renew. Sustain. Energy Rev.* 81, 1378–1392. doi:10.1016/j.rser.2017.05.178

Gorre, J., Ortloff, F., and van Leeuwen, C. (2019). Production costs for synthetic methane in 2030 and 2050 of an optimized power-to-gas plant with intermediate hydrogen storage. *Appl. Energy* 253, 113594. doi:10.1016/j.apenergy.2019.113594

Grobelak, A., Grosser, A., Kacprzak, M., and Kamizela, T. (2019). Sewage sludge processing and management in small and medium-sized municipal wastewater treatment plant-new technical solution. *J. Environ. Manag.* 234, 90–96. doi:10.1016/j.jenvman.2018.12.111

Gu, Y., Li, Y., Li, X., Luo, P., Wang, H., Robinson, Z. P., et al. (2017). The feasibility and challenges of energy self-sufficient wastewater treatment plants. *Appl. Energy* 204, 1463–1475. doi:10.1016/j.apenergy.2017.02.069

He, C., Chen, C.-L., Giannis, A., Yang, Y., and Wang, J.-Y. (2014). Hydrothermal gasification of sewage sludge and model compounds for renewable hydrogen production: a review. *Renew. Sustain. Energy Rev.* 39, 1127–1142. doi:10.1016/j.rser.2014.07.141

He, W., Li, G., Kong, L., Wang, H., Huang, J., and Xu, J. (2008). Application of hydrothermal reaction in resource recovery of organic wastes. *Resour. Conserv. Recycl.* 52 (5), 691–699. doi:10.1016/j.resconrec.2007.11.003

Heidrich, E. S., Curtis, T. P., and Dolfing, J. (2011). Determination of the internal chemical energy of wastewater. *Environ. Sci. Technol.* 45 (2), 827–832. doi:10.1021/es103058w

Hidalgo, D., and Martín-Marroquín, J. M. (2020). Power-to-methane, coupling CO_2 capture with fuel production: an overview. *Renew. Sustain. Energy Rev.* 132, 110057. doi:10.1016/j.rser.2020.110057

Huang, H., Xiao, D., Zhang, Q., and Ding, L. (2014). Removal of ammonia from landfill leachate by struvite precipitation with the use of low-cost phosphate and magnesium sources. *J. Environ. Manag.* 145, 191–198. doi:10.1016/j.jenvman.2014.06.021

Kantor, I., and Santecchia, A. (2016). D5.7—report on LC assessment tools based on the results of MORE and EPOS, 27.

Kataki, S., West, H., Clarke, M., and Baruah, D. C. (2016). Phosphorus recovery as struvite from farm, municipal and industrial waste: feedstock suitability, methods and pre-treatments. *Waste Manag.* 49, 437–454. doi:10.1016/j.wasman.2016.01.003

Li, B., Boiarkina, I., Yu, W., Huang, H. M., Munir, T., Wang, G. Q., et al. (2019). Phosphorous recovery through struvite crystallization: challenges for future design. *Sci. Total Environ.* 648, 1244–1256. doi:10.1016/j.scitotenv.2018.07.166

Maddi, B., Panisko, E., Wietsma, T., Lemmon, T., Swita, M., Albrecht, K., et al. (2017). Quantitative characterization of aqueous byproducts from hydrothermal liquefaction of municipal wastes, food industry wastes, and biomass grown on waste. *ACS Sustain. Chem. Eng.* 5 (3), 2205–2214. doi:10.1021/acssuschemeng.6b02401

Main tables—Eurostat (2018). Available at: https://ec.europa.eu/eurostat/web/energy/data/main-tables (Accessed November 9, 2019).

Maréchal, F., and Kalitventzeff, B. (1998). Energy integration of industrial sites: tools, methodology and application. *Appl. Therm. Eng.* 18 (11), 921–933. doi:10.1016/s1359-4311(98)00018-0

Maronese, S., Ensinas, A. V., Mian, A., Lazzaretto, A., and Maréchal, F. (2015). Optimum biorefinery pathways selection using the integer-cuts constraint method applied to a MILP problem. *Ind. Eng. Chem. Res.* 54 (28), 7038–7046. doi:10.1021/acs.iecr.5b01439

Mayer, B. K., Baker, L. A., Boyer, T. H., Drechsel, P., Gifford, M., Hanjra, M. A., et al. (2016). Total value of phosphorus recovery. *Environ. Sci. Technol.* 50 (13), 6606–6620. doi:10.1021/acs.est.6b01239

Mian, A., Ensinas, A. V., and Marechal, F. (2015). Multi-objective optimization of SNG production from microalgae through hydrothermal gasification. *Comput. Chem. Eng.* 76, 170–183. doi:10.1016/j.compchemeng.2015.01.013

Miguel, C. V., Soria, M. A., Mendes, A., and Madeira, L. M. (2015). Direct CO_2 hydrogenation to methane or methanol from post-combustion exhaust

streams-a thermodynamic study. *J. Nat. Gas Sci. Eng.* 22, 1–8. doi:10.1016/j.jngse.2014.11.010

Molinos-Senante, M., Sala-Garrido, R., and Iftimi, A. (2018). Energy intensity modeling for wastewater treatment technologies. *Sci. Total Environ.* 630, 1565–1572. doi:10.1016/j.scitotenv.2018.02.327

Mørup, A. J., Christensen, P. R., Aarup, D. F., Dithmer, L., Mamakhel, A., Glasius, M., et al. (2012). Hydrothermal liquefaction of dried distillers grains with solubles: a reaction temperature study. *Energy Fuels* 26 (9), 5944–5953.

OECD (2012). *Water quality and agriculture: meeting the policy challenge. OECD studies on water*. Paris: OECD Publishing.

Olajire, A. A. (2010). CO_2 capture and separation technologies for end-of-pipe applications-a review. *Energy* 35 (6), 2610–2628. doi:10.1016/j.energy.2010.02.030

Panepinto, D., Fiore, S., Zappone, M., Genon, G., and Meucci, L. (2016). Evaluation of the energy efficiency of a large wastewater treatment plant in Italy. *Appl. Energy* 161, 404–411. doi:10.1016/j.apenergy.2015.10.027

Pérez-Fortes, M., Schöneberger, J. C., Boulamanti, A., and Tzimas, E. (2016). Methanol synthesis using captured CO_2 as raw material: techno-economic and environmental assessment. *Appl. Energy* 161, 718–732. doi:10.1016/j.apenergy.2015.07.067

Rahimi, S., Modin, O., and Mijakovic, I. (2020). Technologies for biological removal and recovery of nitrogen from wastewater. *Biotechnol. Adv.* 43, 107570. doi:10.1016/j.biotechadv.2020.107570

Rubio-Maya, C., Uche-Marcuello, J., Martínez-Gracia, A., and Bayod-Rújula, A. A. (2011). Design optimization of a polygeneration plant fuelled by natural gas and renewable energy sources. *Appl. Energy* 88 (2), 449–457. doi:10.1016/j.apenergy.2010.07.009

Santibañez-Aguilar, J. E., Martinez-Gomez, J., Ponce-Ortega, J. M., Nápoles-Rivera, F., Serna-González, M., González-Campos, J. B., et al. (2015). Optimal planning for the reuse of municipal solid waste considering economic, environmental, and safety objectives. *AIChE J* 61 (6), 1881–1899. doi:10.1002/aic.14785

Schmidt, O., Gambhir, A., Staffell, I., Hawkes, A., Nelson, J., and Few, S. (2017). Future cost and performance of water electrolysis: an expert elicitation study. *Int. J. Hydrogen Energy* 42 (52), 30470–30492. doi:10.1016/j.ijhydene.2017.10.045

Snowden-Swan, L. J., Zhu, Y., Jones, S. B., Elliott, D. C., Schmidt, A. J., Hallen, R. T., et al. (2016). Hydrothermal liquefaction and upgrading of municipal wastewater treatment plant sludge: a preliminary techno-economic analysis. *Tech. Rep.* 25464, 1258731.

Turton, R. (2018). *Analysis, synthesis and design of chemical processes*. 5th Edn. Boston, MA: Prentice-Hall.

Tzanetis, K. F., Posada, J. A., and Ramirez, A. (2017). Analysis of biomass hydrothermal liquefaction and biocrude-oil upgrading for renewable jet fuel production: the impact of reaction conditions on production costs and GHG emissions performance. *Renew. Energy* 113, 1388–1398. doi:10.1016/j.renene.2017.06.104

Urban, W., Girod, K., and Lohmann, H. (2009). *Technologien und kosten der biogasaufbereitung und einspeisung in das erdgasnetz*. Oberhausen, DE: Fraunhofer UMSICHT.

Wang, L., Pérez-Fortes, M., Madi, H., Diethelm, S., Herle, J. V., and Maréchal, F. (2018). Optimal design of solid-oxide electrolyzer based power-to-methane systems: a comprehensive comparison between steam electrolysis and co-electrolysis. *Appl. Energy* 211, 1060–1079. doi:10.1016/j.apenergy.2017.11.050

Willauer, H. D., Hardy, D. R., Schultz, K. R., and Williams, F. W. (2012). The feasibility and current estimated capital costs of producing jet fuel at sea using carbon dioxide and hydrogen. *J. Renew. Sustain. Energy* 4 (3), 033111. doi:10.1063/1.4719723

Ye, Y., Ngo, H. H., Guo, W., Chang, S. W., Nguyen, D. D., Zhang, X., et al. (Forthcoming 2020). Nutrient recovery from wastewater: from technology to economy. *Bioresour. Technol. Rep.* 100425. doi:10.1016/j.biteb.2020.100425

Zhu, Y., Biddy, M. J., Jones, S. B., Elliott, D. C., and Schmidt, A. J. (2014). Techno-economic analysis of liquid fuel production from woody biomass via hydrothermal liquefaction (HTL) and upgrading. *Appl. Energy* 129, 384–394. doi:10.1016/j.apenergy.2014.03.053

Conflict of Interest: The authors declare that the research was conducted in the absence of any commercial or financial relationships that could be construed as a potential conflict of interest.

frontiers in Energy Research

ORIGINAL RESEARCH
published: 28 September 2020
doi: 10.3389/fenrg.2020.557466

Challenges and Opportunities of Carbon Capture and Utilization: Electrochemical Conversion of CO_2 to Ethylene

Cato A. R. Pappijn[1], *Matthijs Ruitenbeek*[2], *Marie-Françoise Reyniers*[1] *and Kevin M. Van Geem*[1]*

[1] Laboratory for Chemical Technology, Department of Materials, Textiles and Chemical Engineering, Ghent University, Ghent, Belgium, [2] Dow Benelux BV, PSPH R&D, Terneuzen, Netherlands

The discovery and development of efficient technologies that enable the use of CO_2 as a starting material for chemical synthesis (at scale) is probably one of the biggest scientific challenges of our time. But a key question is if the cure will not be worse than the disease? In this work, the economic feasibility of the electrochemical reduction of CO_2 to ethylene is assessed and it is demonstrated that from a Capital expenditure and Operational expenditure point of view the electrochemical production of ethylene from CO_2 is not feasible under the current market conditions. Even in the case that the renewable electricity price would be zero, the feasibility is hampered by the state-of-the-art catalyst performance (selectivity) and the cost of the electrochemical reactor. Turning the installation on and off, if this would be even practically possible, is not interesting because our study shows that because of the high Capital expenditure, the payback time of the process would become unacceptably high. Finally, because of the high electricity requirement, this Carbon Capture and Utilization process has a lower CO_2 avoidance potential than the substitution of gray electricity by green electricity. This means that today the available green electricity would best be used to close coal and gas based power plants instead of powering the electrochemical conversion of CO_2 to ethylene.

Keywords: carbon capture and utilization, CO_2 conversion, electrocatalysis, renewable and sustainable energy, ethylene

OPEN ACCESS

Edited by:
Francois M. A. Marechal, École Polytechnique Fédérale de Lausanne, Switzerland

Reviewed by:
Thomas Alan Adams, McMaster University, Canada
Umberto Desideri, University of Pisa, Italy

***Correspondence:**
Kevin M. Van Geem
kevin.vangeem@UGent.be

Specialty section:
This article was submitted to Process and Energy Systems Engineering, a section of the journal Frontiers in Energy Research

Received: *30 April 2020*
Accepted: *27 August 2020*
Published: *28 September 2020*

Citation:
Pappijn CAR, Ruitenbeek M, Reyniers M-F and Van Geem KM (2020) Challenges and Opportunities of Carbon Capture and Utilization: Electrochemical Conversion of CO_2 to Ethylene. Front. Energy Res. 8:557466. doi: 10.3389/fenrg.2020.557466

INTRODUCTION

Climate change, of which greenhouse gas emission is the main driver, is one of the most urgent challenges humanity is currently facing. As depicted in **Figure 1**, the atmospheric CO_2 concentration has been rising rapidly since the start of the measurements in March 1958, with an average increase of approximately 2 ppm per year over the past decade (Tans, 2019). In 2016, the atmospheric CO_2 concentration stayed above the symbolic 400 ppm mark all year round for the first time, corresponding to a 30% increase compared to the pre-industrial (before circa 1750) levels of 270 ppm (Betts et al., 2016). The Paris Agreement under the United Nations Framework Convention

Abbreviations CCS, carbon capture and sequestration; CCU, carbon capture and utilization; FE, Faradaic efficiency; EE, energy efficiency; CAPEX, capital expenditure; OPEX, operational expenditure; MEA, monoethanolamine; HVC, high-value chemical; BTX, benzene, toluene, xylene

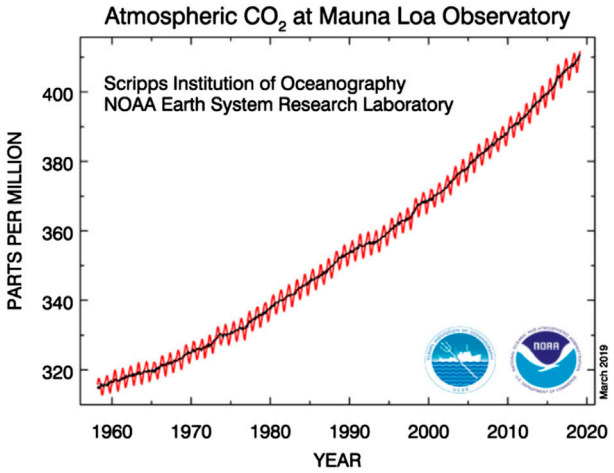

FIGURE 1 | Concentrations of CO_2 in the atmosphere measured at Mauna Loa Observatory (Hawaii) since the beginning of the measurements in March 1958 (316 ppm) (Tans, 2019).

on Climate Change adopted in 2015 illustrates the worldwide commitment to reduce greenhouse gas emissions to mitigate global warming, but this will require an order-of-magnitude increase in public and private investments in research and development between 2019 and 2030 (Rockström et al., 2017).

Strategies to reduce CO_2 emissions can be divided in four categories that focus on either avoidance of CO_2 emissions or binding the emitted CO_2 in a natural or non-natural sink. The first category is improving energy efficiency, which currently provides the greatest return on investment and has already been successfully applied in many industrial contexts. Although this approach still has potential, annual improvements of 1–2% will not be sufficient to meet the climate targets. The second category, using non- or low-carbon energy sources, (e.g., solar, wind, geothermal), is at large scale still challenging due to the fluctuating nature of the energy supply and the slow rate at which the electricity production is becoming more renewable. Carbon Capture and Sequestration (CCS), i.e., a series of technologies combining CO_2 capture from large point sources such as power plants, transportation to a storage site, and sequestration into a (natural) sink, is the third category, but its potential is currently rather limited due to technical and economic hurdles (Spigarelli and Kawatra, 2013; Leung et al., 2014). The fourth category is Carbon Capture and Utilization (CCU), in which CO_2 is converted to (high-value) products. This category can be considered as a special case of the third category with the utilization part acting as a non-natural sink (Whipple and Kenis, 2010; Kuhl et al., 2014; Schouten et al., 2014).

CO_2 is a thermodynamically very stable molecule and thus a substantial input of energy combined with effective reaction conditions and active catalysts are required for its conversion, c.f. **Figure 2**. To obtain the desired overall negative CO_2 balance, the energy required for its conversion should originate from non- or low carbon energy sources. Hence, the development of CO_2 conversion processes has focused on minimizing the required energy input by using the non or low-carbon energy sources in the most efficient way possible. According to a recent study (Voltachem, 2016), the development of new products through the application of innovative technologies powered by renewable energy is one of the main drivers for "electrification" of the chemical industry, i.e., replacing thermal and chemical energy by electrical energy. Other main drivers are economic benefits and improved sustainability through the reduction of feedstocks, by-products, waste, energy use, solvents, and CO_2.

Among all the proposed methods for converting CO_2, which have as common advantage the ease of integration of non- or low carbon energy sources, electrochemical methods are considered to be the most promising (Endrődi et al., 2017), as several advantages have been claimed compared to the other methods: 1) they can be conducted at ambient conditions (allowing for rapid changes in the production rate as the availability of the renewable energy changes), 2) by a careful selection of the electrocatalyst, electrolyte and operating conditions, it is possible to drive the electrochemical conversion of CO_2

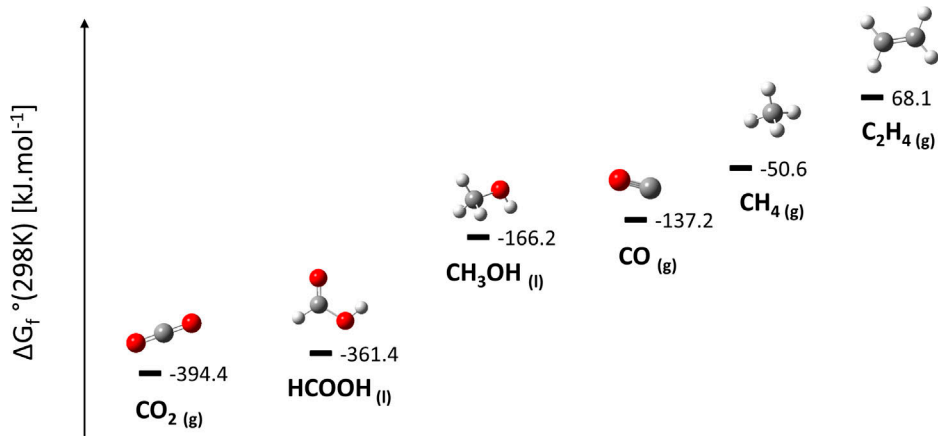

FIGURE 2 | Standard Gibbs free energy of formation (at 298 K), expressed in kJ mol^{-1}, of CO_2 and possible reduction products.

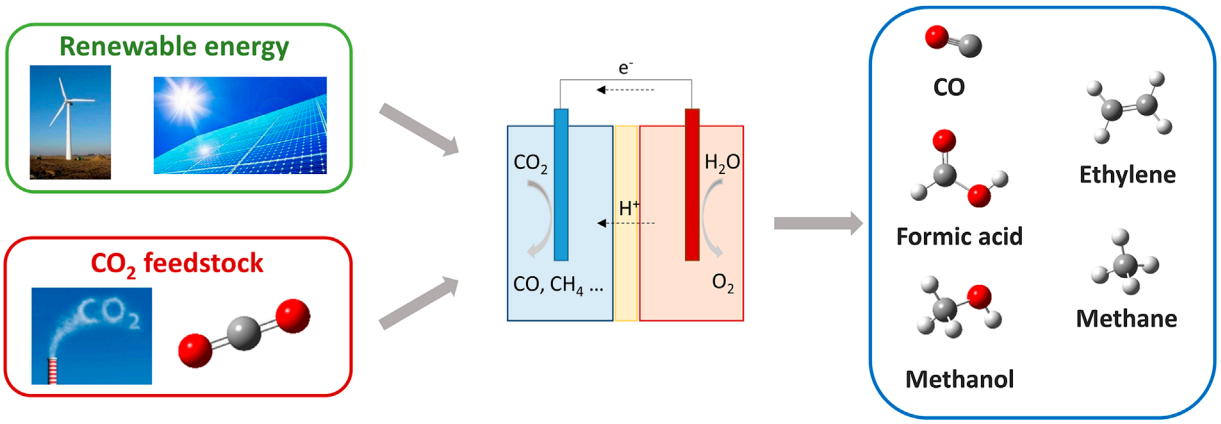

FIGURE 3 | Schematic representation of the production of high-value chemicals by the electrochemical reduction of CO_2 making use of renewable energy sources.

toward the desired products, 3) the chemical consumption can be minimized by recycling the electrolytes, 4) the reaction systems are compact, modular and hence scale-up is relatively straightforward, and 5) the electrons are directly used for product formation. However, there are clear challenges for electrification, such as the overall high cost of electricity, the large investment costs, the often poor selectivities and low conversions related to low reaction rates (resulting in large reactor volumes needed for a world-scale plant), the technical and economic feasibility of turning plants on and off safely on short notice, etc. This implies that there is a lot of skepticism whether electrification of the chemical industry is actually feasible (Van Geem et al., 2019; Gani et al., 2020) or whether it is another hype like the numerous ones that have been presented in the last two decades (Banholzer, 2012; Banholzer and Jones, 2013).

The goal of this study is to explore whether the electrochemical conversion of CO_2 can be a viable alternative production route of ethylene, which is the key building block of the chemical industry and representative for products with a reasonably high added value. First, a short overview is given of the CO_2 reduction process and the performance trends with the focus on ethylene formation. Next, a techno-economic model is developed for a CO_2 conversion plant integrated with CO_2 capture from a blast-furnace flue gas stream. With this model, the economic competitiveness of this alternative ethylene production route is compared against the current state of the art for ethylene production, i.e., naphtha-based steam cracking, under both current and future conditions. Finally, the CO_2 avoidance potential of the process is assessed based on a Life Cycle Analysis, adopting a cradle-to-gate boundary.

METHODOLOGY

Electrochemical Conversion of CO_2

The electrochemical reduction of CO_2 is a complex conversion consisting of multiple elementary proton-electron reactions leading to the (co-)formation of various products of which ethylene has the highest commercial value. As depicted in **Figure 3**, CO_2 is converted at the negatively charged cathode to primarily CO, methane, ethylene and formic acid, while H_2O is oxidized into O_2 at the anode. The half-cell reactions for the electrochemical reduction of CO_2 and the corresponding formal reduction potential are summarized in **Table 1** (Bard et al., 1985). For all possible reduction products, the reaction proceeds *via* CO as intermediate species (Hori, 2008). In aqueous environment, the hydrogen evolution reaction competes with the reduction of CO_2. Aside from the employed electrocatalyst and electrode potential, the product distribution obtained from the electrochemical reduction of CO_2 depends on the choice of electrolyte, the electrolyte concentration, the concentration of dissolved CO_2 and the reaction conditions, i.e., pressure and temperature.

To evaluate the technological performance of this electrochemical process and enable a meaningful comparison between different electrocatalysts, several figures of merit are commonly used (Pander III et al., 2017). Because the reduction of CO_2 has to overcome a kinetic energy barrier, the cell potential at which the redox reaction is experimentally observed (E), is higher than the reversible cell potential (E^0) and the difference between the two is denoted as the overpotential (η), c.f. **Eq. 1**.

TABLE 1 | Half-cell reactions and the corresponding formal redox potential E^0 (V) for the electrochemical reduction of CO_2. All potentials are referenced against the standard hydrogen electrode (Bard et al., 1985).

Half-cell reaction	E^0 (V)
$2H^+ + 2e^- \leftrightarrow H_2$	0.00
$CO_2 + 2H^+ + 2e^- \leftrightarrow HCOOH$	−0.61
$CO_2 + 2H^+ + 2e^- \leftrightarrow CO + H_2O$	−0.53
$CO_2 + 6H^+ + 6e^- \leftrightarrow CH_3OH + H_2O$	−0.38
$CO_2 + 8H^+ + 8e^- \leftrightarrow CH_4 + 2H_2O$	−0.24
$2CO_2 + 12H^+ + 12e^- \leftrightarrow C_2H_4 + 4H_2O$	−0.34
$2H_2O \leftrightarrow O_2 + 4H^+ + 4e^-$	1.23

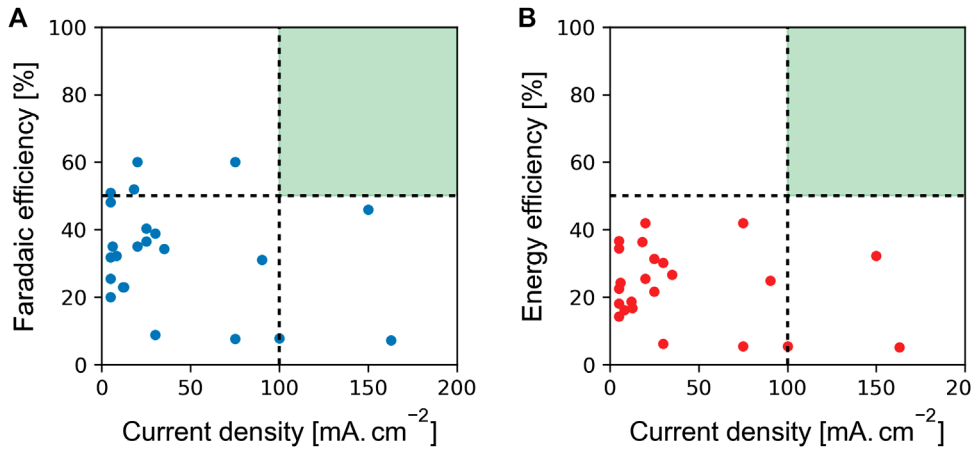

FIGURE 4 | Summary of the electrochemical performance of CO_2 reduction to ethylene from a selection of studies reported in the open literature published in the period from 1986 to 2019: Faradaic efficiencies **(A)** and energy efficiencies **(B)** as a function of current density (mA cm^{-2}) (Hori et al., 1985; Kaneco et al., 1999; Ogura et al., 2004; Hori, 2008; Engelbrecht et al., 2016; Ma et al., 2016; Mistry et al., 2016; Wu et al., 2016; Ke et al., 2017; Peng et al., 2017; Gao et al., 2019).

$$\eta = E - E^0 \tag{1}$$

Minimizing the overpotential of the desired electrochemical reaction minimizes the required energy input. The Faradaic efficiency (*FE*) or current efficiency is a measure for the product selectivity of the reduction process for a given product, and is equal to the ratio of the charge used to generate a given product and the total charge passed during the electrolysis process (**Eq. 2**).

$$FE = \frac{z\,n\,F}{Q} \tag{2}$$

With z the number of electrons transferred in the corresponding half reaction, n the number of moles of a certain product and F Faraday's constant. A second efficiency indicator is the energy efficiency (*EE*), c.f. **Eq. 3**, which is the ratio of the amount of energy in the products and the amount of energy put into the system.

$$EE = \frac{E^0}{E^0 + \eta} \cdot FE \tag{3}$$

In general terms, the lower the overpotential and the higher the Faradaic efficiency, the higher the energy efficiency of the process. Finally, the current density (i), which is defined as the ratio of the current at a given cell potential (R') and the active electrode area (A), determines together with the Faradaic efficiency the specific electrochemical reaction rate, c.f. **Eq. 4**. The lower the current density, the higher the electrode surface area required to obtain a certain reaction rate. Hence, this parameter significantly influences the cost of the electrochemical reactor, and the sensitivity to Capital expenditure (CAPEX) and Operational expenditure (OPEX) has been investigated (Jhong et al., 2013).

$$r = \frac{R'}{A} = \frac{i \cdot FE}{z \cdot F} \tag{4}$$

Process Conditions and Selectivity

To enable a feasible large-scale implementation of an electrochemical CO_2 reduction process, the development of an active, selective, stable, and relatively low-cost electrocatalyst is a prerequisite. Over the last few years, many researchers focused on the exploration of different electrocatalysts with the aim of addressing the key challenges of this electrochemical process (Hori et al., 1985; Hara et al., 1997; Hori, 2008; Rakowski Dubois and Dubois, 2009; Peterson and Nørskov, 2012; Schneider et al., 2012; Qiao et al., 2014; Kortlever et al., 2015; Mao and Hatton, 2015; Engelbrecht et al., 2016; Kortlever et al., 2016; Wu et al., 2016; Tao et al., 2017): 1) reduce the overpotential (or increase energy efficiency), 2) increase the selectivity (or Faradaic efficiency), 3) increase current density, and 4) expand catalyst lifetime (less than 100 h) with order of magnitude. While new studies reporting improved Faradaic efficiencies and lower overpotentials are consistently being published, the important question remains what the performance of the reduction process should be to enable implementation of a feasible large-scale industrial process. As a rule of thumb, industrial reactors are typically operated at geometric current densities above 100 mA cm^{-2} with at least 50% Faradaic efficiency for the required products, in order to minimize investment costs as much as possible (Oloman and Li, 2008). In **Figure 4**, an overview is given of the electrochemical performances for CO_2 reduction to ethylene from a selection of studies reported in the open literature published in the period from 1986 to 2017. The overpotential, which determines the energy efficiency of the process, ranges from −0.8 to −2.4 V. While significant progress has been made over the last few years, the performance of state-of-the art technologies seems to be currently not yet at the level required for an economically viable large-scale process, indicated by the green zone and applying the rule of thumb specified above.

Aside from activity and selectivity issues, rapid deactivation of the catalysts, which leads to a shift in the product distribution favoring the hydrogen evolution reaction, is also one of the main

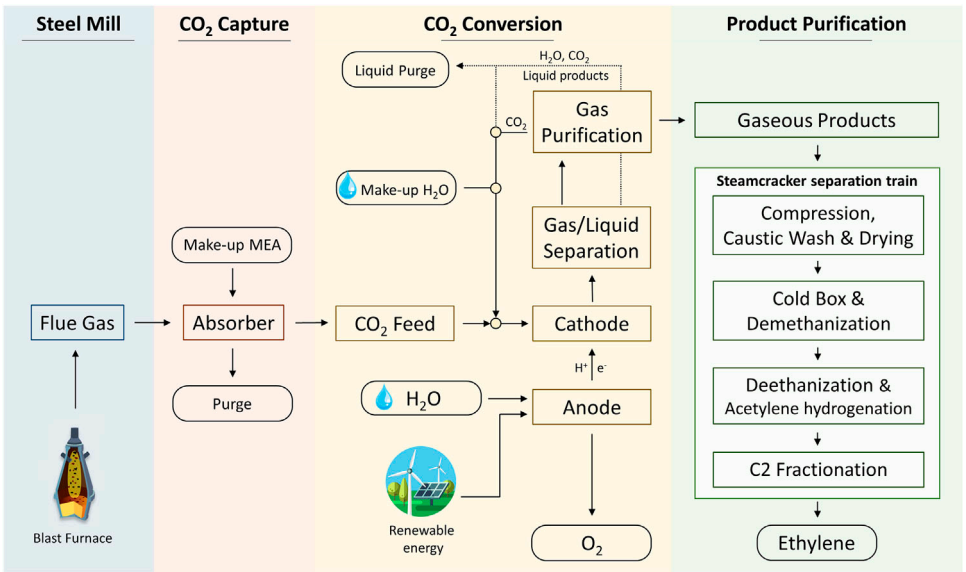

FIGURE 5 | Envisioned process scheme for the electrochemical conversion of a CO_2-containing flue gas stream to high-value chemicals.

challenges. In most cases, the catalyst lifetime is under 100 h (Qiao et al., 2014). The factors influencing the catalyst lifetime have so far not been analyzed in detail, also because most experiments are performed in a limited time span focusing on improving the initial catalyst performance. Although the exact cause for catalyst deactivation is not always clear, several hypotheses have been suggested, including electrolyte trace impurity deposition, accumulation of adsorbed or insoluble reaction by-products and morphological changes of the catalyst. A lifetime in the order of magnitude of thousands of hours is required for a viable large-scale process. Otherwise, frequent regeneration of the electrodes should be foreseen in the process (Dominguez-Ramos et al., 2015; Martin et al., 2015).

It is clear that several technological breakthroughs are needed before the electrochemical reduction of CO_2 can become industrially feasible. A roadmap for the electrochemical reduction of CO_2 has recently been developed within EU's Energy program, proposing both short-term and long-term practical goals (Koper and Roldan, 2019). In the next 5 years, significant progress should be made on the development of CO_2 electrocatalysts and electrolyzers, operating at relevant current densities (>100 mA cm^{-2}), with high Faradaic efficiency for high-value products such as ethylene, at lower overpotential (2.0–2.2 V), and good stability (>100 h). In the long term, the integration with downstream operations as well as integration with upstream CO_2 capture should be considered.

Conceptual Process Design

In **Figure 5**, a conceptual process scheme for the electrocatalytic conversion of CO_2 is depicted. The first step of the process is the capture of CO_2 from the flue gas stream and transport to the conversion unit. The CO_2 source for this study is considered to be blast furnace gas, which contains ~22 mol% CO, ~22 mol% CO_2, ~5 mol% H_2, and ~51 mol% N_2. The CO_2 is captured *via* chemical absorption with monoethanolamine (MEA) as solvent. The blast furnace technology will continue to dominate steel production in the coming decade and the only way to substantially reduce the associated CO_2 emissions is to combine it with CCS or CCU options. In an absorber column the CO_2-containing gas stream is contacted with a solvent, after which it is desorbed again from the solvent in a stripper column. As MEA can undergo degradation and is also lost *via* the gasses that are vented into the atmosphere, a make-up of this chemical is required. Chemical absorption with MEA results in a high CO_2 purity product stream (>98 wt%), with H_2O as the main impurity, while traces of N_2 and MEA can also be present (Li et al., 2016). Gaseous impurities can have an effect on the electrolysis process in different ways, i.e., they can act as 1) as diluents (e.g., N_2), 2) as reducible species (e.g., O_2), and 3) as catalyst poisoning species (e.g., NO_2, SO_2, H_2S, organic gases) (Zhai et al., 2019). To enable industrial application, the influence of gaseous impurities on the electrolysis process needs to be better understood to avoid catalyst degradation. The captured CO_2 is combined with a possible recycle stream and sent to the reactor in which the electrochemical reduction takes place. At the cathode, CO_2 is reduced resulting in the formation of the main products CO, ethylene, methane, hydrogen and formic acid, while at the anode H_2O is oxidized into O_2. The global reaction for the production of ethylene is:

$$2\,CO_2 + 2\,H_2O \leftrightarrow C_2H_4 + 3O_2$$

The product stream that leaves the cathode compartment of the reactor is sent to a flash vessel. The obtained liquid stream contains mainly electrolyte and unconverted CO_2 and can be sent back to the reactor. In order to avoid the accumulation of liquid byproducts (i.e., formic acid), part of this stream is purged. The

gas stream contains ethylene, unconverted CO_2, and significant amounts of other byproducts, such as CO and H_2. A gas purification section is required which serves two main goals: separation of the unconverted CO_2 for re-use and purification of the desired products (in this case ethylene), and byproducts.

Economic Analysis

To assess the actual economic feasibility of this alternative production route for ethylene, the CAPEX and OPEX have been estimated. A grass-roots plant is considered, built in Northwestern Europe. Cost calculations are thus based on European prices. Cost functions are introduced to estimate the CAPEX and OPEX for the different steps of the electrochemical conversion process, i.e., CO_2 capture, CO_2 conversion and product separation and purification. Because of the large scale of this industrial process, the feasibility study is done for the replacement of a part of the installed production capacity based on fossil fuels, i.e., steam cracking of naphtha. This means it is assumed that the gaseous product stream, after CO_2 removal, is further processed on the separation section of an existing steam cracking facility. No costs have thus been estimated for the product separation and purification steps, except for capturing and recycling of the unconverted CO_2. Using estimates from literature data for the specific capital cost and energy requirement, the CAPEX and OPEX are written as a function of four different parameters for the different steps. These parameters, which are related to both the process and to external factors, are: (carbon-based) product selectivity, (single-pass) conversion, CO_2 value, and electricity price. All other parameters appearing in the cost functions are rewritten as a function of these four critical parameters.

Capital Expenditure Estimation

The estimated CAPEX for the CO_2 capture plant is based on a specific capital cost of 70 €/metric ton CO_2/year (Kuramochi et al., 2011). For the installed cost of the electrochemical reactors, a value of 66 million € is reported in literature, for the conversion of 100 metric ton CO_2 per day (Oloman and Li, 2008). This value corresponds to 70 electrochemical flow reactors each with 100 cells of 0.5 m^2. No economies of scale are taken into account for the electrochemical reduction of CO_2, due to the modular character of the electrochemical cells. To improve the overall conversion of the electrochemical process, unconverted CO_2 is separated from the gaseous products and recycled back to the reactor. This is done *via* an additional MEA absorption system, for which the same specific capital cost of 70 €/metric ton CO_2/year is taken (Kuramochi et al., 2011). Because the assumption is made that the gaseous product stream, after CO_2 removal, is further processed in the separation section of the existing steam cracking facility, no costs are associated to further product separation and purification steps. The maintenance cost is estimated as 2.5% of the CAPEX.

Operational Expenditure Estimation

The main energy contribution for the CO_2 capture process is the generation of steam required for the desorption process. This energy is provided making use of natural gas with an efficiency of 85% and a thermal energy price of 8.3 €/GJ (Eurostat (2019)). Mechanical energy required for the pumps and compressors, is assumed to be delivered by electromotors. The thermal and electrical energy requirements for the MEA absorption system are taken from Kuramochi et al. (2011), i.e., 3.2 and 0.50 GJ/metric ton CO_2, respectively. The cost of MEA losses is assumed to be 4.6 €/metric ton CO_2 (Karl et al., 2011). With respect to the OPEX of the electrochemical reactor, there are two main contributions: the usage of chemicals and the consumption of energy (i.e., electricity). The energy required for the conversion of CO_2 is among others determined by the selectivity or equivalently the Faradaic efficiency of the desired reaction, in this case the conversion to ethylene. For a Faradaic efficiency of 60%, approximately 20 MW h per metric ton of converted CO_2 is required. The specific energy consumption decreases with a factor two when considering the limiting case of a Faradaic efficiency of 100% (Agarwal et al., 2011). This confirms the importance of technological advancements regarding the energy efficiency of the process to enable large-scale industrial production. With respect to the cost of chemicals, the critical assumption is made that the electrolytes can be fully recycled, which means that the main cost is included in the CAPEX, and in the OPEX only recycling costs need to be taken into account.

TABLE 2 | Applied pricing (March 2018) level for the major materials in this study (ICIS Pricing Database; Platts Global Ethylene Price Index; Platts Global Propylene Price Index).

	Price (€/metric ton)
Naphtha	500
Ethylene	1,050
Propylene	840
Butadiene	900
Pygas (BTX)	750

Economic Analysis

For the case study, an annual ethylene production of 10^5 metric ton is considered, which corresponds to approximately 5–20% of a typical ethylene production site based on fossil feedstocks. At 100% conversion and selectivity, the electrocatalytic conversion of CO_2 would require 3.14×10^5 metric ton of CO_2 per year, which corresponds to about 5–10% of the CO_2 emissions of that same ethylene production site. As a base case, the production of polymer-grade ethylene based on a fossil feedstock, i.e., steam cracking of naphtha, is taken, as this is and will remain the predominant process for the production of olefins in the coming decades (Amghizar et al., 2017). For this process, a yield of high-value chemicals (HVC) of 55 wt% is assumed, with an ethylene and propylene yield of, respectively, 30 and 15 wt% (after hydrogenation of acetylene, methyl acetylene and propadiene). The detailed effluent composition obtained from Zimmermann and Walzl (2000) can be found in the **Supplementary Material**.

The estimated CAPEX and OPEX for the furnace section of a naphtha-based steam cracker located in Europe are equal to respectively 500 and 225 €/metric ton ethylene (Brown, 2019,

TABLE 3 | Values for the three input parameters, i.e., product selectivity (%), conversion (%), CO_2 value (€/metric ton) and electricity price (€/MW h) for the five different cases.

Parameter	References	High selectivity	High conversion	High CO_2 value	Free electricity
Selectivity (%)	70	100	70	70	70
Conversion (%)	50	50	100	50	50
CO_2 value (€/metric ton)	−30	−30	−30	−100	−30
Electricity price (€/MW h)	35	35	35	35	0

Personal Communication). This corresponds to an energy requirement of approximately 9 GJ/metric ton HVC or 16 GJ/metric ton ethylene for the furnace section, in agreement with the value reported by Ren et al. (2008). Process upsets, technical issues, and turnarounds, are accounted for *via* the plant annual uptime, which is equal to 8,440 h per year or 96.3%. An overview of the main techno economic assumptions can be found in the **Supplementary Material**.

The revenues for the electrochemical process result from the sale of ethylene. Note that high-purity O_2 (90–95 wt%) can be considered as a valuable byproduct from the electrolysis process, but is it not taken into account in the product revenues. If possible, O_2 will be used in nearby chemical plants to avoid the high-cost transport needs. For the conventional steam cracking process the sale of other important products such as propylene, butadiene and BTX is also considered. The prices determined for March 2018, are summarized in **Table 2**, i.e., ethylene at 1,050 €/metric ton, propylene at 840 €/metric ton and naphtha at 500 €/metric ton. The gross margin is calculated as the difference between the revenue from the sale of products and the feedstock cost.

Five hypothetical cases were considered to assess the economic potential of this alternative ethylene production route compared to the base case, i.e., steam cracking of naphtha. These cases, with different values for the four critical parameters as shown in c.f. **Table 3**, are:

(1) Reference case: State-of-the-art electrolyzer performance based on Ogura et al. (2004) with a product selectivity of 70% and conversion of 50%, CO_2 value of −30 €/metric ton and an industrial electricity price of 35 €/MW h (Haegel et al., 2017).
(2) High selectivity: Selectivity of 100% and conversion of 50%, CO_2 value of −30 €/metric ton and an industrial electricity price of 35 €/MW h.
(3) High conversion: Selectivity of 70% and conversion of 100%, CO_2 value of −30 €/metric ton and an industrial electricity price of 35 €/MW h.
(4) High CO_2 cost: Selectivity of 70% and conversion of 50%, CO_2 value of −100 €/metric ton and an industrial electricity price of 35 €/MW h.
(5) Free electricity: Selectivity of 70% and conversion of 50%, CO_2 value of −30 €/metric ton and zero cost electricity.

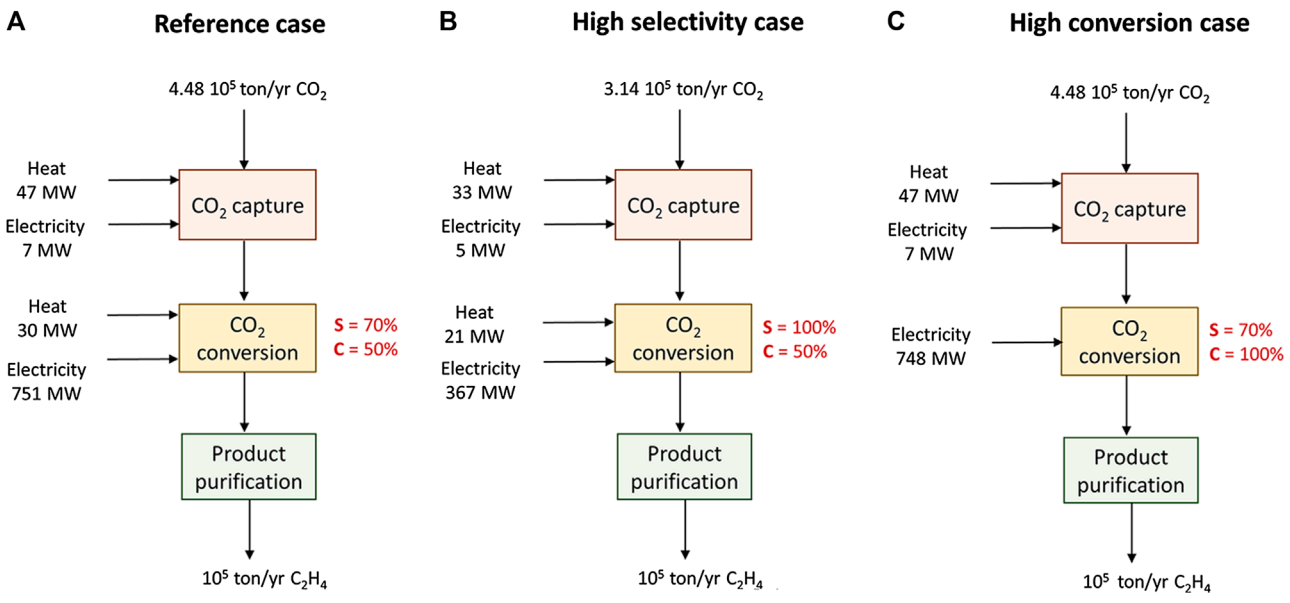

FIGURE 6 | Black box representations of the electrochemical reduction of CO_2 with the electrolyzer performance, i.e., conversion (C) and selectivity (S), energy input and material streams that have been considered in the economic analysis for the **(A)** reference, high CO_2 cost and free electricity cases, **(B)** the high selectivity case, and **(C)** the high conversion case.

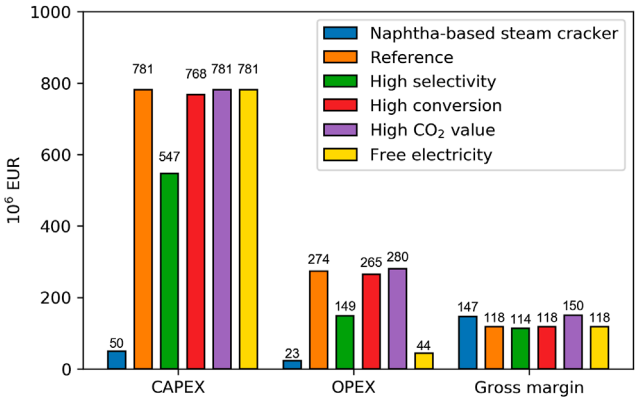

FIGURE 7 | Capital expenditure, Operational expenditure, and gross margin (in 10^6 €) for the naphtha-based steam cracker, the reference electrochemical case, the high selectivity case, the high conversion case, the high CO_2 cost case and the free electricity case.

RESULTS AND DISCUSSION

Economic Evaluation

In **Figure 6**, the main energy input and material streams considered in the economic analysis are shown. Note that for the reference case, the high CO_2 price case and the free electricity case, these values are identical, as the only difference between these three cases is caused by a change in CO_2 and electricity price. For a product selectivity of 70%, a larger flow of CO_2 is required to obtain the desired ethylene production capacity (10^5 metric ton per year), i.e., 4.48×10^5 metric ton CO_2 per year compared to 3.14×10^5 metric ton CO_2 per year in case of a product selectivity of 100%. This lower product selectivity leads to larger energy requirements for the CO_2 capture step. The thermal energy required in the CO_2 capture step is equal to approximately 87% of the total energy need. The thermal energy input in the CO_2 conversion step is used in the recycle loop for the separation of unconverted CO_2 from the gaseous product. In the case of complete conversion of CO_2, there is no need for this separation step and hence the thermal energy input becomes negligible. The energy consumption for the CO_2 conversion step is dominated by the electricity need. Taking into account that the plant runs for 8,440 h in one year (or 96% of the time), this corresponds to a continuous power requirement of 367 MW. If the product selectivity decreases to 70%, the required electrical power increases to 751 MW.

Figure 7 summarizes the CAPEX, OPEX and gross margins, i.e., the difference between revenues and feedstock cost, for the five studied cases and the base case, i.e., naphtha-based steam cracking. It can be seen that currently the main disadvantage of the electrochemical process is the high CAPEX of the electrochemical reactor, which is a consequence of expensive electrode materials combined with limited economies of scale due to the modular character of the electrochemical cells. However, when considering the gross margin, the electrochemical process looks promising compared to the conventional steam cracking route, due to the lower feedstock cost. Hence, future R&D efforts should aim to develop highly active, selective, stable and low-cost electrocatalysts in order to decrease the reactor CAPEX. For each case, the CAPEX, OPEX, and gross margin of the different steps, i.e., CO_2 capture, CO_2 conversion, and product separation, can be found in the **Supplementary Material**.

Sensitivity Analysis

A global sensitivity analysis has been conducted in order to investigate the influence of the dominant parameters, i.e., selectivity, conversion, CO_2 price, and electricity price, on the economics of the electrochemical process. The results for the sensitivity of the CAPEX, OPEX, and gross margin with respect to the reference electrochemical case are shown in **Figure 8**. As expected the selectivity to ethylene is the parameter with the largest influence on the CAPEX and the OPEX of the process. For a lower selectivity, more energy is lost in byproduct formation. More energy is thus required to obtain a desired production capacity of ethylene. A higher electricity consumption also increases the total electrolyzer area, resulting in a higher electrolyzer CAPEX. The conversion, which determines the required capacity of the recycle loop, has only a limited influence. This is also the case for the price of CO_2, which is

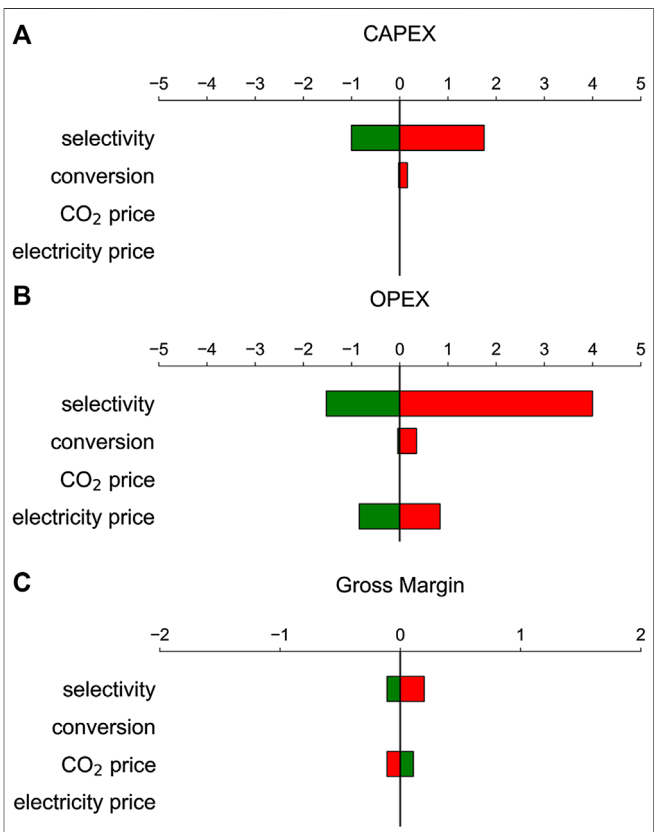

FIGURE 8 | Sensitivity analysis of the **(A)** Capital expenditure (CAPEX), **(B)** Operational expenditure (OPEX), and **(C)** gross margin for a positive (green) or negative (red) change of the model parameters (selectivity, conversion, CO_2 price and electricity price) for the reference electrochemical case.

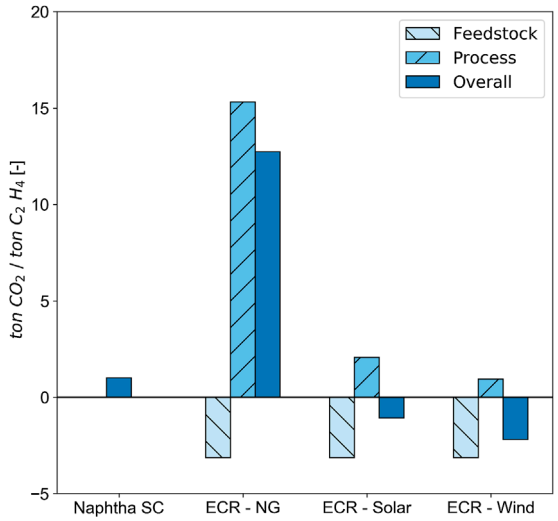

FIGURE 9 | CO_2 emissions per metric ton of ethylene produced: Comparison between steam cracking (SC) of naphtha and the electrochemical reduction (ECR) of CO_2 using electricity from natural gas (NG), solar and wind energy. For the ECR process, both the CO_2 used as feedstock as well as the CO_2 emitted during the complete process is considered.

encouraging as it reduces the dependence of the process on a factor that is mainly determined by macro-economic and political factors ("CO_2 tax" *vs.* capture costs). The electricity price is one of the main parameters influencing the economic feasibility of the process. Some people argue whether or not it would be beneficial to operate an electrochemical process only when the electricity price is below a certain threshold value, i.e., operate the production plant in a flexible manner according to the energy market. The mild operating conditions, i.e., ambient temperature, and the modular character of a world-scale plant would allow rapid changes in production rate. However, due to the extremely high CAPEX of the electrochemical process, we believe that it would be more beneficial to run the process continuously with a fluctuating energy price, rather than operating it as a discontinuous process. This is primarily motivated by the payback time and for the chemical industry this is typically in the order of a decade for large investments (Anderson and Fennell, 2013). Turning the installation on and off would result in an unacceptably high payback time. Also, the practical feasibility of ramping up or down such a large scale production unit should be considered and there is not a lot of published work on the start-up and shutdown of electrochemical reactors (Rousar et al., 1986; Bisang 1997).

Energy Considerations

If the CO_2 reduction process results in an overall negative net CO_2 balance, it can be considered a viable carbon recycling technology. This means that the amount of CO_2 emitted during the complete process needs to be lower than the amount of CO_2 converted. For naphtha-based steam cracking, the CO_2 emissions are approximately 1 metric ton CO_2 per metric ton ethylene (Ren et al., 2006). These emissions are the result of fuel combustion and utilities, both of which use fossil fuel. The main contributor is the furnace with over 90% of the CO_2 emissions (Amghizar et al., 2020). Because the electrochemical reduction of CO_2 to ethylene requires a significant amount of electrical power, it is clear that the electricity needs to come from low-carbon energy sources, such as wind and solar energy, to obtain an overall negative CO_2 balance. Because of their intermittent nature, both solar and wind energy have a reduced capacity factor, which is not accounted for in the presented analysis. We assume that access to green electricity is continuous and steady state operation is possible. The CO_2 emissions of the alternative ethylene production route are based on a Life Cycle Analysis, adopting a cradle-to-gate boundary, i.e., usage and end-of-life treatment are not included (von der Assen et al., 2013). In this analysis, the CO_2 feedstock is considered as a regular feedstock with its own production emissions. The emission intensities for Northwestern Europe, expressed in kg CO_2 equivalents per MW h for natural gas, solar and wind are equal to respectively 490, 48, and 12 kg CO_2eq/MW h (Schlömer et al., 2015). In **Figure 9**, the CO_2 emissions per metric ton of ethylene produced are compared between the base case, i.e., steam cracking of naphtha, and the electrochemical reduction of CO_2 using gray electricity from a natural gas power plant, and green electricity from both solar and wind energy. The overall CO_2 balance for the electrochemical route is based on an ideal electrolyzer, i.e., operating at a conversion and selectivity of 100%. The production of 1 metric ton of ethylene requires 3.14 metric ton of CO_2 as carbon feed, while the electrolyzer uses approximately 10 MW h per metric ton CO_2. The thermal energy demand for the CO_2 capture step, i.e., 3.2 GJ/metric ton CO_2 amounts to 0.56 metric ton CO_2 per metric ton ethylene. The CO_2 emissions related to the conversion step are equal to 1.50 and 0.37 metric ton CO_2 per metric ton ethylene, using respectively solar and wind energy. The small difference in emission intensity between these two low-carbon energy sources leads to a significant difference in CO_2 emissions per metric ton CO_2 due to the large electricity demand. From **Figure 9**, it can be seen that this alternative production route of ethylene can potentially lead to a reduction of CO_2 emissions. Note that the CO_2 emissions related to the product separation and purification steps are not taken into account in this calculation.

As stated before, it is clear that the electroreduction of CO_2 needs to be powered by green electricity in order to obtain an overall negative net CO_2 balance. The fact that reducing CO_2 emissions through CCU processes will only be possible if the electricity (and in some cases the thermal energy) inputs are from renewable sources has been included in earlier studies (Bennett et al., 2014; Jouny et al., 2018; Spurgeon and Kumar, 2018; Mohsin et al., 2020). One of the challenges for electrolyzers powered by renewable energy is the operation at strongly fluctuating power inputs and with frequent interruptions due to low input (Mergel et al., 2013). The dynamic behavior of the electrochemical reactor as well as the downstream system components, (e.g., electrolyte circuit, gas separator) needs to be analyzed such that load changes do not present any problems over a large power input range. For water electrolysis, systems have been developed which allow for a large partial load range (5–100%) and can accommodate extreme overloads. Operating the electrolyzer at

a very low level (i.e., at 10% of peak load) avoids the need to shut down the chemical plant completely and the associated energy losses during start-up (Brauns and Turek, 2020). In case the electrolyzer has been designed for constant conditions, the occurring power fluctuations can be damped by additional energy storage devices, which are charged when excess renewable energy is available. Overall, it can be concluded that more theoretical and experimental work is needed to better understand the dynamic behavior of CO_2 electrolyzers powered by intermittent renewable energy.

Instead of considering the amount of CO_2 emitted or avoided per metric ton ethylene, one can also look at the amount of CO_2 avoided per energy unit of green electricity. In other words, what is the most efficient way to reduce CO_2 emissions with 1 MW h of green electricity? With an electrical energy of 1 MW h, approximately 0.032 metric ton ethylene can be produced, assuming again an ideal electrolyzer performance. This ethylene formation converts 0.10 metric ton of CO_2, but also leads to 0.030 metric ton of CO_2 emitted using wind power as renewable energy source. The production of 0.032 metric ton ethylene *via* the traditional steam cracking route results in approximately 0.058 metric ton of CO_2 emitted. Thus, by producing this ethylene *via* the alternative electrochemical route instead of the fossil-fuel based process, there is a potential of lowering the emitted CO_2 by 0.13 metric ton per MW h. Using the emission intensities, 1 MW h of electricity generated from coal and natural gas, leads to respectively 0.82 and 0.49 metric ton CO_2 emitted per MW h (Schlömer et al., 2015). This implies that from an energy point of view, it is more beneficial to use 1 MW h green electricity to replace 1 MW h gray electricity than use it to convert CO_2 electrochemically in ethylene.

A key performance indicator often used to compare different CCU processes is the cost of CO_2 avoided, i.e., the cost to avoid the emission of 1 metric ton of CO_2 relative to a reference case. The production cost for fossil ethylene considering a plant located in Europe, is dominated by the feedstock cost and equal to approximately 700 € per metric ton of ethylene. For CO_2-based ethylene, the production cost is equal to 1,950 € per metric ton of ethylene, assuming again an ideal electrolyzer, and an electricity price of 35 €/MW h. This value is in agreement with the study of Jouny et al. (2018), in which they report a production cost of approximately 2000 € per metric ton of ethylene, for their "optimistic case," using the same electricity price of 35 €/MW h and a faradaic efficiency of 90%. The net CO_2 emissions for the CO_2 reduction process using solar and wind energy are equal to respectively −1.08 and −2.20 metric ton CO_2 per metric ton ethylene. Based on these values, the CO_2 avoidance cost amounts to 602 and 391 € per metric ton CO_2 avoided. Note that these values are significantly higher than the recent prices of the CO_2 allowances envisioned by the European Emission Trading Scheme, i.e., 28 €/metric ton CO_2 in 2030 and 43 €/metric ton CO_2.

CONCLUSIONS

Electrochemical conversion of CO_2 to ethylene could be of interest to the chemical industry, but several breakthroughs are needed to make this competitive with the current state of the art under current market conditions. Without a substantial decrease of the electricity price and large capacity increases in renewable electricity production (to become a reliable provider at continuous low prices), this alternative ethylene production route seems infeasible for the chemical industry. Due to high capital costs for the electrochemical technology, it makes no sense to run these installations only in times when renewable power would be abundantly available and hence cheap. Turning large scale chemical processes "on" and "off" is today economically unfavorable, not even when assuming that safety would be guaranteed and an instantaneous shut down would be feasible. When combined with green electricity, e.g., wind and solar, the electrochemical reduction of CO_2 can lead to a negative overall CO_2 balance. However, from an energy point of view, using green electricity to replace gray electricity, has a larger CO_2 avoidance potential, compared to using it for the electrochemical production of ethylene.

DATA AVAILABILITY STATEMENT

The raw data supporting the conclusions of this article will be made available by the authors, without undue reservation.

AUTHOR CONTRIBUTIONS

CP: conceptualization, formal analysis, investigation, writing—original draft, visualization, writing—review and editing. MR: conceptualization, data curation, writing—review and editing. M-FR: writing—review and editing. KG: conceptualization, supervision, writing—review and editing, and funding acquisition.

FUNDING

CP acknowledges financial support from a doctoral fellowship from the Research Foundation—Flanders (FWO). The research leading to these results has also received funding from the European Research Council under the European Union's Horizon 2020 research and innovation program (ERC Grant Agreement No. 818607).

ACKNOWLEDGMENTS

Kees Biesheuvel, Ronald Wevers, Hanne Schatteman, Hannes Saeid Bakhsh, and Thomas Vandeputte are thanked for their valuable contributions.

SUPPLEMENTARY MATERIAL

The Supplementary Material for this article can be found online at: https://www.frontiersin.org/articles/10.3389/fenrg.2020.557466/full#supplementary-material

REFERENCES

Agarwal, A. S., Zhai, Y., Hill, D., and Sridhar, N. (2011). The electrochemical reduction of carbon dioxide to formate/formic acid: engineering and economic feasibility. *ChemSusChem* 4, 1301–1310. doi:10.1002/cssc.201100220

Amghizar, I., Vandewalle, L. A., Van Geem, K. M., and Marin, G. B. (2017). New trends in olefin production. *Engineering* 3, 171–178. doi:10.1016/j.eng.2017.02.006

Amghizar, I., Dedeyne, J. N., Brown, D. J., Marin, G. B., and Van Geem, K. M. (2020). Sustainable innovations in steam cracking: CO_2 neutral olefin production. *React. Chem. Eng* 5, 239–257. doi:10.1039/c9re00398c

Anderson, J., and Fennell, A. (2013). Calculate financial indicators to guide investments. *Chem. Eng. Prog* 109, 34–40.

Banholzer, W. F., and Jones, M. E. (2013). Chemical engineers must focus on practical solutions. *AIChE J* 59, 2708–2720. doi:10.1002/aic.14172

Banholzer, W. F. (2012). Practical limitations and recognizing hype. *Energy Environ. Sci* 5, 5478–5480. doi:10.1039/c2ee03146a

Bard, A. J., Parsons, R., and Jordan, J.International Union of Pure and Applied Chemistry (1985). *Standard potentials in aqueous solution*. New York, NY: M. Dekker.

Bennett, S. J., Schroeder, D. J., and Mccoy, S. T. (2014). Towards a Framework for discussing and assessing CO_2 utilisation in a climate context. *Energy Procedia* 63, 7976–7992. doi:10.1016/j.egypro.2014.11.835

Betts, R. A., Jones, C. D., Knight, J. R., Keeling, R. F., and Kennedy, J. J. (2016). El Niño and a record CO_2 rise. *Nat. Clim. Change* 6, 806. doi:10.1038/nclimate3063

Bisang, J. M. (1997). Modelling the startup of a continuous parallel plate electrochemical reactor. *J. Appl. Electrochem* 27, 379–384. doi:10.1023/a:1018401418261

Brauns, J., and Turek, T. (2020). Alkaline water electrolysis powered by renewable energy: a review. *Processes* 8, 248. doi:10.3390/pr8020248

Dominguez-Ramos, A., Singh, B., Zhang, X., Hertwich, E. G., and Irabien, A. (2015). Global warming footprint of the electrochemical reduction of carbon dioxide to formate. *J. Clean. Prod* 104, 148–155. doi:10.1016/j.jclepro.2013.11.046

Endrődi, B., Bencsik, G., Darvas, F., Jones, R., Rajeshwar, K., and Janáky, C. (2017). Continuous-flow electroreduction of carbon dioxide. *Prog. Energy Combust. Sci* 62, 133–154.

Engelbrecht, A., Hämmerle, M., Moos, R., Fleischer, M., and Schmid, G. (2016). Improvement of the selectivity of the electrochemical conversion of CO_2 to hydrocarbons using cupreous electrodes with in-situ oxidation by oxygen. *Electrochim. Acta* 224, 642–648. doi:10.1016/j.electacta.2016.12.059

Eurostat (2019). Natural gas price statistics [Online]. Available: https://ec.europa.eu/eurostat/statistics-explained/index.php/Natural_gas_price_statistics (Accessed February 15, 2019).

Gani, R., Bałdyga, J., Biscans, B., Brunazzi, E., Charpentier, J.-C., Drioli, E., et al. (2020). A multi-layered view of chemical and biochemical engineering. *Chem. Eng. Res. Des* 155, A133–A145. doi:10.1016/j.cherd.2020.01.008

Gao, J., Zhang, H., Guo, X., Luo, J., Zakeeruddin, S. M., Ren, D., et al. (2019). Selective C-C coupling in carbon dioxide electroreduction via efficient spillover of intermediates as supported by operando Raman spectroscopy. *J. Am. Chem. Soc* 141, 18704–18714. doi:10.1021/jacs.9b07415

Haegel, N. M., Margolis, R., Buonassisi, T., Feldman, D., Froitzheim, A., Garabedian, R., et al. (2017). Terawatt-scale photovoltaics: trajectories and challenges. *Science* 356, 141–143. doi:10.1126/science.aal1288

Hara, K., Kudo, A., and Sakata, T. (1997). Electrochemical CO_2 reduction on a glassy carbon electrode under high pressure. *J. Electroanal. Chem* 421, 1–4. doi:10.1016/s0022-0728(96)01028-5

Hori, Y., Kikuchi, K., and Suzuki, S. (1985). Production of Co and CH_4 in electrochemical reduction of CO_2 at metal electrodes in aqueous hydrogencarbonate solution *Chem. Lett* 14, 1695–1698. doi:10.1246/cl.1985.1695

Hori, Y. (2008). "Electrochemical CO_2 reduction on metal electrodes," in *Modern aspects of electrochemistry*. Editors C. G. Vayenas, R. E. White and M. E. Gamboa-Aldeco (New York, NY: Springer New York), 89–189.

ICIS Pricing Database. Available at: https://www.icis.com/explore/commodities/energy/gas/europe/ (Accessed February 15, 2019).

Jhong, H.-R. M., Ma, S., and Kenis, P. J. (2013). Electrochemical conversion of CO_2 to useful chemicals: current status, remaining challenges, and future opportunities. *Curr. Opin. Chem. Eng* 2, 191–199. doi:10.1016/j.coche.2013.03.005

Jouny, M., Luc, W., and Jiao, F. (2018). General techno-economic analysis of CO_2 electrolysis systems. *Ind. Eng. Chem. Res* 57, 2165–2177. doi:10.1021/acs.iecr.7b03514

Kaneco, S., Iiba, K., Suzuki, S.-K., Ohta, K., and Mizuno, T. (1999). Electrochemical reduction of carbon dioxide to hydrocarbons with high faradaic efficiency in LiOH/methanol. *J. Phys. Chem. B* 103, 7456–7460. doi:10.1021/jp990021j

Karl, M., Wright, R. F., Berglen, T. F., and Denby, B. (2011). Worst case scenario study to assess the environmental impact of amine emissions from a CO_2 capture plant. *Int. J. Greenh. Gas Con* 5, 439–447. doi:10.1016/j.ijggc.2010.11.001

Ke, F.-S., Liu, X.-C., Wu, J., Sharma, P. P., Zhou, Z.-Y., Qiao, J., et al. (2017). Selective formation of C_2 products from the electrochemical conversion of CO_2 on CuO-derived copper electrodes comprised of nanoporous ribbon arrays. *Catal. Today* 288, 18–23. doi:10.1016/j.cattod.2016.10.001

Koper, M., and Roldan, B. (2019). Research needs towards sustainable production of fuels and chemicals (EnergyX). Available: https://energy-x.eu/wp-content/uploads/2019/10/Energy-X-Research-needs-report.pdf (Accessed February 10, 2019).

Kortlever, R., Shen, J., Schouten, K. J. P., Calle-Vallejo, F., and Koper, M. T. M. (2015). Catalysts and reaction pathways for the electrochemical reduction of carbon dioxide. *J. Phys. Chem. Lett* 6, 4073–4082. doi:10.1021/acs.jpclett.5b01559

Kortlever, R., Peters, I., Balemans, C., Kas, R., Kwon, Y., Mul, G., et al. (2016). Palladium-gold catalyst for the electrochemical reduction of CO_2 to C1–C5 hydrocarbons. *Chem. Commun* 52, 10229–10232. doi:10.1039/c6cc03717h

Kuhl, K. P., Hatsukade, T., Cave, E. R., Abram, D. N., Kibsgaard, J., and Jaramillo, T. F. (2014). Electrocatalytic conversion of carbon dioxide to methane and methanol on transition metal surfaces. *J. Am. Chem. Soc* 136, 14107–14113. doi:10.1021/ja505791r

Kuramochi, T., Ramírez, A., Turkenburg, W., and Faaij, A. (2011). Techno-economic assessment and comparison of CO_2 capture technologies for industrial processes: preliminary results for the iron and steel sector. *Energy Procedia* 4, 1981–1988. doi:10.1016/j.egypro.2011.02.079

Leung, D. Y. C., Caramanna, G., and Maroto-Valer, M. M. (2014). An overview of current status of carbon dioxide capture and storage technologies. *Renew. Sustain. Energy Rev* 39, 426–443. doi:10.1016/j.rser.2014.07.093

Li, K., Cousins, A., Yu, H., Feron, P., Tade, M., Luo, W., et al. (2016). Systematic study of aqueous monoethanolamine-based CO_2 capture process: model development and process improvement. *Energy Sci. Eng* 4, 23–39. doi:10.1002/ese3.101

Ma, S., Sadakiyo, M., Luo, R., Heima, M., Yamauchi, M., and Kenis, P. J. A. (2016). One-step electrosynthesis of ethylene and ethanol from CO_2 in an alkaline electrolyzer. *J. Power Sources* 301, 219–228. doi:10.1016/j.jpowsour.2015.09.124

Mao, X., and Hatton, T. A. (2015). Recent advances in electrocatalytic reduction of carbon dioxide using metal-free catalysts. *Ind. Eng. Chem. Res* 54, 4033–4042. doi:10.1021/ie504336h

Martín, A. J., Larrazábal, G. O., and Pérez-Ramírez, J. (2015). Towards sustainable fuels and chemicals through the electrochemical reduction of CO_2: lessons from water electrolysis. *Green Chem* 17, 5114–5130. doi:10.1039/c5gc01893e

Mergel, J., Carmo, M., and Fritz, D. (2013). "Status on technologies for hydrogen production by water electrolysis," in *Transition to renewable energy systems*. (Weinheim, Germany: Wiley-VCH Verlag GmbH & Co. KGaA), 423–450.

Mistry, H., Varela, A. S., Bonifacio, C. S., Zegkinoglou, I., Sinev, I., Choi, Y.-W., et al. (2016). Highly selective plasma-activated copper catalysts for carbon dioxide reduction to ethylene. *Nat. Commun* 7, 12123. doi:10.1038/ncomms12123

Mohsin, I., Al-Attas, T. A., Sumon, K. Z., Bergerson, J., Mccoy, S., and Kibria, M. G. (2020). Economic and environmental assessment of integrated carbon capture and utilization. *Cell Rep. Phys. Sci* 1, 100104. doi:10.1016/j.xcrp.2020.100104

Ogura, K., Yano, H., and Tanaka, T. (2004). Selective formation of ethylene from CO_2 by catalytic electrolysis at a three-phase interface. *Catal. Today* 98, 515–521. doi:10.1016/j.cattod.2004.09.006

Oloman, C., and Li, H. (2008). Electrochemical processing of carbon dioxide. *ChemSusChem* 1, 385–391. doi:10.1002/cssc.200800015

Pander, III, J. E., Ren, D., and Yeo, B. S. (2017). Practices for the collection and reporting of electrocatalytic performance and mechanistic information for the CO_2 reduction reaction. *Catal. Sci. Technol* 7, 5820–5832. doi:10.1039/c7cy01785e

Peng, Y., Wu, T., Sun, L., Nsanzimana, J. M. V., Fisher, A. C., and Wang, X. (2017). Selective electrochemical reduction of CO_2 to ethylene on nanopores-modified https://www.spglobal.com/platts/en/our-methodology/price-assessments/petrochemicals/pgpi-propylene copper electrodes in aqueous solution. *ACS Appl. Mater. Interfaces* 9, 32782–32789. doi:10.1021/acsami.7b10421

Peterson, A. A., and Nørskov, J. K. (2012). Activity descriptors for CO_2 electroreduction to methane on transition-metal catalysts. *J. Phys. Chem. Lett* 3, 251–258. doi:10.1021/jz201461p

Platts Global Ethylene Price. Index. Available at: https://www.spglobal.com/platts/en/our-methodology/price-assessments/petrochemicals/pgpi-ethylene (Accessed February 15, 2019).

Platts Global Propylene Price. Index. Available at: https://www.spglobal.com/platts/en/our-methodology/price-assessments/petrochemicals/pgpi-propylene (Accessed February 15, 2019).

Qiao, J., Liu, Y., Hong, F., and Zhang, J. (2014). A review of catalysts for the electroreduction of carbon dioxide to produce low-carbon fuels. *Chem. Soc. Rev* 43, 631–675. doi:10.1039/c3cs60323g

Rakowski Dubois, M., and Dubois, D. L. (2009). Development of molecular electrocatalysts for CO_2 reduction and H_2 production/oxidation. *Acc. Chem. Res* 42, 1974–1982. doi:10.1021/ar900110c

Ren, T., Patel, M., and Blok, K. (2006). Olefins from conventional and heavy feedstocks: energy use in steam cracking and alternative processes. *Energy* 31, 425–451. doi:10.1016/j.energy.2005.04.001

Ren, T., Patel, M. K., and Blok, K. (2008). Steam cracking and methane to olefins: energy use, CO_2 emissions and production costs. *Energy* 33, 817–833.

Rockström, J., Gaffney, O., Rogelj, J., Meinshausen, M., Nakicenovic, N., and Schellnhuber, H. J. (2017). A roadmap for rapid decarbonization. *Science* 355, 1269–1271. 10.1126/science.aah3443

Rousar, I., Micka, K., and Kimla, A. (1986). *Electrochemical engineering.* Amsterdam, Netherlands: Elsevier.

Schlömer, S., Bruckner, T., Fulton, L., Hertwich, E., Mckinnon, A., Perczyk, D., et al. (2015). "Technology-specific cost and performance parameters," in *Climate change 2014: mitigation of climate change: working group III contribution to the IPCC fifth assessment report.* Editor S. Schlömer (Cambridge, UK: Cambridge University Press), 1329–1356.

Schneider, J., Jia, H., Muckerman, J. T., and Fujita, E. (2012). Thermodynamics and kinetics of CO_2, CO, and H^+ binding to the metal centre of CO_2 reductioncatalysts. *Chem. Soc. Rev* 41, 2036–2051. doi:10.1039/c1cs15278e

Schouten, K. J. P., Calle-Vallejo, F., and Koper, M. T. M. (2014). A step closer to the electrochemical production of liquid fuels. *Angew. Chem. Int. Ed* 53, 10858–10860. doi:10.1002/anie.201406174

Spigarelli, B. P., and Kawatra, S. K. (2013). Opportunities and challenges in carbon dioxide capture. *J. CO2 Util* 1, 69–87. doi:10.1016/j.jcou.2013.03.002

Spurgeon, J. M., and Kumar, B. (2018). A comparative technoeconomic analysis of pathways for commercial electrochemical CO_2 reduction to liquid products. *Energy Environ. Sci* 11, 1536–1551. doi:10.1039/c8ee00097b

Tans, P. (2019). Trends in atmospheric carbon dioxide. NOAA/ESRL. Available: www.esrl.noaa.gov/gmd/ccgg/trends/ (Accessed February 10, 2019).

Tao, M., Qun, F., Hengcong, T., Zishan, H., Mingwen, J., Yunnan, G., et al. (2017). Heterogeneous electrochemical CO_2 reduction using nonmetallic carbon-based catalysts: current status and future challenges. *Nanotechnology* 28, 472001.

Van Geem, K. M., Galvita, V. V., and Marin, G. B. (2019). Making chemicals with electricity. *Science* 364, 734. doi:10.1126/science.aax5179

Voltachem (2016). *Empowering the chemical industry: opportunities for electrification.* Den Haag, Netherlands: TNO.

Von Der Assen, N., Jung, J., and Bardow, A. (2013). Life-cycle assessment of carbon dioxide capture and utilization: avoiding the pitfalls. *Energy Environ. Sci* 6, 2721–2734. doi:10.1039/c3ee41151f

Whipple, D. T., and Kenis, P. J. A. (2010). Prospects of CO_2 Utilization via direct heterogeneous electrochemical reduction. *J. Phys. Chem. Lett* 1, 3451–3458. doi:10.1021/jz1012627

Wu, J., Ma, S., Sun, J., Gold, J. I., Tiwary, C., Kim, B., et al. (2016). A metal-free electrocatalyst for carbon dioxide reduction to multi-carbon hydrocarbons and oxygenates. *Nat. Commun* 7, 13869. doi:10.1038/ncomms13869

Zhai, Y., Chiachiarelli, L., and Sridhar, N. (2019). Effect of gaseous impurities on the electrochemical reduction of CO_2 on copper electrodes. *ECS Trans* 19, 1–13. doi:10.1149/1.3220175

Zimmermann, H., and Walzl, R. (2000). "Ethylene," in Ullmann's Encyclopedia of Industrial Chemistry. (Wiley-VCH Verlag GmbH & Co. KGaA).

Conflict of Interest: Author MR was employed by the company Dow Benelux BV.

The remaining authors declare that the research was conducted in the absence of any commercial or financial relationships that could be construed as a potential conflict of interest.

frontiers in Energy Research

ORIGINAL RESEARCH
published: 29 September 2020
doi: 10.3389/fenrg.2020.00161

Mixed-Integer Linear Programming (MILP) Approach for the Synthesis of Efficient Power-to-Syngas Processes

Andrea Maggi[1]*, *Marcus Wenzel*[1] and *Kai Sundmacher*[1,2]

[1] Department for Process Systems Engineering, Max-Planck-Institute for Dynamics of Complex Technical Systems, Magdeburg, Germany, [2] Department for Process Systems Engineering, Otto-von-Guericke University, Magdeburg, Germany

Within the context of energy transition scenarios toward renewable resources, superstructure optimization is implemented for the synthesis of sustainable and efficient Power-to-Syngas processes. A large number of reactors (reverse water-gas-shift, steam reforming, dry reforming, tri-reforming, methane partial oxidation reactor, and water electrolyzer) and separators (PSA, TSA, cryogenics, membranes, and gas-liquid scrubbing) are included within a single MILP framework, accounting for typical operating conditions of each process-unit, under the specified simplifying assumptions. Power is minimized in the context of sustainable feedstocks: water and biogas or carbon dioxide from direct air-capture. The objective function adds the thermal to the electrical contribution to the total power, the latter being weighted by a pseudo-price of null (i.e., sustainable, in-house electricity production), or unitary value (i.e., electricity purchased, possibly generated from non-sustainable sources). Simultaneous operations of multiple reactor technologies are allowed to identify possible synergies. With biogas and null value of the pseudo-price, the results identify plant configurations mainly run via electricity, which constitutes up to 97% of the total power for co-operating partial oxidation of methane and water electrolysis. Alternatively, lower total demands are attained at the expenses of thermal duty when electricity is penalized: the endothermic reactors are operated. With carbon dioxide, the total power demand dramatically increases due to the large consumptions of direct-air capture and water electrolysis. The resulting topologies always favor membrane separation, adsorption, and cryogenics over absorption technologies.

Keywords: sustainability, syngas, superstructure, biogas, CO_2 utilization, Power-to-X, process synthesis

OPEN ACCESS

Edited by:
Theodoros Damartzis, École Polytechnique Fédérale de Lausanne, Switzerland

Reviewed by:
Mariano Martín, University of Salamanca, Spain
Ligang Wang, École Polytechnique Fédérale de Lausanne, Switzerland

***Correspondence:**
Andrea Maggi
maggi@mpi-magdeburg.mpg.de

Specialty section:
This article was submitted to Process and Energy Systems Engineering, a section of the journal Frontiers in Energy Research

Received: *06 April 2020*
Accepted: *24 June 2020*
Published: *29 September 2020*

Citation:
Maggi A, Wenzel M and Sundmacher K (2020) Mixed-Integer Linear Programming (MILP) Approach for the Synthesis of Efficient Power-to-Syngas Processes. Front. Energy Res. 8:161. doi: 10.3389/fenrg.2020.00161

INTRODUCTION

It is generally agreed that immediate large-scale actions are required worldwide to cease further CO_2 emissions and to reduce its current concentration in the atmosphere (IPCC, 2013). To achieve this goal, a shift from fossil fuels toward renewable energy carriers is necessary. Products, intermediates, and raw materials that contribute to high CO_2 emissions must be identified alongside suitable technologies for the conversion of CO_2 and biological feedstocks into useful chemicals and fuel. This can be achieved by Power-to-X technologies, which are capable of transforming renewable electricity and sustainable feedstock into useful components such as syngas.

Synthesis gas (syngas), a mixture of H_2 and CO in variable proportions, is an important intermediate and precursor necessary for the production of a wide range of products. Its worldwide production requires approximately 2% of the global primary energy demand (El-Nagar and Ghanem, 2019). However, since most of the syngas production is based on fossil fuels, it entails large, positive CO_2 emissions. Therefore, the sustainable production of syngas offers high potential for the reduction of CO_2 emissions. Furthermore, its intermediate location within the overall production chain, from feedstocks to chemicals or fuels, allows for existing downstream processes to be run without any substantial modifications and, simultaneously, to benefit from a sustainable feed stream. Due to the fact that syngas can be readily converted into liquid fuels, i.e., via Fischer-Tropsch synthesis (Gruber et al., 2019), it plays a crucial role in decarbonizing the transportation system.

In recent years, Power-to-Syngas related processes have been an object of interest in the scientific community on different scales. Detailed catalytic studies were performed on the reaction steps. Abdullah et al. (2017) and Arora and Prasad (2016) proposed an extensive review of the role of Ni-based catalysts in dry-reforming of methane, effective in terms of the efficient, direct utilization of biogas, although negatively affected by its endothermic nature. Rh-based catalysts were studied in the context of oxygen-enhanced dry-reforming (oxy-dry reforming): oxygen debottlenecks the dry reforming process by reducing coking effects (Moral et al., 2018). Singha et al. (2016) characterized nanocrystalline Ni-ZrO_2 catalysts for tri-reforming, particularly suited to accept flue gases without the need for previous separation. In the context of partial oxidation, a study by Pantaleo et al. (2016) proposes the use of CeO_2-supported nickel catalysts: the catalyst activity and stability are revealed to be deeply affected by the crystallite size and interaction between nickel oxide and ceria. Furthermore, high conversion and selectivity were obtained. The analysis of a synergistic combination of partial oxidation and dry reforming of methane was explored by Kang et al. (2018): a non-stoichiometric dry reforming feed-stream (excess methane over carbon dioxide) is fed to a fixed bed reactor previously oxidized by air. The subsequent oxidation of methane accompanies the endothermic dry reforming, with a resulting decrease in energy demand. Chemical looping was also dealt with by Wenzel et al. (2018) in the context of the reverse water-gas shift reaction. The author simulated and compared fixed-bed and fluidized-bed reactors filled with iron oxide and ceria oxygen-storage material (OSM) with a novel reaction kinetic. The study concluded that fixed-bed outperforms fluidized-bed with respect to OSM and carbon monoxide concentration in the outlets.

Methodological advancements were achieved in terms of process networks by Schack et al. (2016), who combined several renewable-to-chemical processes within the same optimization framework by means of large linear models. In this context, process pathways were identified via linear programming and with respect to the cost of resources. More recently, Liesche et al. (2019) and Schack et al. (2020) proposed an optimization technique based on the linearization of the states for process and unit optimization (FluxMax). The benefits of implementing linear programming techniques combines the guarantee for global optimality with the advancement achieved by the underlying algorithms, capable of exploring large scenarios with little computational effort, thus making them suitable for large-scale analyses.

TABLE 1 | Syngas downstream applications, molar ratios, temperature, and pressure requirements.

Downstream application	Molar ratio H_2/CO	(*T* [K], *p* [bar])
Phosgene	0	(323,3)
Monsanto process	0.1	(473,60)
Hydroformylation	1.1	(428,170)
Iron ore	1.4	(973,1)
Fischer-Tropsch	1.95	(30,473)
Methanol production	2.15	(140,473)

Data adapted from Wenzel et al. (2017).

In the present contribution, a superstructure optimization approach is used to identify which reaction and separation steps should be chosen to produce syngas with a minimum overall energy demand. Special emphasis is put on differentiating between energy inputs in the form of heat and electricity. Biogas from anaerobic digestion, water, and CO_2 from direct air-capture are considered as renewable raw materials. Essentially, biogas is a carbon-neutral resource, and it does therefore not contribute significantly to the increase in atmospheric CO_2 levels (Paolini et al., 2018). As chemical reaction steps, water electrolysis, methane steam reforming, dry reforming, partial oxidation, tri-reforming, and reverse water-gas shift are considered and possible synergies allowed. For the subsequent separation of the mixtures, both state-of-the-art as well as new and emerging technologies are considered. The aim is to highlight most promising flowsheets for current and future implementation, for the downstream applications reported in **Table 1**. The overall idea is sketched in **Figure 1**. An analysis of costs is omitted in this contribution for two reasons: (1) reliable cost estimates are not readily available for all unit operations, especially for emerging technologies, and (2) the analysis should not be biased toward existing, commercially available technologies but should reflect a wide range of opportunities to identify possible future research needs.

METHODS

System Description

Syngas is produced by chemical conversion steps followed by separation and conditioning of the molar H_2/CO ratio. **Figure 2** represents a simplified flowsheet of the system described in this section. Purified biogas (BG) from anaerobic digestion and CO_2 from direct air-capture are the candidate carbon sources. Several reactors generate raw syngas from the feedstocks. Biogas purification steps are not included in the analysis. Nevertheless, a 2-to-3 CO_2/CH_4 biogas mixture can be fed directly to dry-reforming (DR) or tri-reforming (TRI), or separated into its components CO_2 and CH_4, reactants for reverse water-gas-shift

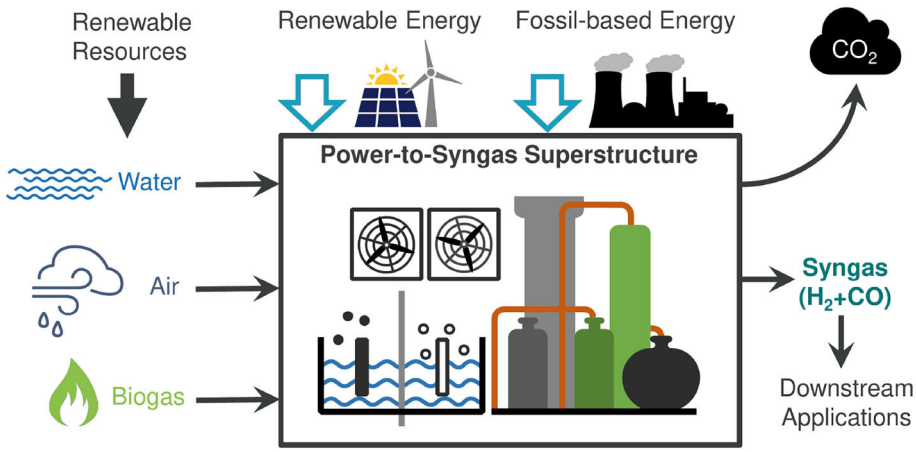

FIGURE 1 | General representation of the syngas production framework.

(RWGS), methane steam-reforming (SR), and methane partial oxidation (POX). CO_2 from direct air capture can be fed to the RWGS reaction. With the exception of DR, the other chemical reactors require H_2O, O_2, or H_2. Consequently, a make-up stream of H_2O is also allowed, which either feeds SR and TRI or is split into pure H_2 and O_2 via an electrolyzer (EL). The raw syngas is composed of unreacted components and side products. Recycle and outlet streams are therefore introduced. Excess O_2 can be utilized for power generation by oxy-combustion of excess CH_4, or released into the atmosphere. Unreacted CO_2 is also released into the atmosphere. However, such emissions are biogenic due to the selected carbon sources for the process. Excess H_2 is pressurized and stored at 300 bar (Di Profio et al., 2009). EL can provide green H_2 directly into the outlet syngas stream, bypassing the battery of reactors.

The product separation can be accomplished by a number of state-of-the-art or emerging technologies. For a single separation task, e.g., separation of component A from an initial mixture ABC, the superstructure comprises one or more separation methods. As an example, the task of separating H_2 from CO_2, CO and CH_4 can be accomplished by three competing methods: layered bed pressure-swing adsorption, polymeric membrane and palladium membranes. This contribution is intended to provide a conservative energy analysis of the system. Electricity is therefore not recovered by expansion and cooling utility consumption not accounted for. The power required for pumping cooling water is assumed to be negligible compared to the major energy contributions in the system.

General Modeling Assumptions for Reactors and Separators

The underlying modeling assumptions for reactors are the following:

- Reactor temperature, pressure, and feed composition are assigned prior to optimization;
- RWGS, SR, DR, and POX are modeled as Gibbs reactors, and a stoichiometric feed is assigned. Their outlet composition is calculated prior to optimization;
- Side reactions occurring in SR, DR, and POX are considered;
- Due to the intrinsic system complexity, representative temperature, pressure, and inlet and outlet composition for TRI are retrieved from literature (Song and Pan, 2004);
- Water conversion at EL is 100%;
- Each reactor is associated with a single set of temperature, pressure, feed, and outlet composition.

All reactors specifications are reported in **Table 2**.

For separators, the following most general assumptions are applied:

- Sharp-split separators;
- The generic separator is decomposed into operation and regeneration steps;
- Typical temperature and pressure levels are assigned prior to optimization;
- Unit-specific calculations are embedded if required;
- The components in gas phase obey the ideal gas law;
- Compression and expansion steps are adiabatic;

Scope of the contribution is to underline dominant process paths in a topological perspective. For this reason, the optimization of the operating conditions of each process element is not part of this study.

Modeling of Reactors

The complete set of parameters implemented at a reactor-level is reported in **Table 2**. The current section discusses the rationale behind its identification.

Mass Balances

When a non-adiabatic system is at thermodynamic equilibrium, it is sufficient to define the molar composition by the following set of algebraic equations for each given independent stoichiometric

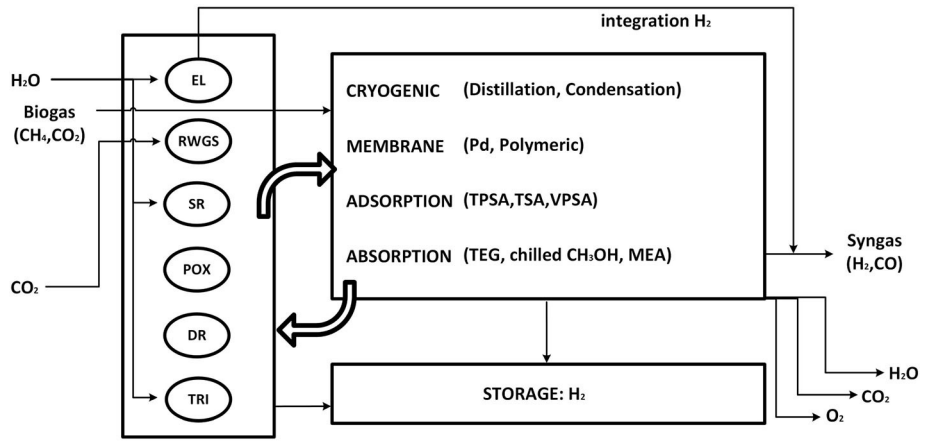

FIGURE 2 | Simplified process flowsheet. EL, electrolyzer; RWGS, reverse water-gas-shift reactor; SR, methane steam reforming; POX, methane partial oxidation; DR, dry reforming of methane; TRI, tri-reforming of methane; TPSA,TSA,VPSA, temperature/pressure/vacuum swing adsorption; TEG, ethylene glycol absorption; MEA, mono-ethanol amine.

TABLE 2 | Parameters for the description of reactors.

Reactor	Components	Inlet Composition %	Outlet Molar composition %	Molar ratio Outlet/inlet flowrate
RWGS	H_2,CO_2,H_2O,CO	[50 50 0 0]	[27.4 27.4 22.6 22.6]	0
SR	H_2,CO_2,H_2O,CO,CH_4	[0 0 50 0 50]	[56.2 2.6 11.7 15.3 14.2]	1.55
POX	H_2,CO_2,H_2O,CO,CH_4,O_2	[0 0 0 0 66.7 33.3]	[58.6 1.32 4.3 30.1 5.6 0]	1.80
DR	H_2,CO_2,H_2O,CO,CH_4	[0 50 0 0 50]	[28.5 10.8 5.4 39.2 16.1]	1.51
TRI	H_2,CO_2,H_2O,CO,CH_4,O_2	[0 32.3 32.3 0 32.3 3.2]	[45.3 9.4 14.7 30.6 0.04 0]	1.61
EL	H_2,H_2O,O_2	[0 100 0]	[66.7 0 33.3]	1.5

Reactor	T [K]	p [bar]	$\tilde{q}$ [kJ/mol]	$\tilde{w}$ [kJ/mol]	θ_j %
RWGS	1000	5	$35{\cdot}\theta_{RWGS}$	0	θ_{RWGS} = 22.6
SR	1173	30	$227{\cdot}\theta_{SR}-33{\cdot}\theta_{WGS}$	0	θ_{SR} = 27.8; θ_{WGS} = 4.0
POX	1328 (in: 773)	30	adiabatic	0	–
DR	1000	5	$260{\cdot}\theta_{DR}+35{\cdot}\theta_{RWGS}$	0	θ_{DR} = 25.6; θ_{RWGS} = 8.1
TRI	1123	1	$58{\cdot}n_{in}$	0	–
EL	333	1	0	327	–

θ represents the ratio between extent of reaction and feed flowrate. Specific heat demands ($\tilde{q}$) and electrical energy demands ($\tilde{w}$) per mole flowrate of feed are included.

relation j:

$$f_j\left(T,p,\lambda\right)=0,\quad \forall j\in J, \tag{1}$$

where f is a function of the system temperature, pressure, and the extent of reaction λ. Hence, for the RWGS reactor, $J = \{j \mid j = \{\text{RWGS}\}\}$; for SR $J = \{j \mid j = \{\text{SR}, \text{WGS}\}\}$, and for DR $J = \{j \mid j = \{\text{DR}, \text{RWGS}\}\}$, where WGS denotes the water gas shift reaction. The outlet composition can thus be determined. Given that (T, p) are fixed and that the feed to the reactor is stoichiometric, the ratio between outlet and inlet flowrates remains constant for any given inlet flowrate. As a result, the outlet molar flowrate is linearly proportional to the feed flowrate, and the compositions are fixed for all streams.

POX is run within an adiabatic reactor with irreversible reactions of partial and total oxidation:

$$2CH_4 + O_2 \longrightarrow 2CO + 4H_2 \tag{2}$$
$$CH_4 + 2O_2 \longrightarrow 2H_2O + CO_2. \tag{3}$$

As a consequence, Equation set (1) is not sufficient to characterize the equilibrium. For this process-step, T is the temperature after adiabatic reaction, which is calculated from the following energy balance

$$H^{\circ}_{in}(T_{in}) - H^{\circ}(T) = 0, \tag{4}$$

which expresses the conservation of energy in terms of total enthalpy change. Furthermore, atomic balances for the elements

saturate the degrees of freedom, leading to the set of equations

$$f_j(\mathbf{n}) = 0, \forall j \in J := \{\text{DR}, \text{SR}\}, \tag{5}$$

$$H^\circ(T_{in}, \mathbf{n}) - H^\circ(T) = 0, \tag{6}$$

$$n_{i,in} - n_i = 0, \forall i \in I := \{\text{C}, \text{O}, \text{H}\}, \tag{7}$$

which is solved for T and $\mathbf{n}$ (vector of molar outlet flowrates). Here, C, O, and H belong to set I and denote the chemical elements carbon, oxygen, and hydrogen, respectively. As for RWGS, SR, and DR, feed composition, temperature, and pressure are fixed, and the outlet composition and reactor temperature can be calculated.

The ratio between outlet and inlet mole flowrate is calculated accounting for the conversion of methane and the outlet composition.

Energy Balances

The process system includes endothermic reactors (RWGS, SR, DR, and TRI) and an adiabatic reactor (POX). In all the cases, preconditioning of the feed streams to the reactors is performed by compression and pre-heating, thus enabling the internal energy of reactants to reach the requirements for chemical conversion.

Each endothermic reactor requires a thermal power input, expressed by a linear combination such as

$$\sum_{j \in J} \lambda_j \Delta H_j^\circ(T) = n_{in} \sum_{j \in J} \theta_j \Delta H_j^\circ(T), \tag{8}$$

where θ_j is the constant ratio between the extent of reaction j and n_{in} the feed flowrate. POX is adiabatic and requires no modeling of excess heat. For TRI, the summation appearing in the right-hand side of Equation (8) is determined from the standard reaction enthalpy of the main reactions—dry, steam reforming, and partial oxidation of methane—and from their extent of reaction, estimated from Song and Pan (2004).

The electrolyzer requires power in the form of electrical input. As reported in Bensmann et al. (2013), the Gibbs free energy of reaction provides a reasonable estimation for the reversible power requirement, which is divided by an efficiency factor of 72% to obtain the real demand. As for the reactors, EL requires feed preconditioning to reach the operative temperature at atmospheric pressure.

Modeling of Separators

An extensive literature survey was conducted to identify unit-specific calculations. The energy requirements are therefore characterized for each specific case, resulting in linear gray-box models. The superstructure embeds the following families of separation methods: adsorption (temperature- and pressure-swing), absorption (glycol, amine, and methanol), membrane separation (polymeric and palladium), and cryogenic operations (chilled methanol and cryogenic distillation). **Table 3** introduces the set of separators allowed within the control volume and their parameters selection.

TABLE 3 | Separation methods and identifier adopted in **Table 4**.

Separator	ID	$(T, p)_{op}$	$(T, p)_{reg}$	$\tilde{C}p_e$ [J/kg/K]	θ [kg/kg]	$\tilde{q}_{reg}$ [J/mol]	COP	References
TPSA (Al_2O_3+CuCl/Z)	I	$(298, 8)_{op}$	$(393, 1)_{reg}$	Al_2O_3: 240 CuCl/Z: 240	Al_2O_3: 5.5 CuCl/Z: 5.5	H_2O: 4.8E4 CO_2: 3.4E4 CO: 3.5E4 CH_4: 1.1E4	-	Netusil and Ditl, 2011
TSA (Silica Gel)	II	$(298, 1)_{op}$	$(393, 1)_{reg}$	silica: 920	silica: 8	H_2O: 3.1E4	-	Netusil and Ditl, 2011
TPSA (Al_2O_3)	III	$(298, 8)_{op}$	$(393, 1)_{reg}$	Al_2O_3: 240	Al_2O_3: 5.5	H_2O: 4.8E4	-	Netusil and Ditl, 2011
TSA (ASMS-3A+CuCl/Z)	IV	$(298, 8)_{op}$	$(393, 1)_{reg}$	ASMS-3A: 920 CuCl/Z: 240	ASMS-3A:8 CuCl/Z: 5.5	H_2O: 2.3E4 CO_2: 2.3E4 CO: 3.5E4	-	Li et al., 2007; Morishige, 2011
VPSA	V	$(298, 8)_{op}$	$(298, 0.1)_{reg}$	-	-	-	-	-
Membrane (Polymeric)	VI	$(298, 2)_{op}$	$(298, 0.1)_{reg}$	-	-	-	-	-
Membrane (Palladium)	VII	$(298, 21)_{op}$	$(298, 1)_{reg}$	-	-	-	-	-
Absorption (Glycol)	VIII	$(308, 10)_{op}$	$(473, 1)_{reg}$	TEG: 2225	49	H_2O: 3.2E5	-	Bahadori and Vuthaluru, 2009
Absorption (Methanol)	IX	$(233, 30)_{op}$	$(298, 1)_{reg}$	-	-	-	40	Sun and Smith, 2013
Absorption (Amine)	X	$(313, 1)_{op}$	$(393, 2)_{reg}$	MEA: 3325	3.5	CO_2: 4.1E4	-	Ziaii et al., 2009
Cryogenics (CH_4/CO_2)	XI	$(263, 40)_{op}$	$(223, 40)_{reg}$	-	-	-	54	Maqsood et al., 2014
Cryogenics (CH_4/H_2)	XII	$(103, 1)_{op}$	$(103, 1)_{reg}$	-	-	-	775	Sun and Smith, 2013

Deviations from the reported values for (T [K], p [bar]) are possibly implemented in the constraints, e.g., membranes for H_2 separation adjacent to the reactor are operated at temperatures higher than 298 K (Pd membrane, polymeric membrane).

Mass Balances

The sharp-split assumption allows for a linear mathematical description only if the composition at the beginning of the separation train is fixed. For this reason, the modeling choice of fixing temperature and pressure at the Gibbs reactors introduced in section (2.2) is justified. This approach has been adopted in literature (Biegler et al., 1997) for the screening of distillation sequences, while the current contribution extends the method to a wider choice of separators. The underlying mathematical formulation reads

$$n_A = n_{(A,B,C)} \frac{x_A}{x_A + x_B + x_C} = n_{(A,B,C)} \xi_{A/(B,C)}, \tag{9}$$

where a generic component A is ideally separated out of a mixture (A, B, and C), and the split factor ξ is given by the ratio of the mole fractions x at the outlet stream of the reactor. The splits modeled in the framework are listed in **Table 4** together with the corresponding feasible separation methods and literature references. It is here stressed that not all the separation techniques are at high readiness level. A few separators are considered feasible for specific separation tasks if characteristic properties, such as kinetic diameter, relative permeability, dew points, etc., suggest so. Nevertheless, most of the separators are state-of-the-art technologies in industry or in laboratory-scale applications.

Energy Balances

The generic separator is divided into an operation and regeneration step. A membrane separates the permeate from the retentate stream, a gas-liquid absorption process is followed by stripping, and an adsorption step via VPSA/TSA is periodically switched into regeneration mode by vacuum generation or heating, respectively. Each method is therefore associated with two distinct (T, p) values for operation $(T, p)_{ops}$ and regeneration $(T, p)_{reg}$, respectively: the feed stream, as well as the outlet from the operation-step, are at $(T, p)_{ops}$. In order to model the adjustment of the internal energy between consecutive separators, heating or cooling, compression or expansion are considered. For thermal-power calculations, the heat capacity $\tilde{C}p$ is calculated as a weighted average for pure components, accounting for the actual mixture composition and the initial and final temperature.

As formerly stated in section (2.1), power recovery by expansion and cooling are not considered as long as they occur above the atmospheric conditions ($T = 298\,\mathrm{K}$, $p = 1\,\mathrm{bar}$). Nevertheless, the expansion of gas may require inter-heating steps. Similarly, compression may require cooling. The temperature attained after isentropic transformation is calculated as

$$T_{2,id} = T_1 \left(\frac{p_2}{p_1} \right)^{\frac{R}{\tilde{C}p}}, \tag{10}$$

where R is the universal gas constant. The real temperature is calculated assuming an efficiency factor of $T = 80\%$. In agreement with the conservative framework, the power requirement for compression is over-estimated by a single, isentropic step as well as the temperature out of compression and expansion. As an example, whenever a process stream delivers gas to higher (T, p) values, the pressurization can be deployed to partly satisfy the need for thermal power input. For an adiabatic compression step, the specific molar electrical work is estimated as

$$\tilde{w} = \frac{\gamma}{(\gamma - 1)} R T_1 \left(\left(\frac{p_2}{p_1} \right)^{\frac{\gamma - 1}{\gamma}} - 1 \right) \frac{1}{\eta}, \tag{11}$$

$$\gamma = \frac{\tilde{C}p}{\tilde{C}v} \tag{12}$$

TABLE 4 | Numbered list of splits allowed in the superstructure and available separation methods.

(ID)	Splits	ID available methods	References
(1)	$(H_2,CH_4)/(CO_2,CO,H_2O)$	IV	[4,5]
(2)	$(H_2)/(CO_2,CO,H_2O,CH_4)$	VII	[11,30]
(3)	$(H_2O)/(CO_2,H_2,CO,CH_4)$	VI	[21,23,30,33]
(4)	$(H_2O)/(CO_2,CO,CH_4)$	VI,VIII,II	[20,21,23,33,38]
(5)	$(CH_4)/(CO_2,CO,H_2O)$	II	[4,5,31]
(6)	$(H_2)/(CO_2,CO,CH_4)$	V,VI,VII	[2,4,5,8,10,11,12,34]
(7)	$(CO)/(CO_2,H_2,CH_4)$	V	[4,5]
(8)	$(CO_2,H_2O)/(H_2,CO)$	III,X	[12,16,32]
(9)	$(H_2O)/(CO_2,H_2,CO)$	VI,VIII,II	[20,21,23,30,33,38]
(10)	$(H_2)/(CO_2,CO,H_2O)$	I,VII	[3,11,12,31,34,38]
(11)	$(CO)/(CO_2,H_2O)$	V	[3,5]
(12)	$(H_2O)/(CO_2,CO)$	VI,VIII,II	[20,21,23,30,33,38]
(13)	$(CO_2)/(H_2,CO)$	V,IX,X	[6,12,14,15,16,17,18,27,28]
(14)	$(H_2)/(CO_2,CO)$	VI,V,VII	[3,7,8,9,13,20,34,37]
(15)	$(CO)/(CO_2,H_2)$	V	[3,5]
(16)	$(CO_2)/(CO,CH_4)$	V	[19]
(17)	$(CO_2)/(H_2,CH_4)$	V	[9,19]
(18)	$(H_2)/(CO_2,CH_4)$	V,VII,VI	[4,8,10,11,12,34,35,36]
(19)	$(CO)/(CO_2,CH_4)$	V	[3,5]
(20)	$(CO)/(CH_4)$	V	[4,5]
(21)	$(H_2)/(CH_4)$	VI,XII,V	[8,10,14,24,28]
(22)	$(CO_2)/(CH_4)$	VI,V,X,XI	[12,15,16,19,25,26]
(23)	$(CO_2)/(H_2O)$	II,VIII,VI,	[20,21,22,23]
(24)	$(CO_2)/(CO)$	V	[1,3,4,5,14,19]
(25)	$(CO_2)/(H_2)$	V,X,IX,VI,VII	[3,8,10,11,12,13,14,15,16,17,18,34]
(26)	$(CO)/(H_2)$	V,VI,VII	[1,2,3,4,5,6,7,8,10,11,12]

References are included: [1] Battrum and Thomas (1991); [2] Jang et al. (2011); [3] Ritter and Ebner (2007); [4] Dutta and Patil (1995); [5] Gao et al. (2018, 2016); [6] DiMartino et al. (1988); [7] Kim et al. (2013); [8] MEDAL™ Air Liquide - hydrogen purification; [9] Uebbing et al. (2019); [10] Poudel et al. (2019); [11] Li et al. (2000); [12] Häussinger et al. (2011); [13] Sircar and Golden (2000); [14] Wang et al. (2008); [15] MEDAL™ Air Liquide - biogas purification; [16] Ziaii et al. (2009); [17] Burr and Lyddon (2008); [18] Hochgesand (1970); [19] Grande et al. (2017); [20] Wang and LeVan (2009); [21] Sijbesma et al. (2008); [22] Han et al. (2015); [23] Scholes et al. (2012); [24] Yang et al. (1997); [25] Maqsood et al. (2014); [26] SGC (2012); [27] Reimert et al. (2015); [28] Mulgundmath and Tezel (2010); [29] Merel et al. (2008); [30] Metz et al. (2005); [31] Delgado et al. (2014); [32] Wurzbacher et al. (2012); [33] Merkel et al. (2001); [34] Agarwal et al. (2010); [35] Mondal et al. (2012); [36] Park et al. (2000); [37] Lin et al. (2012); [38] Netusil and Ditl (2011).

where $\eta = 0.8$ is the efficiency, and γ is the ratio of specific heats at constant pressure and constant volume (see Grande and Rodrigues, 2007). Equation (11) defines a coefficient which multiplies the gas flowrate, i.e., the mathematical description is linear. The same formula is adopted to model vacuum operations as in Grande and Rodrigues (2007), e.g., vacuum normalization in VPSA or membrane separators. For the latter, the pressure in the retentate is assumed to be 20 times higher than in the permeate side, set at $p = 0.1$ bar is assumed (Huang et al., 2014). In order to describe the energy demand of each separator, additional and method-specific calculations are included.

Cryogenic separator

The non-ideal coefficient of performance (COP) describes the ratio between the thermal power absorbed by the refrigerant and the real electrical power required at the compressor in a cryogenic loop. The definition of COP reads

$$COP_{real} = COP_{id}\eta = \frac{Q}{W_{id}}\eta = \frac{T^R_{ev}}{T^R_{cond} - T^R_{ev}}\eta, \tag{13}$$

where W_{id} is the ideal electrical power requirement. In an ideal case, it corresponds to a reverse Carnot cycle between the cryogenic evaporation temperature of the refrigerant, T^R_{ev} and the temperature at which the refrigerant releases its internal energy by condensation, T^R_{cond}. The ideal COP is corrected by a thermodynamic efficiency factor η of 60% (Smith, 2005). Q is the thermal power acquired by the refrigerant during cryogenic evaporation and is lost by the cooling process fluid in order to reach the required cryogenic temperature. A proportionality coefficient for the estimation of the power requirement in cryogenic operations is derived by rearranging Equation (13):

$$\tilde{w} = \frac{1}{COP_{id}\eta}Q = \frac{1}{\eta}\frac{T^R_{cond} - T^R_{ev}}{T^R_{ev}}\tilde{C}p\left(T_{amb} - T_{cryo}\right). \tag{14}$$

In Equation (14), a distinction is made between the cryogenic temperatures T_{cryo} and T^R_{ev}, the former being 15 K higher than the latter, thus ensuring the heat transfer.

Temperature-swing adsorption: TSA

TSA operations consist of cyclic switch between operation and regeneration at high temperature of the adsorbent bed. Consequently, the relevant contributions for regenerations are the heat of desorption for the entrained components Q_{des} and the heat input to raise the bed temperature Q_{bed}:

$$Q_{TSA} = Q_{bed} + Q_{des} = \left(\tilde{q}_{des} + \tilde{q}_{bed}\right) n_{feed} \tag{15}$$

$$\tilde{q}_{bed} = \left(T_{reg} - T_{op}\right) \sum_{k\subset K}\left(\frac{1}{\theta_i}\hat{C}p_{bed,l}MW_i x_i\right), \tag{16}$$

$$\tilde{q}_{des} = \sum_{k\subset K}\left(\tilde{q}^*_{des,i}x_i\right). \tag{17}$$

For Equations (16) and (17), sets k and K are introduced:

$$\begin{aligned} &k \subset K, \\ &k = \{i, l \mid i = \{\text{components adsorbed by adsorbent-type } l\}, \\ &l = \{\text{adsorbent-type } l\}\}. \end{aligned} \tag{18}$$

In Equation (16), $\theta_i^{-1}MW_i$ is the molar mass of adsorbent required to adsorb component i, which is multiplied by the specific heat per unit of mass of adsorbent $\hat{C}p$. Furthermore, MW_i is the molecular weight. In Equation (17), $\tilde{q}^*_{des,i}$ is the molar heat of desorption for component i.

Layered beds are also considered, which necessitates the subscript l and the summation operator in Equations (16) and (17).

Absorption in glycol, amines, or chilled methanol

The gas-liquid absorption processes require high-temperature regeneration. It is often the case that the absorption operation is performed in pressurized vessels. Unit-specific calculations must account for the change of the internal energy of the fluid sent to regeneration. The specific thermal power input reads

$$\tilde{q}_{rec} = \theta_{rec}\tilde{C}p_{entrainer}\left(T_{reg} - T_{op}\right), \tag{19}$$

where θ_{rec} is the ratio between the flowrate of entrainer required per unit of entrained key component (circulation rate). The description of amine and glycol absorption resort to Equation (19). The absorption of CO_2 in methanol occurs at cryogenic conditions, whereas the regeneration is operated at ambient temperature. As a consequence, this specific separator is described by the relations already introduced for cryogenic systems in section (2.4.2).

Modeling of Interconnections

This section discusses the conceptual structures that enable to build the final set of problem constraints in a linear form.

Mixture

For a given mixture ϕ, there are two sets of mass balances:

$$\xi^\phi_i n_i - \sum_j n_{ji} = 0 \qquad \forall i \in I, \tag{20}$$

$$n_j - \sum_i n_{ji} = 0 \qquad \forall j \in J. \tag{21}$$

Sets I and J in Equations (20) and (21) incorporate the feed streams to the separators that generate and accept ϕ, respectively. Furthermore, n_i and n_j are the feed flowrates to the separators, while n_{ji} represents the flowrate of the connecting stream from separator i to j; ξ^ϕ_i is the split factor associated with separator i and its outlet mixture ϕ. Coefficients of molar thermal energy and work (see section Modeling of Separators) are multiplied by the corresponding flowrates n_{ji}. The linear description of the change in (T, p) between consecutive separators is formulated as

$$Q_{ji} - \tilde{q}_{ji}n_{ji} = 0, \tag{22}$$

$$W_{ji} - \tilde{w}_{ji}n_{ji} = 0, \tag{23}$$

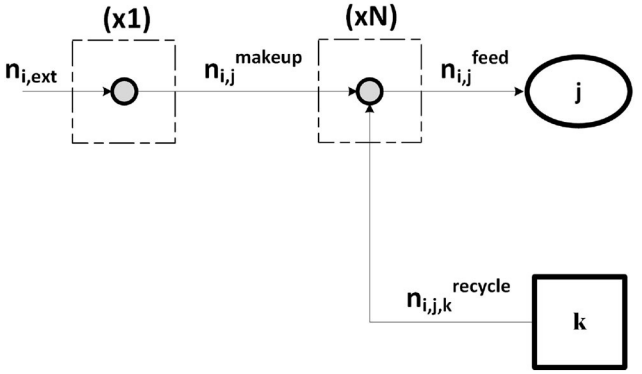

FIGURE 3 | Substance-node balances associated to component *i* fed to the plant. Stream $n_{i,ext}$ is split into *N* streams $n_{i,j}^{makeup}$, each contributing to the reactor feed $n_{i,j}^{feed}$ together with other streams $n_{i,j,k}^{recycle}$ from the plant.

where Q and W denote the thermal and electrical power, respectively.

Set Φ is introduced. It groups Equations (20, 21, 22, 23), related to the specified mixture ϕ.

Separation Train

Each stream j, belonging to set Φ_1 (see nomenclature in section Mixture), is associated with two streams i belonging to Φ_2 and Φ_3, respectively. Therefore, two equations describing the connectivity between equations sets Φ_1 and Φ_2, and Φ_1 and Φ_3, can be formulated:

$$n_{j,\Phi_1} - n_{i,\Phi_2} = 0, \tag{24}$$

$$n_{j,\Phi_1} - n_{i,\Phi_3} = 0, \tag{25}$$

indicating that stream j in set Φ_1 coincides with i in Φ_2 and Φ_3, respectively. Such concatenation constraints make sure that the mass balances downstream of each conversion technology are fulfilled.

Substance Nodes

Each component is associated with $1 + N$ nodes, where N is the number of reactors it is fed to, belonging to set J (reference to **Figure 3**). The first node balance reads

$$n_{i,ext} - \sum_{j \in J} n_{i,j}^{makeup} = 0, \tag{26}$$

indicating that component i, provided from an external source, can be delivered to any j^{th} reactor $\in J$, "make-up" stream. For each reactor feed in set J, a constraint is imposed with respect to i:

$$n_{i,j}^{makeup} + \sum_{k \in K} n_{i,j,k}^{recycle} - n_{i,j}^{feed} = 0, \tag{27}$$

where K is the set of process units which produce a stream of pure i. Equation (27) binds the component flowrate of i in the reactor feed to the make-up stream for the same reactor as well as to all the relevant recycles within the plant.

Outlet and Syngas Nodes

As previously discussed in section (2.1), excess H_2 and CH_4 can leave the plant after pressurization, as excess CO_2 and H_2O can be released into the environment, whereas O_2 can be used in oxy-combustion for heat generation. For each component leaving the plant, a node balance is introduced:

$$\sum_{j \in J} n_{i,j} - n_{i,out} = 0, \tag{28}$$

where J is the set of process-units which produce or separate component i, leaving the battery limit. Similarly, the following syngas node balances are required:

$$\sum_{j \in J} n_{\mathrm{CO},j} - n_{\mathrm{CO},syngas} = 0, \tag{29}$$

$$\sum_{k \in K} n_{\mathrm{H_2},k} - n_{\mathrm{H_2},syngas} = 0, \tag{30}$$

$$n_{\mathrm{H_2},syngas} - \psi\, n_{\mathrm{CO},syngas} = 0, \tag{31}$$

Equation (31) sets the syngas ratio to the desired value for downstream applications.

Logical Constraints

Logical constraints are imposed such that at most one separation method per task is active. Binary variables support such logical conditions:

$$\sum_{i \in I} y_i - 1 = 0, \tag{32}$$

$$n_i - M y_i \leq 0, \qquad \forall i \in I. \tag{33}$$

When the binary operator y_i in Equations (32) and (33) is zero, the feed flowrate n_i to separator i belonging to the set I of methods accomplishing the given task is also zero. On the contrary, if $y_i = 1$ the separator is active. M is a constant whose value is big enough but possibly of the same order of magnitude. The selected value for implementation is four times the specified syngas productivity. If the value of M exceeds the value of the underlying flowrate for several orders of magnitude, numerical issues might be encountered, and the condition of mutual exclusivity among separators is violated.

Each reactor has an associated separation sequence. Even though RWGS, SR, POX, DR, and TRI could share the same separators, five distinct separation-trains are implemented, which allows for linearity to be preserved. In case the selected route for separation strongly depends on the outlet composition from the reactor, redundancies may occur if more reactors are simultaneously operated. For instance, membrane and adsorption technologies may entrain the same key component out of a given mixture in the downstream of two distinct reactors. The optimal separation sequence can therefore be homogenized by introducing complexity-reduction constraints.

For each separator shared among N different separation-trains, an inequality is implemented:

$$\frac{1}{N}\sum_{i\in I} y_i - y^{CC} \leq 0. \tag{34}$$

The new binary variable y^{CC} appears in the final inequality which sets the maximum number of units allowed within the plant N_{max} as

$$\sum_{j\in J} y_j^{CC} + \sum_{k\in K} y_k - N_{max} \leq 0. \tag{35}$$

Inequality (35) combines the binary variables associated to the possibly redundant units, set J, with the binaries of unique units, set K, i.e., reactors and non-redundant separators. For $N_{max} = +\infty$, unitary binaries can be paired with zero-flow units. In case the maximum number of units allowed is less than the number generated by MILP in the unconstrained case, $N_{max} \leq N_{unconstrained}$ the plant is forced toward higher power requirements. Each binary variable therefore assumes unitary value only if the corresponding unit operation is active and N_{max} coincides with the actual number of operating units.

Objective Function

The general formulation of the objective function reads

$$\min_{\boldsymbol{n},\boldsymbol{y}} (Q + \omega W), \tag{36}$$

where a pseudo-price $\omega \in [0, 1]$ is introduced. The process is optimized with respect to the molar flowrates, in vector $\boldsymbol{n}$, and of binary variables, in vector $\boldsymbol{y}$. The objective penalizes the electrical power demand, W, added to the thermal power demand Q. The values of ω, spanning within its boundaries, generates a Pareto front with respect to the power consumption. For decreasing values of ω, less relevance is given to the electricity demand. This reflects a transition toward plant layouts favoring the use of sustainable, carbon-neutral sources of electricity.

In this contribution, topological results and total power consumption are explored at the boundaries of the pseudo-price domain, namely $\omega = 1$, objective (A):

$$\min_{\boldsymbol{n},\boldsymbol{y}} (Q + W), \tag{37}$$

and $\omega = 0$, objective (B):

$$\min_{\boldsymbol{n},\boldsymbol{y}} Q. \tag{38}$$

Objectives and constraints are linear, and decision variables are either continuous or integer. The resulting MILP problems are solved in MATLAB® 2018b using the function *intlinprog*. The algorithm solves and tightens LP relaxations before implementing heuristics and branch-and-bound strategies.

TABLE 5 | Topological results for unconstrained plant complexity.

(A) $\min_{n,y}(Q + W)$

Downstream	Reactors	ID separation methods	n° units	redundancies
Phosgene	RWGS,DR	V,VI	10	4
Monsanto	RWGS,DR	V,VI	10	4
Hydroformylation	SR,DR,TRI,EL	I,V,VI	12	4
Iron ore	SR,DR,TRI,EL	V,VI,VII	12	4
Fischer Tropsch	SR,DR,TRI,EL	V,VI	9	1
Methanol	SR,DR,TRI,EL	I,V,VI	11	4

(B) $\min_{n,y} Q$

Downstream	Reactors	ID separation methods	n° units	redundancies
Phosgene	POX,EL	V,VI,XII	7	1
Monsanto	POX,EL	V,VI,XII	7	1
Hydroformylation	POX,EL	V,VI,XII	7	1
Iron ore	POX,EL	V,VI,XII	7	1
Fischer Tropsch	POX,EL	V,VI,XII	7	1
Methanol	POX,EL	V,VI,XII	7	1

The number of redundant units is derived according to the criteria presented in section (3.1).

RESULTS AND DISCUSSION

The aim of this section is to introduce and discuss the optimization results resulting from the enforcement of objective (A) and (B).

Firstly, biogas is considered as feedstock for unconstrained plant complexity. Thereafter, redundancies are removed by application of Equation (35). Total, thermal, and electrical power demands are reported for the resulting plant topologies and compared with the respective requirements after heat integration (pinch analysis, minimum $\Delta T = 15$ K). Subsequently, the feed is limited to CO_2 from DAC. The power contributions are expressed per molar flow of syngas.

Feedstock: Biogas

Plant topologies obtained for objective (A) and (B) and unconstrained plant complexity are reported in **Tables 5A,B**. The number of units account for possible redundancies. As an example, for objective (A) and phosgene synthesis, the optimizer identifies an interaction between RWGS and DR and a plant comprising 10 units. The quinary outlet gas from DR shares 4 components with the outlet from RWGS, including the components of the biogas feed stream: CO_2 and CH_4. At most, therefore, three separators can be shared between DR and RWGS, one of which splits the biogas stream into pure CO_2 and CH_4. As a matter of fact, four separators and two reactors are sufficient to perform the production, and four units are redundant. Interactions among reactors are not deemed redundant.

Results show that for unconstrained complexity, redundancies always occur. These results are therefore not representative of implementable solutions in terms of downstream operations.

TABLE 6 | Plant topology and power consumption, divided into thermal percent (T%), electrical percent (E%), and total power (tot.) and compared with total power required after heat integration via pinch (HI).

(A) $\min_{n,y}(Q+W)$				
Downstream	**Reactors (separators)**	**T %**	**E %**	**tot.; (with HI) [kJ/mol$_{syngas}$]**
Phosgene	DR(3_{VI},6_{VI},19_{V},22_{VI})	70.1	29.9	232; (188)
Monsanto	DR(3_{VI},6_{VI},19_{V},22_{VI})	61.6	38.4	262; (219)
Hydroformylation	DR,SR(1_{IV},11_{V},21_{V},23_{VI})	77.1	22.9	147; (96)
Iron Ore	EL;DR,SR,TRI(3_{VI},6_{VI},19_{V},22_{VI})	75.7	24.3	125; (110)
Fischer Tropsch	EL;SR,TRI(3_{VI},7_{V},18_{V},22_{VI})	63.5	36.5	128; (112)
Methanol	EL;SR,TRI(3_{VI},7_{V},18_{V},22_{VI})	57.0	43.0	139; (116)
(B) $\min_{n,y} Q$				
Downstream	**Reactors (separators)**	**T %**	**E %**	**tot.; (with HI) [kJ/mol$_{syngas}$]**
Phosgene	EL;POX(3_{VI},6_{VII},19_{V},22_{VI})	2.8	97.2	638; (620)
Monsanto	EL;POX(3_{VI},6_{VII},19_{V},22_{VI})	2.7	97.3	662; (644)
Hydroformylation	EL;POX(3_{VI},6_{VII},19_{V},22_{VI})	2.7	97.3	323; (314)
Iron Ore	EL;POX(3_{VI},7_{V},18_{VI},22_{VI})	7.1	92.9	247; (229)
Fischer Tropsch	EL;POX(2_{VII},4_{VI},19_{V},22_{VI})	3.1	96.9	200; (194)
Methanol	EL;POX(2_{VII},4_{VI},19_{V},22_{VI})	2.7	97.3	206; (200)

Biogas as feedstock.

Nevertheless, relevant general features of the resulting configurations can be observed:

- POX is never part of the solution with objective (A) but is always selected with (B);
- DR results from all syngas applications with objective (A);
- The pair TRI-EL is selected for high syngas ratios with (A) while RWGS is for low syngas ratios;
- None of the separation trains allows for absorption-based methods;
- Cryogenics is selected by enforcement of objective (B) and for any downstream application, i.e., separation of CH_4 from H_2 (method VII).

Redundancies are thus removed in the setting $N_{max} = n^{\circ}_{Units} - n^{\circ}_{Redundancies}$ in Equation (35). In case redundancies are still present after reduction, e.g., if a lower number of reactors is selected, N_{max} is updated and the procedure reiterated. The **Tables 6A,B** include the plant configurations thus obtained. Reactor-wise, they reflect the same pattern discussed for the case of unconstrained complexity in **Table 5**: EL and POX come with objective (B), whereas POX does not activate with (A). In (A), DR is the only reactor active for low syngas ratios, whereas combinations of TRI, EL, and SR are better suited for higher ratios. Separator-wise, the predominance of adsorption and membranes over absorption methods is confirmed, whereas cryogenics with objective (B) is not due to the restriction imposed on the number of units: if biogas has to be split, the binary mixture to be separated in the biogas train is necessarily (CH_4/CO_2), split 22 in **Table 4** and is thus shared with the downstream of POX. The only cryogenic method available for this task is distillation, conducted at pressure higher than POX reactor—**Table 3**. The thermal power input to adjust the temperature of CH_4 to the reactor level is therefore far higher than the input required from the selected separator, the polymeric membrane, which can decrease this thermal duty by adiabatic temperature increase after vacuum normalization and pressurization (adiabatic temperature increase). Palladium membrane for the separation of H_2 is the result if the electrical power is not penalized.

In objective (A), the predominant power contribution is thermal, whereas most of the power required with objective (B) is electrical. Partial contributions to the total power without heat integration are represented in **Figures 4**, **5**. The sum of *reactor* and *preconditioning* gives the total reactor power input, the former being associated with the chemical reaction in the reactor only, while the latter accounts for the pressure and temperature adjustment to bring the reactants to feed conditions. *Adjustment* denotes the power input to meet the (T, p) level at which syngas is required for its further downstream applications; *storage* is associated with the power for pressurization of surplus H_2, while *separation* comprises the remaining contributions.

With both objectives (A) and (B), the reactors dominate the total power demand and exhibit a decreasing trend with H_2/CO. The high power requirement for storage with objective (B) is determined by the large H_2 surplus, accompanying the large O_2 demand at the POX reactor to sustain the CO production (see **Table 2** for POX stoichiometry).

Within the context of objective (A), the pinch analysis determines a substantial recovery of heat within the separation train and complete recovery in the context of (B). Nevertheless, all the reactors in (A) are heat sinks at high temperatures. Consequently, they cannot benefit from heat integration. As highlighted by the energy contributions in **Figure 4**, the power requirement at the reactors dominates over the other

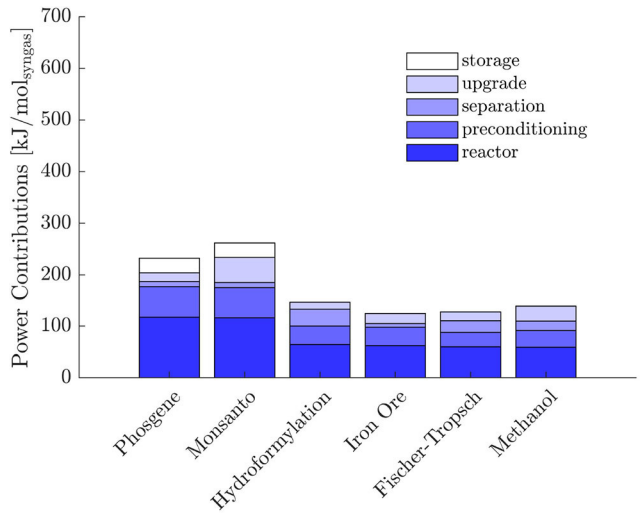

FIGURE 4 | Contributions to the total power requirements for $\min_{n,y}(Q+W)$, biogas as feedstock.

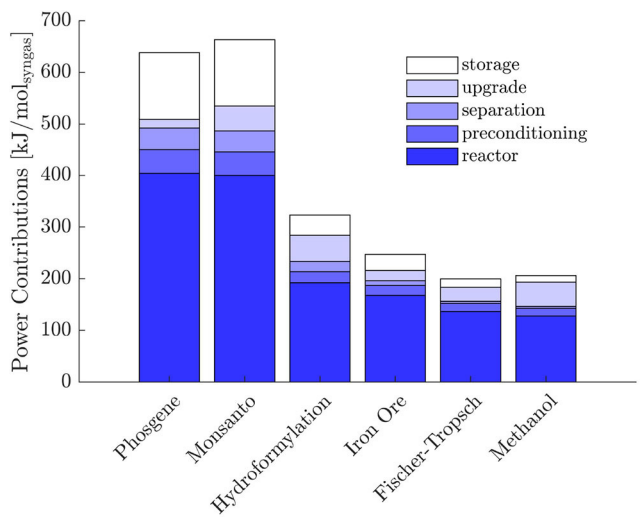

FIGURE 5 | Contributions to the total power requirements for $\min_{n,y} Q$, biogas as feedstock.

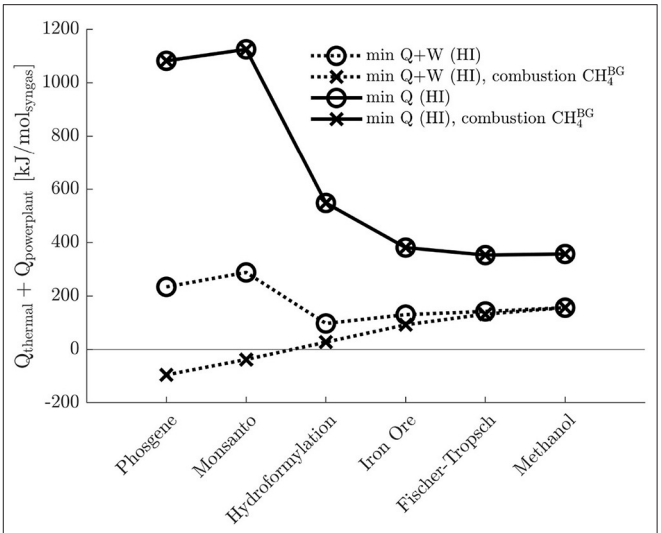

FIGURE 6 | Comparison among total power demands after heat integration (HI) for the two objectives, $\min_{n,y}(Q+W)$ and $\min_{n,y} Q$, for biogas as feedstock, with and without surplus bio-CH_4 utilization. The electrical power is generated by gas-fired power plant of 60% efficiency, $Q_{powerplant} = W/0.6$.

contributions, which justifies the modest reduction in total power demand reported in **Table 6**. Moreover, if heat integration is beneficial in terms of utility minimization, it neglects the effect of poor overall heat transfer coefficients typical of gas-gas economizers. Excluding the phase transition required for water to adjust to SR and TRI reactor conditions and a liquid make-up stream for EL, the process system encompasses gas streams only. The overall heat transfer coefficients are normally greatly improved in presence of phase-changing fluids, typically condensing steam, which can justify the more conservative approach of sequential optimization and heat integration.

Biogas is totally or partially separated into its components and utilized as a reactant. Nevertheless, surplus bio-CH_4 could be used to generate carbon-neutral hot and electrical utilities by combustion. **Figure 6** depicts the net total power demand, or demand for possibly fossil-based power, in terms of hot utility after heat integration and with objectives (A) and (B). It is assumed that

I Electricity is generated by a gas-fired power plant (worst-case scenario) with an efficiency of 60%: $Q_E = W/0.6$;
II The hot utility at the syngas and power plant is provided directly by the combustion of CH_4 (low heating value $LHV = 785\,\text{kJ/mol}$);
III The heat generated by combustion of surplus bio-CH_4 can be directly transferred to the process or the power plant, thus neglecting the generation of steam and the irreversibilities.

Assumption III necessarily outlines the most optimistic scenario, which is to be benchmarked against the demand which does not account for bio-CH_4 utilization: the actual power demand is expected to fall between these boundaries. As indicated by **Figure 6**, plant configurations resulting with objective (A) can greatly benefit from the utilization of surplus bio-CH_4, especially for low syngas ratios. On the contrary, with objective (B), bio-CH_4 is entirely converted, as CH_4 is the only feedstock for POX.

Feedstock: CO_2 From DAC

Direct air capture (DAC) provides pure CO_2 to the plant and substitutes biogas as a source of carbon for the system. In this system, low temperature (LT) solid sorbent performs DAC with a thermal and electrical power input of 277 and 39 kJ/mol_{CO2}, respectively. The values are adapted from Fasihi et al. (2019). **Table 7** shows that the combination of EL and RWGS, the only technology available for the feedstock, is followed by combinations of membranes (polymeric and Pd)

TABLE 7 | Plant topology and power consumption, divided into thermal percent (T%), electrical percent (E%), and total power (tot.).

(A) $\min_{n,y}(Q+W)$					
Downstream	**Reactors (separators)**	**T %**	**E %**	**tot. [kJ/mol$_{syngas}$]**	**DAC [kJ/mol$_{syngas}$]**
Phosgene	EL;RWGS(9_{VI},13_{V},26_{VII})	46.5	53.5	841	316
Monsanto	EL;RWGS(9_{VI},13_{V},26_{VII})	45.9	54.1	845	313
Hydroformylation	EL;RWGS(9_{VI},13_{V},26_{VII})	31.8	68.2	585	151
Iron Ore	EL;RWGS(9_{VI},14_{VI},24_{V})	32.6	67.4	557	132
Fischer Tropsch	EL;RWGS(9_{VI},13_{V})	26.2	73.8	510	107
Methanol	EL;RWGS(9_{VI},13_{V})	24.5	75.5	510	101
(B) $\min_{n,y} Q$					
Downstream	**Reactors (separators)**	**T %**	**E %**	**tot. [kJ/mol$_{syngas}$]**	**DAC [kJ/mol$_{syngas}$]**
Phosgene	EL;RWGS(9_{VI},15_{V},25_{VII})	45.9	54.1	851	316
Monsanto	EL;RWGS(9_{VI},15_{V},25_{VII})	44.0	56.0	878	313
Hydroformylation	EL;RWGS(9_{VI},13_{V},26_{VII})	31.8	68.2	585	151
Iron Ore	EL;RWGS(9_{VI},13_{V},26_{VI})	31.2	68.8	572	132
Fischer Tropsch	EL;RWGS(9_{VI},13_{V},26_{V})	25.5	74.5	522	107
Methanol	EL;RWGS(9_{VI},15_{V},25_{V})	23.9	76.1	523	101

Consumptions for direct air capture (DAC) are reported. CO_2 as feedstock.

and VPSA operations. The contributions to the total power, similar between objectives (A) and (B), are shifted toward electricity and proportional to the syngas ratio. Compared with the corresponding values in **Table 6**, the power demands are conspicuously higher due to the presence of DAC, the latter spanning between 19 and 37% of the required total input.

CONCLUSIONS

Candidate process topologies for Power-to-Syngas applications are embedded within a superstructure. Mixed-integer, linear constraints are set for alternative feedstock scenarios: biogas and CO_2 from DAC (LT-solid sorbent). A general objective-function formulation combines thermal and electrical power input linearly. The electrical power contribution is weighted by a pseudo price $\omega \in [0,1]$. For $\omega \to 1$, electricity is penalized, e.g., purchased from fossil-based power plant facilities, whereas $\omega \to 0$ assumes carbon-free in-house electricity production. The resulting MILP problems are solved for extreme-value scenarios: objective (A) for $\omega = 1$ and objective (B) for $\omega = 0$. Results show that the higher total power demand with (B) with respect to (A) is compensated by the predominance of electricity demand, up to 97%, possibly increasing after heat integration. Furthermore, topological configurations with (B) include two reactors for any syngas application, EL and POX, whereas interaction among EL, SR, TRI, and DR result in (A). Forcing the plant complexity toward a single reactor would therefore increase the total energy values. Surplus bio-CH_4 can relieve the demand for external fossil-based fuel, especially for downstream applications requiring low syngas ratios.

Membranes and adsorption-based separators prevail over absorption and scrubbing methods. Cryogenics possibly result with (B). For CO_2 as feedstock, the combination of EL, RWGS, and DAC enhances the total power requirements even though the electricity demand prevails over thermal inputs.

Assuming that proper storage strategies to face the intermittent nature of renewable resources are available, such as batteries for electricity and biogas buffer tanks, process configuration favoring electricity over thermal inputs are preferable for applications requiring high syngas ratios, suggesting the implementation of POX in conjunction with EL. On the contrary, for low ratios, surplus bio-CH_4 can be utilized to mitigate the thermal power requirements for DR, resulting with (A). Nevertheless, in case the effect of coking in DR were mitigated by introduction of oxygen (oxy-DR), the energy demand is expected to increase substantially due to the introduction of EL.

The possibility of a severe drop in biogas availability over the long-term suggests the implementation of reverse water-gas-shift to allow for operations based on CO_2 as feedstock.

DATA AVAILABILITY STATEMENT

The raw data supporting the conclusions of this article can be made available by the authors upon request, without undue reservation.

AUTHOR CONTRIBUTIONS

KS conceived of the general framework: the application of superstructure optimization for the Power-to-Syngas processes. AM identified the specific system elements of interest, developed the underlying theory, and produced the numerical results. AM interpreted the results and generated the manuscript. MW supervised AM through his work, providing suggestions concerning the theoretical background and the interpretation of results. Furthermore, MW also contributed to the generation of the manuscript.

ACKNOWLEDGMENTS

The authors acknowledge their Partners within the context of P2Chem, a project financially supported by the Federal Ministry of Education and Research of Germany (support code: 05M18OCB). Johanna Klüsener and Stefan Bube are gratefully acknowledged for providing icons for **Figure 1** used in the manuscript.

REFERENCES

Abdullah, B., Ghani, N. A. A., and Vo, D.-V. N. (2017). Recent advances in dry reforming of methane over Ni-based catalysts. *J. Clean. Product*. 162, 170–185. doi: 10.1016/j.jclepro.2017.05.176

Agarwal, A., Biegler, L. T., and Zitney, S. E. (2010). A superstructure-based optimal synthesis of PSA cycles for post-combustion CO2 capture. *AIChE J*. 56, 1813–1828. doi: 10.1002/aic.12107

Arora, S., and Prasad, R. (2016). An overview on dry reforming of methane: strategies to reduce carbonaceous deactivation of catalysts. *RSC Adv*. 6, 108668–108688. doi: 10.1039/C6RA20450C

Bahadori, A., and Vuthaluru, H. B. (2009). Simple methodology for sizing of absorbers for TEG (Triethylene Glycol) gas dehydration systems. *Energy* 34, 1910–1916. doi: 10.1016/j.energy.2009.07.047

Battrum, M., and Thomas, W. (1991). Carbon monoxide recovery by pressure swing adsorption. *Chem. Eng. Res. Design* 69, 119–129.

Bensmann, B., Hanke-Rauschenbach, R., Arias, I. P., and Sundmacher, K. (2013). Energetic evaluation of high pressure PEM electrolyzer systems for intermediate storage of renewable energies. *Electrochim. Acta* 110, 570–580. doi: 10.1016/j.electacta.2013.05.102

Biegler, L. T., Grossmann, I. E., and Westerberg, A. W. (1997). *Systematic Methods for Chemical Process Design*. Old Tappan, NJ: Prentice Hall.

Burr, B., and Lyddon, L. (2008). "A comparison of physical solvents for acid gas removal," in 87th Annual Convention of the Gas Processors Association (Red Hook, NY: Curran).

Delgado, J. A., Águeda, V., Uguina, M., Sotelo, J., Brea, P., and Grande, C. A. (2014). Adsorption and diffusion of H2, CO, CH4, and CO2 in BPL activated carbon and 13X zeolite: evaluation of performance in pressure swing adsorption hydrogen purification by simulation. *Indus. Eng. Chem. Res*. 53, 15414–15426. doi: 10.1021/ie403744u

Di Profio, P., Arca, S., Rossi, F., and Filipponi, M. (2009). Comparison of hydrogen hydrates with existing hydrogen storage technologies: energetic and economic evaluations. *Int. J. Hydrogen Energy* 34, 9173–9180. doi: 10.1016/j.ijhydene.2009.09.056

DiMartino, S., Glazer, J., Houston, C., and Schott, M. (1988). Hydrogen/carbon monoxide separation with cellulose acetate membranes. *Gas Separat. Purif*. 2, 120–125. doi: 10.1016/0950-4214(88)80027-6

Dutta, N., and Patil, G. (1995). Developments in CO separation. *Gas Separat. Purif*. 9, 277–283. doi: 10.1016/0950-4214(95)00011-Y

El-Nagar, R. A., and Ghanem, A. A. (2019). "Syngas production, properties, and its importance," in *Sustainable Alternative Syngas Fuel*, eds C. Ghenai and A. Inayat (Rijeka: IntechOpen), 1–408.

Fasihi, M., Efimova, O., and Breyer, C. (2019). Techno-economic assessment of CO2 direct air capture plants. *J. Clean. Product*. 224, 957–980. doi: 10.1016/j.jclepro.2019.03.086

Gao, F., Wang, S., Wang, W., Duan, J., Dong, J., and Chen, G. (2018). Adsorption separation of CO from syngas with CuCl@ AC adsorbent by a VPSA process. *RSC Adv*. 8, 39362–39370. doi: 10.1039/C8RA08578A

Gao, F., Wang, Y., Wang, X., and Wang, S. (2016). Selective CO adsorbent CuCl/AC prepared using CuCl 2 as a precursor by a facile method. *RSC Adv*. 6, 34439–34446. doi: 10.1039/C6RA03116A

Grande, C. A., Blom, R., Andreassen, K. A., and Stensrød, R. E. (2017). Experimental results of pressure swing adsorption (PSA) for pre-combustion CO2 capture with metal organic frameworks. *Energy Proc*. 114, 2265–2270. doi: 10.1016/j.egypro.2017.03.1364

Grande, C. A., and Rodrigues, A. E. (2007). Layered vacuum pressure-swing adsorption for biogas upgrading. *Indus. Eng. Chem. Res*. 46, 7844–7848. doi: 10.1021/ie070942d

Gruber, H., Groß, P., Rauch, R., Reichhold, A., Zweiler, R., Aichernig, C., et al. (2019). Fischer-Tropsch products from biomass-derived syngas and renewable hydrogen. *Biomass Conv. Bioref*. doi: 10.1007/s13399-019-00459-5

Han, C., Zahid, U., An, J., Kim, K., and Kim, C. (2015). CO2 transport: design considerations and project outlook. *Curr. Opin. Chem. Eng*. 10, 42–48. doi: 10.1016/j.coche.2015.08.001

Häussinger, P., Lohmüller, R., and Watson, A. M. (2011). *Hydrogen, 3. Purification*. Weinheim: American Cancer Society. doi: 10.1002/14356007.o13_o04

Hochgesand, G. (1970). Rectisol and purisol. *Indus. Eng. Chem*. 62, 37–43. doi: 10.1021/ie50727a007

Huang, Y., Merkel, T. C., and Baker, R. W. (2014). Pressure ratio and its impact on membrane gas separation processes. *J. Memb. Sci*. 463, 33–40. doi: 10.1016/j.memsci.2014.03.016

IPCC (2013). *Climate Change 2013: The Physical Science Basis. Contribution of Working Group I to the Fifth Assessment Report of the Intergovernmental Panel on Climate Change*. Cambridge, UK; New York, NY: Cambridge University Press.

Jang, S.-C., Yang, S.-I., Oh, S.-G., and Choi, D.-K. (2011). Adsorption dynamics and effects of carbon to zeolite ratio of layered beds for multicomponent gas adsorption. *Korean J. Chem. Eng*. 28, 583–590. doi: 10.1007/s11814-010-0399-9

Kang, D., Lim, H. S., Lee, M., and Lee, J. W. (2018). Syngas production on a Ni-enhanced Fe2O3/Al2O3 oxygen carrier via chemical looping partial oxidation with dry reforming of methane. *Appl. Energy* 211, 174–186. doi: 10.1016/j.apenergy.2017.11.018

Kim, H. W., Yoon, H. W., Yoon, S.-M., Yoo, B. M., Ahn, B. K., Cho, Y. H., et al. (2013). Selective gas transport through few-layered graphene and graphene oxide membranes. *Science* 342, 91–95. doi: 10.1126/science.1236098

Li, A., Liang, W., and Hughes, R. (2000). The effect of carbon monoxide and steam on the hydrogen permeability of a Pd/stainless steel membrane. *J. Memb. Sci*. 165, 135–141. doi: 10.1016/S0376-7388(99)00223-9

Li, X., Li, Z., Xia, Q., and Xi, H. (2007). Effects of pore sizes of porous silica gels on desorption activation energy of water vapour. *Appl. Thermal Eng*. 27, 869–876. doi: 10.1016/j.applthermaleng.2006.09.010

Liesche, G., Schack, D., and Sundmacher, K. (2019). The FluxMax approach for simultaneous process synthesis and heat integration: production of hydrogen cyanide. *AIChE J*. 65:e16554. doi: 10.1002/aic.16554

Lin, H., Thompson, S. M., Serbanescu-Martin, A., Wijmans, J. G., Amo, K. D., Lokhandwala, K. A., et al. (2012). Dehydration of natural gas using membranes. Part I: composite membranes. *J. Memb. Sci*. 413, 70–81. doi: 10.1016/j.memsci.2012.04.009

Maqsood, K., Mullick, A., Ali, A., Kargupta, K., and Ganguly, S. (2014). Cryogenic carbon dioxide separation from natural gas: a review based on conventional and novel emerging technologies. *Rev. Chem. Eng*. 30, 453–477. doi: 10.1515/revce-2014-0009

Merel, J., Clausse, M., and Meunier, F. (2008). Experimental investigation on CO2 post- combustion capture by indirect thermal swing adsorption using 13X and 5A zeolites. *Indus. Eng. Chem. Res*. 47, 209–215. doi: 10.1021/ie071012x

Merkel, T., Gupta, R., Turk, B., and Freeman, B. D. (2001). Mixed-gas permeation of syngas components in poly (dimethylsiloxane) and poly (1-trimethylsilyl-1-propyne) at elevated temperatures. *J. Memb. Sci*. 191, 85–94. doi: 10.1016/S0376-7388(01)00452-5

Metz, S. J., Van de Ven, W., Potreck, J., Mulder, M., and Wessling, M. (2005). Transport of water vapor and inert gas mixtures through highly selective and highly permeable polymer membranes. *J. Memb. Sci*. 251, 29–41. doi: 10.1016/j.memsci.2004.08.036

Mondal, M. K., Balsora, H. K., and Varshney, P. (2012). Progress and trends in CO2 capture/separation technologies: a review. *Energy* 46, 431–441. doi: 10.1016/j.energy.2012.08.006

Moral, A., Reyero, I., Alfaro, C., Bimbela, F., and Gandia, L. M. (2018). Syngas production by means of biogas catalytic partial oxidation and

dry reforming using Rh-based catalysts. *Catalysis Tdy* 299, 280–288. doi: 10.1016/j.cattod.2017.03.049

Morishige, K. (2011). Adsorption and separation of CO2/CH4 on amorphous silica molecular sieve. *J. Phys. Chem. C* 115, 9713–9718. doi: 10.1021/jp202572w

Mulgundmath, V., and Tezel, F. H. (2010). Optimisation of carbon dioxide recovery from flue gas in a TPSA system. *Adsorption* 16, 587–598. doi: 10.1007/s10450-010-9255-9

Netusil, M., and Ditl, P. (2011). Comparison of three methods for natural gas dehydration. *J. Nat. Gas Chem*. 20, 471–476. doi: 10.1016/S1003-9953(10)60218-6

Pantaleo, G., La Parola, V., Deganello, F., Singha, R., Bal, R., and Venezia, A. (2016). Ni/CeO2 catalysts for methane partial oxidation: synthesis driven structural and catalytic effects. *Appl. Catal. Environ*. 189, 233–241. doi: 10.1016/j.apcatb.2016.02.064

Paolini, V., Petracchini, F., Segreto, M., Tomassetti, L., Naja, N., and Cecinato, A. (2018). Environmental impact of biogas: a short review of current knowledge. *J. Environ. Sci. Health A* 53, 899–906. doi: 10.1080/10934529.2018.1459076

Park, J.-H., Kim, J.-N., and Cho, S.-H. (2000). Performance analysis of four-bed H2 PSA process using layered beds. *AIChE J*. 46, 790–802. doi: 10.1002/aic.690460413

Poudel, J., Choi, J. H., and Oh, S. C. (2019). Process design characteristics of syngas (CO/H2) separation using composite membrane. *Sustainability* 11:703. doi: 10.3390/su11030703

Reimert, R., Marschner, F., Renner, H.-J., Boll, W., Supp, E., Brejc, M., et al. (2015). "Ullmann's energy: resources, processes, products," in *Gas Production, 2 Processes: Natural Gas*, ed Wiley-VCH (Weinheim: Wiley-VCH).

Ritter, J. A., and Ebner, A. D. (2007). State-of-the-art adsorption and membrane separation processes for hydrogen production in the chemical and petrochemical industries. *Separat. Sci. Technol*. 42, 1123–1193. doi: 10.1080/01496390701242194

Schack, D., Liesche, G., and Sundmacher, K. (2020). The FluxMax approach: simultaneous flux optimization and heat integration by discretization of thermodynamic state space illustrated on methanol synthesis process. *Chem. Eng. Sci*. 215:115382. doi: 10.1016/j.ces.2019.115382

Schack, D., Rihko-Struckmann, L., and Sundmacher, K. (2016). "Structure optimization of power-to-chemicals (P2C) networks by linear programming for the economic utilization of renewable surplus energy," in *Computer Aided Chemical Engineering*, Vol. 38, eds Z. Kravanja and M. Bogataj (Elsevier), 1551–1556. doi: 10.1016/B978-0-444-63428-3.50263-0

Scholes, C. A., Bacus, J., Chen, G. Q., Tao, W. X., Li, G., Qader, A., et al. (2012). Pilot plant performance of rubbery polymeric membranes for carbon dioxide separation from syngas. *J. Memb. Sci*. 389, 470–477. doi: 10.1016/j.memsci.2011.11.011

SGC (2012). *Basic Data on Biogas*.

Sijbesma, H., Nymeijer, K., van Marwijk, R., Heijboer, R., Potreck, J., and Wessling, M. (2008). Flue gas dehydration using polymer membranes. *J. Memb. Sci*. 313, 263–276. doi: 10.1016/j.memsci.2008.01.024

Singha, R. K., Shukla, A., Yadav, A., Adak, S., Iqbal, Z., Siddiqui, N., et al. (2016). Energy efficient methane tri-reforming for synthesis gas production over highly coke resistant nanocrystalline Ni/ZrO2 catalyst. *Appl. Energy* 178, 110–125. doi: 10.1016/j.apenergy.2016.06.043

Sircar, S., and Golden, T. (2000). Purification of hydrogen by pressure swing adsorption. *Separat. Sci. Technol*. 35, 667–687. doi: 10.1081/SS-100100183

Smith, R. (2005). *Chemical Process: Design and Integration*. West Sussex: John Wiley & Sons.

Song, C., and Pan, W. (2004). Tri-reforming of methane: a novel concept for catalytic production of industrially useful synthesis gas with desired H2/CO ratios. *Catalysis Tdy* 98, 463–484. doi: 10.1016/j.cattod.2004.09.054

Sun, L., and Smith, R. (2013). Rectisol wash process simulation and analysis. *J. Clean. Product*. 39, 321–328. doi: 10.1016/j.jclepro.2012.05.049

Uebbing, J., Rihko-Struckmann, L. K., and Sundmacher, K. (2019). Exergetic assessment of CO2 methanation processes for the chemical storage of renewable energies. *Appl. Energy* 233, 271–282. doi: 10.1016/j.apenergy.2018.10.014

Wang, B., Cote, A. P., Furukawa, H., O'Keeffe, M., and Yaghi, O. M. (2008). Colossal cages in zeolitic imidazolate frameworks as selective carbon dioxide reservoirs. *Nature* 453, 207–211. doi: 10.1038/nature06900

Wang, Y., and LeVan, M. D. (2009). Adsorption equilibrium of carbon dioxide and water vapor on zeolites 5A and 13X and silica gel: pure components. *J. Chem. Eng. Data* 54, 2839–2844. doi: 10.1021/je800900a

Wenzel, M., Rihko-Struckmann, L., and Sundmacher, K. (2017). Thermodynamic analysis and optimization of RWGS processes for solar syngas production from CO2. *AIChE J*. 63, 15–22. doi: 10.1002/aic.15445

Wenzel, M., Rihko-Struckmann, L., and Sundmacher, K. (2018). Continuous production of CO from CO2 by RWGS chemical looping in fixed and fluidized bed reactors. *Chem. Eng. J*. 336, 278–296. doi: 10.1016/j.cej.2017.12.031

Wurzbacher, J. A., Gebald, C., Piatkowski, N., and Steinfeld, A. (2012). Concurrent separation of CO2 and H2O from air by a temperature-vacuum swing adsorption/desorption cycle. *Environ. Sci. Technol*. 46, 9191–9198. doi: 10.1021/es301953k

Yang, J., Lee, C.-H., and Chang, J.-W. (1997). Separation of hydrogen mixtures by a two-bed pressure swing adsorption process using zeolite 5A. *Indus. Eng. Chem. Res*. 36, 2789–2798. doi: 10.1021/ie960728h

Ziaii, S., Cohen, S., Rochelle, G. T., Edgar, T. F., and Webber, M. E. (2009). Dynamic operation of amine scrubbing in response to electricity demand and pricing. *Energy Proc*. 1, 4047–4053. doi: 10.1016/j.egypro.2009.02.211

Conflict of Interest: The authors declare that the research was conducted in the absence of any commercial or financial relationships that could be construed as a potential conflict of interest.

frontiers in Energy Research

ORIGINAL RESEARCH
published: 30 September 2020
doi: 10.3389/fenrg.2020.00190

Optimizing the Design of Supply Chains for Carbon Capture, Utilization, and Sequestration in Europe: A Preliminary Assessment

*Federico d'Amore and Fabrizio Bezzo**

Computer-Aided Process Engineering Laboratory (CAPE-Lab), Department of Industrial Engineering, University of Padova, Padova, Italy

Carbon capture and storage represents a key technology for reducing the anthropogenic emissions of greenhouse gases. In addition to this, carbon utilization has often been considered as a viable option for increasing the environmental benefits, while decreasing costs of the mere capture and storage system. This contribution proposes an optimization framework for the design of carbon capture, transport, utilization, and storage supply chains in the European context. Based on literature data, technologies converting CO_2 into methanol and polyether carbonate polyols were selected as the most promising and incorporated into the optimization framework. The goal is to reduce 50% of European emissions from large stationary sources by 2030. Results highlight that, under our assumptions, the significance of carbon utilization in terms of a reduction of the environmental impact is likely to be a minor one: considering the current state of technologies only about 2.4% of the overall CO_2 emitted from large stationary sources can be removed by chemical utilization. However, significant benefits can be obtained in terms of overall cost reduction thanks to revenues deriving from the chemicals being produced.

Keywords: carbon capture utilization and storage, supply chain optimization, mixed integer linear programming, European framework, CO_2 chemical conversion and utilization

OPEN ACCESS

Edited by:
Antonio Espuña, Universitat Politecnica de Catalunya, Spain

Reviewed by:
Athanasios I. Papadopoulos, Centre for Research and Technology Hellas (CERTH), Greece
Rajagopalan Srinivasan, Indian Institute of Technology Madras, India

****Correspondence:***
Fabrizio Bezzo
fabrizio.bezzo@unipd.it

Specialty section:
This article was submitted to Process and Energy Systems Engineering, a section of the journal Frontiers in Energy Research

Received: *26 February 2020*
Accepted: *17 July 2020*
Published: *30 September 2020*

Citation:
d'Amore F and Bezzo F (2020) Optimizing the Design of Supply Chains for Carbon Capture, Utilization, and Sequestration in Europe: A Preliminary Assessment. Front. Energy Res. 8:190. doi: 10.3389/fenrg.2020.00190

1. INTRODUCTION

The anthropogenic generation of greenhouse gases (GHGs) has led to an increment of the average surface temperature, with dramatic consequences for the natural environment. The target of limiting the rise in average temperature to +1.5°C by 2050 was indicated (IPCC, 2018). In the European Union (EU), in order to comply with the Paris Agreement, it has been proposed to reduce GHGs and particularly CO_2 emissions by 43% by 2030 with respect to 2005 values. Carbon capture and storage (CCS) technologies represent a promising candidate for attaining sustainable development (Li et al., 2019), i.e., an economic growth that aims at tackling major environmental issues (global warming), in an era when power and industry still massively rely on carbon and, more in general, fossil fuels.

Overall, CCS is employed to dispose the CO_2 emitted by the operation of carbon intensive facilities into appropriate geological basins (CCS), in opposition to the possibility of converting it into useful products (CCU), or exploiting a combination of both sequestration and utilization (CCUS). The typical CCS scheme is composed of three echelons: capture, transport, and sequestration (IPCC, 2005). Three main technologies are currently available for capturing CO_2

from the use of fossil fuels: post-combustion capture, oxy-fuel combustion capture, and pre-combustion capture (Bui et al., 2018). The concentrated CO_2 flow is then purified and compressed to be transported in a cost-effective way. Finally, the third step is the injection of CO_2 below the Earth's surface and its consequent sequestration. As an alternative to geological sequestration into appropriate basins, CO_2 could be diverted for the use of processes traditionally fed by fossil fuels, with the aim of producing commodities while pursuing a negative carbon footprint (Smit et al., 2014). Regarding utilization pathways, different options have been highlighted as promising in attaining a reduction of the costs of CCS through either CCU or CCUS, and have been gathered into groups of mineral carbonation, chemical conversion, and biological utilization (US National Academy of Sciences, 2019). Several studies have considered the technological feasibility of different routes, among which chemical conversion has emerged as the most appropriate option (at least in techno-economic terms) for an early-stage implementation of CCU (Lehtonen et al., 2019). For instance, Alper and Yuksel Orhan (2017) recently reviewed the possible chemical conversion options for CO_2 and from their analysis a broad variety of families of both pathways and products, attractive for CCUS, emerged (e.g., C1-chemicals, catalytic processes, polymers, inorganics, fine chemicals). Sternberg et al. (2017) analyzed the CO_2-based production of some C1-chemicals by assessing the potential benefits in terms of lowering global warming and fossil depletion; Barbera et al. (2020) assessed the technical performance of conversion paths into C1-chemicals. Armstrong and Styring (2015) highlighted the environmental benefits achievable in treating CO_2 as a commodity chemical rather than a waste product. On the other hand, other studies questioned the actual effectiveness of the chemical conversion of CO_2 and indicated that only minor environmental benefits could be obtained (Mac Dowell et al., 2017).

Recently, a noteworthy research effort has laid the foundations for several studies on CCS and CCUS, which have provided a large increase in the techno-economic knowledge of each single stage of the supply chain (SC). Moreover, the necessity of investigating the design, cost, and integration of the CCS/CCUS stages for different geographic contexts and applicative frameworks has emerged (Bui et al., 2018). Several contributions analyzed, mostly through mixed integer linear programming (MILP) techniques, the design and optimization of CCS systems for different geographic contexts and scales (**Table 1**). Han and Lee (2012) optimized a CCS SC for North Korea through a MILP formulation under uncertainty in market prices while, again for North Korea, a subsequent contribution considered preference on risk as a measure of data uncertainty (Lee et al., 2017). Middleton et al. (2012) proposed a MILP model for CCS located in Texas that also took into account uncertainty in storage physics. Again, the response toward uncertainty in storage physics was investigated by Middleton and Yaw (2018) for the case of a CCS SC in Alberta, Canada. Another MILP CCS optimization was published for the United Kingdom by Elahi et al. (2014), which has subsequently been updated by also including uncertainty in carbon prices (Elahi et al., 2017). Again, for the United Kingdom, another MILP optimization under uncertainty in market prices and subsidies was developed by Nie et al. (2017). Similarly, Kalyanarengan Ravi et al. (2016) proposed a CCS SC modeling framework for the context of the Netherlands. d'Amore and Bezzo (2017) optimized a European CCS SC, also considering the risk of leakage related to the pipeline transport (d'Amore et al., 2018), and aspects of social acceptance and risk perception (d'Amore et al., 2020). Zhang et al. (2018) proposed a theoretical MILP modeling tool for the optimization of CCS systems under both storage physics and cost uncertainties.

The first model on CCUS SC optimization was proposed by Turk et al. (1987) and included the possibility of employing CO_2 for enhanced oil recovery (EOR) in Ohio (United States). Klokk et al. (2010) adopted a similar approach for an infrastructure located in Norway. Hasan et al. (2015) in their US-wise optimization framework took again into account EOR as the only possible utilization option. A theoretical modeling framework for EOR was proposed by Wu et al. (2015), too. Ağrali et al. (2018) proposed an optimization model for CCUS located in Turkey, where again, only EOR was adopted as a carbon utilization sink. An even more limited number of scientific contributions optimize CCUS systems by considering the conversion and utilization of CO_2 to generate valuable products. For South Korea, Han and Lee (2013) and Lee et al. (2019) considered the conversion of CO_2 into either biobutanol or green polymers as an alternative to geological storage within a comprehensive CCUS modeling framework. For Germany Leonzio et al. (2019) optimized a CCUS SC through a MILP modeling tool that included the possibility to produce methanol as an alternative to geological storage. Finally, Kim et al. (2019) produced a MILP formulation for the integration of a hydrogen/CCUS SC in the context of South Korea.

Overall, considering the framework of modeling, simulation, and optimization of CO_2 SCs, very few contributions optimized comprehensive CCUS superstructures (i.e., continent-wide) and, in particular, most of these considered only EOR as a unique utilization pathway, given its well-known practice and capability of generating profits. However, although there is great potential with EOR, it is not recognized as a viable and large-scale solution in Europe (Geske et al., 2015). On the other hand, those very few articles including other routes (such as methanol, bio-butanol, and polymers) are focused on a regional-to-countrywide level, and never address the problem of CO_2 conversion and utilization at the European scale. This contribution aims at filling this gap by proposing a large-scale European CCUS SC optimization, with the main goal of addressing the echelon of CO_2 conversion into useful products through a tailored design stage. Regarding the possible CO_2 conversion options, major research issues remain open and need to be tackled, such as scalability and costs, especially for mineral carbonation and biological pathways (US National Academy of Sciences, 2019). This study will only take into account chemical conversion as a potential utilization route, in opposition to the mere geological sequestration into appropriate basins. The resulting MILP modeling tool will provide insights into the optimal design of comprehensive CCUS systems at a noteworthy geographic scale, to provide researchers,

TABLE 1 | Literature review on published contributions on SC optimization for CCS/CCUS.

References	CC(U)S	Utilization	Scale (Area)	Uncertainty
Turk et al. (1987)	CCUS	EOR	Region (Ohio, United States)	–
Klokk et al. (2010)	CCUS	EOR	Country (Norway)	–
Han and Lee (2012)	CCS	–	Region (Pohang, South Korea)	Prices, costs
Middleton et al. (2012)	CCS	–	Region (Texas, United States)	Storage physics
Han and Lee (2013)	CCUS	Biobutanol, polymers	Region (Pohang, South Korea)	Prices, costs
Elahi et al. (2014)	CCS	–	Country (United Kingdom)	–
Hasan et al. (2015)	CCUS	EOR	Country (United States)	–
Wu et al. (2015)	CCUS	EOR	Region (theoretical)	Inexact parameters
Kalyanarengan Ravi et al. (2016)	CCS	–	Country (the Netherlands)	–
d'Amore and Bezzo (2017)	CCS	–	Continent (Europe)	–
Elahi et al. (2017)	CCS	–	Country (United Kingdom)	Carbon prices
Lee et al. (2017)	CCS	–	Region (Pohang, South Korea)	Preference on risk
Nie et al. (2017)	CCS	–	Country (United Kingdom)	Market, subsidies
Ağrali et al. (2018)	CCUS	EOR	Country (Turkey)	–
d'Amore et al. (2018)	CCS	–	Continent (Europe)	–
Middleton and Yaw (2018)	CCS	–	Region (Alberta, Canada)	Storage physics
Zhang et al. (2018)	CCS	–	Region (theoretical)	Storage physics, costs
d'Amore et al. (2019)	CCS	–	Continent (Europe)	Storage capacity
Lee et al. (2019)	CCUS	Biobutanol, polymers	Region (Pohang, South Korea)	Preference on risk
Leonzio et al. (2019)	CCUS	Methanol	Country (Germany)	–
Kim et al. (2019)	CCUS	Hydrogen	Country (South Korea)	–
d'Amore et al. (2020)	CCS	–	Continent (Europe)	–
d'Amore and Bezzo (2020)	CCS	–	Continent (Europe)	–

investors, and policy makers with a methodological framework for quantitative and strategic analysis of a range of possible alternatives for a significant decrease in European CO_2 emissions.

The article is organized as follows. The modeling framework and its main assumptions will be characterized within the next section, after which the description of the MILP model will follow. Further input parameters and the complete mathematical formulation are reported in the **Supplementary Material**. Subsequently, the case studies and results will be presented, and the main limitations of the study will be critically analyzed and discussed. Some final remarks will conclude the work.

2. MODELING FRAMEWORK

This contribution proposes a MILP model for the economic optimization of European CCUS SCs. Although based on a time-static architecture (to reduce the computational burden), the model is conceived to capture a fixed quota of the CO_2 emissions that it is forecasted to be produced from large-stationary sources throughout the next decade (i.e., from 2020 to 2030). In particular, the SC takes into account (**Figure 1**):

- the location and emission of large stationary sources of CO_2 in Europe, according to data provided by the EDGAR Database (JRC, 2016) and reported in d'Amore and Bezzo (2017);
- the spatially-explicit features of the European territory, discretized through a grid $g = \{1,..., 134\}$ of cells as retrieved from d'Amore et al. (2018);
- the techno-economic description through set $k = \{post_{coal}^{comb}, post_{gas}^{comb}, oxy_{coal}^{fuel}, pre^{comb}\}$ of carbon capture options, that include post-combustion from coal-fired power plants, post-combustion from gas-fired power plants, pre-combustion from gas-fired power plants, and oxy-fuel combustion (d'Amore and Bezzo, 2017);
- the implementation of techno-economic parameters through set $l = \{pipeline, ship\}$ of transport modes, that include both pipelines (onshore and offshore) and ships; transported flowrates are discretized through a set $p = \{1,..., 7\}$ which ranges from 1 to 30 Mt/year (d'Amore and Bezzo, 2017).
- the location of onshore and offshore basins $s = \{saline\ aquifer, gas\ field, coal\ field\}$ that are able to efficiently trap the CO_2 for long term geological sequestration, according to data provided by the EU GeoCapacity Project (2009) and mapped in d'Amore et al. (2019);
- the techno-economic features of the CO_2 utilization stage through set ψ of chemical outputs, which will be described subsequently.

Overall, this European CCUS model is capable of providing:

- the selection, location, scale, and cost of capture nodes;
- the definition, scale, and cost of the transport infrastructure between geographic nodes;
- the location, scale, and cost of geological sequestration nodes;
- the selection, location, scale, and profit of chemical conversion nodes;

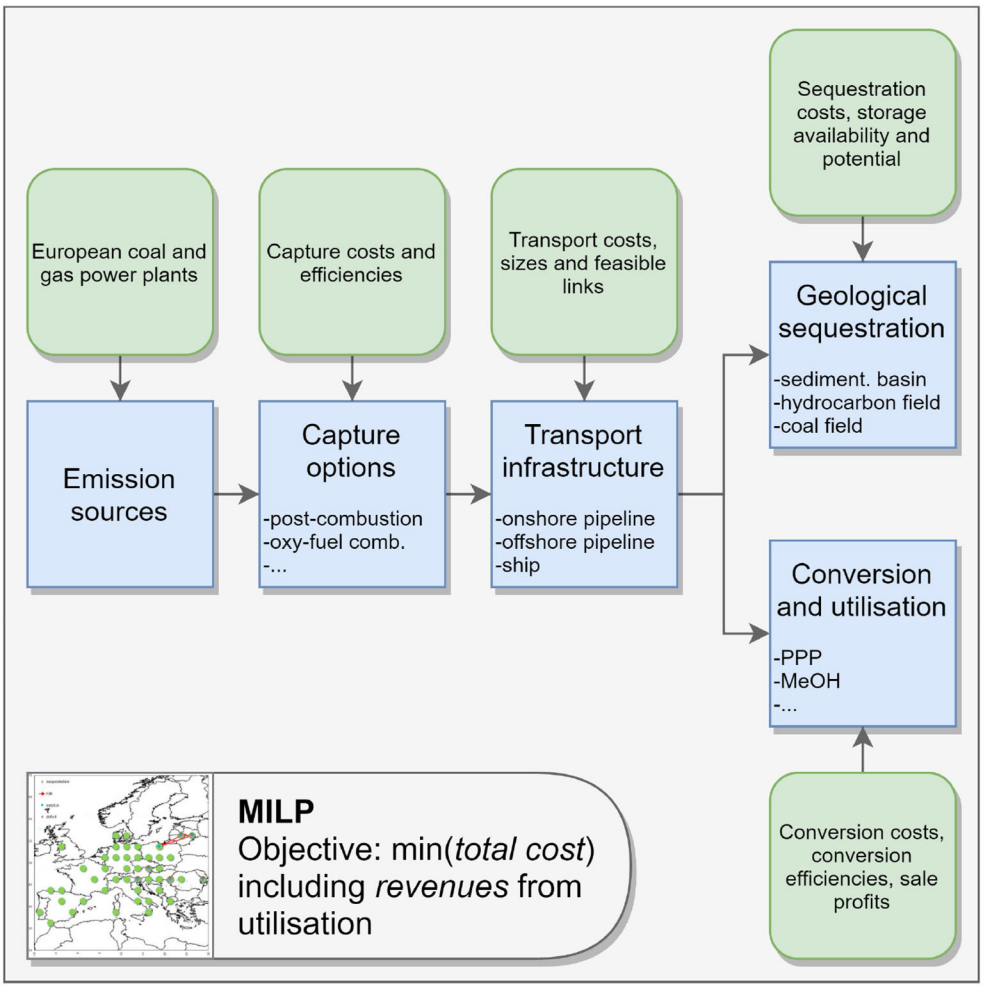

FIGURE 1 | Overview of the proposed framework for the CCUS SC optimization.

- the final CCUS SC configuration according to the chosen European carbon reduction target;
- the differences in SC behavior according to the rates of chemical production;
- the differences in SC behavior according to national regulations on onshore storage.

This study, given the high number of potential reaction mechanisms for CO_2 conversion (Aresta et al., 2013), proposes a screening of the processes according to the following principles:

- (*i*) *minimum production threshold*: a conversion path is taken into account only if the European demand for the chemical output is a relevant one; the reason for this relies on the large flowrates of CO_2 (i.e., $\geq$ 1 Mt/year) deriving from stationary sources and consequently on the necessity of exploiting these carbon streams at scale for producing chemicals. Therefore, this model assumes that at least 1 Mt/year of CO_2 should be converted in order to satisfy the market demand;
- (*ii*) *techno-economic data availability*: the maturity of the technology should be at least such that basic technical (productivity) and economic (production cost) information is available. This means that the current state of research and/or industrial application must be capable of providing complete techno-economic information on the specific conversion process;
- (*iii*) *environmentally promising*: the conversion process must produce in general less CO_2 than that employed to feed it, thus, the process CO_2 net balance should be negative (i.e., CO_2 emissions are lower than CO_2 consumption); regarding energy requirements, as detailed in the next sections, a first scenario will optimistically assume to exploit only low carbon emission sources (e.g., renewable energy, nuclear energy) to generate the additional electricity required to operate the conversion processes, while a subsequent analysis will take into account the different carbon intensities which are countrywide specific and depend on the local energy mix;

- (*iv*) *economically promising*: in order to be sustainable from an economic standpoint, the conversion process should be capable of providing a profit from the sale of the chemical output.

As a result, after excluding those products from the CCUS framework, whose processes do not meet the requirements listed above according to information found in the scientific literature (**Table 2**), two chemical products, i.e., polyether carbonate polyols (PPP) and methanol (MeOH), were selected and included as options for CO_2 utilization in set $\psi = \{PPP, MeOH\}$. Regarding the compliance with both the minimum production threshold and the availability of techno-economic data, PPP are bulk chemicals generally employed in the production of polyurethanes and are one of the most commonly produced polymers, with a yearly world production of 9.4 Mt, of which 2.4 Mt is produced just in Europe (Covestro, 2017), whereas MeOH is one of the most versatile and produced chemicals, with a world plant capacity of 125 Mt/year and a European demand of 12 Mt/year (IHS, 2017). When studying the compliance with the environmental requirements, the chemical conversion of CO_2 into PPP (with 20% weight of CO_2) generates 2.65–2.86 kg CO_2-eq per kg of product, leading to a GHG emission reduction of about 11% with respect to traditional production technologies (von der Assen and Bardow, 2014). Similarly, the conversion of CO_2 into MeOH allows saving about 1.2 kg of CO_2 per kg of MeOH with respect to its traditional production through steam reforming of natural gas (Roh et al., 2016). According to the literature, the two selected processes for CO_2 chemical conversion are also promising from an economic standpoint. Regarding the conversion of CO_2 into PPP, this process can be specifically designed to generate profits (Fernández-Dacosta et al., 2017), while concerning the production of MeOH, several options have been demonstrated to be economically feasible (e.g., Mondal et al., 2016; Pérez-Fortes et al., 2016; Rivera-Tinoco et al., 2016; Bellotti et al., 2017). It should be noted that the conversion into dimethylcarbonate (DMC), despite looking attractive from both an environmental and an economic point of view (**Table 1**), does not comply with the minimum production threshold that is imposed here (Covestro, 2017).

TABLE 2 | List of chemicals that can be produced from CO_2 and their effective compliance with the design requirements: (i) minimum production threshold, (ii) techno-economic data availability, (iii) environmentally promising, and (iv) economically promising.

		Compliances			
Chemical	**References**	**(i)**	**(ii)**	**(iii)**	**(iv)**
Urea	Heffer and Prud'homme (2016)	V	V	X	V
Polyurethanes	Covestro (2017)	V	V	–	–
Mineral carbonates	Aresta et al. (2013)	V	V	V	X
Syngas	Cairns (2016)	X	V	–	–
MeOH	IHS (2017)	V	V	V	V
Formaldehyde	MC Group (2017)	V	X	–	–
Formic Acid	Aresta et al. (2013)	X	V	V	X
Ethylene	Statista (2013)	X	X	–	–
Ethylene glycol	Aresta et al. (2013)	X	X	–	–
Acetic acid	Aresta et al. (2013)	X	V	–	–
Acrylic acid	Aresta et al. (2013)	X	X	–	–
DMC	Aresta et al. (2013)	X	V	V	V
Salicylic acid	Aresta et al. (2013)	V	X	–	–
Polyoxymethylene	PIE (2016)	X	X	–	–
Polycarbonate	Covestro (2017)	X	X	–	–
Kerosene	CNN (2014)	X	V	V	X
Biodiesel	Lam et al. (2012)	X	V	V	X
Dimethoxyethane	Methanol Institute (2016)	V	X	–	–
Methyl tert-butyl ether	Argus De Witt (2015)	V	X	–	–
PPP	Aresta et al. (2013)	V	V	V	V

Only PPP and MeOH meet all the requirements.

3. MATHEMATICAL FORMULATION

The objective is to minimize the total cost *TC* [€] to install and operate the entire European CCUS network, including the expenditures related to capture facilities *TCC* [€], transport infrastructure *TTC* [€], and injection of the CO_2 into geological basins *TSC* [€], and also considers the *profit* [€] from the utilization stage:

$$\begin{cases} objective = min(TC) \\ TC = TCC + TTC + TSC - profit \\ s.t. \\ capture\ problem\ model \\ transport\ problem\ model \\ sequestration\ problem\ model \\ utilization\ problem\ model \end{cases} \quad (1)$$

The *capture problem model* entails a set of equations needed to set the optimal captured amounts of CO_2 in regions *g* through the most appropriate capture technologies *k*, to calculate the value of capture costs *TCC*. The *transport problem model* defines the mass balances among regions *g* and *g*′, to determine the optimal size and routing of the CO_2 flowrates through the different transport means *l*, in order to evaluate transport costs *TTC*. The *sequestration problem model* describes the optimal positioning of properly sized injection wells in regions *g*, to determine costs for storage *TSC*. These SC echelons are defined on the basis of techno-economic characteristics of capture options *k*, transport modes *l*, and sequestration wells, which are all extensively described in d'Amore and Bezzo (2017). In particular, the *capture problem model*, the *transport problem model*, and the *sequestration problem model* have already been discussed in d'Amore and Bezzo (2017) and d'Amore et al. (2018), and their main characteristics are briefly summarized in the **Supplementary Material**. On the other hand, to highlight the key challenge of this contribution, the *utilization problem model* will be entirely described below, on the basis of the conversion processes modeled for producing either PPP (**Figure 2A**) or MeOH (**Figure 2B**).

The total *profit* of Equation (1) obtained from the conversion of CO_2 is calculated according to the cash flow $CF_{\psi,g}$ [€] that can be generated by the production and sale of chemical ψ in

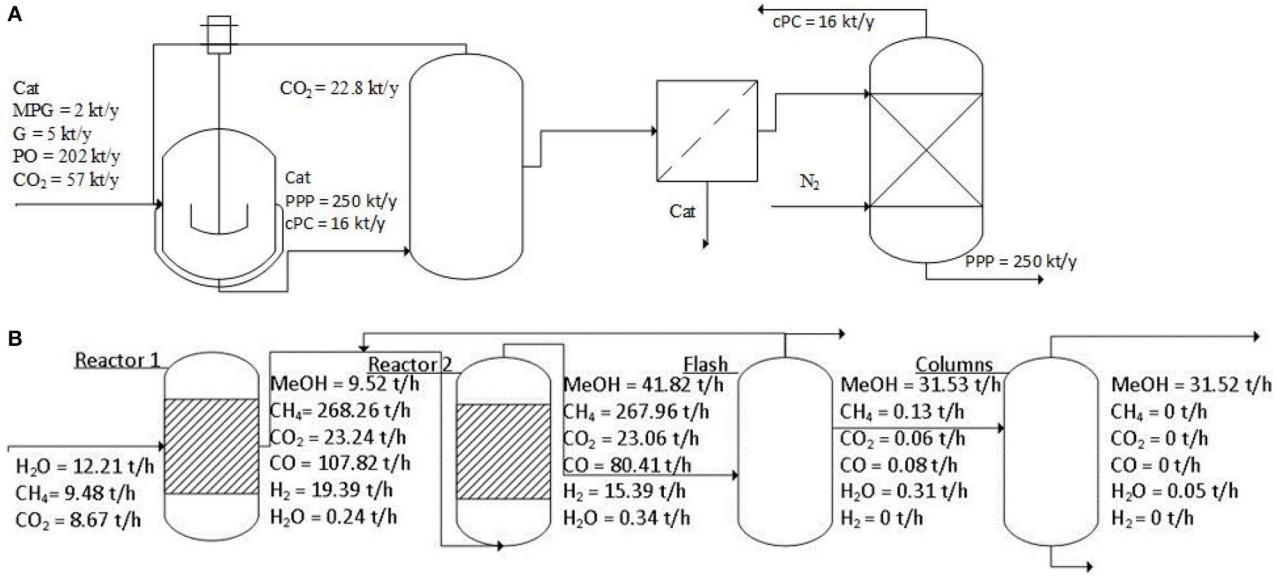

FIGURE 2 | Principal flowrates and conversion schemes for producing: **(A)** PPP (Fernández-Dacosta et al., 2017), or **(B)** MeOH (Wiesberg et al., 2016).

region g:

$$profit = \sum_{\psi,g} CF_{\psi,g} \tag{2}$$

In particular, $CF_{\psi,g}$ of Equation (2) is defined as:

$$CF_{\psi,g} = (R_{\psi,g} + COM_{\psi,g}) \cdot (1 - tax_g) + d_{\psi,g} \qquad \forall \psi, g \tag{3}$$

The revenue $R_{\psi,g}$ [€] is calculated assuming the sale of both the main product and by-products derived from the production of chemical ψ in region g, whereas $COM_{\psi,g}$ [€] represents the manufacturing cost of chemical ψ in region g. Furthermore, tax_g [%] (**Supplementary Table 1** reported in the **Supplementary Material**) is a country-based parameter that describes the corporate tax rates in each region g, while $d_{\psi,g}$ [€] accounts for the depreciation of chemical ψ in region g.

As regards the revenue $R_{\psi,g}$ of Equation (3) of chemical ψ in region g, it is given by:

$$R_{\psi,g} = \widehat{R}_{\psi,g} \cdot U^{chem}_{\psi,g} \qquad \forall \psi, g \tag{4}$$

where $U^{chem}_{\psi,g}$ [t] is the amount of chemical ψ that is produced in region g as a result of the model solution, whereas $\widehat{R}_{\psi,g}$ [€/t] is a parameter representing the unitary revenues that can be earned from chemical ψ in region g. In particular, $\widehat{R}_{\psi,g}$ of Equation (4) is calculated according to the unitary price $P_{\zeta,g}$ [€/t] set on output products ζ in region g, and to the mass flowrates $\dot{m}_{\zeta,\psi}$ [t/year] of output commodities ζ that are generated along with chemical ψ:

$$\widehat{R}_{\psi,g} = \sum_{\zeta} \frac{P_{\zeta,g} \cdot \dot{m}_{\zeta,\psi}}{U^{ref}_{\psi}} \qquad \forall \psi, g \tag{5}$$

The parameter U^{ref}_{ψ} [set equal to 250 kt/year], representing the reference plant output capacity, the output flowrates $\dot{m}_{\zeta,\psi}$, and the unitary prices $P_{\zeta,\psi}$ set for the production, are retrieved from Souza et al. (2014), Wiesberg et al. (2016), and Fernández-Dacosta et al. (2017), and finally differentiated among the European countries c according to the different costs of natural gas and electricity (**Supplementary Table 1** reported in the **Supplementary Material**).

The manufacturing cost $COM_{\psi,g}$ of Equation (3) is calculated according to the formulation proposed by Turton et al. (2015):

$$COM_{\psi,g} = U^{chem}_{\psi,g} \cdot [A^{\psi} \cdot (raw_{\psi,g} + util_{\psi,g})] + B^{\psi} \cdot FCI_{\psi,g} + C^{\psi} \cdot lab_{\psi,g} \cdot \delta^{chem}_{\psi,g} \qquad \forall \psi, g \tag{6}$$

Accordingly, the manufacturing cost depends on the amount of chemical $U^{chem}_{\psi,g}$ of Equation (6), which is multiplied by a scalar $A^{\psi} = 1.23$, that conversely weights the sum of $raw_{\psi,g}$ [€/t] (**Supplementary Table 2** reported in the **Supplementary Material**) and $util_{\psi,g}$ [€/t] (**Supplementary Table 3** reported in the **Supplementary Material**), these representing the unitary costs of raw materials and utilities for chemical ψ in region g, respectively. Furthermore, $COM_{\psi,g}$ also depends on the fixed capital investment $FCI_{\psi,g}$ [€] for producing chemical ψ in region g (weighted by $B^{\psi} = 0.28$) and on the labor cost $lab_{\psi,g}$ [€/t] (the latter, reported in **Supplementary Table 1**, is weighted by $C^{\psi} = 2.73$). The binary variable $\delta^{chem}_{\psi,g}$ determines whether the productivity $U^{chem}_{\psi,g}$ of chemical ψ in region g falls to a null value, and in that case the contribution of labor costs is also consequently nullified. In fact, $\delta^{chem}_{\psi,g}$ is a decision variable determining whether there is production of chemical ψ in region g, or not, according to the productivity upper bound $U^{max}_{\psi,g}$ [t

of chemical] (retrieved from IHS, 2017 and Covestro, 2017) of chemical ψ in region g:

$$U^{chem}_{\psi,g} \leq \delta^{chem}_{\psi,g} \cdot U^{max}_{\psi,g} \qquad \forall \psi, g \tag{7}$$

Regarding the term $FCI_{\psi,g}$ of Equation (6), it has been evaluated following the non-linear formulation provided by Sinnot and Towler (2009). Then, given the MILP mathematical architecture of this optimization problem, that formulation has been linearized and eventually the following equation has been implemented to calculate $FCI_{\psi,g}$, given a non-null amount $U^{chem}_{\psi,g}$ of chemical ψ in region g, and according to the binary decision variable $\delta^{chem}_{\psi,g}$:

$$FCI_{\psi,g} = U^{chem}_{\psi,g} \cdot FCI^{slope}_{\psi} + \delta^{chem}_{\psi,g} \cdot FCI^{intercept}_{\psi} \qquad \forall \psi, g \tag{8}$$

where FCI^{slope}_{ψ} [€/t of chemical] and $FCI^{intercept}_{\psi}$ [€] (**Table 3**) are respectively the arrays of slope and the intercept coefficients of the linearized facility capital costs for producing each chemical ψ, and are calculated from the results provided by Aasberg-Petersen et al. (2008).

Having defined $FCI_{\psi,g}$ through Equation (8), it is then possible to evaluate the depreciation $d_{\psi,g}$ of Equation (3) of chemical ψ in region g as a fixed percentage (set equal to 10% according to d'Amore and Bezzo, 2016) over facility capital cost:

$$d_{\psi,g} = 0.1 \cdot FCI_{\psi,g} \qquad \forall \psi, g \tag{9}$$

As seen before in Equations (4), (6), $U^{chem}_{\psi,g}$ represents the optimal amount of chemical ψ to be produced in region g according to the model solution.

It is possible to link the chemical output $U^{chem}_{\psi,g}$ with the actual CO_2 exploited for utilization, according to the total quantity of CO_2 sent to the conversion process $U_{\psi,g}$ [t of CO_2] for producing ψ in region g:

$$U_{\psi,g} = U^{conv}_{\psi,g} + U^{lost}_{\psi,g} \qquad \forall \psi, g \tag{10}$$

In particular, $U^{conv}_{\psi,g}$ [t of input CO_2 to the conversion stage] represents the actual quantity of CO_2 that is exploited for conversion and utilization in chemical ψ in region g, while $U^{lost}_{\psi,g}$ [t of emitted CO_2 from the conversion stage] takes into account the direct CO_2 emissions generated by the process when producing chemical ψ in region g:

$$U^{conv}_{\psi,g} = \eta^{R}_{\psi} \cdot U^{chem}_{\psi,g} \qquad \forall \psi, g \tag{11}$$

$$U^{lost}_{\psi,g} = (1 - \eta^{C}_{\psi}) \cdot U_{\psi,g} \qquad \forall \psi, g \tag{12}$$

The parameter η^{R}_{ψ} [t of input CO_2 to the conversion stage/t of chemical ψ] (**Table 3**) of Equation (11) represents the amount of CO_2 that is needed to produce a unitary amount of chemical ψ. Conversely, the parameter η^{C}_{ψ} [t of captured CO_2/t of input CO_2 to the conversion stage] (**Table 3**) of Equation (12) is introduced to take into account the CO_2 conversion efficiency of the process that generates chemical ψ (Sakakura and Kohno, 2009; Langanke et al., 2014; Roh et al., 2016; Barbera et al., 2020). Given the actually converted CO_2 quantity $U^{conv}_{\psi,g}$, it is also possible to evaluate the indirect CO_2 emissions U^{ind}_{g} [t of indirect CO_2 from conversion processes]:

$$U^{ind}_{g} = \sum_{\psi} (CI_g \cdot EEC_{\psi} \cdot U^{conv}_{c,g}) \qquad \forall g \tag{13}$$

where CI_g [t of indirect CO_2/GJ] is the carbon intensity for electricity generation in region g (**Supplementary Table 4** reported in the **Supplementary Material**) (EEA, 2019; ElectricityMap, 2019; IEA, 2019), whereas EEC_{ψ} [GJ/t of input CO_2] (**Table 3**) is the specific electric energy consumption for producing chemical ψ (Fernández-Dacosta et al., 2017; Barbera et al., 2020). Note that in case of exploiting only low carbon energy sources (e.g., renewables, nuclear energy) it will be here assumed that $CI_g = 0$ thus, the contribution of indirect CO_2 emissions generated from conversion processes is completely neglected.

Finally, the total amount of CO_2 converted into chemicals (i.e., $U^{conv}_{\psi,g}$) is constrained to be larger than that generated by both direct (i.e., $U^{lost}_{\psi,g}$) and indirect (i.e., U^{ind}_{g}) emissions produced by the utilization stage:

$$\sum_{\psi,g} U^{conv}_{\psi,g} \geq \sum_{\psi,g} U^{lost}_{\psi,g} + \sum_{g} U^{ind}_{g} \tag{14}$$

TABLE 3 | Arrays of slopes FCI^{slope}_{ψ} [€/t of chemical] and intercepts $FCI^{intercept}_{\psi}$ [€] coefficients for the calculation of the facility capital costs of producing chemical ψ (Aasberg-Petersen et al., 2008).

	FCI_{ψ}				
	Slope [€/t]	**Intercept [M€]**	η^{R}_{ψ} **[t/t]**	η^{C}_{ψ} **[t/t]**	EEC_{ψ} **[GJ/t]**
PPP	33.96	20.97	0.228	0.6500	0.3754
MeOH	79.79	229.02	1.370	0.9385	29.4000

Carbon quantity η^{R}_{ψ} [t of input CO_2 to the conversion stage/t of chemical ψ] that is reacted and converted to generate chemical ψ, carbon conversion efficiency η^{C}_{ψ} [t of captured CO_2/t of input CO_2 to the conversion stage] in producing chemical ψ, and electric energy consumption EEC_{ψ} [GJ/t of input CO_2 to the conversion stage] for producing chemical ψ (Sakakura and Kohno, 2009; Langanke et al., 2014; Roh et al., 2016; Barbera et al., 2020).

3.1. Scenarios

The time-static CCUS model was optimized using the GAMS CPLEX solver for MILP problems on a 32 GB RAM computer in about 2 h (an optimality gap always lower than 0.5% was reached). Results from the optimal CCS network (hence, without utilization stage) are reported as a matter of comparison (Scenario 0). The CCUS network is here optimized according to the selection of a minimum European reduction target $\alpha = 50\%$ of overall European CO_2 emissions from large stationary sources, therefore consistent with the recent directives (EC,

TABLE 4 | Main assumptions and results for Scenario 0, Scenario A, Scenario B, and Scenario C.

Scenario	Model	E. source		Demand	*TC*	*TCC*	*TTC*	*TSC*	*profit*
		ren.	mix		[€/t]	[€/t]	[€/t]	[€/t]	(€/t)
0	CCS	–	–	–	32.59	30.69	1.64	0.25	–
A_{D1}	CCUS	V		1×	31.16	30.77	1.57	0.25	1.44
A_{D2}	CCUS	V		2×	29.78	30.80	1.61	0.24	2.87
A_{D3}	CCUS	V		3×	28.46	30.86	1.64	0.23	4.27
B	CCUS	V		1×	32.07	30.78	2.32	0.42	1.44
C	CCUS		V	1×	31.90	30.77	1.64	0.25	0.76

All scenarios aim at reaching a European carbon reduction target $\alpha = 50\%$. Results are summarized in terms of total cost TC, total capture cost TCC, total transport cost TTC, total sequestration cost TSC, and profit. Intensive values (i.e., [€/t]) refer to the overall sequestered and converted quantity of CO_2.

TABLE 5 | Main assumptions and results for Scenario 0, Scenario A, Scenario B, and Scenario C.

Scenario	Model	E. source		Demand	U^{seq}	U^{conv}	U^{lost}	U^{ind}_{mix}
		ren.	mix		[Mt/year]	[Mt/year]	[Mt/year]	[Mt/year]
0	CCS	–	–	–	698.57	0.00	0.00	0.00
A_{D1}	CCUS	V		1×	681.59	16.99	1.37	64.39
A_{D2}	CCUS	V		2×	664.60	33.97	2.74	128.72
A_{D3}	CCUS	V		3×	647.61	50.96	4.11	193.06
B	CCUS	V		1×	681.59	16.99	1.37	64.39
C	CCUS		V	1×	681.59	16.99	1.37	15.62

All scenarios aim at reaching a European carbon reduction target $\alpha = 50\%$. Results are summarized in terms of yearly sequestered CO_2 U^{seq} [Mt/year] yearly converted CO_2 U^{conv} [Mt/year], yearly direct CO_2 emissions due to conversion processes U^{lost} [Mt/year], and yearly indirect CO_2 emissions due to conversion processes (if local energy mixes were/are considered) U^{ind}_{mix} [Mt/year].

2017). Three scenarios have been investigated here (**Table 4**). In Scenario A_{D1} it is assumed that the production of PPP and MeOH cannot be higher than the current European production and that all the electricity needed to perform the conversion and utilization processes comes from zero-carbon energy sources, thus, indirect CO_2 emissions are neglected from the carbon balance and consequently, the constraint imposed through Equation (14) is excluded from the model optimization. Then, Scenario A is also tested on hypothetical higher demands of the two chemicals, i.e., Scenario A_{D2} and Scenario A_{D3} considering demands that are two and three times, respectively, higher than the current one. A case-study subsequently described, still assuming that no contribution from indirect emissions is accounted for, investigated the fact that some European countries do not allow onshore CO_2 sequestration (Scenario B). Finally, Scenario C analyzes the response of the model to the nation-wide characteristics in terms of electricity carbon intensity to determine the optimal CCUS SC while limiting the generation of indirect emissions from conversion and utilization processes therefore, the constraint set by the aim of Equation (14) is included within the model optimization.

4. RESULTS

4.1. Scenarios A

Scenario A_{D1} entails a total cost *TC* for installing and operating the CCUS SC that is 4.4% lower than that obtained for Scenario 0 (**Table 4**). This is due to the fact that the introduction of chemical conversion brings in some revenues (the profit in Scenario A_{D1} is equal to 1.44 €/t). In particular, the possibility of chemical conversion of CO_2 entails an almost identical capture cost *TCC*, which slightly increases from 30.69 €/t (Scenario 0) to 30.77 €/t (Scenario A_{D1}). On the other hand, Scenario A_{D1} exhibits a nearly unchanged transport infrastructure with respect to Scenario 0, despite the necessity of transporting not only the CO_2 that is destined to sequestration, but also the CO_2 fed to the conversion plants (the latter quantity is so small that does not affect the overall structure of the transport network). This result is not surprising if we consider that the same total quantity of CO_2 is imposed to be captured from stationary sources in all scenarios, and therefore the same total flowrate must be shipped between the nodes (independently of the choice of either sequestration or utilization). As a result, the total transport cost *TTC* just slightly varies from 1.64 €/t (Scenario 0) to 1.57 €/t (Scenario A_{D1}). The exploitation of geological storage slightly diminishes with respect to Scenario 0 (i.e., −2.43%) (**Table 5**). Total sequestration costs *TSC* are unchanged between Scenario 0 and Scenario A_{D1} (0.25 €/t). The net impact of utilization amounts to 2.43% of the overall captured CO_2 therefore, the result is comparable with the 1% upper bound for chemical conversion estimated by Mac Dowell et al. (2017).

Scenario A_{D2} and Scenario A_{D3} focus on investigating how the cost of a CO_2 SC would vary if the production of chemicals was increased progressively from the current European values (i.e., with respect to Scenario A_{D1}) to three times that (**Tables 4**, **5**). Accordingly, tripling the production of both chemicals corresponds to an increase of the European production quota from 25.5%^{PPP} and 9.6%^{MeOH} (Scenario A_{D1}) to 76.6%^{PPP} and 28.8%^{MeOH} (Scenario A_{D3}) of actual world capacity. Under these assumptions, the results from the optimal CCUS configuration show that overproduction of the two chemicals mainly affects the total cost of the SC, which could be reduced by about 12.67% in case the production of both chemicals was tripled with respect to current values. On the other hand, the contribution of CO_2 utilization over capture would go from 2.43% (Scenario A_{D1}) to a maximum of about 7.29% (Scenario A_{D3}) (**Figure 3A**). This means that, in order to completely avoid the necessity of CO_2 sequestration, a massive increase to over 38 times the current European production of PPP and MeOH would be required. In terms of GHGs savings, Scenario A_{D3} would allow a net CO_2 yearly decrease due to utilization equal to 50.96 Mt/year, against just 16.99 Mt/year for Scenario A_{D1} (**Figure 3B**).

The final SC configuration is reported in **Figure 4** for both Scenario 0 (**Figure 4A**) and Scenario A_{D1} (**Figure 4B**). Note that

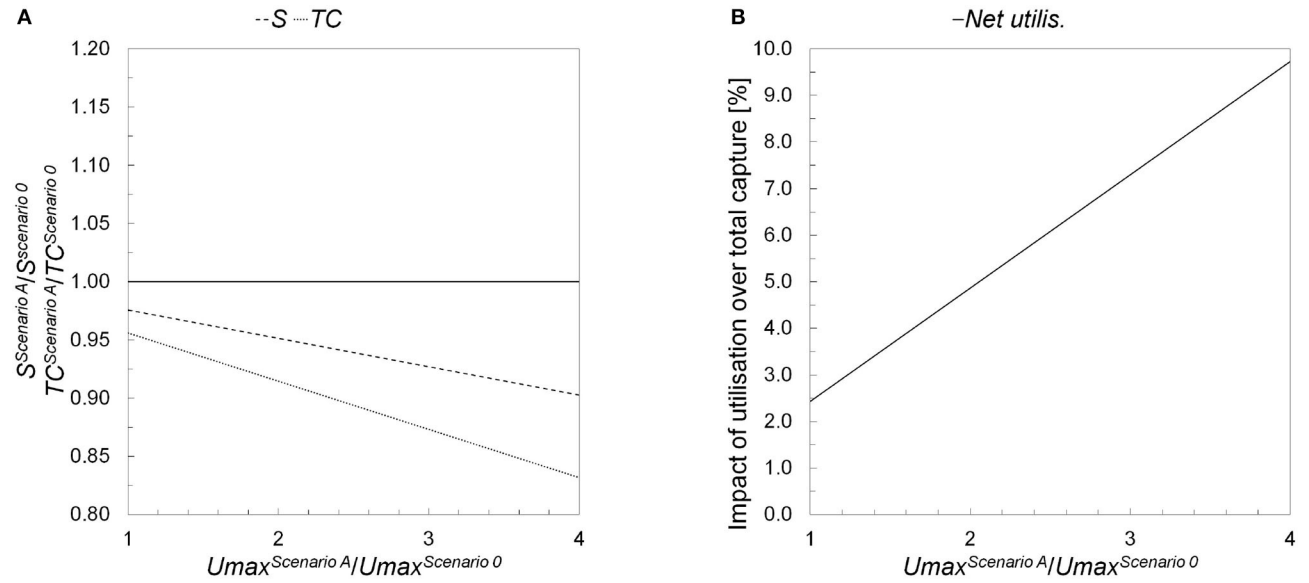

FIGURE 3 | Comparison between Scenario 0 and Scenario A in terms of: **(A)** relative variations in total cost (*TC*) and exploitation of geological sequestration (*S*); and **(B)** effective net CO_2 utilization (Net utilis.), with respect to the change in the productions of the chemical being considered (U^{max}).

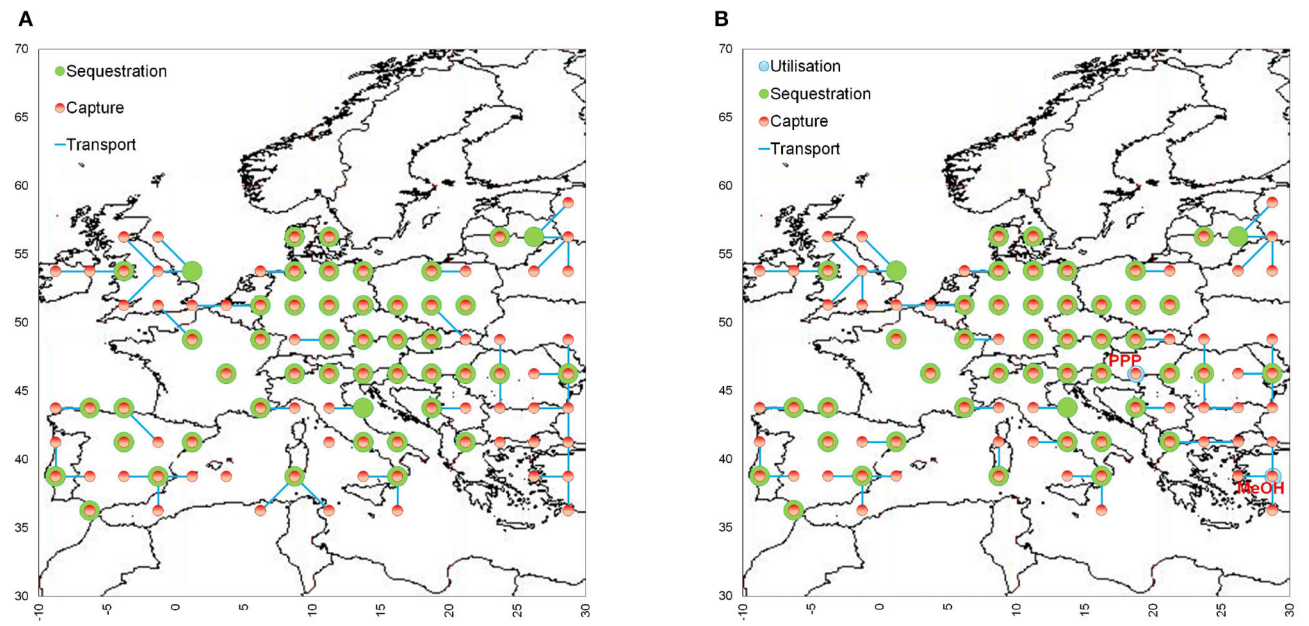

FIGURE 4 | Final SC configurations for **(A)** Scenario 0 and **(B)** Scenario A_{D1}.

for the cases of Scenario A_{D2-D3} the SC design is unchanged with respect to Scenario A_{D1}, since varying the demands of the two chemicals only determines the installation of larger conversion facilities, while their location and infrastructure is not affected. **Figure 4** highlights that the resulting networks are almost identical between Scenario 0 and Scenario A_{D1}. Capture nodes do not change and, consequently, the main driver in establishing the transportation arcs is the location of the sequestration sites. Regarding the utilization stage, the conversion facilities are located in regions allowing for a reduction of production costs, i.e., Hungary (PPP) and Turkey (MeOH). In fact, it was verified that the key parameters affecting the selection of the plant sites are corporate tax rate, cost of materials, and energy price. Regarding corporate tax rates, there is a large variability across Europe (**Supplementary Table 1** reported in the **Supplementary Material**), from a minimum

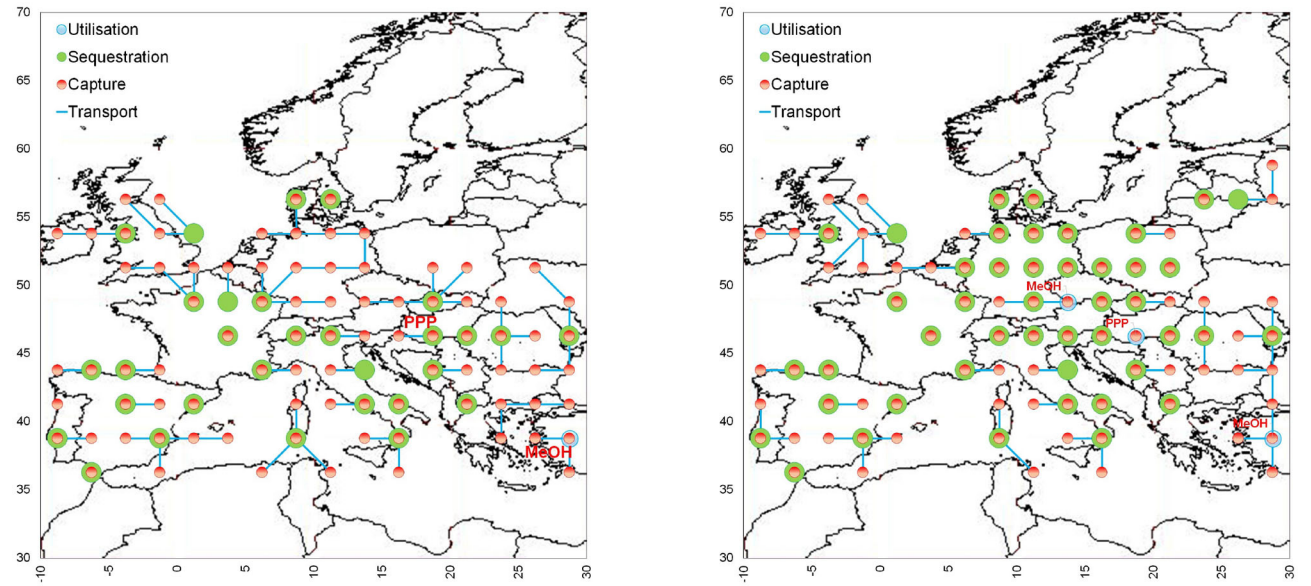

FIGURE 5 | Final SC configurations for **(A)** Scenario B and **(B)** Scenario C.

of 9% (Hungary) up to a maximum of 34% (Belgium). The corporate tax rate of Macedonia is just slightly higher than that of Hungary, while the one of Turkey is close to the European mean (i.e., 20%). As a consequence, the construction of plants in Hungary is mainly justified by their competitiveness in corporate tax rates. On the other hand, Turkey is characterized by low costs of raw materials (**Supplementary Table 2** reported in the **Supplementary Material**) and utilities (**Supplementary Table 3** reported in the **Supplementary Material**). In particular, Turkey has the cheapest electricity price among the analyzed countries (0.0187 €/kWh) (**Supplementary Table 1** reported in the **Supplementary Material**). Accordingly, the presence of a plant for producing MeOH in Turkey is quite justifiable despite the high energy intensity required by its production process. Summarizing, the location of plants for CO_2 conversion into PPP is mainly driven by low taxation, since this process is less energy intensive. Conversely, regarding the production of MeOH, its optimal positioning is mainly determined by the cost of raw materials and utilities (and, in particular, of electricity). Labor costs do not seem to have a relevant impact for choosing the locations of CO_2 conversion facilities.

4.2. Scenario B

Scenario B considers the fact that some countries restrict (Czech Republic, Germany, Poland, Sweden, the Netherlands, and the United Kingdom) or forbid (Austria, Croatia, Estonia, Ireland, Latvia, Finland, and Belgium) onshore sequestration (EC, 2017). Even though the United Kingdom, Poland, and the Netherlands are in the process of authorizing it (EC, 2017), Scenario B prudently optimizes the CCUS SC while excluding all the aforementioned states from those in which onshore storage is allowed. Results show that the total cost *TC* does not change significantly (about 3% more expensive with respect to Scenario A_{D1}), while capture costs *TCC* and *profit* are also unchanged between the two analyzed case studies (**Table 4**). On the other hand, analogously to that observed in d'Amore and Bezzo (2017) for CCS SCs, the optimal CCUS network entails a more complex and expensive transport infrastructure (+48% in terms of *TTC*) and sequestration stage (+68% in terms of *TSC*). These additional expenditures are a consequence of the necessity of routing CO_2 flowrates toward those sequestration basins that are still available once countrywide legal frameworks are taken into account (**Figure 4A**). Regarding the CO_2 exploited for conversion and utilization purposes, the restrictive legal framework for onshore storage produces the same identical results obtained in Scenario A_{D1}.

4.3. Scenario C

The previously discussed scenarios A-B investigated the design of optimal European CCUS SCs while neglecting the indirect CO_2 emissions that may be generated by the energy requirements of conversion processes. As shown in **Table 5**, if these network considered the contribution of the local energy mixes toward indirect emissions from chemicals production, the overall amount of CO_2 generated (directly and indirectly from its conversion) would be higher than that captured. To overcome this simplification, which may lead to unrealistic results, Scenario C optimizes the European CCUS network while taking into account the country-specific electricity carbon intensities. As a result, most of the production of MeOH is now located in Austria, which is a country characterized by a particularly attractive compromise between a low electricity carbon intensity (i.e.,

0.024 t of CO_2/GJ) and production cost parameters (**Figure 5B**). As in Scenario A_{D1}, a residual production of MeOH is still located in Turkey and a PPP plant is installed in Hungary. The drawback of keeping net CO_2 emissions negative lays on the slight increase in total costs *TC* (+2.4% with respect to Scenario A_{D1}), which is due to a drop in total *profit* earned from the sale of chemical outputs (−47.2% with respect to Scenario A_{D1}) (**Table 4**). Overall, Scenario C demonstrates that indirect CO_2 emissions generated from CO_2 conversion processes (i.e., U^{ind}) might play a key role in determining the economics and design of a European CCUS network, but that in general, a satisfactory solution entailing negative CO_2 emissions can be obtained while still generating some profit from both PPP and MeOH. Moreover, the contribution of direct additional CO_2 emissions from utilization (i.e., U^{lost}) was always negligible in all analyzed scenarios.

5. DISCUSSION

Results of the optimization show that for the case study being considered, CO_2 utilization may have a non-negligible economic impact (overall costs decrease by 4.4%); however, as suggested by other studies (e.g., Mac Dowell et al., 2017), its environmental impact is a minor one (in our case study, the contribution amounts to 2.4% reduction in GHGs emissions). Thus, the major benefit of CO_2 utilization seems to be that of a slight reduction in taxpayer costs in establishing a CCS infrastructure.

Having stated that, we need to highlight the limitations, too, of this study. First, the focus was on the very few chemical technologies that are currently demonstrated to be sufficiently mature to provide a reduction in CO_2 emissions, and to guarantee some profitability. Although material balances (Mac Dowell et al., 2017) and thermodynamics (Stevenson, 2019) still limit the potential of the chemical industry in terms of CO_2 utilization, alternative pathways may nonetheless disclose wider and more positive scenarios. For instance the application of CCU technologies in the cement industry could foster the routing toward an "ideally carbon-free" market in which construction materials are generated from the same CO_2 captured within the plant itself or from large stationary sources (US National Academy of Sciences, 2019). Furthermore, this study does not consider the possibility that the unsatisfactory environmental performance of a technology could be balanced by negative emissions in a different location, thanks to some sort of carbon trading mechanisms or cooperative actions. Similarly we did not consider the possibility of favorable local situations (e.g., a conversion facility fed by renewable power plant producing electricity at a cheap price), which could change the economic and/or environmental sustainability of some technologies in some specific cases. The energy sector, too, may provide a huge market for CO_2-derived fuels. As a matter of fact, methanol is currently envisioned for a wide range of applications beyond its current use, e.g., as fuel for transport, in energy sectors, or for the synthesis of hydrocarbons, including several major large-volume chemicals (Pérez-Fortes et al., 2016). Hence, imposing the current production volumes as an upper bound for the calculation of utilization potential may neglect a wide range of additional options. Furthermore, focusing on large stationary sources may neglect the fact that more effective conversion routes could be established at an industrial level, e.g., by integrating conversion technologies within a petrochemical plant. Governmental subsidies, too, may help support some technologies and accelerate the transition toward a CO_2 derived chemical industry. However, the definition of the most suitable mechanisms and their effect on the deployment of alternative technologies is beyond the scope of this work. We need to recognize, though, that currently, many potential routes are just possibilities and that their practical implementation is far from being demonstrated at a large scale (US National Academy of Sciences, 2019): the degree of uncertainty in terms of costs, productivity, GHGs emissions is so high that any modeling and optimization framework may simply result in a speculative exercise with questionable practical benefits. This is why we decided to exclude such routes in the current analysis.

On the other hand, even our "conservative" approach could be alleged by someone to be over-optimistic. In fact, it is assumed that traditional routes for the chemicals being considered would move to alternative technologies based on CO_2 conversion so that all European production would rely on CO_2 as a feedstock. In the current situation, such a scenario does not appear to be very plausible unless significant incentives are introduced or whole world production follows a similar path.

To sum up, even if there are limitations, we believe that the proposed analysis may represent a sound preliminary assessment of current potential of CCUS in Europe, when CO_2 emissions from large stationary sources are taken into account.

6. CONCLUSIONS

This article assessed the potential impact of a European carbon capture, transport, utilization, and storage supply chain. Results suggested that CO_2 utilization can contribute only marginally to achieve the European climate target set for 2030 in terms of emissions reduction. The positive effect is that it can generate some profits and consequently help to decrease costs related to the overall carbon capture and sequestration infrastructure. Moreover, this analysis demonstrated the key role played by national energy mixes (thus, energy carbon intensities) in determining the optimal positioning of conversion plants as a consequence of accounting for both direct and indirect CO_2 emissions from the conversion stage; furthermore, the study was able to show the response in terms of a network design to countrywide legal frameworks on onshore geological storage.

This work sets the basis for future research on the strategic optimization of carbon capture, transport, utilization, and sequestration supply chains at a wide continent-level scale. The proposed methodology is general, since it could be applied to different geographic contexts, and could be

improved by adding more CO_2 conversion and utilization pathways, in order to achieve a more comprehensive modeling framework.

DATA AVAILABILITY STATEMENT

All datasets generated for this study are either included in the article/**Supplementary Material**, or available upon request to the corresponding author.

AUTHOR CONTRIBUTIONS

FB conceived and led this study. Fd'A developed the model formulation and implementation, carried out the analyses, and wrote the paper. Fd'A and FB contributed to the text and edited the paper. All authors contributed to the article and approved the submitted version.

FUNDING

This research was supported by the Department of Industrial Engineering, University of Padova (Grant 2019DII126): Optimising supply chains for carbon capture, transport, utilisation, and sequestration, including emission points from industrial clusters.

ACKNOWLEDGMENTS

The authors would like to thank Mr. Victor Baldo for some preliminary simulation work.

SUPPLEMENTARY MATERIAL

The Supplementary Material for this article can be found online at: https://www.frontiersin.org/articles/10.3389/fenrg.2020.00190/full#supplementary-material

REFERENCES

Aasberg-Petersen, K., Nielsen, C. S., Dybkjær, I., and Perregaard, J. (2008). *Large Scale Methanol Production From Natural Gas*. Haldor Topsoe, 22. Available online at: http://www.topsoe.com/sites/default/files/topsoe_large_scale_methanol_prod_paper.ashx_.pdf (accessed March 29, 2018).

Ağrali, S., Üçtuğ, F. G., and Türkmen, B. A. (2018). An optimization model for carbon capture and storage/utilization vs. carbon trading: a case study of fossil-fired power plants in Turkey. *J. Environ. Manage.* 215, 305–315. doi: 10.1016/j.jenvman.2018.03.054

Alper, E., and Yuksel Orhan, O. (2017). CO_2 utilization: developments in conversion processes. *Petroleum* 3, 109–126. doi: 10.1016/j.petlm.2016.11.003

Aresta, M., Dibenedetto, A., and Angelini, A. (2013). The changing paradigm in CO_2 utilization. *J. CO_2 Util.* 3–4, 65–73. doi: 10.1016/j.jcou.2013.08.001

Argus De Witt, A. (2015). *Argus DeWitt 2015 Fuels and Oxygenates Annual*. Available online at: https://www.argusmedia.com/~/media/files/pdfs/petchems/mtbe-2015-annual-flyer.pdf?la=en (accessed March 29, 2018).

Armstrong, K., and Styring, P. (2015). Assessing the potential of utilization and storage strategies for post-combustion CO_2 emissions reduction. *Front. Energy Res.* 3, 1–9. doi: 10.3389/fenrg.2015.00008

Barbera, E., Mantoan, F., Bertucco, A., and Bezzo, F. (2020). Hydrogenation to convert CO_2 to C1 chemicals: technical comparison of different alternatives by process simulation. *Can. J. Chem. Eng.* 98, 1893–1906. doi: 10.1002/cjce.23755

Bellotti, D., Rivarolo, M., Magistri, L., and Massardo, A. F. (2017). Feasibility study of methanol production plant from hydrogen and captured carbon dioxide. *J. CO_2 Util.* 21, 132–138. doi: 10.1016/j.jcou.2017.07.001

Bui, M., Adjiman, C. S., Bardow, A., Anthony, E. J., Boston, A., Brown, S., et al. (2018). Carbon capture and storage (CCS): the way forward. *Energy Environ. Sci.* 11, 1062–1176. doi: 10.1039/c7ee02342a

Cairns, H. (2016). *Global Trends in Syngas*, Technical report. Stratas Advisors. Available online at: https://stratasadvisors.com/Insights/072216-Global-Sybgas-Trends (accessed September 15, 2020).

CNN (2014). *Desert Plants and Green Diesel: Meet the Jet Fuels of the Future*. Available online at: http://edition.cnn.com/travel/article/boeing-biofuel/index.html (accessed September 15, 2020)

Covestro (2017). *Investor Presentation Technical Report*. Available online at: http://investor.covestro.com/en/presentations/presentations/ (accessed September 15, 2020)

d'Amore, F., and Bezzo, F. (2016). Strategic optimisation of biomass-based energy supply chains for sustainable mobility. *Comput. Chem. Eng.* 87, 68–81. doi: 10.1016/j.compchemeng.2016.01.003

d'Amore, F., and Bezzo, F. (2017). Economic optimisation of European supply chains for CO_2 capture, transport and sequestration. *Int. J. Greenh. Gas Control* 65, 99–116. doi: 10.1016/j.ijggc.2017.08.015

d'Amore, F., and Bezzo, F. (2020). Optimal design of European cooperative supply chains for carbon capture, transport and sequestration with costs share policies. *AIChE J.* 66:e16872. doi: 10.1002/AIC.16872

d'Amore, F., Lovisotto, L., and Bezzo, F. (2020). Introducing social acceptance into the design of CCS supply chains: a case study at a European level. *J. Clean. Prod.* 249:119337. doi: 10.1016/j.jclepro.2019.119337

d'Amore, F., Mocellin, P., Vianello, C., Maschio, G., and Bezzo, F. (2018). Economic optimisation of European supply chains for CO_2 capture, transport and sequestration, including societal risk analysis and risk mitigation measures. *Appl. Energy* 223, 401–415. doi: 10.1016/j.apenergy.2018.04.043

d'Amore, F., Sunny, N., Iruretagoyena, D., Bezzo, F., and Shah, N. (2019). European supply chains for carbon capture, transport and sequestration, with uncertainties in geological storage capacity: insights from economic optimisation. *Comput. Chem. Eng.* 129:106521. doi: 10.1016/j.compchemeng.2019.106521

EC (2017). *Report From the Commission to the European Parliament and the Council on Implementation of Directive 2009/31/EC on the Geological Storage of Carbon Dioxide*. Available online at: https://ec.europa.eu/commission/sites/beta-political/files/report-carbon-capture-storage_en.pdf (accessed September 15, 2020)

EEA (2019). *CO_2 Emission Intensity*. Available online at: https://www.eea.europa.eu/data-and-maps (accessed September 15, 2020)

Elahi, N., Shah, N., Korre, A., and Durucan, S. (2014). Multi-period least cost optimisation model of an integrated carbon dioxide capture transportation and storage infrastructure in the UK. *Energy Procedia* 63, 2655–2662. doi: 10.1016/j.egypro.2014.11.288

Elahi, N., Shah, N., Korre, A., and Durucan, S. (2017). Multi-stage stochastic optimisation of a CO_2 transport and geological storage in the UK. *Energy Procedia* 114, 6514–6525. doi: 10.1016/j.egypro.2017.03.1787

ElectricityMap (2019). *Climate Impact by Area: Ranked by Carbon Intensity of Electricity Consumed*. Available online at: https://www.electricitymap.org/ (accessed September 15, 2020)

EU GeoCapacity Project (2009). *Assessing European Capacity for Geological Storage of Carbon Dioxide*. Available online at: www.geology.cz/geocapacity/publications(accessed September 15, 2020)

Eurostat (2017a). *Energy Price Statistics*. Available online at: http://ec.europa.eu/eurostat/statistics-explained/index.php/Energy_price_statistics(accessed September 15, 2020)

Eurostat (2017b). *Labour Costs Database*. Available online at: http://ec.europa.eu/eurostat/web/labour-market/labour-costs/database (accessed September 15, 2020)

Eurostat (2017c). *Natural Gas Price Statistics*. Available online at: http://ec.europa.eu/eurostat/statistics-explained/index.php/Natural_gas_price_statistics (accessed September 15, 2020)

Fernández-Dacosta, C., Van Der Spek, M., Hung, C. R., Oregionni, G. D., Skagestad, R., Parihar, P., et al. (2017). Prospective techno-economic and environmental assessment of carbon capture at a refinery and CO_2 utilisation in polyol synthesis. *J. CO_2 Util.* 21, 405–422. doi: 10.1016/j.jcou.2017.08.005

Geske, J., Berghout, N., and van den Broek, M. (2015). Cost-effective balance between CO_2 vessel and pipeline transport: part II–design of multimodal CO_2 transport: the case of the West Mediterranean region. *Int. J. Greenh. Gas Control* 33, 122–134. doi: 10.1016/j.ijggc.2014.12.005

Han, J. H., and Lee, I. B. (2012). Multiperiod stochastic optimization model for carbon capture and storage infrastructure under uncertainty in CO_2 emissions, product prices, and operating costs. *Ind. Eng. Chem. Res.* 51, 11445–11457. doi: 10.1021/Ie3004754

Han, J. H., and Lee, I. B. (2013). A comprehensive infrastructure assessment model for carbon capture and storage responding to climate change under uncertainty. *Ind. Eng. Chem. Res.* 52, 3805–3815. doi: 10.1021/ie301451e

Hasan, M. M. F., First, E. L., Boukouvala, F., and Floudas, C. A. (2015). A multi-scale framework for CO_2 capture, utilization, and sequestration: CCUS and CCU. *Comput. Chem. Eng.* 81, 2–21. doi: 10.1016/j.compchemeng.2015.04.034

Heffer, P., and Prud'homme, M. (2016). "Fertilizer outlook 2016–2020," in *84th IFA Annual Conference, Moscow, 30 May–1 June 2016* (Moscow: International Fertilizer Industry Association (IFA)).

IEA (2019). *Data and Statistics: Explore Energy Data by Category, Indicator, Country or Region*. Available online at: https://www.iea.org/data-and-statistics (accessed September 15, 2020)

IHS (2017). *Global Methanol Demand Growth Driven by Methanol to Olefins as Chinese Thirst for Chemical Supply Grows*. IHS Markit Says. Available online at: http://news.ihsmarkit.com/press-release/country-industry-forecasting-media/global-methanol-demand-growth-driven-methanol-olefi (accessed September 15, 2020)

IPCC (2005). *IPCC Special Report on Carbon Dioxide Capture and Storage. Prepared by Working Group III of the Intergovernmental Panel on Climate Change*. Cambridge University Press, 442. Available online at: https://www.ipcc.ch/pdf/special-reports/srccs/srccs_wholereport.pdf (accessed September 15, 2020)

IPCC (2018). *Global Warming of 1.5°C. An IPCC Special Report on the Impacts of Global Warming of 1.5°C Above Pre-industrial Levels and Related Global Greenhouse Gas Emission Pathways, in the Context of Strengthening the Global Response to the Threat of Climate Change*. Available online at: http://report.ipcc.ch/sr15/pdf/sr15_spm_final.pdf (accessed September 15, 2020)

JRC (2016). *Emission Database for Global Atmospheric Research (EDGAR)*. Available online at: edgar.jrc.ec.europa.eu/index.php (accessed September 15, 2020)

Kalyanarengan Ravi, N., Van Sint Annaland, M., Fransoo, J. C., Grievink, J., and Zondervan, E. (2016). Development and implementation of supply chain optimization framework for CO_2 capture and storage in the Netherlands. *Comput. Chem. Eng.* 102, 40–51. doi: 10.1016/j.compchemeng.2016.08.011

Kim, M., Kim, K., Kim, T. H., and Kim, J. (2019). Economic and environmental benefit analysis of a renewable energy supply system integrated with carbon capture and utilization framework. *Chem. Eng. Res. Des.* 147, 200–213. doi: 10.1016/j.cherd.2019.05.008

Klokk, Ø, Schreiner, P. F., Pagès-Bernaus, A., and Tomasgard, A. (2010). Optimizing a CO_2 value chain for the Norwegian continental shelf. *Energy Policy* 38, 6604–6614. doi: 10.1016/j.enpol.2010.06.031

Lam, M. K., Lee, K. T., and Mohamed, A. R. (2012). Current status and challenges on microalgae-based carbon capture. *Int. J. Greenh. Gas Control* 10, 456–469. doi: 10.1016/J.IJGGC.2012.07.010

Langanke, J., Wolf, A., Hofmann, J., Böhm, K., Subhani, M. A., Müller, T. E., et al. (2014). Carbon dioxide (CO_2) as sustainable feedstock for polyurethane production. *Green Chem.* 16, 1865–1870. doi: 10.1039/C3GC41788C

Lee, S. Y., Lee, I. B., and Han, J. (2019). Design under uncertainty of carbon capture, utilization and storage infrastructure considering profit, environmental impact, and risk preference. *Appl. Energy* 238, 34–44. doi: 10.1016/j.apenergy.2019.01.058

Lee, S. Y., Lee, J. U., Lee, I. B., and Han, J. (2017). Design under uncertainty of carbon capture and storage infrastructure considering cost, environmental impact, and preference on risk. *Appl. Energy* 189, 725–738. doi: 10.1016/j.apenergy.2016.12.066

Lehtonen, J., Järnefelt, V., Alakurtti, S., Arasto, A., Hannula, I., Harlin, A., et al. (2019). *The Carbon Reuse Economy: Transforming CO_2 From a Pollutant Into a Resource*. Espoo: VTT Technical Research Centre of Finland.

Leonzio, G., Foscolo, P. U., and Zondervan, E. (2019). An outlook towards 2030: optimization and design of a CCUS supply chain in Germany. *Comput. Chem. Eng.* 125, 499–513. doi: 10.1016/j.compchemeng.2019.04.001

Li, H., Jiang, H. D., Yang, B., and Liao, H. (2019). An analysis of research hotspots and modeling techniques on carbon capture and storage. *Sci. Total Environ.* 687, 687–701. doi: 10.1016/j.scitotenv.2019.06.013

Mac Dowell, N., Fennell, P. S., Shah, N., and Maitland, G. C. (2017). The role of CO_2 capture and utilization in mitigating climate change. *Nat. Clim. Change* 7, 243–249. doi: 10.1038/nclimate3231

MC Group (2017). *World Formaldehyde Production to Exceed 52 Mln Tonnes in 2017*. Available online at: https://mcgroup.co.uk/news/20140627/formaldehyde-production-exceed-52-mln-tonnes.html (accessed September 15, 2020)

Methanol Institute (2016). *DME: An Emerging Global Fuel*, Technical report. Available online at: http://www.methanol.org/wp-content/uploads/2016/06/DME-An-Emerging-Global-Guel-FS.pdf

Middleton, R. S., Keating, G. N., Viswanathan, H. S., Stauffer, P. H., and Pawar, R. J. (2012). Effects of geologic reservoir uncertainty on CO_2 transport and storage infrastructure. *Int. J. Greenh. Gas Control* 8, 132–142. doi: 10.1016/j.ijggc.2012.02.005

Middleton, R. S., and Yaw, S. (2018). The cost of getting CCS wrong: uncertainty, infrastructure design, and stranded CO_2. *Int. J. Greenh. Gas Control* 70, 1–11. doi: 10.1016/j.ijggc.2017.12.011

Mondal, K., Sasmal, S., Badgandi, S., Chowdhury, D. R., and Nair, V. (2016). Dry reforming of methane to syngas: a potential alternative process for value added chemicals–a techno-economic perspective. *Environ. Sci. Pollut. Res.* 23, 22267–22273. doi: 10.1007/s11356-016-6310-4

Nie, Z., Korre, A., Elahi, N., and Durucan, S. (2017). Real options analysis of CO_2 transport and storage in the UK continental shelf under geological and market uncertainties and the viability of subsidies for market development. *Energy Procedia* 114, 6612–6622. doi: 10.1016/j.egypro.2017.03.1815

Pérez-Fortes, M., Schöneberger, J. C., Boulamanti, A., and Tzimas, E. (2016). Methanol synthesis using captured CO_2 as raw material: techno-economic and environmental assessment. *Appl. Energy* 161, 718–732. doi: 10.1016/j.apenergy.2015.07.067

PIE (2016). *POM Technical Report*. Available online at: https://pieweb.plasteurope.com/Default.aspx?pageid=302&node=100212 (accessed September 15, 2020)

Rivera-Tinoco, R., Farran, M., Bouallou, C., Auprêtre, F., Valentin, S., Millet, P., et al. (2016). Investigation of power-to-methanol processes coupling electrolytic hydrogen production and catalytic CO_2 reduction. *Int. J. Hydrogen Energy* 41, 4546–4559. doi: 10.1016/j.ijhydene.2016.01.059

Roh, K., Frauzem, R., Nguyen, T. B. H., Gani, R., and Lee, J. H. (2016). A methodology for the sustainable design and implementation strategy of CO_2 utilization processes. *Comput. Chem. Eng.* 91, 407–421. doi: 10.1016/j.compchemeng.2016.01.019

Sakakura, T., and Kohno, K. (2009). The synthesis of organic carbonates from carbon dioxide. *Chem. Commun.* 11, 1312–1330. doi: 10.1039/b819997c

Sinnot, R., and Towler, G. (2009). *Chemical Engineering Design. 5th Edn* (Oxford: Butterworth-Heinemann).

Smit, B., Park, A. H. A., and Gadikota, G. (2014). The grand challenges in carbon capture, utilization, and storage. *Front. Energy Res.* 2, 2013–2015. doi: 10.3389/fenrg.2014.00055

Souza, L. F. S., Ferreira, P. R. R., Medeiros, J. L. De, Alves, R. M. B., and Arau, Q. F. (2014). Production of DMC from CO_2 via indirect route: technical–economical–environmental assessment and analysis. *ACS Sustain. Chem. Eng.* 2, 62–69. doi: 10.1021/sc400279n

Statista (2013). *Ethylene Production Capacity Worldwide in 2013 by Region*. Available online at: https://www.statista.com/statistics/270007/capacity-of-ethylene-by-region/ (accessed September 15, 2020)

Sternberg, A., Jens, C. M., and Bardow, A. (2017). Life cycle assessment of CO_2-based C1-chemicals. *Green Chem.* 19, 2244–2259. doi: 10.1039/c6gc02852g

Stevenson, S. A. (2019). Thermodynamic considerations in CO_2 utilization. *AIChE J.* 65, 1–15. doi: 10.1002/aic.16695

Turk, G. A., Cobb, T. B., Jankowski, D. J., Wolsky, A. M., and Sparrow, F. T. (1987). CO_2 transport: a new application of the assignment problem. *Energy* 12, 123–130. doi: 10.1016/0360-5442(87)90116-2

Turton, R., Baile, R. C., Whiting, W. B., Shaeiwitz, J. A., and Bhattacharyya, D. (2015). *Analysis, Synthesis, and Design of Chemical Processes. 4th Edn.* Upper Saddle River, NJ: Pearson Education, Inc.

US National Academy of Sciences (2019). *Gaseous Carbon Waste Streams Utilization: Status and Research Needs*. Washington, DC: The National Academies Press.

von der Assen, N., and Bardow, A. (2014). Life cycle assessment of polyols for polyurethane production using CO_2 as feedstock: insights from an industrial case study. *Green Chem.* 16, 3272–3280. doi: 10.1039/C4GC00513A

Wiesberg, I. L., de Medeiros, J. L., Alves, R. M. B., Coutinho, P. L. A., and Araújo, O. Q. F. (2016). Carbon dioxide management by chemical conversion to methanol: hydrogenation and bi-reforming. *Energy Convers. Manage.* 125, 320–335. doi: 10.1016/j.enconman.2016.04.041

Wu, Q., Lin, Q. G., Wang, X. Z., and Zhai, M. Y. (2015). An inexact optimization model for planning regional carbon capture, transportation and storage systems under uncertainty. *Int. J. Greenh. Gas Control* 42, 615–628. doi: 10.1016/j.ijggc.2015.09.017

Zhang, S., Liu, L., Zhang, L., Meng, Q., and Du, J. (2018). Optimal planning for regional carbon capture and storage systems under uncertainty. *Chem. Eng. Trans.* 70, 1207–1212. doi: 10.3303/CET1870202

Conflict of Interest: The authors declare that the research was conducted in the absence of any commercial or financial relationships that could be construed as a potential conflict of interest.

GLOSSARY

Acronyms

CCS	Carbon dioxide capture and storage
CCU	Carbon dioxide capture and utilization
CCUS	Carbon dioxide capture, utilization, and storage
DMC	Dimethylcarbonate
EOR	Enhanced oil recovery
EU	European Union
GHG	Greenhouse gas
MeOH	Methanol
MILP	Mixed integer linear programming
PPP	Polyether carbonate polyols
SC	Supply chain

Sets

g	Region, g ={1, 2,..., 133, 134}
k	Capture option, k ={$post^{comb}_{coal}$, $post^{comb}_{gas}$, oxy^{fuel}_{coal}, pre^{comb}}
l	Transport mode, l ={*pipeline*, *ship*}
p	Transport capacity, p ={1, 2,..., 6, 7}
ψ	Chemical output, ψ ={*PPP*, *MeOH*}
s	Basin, s ={*saline aquifer*, *gas field*, *coal field*}

Scalars

A^{ψ}	Scalar A for calculation of manufacturing cost of chemical ψ
B^{ψ}	Scalar B for calculation of manufacturing cost of chemical ψ
C^{ψ}	Scalar C for calculation of manufacturing cost of chemical ψ

Parameters

α	European carbon reduction target [%]
CI_g	Electricity carbon intensity in region g [t/GJ]
EEC_{ψ}	Specific electric energy requirements for producing chemical ψ [GJ/t]
$FCI^{intercept}_{\psi}$	Array of intercept coefficients of the linearized facility capital cost for producing chemical ψ [€]
FCI^{slope}_{ψ}	Array of slope coefficients of the linearized facility capital cost for producing chemical ψ [€/t]
$lab_{\psi,g}$	Labor cost for producing chemical ψ in region g [€/t]
$\dot{m}_{\zeta,\psi}$	Mass flowrate of output ζ for producing chemical ψ [t/year]
η^{C}_{ψ}	Conversion efficiency of the process that generates chemical ψ [t/t]
η^{R}_{ψ}	Amount of CO_2 that is needed to produce a unitary amount of chemical ψ [t/t]
$P_{\zeta,g}$	Unitary price of commodity ζ for producing chemical ψ [€/t]
P^{max}_{g}	Amount of anthropogenic CO_2 that is generated in region g [t of CO_2]
$raw_{\psi,g}$	Unitary cost of raw materials for producing chemical ψ in region g [€/t]
$\widehat{R}_{\psi,g}$	Unitary revenue from chemical ψ in region g [€/t]
tax_g	Taxation in region g
$util_{\psi,g}$	Unitary cost of utilities for producing chemical ψ in region g [€/t]
$U^{max}_{\psi,g}$	Productivity upper bound for chemical ψ in region g [t]
U^{ref}_{ψ}	Reference chemical plant capacity [t/year]

Continuous Variables

$CF_{\psi,g}$	Cash flow from sale of chemical ψ in region g [€]
$COM_{\psi,g}$	Manufacturing cost for chemical ψ in region g [€]
$d_{\psi,g}$	Depreciation of chemical ψ in region g [€]
$FCI_{\psi,g}$	Fixed capital investment for producing chemical ψ in region g [€]
profit	Profit earned from sale of chemicals [€]
$R_{\psi,g}$	Revenue from sale of chemical ψ (and by-products) in region g [€]
S	Geologically sequestered CO_2 [t]
TC	Total cost [€]
TCC	Total capture cost [€]
TSC	Total sequestration cost [€]
TTC	Total transport cost [€]
$U_{\psi,g}$	Quantity of CO_2 sent to conversion process for producing chemical ψ in region g [t]
$U^{chem}_{\psi,g}$	Amount of chemical ψ produced in region g [t]
$U^{conv}_{\psi,g}$	Quantity of CO_2 converted and utilized for producing chemical ψ in region g [t]
U^{conv}	European converted CO_2 [t]
$U^{lost}_{\psi,g}$	Direct CO_2 emissions generated by conversion into chemical ψ in region g [t]
U^{lost}	European direct CO_2 emissions due to conversion facilities [t]
U^{ind}_{g}	Indirect CO_2 emissions generated by conversion processes in region g [t]
U^{ind}	European indirect CO_2 emissions due to conversion facilities [t]
U^{seq}	European sequestered CO_2 [t]

Binary Variables

$\delta^{chem}_{\psi,g}$	1 if chemical ψ is produced in region g, 0 otherwise

frontiers in Energy Research

ORIGINAL RESEARCH
published: 09 October 2020
doi: 10.3389/fenrg.2020.571787

Modeling and Optimization of Rectangular Latent Heat Storage Elements in an Air-Guided Heat Storage System

*Matti Grabo, Christoph Staggenborg, Kai Alexander Philippi and Eugeny Y. Kenig**

Chair of Fluid Process Engineering, Faculty of Mechanical Engineering, Paderborn University, Paderborn, Germany

The thermal performance of macro-encapsulated latent heat storage elements in form of thin, rectangular plates within an air-driven heat storage system is investigated. The plates are made of high-density polyethylene and filled with phase change material. Several plates are stacked together and inserted into a box which can be installed in a heating/air conditioning system. First, an experimental test rig was designed. Measured temperature and pressure drop data retrieved from the rig was then used to validate a simplified computational fluid dynamics model describing a section of the test set-up including a stack of ten plates. Afterward, the model was reduced in complexity in order to perform a parametric study by varying geometric parameters of the storage plates. In total, 217 different geometries were simulated and their thermo-hydraulic efficiency was evaluated. As a result, geometries were proposed, which can potentially increase the thermo-hydraulic efficiency of the storage plates by over 50%.

Keywords: heat transfer, latent heat, heat storage, computational fluid dynamics, phase change material

OPEN ACCESS

Edited by:
Theodoros Damartzis, École Polytechnique Fédérale de Lausanne, Switzerland

Reviewed by:
Gerhard Schmitz, Hamburg University of Technology, Germany
Amin Ghobeity, Sheridan College, Canada

****Correspondence:***
Eugeny Y. Kenig
eugeny.kenig@upb.de

Specialty section:
This article was submitted to Process and Energy Systems Engineering, a section of the journal Frontiers in Energy Research

Received: *11 June 2020*
Accepted: *31 August 2020*
Published: *09 October 2020*

Citation:
Grabo M, Staggenborg C, Philippi KA and Kenig EY (2020) Modeling and Optimization of Rectangular Latent Heat Storage Elements in an Air-Guided Heat Storage System. Front. Energy Res. 8:571787. doi: 10.3389/fenrg.2020.571787

INTRODUCTION

As reported by the International Energy Agency, only 10% of the global heat production was covered by renewable energy sources in 2018 (International Energy Agency, 2019). One of the ways toward increasing the usability of renewable energies is to adapt the supply of heating and cooling to the current demand and to minimize the cost-intensive consumption of electricity and fossil fuels. Among others, this can be achieved by using heat and cold storages, which increasingly have become a major focus of the heating, ventilation and air conditioning (HVAC) sector. One of the available heat storage technologies are latent heat storages, which use the phase change energy of the storage material and, compared to sensible heat storages, significantly increase the volume-specific storage capacity over a relatively small temperature interval. Materials used in latent heat storage systems are usually referred to as phase change materials (PCM). A typical application of such heat storages can be an air-conditioning system powered by a solar thermal collector, as illustrated in **Figure 1**. The system is charged during the day, when the thermal solar collector heats up an air flow, which is guided through the storage causing the PCM to melt. After leaving the storage, the air has the temperature of the PCM melting point and is distributed to the consumer. During the night, colder air can be pumped through the storage, which causes the PCM to solidify while heating up the air flow to the PCM melting point. Altogether, if properly designed, such a system is able to keep a constant indoor temperature.

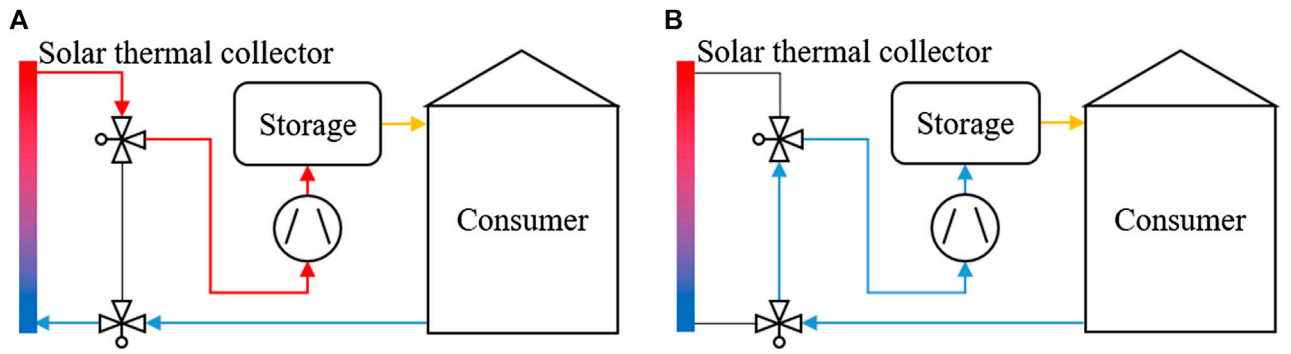

FIGURE 1 | Operation modes of a possible latent heat storage system: charging during the day **(A)** and discharging during the night **(B)**.

In literature, studies of different latent heat storage systems, both experimental and numerical, can be found. Types of latent heat storage include shell-and-tube heat exchangers or direct contact designs as well as packed bed storage tanks. The latter were investigated, among others, by Saitoh and Hirose (1986), Ismail and Henríquez (2002), and Loem et al. (2019). In such systems, the PCM capsules are randomly packed in a tank, and a heat transfer fluid releases heat to the bed while charging or extracts heat while discharging. Storages of structured PCM element arrangements were, for example, described by Darzi et al. (2013). In their numerical study, rectangular, plane PCM plates were used and the influence of operational parameters, such as mass flow rate and inlet temperature, as well as geometrical parameters, such as plate thickness, was investigated. Darzi et al. (2013) found that the plate thickness linearly correlates with the melting duration. Gowreesunker et al. (2013) studied the performance of a PCM plate heat exchanger for air-conditioning of an airport terminal building by using a coupled numerical model. They found that the cooling and partially the heating efforts can be reduced by using PCM and that energy savings of more than 30% can be achieved. The plate encapsulation used in their work was metallic and had surface extensions in form of pin fins in order to increase heat transfer. A recent study of a system consisting of in-duct PCM plates of the same type as used by Gowreesunker et al. (2013) was published by Kumirai et al. (2019). They varied operational parameters, such as inflow velocity and temperature, and compared different PCM in terms of thermal effectiveness. A similar rectangular plate design was investigated by Larrinaga et al. (2020) who investigated the effect of the arrangement of the plate stacks. They found that higher mass flow rates reduce the charging and discharging duration of the storage and that arranging plate stacks in series increases the duration.

Since the performance of the heat storage depends on the ability of the storage elements to effectively transfer energy to the heat transfer fluid, the focus of this study was laid on the design and optimization of new PCM heat storage plates similar to those investigated in the last three studies mentioned above. A new plate design was introduced, which had surface extensions in form of a square based pyramid. The encapsulation material of this plate was high-density polyethylene (HDPE) and the PCM was a salt hydrate. In practice, these plates are stacked and inserted into a box, which has connecting fittings for the installation in air ducts. The plates and the storage box are illustrated in **Figure 2**. Further, a test rig was set-up in order to evaluate the thermal and pressure drop performance of the plates. Based on the experimental setup, a computational fluid dynamics (CFD) model was developed and validated. Next, this model was reduced in complexity in order to perform a parametric study with respect to several geometry parameters of the plate.

METHODS

As can be seen in **Figure 2**, the PCM plates were designed with an extended surface in the form of a pyramidal frustum. The dimensions of the frustum are 15 mm by 15 mm on the base; the frustum height is 3 mm. The angle between the frustum side faces and the base area is 30°. It should be noted, that the thickness of the plate is constant, which means that the bulges on the top side have similar indentations on the bottom side. The overall thickness of the plate is 5 mm, while the HDPE capsule wall is 1 mm thick, thus resulting in a PCM layer thickness of 3 mm. The PCM volume per plate is around 100 ml. The plates can be stacked up to a variable number, and multiple stacks can be inserted into the container allowing for a variable storage capacity. In order to allow for an improved charging/discharging rate, the surface extensions of the plates were evaluated with the help of CFD.

Experimental

A test rig illustrated in **Figure 3** was set-up in order to acquire data for the validation of numerical results. It comprised a duct, in which a stack of ten PCM plates was inserted. Dry air was pumped through the duct by a compressor, then heated and straightened by a filter element before entering the stack. Temperatures were measured with six PT100 class-A sensors with an accuracy of 0.35 K. Two sensors were installed upstream and four sensors downstream of the plate stack in order to determine the thermal performance of the plates under varying inflow temperatures T_{in}. The temperature sensors were evenly distributed within the cross-section of the duct. The

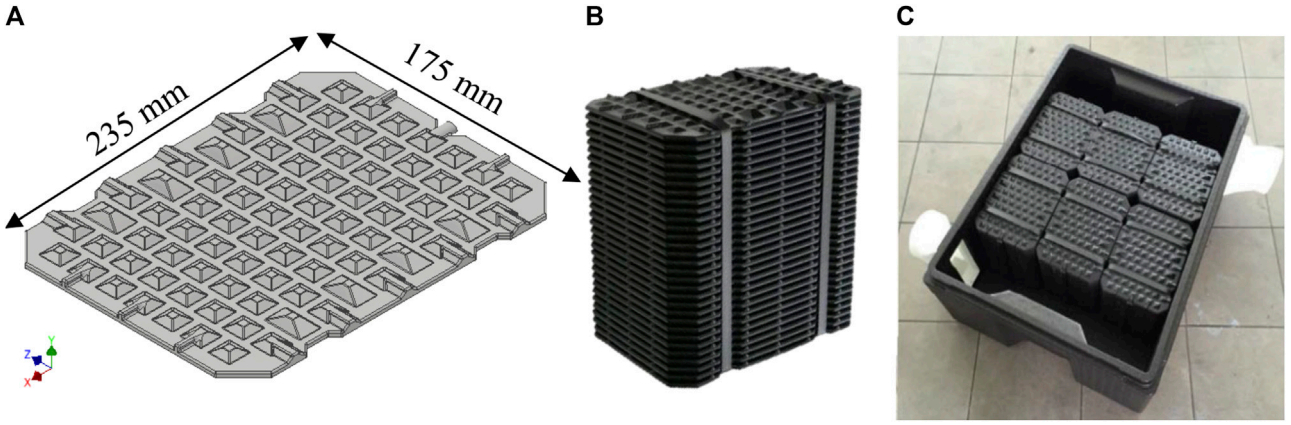

FIGURE 2 | The geometric model of a single storage plate **(A)**, a stack of plates **(B)**, and a storage container filled with six stacks of plates **(C)**.

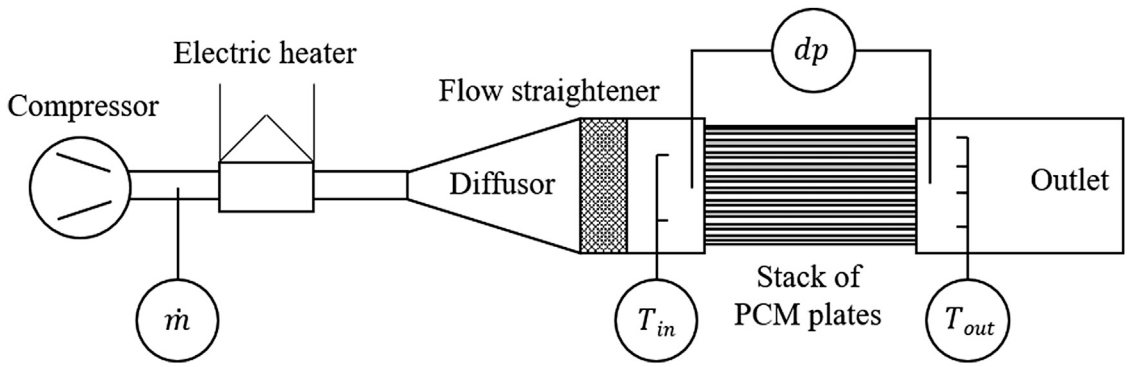

FIGURE 3 | Conceptual design of the experimental test rig: measured data include flow rate $\dot{m}$, pressure drop dp, temperatures upstream T_{in} and downstream T_{out} of one stack of plates.

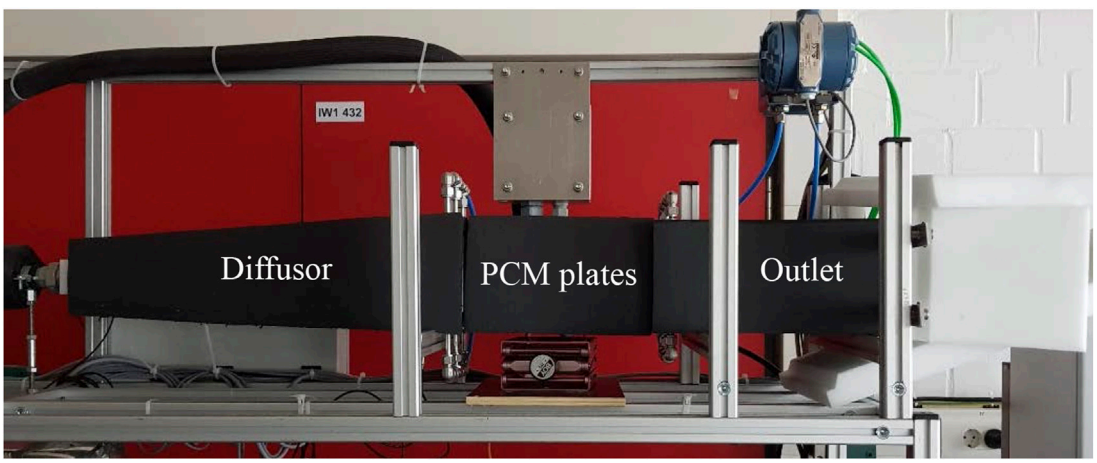

FIGURE 4 | The experimental setup.

TABLE 1 | Properties of PCM and HDPE.

	PCM	HDPE
Density (kg/m³)	1,300	945
Specific heat capacity [J/(kgK)]	2,000	1,845
Thermal conductivity [W/(mK)]	0.6	0.4
Thickness (mm)	3	1
Latent heat of fusion (kJ/kg)	220	—

PCM, phase change material; HDPE, high-density polyethylene.

pressure drop dp was measured with a Rosemount 3051S1CD differential pressure flow transmitter with 0.09% span accuracy. A Brooks 5853S mass flow controller with an accuracy of 0.7% was located between the compressor and the heater in order to control the incoming flow. To minimize ambient temperature influence, the whole setup was insulated with ArmaFlex elastomeric foam. A photograph of the experimental setup is shown in **Figure 4**. Experiments were carried out with flow rates of 150, 275, and 400 L/min and inlet temperatures of 35 and 39°C for melting and 25°C for solidification. The Reynolds numbers $Re = \rho u d_h/\mu$ within the channels for the highest volumetric flow rate were around 560 corresponding to an average flow velocity u of 1.6 m/s. Here, ρ and μ denote density and dynamic viscosity of air, respectively. The hydraulic diameter $d_h = 4A_c/P$ was calculated from the cross-sectional area A_c of a channel between two plates and the wetted perimeter P of such a channel. For the inlet region, Reynolds numbers around 3,800 were obtained.

The PCM used was the salt hydrate ATS30 by the manufacturer Axiotherm GmbH, with a solidus temperature T_s = 28°C and a liquidus temperature T_l = 33°C for melting and T_s = 27°C and T_l = 30°C for solidification (Axiotherm, 2020). The encapsulation material was HDPE. The properties of the PCM and HDPE are given in **Table 1**. **Figure 5** shows the partial enthalpy distribution of the used PCM provided by the manufacturer.

Computational Fluid Dynamics Model of the Test Rig

In order to optimize the plate design, a simplified CFD model of the air duct containing the plate stack was developed. The simulation tool used to implement the model was STAR-CCM+ 13.04. Due to the symmetry of the plates, only a thin slice section in the center of the stack was modeled, which enabled a significant reduction of the computational effort. The CFD model is illustrated in **Figure 6**.

The computational model consisted of two domains: air and PCM. The thickness of the capsule walls was not explicitly resolved, rather it was accounted for by applying a thermal resistance at the boundary that separates the air and the PCM. The thermal resistance was determined from the thickness and the thermal conductivity of the HDPE capsule walls (**Table 1**). At the air inlet, a constant mass flow rate and a specific temperature was defined. Assuming a perfect thermal insulation of the duct, the top and bottom sides were considered as adiabatic, with a no-slip boundary condition. The left and right side of the computational domain were described by symmetry boundary conditions, as shown in **Figure 6**. At the outlet, zero-gradient boundary conditions for pressure and temperature were applied. Note that due to the particular installation of the plate stack on the test rigs, three channels were blocked, as indicated in **Figure 6**. In order to properly attach the plates to the test rig, a special console had to be designed, which contained a stack of 10 plates. Since some part of the cross-sectional area of the stack was covered by the console, one plate was removed in the simulation, because no circulation around this plate was expected. However, during the installation of the test rig, it became clear, that more than just one plate was covered by the console. This was accounted for in the model by closing another channel at the top.

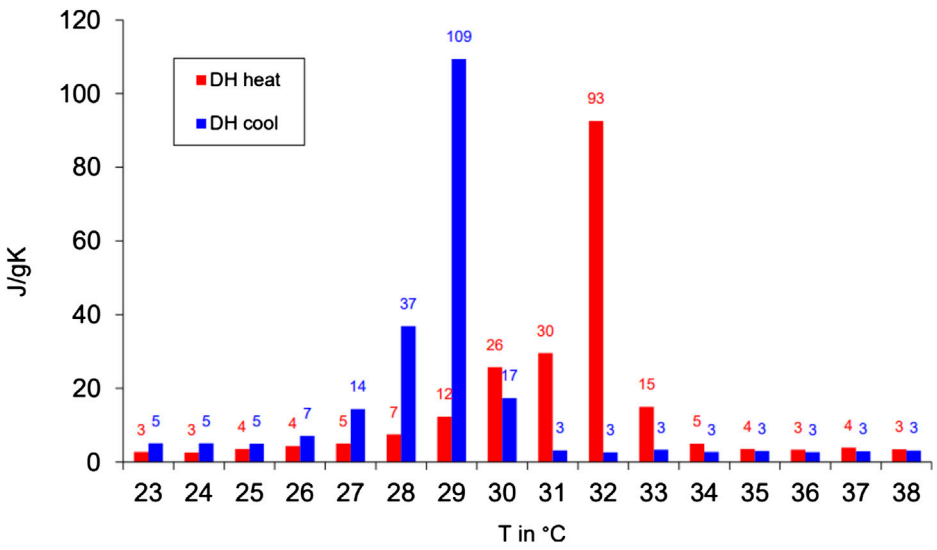

FIGURE 5 | Partial enthalpy distribution of the phase change material ATS30 (Axiotherm, 2020).

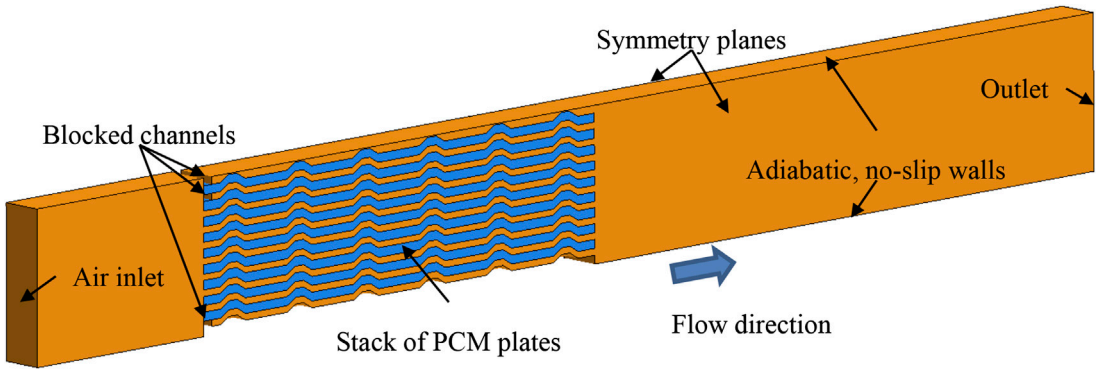

FIGURE 6 | Setup of the computational fluid dynamics (CFD) model of a test rig section containing the air duct and the phase change material (PCM) plate stack: air domain (orange) and PCM domain (blue).

Due to relatively low flow velocities, the Mach number was not expected to exceed 0.3. Therefore, the air flow was assumed to be incompressible and modeled by the following governing equations:

$$\frac{\partial u}{\partial t} + (u \cdot \nabla)u = -\nabla p + \mu \Delta u \tag{1}$$

$$\nabla \cdot u = 0 \tag{2}$$

Heat transport was described by the energy equation:

$$\frac{\partial T}{\partial t} + \nabla \cdot (uT) = a\nabla^2 T \tag{3}$$

Here, u denotes velocity, t time, p pressure field, μ dynamic viscosity, T temperature and a thermal diffusivity. Turbulence was modeled using an extended version of the k-ε model, namely, the elliptic blending model by Billard and Laurence (2012), which is suggested for internal flows involving heat transfer at moderate Reynolds numbers. For the heat transfer inside the plates, it was assumed that, due to the low thickness and high viscosity of the liquid PCM, only heat conduction takes place and any type of convection can be neglected. The phase change process was described using the following equation:

$$\rho c_p \frac{\partial T}{\partial t} = k\nabla^2 T - \rho L \frac{\partial \gamma}{\partial t} \tag{4}$$

The thermal conductivity k, the density ρ and the specific heat capacity c_p were assumed to be constant. L denotes the latent heat of fusion. The liquid fraction of the PCM γ is usually a function of temperature (Voller and Swaminathan, 1991). In this work, a linear γ-T relation was applied:

$$\gamma = \begin{cases} 0 & T < T_s \\ \dfrac{T - T_s}{T_l - T_s} & T_s \leq T \leq T_l \\ 1 & T > T_l \end{cases} \tag{5}$$

Meshing was performed with polyhedral elements and prism layers near the walls. A grid independence study yielded a mesh element size of 0.1 mm and a time step of 0.5 s as sufficient. Multiple simulations were carried out with flow rates of 150, 275, and 400 L/min. As inlet temperature, the measured inlet temperature curves were used. The temperature and pressure drop were evaluated at the same positions as on the real test rig, upstream and downstream of the plate stack. The simulated outlet temperatures and pressure drops were compared to the measured data.

As can be seen in **Figure 7**, the simulated outlet temperatures deviate strongly from the measured ones, especially after the start of the phase change process at approximately 50 min. A possible explanation is the thermal mass of the test rig components, such as the diffusor, duct, outlet, etc., which could not be considered in the CFD model. Besides, by simulating only a slice section of the duct geometry, side effects were neglected. Further, the model assumed a perfectly insulated duct, and hence, heat losses to the environment were neglected. These effects lead to a much slower temperature rise in the experiments. Based on these results, we can conclude that it is not practical to model the actual heat transport within the duct. However, the simulated and measured pressure drop values are in good agreement, which indicates that the flow phenomena within the duct are properly captured.

Representative Element for Parametric Study

The simulated flow distribution is shown in **Figure 8**. It can be seen that the flow pattern inside the individual channels between two plates is similar. This similarity can be used to reduce the initial computational domain to a small representative element.

This element was used to perform a parametric study to identify optimized plate geometries with increased heat transfer and/or lower pressure drop compared to the original design. The model of the representative element, which has the dimensions 10 mm by 40 mm, is illustrated in **Figure 9**.

The phase change phenomena inside the PCM were not modeled, since the actual heat transport into the capsule as well as the pressure drop entirely depend on the actual shape of the capsule surface and operational parameters, such as air flow velocity or inlet temperature. This allows to consider the air flow as steady-state and evaluate the pressure drop and heat transfer

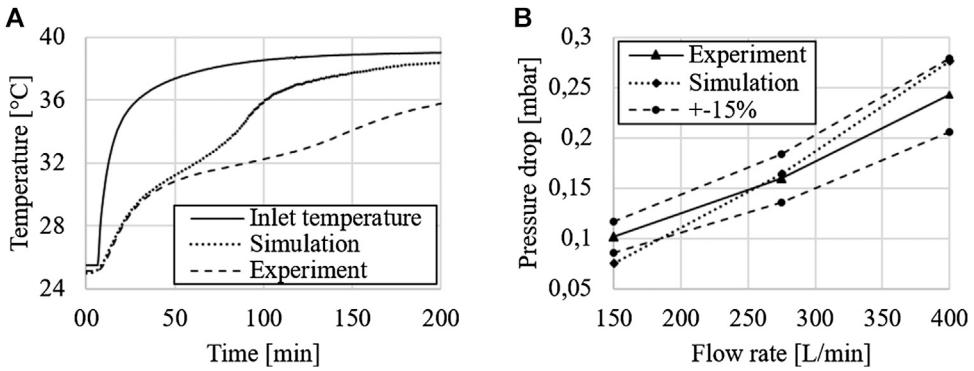

FIGURE 7 | Outlet temperatures (**A**) and pressure drop (**B**) at a flow rate of 400 L/min.

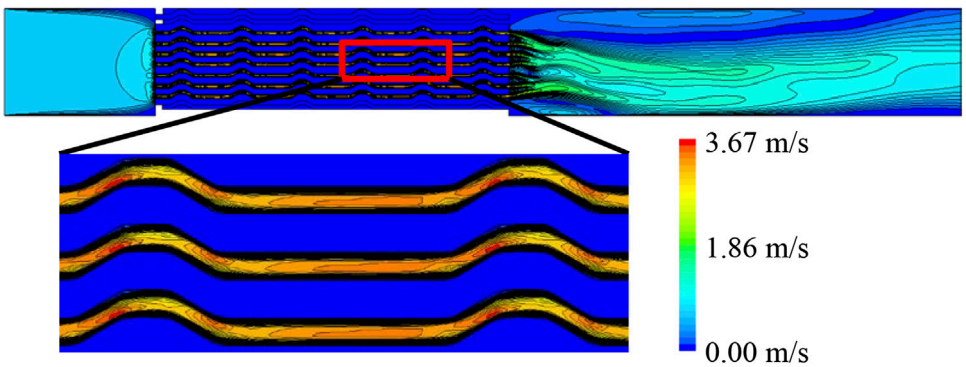

FIGURE 8 | Simulated velocity plots of the test rig duct: similar flow patterns can be observed in the channels between the plates.

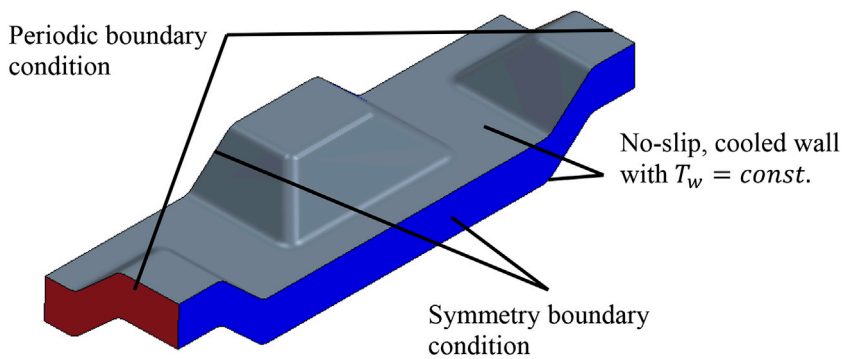

FIGURE 9 | Model of a representative channel element.

under steady-state conditions. By applying a periodic boundary condition at the inlet and outlet of the element, this steady-state was enforced. The wall temperature T_w was kept constant at 20°C, the inflow velocity u was set to 3 m/s and the inlet temperature to 30°C. The mesh consisted of polyhedral cells in the bulk flow and prism layers near the walls. After performing a grid independence study of the representative element, a mesh element size of 0.15 mm was chosen. Comparing the pressure drop over the representative element with that in equivalent sections of the duct model, only small differences (<10%) were found, which indicates that the element represents the whole duct model reasonably well and can be used for a parametric study.

In this study, different plate surface geometries were created and evaluated based on their thermo-hydraulic efficiency ε, which is the ratio of the heat transferred through the element wall and

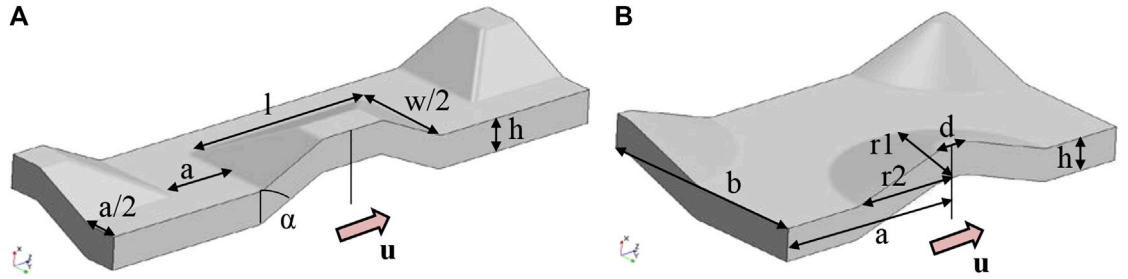

FIGURE 10 | Shapes of plate surface elements and their geometrical parameters based on pyramidal frustum **(A)** and ellipsoid **(B)**.

the pumping effort (**Eq. 6**). This criterion was used before by, for example, Mitrovic and Maletic (2011) for the evaluation of pillow plate heat exchangers.

$$\varepsilon = \frac{A_w \dot{q}_w}{u_{\text{in}} A_{\text{ce}} \Delta p} \tag{6}$$

In **Eq. 6**, A_w denotes the wetted wall area of the element, $\dot{q}_w$ is the heat flux through the wall, u_{in} is the inlet flow velocity, A_{ce} is the cross-sectional area of the element and Δp is the pressure drop across the element. The thermo-hydraulic efficiency was determined for all considered geometries and then compared to ε_{ref}, which represents the thermo-hydraulic efficiency of the

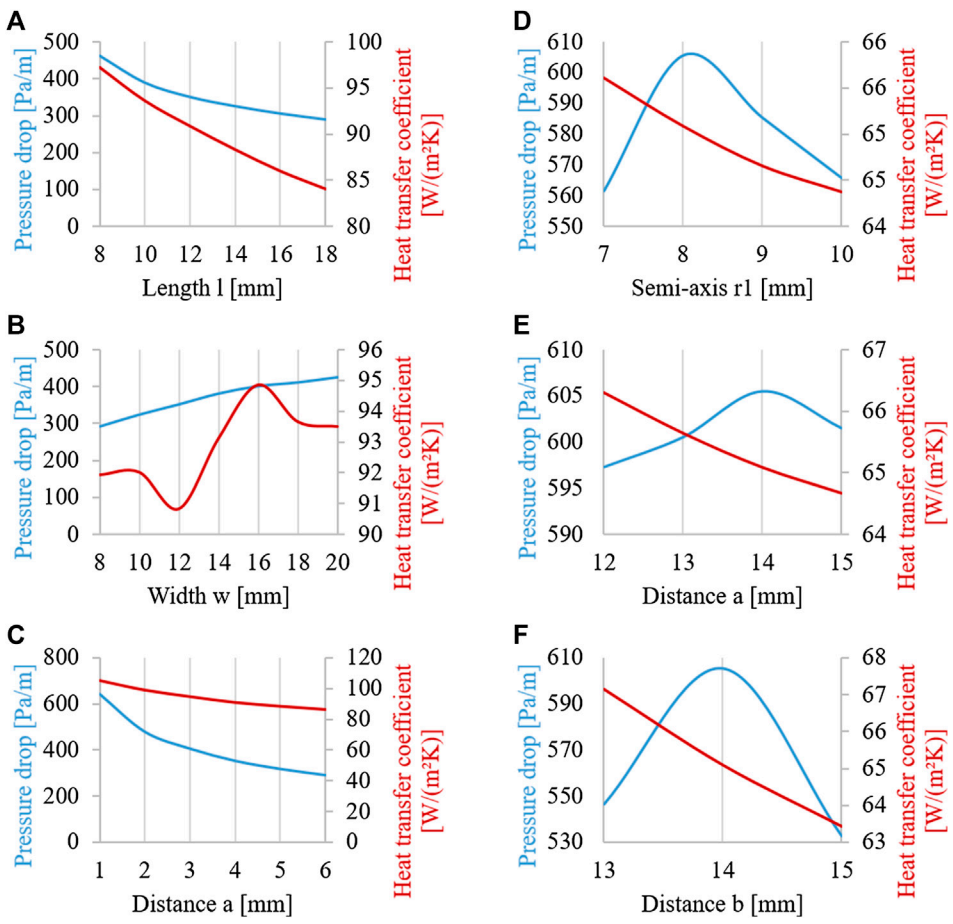

FIGURE 11 | Some pressure drop and heat transfer coefficient results of the parametric study for a pyramidal frustum **(left)** and an ellipsoid **(right)** based geometry: variation of frustum base length l **(A)**, base width w **(B)** and distance a between frustums **(C)** as well as variation of ellipsoid axis r1 **(D)**, distance a **(E)** and distance b **(F)**.

original geometry. The ratio $\varepsilon/\varepsilon_{ref}$ evaluates the relative improvement or worsening of the respective geometry. Multiple geometry parameters were changed in the course of the study, which are shown in **Figure 10**. The original geometry was based on a square pyramidal frustum. The shape of the frustums as well as their arrangement and the height of the channel were varied. Further, an ellipsoid based geometry was investigated, for which the length of the minor and major axis, the arrangement of the elliptic elements and the channel height were varied. In total, 217 different geometry variations were tested and compared to the original geometry.

RESULTS

The influence of some investigated geometrical parameters is shown at the left of **Figure 11** for a frustum reference shape with l = w = 12 mm, a = 4 mm, h = 3 mm and $\alpha = 45^{\circ}$. Each parameter was changed, while the other were kept constant. Also, combinations were tested, when more than one parameter was changed attempting to find additional local optima. As can be seen in the plots in **Figure 11**, similar trends in the behavior of both heat transfer coefficient and pressure drop can usually be encountered. For instance, when pressure drop decreases, the heat transfer coefficient decreases as well. However, the slopes are different, and therefore, the optimal compromise between heat transfer and pressure drop can only be found by analyzing the thermo-hydraulic efficiency (**Eq. 6**). Using this analysis, we found that the frustum based geometries have an improvement potential of only 14% compared to the original.

The same procedure was performed for the ellipsoid based geometries; some illustrative results for a base shape of a = b = 14 mm, h = 3 mm, d = 2 mm, r_1 = 6 mm and r_2 = 8 mm are shown at the right of **Figure 11**. As can be seen, the ellipsoidal shapes usually show a maximum of pressure drop, while the heat transfer coefficient decreases with higher geometrical dimensions. The reason for this behavior is the lower surface area available for heat transfer, since with increasing distance between the surface elements, the number of elements per plate decreases. This results in a lower surface area per plate and therefore in reduced heat transfer. The behavior of the pressure drop was somewhat surprising, since we expected its increase together with increasing surface area. However, as can be seen in **Figure 11**, there is a maximum instead. Such a maximum can also be encountered for other combinations of geometry parameters and geometry variants not shown here, which indicates a higher potential of the ellipsoidal shape for increasing the thermo-hydraulic efficiency. This was indeed confirmed after evaluating 126 different geometry variants based on the ellipsoidal shape, when a possible ϵ improvement of 46% compared to the original geometry was found. Based on the ellipsoidal shape, an alternative, non-symmetric shape in form of a falling droplet was also investigated, while 38 geometry variants were studied and a further improvement of ε up to 52% could be achieved. The optimized droplet geometry is illustrated in **Figure 12**.

CONCLUDING REMARKS

In this work, rectangular, thin heat storage capsules filled with PCM were investigated with respect to their heat transfer performance and pressure drop. The focus was laid on the CFD modeling of the flow and heat transfer in the channels between the plates in order to optimize their shape. Therefore, a test rig was set-up to experimentally evaluate reference plates, and the measured data was used to validate the CFD model of the duct containing a stack of PCM plates. Afterward, the model was reduced in complexity and a representative element was identified, for which a parametric study was performed. Different base geometries were tested as surface extension elements for the storage plates, including pyramidal frustum and ellipsoidal shapes, by changing various geometrical parameters. In total, 217 different geometry variants were simulated and their thermo-hydraulic efficiency was evaluated. Comparing the respective efficiency of each variant with the reference geometry shown in **Figure 2**, a maximal improvement

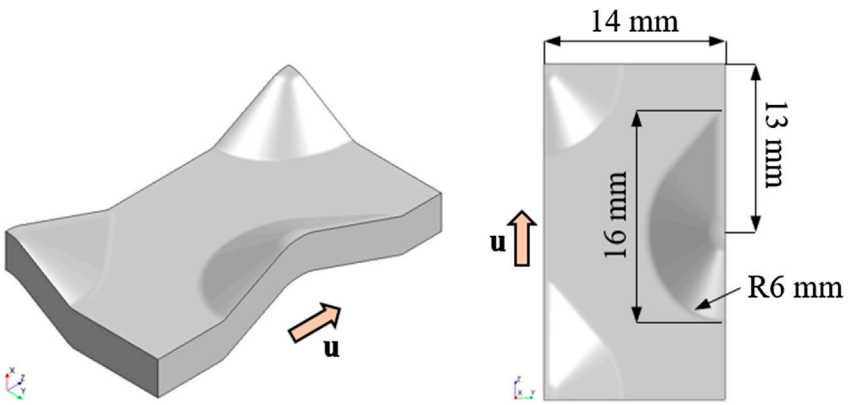

FIGURE 12 | The optimized surface element based on the shape of a droplet.

of 52% was achieved. The optimized shape of surface element based on a droplet shape is shown in **Figure 12**.

The optimized surface geometry of the representative element can be used for the design of improved PCM plates. For an upcoming project, it is planned to manufacture several of these optimized plates together with a consortium partner and to perform further experimental studies. Besides, the storage container in which the plates are stacked will also be investigated to reach further improvement in order to allow for an even flow distribution. Subsequently, future investigations will involve the performance testing of the optimized plates under real operational conditions in a demonstrator building.

DATA AVAILABILITY STATEMENT

All datasets presented in this study are included in the article.

AUTHOR CONTRIBUTIONS

All authors listed have made a substantial, direct and intellectual contribution to the work, and approved it for publication.

FUNDING

The authors are grateful to the German Federal Ministry of Economic Affairs and Energy for their financial support of the project "MoLaWS: Development of a modular heat storage system using high-capacity, innovative latent heat storage elements" (Reference Number: ZF4032917ST7).

ACKNOWLEDGMENTS

Calculations leading to the results presented here were performed on resources provided by the Paderborn Center for Parallel Computing.

REFERENCES

Axiotherm GmbH (2020). Data sheet—ATS 30. Available at: https://www.axiotherm.de/de/download/project/productdatasheet/file/14/ (Accessed August 14, 2020).

Billard, F., and Laurence, D. (2012). A robust k-ε-v^2/k elliptic blending turbulence model applied to near-wall, separated and buoyant flows. *Int. J. Heat Fluid Flow* 33 (1), 45–58. doi:10.1016/j.ijheatfluidflow.2011.11.003

Darzi, A. R., Moosania, S. M., Tan, F. L., and Farhadi, M. (2013). Numerical investigation of free-cooling system using plate type PCM storage. *Int. Commun. Heat Mass Transf* 48, 155–163. doi:10.1016/j.icheatmasstransfer.2013.08.025

Gowreesunker, B. L., Tassou, S. A., and Kolokotroni, M. (2013). Coupled TRNSYS-CFD simulations evaluating the performance of PCM plate heat exchangers in an airport terminal building displacement conditioning system. *Build. Environ* 65, 132–145. doi:10.1016/j.buildenv.2013.04.003

International Energy Agency (2019). Renewables 2019—market analysis and forecast from 2019 to 2024. Available at https://www.iea.org/reports/renewables-2019/heat. (Accessed June 5, 2020).

Ismail, K. R., and Henríquez, J. R. (2002). Numerical and experimental study of spherical capsules packed bed latent heat storage system. *Appl. Therm. Eng* 22 (15), 1705–1716. doi:10.1016/S1359-4311(02)00080-7

Kumirai, T., Dirker, J., and Meyer, J. (2019). Experimental analysis for thermal storage performance of three types of plate encapsulated phase change materials in air heat exchangers for ventilation applications. *J. Build. Eng* 22, 75–89. doi:10.1016/j.jobe.2018.11.016

Larrinaga, P., Diarce, G., Campos-Celador, A., and García-Romero, A. (2020). Parametric characterization of a full-scale plate-based latent heat thermal energy storage system. *Appl. Therm. Eng.* 178, 115441. doi:10.1016/j.applthermaleng.2020.115441

Loem, S., Deethayat, T., Asanakham, A., and Kiatsiriroat, T. (2019). Thermal characteristics on melting/solidification of low temperature PCM balls packed bed with air charging/discharging. *Case Stud. Therm. Eng* 14, 100431. doi:10.1016/j.csite.2019.100431

Mitrovic, J., and Maletic, B. (2011). Numerical simulation of fluid flow and heat transfer in thermoplates. *Chem. Eng. Technol* 34 (9), 1439–1448. doi:10.1002/ceat.201100271

Saitoh, T., and Hirose, K. (1986). High-performance phase-change thermal energy storage using spherical capsules. *Chem. Eng. Commun* 41 (1–6), 39–58. doi:10.1080/00986448608911711

Voller, V. R., and Swaminathan, C. R. (1991). General source-based method for solidification phase change. *Numer. Heat Trans. B* 19 (2), 175–189. doi:10.1080/10407799108944962

Conflict of Interest: The remaining authors declare that the research was conducted in the absence of any commercial or financial relationships that could be construed as a potential conflict of interest.

frontiers in Energy Research

ORIGINAL RESEARCH
published: 16 November 2020
doi: 10.3389/fenrg.2020.549615

Decarbonization in Complex Energy Systems: A Study on the Feasibility of Carbon Neutrality for Switzerland in 2050

Xiang Li[1]*, *Theodoros Damartzis*[1], *Zoe Stadler*[2], *Stefano Moret*[1], *Boris Meier*[2], *Markus Friedl*[2] and *François Maréchal*[1]

[1]Industrial Processes and Energy Systems Engineering, Institute of Mechanical Engineering, Sion, Ecole Polytechnique Fédérale de Lausanne, Lausanne, Switzerland, [2]Hochschule für Technik Rapperswil, Rapperswil, Switzerland

Decarbonization gained prominence with the witnessed rise of temperature over recent years, particularly in the aftermath of the adoption of the Paris agreement for limiting the temperature increase within 2°C until 2050. Biogenic resources are explicitly indicated as carbon-neutral from Life Cycle Assessment perspective by the IPCC, shedding light on the carbon-neutral society by applying Biogenic Energy Carbon Capture for creating negative emissions. This article proposes a novel modeling approach by introducing carbon layers with specification on the principal carbon sources and sinks based upon an optimization algorithm, in order to solve the carbon loop issue in a highly interconnected energy system due to increasing penetration of biomass and carbon capture, use, and storage. This study contributes to quantifying biogenic and nonbiogenic carbon footprints, and optimizing the circular economy associated with a net-zero-emission society, in favor of policy-making for sustainable development in long terms.

Keywords: carbon neutrality, carbon capture, use, and storage, circular carbon flow, energy planning, biogenic energy with carbon capture, mixed-integer linear programming optimization

OPEN ACCESS

Edited by:
Rangan Banerjee, Indian Institute of Technology Bombay, India

Reviewed by:
Xiaofeng Guo, ESIEE Paris, France
Rajagopalan Srinivasan, Indian Institute of Technology Madras, India

***Correspondence:**
Xiang Li
xiang.li@epfl.ch

Specialty section:
This article was submitted to Process and Energy Systems Engineering, a section of the journal Frontiers in Energy Research

Received: *06 April 2020*
Accepted: *28 September 2020*
Published: *16 November 2020*

Citation:
Li X, Damartzis T, Stadler Z, Moret S, Meier B, Friedl M and Maréchal F (2020) Decarbonization in Complex Energy Systems: A Study on the Feasibility of Carbon Neutrality for Switzerland in 2050. Front. Energy Res. 8:549615. doi: 10.3389/fenrg.2020.549615

1. INTRODUCTION

Carbon mitigation is becoming an essential and urgent issue in human activities, infiltrating into various societal fields, including politics, culture, economy, environment, lifestyle, ecology, resource, and so on. In the context of striving for a sustainable society, participating countries in the Paris Climate Summit which took place in 2015 reached an agreement, declaring the objective of keeping the increase in global average temperature to well below 2°C above preindustrial levels within this century, and further to pursue efforts to limit the increase to 1.5°C (IPCC, 2014). In this context, European countries are pioneering the exploration of plausible pathways toward carbon mitigation: the Netherlands announced that all Dutch cars must be emission free by 2030 (NLTimes, 2017); Germany planned to phase out the coal power plants by 2038 (Rinscheid and Wüstenhagen, 2019); and the Danish government decided to provide 100% of Denmark's energy requirements in electricity, heating, and transport from renewable sources by 2050 (Madsen et al., 2018). In terms of Switzerland, there is a host of energy policies that range from rules for market liberalization to programs for energy conservation, subsidies for renewables, and regulations for CO_2 reduction (Markard et al., 2016). In 2011, the Swiss government and parliament decided to phase out nuclear power plants following the Fukushima nuclear accident, and to stimulate energy

efficiency and the use of renewable energies instead. As a consequence, the government developed the Energy Strategy 2050, setting long-term targets for the reduction of energy consumption (54% reduction until 2050) and the expansion of renewable electricity generation and combined generation of power and heat. Concerning climate policy, Switzerland undertook a commitment to halve its greenhouse gas emissions vs. the 1990 level by 2030. To accomplish this, the existing Federal CO_2 Act has to be revised for the period beyond 2020. The corresponding bill is currently being debated in Parliament. In 2019, the Swiss Federal Council resolved that, as of 2050, Switzerland is to reduce its net greenhouse gas emissions to zero (net-zero-emission target) (SFOE, 2020). This declares it is aiming to meet the internationally agreed goal of limiting global climate warming to a maximum of 1.5°C vs. the preindustrial period. To realize this objective, two methods are generally considered:

- mitigation of carbon sources: predominately translated by the massive penetration of renewable resources, and efficiency improvement for carbon-intensive areas;
- reinforcement of carbon sinks: in either natural way, such as afforestation and reforestation, or artificial way, typically the deployment of CCUS technologies.

Therefore, it is necessary to analyze the carbon flows of the energy system, by distinguishing carbon categories and identifying various carbon sources and sinks. This article proposes a modeling approach by defining specific carbon layers based upon distinguished carbon categories and identified carbon sources and sinks, in order to clarify the murkiness in energy system models on carbon loop issues, especially in the context of increasing biogenic energy with carbon capture (BECC) where the biomass serves as both a carbon source and a sink. This approach contributes to quantifying the carbon footprints of the system and discovering potential opportunities for a breakthrough, especially with respect to certain key technologies.

This article hereafter is organized in the following way: **Section 2** resumes the state-of-the-art from the literature review; **Section 3** clarifies the modeling methodology for the MILP (mixed-integer linear programming) optimization, with specification on the carbon flow modeling; **Section 4** presents the key data and assumptions used in this research; **Section 5** defines decarbonization scenarios and analyzes the results, followed by a discussion on how to achieve carbon neutrality; at last, a conclusion is drawn in **Section 6** by resuming the core achievements and limitations of the research.

2. STATE-OF-THE-ART

With increasing attention to the decarbonization of the energy system, numerous articles mentioned the essence of biomass playing in achieving this goal. National Academies of Sciences, Engineering and Medicine (2018) emphasized two technologies for conversing biomass to fuels, namely, pyrolysis and gasification; other possible technologies, such as biomass Fischer–Tropsch processes, hydrothermal gasification, etc., had yet not been accounted for. Celebi et al. (2017) reviewed and analyzed various lignocellulosic biorefineries and suggested process design methodology for improving thermo-environmental performance, which is nevertheless not able to quantify the impact of these improvements on the multisector energy system structure. Dahiya et al. (2018) proposed a concept of circular bio-economy with biorefinery, which focused merely on the biomass field, without analysis on the impact of the biomass on the whole energy system. Similar topics include Pfeffer et al. (2007), Santibañez-Aguilar et al. (2011), and Peduzzi (2015). Smith (2016) came up with seven scenarios elaborating fossil CCS (carbon capture and storage) and BECCS, and the production of biofuels, but no further information on how to optimize the usage of the synthesized biofuels, and their corresponding impact to the other energy conversion technologies. In parallel, Creutzig et al. (2015) emphasized the role that CCS plays in biogenic carbon treatment, but ignored the possibility of CCU application. Instead, SAPEA (2018) took into account the role of CCU, but simply concluding the CCU is not able to abate the carbon emission, since the captured carbon is finally released back to the atmosphere, where the effect of the decreased utilization of fossil fuels is neglected.

Concerning BECC, the majority of current researches focus principally on the improvement of the performance of standalone BECC processes within limited boundaries, for instance at an industrial site level, rendering a lack of holistic view on the interactive impacts on the whole energy systems. Another challenge is arising with the increasing advocation for carbon capture and utilization (CCU), which unavoidably releases back the captured carbon into the atmosphere, resulting in carbon flow loops as long as the carbon products are not chemically stable and nonreleasable, typically recyclable plastics. The loop issue is even more tough to be tackled taking into consideration the double nature of biomass as both carbon source and sink. In addition, current studies have paid limited attention to the relationship of carbon capture and renewable development, which cannot be simply regarded as *synergistic* or *mutually exclusive* due to the intrinsic complexity of the interactions between resources and technologies.

As to the modeling of carbon flows, the majority of articles are dedicated to depicting the inter-regional import and export of carbon fuels, such as Aichele and Felbermayr (2010), Ackerman et al. (2007), and Chen et al. (2017), with limited attention on the intrinsic complexity of the energy system. Some focused on carbon economics on the market such as Spaargaren and Mol (2013) with up-bottom approaches, rendering a lack of details on the technological aspects of the system. Gounand et al. (2018) analyzed the impact of carbon flows on the ecosystems, with limited information on the energy sides; Chen and Chen (2017) emphasized the correlation between energy consumption and carbon emissions; however, the proposed methodology is still an acylic model, implying circular carbon flows are not considered. Ramaswami et al. (2011) and Suciu et al. (2018) analyzed the carbon footprints within city scale, which is yet difficult to be

generalized into a national level, which requires scrutiny since limited freedom of technologies and resources in small cases may restrict the flexibility of a system with diverse possibilities.

Currently, many researchers demonstrate that decarbonizing a specific energy sector within limited boundary is feasible, such as Schiffer and Manthiram (2017) for chemical industry, Braune et al. (2019) for building, and Hannula and Reiner (2017) for transport. However, it should be highlighted that decarbonization of a certain sector may not be substantially beneficial to the decarbonization of the whole energy system, since it might simply shift the carbon emission from one sector to other sectors. For instance, a steel-manufacturing factory opts to consume more electricity than conventional coal/gas as energy carriers in order to mitigate carbon emission, which in nature is risky of transferring the emission pressure to the power sector if the electricity mix is still fossil-dominant. Up to now, there are few models capable of studying circular carbon flow in complex energy systems with multisectors for quantifying the impact of increasing penetration of biogenic carbon sources with CCUS.

From the authors' perspective, a holistic model allows for an in-depth exploration on the interaction between approaches, some of which are supposed to be mutually exclusive; e.g., the implementation of CCS is likely to be impeded by the increasing penetration of intermittent renewables due to lack of available carbon sources, while some are reckoned synergistic, e.g., the development of storage technologies is expected to be in parallel to the renewables' evolution. Therefore, without a holistic view of the whole system, it is difficult to judge the role of a standalone process/sector in the energy transition.

Conventional methods for dealing with complex systems involve simulation and optimization: Simulation is the most straight-forward method with computational efficiency competence for projection modeling by fixing assumptions and observing the consequent pathways. Its application is however limited particularly in the presence of loop problems, where it is difficult to get the optimal solution from limited tests; conversely, optimization deals with a problem by exploring part of (or the whole) feasible zone at a sacrifice of heavy computational complexity and is commonly used as an auxiliary tool for decision-making. Additionally, an optimization problem can be transformed into a simulation problem by enforcing constraints. Taking into consideration the multilateral interactions in the energy systems, an optimization model based upon AMPL (A Mathematical Programming Language) was applied in this research and is elaborated in **Section 3**.

3. MODELING METHODOLOGY

3.1. Model Description

3.1.1. General Introduction

This research is conducted based upon Energyscope, a bottom-up energy system model developed in the Industrial Process and Energy Systems Engineering (IPESE) group in favor of decision-making for techno-economic and ecological optimization. Compared to other existing energy models, which are often proprietary, computationally expensive, and mostly focused on the electricity sector (Limpens et al., 2019), Energyscope optimizes both the investment and operation strategies of an entire energy system (including electricity, heating, and mobility) by taking a "snapshot" for a given objective year. In this study, the time horizon in consideration is 2050 with a monthly resolution. Having a good performance in the trade-off between the modeling scope and computational time, Energyscope was applied to analyze the uncertainty by Moret et al. (2017) and Li et al. (2019). This open-source platform provides users with the flexibility to define tailored scenarios and analyze the corresponding economic and ecological impacts.

In this model, we highlight the difference in final energy consumption (FEC) and end-use demand (EUD). FEC is defined as the amount of input fuel needed to satisfy the EUD. For instance, FEC refers to, in an oil heat boiler, the amount of oil consumed, while EUD corresponds to the heat generated. The efficiency of the boiler is thus defined by the ratio of EUD over FEC. As presented in **Figure 1**, the EUD in Energyscope covers the process heat (HT), low-temperature heat (LT), including space heating and hot water supply, electricity, passenger mobility, and freight mobility, where space heating varies in different months according to the distribution ratios given by Moret et al. (2017), while the other demands are supposed to be uniformly distributed within the whole year. In Energyscope, the links between FEC and EUD are bridged by end-use technologies (EUT), such as the boiler aforementioned. One technology can have multi-inputs and outputs, e.g., a cogeneration gas plant provides both heat and electricity with corresponding efficiencies. Additional to EUT, a part of technologies are responsible for intermediate conversions without direct participation in supply for EUD, such as the storage technologies. From the FEC side, Energyscope involves 1) fossil fuels: natural gas, coal, nonbiogenic waste, heating oil, diesel, and gasoline; and 2) nonfossil resources: uranium, solar, wind, geothermal, and biomass. Intermediate resources include electricity, hydrogen, biogas, and bio-liquids (gasoline and diesel). In particular, electricity is regarded as a resource if it serves as an input of one technology, for instance in the electrolysis process; or as an EUD by household appliances. Specifically, CO_2 is of double nature in this model: It is regarded as an output associated with positive-emission technologies, and as an input resource in negative emission technologies such as synthesizing fuels/plastics. In order to simulate the energy/mass flows, the concept of layers is introduced, which serves as dynamic tanks for balancing all the inputs and outputs in each time period taking into account corresponding conversional efficiencies. Detailed mathematical interpretation of the layers' behavior is presented in **Section 3.1.2**.

3.1.2. Mathematical Formulation

In this article, all decision variables are marked in bold format. The objective function of the Energyscope is to minimize the

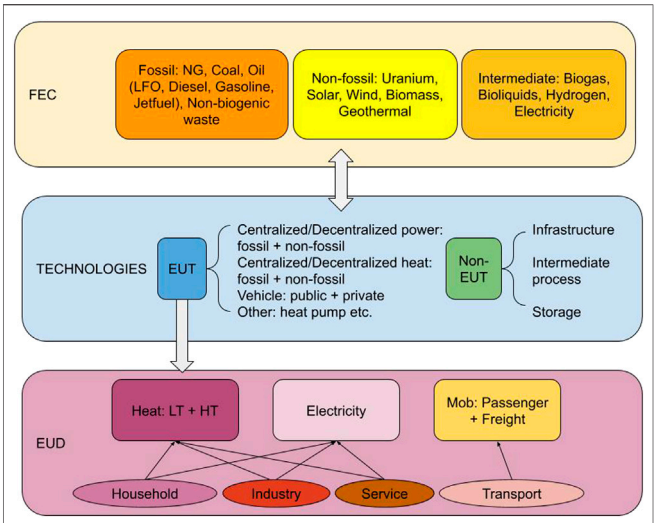

FIGURE 1 | Typology of Energyscope.

annual total cost $\mathbf{C_{tot}}$ expressed by the sum of the annualized CAPEX ($\mathbf{C_{inv}}$), the annual fixed OPEX for the maintenance ($\mathbf{C_{maint}}$) and the annual variable OPEX costs ($\mathbf{C_{op}}$) for purchase of resources, as shown in **Eq. 1**, where the sets $\mathcal{E}$, $\mathcal{R}$, and $\mathcal{T}$ represent the technologies, the resources (renewables and non-renewables as well as electricity import) and the time periods (twelve months within one year), respectively. $t_{op}(t)$ denotes the duration of the period t. The investment cost $\mathbf{C_{inv}}(j)$ is annualized by a factor $\tau(i, n(j))$ expressed in **Eq. 2**, with i the discount rate assumed to be 2.215% and $n(j)$ the expected lifetime for the technology j. The investment cost and fixed operational cost (maintenance) for a given technology are proportional to its installed capacity $\mathbf{F}(j)$, which defines the annual capacity factor $cp(j)$ in **Eq. 3** as the ratio of the annual production (by summing the power output $\mathbf{F_t}(j)$ in GW multiplied by the corresponding period duration $t_{op}(t), t \in \mathcal{T}$) over the theoretical annual production at full load. The annual output $\mathbf{F_a}(j)$ is expressed as the sum of monthly outputs. As to the variable operational cost, it depends on the amount of resources consumed, and specific cost for each resource (nonrenewable and renewable) available in the **Supplementary Material**. It should be highlighted that the monthly outputs of intermittent renewable technologies ($j \in \mathcal{I}$), namely, solar and wind as well as hydro power, are limited by the corresponding monthly capacity factor $cp_{\mathbf{t}}(j)$. Other constraints include: the proportional relationship of investment cost and the installed capacity by **Eq. 6** for every technology in consideration; the same for maintenance cost (fixed OPEX) by **Eq. 7**. Each technology emits GHG during their construction period, which is noted by $\mathbf{GWP_{constr}}$ and is also assumed to be in line with its installed capacity by **Eq. 8**, which is scaled by **Eq. 9** between its minimal and maximal values. Different from the investment and maintenance cost, the variable operational cost is decided by the sum of purchase amounts of resources in each period as expressed in **Eq. 10**, and the availability of resources is capped by **Eq. 11**. For example, the availability of waste for incineration is limited to an upper bound determined by the population. **Equation 12** reflects the concept of layer balance in each period, where $f(i, l)$ stands for the conversional efficiency of a technology i contributing to a certain layer $l \in \mathcal{L}$, or for the resource purchase if $i \in \mathcal{R}$ and $i = l$ where f is set to be 1. Take electricity layer as an example, the layer's level at time period t is expressed as the sum of import (positive value for f), the domestic production by technologies (positive value for f, such as by PV) and internal consumption (negative value for f, such as by an electric heat pump), which is supposed to match the EUD for electricity in the same period. DHN installed capacity is decided by two aspects: 1) it is defined as a value larger than or equal to the total installed capacity of all DHN technologies by **Eq. 13**; 2) taking into account the energy supply security, DHN should be more than "just enough" in order to meet the demand in peak period, and as a result, a peak parameter $\%_{peak}$ is defined in **Eq. 14**, and in this model, we assume it to be 200% of the maximal district heating demand. Energy loss is considered in **Eq. 15**, where $\mathcal{G}$ stands for the electricity and district heating. It is assumed the electricity loss in each period is proportional to the total production from all the power generation technologies, the same for DHN heat loss. In terms of Switzerland, we assume the loss percentages ($\%_{loss}$) 7% and 5% for electricity grid and DHN network, respectively.

$$\min \mathbf{C_{tot}} = \min\left(\tau(i, n(j)) \sum_{j \in \mathcal{E}} \mathbf{C_{inv}}(j) + \sum_{j \in \mathcal{E}} \mathbf{C_{maint}}(j) + \sum_{r \in \mathcal{R}} \sum_{t \in \mathcal{T}} \mathbf{C_{op}}(r, t) \right), \tag{1}$$

$$\tau(i, n(j)) = \frac{i(1+i)^{n(j)}}{(1+i)^{n(j)} - 1}, \tag{2}$$

$$\mathbf{F}(j) cp(j) \sum_{t \in \mathcal{T}} t_{op}(t) \geq \sum_{t \in \mathcal{T}} \left(\mathbf{F_t}(j) t_{op}(t) \right) \quad \forall j \in \mathcal{E}, \tag{3}$$

$$\mathbf{F}(j) cp_{\mathbf{t}}(j) \geq \mathbf{F_t}(j) \geq 0 \quad \forall j \in \mathcal{I}, t \in \mathcal{T}, \tag{4}$$

$$\sum_{t \in \mathcal{T}} \mathbf{F_t}(j) t_{op}(t) = \mathbf{F_a}(j) \quad \forall j \in \mathcal{E}, \tag{5}$$

$$\mathbf{C_{inv}}(j) = c_{inv}(j) \mathbf{F}(j) \quad \forall j \in \mathcal{E}, \tag{6}$$

$$\mathbf{C_{maint}}(j) = c_{maint}(j) \mathbf{F}(j) \quad \forall j \in \mathcal{E}, \tag{7}$$

$$\mathbf{GWP_{constr}}(j) = \mathrm{gwp_{constr}}(j) \mathbf{F}(j) \quad \forall j \in \mathcal{E}, \tag{8}$$

$$f_{min}(j) \leq \mathbf{F}(j) \leq f_{max}(j) \quad \forall j \in \mathcal{E}, \tag{9}$$

$$\mathbf{C_{op}}(i) = \sum_{t \in \mathcal{T}} c_{op}(i, t) \mathbf{F_t}(i) t_{op}(t) \quad \forall i \in \mathcal{R}, \tag{10}$$

$$\sum_{t \in \mathcal{T}} \mathbf{F_t}(i) t_{op}(t) \leq avail(i) \quad \forall i \in \mathcal{R}, \tag{11}$$

$$\sum_{i \in \mathcal{R} \cup \mathcal{E}} f(i, l) \mathbf{F_t}(i) - \mathbf{EndUses}(l, t) = 0 \quad \forall l \in \mathcal{L}, \forall t \in \mathcal{T}, \tag{12}$$

$$\mathbf{F}(DHN) \geq \sum_{j \in DHN\_TECH} \mathbf{F}(j), \tag{13}$$

$$\mathbf{F}(DHN) \geq \%_{Peak} \max_{t \in \mathcal{T}} \{ \mathbf{EndUses}(HeatLowTDHN, t) \}, \tag{14}$$

$$\mathbf{Loss}(\mathrm{g},t)=\left(\sum_{i\in\mathcal{R}\cup\mathcal{E}|f(i,\mathrm{g})>0} f(i,\mathrm{g})\mathbf{F_t}(i)\right)\%_{loss}(\mathrm{g}) \quad \forall \mathrm{g}\in\mathcal{G},\forall t\in\mathcal{T}, \tag{15}$$

$$\mathbf{F_t}(j)+\mathbf{F_t}(k)\mathbf{Y_{Solar}}(j)\geq \frac{\mathbf{EndUses}(HeatLowTDHN,t)+\mathbf{EndUses}(HeatLowTDec,t)}{\mathrm{endUsesInput}(HeatLowTSH)+\mathrm{endUsesInput}(HeatLowTHW)}\sum_{t\in\mathcal{T}}\mathbf{F_t}(j)t_{op}(t),$$
$$k=DEC_{\mathbf{Solar}},\forall j\in HeatLowTDec, j\neq k,\forall t\in\mathcal{T} \tag{16}$$

$$\sum_{j\in\mathcal{E}}\mathbf{Y_{Solar}}(j)\leq 1, \tag{17}$$

$$\mathbf{F}(GRID)=1+\frac{9400}{c_{inv}(GRID)}\frac{\mathbf{F}(WIND)+\mathbf{F}(PV)}{f_{max}(WIND)+f_{max}(PV)}, \tag{18}$$

$$\begin{aligned}&\mathrm{STO}_{in,r}(t)+\mathbf{STO}_{out,r}(t)\leqslant 1 \quad \forall t\in\mathcal{T}\\ &0\leqslant\mathbf{F}_{t,in}(j)\leqslant\mathbf{STO}_{in,r}(j,t)\mathbf{F}(j)\eta(j) \quad \forall j\in\mathcal{S}_r,\forall t\in\mathcal{T},\\ &0\leqslant\mathbf{F}_{t,out}(j)\leqslant\mathbf{STO}_{out,r}(j,t)\mathbf{F}(j)\eta(j) \quad \forall j\in\mathcal{S}_r,\forall t\in\mathcal{T}\end{aligned} \tag{19}$$

$$\mathbf{SL}_{\mathrm{r}}(t)=\mathbf{SL}_{\mathrm{r}}(t-1)+\mathbf{F}_{t,in}(j)t_{op}(t)-\mathbf{F}_{t,out}(j)t_{op}(t) \quad \forall j\in\mathcal{S}_r,t\in\mathcal{T}. \tag{20}$$

A couple of constraints are dedicated for renewable energies. **Equations 16** and **17**, expressed in a compact nonlinear formulation, where the nominator and denominator represent the low-temperature heat demand in month t and in the whole year, respectively, render the model more realistic by defining the operating strategy for decentralized heating: the relative use of each technology in each period should be constant, except for the solar thermal (DecSolar): if solar thermal k is installed ($\mathbf{Y}_{\mathrm{Solar}}=1$), then at maximum, one technology j is used as backup. In order to reflect the impact of increasing penetration of intermittent renewables, particularly PV and wind, we assume the scale of power grid as a linear function expressed by **Eq. 18** in correspondence to the total installed capacity of PV and wind, with a specific additional investment cost of 9.4 billion CHF according to Moret (2017). Additionally, with increasing penetration of renewables, seasonal storage is regarded as an effective method in transferring excessive energy from peak to deficit periods. The technologies for seasonal storage in Energyscope involve: hydrogen storage and natural gas storage. Short-term storage, such as pumped hydro and battery storage, is not considered in the model due to time resolution incompatibility, typically in hourly or daily granularity. The lack of short-term storage technologies are not supposed to have obvious influence on the monthly-modelling results: on one hand, it is difficult to precisely predict the daily or hourly behaviors of the energy system in 2050, while the monthly-level data contribute to the alleviation of short-term fluctuations and by consequence regarded more stable; on the other hand, the short-term storage serves only as buffer and occurs merely in the daily level, implying no influence on the monthly net energy surplus or deficit that is determined by the difference of monthly demand and production. The associated data for the long-term storage technologies are listed in **Table 1**. In order to model the dynamics of the storage behavior of the energy system, two binary variables $\mathbf{STO}_{in,r}, \mathbf{STO}_{out,r}$ were introduced for the three storage resources r, respectively, subject to the constraints defined in **Eq. 19**. $\mathbf{STO}_{in}$ is set to be one in a storage-dominant month, and in correspondence $\mathbf{STO}_{out}$ is assigned to be zero in the same period. As a result, $\mathbf{F}_{t,in}$ represents the net storage (storage-release). Vice versa for a release-dominant month. This approach rules out the possible simultaneous storage and release within each period due to independent operations in different plants, facilitating the modeling on a national scale. Here, $\mathcal{S}_r$ represents the storage technologies (storing and releasing) for the resource r, and η denotes the capacity factor. Since the last two constraints in **Eq. 19** are *quadratic*, rendering the problem into an MINLP (Mix Integer Non-linear Programming), eight equivalent equations are introduced for linearizing the quadratic model in order to achieve computational effectiveness without loss of quality. The accumulated storage level *SL* for each storage resource r is given by a time-continuous and cyclic **Eq. 20**. Other constraints dedicated to carbon flows will be explained in **Section 3.2**.

TABLE 1 | Storage cost, summarized from Gorre et al. (2018) and Leeuwen and Zauner (2018).

	Storage method	c_{inv}[a] (€/kWh)	$c_{op,\ maint}$ (€/kWh)
Hydrogen	Salt caverns	0.036	0.00072
	High-pressure steel tanks[a]	33.33	0.49995
Methane	Depleted natural gas reservoir	0.009	0.00018
	Salt caverns	0.012	0.00024
	High-pressure steel tanks[b]	10.78	0.2156

[a]*The investment cost is based upon the maximal volume of storage, multiplied by the specific investment cost.*
[b]*Based upon 100 €/m³ capital expenditures; not integrated into Energyscope since it is commonly used for short-term storage.*

3.2. Carbon Flow Modeling

This section focuses on presenting the modeling approach for circular carbon flows in energy systems. The major carbon sources and sinks, as well as key technologies, are analyzed in **Sections 3.2.1.–3.2.4**, followed by **3.2.5** presenting the modeling concepts of carbon layers in Energyscope. In order to quantify the carbon flows, a parameter named carbon content linking the energy and carbon mass for each carbon resource and product r is defined by **Eq. 21**:

$$carbon\ content_r=\frac{m(C)}{m(r)^{*}\mathrm{LHV_r}} \tag{21}$$

where the $\frac{m(C)}{m(r)}$ denotes the carbon element mass fraction (%) of r, and the LHV_r refers to its *lower heating value*. Without specification, all mass–energy conversion in this article is based upon *LHV*.

Carbon management is considered by taking into account various carbon-containing resources, either biogenic or nonbiogenic, carbon sinks in the form of CO_2 capture technologies, CO_2 emissions from biomass conversion, as well as CO_2 utilization to produce synthetic chemicals and fuels. Apart from the conventional carbon balance between sources and sinks,

conversion of biogenic resources yields useful energy products but also CO_2 that can be considered a waste stream, which can be further transformed into useful products via different chemical synthesis routes. Both these conversion technology groups are used in the Energyscope model to fulfill a two-fold purpose. On one hand, the produced fuels and products from biomass or CO_2 are used to substitute fossil carbon with biogenic one, thus reducing the needs for conventional fossil resources, while at the same time, the circular utilization of CO_2 within the energy system itself leads to a significant reduction of the overall carbon emissions to the atmosphere. The use of **Eq. 21** enables not only the quantification of the carbon in each of the system flows, but also provides a method to help track the footprint of these contributing flows within the complex energy system.

3.2.1. Carbon Sources

- Biogenic carbon sources, including

  (1) domestic wood: waste wood, wood residues, and forest wood (soft and hard);
  (2) domestic wet biomass: sewage sludge, manure, industry waste, and household garbage;
  (3) domestic plant (crops): agriculture residues.

- Nonbiogenic carbon sources, including

  (1) fossil fuels import: NG (natural gas) and LFO (light fuel oil), diesel, gasoline, and jet-fuel (kerosene);
  (2) domestic fuels: nonbiogenic waste;
  (3) others: construction emission for technologies and direct cement manufacturing emission.

Coal import is not considered in this model due to the Swiss policy of phasing out coal. **Table 2** summarized the domestic biomass potential for energy usage by aggregating all the corresponding subcategories listed in the biogenic carbon sources. It is highlighted that only the sustainable part of the biomass potential was integrated in Energyscope.

In addition to domestic biomass resources, biofuel import contributes to the energy supply as well. In Switzerland, all nonbiogenic energy fuels depend on import, except nonbiogenic wastes. Among the carbon sources, cement manufacturing calls for special scrutiny due to the large amount of the direct emission from $CaCO_3 \rightarrow CaO + CO_2$. Approximately 60% (Dean et al., 2011) of CO_2 emissions from cement production arise from the calcination of limestone ($CaCO_3$) to form CaO (the main precursor for cement production), with the remaining emissions from the process of fuel utilization for heating the kiln and effecting the clinkering reactions (Bui et al., 2018). In Energyscope, the indirect emission of cement manufacturing associated with heat supply is reckoned in industry heat demand, while the direct emission that amounts to 1.62 Mt CO_2 per year (Zuberi and Patel, 2017) is counted separately with the hypothesis of a uniform distribution over all periods.

In 2017, Switzerland generated in total 80–90 Mt waste (FOEN, 2018), of which 86% stemmed from construction waste, including excavated waste (57 Mt) and deconstruction waste (17 Mt). Approximately 30% deconstruction waste went further to incineration and landfill. Additionally, 7% of the total waste is composed of the municipal solid waste (MSW), where 53% was recycled and the remaining 2.9 Mt went to incineration. The third-largest source, biogenic waste, took account of approximately 6% of the waste stock, including food waste, agricultural waste, and dry sewage sludge, etc. In order to avoid double counting the biomass, the waste in Energyscope refers to merely the nonbiogenic waste, i.e., the nonrecyclable MSW for energy usage: construction waste is not considered since it is accounted in the availability of wood; similarly, biogenic waste is incorporated into the wet biomass category. By this approach, the annual waste in 2017 amounts to 9.835 TWh, with an average LHV value of MSW 12.35 MJ/kg (Michel, 2012). We further assume an increase in waste availability by 42.8% in 2050 in correspondence to the estimation of GDP development by SECO (2020). One constraint (**Eq.22**) is integrated into the model reflecting the following two assumptions:

TABLE 2 | Domestic biomass potential for Switzerland, extracted from Burg et al. (2018).

	Wood	Wet biomass	Plant
Sustainable potential (GWh)	14,000	8,856	4,300
Total potential (GWh)	41,667	10,097	4,903

- waste generation rate is uniform over the year;
- waste can be neither accumulated nor exported, implying immediate disposal (e.g., burning in a CHP boiler) when generated.

$$\mathbf{F_t}(WASTE)\sum_{t'\in\mathcal{T}} t_{op}(t') = avail(WASTE), \tag{22}$$

where the *avail* represents the annual amount of waste generated within Switzerland.

3.2.2. Carbon Conversion Technologies

Conventional boilers, oil-based vehicles are the major technologies for conversing FEC to satisfy EUD with associated efficiencies. These technologies are mature and have been discussed in numerous articles. In this section, we focus on biomass-based technologies including the following:

- Pyrolysis: The thermal cracking of wood, or solid biomass in general, in the absence of oxidizing conditions. Pyrolysis can deliver a variety of products including gaseous, liquid, and solid mixtures of organic and inorganic compounds, depending on the operating conditions. The heating rate is prevalent among them, determining the intensity of the carbon bond scission and thus, the final distribution of the product mix. Although pyrolysis is considered to be the first step of biomass gasification in order to produce a gaseous fuel, a standalone process can be utilized and targeted

toward the production of bio-crude, a liquid hydrocarbon mixture that should undergo further treatment to produce biodiesel.

- Gasification: Woody biomass can be converted to a gaseous fuel stream comprised mainly CO and H_2 (syngas) and to a smaller extent CO_2 and CH_4 through gasification, a thermochemical process that employs biomass oxidation in substoichiometric conditions to favor the production of CO instead of CO_2. Different oxidizing media such as steam, air, or pure oxygen directly affect the product distribution in the outlet stream. Gasification is a mature technology that uses a variety of different reactor configurations depending on the intended use of the produced syngas. Temperatures inside the gasifier can reach up to 700°C and usually, the heat is partially provided by combustion of a fraction of the product gas. Syngas from the gasifier can be used in a diverse number of ways including the focus on gaseous fuel production such as H_2 or CH_4 as well as liquid fuel synthesis. Hydrogen production is controlled by the process setup including the type and operation of the gasifier, nature of the oxidizing medium, and operating conditions such as the reactor temperature and the feed stream composition. On the other hand, production of biomethane requires a subsequent upgrade of the syngas with reaction with H_2 results in enriching the product gaseous fuel in CH_4 as CO and CO_2 are converted into methane through the Sabatier reactions.
- Fischer–Tropsch synthesis: The Fischer–Tropsch (FT) reaction, first developed by Franz Fischer and Hans Tropsch in the 1920s, is a catalytic synthesis process realized as polymerization of carbon atoms. It is mainly used to produce synthetic biofuels from gasification-derived syngas. The chemical reaction is described by a simple representation of the form:

$$(2n + 1)H_2 + nCO \rightarrow C_nH_{2n+2} + nH_2O, \quad (23)$$

where n is the number of carbon atoms in the polymer chain. The conversion conditions (around 200–300°C and pressure in the range of tens of bars) are used to inhibit the formation of small alkanes, but rather push toward the production of long-chain hydrocarbons with carbon chains of 10–20 atoms, according to the Anderson–Schulz–Flory (ASF) distribution. The FT process uses catalysts to promote the growth of the carbon chain, with nickel or cobalt being the most commonly used ones. However, their low poisoning resistance to sulfuric derivatives dictates stringent syngas cleaning steps prior to insertion in the FT reactor. The produced hydrocarbon blend must then undergo hydrotreatment in order to obtain the desired biofuel quality. The addition of hydrogen in a subsequent hydrocracking reactor leads to the chemical cleavage of the long-chain hydrocarbons and under controlled conditions, the acquisition of a paraffin blend (biodiesel) of the desired quality.

- Anaerobic digestion: Anaerobic digestion (AD) is a biochemical process that is used to break the biogenic carbon of wet biomass and release it in the form of biogas, a gaseous mixture of CH_4 and CO_2. Digestion of wet biomass under anaerobic conditions is realized with the aid of suitable bacteria and proceeds through a complex series of (bio-)chemical reactions that can be grouped in four main stages, namely, hydrolysis, acidogenesis, acetogenesis, and methanogenesis. A set of parameters including the temperature and pH are decisive for the efficient operation of anaerobic digestion. In particular, three types of bacteria are used depending on the temperature of operation: thermophilic (45–55°C), mesophilic (25–45°C), and cryophilic (below 25°C). The production of methane is directly linked with the type of the employed bacteria and is positively affected by temperature; a direct compromise between methane production and energetic demands to sustain the operating temperature to levels above room temperature. Anaerobic digestion results also to a liquid by-product stream, the digestate, which contains all undigested biomass as well as the valuable nutrients originally in the feed stream. Due to the latter, digestate streams are mostly used nowadays as soil fertilizers. However, the high carbon content of this residual stream leaves room for additional retrieval in the form of fuels by hydrothermal treatment. The energy efficiency of anaerobic digestion greatly depends on both the nature of the digested biomass and the operating conditions. Together, they define the methane potential for each case (i.e., the produced volume of methane per mass unit of digestible matter). As the energetic content of methane is the only source of contained energy in the output biogas stream, the methane potential is a crucial parameter to define the energy efficiency of the process.
- Hydrothermal gasification (HTG): Hydrothermal gasification (HTG) offers the possibility of converting wet organic streams into methane using high pressure to reach supercritical water conditions in a complex reactor scheme. Compared to traditional gasification, it offers the advantage of utilizing the wet stream as it is, avoiding the preceding energy-intensive drying step. Moreover, water in its supercritical condition has a low density and dielectric constant. Consequently, it changes from polar to nonpolar solvent, and thus, the organic compounds dissolve easily in it. Furthermore, the supercritical conditions that prevail within the HTG reactor also ensure that the nitrous and phosphoric minerals contained in some forms of wet biomass such as sewage sludge and manure are released unharmed in the residual output stream. Apart from the direct processing of wet biomass streams, HTG can be used to convert the lignin-rich digestates from anaerobic digestion. On the drawbacks of the process stand the energy needed to reach the operating conditions (around the critical point of water, i.e., 370°C and 220 bars) as well as the use of a catalyst, which in turn requires special attention with regard to maintenance (poisoning prevention, degradation handling, etc.)

- Biomass to alcohols: Primary alcohols such as methanol and ethanol are not only individually used fuels, but also constitute chemicals used as the basis for the synthesis of higher fuels, e.g., aviation fuels. Alcohols can be produced from both woody and nonwoody biomass using different conversion pathways. Methanol can be produced from wood gasification followed by a synthesis step to convert the produced syngas. Ethanol is primarily produced via the biochemical fermentation of biomass crops such as corn, wheat, or sugarcane. Fermentation is usually preceded by pretreatment and handling steps such as milling and hydrolysis, which aims to isolate the sugars from the biomass matrix. Then, the biological degradation step is able to transform the sugars in chemicals of fuels such as ethanol depending on the design of the process.

3.2.3. Carbon Sinks

Two categories of carbon sinks are considered in Energyscope:

- natural carbon sinks: Biomass is regarded as a carbon sink in the process of biogenic formation. As presented, it serves also as a carbon source by combustion.
- artificial carbon sinks: CCUS, where the three processes, CC (carbon capture), CCS (carbon sequestration), and CCU (carbon utilization) are treated separately. Carbon capture occurs previously to the sequestration and utilization. The captured carbon has to be either stored or used.

In terms of CC process, two categories are distinguished according to their application fields: one is from large point sources with high CO_2 concentration where "conventional" carbon capture technologies could be deployed on large scales, such as a gas power plant, or a cement factory, etc. Three typical technologies are commonly applied in this category for mitigating the carbon emission, namely,

- postcombustion: One of the most relatively mature technologies for carbon capture. It applies to almost all industrial sectors, typically gas/coal power stations and heavy manufacturing plants. Carbon dioxide is captured from flue gases after combustion of fossil fuel at power stations or other large point sources. Postcombustion capture is most popular in research because existing fossil fuel power plants can be retrofitted to include CCS technology in this configuration (Sumida et al., 2012).
- precombustion: This applies to the majority of biofuels and chemical industry. There are several advantages and disadvantages compared to conventional postcombustion CC. The CO_2 is removed after the combustion of fossil fuels, but before the flue gas is expanded to atmospheric pressure. The capture before expansion, i.e., from pressurized gas, is standard in almost all industrial CO_2 capture processes, at the same scale as required for power plants (Bryngelsson and Westermark, 2009; Starr, 2009).
- oxy-fuel: The fuel is burned in oxygen instead of air in order to obtain an almost pure carbon dioxide stream that can be transported to the sequestration site or reused. The cement industry is considered one of the most promising application fields for deploying this technology.

By contrast, the other category of CC process is specified for the nonconcentrated carbon emission, typically involving transportation (including aviation) and other fugitive emissions, e.g., the emission to the atmosphere due to incomplete absorption/adsorption of conventional carbon capture technologies. These emissions are not supposed to be capturable except via natural carbon sinks (biomass) or DAC (direct air capture). As an emerging technology, the latter is commonly as much as 3–5 times that of conventional CC technologies.

Following carbon capture, either CCS or CCU should be applied. Carbon storage implies deposing the captured CO_2 into an underground formation for preventing release into the atmosphere in a long period, typically hundreds or thousands of years. According to the geological and geographical analysis conducted by Chevalier et al. (2010), Switzerland has a CCS potential in aquifer amounting to 2.7 billion tons that is approximately 67 times compared to the current anthropogenic emission 47.24 Mt/year (Stadler et al., 2019).

Different from carbon storage, carbon utilization consists in making use of the captured CO_2 to produce fuels or chemical products, such as methane, methanol, and ethylene. In these cases, CO_2 serves as a necessary raw material for production. Despite the relatively high cost compared to CCS, carbon utilization facilitates energy systems' coupling in transferring CO_2 among sectors as intermediate energy carriers. This feature, together with e-hydrogen (stemming from electrolysis), is promising in alleviating the increasing intermittency from massive penetration of renewables. The following section will present several typical CCU processes and their roles in the energy transition.

3.2.4. CO_2-to-X

In the context of the energy system decarbonization, CO_2 can be treated as a carbon source, an input material for the production of synthetic fuels and products. This is realized through a number of considered CO_2-to-X processing technologies, able to transform CO_2 to valuable outputs. The main considered CO_2-to-X technologies are listed below:

- Methanation: Methanation is a catalytic conversion process through which, CO_2 reacts with H_2 in order to produce synthetic methane. Methanation is often referred to as the Sabatier process and is described by the following chemical reactions:

$$\begin{aligned} CO_2 + 4H_2 &\leftrightarrow CH_4 + 2H_2O \\ CO + 3H_2 &\leftrightarrow CH_4 + H_2O \end{aligned} \tag{24}$$

Methanation requires moderate temperatures (in the range of 250C–350°C) and pressures as high as 20–25 bars. As the reaction makes use of a catalyst to aid with the conversion, the latter usually being nickel or cobalt, it is evident that the input streams

must be rid of any impurities such as sulfur and hydrocarbons that could poison the catalyst either by deactivation or by coke deposit.

- CO_2-to-diesel: Biodiesel, being a blend of mainly linear hydrocarbons, can be mainly produced through Fischer–Tropsch synthesis using a carbon source and hydrogen. In the examined case, captured CO_2 undergoes a shift reaction in order to create an input stream compatible with the prerequisites of the mainstream FT catalysts in terms of H/C ratio and is then inserted to the FT reactor along with a hydrogen-rich stream. As the origin of the utilized hydrogen plays no part in the operation of this particular process, it is assumed to be taken as a product from other processes such as water electrolysis.
- CO_2-to-jet-fuel: In a process similar to the above, captured CO_2 is used to synthesize a fuel blend through Fischer–Tropsch synthesis. Using appropriate composition tailoring of the produced mixture as well as subsequent fuel upgrading, a liquid blend similar to jet-fuels can be obtained. The bio-jet-fuel blend is assumed to be able to be used as a substitute for conventional fossil jet-fuels.
- CO_2-to-methanol-to-X: Methanol is one of the key chemical compounds, not only due to its use as a standalone chemical, but also its further application as a material for synthesizing other chemicals. It is thermochemically produced from CO_2 hydrogenation in a process that is similar to biodiesel synthesis. Methanol can be then further processed to give a variety of different useful chemicals. Low carbon chain olefins such as ethylene and propylene can be produced by catalytic conversion of methanol via dimethyl ether (DME) in a process known as methanol to olefins (MTO), which follows the following reaction scheme:

$$\begin{aligned} 2CH_3OH &\rightarrow CH_3OCH_3 + 2H_2O \\ CH_3OCH_3 &\rightarrow C_2H_4 + H_2O \\ 3CH_3OCH_3 &\rightarrow 2C_3H_6 + 2H_2O \end{aligned} \tag{25}$$

Both ethylene and propylene constitute chemicals that mainly represent building blocks for subsequent synthesis of polymers widely used in the plastics industry, namely, polyethylene and polypropylene, respectively, or raw materials for the production of other chemicals such as acetic acid. In this study, acetic acid can be either produced through either ethylene cracking or more directly, from carbonylation of methanol. Methanol itself can also be transformed into a mixture of aromatics, mostly benzene and toluene as well as a blend of xylenes (dominated by o- and p-xylene). The latter conversion process serves as a method of synthesizing the aforementioned aromatics directly from captured CO_2, despite its low energy yields due to various processing steps.

3.2.5. Carbon Flows

As stated, carbon flows with in-depth penetration of biomass and CO_2-to-X technologies are complicated in the presence of interconnected loops. **Figure 2** depicts the conceptual carbon flows in the system, where carbon sources are divided into biogenic and nonbiogenic parts:

- biogenic carbon inputs lead to at maximal net-zero emission; negative emission could be realized in the presence of BECCS.
- nonbiogenic carbon inputs result in at least net-zero emission. In reality, it is impossible to realize 100% carbon capture and as a result, nonbiogenic carbon emission keeps always positive.

In Energyscope, the carbon balance is handled by the CO_2 layers that behave as tanks with incoming carbon flows from various sources and outgoing flows to different locations. The following list summarizes the CO_2 layers defined in the MILP model:

- CO_{2A}: the carbon emission from carbon-intensive fields. This amount of carbon emission is capturable by applying conventional carbon capture technologies. In Energyscope, emissions from centralized thermal plants are computed into this category.
- CO_{2C}: the captured carbon, which is assumed to either be used or stored later; in this level, CO_2 storage could be further categorized as:
  - CO_{2S}: sequestration, where the CO_2 is buried into underground formation and cannot be reused;
  - CO_{2SS}: temporary storage, implying the CO_2 is capable of being used later.
- CO_{2E}: in contrast to CO_{2A}, the CO_{2E} refers to the carbon emission from nonconcentrated spot sources, e.g., a car or a household wood furnace. In addition, it includes the fugitive emission in conventional carbon capture processes, as well as the emission from construction periods. These emissions are not supposed to be mitigated without biomass photosynthesis or direct air capture (DAC). In Energyscope, all emissions stemming from decentralized (DEC) technologies belong to this category.

Figure 2 illustrates the relationship of the CO_2 layers defined in the model. All technologies are linked to one or more CO_2 layer(s) with corresponding emission factors. Through this approach, each technology in Energyscope emits or absorbs certain amount of CO_2 from corresponding layers, leading to the net emission in each period t expressed by:

$$\begin{aligned} \textbf{Emission}(t) &= \sum_{j \in \mathcal{E}, c \in \mathcal{C}} \mathbf{F_t}(j) t_{op}(t) \eta(j,c) \quad \forall t \in \mathcal{T} \\ \sum_{t \in \mathcal{T}: t \leqslant t'} \textbf{Emission}(t) &\leqslant \epsilon \quad \forall t' \in \mathcal{T}, \end{aligned} \tag{26}$$

where $\mathcal{T}$ represents the set of periods, and $\mathcal{C}$ denotes the carbon layers of CO_{2A} and CO_{2E} covering both concentrated and dispersed carbon emissions. η denotes the emission factor with unit $ktCO_2/GWh$ for the technology j in a certain layer c. Instead of limiting merely the annual emission, a more strict ϵ-control is

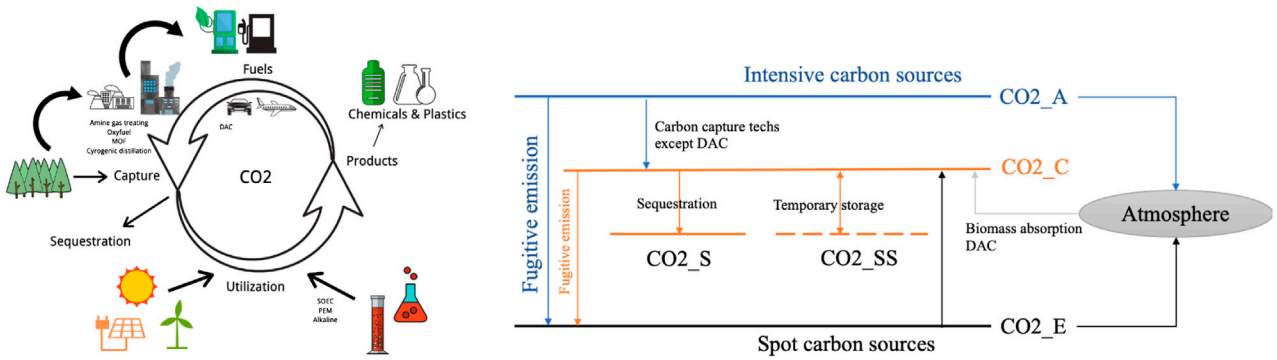

FIGURE 2 | Carbon flow modeling **(A)** circular carbon flow in energy systems, **(B)** modeling concept of CO_2 layers.

introduced to ensure that the total emission levels within all periods previous to t' ($t' \in \mathcal{T}$) do not reach the limit set by ϵ.

As illustrated in the **Figure 2B**, the captured CO_2 (CO_{2C}) can either be transformed to fuels and chemical products, or be stored temporarily or permanently (sequestrated underground). This concept is translated into **Eq. 27**:

$$\sum_{j\in\mathcal{CC}} \mathbf{F_t}(j) = \sum_{j\in\mathcal{CCS}} \mathbf{F_t}(j) + \sum_{j\in\mathcal{CCU}} \mathbf{F_t}(j) + \sum_{j\in\mathcal{CTS}_{\text{in}}} \mathbf{F_t}(j) - \sum_{j\in\mathcal{CTS}_{\text{out}}} \mathbf{F_t}(j) \quad \forall t \in \mathcal{T} \tag{27}$$

which reflects the carbon balance of carbon sources and sinks, where the inputs stem from all carbon capture technologies $\mathcal{CC}$, and the outputs flow to $\mathcal{CCS}$ and $\mathcal{CCU}$, representing all the carbon sequestration and utilization technologies, respectively. Specifically, the cost for a given CC or CCS technology $c(j)$ is expressed as Swiss franc per ton of CO_2 captured or sequestrated. This practice takes into account the whole lifespan of a technology into consideration. Therefore, the annual cost of a given CC or CCS technology j could be expressed by **Eq. 28**:

$$c(j)\sum_{t\in\mathcal{T}} \mathbf{F}_t(j)t_{op}(t) \quad \forall j \in \mathcal{CC}\cup\mathcal{CS}, \tag{28}$$

where $\mathbf{F_t}$ is of unit kt-CO_2 captured per hour.

4. HISTORICAL DATA AND ASSUMPTIONS ON SWISS ENERGY SYSTEM

4.1. Demand

Figure 3 illustrates the historical EUD in Switzerland and defines three scenarios according to JASM (2020): scenario REF representing the base scenario; scenarios HIGH and LOW depicting the high- and low-energy demands in respective sectors. This article adopts the scenario REF as the base scenario for analysis.

Additionally, plastics and chemicals demands are integrated into EUD (**Figure 4**) in order to have a holistic view on the carbon flow chains. It is assumed that the demands for chemicals and plastics in 2050 keep the same as 2017 due to a trade-off between increasing population and recycling rate. Intermediate products include ethane, ethylbenzene, benzene, propylene, ethylene, styrene, p-xylene, and toluene.

Transportation accounts for more than 1/3 of final energy consumption in the current Swiss system. The passenger and freight demand (excluding aviation) in 2050 are estimated to be 140,300 Mpkm (million passenger kilometer) and 39,700 Mtkm (million ton kilometer), respectively (Stadler et al., 2019). In terms of aviation, we distinguish the short-distance and long-distance flight, and estimate the demand via **Eq. 29**:

$$\sum_{i\in\mathcal{F},j\in\mathcal{C}} r(i)f(i,j), \tag{29}$$

where the r represents the share of flight category for short distance (within Europe) and long distance (outside Europe) in the flight set $\mathcal{F}$. The f indicates the conversion factor of energy consumption (unit MJ) with respect to 1 pkm EUD in different classes $\mathcal{C}$ (economy, business, and first class) for short- and long-distance aviation, respectively. This approach results in the specific weighted energy consumption for Swiss aviation: 2.1226 MJ/pkm, translated to 22.6 TWh kerosene equivalent (see **Supplementary Material**). This value corresponds well to the amount of kerosene consumption 21.4 TWh/y reported by Stadler et al. (2019). By taking a projection factor of 1.33 in 2050 compared to 2015 defined in Commission européenne and Direction générale de la mobilité et des transports (2016), the passenger aviation demand is estimated to be 50,800 Mpkm in 2050.

4.2. Current Energy Mix

As a country lacking fossil fuels, the current energy supply of Switzerland depends predominantly on imports. Petroleum products and natural gas accounted for approximately 60% in the energy mix. In the power sector, hydro power dominated with around 50% share, and wind and PV were developing rapidly [PV production in 2018 was roughly 40 times the value in 2008 according to BFE (2018a)]. First, we applied Energyscope on the energy system of Switzerland in 2017 for calibration. From the corresponding results shown in **Figure 5**, the renewable penetration accounted for around 30% in the Swiss FEC mix, associated with carbon emissions from fossil and nonfossil fuels 40.7 and 10.0 Mt/y, respectively.

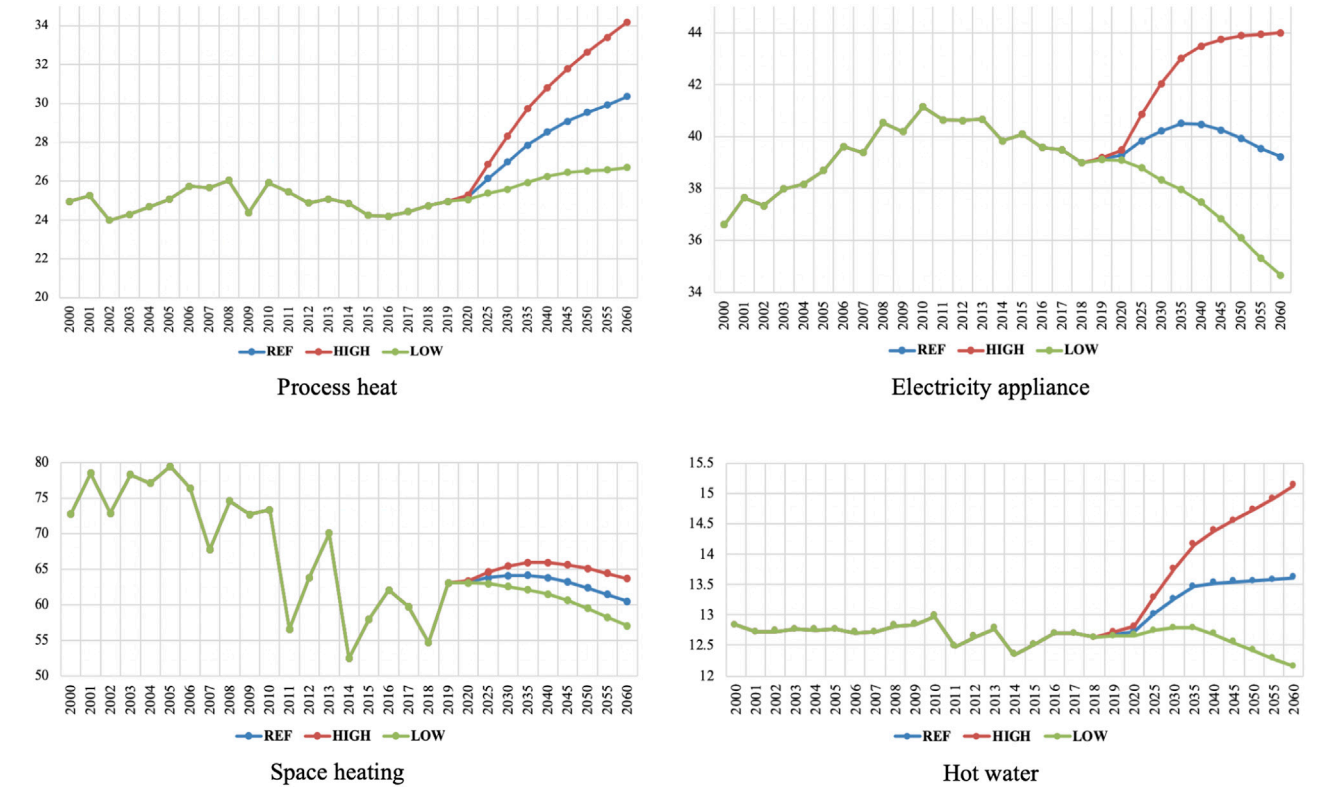

FIGURE 3 | History and projection of Swiss energy demand (TWh) for process heat, electricity appliance, space heating, and hot water in three scenarios.

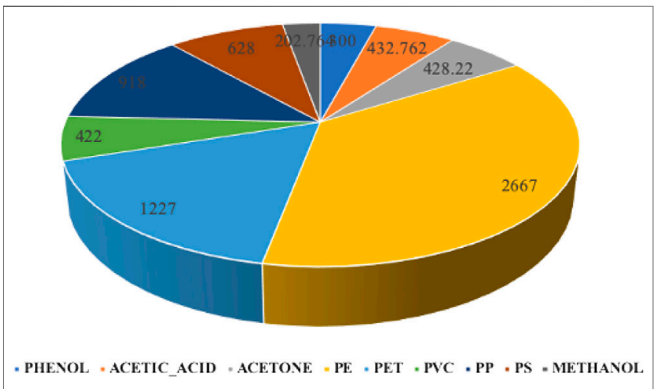

FIGURE 4 | Chemicals and plastics demand (GWh) of Switzerland, 2017.

5. DECARBONIZATION SCENARIOS

5.1. Scenario Definition

This section focuses on two issues: 1) Is it possible to realize carbon neutrality in 2050 for Switzerland? 2) If yes, what does the optimal energy system look like? First, the ϵ value of CO_2 limit is fixed to zero in **Eq. 26**, and second, two scenarios are defined:

- scenario a: allowing the utilization of fossil fuels
- scenario b: banning the utilization of fossil fuels

Additionally, electricity import is prohibited within both scenarios in order to realize power autonomy. The availability for wood, wet biomass, and plants (crops) follow the definition in **Table 2**. PV potential varies in literature: according to SFOE (2019), Swiss roofs and facades have the potential to generate 67 TWh of electricity per year, where 50 TWh is estimated from roofs larger than 10 m^2, and 17 TWh from walls for at least 20 m^2 average exposure to excellent sunlights with hypothesis that 45–60% of their surfaces can be covered with PV panels. Assouline et al. (2016) indicated the PV power production for urban areas in Switzerland in 2050 was expected to reach about 32 TWh. In this article, the maximal installed capacity of PV panels in Switzerland in 2050 is set to be 40 GW. Compared to the solar energy, the development potential for wind is limited and estimated to be 4.4 GW (BFE, 2018b) in 2050. **Table 3** lists the key assumptions in the scenarios.

In Energyscope, imported resources are regarded as nonstorable due to techno-economic consideration, implying "import only when needed". Domestic fuel products, such as hydrogen from electrolysis, are assumed to be storable. In the following paragraphs, the results of scenarios a and b are analyzed, respectively, with further discussion in **Section 5.3**.

5.2. Results

5.2.1. Net-Zero Emission With Fossil Fuels

The Sankey diagram in **Figure 6** illustrates the optimal carbon flows of the considered energy system with fossil fuel utilization.

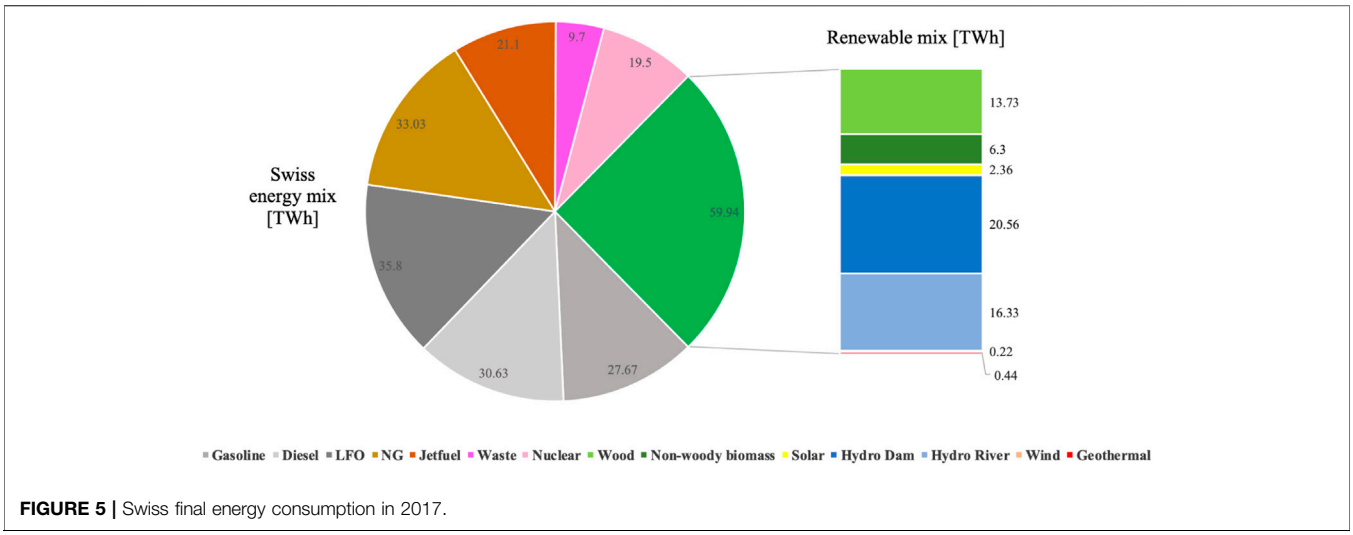

FIGURE 5 | Swiss final energy consumption in 2017.

TABLE 3 | Assumptions in Energyscope.

Parameter	Range		Note
	Min	Max	
Public mobility share in passenger transportation	21%	50%	The min is set to the value in 2017
Train ratio in freight transportation	37%	80%	The min is set to the value in 2017
Share of (bio) gasoline and (bio) diesel vehicles	20%	100%	The min value is based upon experts' opinion
District heating share in low-temperature heat supply	5%	70%	The min is set to the value in 2017
District heating loss	5%	5%	According to Moret (2017)
Geothermal share in district heating	0%	30%	Assumption
Transmission and distribution power loss	7%	7%	According to SFOE (2015)

The width of the arrow is proportional to the amount of carbon flow expressed as kt of C element per year. For instance, a part of CO_2 (CO_2E) in the atmosphere is captured by wood and then converted to diesel via FT (Fischer–Tropsch) process, which is further converted into CO_2 again after combustion in a truck engine, and is released back to the atmosphere, thus forming a closed loop that represents a complete carbon flow chain. In this figure, DHN, DEC, and IND represent district heating, decentralized technologies, and industrial energy supply technologies, respectively.

In terms of nonbiogenic carbon, natural gas import in this scenario amounts to 31.64 TWh/y, approximately the same level as today (33 TWh): the majority (84%) is used for power and heat supply, while 15% serves for transportation and the remaining part is transformed to methanol. Nonbiogenic waste is predominantly incinerated in combined heat and power plants. As the most important energy carriers, the two sources contribute to 3,780 kt-C/y. Other nonbiogenic carbon sources stem mainly from jet-fuel (excluding the biogenic part coming from ethanol upgrading), construction, and cement industry, as well as a small part of gasoline and diesel. The significant drop in fuel consumption results principally from deep electrification in the mobility sector. As for biogenic carbon, the saturation of domestic biomass sustainability is witnessed, translated to 2,829 kt-C/y contributing 27.2 TWh/y to the energy system. Wood is largely converted to hydrogen and diesel, while wet biomass is all consumed by hydrothermal gasification for producing synthetic natural gas. Plants are in majority converted to jet-fuel (441 kt-C/y) via fermentation processes.

Based upon the optimization results, chemicals and plastics depend mainly on import, except PVC, PE, and methanol, which could be synthesized from intermediate materials. 3% of the captured carbon (CO_{2C}) participates in the formation of chemicals/fuels/plastics with the remaining 97% being sequestrated underground. The results suggest that carbon neutrality for Switzerland in 2050 is theoretically feasible by exploiting domestic biomass up to its limit and deploying considerable CCS (5,820 kt-C) in order to offset nonbiogenic emissions. Neither natural gas storage nor hydrogen storage is observed in this case due to a higher cost of domestic synthesis compared to imports.

5.2.2. Net-Zero Emission Without Fossil Fuels

Scenario b aims at decarbonizing the energy system without importing fossil fuels. Similarly, biomass is fully exploited and the majority of biogenic carbon is converted to biogas and liquid biofuels. Waste serves as a major source for nonbiogenic carbon. With regard to the carbon sinks, CCS declines to 3,744 kt-C/y from 5,820 kt-C/y in scenario a, while CCU climbs due to the production of diesel (766 kt-C/y) and jet-fuel 663 kt-C/y, as well

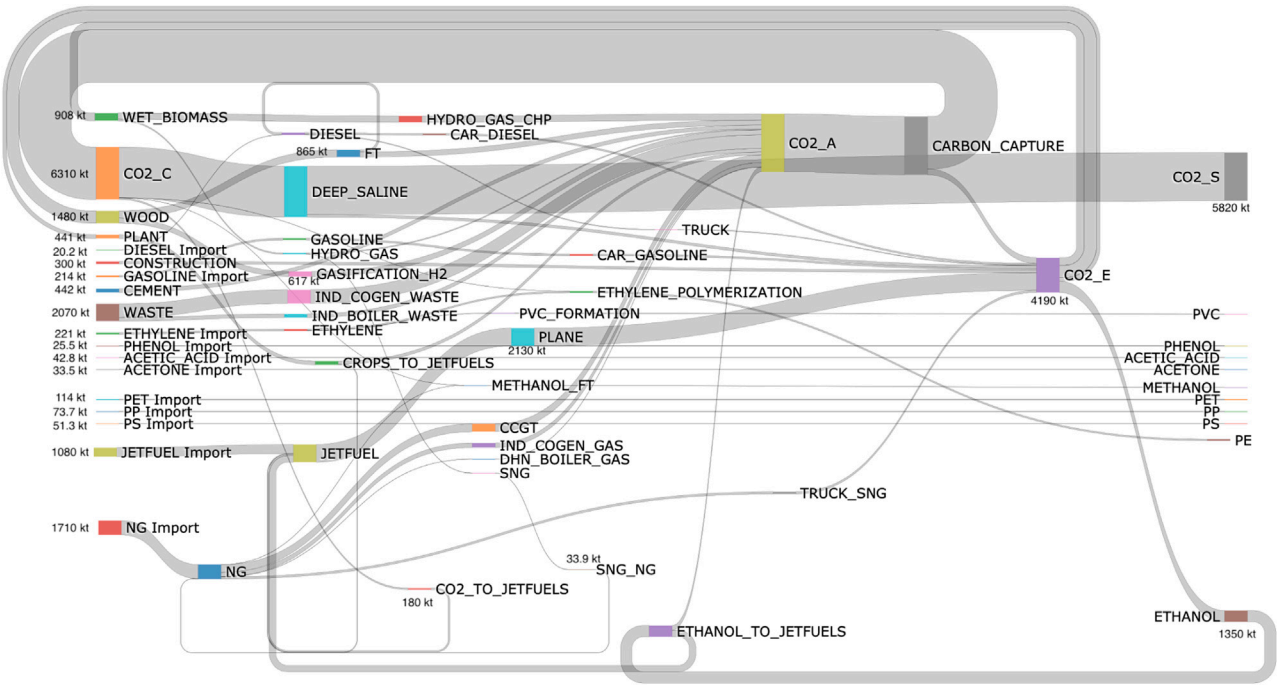

FIGURE 6 | Annual carbon flow (kt-C) in a net-zero-emission system with fossil fuel import.

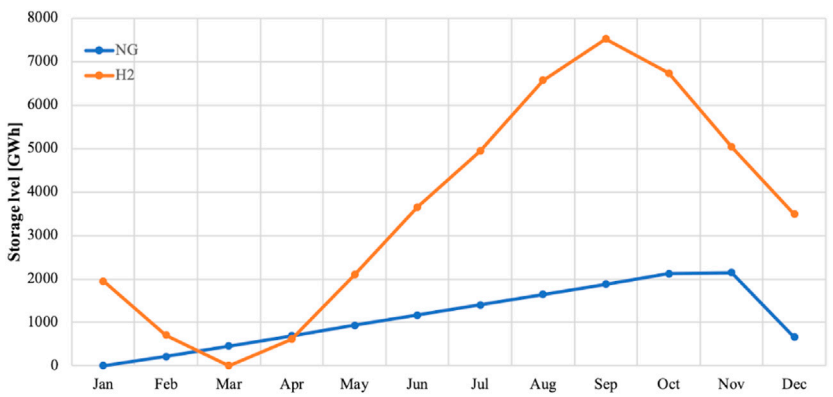

FIGURE 7 | Seasonal storage levels of natural gas and hydrogen (GWh).

as plastics (8 kt-C/y). The results demonstrate the dominance of CCS as the major negative emission technology and the principal role of CCU as clean fuel supplier.

In **Figure 9**, the annual natural gas storage level is represented via the loop NG → NG_STO → NG, where hydrogen storage is not included due to its zero carbon content. Furthermore, **Figure 7** depicts the monthly storage variation of both natural gas and hydrogen, where a continuous increase of hydrogen level is observed from March to September, after which the system starts to discharge. Similarly, natural gas storage begins in February and assumes the maximum in October. This trend corresponds well to the reverse-seasonality of PV production and energy demands: in summer, the energy surplus reaches the peak where the maximal storage level amounts to 10 TWh. As to the monthly variation of CO_2 storage level shown in **Figure 8**, the peak and the trough appear in winter and summer, respectively, in correspondence to the distribution of energy demand intensity of Switzerland.

Based upon the modeling results, a massive penetration of renewables is obligatory for realizing carbon neutrality: **Figure 10** reflects the output of renewable technologies (positive value) as well as electrolysis (negative value). Biomass is not included here since it is mainly used for fuel production as discussed previously. An obvious positive correlation is observed between electrolysis and the renewable power outputs, especially the intermittent renewables (PV and wind). Hydropower accounts for nearly

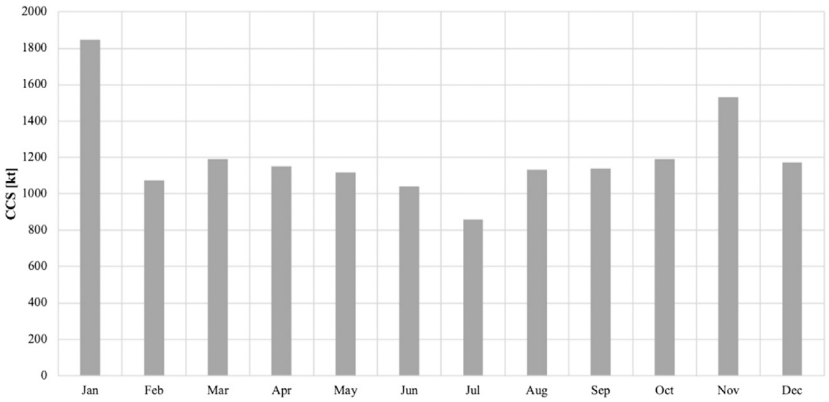

FIGURE 8 | Monthly carbon sequestration (kt-CO_2).

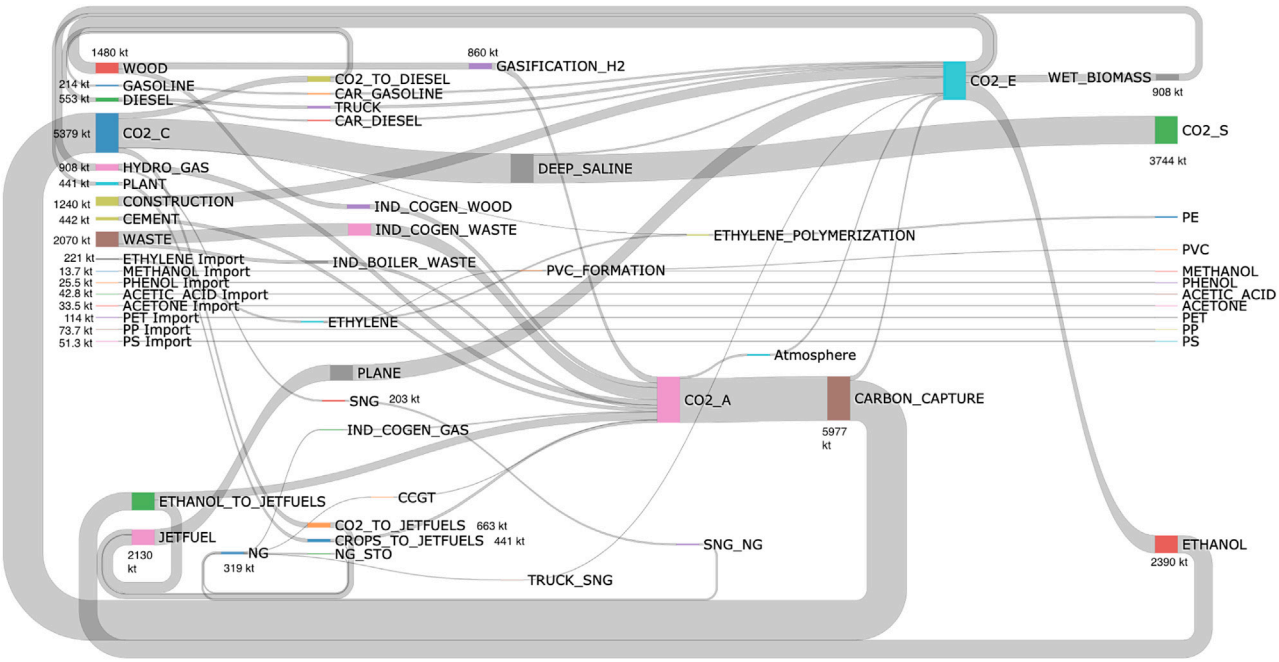

FIGURE 9 | Annual carbon flow (kt-C) in a fossil-fuel-free and net-zero-emission system.

half of the total renewable outputs and is distributed relatively uniformly among the months. In summer, PV and hydro contribute approximately the same amount of power to the system. Geothermal is predominantly used for heat supply in cold seasons.

5.3. Discussion

Table 4 summarizes the key findings on the carbon flows from the two scenarios. In the presence of fossil fuels, CCS is deployed on a large scale with limited CCU due to the relatively lower cost of imports than domestic production. Phasing out fossil fuels results in an explicit increase for CCU and a decline for CCS as a result of the deficit for fuels. CCU is capable of shifting emissions among different technologies and in different periods due to seasonal storage, which is yet not able to directly mitigate the anthropogenic carbon emission by nature, except the small part in plastics synthesis. However, CCU results in a steep decline of nonbiogenic carbon entering the energy system by providing alternative e-fuels and biofuels. From this perspective, all the carbon emissions stem originally from "above the ground" and circulate internally, implying no carbon accumulation in the energy system. Despite an increase of the total cost around 3.3 billion CHF/y, scenario b is considered more radical in terms of realizing fossil-free society and diminishing the overdependence on CCS, which may result in unexpected geologic impacts. It should be highlighted that the total cost of

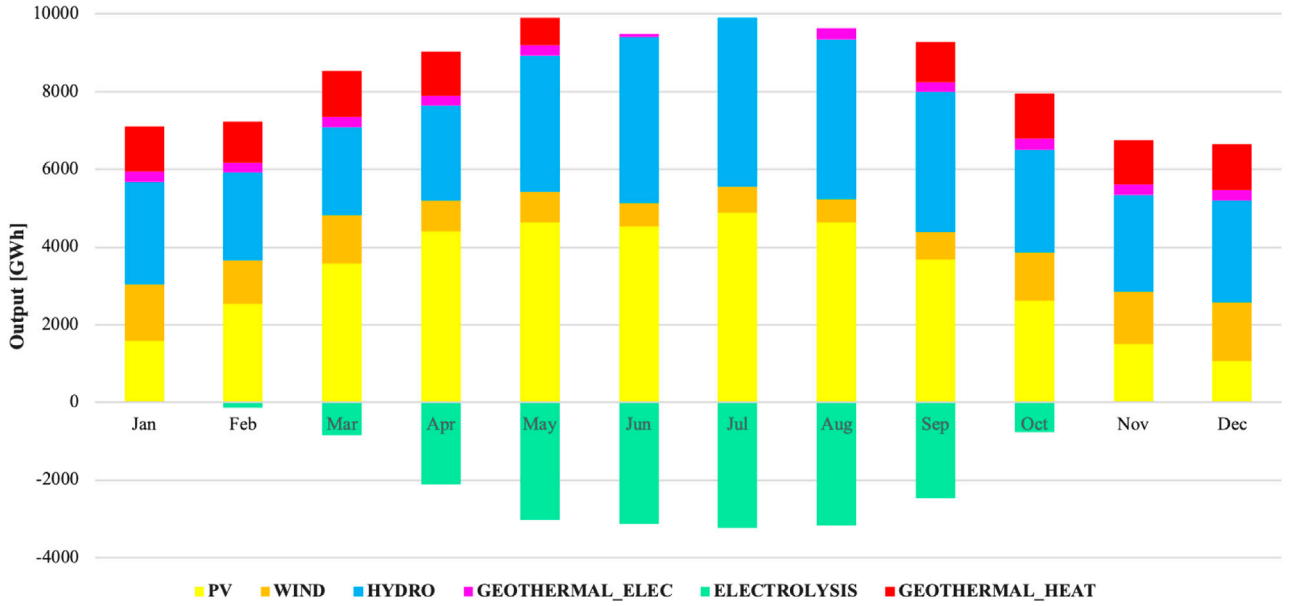

FIGURE 10 | Monthly production of renewables.

TABLE 4 | Scenario comparison.

	Scenario a	Scenario b
Total cost (MCHF/y)	25,152	28,451
Net carbon emission (kt-C/y)	0	0
Biogenic carbon inputs (kt-C/y)	4,179	5,219
Wood	1,480	1,480
Wet biomass	908	908
Plant (crops)	441	441
Ethanol import	1,350	2,390
Nonbiogenic carbon inputs (kt-C/y)	6,390.5	4,327.5
Fuel/construction/cement[a]	5,828.7	3,752
Chemicals/plastics	561.8	575.5
Carbon capture (kt-C/y)[b]	6,310	5,379
Carbon sequestration (kt-C/y)	5,820	3,744
Fugitive emission (kt-C/y)	301.3	198
Carbon utilization (kt-C/y)	188.7	1,437
Fuel	180	1,429
Chemicals/plastics[c]	8.7	8

[a]*Emission in cement manufacturing stemming from fuels not included.*
[b]*Including biogenic and nonbiogenic CC.*
[c]*Processes without direct participation of CO_2 are not included in CCU.*

the energy system is of large uncertainty depending predominantly on the specific investment and operational costs for the considered resources and technologies, which was discussed in the previous studies (Moret et al., 2017; Li et al., 2019). The results in this article are based upon the EUD projection in **4.1**, which could be further reduced by energy efficiency improvement, for instance, building renovation and innovative industrial process design, as well as lifestyle change, such as substitution of private cars by increasing bicycles. All these effective measures contribute to the acceleration of the decarbonization process and by consequence, reinforcing the plausibility of the realization of carbon neutrality illustrated in this study.

Concerning the limitations of this research: The infrastructures in the energy system are not fully modeled, e.g., the pipelines for hydrogen. In addition, the emission factors for each technology during construction in the future are based upon the present values that are supposed to decline due to the intensification of carbon mitigation. In terms of CCS, this model reports the amount of CO_2 needed to be sequestrated, but no further information on where to store and how to transport the CO_2 from sources to sinks. Therefore, it requires industrial pilot projects for further demonstration and benchmarking; in particular the development of biomass and CCUS technologies as well as auxiliary infrastructures.

6. CONCLUSION

This article comes up with a systematic methodology of modeling carbon flows in a complex energy system in favor of sustainable strategy decisions for the long-term energy transition toward a carbon-neutral society. It proposes an optimization approach for solving the complex carbon loop issues emerging from the massive penetration of renewables and CCUS technologies. Results demonstrate that a radical reformulation of the current energy system is obligatory, where the participation of biomass is indispensable. By quantifying the carbon flows among various sources and sinks, this article depicts the optimal configurations of the Swiss energy system in terms of techno-economic consideration, concluding the following:

- for nonbiogenic carbon: CCS serves as an absolute carbon sink in offsetting the nonbiogenic carbon inputs;
- for biogenic carbon: CCU with biogenic carbon sources strengthens the coupling of the whole system via power-to-X and energy storage, with net-zero (even negative) carbon emission.

In terms of Switzerland, biomass-based plants, waste incineration, and cement industry are the key areas for the deployment of carbon capture technologies. Although the applied case study is based on Switzerland, the modeling approach presented by this article is generic and applicable to different energy systems of different scales.

DATA AVAILABILITY STATEMENT

The original contributions presented in the study are included in the article/**Supplementary Material**, and further inquiries can be directed to the corresponding author.

AUTHOR CONTRIBUTIONS

XL for modeling, results analysis, and writing. TD for data management. SM for initial conceptual development of the modelling framework. The others for data collection and review.

FUNDING

The research work for this paper was financially supported by the Swiss Competence Center for Energy Research - Joint Activity Scenario Modeling (JASM). The research work for this paper was financially supported by the Swiss Competence Center for Energy Research - Biomass for Swiss Energy Future (BIOSWEET). The research work for this paper was financially supported by the Swiss National Science Foundation, the Swiss Federal Office of Energy as well as the Federal Office for the Environment. SM acknowledges partial support from the Swiss National Science Foundation (SNSF) under Grant no P2ELP2_188028.

SUPPLEMENTARY MATERIAL

The Supplementary Material for this article can be found online at: https://www.frontiersin.org/articles/10.3389/fenrg.2020.549615/full#supplementary-material

REFERENCES

Ackerman, F., Ishikawa, M., and Suga, M. (2007). The carbon content of Japan–US trade. *Energy Pol.* 35, 4455–4462. doi:10.1016/j.enpol.2007.03.010

Aichele, R., and Felbermayr, G. (2010). *Kyoto and the carbon content of trade*. Stuttgart, Germany: Hohenheim University, Vol. 69.

Assouline, D., Mohajeri, N., and Scartezzini, J. L. (2016). Solar photovoltaic electricity potential for Switzerland—SCCER FEEB&D. Available at: https://www.sccer-feebd.ch/solar-photovoltaic-electricity-potential-for-switzerland/[Dataset] (Accessed January 10, 2020).

BFE (2018a). Gesamtenergiestatistik, Bundesamt für Energie. Available at: https://www.bfe.admin.ch/bfe/de/home/versorgung/statistik-und-geodaten/energiestatistiken/gesamtenergiestatistik.html[Dataset].

BFE (2018b). Office fédéral de l'énergie - storymap Installations éoliennes. Available at: https://www.uvek-gis.admin.ch/BFE/storymaps/EE_WEA/index.php?lang=fr[Dataset].

Braune, A., Geiselmann, D., Oehler, S., and Ruiz Durán, C. (2019). Implementation of the DGNB framework for carbon neutral buildings and sites. *IOP Conf. Ser. Earth Environ. Sci.* 290, 012040. doi:10.1088/1755-1315/290/1/012040

Bryngelsson, M., and Westermark, M. (2009). CO2 capture pilot test at a pressurized coal fired CHP plant. *Energy Procedia* 1, 1403–1410. doi:10.1016/j.egypro.2009.01.184

Bui, M., Adjiman, C. S., Bardow, A., Anthony, E. J., Boston, A., and Brown, S. (2018). Carbon capture and storage (CCS): the way forward. *Energy Environ. Sci.* 11, 1062–1176. doi:10.1039/C7EE02342A

Burg, V., Bowman, G., Erni, M., Lemm, R., and Thees, O. (2018). Analyzing the potential of domestic biomass resources for the energy transition in Switzerland. *Biomass Bioenergy* 111, 60–69. doi:10.1016/j.biombioe.2018.02.007

Celebi, A. D., Ensinas, A. V., Sharma, S., and Maréchal, F. (2017). Early-stage decision making approach for the selection of optimally integrated biorefinery processes. *Energy* 137, 908–916. doi:10.1016/j.energy.2017.03.080

Chen, B., Yang, Q., Zhou, S., Li, J. S., and Chen, G. Q. (2017). Urban economy's carbon flow through external trade: spatial-temporal evolution for Macao. *Energy Pol.* 110, 69–78. doi:10.1016/j.enpol.2017.08.010

Chen, S., and Chen, B. (2017). Coupling of carbon and energy flows in cities: a meta-analysis and nexus modelling. *Appl. Energy* 194, 774–783. doi:10.1016/j.apenergy.2016.10.069

Chevalier, G., Diamond, L. W., and Leu, W. (2010). Potential for deep geological sequestration of CO2 in Switzerland: a first appraisal. *Swiss J. Geosci.* 103, 427–55. doi:10.1007/s00015-010-0030-4

Commission Européenne and Direction Générale de la Mobilité et des Transports (2016). *EU energy, transport and GHG emmissions: trends to 2050: reference scenario 2016* (Luxembourg: Office for Official Publications of the European Communities).

Creutzig, F., Ravindranath, N. H., Berndes, G., Bolwig, S., Bright, R., and Cherubini, F. (2015). Bioenergy and climate change mitigation: an assessment. *GCB Bioenergy* 7, 916–944. doi:10.1111/gcbb.12205

Dahiya, S., Kumar, A. N., Shanthi Sravan, J., Chatterjee, S., Sarkar, O., and Mohan, S. V. (2018). Food waste biorefinery: sustainable strategy for circular bioeconomy. *Bioresour. Technol.* 248, 2–12. doi:10.1016/j.biortech.2017.07.176

Dean, C. C., Blamey, J., Florin, N. H., Al-Jeboori, M. J., and Fennell, P. S. (2011). The calcium looping cycle for CO_2 capture from power generation, cement manufacture and hydrogen production. *Chem. Eng. Res. Des.* 89, 836–855. doi:10.1016/j.cherd.2010.10.013

FOEN (2018). Waste and raw materials: in brief. Available at: [Dataset].

Gorre, J., Van Leeuwen, C., and Ortloff, F. (2018). "Innovative large-scale energy storage tech- nologies and power-to-gas concepts after optimisation: store&GO D8.6: report on the optimal time profile and operation of the conversion technology during a representative year," in *The perspective of the available storage capacities*. STORE&GO Technical Rep. EU-H2020.

Gounand, I., Little, C. J., Harvey, E., and Altermatt, F. (2018). Cross-ecosystem carbon flows connecting ecosystems worldwide. *Nat. Commun.* 9, 1–8. doi:10.1038/s41467-018-07238-2

Hannula, I., and Reiner, D. (2017). *The race to solve the sustainable transport problem via carbon-neutral synthetic fuels and battery electric vehicles*. Cambridge, UK: University of Cambridge. Working paper. doi:10.17863/CAM.17544

IPCC (Editor) (2014). *Climate change 2014: mitigation of climate change: working group III contribution to the fifth assessment report of the intergovernmental panel on climate change* (New York, NY: Cambridge University Press)

JASM (2020). Database: the joint activity scenarios and modelling (JASM). Available at: https://sccer-jasm.ch/[Dataset].

Leeuwen, C., and Zauner, A. (2018). Innovative large-scale energy storage technologies and power-to-gas concepts after optimisation, STORE&G D8.3, report on the costs involved with PtG technologies and their potentials across the EU. STORE&GO Technical Rep. EU-H2020

Li, X., Moret, S., Baldi, F., and Marechal, F. (2019). Are renewables really that expensive? The impact of uncertainty on the cost of the energy transition. *Comput. Aided Chem. Eng.* 46, 1753–1758. doi:10.1016/B978-0-128-18634-3.50293-9

Limpens, G., Moret, S., Jeanmart, H., and Maréchal, F. (2019). EnergyScope TD: a novel open-source model for regional energy systems. *Appl. Energy* 255, 113729. doi:10.1016/j.apenergy.2019.113729

Madsen, J. S., Bach, L., Knudsen, K. B., Sørensen, M., and Holbech, C. (2018). From policy to action, state of green. State of Green Technical report.

Markard, J., Suter, M., and Ingold, K. (2016). Socio-technical transitions and policy change – advocacy coalitions in Swiss energy policy. *Environ. Innovat. Soc. Trans.* 18, 215–237. doi:10.1016/j.eist.2015.05.003

Michel, L. (2012). "Complémentarité entre plusieurs ressources énergétiques pour une même prestation," in *Le Cas Du Réseau de Chauffage à Distance de Lausanne*. PhD thesis. Geneve: Université de Geneve.

Moret, S., Codina Gironès, V., Bierlaire, M., and Maréchal, F. (2017). Characterization of input uncertainties in strategic energy planning models. *Appl. Energy* 202, 597–617. doi:10.1016/j.apenergy.2017.05.106

Moret, S. (2017). Strategic energy planning under uncertainty. No. 796. Ph.D. thesis. Paris: EPFL.

National Academies of Sciences, Engineering and Medicine (2018). *Bioenergy with carbon capture and storage approaches for carbon dioxide removal and reliable sequestration: proceedings of a workshop—in brief*. Washington, DC: The National Academies Press. doi:10.17226/25170

NLTimes (2017). New Dutch government's plans for the coming years. Available at: https://nltimes.nl/2017/10/10/new-dutch-governments-plans-coming-years [Dataset].

Peduzzi, E. (2015). Biomass to liquids: thermo-economic analysis and multi-objective optimisation. PhD thesis. Paris: EPFL.

Pfeffer, M., Wukovits, W., Beckmann, G., and Friedl, A. (2007). Analysis and decrease of the energy demand of bioethanol-production by process integration. *Appl. Therm. Eng.* 27, 2657–2664. doi:10.1016/j.applthermaleng.2007.04.018

Ramaswami, A., Chavez, A., Ewing-Thiel, J., and Reeve, K. E. (2011). Two approaches to greenhouse gas emissions foot-printing at the city scale. *Environ. Sci. Technol.* 45, 4205–4206. doi:10.1021/es201166n

Rinscheid, A., and Wüstenhagen, R. (2019). Germany's decision to phase out coal by 2038 lags behind citizens' timing preferences. *Nature Energy* 4, 856–863. doi:10.1038/s41560-019-0460-9

Santibañez-Aguilar, J. E., González-Campos, J. B., Ponce-Ortega, J. M., Serna-González, M., and El-Halwagi, M. M. (2011). Optimal planning of a biomass conversion system considering economic and environmental aspects. *Ind. Eng. Chem. Res.* 50, 8558–8570. doi:10.1021/ie102195g

SAPEA (2018). Novel carbon capture and utilisation technologies. Technical report. Science Advice for Policy by European Academies.

Schiffer, Z. J., and Manthiram, K. (2017). Electrification and decarbonization of the chemical industry. *Joule* 1, 10–14. doi:10.1016/j.joule.2017.07.008

SECO (2020). Staatssekretariat für Wirtschaft SECO. Available at: https://www.seco.admin.ch/seco/de/home.html [Dataset].

SFOE (2019). Les toits et les façades des maisons suisses pourraient produire 67 TWh d'électricité solaire par an. Available at: https://www.bfe.admin.ch/bfe/fr/home/actualites-et-medias/communiques-de-presse/mm-test.msg-id-74641.html[Dataset].

SFOE (2015). Swiss electricity statistics 2015. Swiss Federal Office of Energy Technical report.

SFOE (2020). What is the energy strategy 2050? Available at: https://www.bfe.admin.ch/bfe/en/home/politik/energiestrategie-2050/was-ist-die-energiestrategie-2050.html [Dataset].

Smith, P. (2016). Soil carbon sequestration and biochar as negative emission technologies. *Global Change Biol.* 22, 1315–1324. doi:10.1111/gcb.13178

Spaargaren, G., and Mol, A. P. J. (2013). Carbon flows, carbon markets, and low-carbon lifestyles: reflecting on the role of markets in climate governance. *Environ. Polit.* 22, 174–193. doi:10.1080/09644016.2013.755840

Stadler, Z., Meier, B., Friedl, M., Damartzis, T., Moret, S., and Li, X. (2019). Carbon flows in the energy transition. Technical report. Swiss Federal Office of the Environment.

Starr, F. (2009). Integrated gasification combined cycle for carbon capture & storage. Claverton Group Conference December 3, 2019. Available at: https://claverton-energy.com/integrated-gasification-combined-cycle-for-carbon-capture-storage.html.

Suciu, R., Girardin, L., and Maréchal, F. (2018). Energy integration of CO2 networks and power to gas for emerging energy autonomous cities in Europe. *Energy* 157, 830–842. doi:10.1016/j.energy.2018.05.083

Sumida, K., Rogow, D. L., Mason, J. A., McDonald, T. M., Bloch, E. D., and Herm, Z. R. (2012). Carbon dioxide capture in metal–organic frameworks. *Chem. Rev.* 112, 724–781. doi:10.1021/cr2003272

Zuberi, M. J. S., and Patel, M. K. (2017). Bottom-up analysis of energy efficiency improvement and CO_2 emission reduction potentials in the Swiss cement industry. *J. Clean. Prod.* 142, 4294–4309. doi:10.1016/j.jclepro.2016.11.178

Conflict of Interest: The authors declare that the research was conducted in the absence of any commercial or financial relationships that could be construed as a potential conflict of interest.

frontiers in Energy Research

ORIGINAL RESEARCH
published: 12 January 2021
doi: 10.3389/fenrg.2020.549298

Novel Multiplicity and Stability Criteria for Non-Isothermal Fixed-Bed Reactors

Jens Bremer[1]* *and Kai Sundmacher*[1,2]

[1]Process Systems Engineering, Max Planck Institute for Dynamics of Complex Technical Systems, Magdeburg, Germany, [2]Chair for Process Systems Engineering, Otto-von-Guericke University, Magdeburg, Germany

With the increasing need to utilize carbon dioxide, fixed-bed reactors for catalytic hydrogenation will become a decisive element for modern chemicals and energy carrier production. In this context, the resilience and flexibility to changing operating conditions become major objectives for the design and operation of real industrial-scale reactors. Therefore steady-state multiplicity and stability are essential measures, but so far, their quantification is primarily accessible for ideal reactor concepts with zero or infinite back-mixing. Based on a continuous stirred tank reactor cascade modeling approach, this work derives novel criteria for stability, multiplicity, and uniqueness applicable to real reactors with finite back-mixing. Furthermore, the connection to other reactor features such as runaway and parametric sensitivity is demonstrated and exemplified for CO_2 methanation under realistic conditions. The new criteria indicate that thermo-kinetic multiplicities induced by back-mixing remain relevant even for high Bodenstein numbers. In consequence, generally accepted back-mixing criteria (e.g., Mears' criterion) appear insufficient for real non-isothermal reactors. The criteria derived in this work are applicable to any exothermic reaction and reactors at any scale. Ignoring uniqueness and multiplicity would disregard a broad operating range and thus a substantial potential for reactor resilience and flexibility.

Keywords: fixed-bed reactors, multiplicity, uniqueness, back-mixing, stability, modeling, methanation (Sabatier) reaction, flexibility

OPEN ACCESS

Edited by:
Francois M. A. Marechal, École Polytechnique Fédérale de Lausanne, Switzerland

Reviewed by:
C. K. Cheng, Universiti Malaysia Pahang, Malaysia
Frederic Marias, Université de Pau et des Pays de l'Adour, France

***Correspondence:**
Jens Bremer
bremerj@mpi-magdeburg.mpg.de

Specialty section:
This article was submitted to Process and Energy Systems Engineering, a section of the journal Frontiers in Energy Research

Received: *05 April 2020*
Accepted: *31 August 2020*
Published: *12 January 2021*

Citation:
Bremer J and Sundmacher K (2021) Novel Multiplicity and Stability Criteria for Non-Isothermal Fixed-Bed Reactors. Front. Energy Res. 8:549298. doi: 10.3389/fenrg.2020.549298

INTRODUCTION

Currently, we see many incentives for more sustainable chemicals and energy carrier production based on CO_2 and H_2. Chemical reactors for CO_2 hydrogenation play a crucial role in setting up sustainable production chains (e.g., via Fischer–Tropsch synthesis, CO_2 methanation, CO methanation, methanol synthesis, reverse water-gas shift). Especially for chemical energy conversion systems, as currently evaluated in the context of Power-to-X, these reactors are decisive for the overall process efficiency. Moreover, sustainable production increasingly demands for more flexible usage of chemical reactors accessing broader operation ranges and faster load changes. Encountering these new challenges demands a reassessment of former perspectives on reactor design and operation.

Due to the exothermic nature of most CO_2 hydrogenations, strong heat releases may result in harmful temperature excursions within the reactor interior, influencing catalyst lifetime, process safety, and performance. Cooled fixed-bed reactors allow for effective heat management and better controllability (Bremer and Sundmacher, 2019). These polytropic

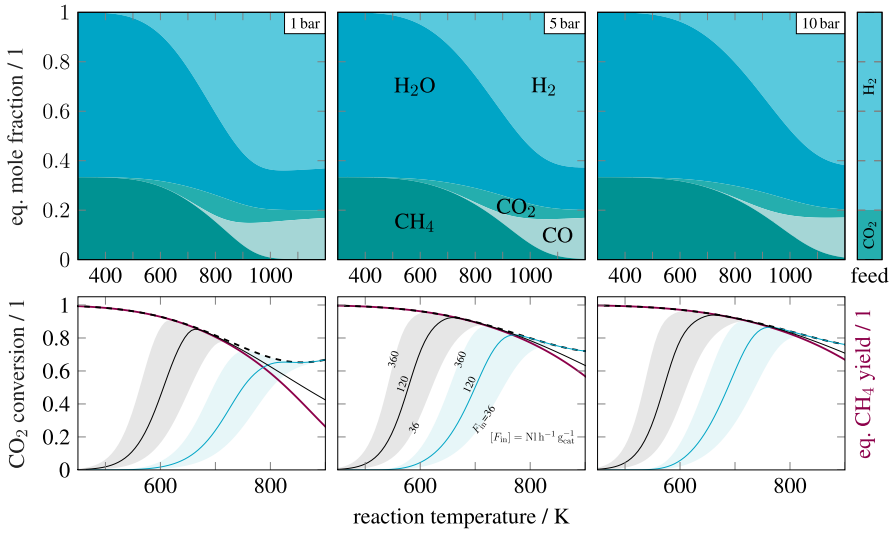

FIGURE 1 | Mole fractions at chemical equilibrium **(top row)** and kinetic conversion **(bottom row)** over temperature for pure, stoichiometric feed (H_2/CO_2 = 4) at different pressures and flows, computed via Gibbs-free-energy minimization, kinetic model according to Koschany et al. (2016) (—) and Xu and Froment (1989) (—), equilibrium CO_2 conversion (- - - -), equilibrium CH_4 yield (—).

reactor concepts are often the first choice for the hydrogenation of CO_2 (Kopyscinski et al., 2010; Wood et al., 2012; Biollaz and Schildhauer, 2016).

However, designing and operating polytropic fixed-bed reactors is a rather challenging task, due to a variety of possible physiochemical phenomena (e.g., runaway, parametric sensitivity), which can lead to performance losses or critical process failures (see e.g., Kreitz et al., 2019; Kiewidt and Thöming, 2019; Moioli et al., 2019; Theurich et al., 2019; Fache et al., 2020; Fischer and Freund, 2020; Zimmermann et al., 2020). Such instances correlate with features from systems theory, i.e., uniqueness, multiplicity, and stability. Much work has been done in this direction for ideal plug flow tubular reactors (PFTRs) and continuous stirred tank reactors (CSTRs), providing explicit criteria based on fundamental reactor parameters (Zaldívar et al., 2003; Szeifert et al., 2007; Dochain, 2018). However, real polytropic reactors with finite back-mixing are yet inaccessible for these criteria and are therefore usually subject to qualitative descriptions.

This work intends to review the current perspective on uniqueness and multiplicity of real polytropic reactors under non-isothermal conditions and demonstrates their close connection to stability. Therefore, we perform a bifurcation analysis on a cascade of CSTRs with unlimited stage numbers. As a result, novel criteria for uniqueness and multiplicity are derived that underline the importance of back-mixing within fixed-bed reactors, even at an industrial scale. The theoretical discussions are exemplified for CO_2 methanation — a highly exothermic reaction that is currently under intensive investigation for future energy storage.

Carbon Dioxide Methanation

The key reaction for methanation of CO_2 and H_2 reads

$$CO_2 + 4H_2 \rightleftharpoons CH_4 + 2H_2O, \quad \Delta_R\tilde{H}^0 = -164.9\ \mathrm{kJmol^{-1}}. \quad (1)$$

Methanation is one of several possibilities to activate the inert carbon dioxide. Further reactions are, for instance, dry reforming, reverse water-gas shift (RWGS), and methanol synthesis. Among these reactions, CO_2 methanation is thermodynamically the most favored, as it exhibits the lowest Gibbs free energy of reaction in a temperature range from ambient to 900 K ($\Delta_R\tilde{G}^0 = -142\,\mathrm{kJmol^{-1}}$) (Wenzel, 2018). As depicted in **Reaction 1**, CO_2 methanation also features a strong exothermicity, such that lower temperatures shift the chemical equilibrium to the product side. This fact is supported by **Figure 1**, which shows the result of chemical equilibrium calculations assuming stoichiometric feed over a wide temperature range and for technical relevant pressures (thermochemistry data taken from Lemmon et al., 1998; Haynes, 2017).

Figure 1 also illustrates two relevant kinetic models for nickel catalysts. The model from Koschany et al. (2016) differs significantly at temperatures above 700 K and shows higher methane contents due to the exclusion of carbon monoxide. Xu and Froment (1989), in contrast, considered the CO methanation and RWGS reaction to account for carbon monoxide. This was certainly motivated by the lower activity, which achieves sufficient conversions only at higher temperatures where CO formation becomes relevant. Although CO methanation and RWGS reaction certainly occur, they are not favored at elevated pressures and temperatures below 800 K. An

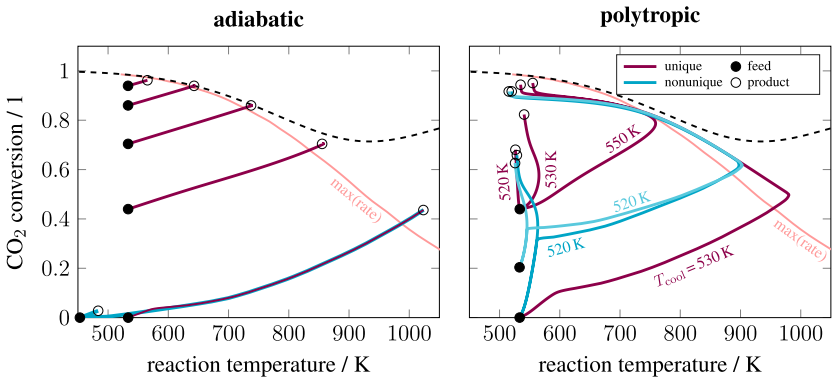

FIGURE 2 | State-space diagram for adiabatic and polytropic reactors with exemplary reaction pathways, reactor length: 2 m, pressure: 5 bar, reaction: CO_2 methanation according to Koschany et al. (2016), equilibrium CO_2 conversion (- - - -).

analysis of thermodynamic limitations is comprehensively illustrated by Gao et al. (2012), who also showed possible amounts of solid carbon under CO_2 excess. More detailed calculations are presented by Kiewidt (2017), who identified considerable amounts of solid carbon at feed ratios $H_2/CO_2 < 3.2$.

Regardless of the many details on chemistry, this work considers methanation mainly as a well-studied and highly relevant reference reaction. However, the presented results and criteria are easily applicable to other exothermic reactions.

Reactor Concepts for Exothermic Reactions

Reactor concepts for exothermic reactions are mainly determined by the expected temperature rise and the corresponding heat generation. In order to assess the temperature increase, the adiabatic temperature rise (ATR) is considered as an appropriate worst-case estimate. The ATR is defined as

$$\Delta T_{\mathrm{ad}} = \frac{c_{\mathrm{CO_2}}\left(-\Delta_R \tilde{H}\right)}{\rho_{\mathrm{gas}} c_{p,\mathrm{gas}}} = \frac{w_{\mathrm{CO_2}}\left(-\Delta_R \tilde{H}\right)}{M_{\mathrm{CO_2}} c_{p,\mathrm{gas}}}, \tag{2}$$

and exemplary evaluated for methanation at standard, stoichiometric feed conditions

$$\Delta T_{\mathrm{ad}}^{0} = \frac{0.845\,(164'900\ \mathrm{J mol^{-1}})}{0.044\ \mathrm{kg mol^{-1}}\, 2'950\ \mathrm{J kg^{-1}\, K^{-1}}} = 1073.5\ \mathrm{K}.$$

Looking at **Eq. 2** reveals that the ATR is pressure-independent, since $\Delta_R \tilde{H}$ and $c_{p,\mathrm{gas}}$ depend exclusively on temperature under ideal gas conditions. Although a higher pressure leads to more reactants and thus more heat generation, the gas heat capacity increases simultaneously and compensates for a further temperature rise. The temperature dependence of the ATR is also rather negligible.

Technologically, this large temperature increase is answered with a series of adiabatic or polytropic fixed-bed reactors (with or without product recycles). **Figure 2** illustrates exemplary state-space diagrams for both concepts. Which concept is used for a particular application is often driven by several aspects (e.g., plant size, product quality, costs, safety, reliability, flexibility). However, for modern hydrogenation, we see an increasing application of polytropic fixed-bed reactors (Kopyscinski et al. 2010).

Switching the reactor concept from adiabatic to polytropic (e.g., by cooled multi-tubular bundle reactors) potentially enables a lower catalyst volume, fewer reactor stages, better heat management, and the elimination of gas recycling. Nevertheless, such reactors are more difficult to construct and maintain (e.g., in case of catalyst replacements), which is, in particular, difficult for process scale-up. Hence, the performance benefit must outweigh the increased complexity of the reactor. In the context of gas-to-liquids, Fischer–Tropsch synthesis is an example of the successful use of multi-tubular reactors on a large scale (Wood et al., 2012).

Figure 2 also highlights the relevance of uniqueness. Under certain conditions, both adiabatic and polytropic reactor concepts allow for nonunique operating states (here illustrated for CO_2 methanation with respect to cooling or inlet temperature). Especially for polytropic reactors, these nonunique states allow for large conversions and reduced peak temperatures in one single reactor stage, even for undiluted feeds (Bremer and Sundmacher, 2019). Furthermore, uniqueness is very much related to potential reactor runaways and is, thus, relevant to guarantee safe operation. Consequently, a clear determination of uniqueness is of great value for the design and operation of real non-isothermal fixed-bed reactors but has not been sufficiently addressed in the literature yet. This work shall contribute to close this gap and proceeds with a brief literature overview on state-space multiplicity.

State-Space Multiplicity

State-space multiplicity of fixed-bed reactors is differentiated in extrinsic and intrinsic (Bremer and Sundmacher, 2019), whereas this work exclusively deals with the intrinsic version. There are numerous sources for intrinsic state-space multiplicity. Three

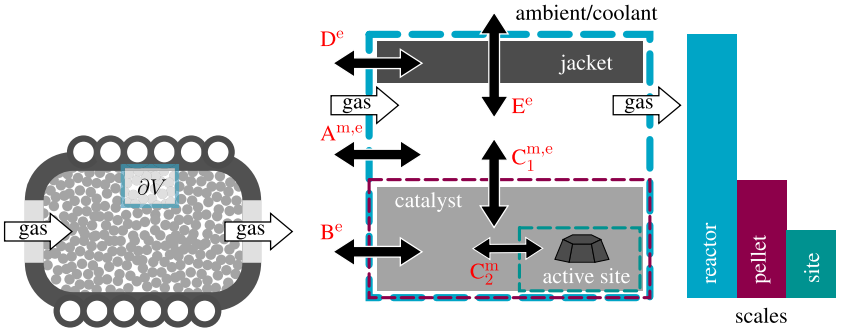

FIGURE 3 | Flux network and sources A to E for intrinsic multiplicity within fixed-bed reactors, double arrows indicate mass (m) and/or energy (e) fluxes to be part of the respective source.

scales are in particular of interest: the scale of the active site, the catalyst pellet (including pores), and the reactor (Sheintuch, 1987). **Figure 3** illustrates all three scales and the corresponding multiplicity sources (A to E) that have been most discussed in the literature.

These sources typically relate to mass and energy fluxes within a reactor control volume (∂V) and their natural drive to equalize temperature and concentration differences caused by reactive sources and sinks. All fluxes are determined by corresponding transport resistances and linked in a network connecting scales and phases. Depending on inlet and surrounding conditions of the control volume, some resistances are rate-determining for the overall mass and energy transport. According to conservation laws, at steady state all fluxes, sources, and sinks are in equilibrium. A change of inlet and surrounding conditions disturbs the entire network, and a new flux equilibrium emerges. At reactor scale, there exists a unique flux equilibrium if all individual fluxes are unique and if inlet and surrounding of the control volume are not influenced by the control volume itself. If the control volume influences its inlet and/or surrounding (e.g., due to back-mixing), multiple flux equilibria, and, thus, multiple steady states are possible. This interaction is typically denoted as feedback at reactor scale. Similarly, these feedbacks may also occur at catalyst and site scale due to the interaction with neighboring scales.

When steady-state multiplicities in fixed-bed reactors are observed (either numerically or experimentally), they often result from several sources simultaneously. In order to assign the observed multiplicity to the correct source, careful evaluation of each source is required. Therefore, Sheintuch (1987) divided intrinsic multiplicity sources from **Figure 3** into three classes:

- purely kinetic (C_2^m),
- isothermal (A^m, C_1^m),
- thermo-kinetic (A^e, B^e, C_1^e, D^e, E^e).

Purely kinetic sources belong to mass transport at the active site induced by nonlinear kinetics (e.g., adsorption vs. reaction) (Nibbelke et al., 1998), concurrent reactions/reaction networks (Balakotaiah and Luss, 1983; Elnashaie and Elshishini, 1993; Nibbelke et al., 1998; Mohl et al., 2001), or catalyst deactivation (Gilles, 1977; Eigenberger, 1983). *Isothermal* sources arise from mass transport at catalyst (diffusion) (Morbidelli et al., 1986; Lee et al., 1987) or reactor scale (convection, dispersion). *Thermo-kinetic* sources are mainly caused by nonisothermicities, which influence the nonlinear reaction rate coefficients according to the Arrhenius relation (Eigenberger, 1972a; Heinemann and Poore, 1982; Wagialla and Elnashaie, 1995).

Furthermore, multiplicities are also able to propagate through different scales and along with spatial directions. As a result, a large amount of multiple steady states (in theory up to infinity) at reactor scale can be produced by only a few (typically three) multiple steady states at pallet or site scale (Lee et al., 1987; Arce and Ramkrishna, 1991; Nibbelke et al., 1998). Due to the variety of different sources and their ability to propagate through scales, literature (going back to the early 60s) reports very differently or even controversially about total number, relevant sources, and necessary conditions of multiple steady states in fixed-bed reactors. This aspect is demonstrated by a brief literature review in **Table 1**.

As shown in **Table 1**, the investigation of steady-state multiplicity is mainly performed via cell models and dispersion models (see **Materials and Methods**). Both model types have been used to outline the two theoretical limiting cases: a reactor without and with an infinite number of multiple steady states. The dominating opinion is that the ideal PFTR is free of any state-space multiplicity due to the absence of transport in countercurrent direction (feedback). However, some studies opposed that the ideal PFTR is rather characterized by an infinite number of steady states (Liu and Amundson, 1962; Wagialla and Elnashaie, 1995; Nibbelke et al., 1998). These studies refer to the fact that the continuum description of an ideal PFTR corresponds to a series of infinite CSTRs. Assuming that the ignition can occur at any CSTR within the series gives rise to an ignition possible at any position along the reactor axis. This thought experiment allows for discontinuous solutions in packed-beds, which is often correlated to multiple steady states of single particles (Arce and Ramkrishna, 1991) or active sites (Nibbelke et al., 1998). Although the confusing concept of infinite solutions was discussed very controversially, it was certainly the main

TABLE 1 | Review on multiplicity sources within fixed-bed reactor models and experiments.

Active Source Figure 3	Class	# MSS	Bo^m, Bo^e Eq. 4	Model Type	References
None	None	1 (stable)	$\rightarrow\infty^{m,e}$	Id. PFTR	Schmitz and Amundson (1963), Sinkule et al. (1976a), Varma (1980), Jensen and Ray (1982)
None	None	∞	$\rightarrow\infty^{m,e}$	Id. PFTR	Liu and Amundson (1962), Wagialla and Elnashaie (1995), Nibbelke et al. (1998)
Pseudo-homogeneous models (lumped gas and solid phase)					
A^e, B^e, E^e	tk	1^{exp}, 2^{exp}	100^e	DM	Kalthoff and Vortmeyer (1980)
$A^{m,e}$, B^e, E^e	tk	1, 2 (stable)	$40–1'900^m$, $3–160^e$	DM	Puszyński et al. (1981)
$A^{m,e}$, B^e, E^e	tk	1, 3, 5, 7	$1–5^{m,e}$	DM	Heinemann and Poore (1981), Heinemann and Poore (1982)
$A^{m,e}$, B^e, E^e	tk	1, 3, 5	$1–320^m$, $1–100^e$	DM	Jensen and Ray (1982)
$A^{m,e}$, B^e	tk	1^{exp}, 2^{exp}, 3	300^m, $8^{e,exp}$, 30^e	DM	Wedel and Luss (1984)
A^e, B^e, E^e	tk	1, 3	$10–10'000^e$	DM	Pita et al. (1989)
A^m, C_2^m	k,i	∞	$1-\infty^m$	CM, DM	Nibbelke et al. (1998)
C_2^m	k,i	1, 3, 5	∞^m	CM, DM	Nibbelke et al. (1998)
$A^{m,e}$, B^e	tk	1, 2, 3	$6^{m,e}$	DM	Dochain (2018), Dramé et al. (2008)
Heterogeneous models					
$A^{m,e}$	tk	∞	$100–300^{mg,eg}$	DM	Liu and Amundson (1963)
B^e, E^e	tk	1, 3, 5	280^{ec}	DM	Eigenberger (1972a), Eigenberger (1972b)
$A^{m,e}$, $C_1^{m,e}$	tk	∞	$9.5–43^{mg}$, $40–172^{eg}$	CM, DM	Sinkule et al. (1976b)
C_1^m	i	1, 3	∞^{mg}	DM	Morbidelli et al. (1986), Lee et al. (1987)
A^m, C_1^m	i	1, 3, 5, 7, 9	$0 < Bo^{mg} < \infty$	DM	Lee et al. (1987)
A^m, C_1^m	i	1, 3	0^{mg}	DM	Lee et al. (1987)
A^m, C_1^m	i	∞	0^{mg}	CM	Arce and Ramkrishna (1991)
$A^{m,e}$, B^e	tk	1, 3, ∞	$40^{mg,eg}$, $> 40^{eg}$	CM	Wagialla and Elnashaie (1995)
C_1^m	i	∞	∞^{mg}	DM	Trinh and Ramkrishna (1996)
A^m, C_1^m	i	∞	$1–10^{mg}$	DM	Trinh and Ramkrishna (1997)
B^e, C_2^m	tk,k	∞	Similar to (Eigenberger, 1972a)	CM, DM	Nibbelke et al. (1998)
$C_1^{m,e}$	tk	1, 3	$\infty^{mg,eg}$	DM	Dommeti et al. (1999)
B^e, $C_1^{m,e}$	tk	1, 3, 5, 11	$\infty^{mg,eg}$, $50–3'000^{ec}$	DM	Agrawal et al. (2007)
$A^{m,e}$, B^e, E^e	tk	1, 3, 5	$0–560^{eg}$, $0–5'600^{ec}$, $0–1'680^{mg}$	DM	Bostandzhiyan and Shkadinskii (2010)
Purely experimental studies—comprehensive reviews given by Padberg and Wicke (1967), Wedel and Luss (1984), Harold and Luss (1985), Adaje and Sheintuch (1990)					
		2^{exp} (stable)			Puszyński and Hlavacek (1984), Adaje and Sheintuch (1990)
		4^{exp} (stable)			Harold and Luss (1985)

m - mass; e - energy; g - gas; c - catalyst; exp - experimental; k - kinetic; i - isothermal; tk - thermo-kinetic; CM - cell model; DM - dispersion model; MSS - multiple steady states.

driver behind many investigations. Thereby, two objectives became the most relevant for technical applications: Firstly, the ability to operate at various states promises performance improvements. Secondly, state-space uniqueness is of great value for safety reasons (e.g., to avoid runaways).

Apart from ideal reactors, many studies in **Table 1** also focus on real reactors considering finite Bodenstein numbers (see definition in **Materials and Methods**) within dispersion models or finite numbers n of representative CSTRs within cell models. As shown in Levenspiel (1999), both concepts are interchangeable due to the relation

$$\frac{1}{n} = \frac{2}{\mathrm{Bo}} - \frac{2}{\mathrm{Bo}^2}\left(1 - \exp(-\mathrm{Bo})\right), \quad \text{and}$$
$$n = \frac{\mathrm{Bo}}{2} \quad (\text{if } \mathrm{Bo} > 100). \tag{3}$$

Besides the different model concepts, various assumptions are made in order to uncover the influence of specific sources of steady-state multiplicity. Therefore, the studies in **Table 1** differ in many aspects of the model constitution (e.g., heterogeneous vs. homogeneous, isothermal vs. non-isothermal, first-order reaction vs. Langmuir-Hinshelwood Hougen-Watson-type reaction, with vs. without radial dispersion). For instance, the use of isothermal reactor models eliminates all thermo-kinetic multiplicities and allows for investigations on purely kinetic and/or isothermal multiplicities. On the contrary, the study of purely thermo-kinetic multiplicities is preferably done in the absence of kinetic and isothermal multiplicities.

Most studies dealing with *thermo-kinetic multiplicity* sources agree that axial dispersion of heat plays a vital role in the existence of multiple steady states in fixed-bed reactors. Eigenberger (1972b), in particular, argued that heat conduction through the solid phase (source B^e) must reduce an infinite multiplicity to a finite number of multiple steady states. The author also identified a maximum number of three or five multiple steady states, depending on the boundary conditions of the solid phase. It took about 20 years before this finding was revised. Therefore, Nibbelke et al. (1998) extended the model of Eigenberger (1972b) and considered a reaction kinetic with multiplicities at the active site (source C_2^m). The authors could prove that an infinite number of steady states is maintained even if axial heat dispersion through the solid phase is incorporated. Unfortunately, this research direction is still very narrow, which is certainly due to the fact that the required heterogeneous model is a rather sophisticated

numerical tool for such analyses. The use of pseudo-homogeneous models provides a possible remedy. Although pseudo-homogeneous models are not able to distinguish between energy transport in source A and B, their results point in the same direction. By making use of dimensionless model formulations and bifurcation techniques Heinemann and Poore (1981), Jensen and Ray (1982), Heinemann and Poore (1982) classified several aspects that also contribute to the existence of multiplicity. Both stated that a nonadiabatic reactor with unequal Bodenstein numbers for heat and mass dispersion shows a unique solution, either for sufficiently high values of the Bodenstein numbers, large heat transfer coefficients, or small values of the Damköhler number. These conditions also hold for industrial fixed-bed reactors; such that multiplicity was found to be relevant even for technical configurations (Puszyński et al., 1981; Pita et al., 1989). This is reflected in **Table 1** by the broad range of Bodenstein numbers in which multiple steady states are observed. In most investigations, the number of three multiple steady states is confirmed. Beyond that, some studies report up to eleven multiple steady states. However, experimental evidence above four multiple steady states was not found. For instance, Wedel and Luss (1984) validated their results with an experimental setup for CO and CO_2 methanation in a fixed-bed of 25 cm in length and 2.5 cm in diameter. The authors could reproduce predicted model solutions of one ignited and one extinguished state with identical feed concentration. Therefore, a one-dimensional axial dispersion model, which accounts for the diffusion-reaction interactions within the pellets, was found to be well suited for multiplicity analysis. Since their experimental setup has a low bed length and, thus, a low Bodenstein number ($Bo^e = 8$), conclusions for industrial reactors are rather limited. Nevertheless, the good agreement between model and experiment verified and proved that state-space multiplicity is of significance within fixed-bed reactors. More recently, Agrawal et al. (2007) pointed out that the often reported high number of multiple solutions originates from the assumption of constant transport coefficients, which leads to many fragile solutions that emerge from unstable branches. Accounting for the variation of heat and mass transfer coefficients with local flow and reaction properties eliminates these nonphysical solutions. For this reason, recent works are often motivated to add more physical meaning to their models. This allows to additionally focus on effects of secondary order (e.g., flow maldistributions, localized hot-spots, spatial and spatiotemporal patterns) (Sheintuch, 1997; Trinh and Ramkrishna, 1997; Jaree et al., 2001; Papadias et al., 2001; Marwaha and Luss, 2003; Agrawal et al., 2007; Viswanathan et al., 2008; Nekhamkina and Sheintuch, 2012), which is, however, not object of this work. Similarly, stable oscillatory solutions are also disregarded in this work, since they are unlikely to occur in fixed-bed reactors on an industrial scale due to their high thermal inertia (Jensen and Ray, 1982).

In order to identify the full operating range of fixed-bed reactors, this work considers state-space multiplicity as a crucial feature. Therefore, thermo-kinetic sources are of major interest, since purely kinetic and isothermal multiplicities are reported to be rather fragile. The literature survey from above reveals that axial dispersion, as well as the diffusion-reaction interaction, are essential model components to obtain consistent results. However, for specific applications, these studies rather provide trends than generally valid correlations and criteria. The impact of several simultaneously interacting features is certainly the main reason for this obstacle. Furthermore, the operation at unstable states is also underrepresented in the literature and needs further elaboration (see e.g., Bremer and Sundmacher, 2019). Therefore, the following sections intend to provide more insights and propose general criteria that unifies the aspects uniqueness, multiplicity, and stability.

MATERIALS AND METHODS

Analyzing chemical fixed-bed reactors requires to incorporate a variety of physicochemical interactions and is often motivated by models from first-principles. Solving these models can lead to a challenging computational task due to the complex coupling of mass, energy, and momentum transport. However, putting all available details into consideration is not always necessary. For instance, the basic phenomena described in this work are fully representable by mass and energy transport alone, which agrees well with previous works (see **Table 1**). In addition to physical assumptions, the considered control volume boundary also determines the relevant balance components. This differentiation meets the two *ideal reactor* concepts for continuously operated reactors:

- the ideal CSTR,
- the ideal PFTR.

The CSTR concept often considers a control volume around the entire reactor volume (integral balance). In contrast, the control volume for the ideal PFTR typically refers to an infinitesimally small volume segment within the reactor volume (differential balance). The PFTR allows to describe in detail spatial distributions of the reactors state variables (e.g., temperature and mass fraction), but also requires higher numerical efforts. Both ideal reactors also represent the two limiting cases for back-mixing/axial dispersion, which is typically measured by the axial Bodenstein number for mass and energy according to

$$\mathrm{Bo}^{\mathrm{m}} = \frac{v_z L}{\mathscr{D}_z}, \quad \mathrm{Bo}^{\mathrm{e}} = \frac{v_z \rho_{\mathrm{gas}} c_{p,\mathrm{gas}} L}{\lambda_z}, \tag{4}$$

which are essential for later discussions. In case of an ideal CSTR the reactive volume is fully mixed ($\mathscr{D}_z = \lambda_z \to \infty$, $\mathrm{Bo}^{\mathrm{m}} = \mathrm{Bo}^{\mathrm{e}} \to 0$), whereas in case of the ideal PFTR no back-mixing/dispersion exists ($\mathscr{D}_z = \lambda_z \to 0$, $\mathrm{Bo}^{\mathrm{m}} = \mathrm{Bo}^{\mathrm{e}} \to \infty$) (Levenspiel, 1999).

Real reactors, as considered in this work, are allocated right in between these two limiting cases. The corresponding model approaches are

- the CSTR cascade (tanks-in-series model, cell model),
- the tubular reactor model with axial dispersion (dispersion model, continuous model).

In order to represent real reactors more accurately, the control volume might also differentiate between bulk gas phase and catalyst phase. Two model concepts are commonly applied:

- the pseudo-homogeneous model (no phase distinction),
- the heterogeneous model (phase distinction with interfacial and intraparticle mass and energy transport).

Depending on the considered model, the energy dispersion coefficient in **Eq. 4** is considered differently. The pseudo-homogeneous model lumps solid and gas phase, which requires an effective energy dispersion term ($\lambda_z = \lambda_z^{\mathrm{eff}}$). On the contrary, the heterogeneous model allows for the distinction between gas and catalyst-phase dispersion and, thus, accounts for two separate energy-based Bodenstein numbers ($\mathrm{Bo}^{\mathrm{eg}}$, $\mathrm{Bo}^{\mathrm{ec}}$). For real fixed-bed reactors, the mass-based Bodenstein number is reported to be three to ten times higher than the energy-based Bodenstein number (Puszyński et al., 1981; Bostandzhiyan and Shkadinskii, 2010). Thus, energy back-mixing is the dominating axial dispersion mechanism within fixed-bed reactors (Mears, 1976). Note that some studies define the here stated Bodenstein number as Péclet number. In this work, these numbers are distinguished by the characteristic length, which is the reactor length L for the Bodenstein number and the particle diameter d_{p} for the Péclet number.

Both model concepts offer different levels of sophistication, e.g., one-, two-, or three-dimensional spatial resolution, stationary or dynamic, with or without axial dispersion. How sophisticated a model needs to be is often rated by criteria (e.g., Mears' criterion), which incorporate dominating transport phenomena and reactor design. A comprehensive overview is provided by Pérez-Ramírez (2000). Besides these criteria, distinct model or transport components may be examined separately. This decoupling approach is well-established to identify and analyze, for instance, different sources of state-space multiplicity. In this context, Nibbelke et al. (1998) emphasized that the identification of multiplicity sources is inevitable for a correct interpretation of numerical and also experimental results. This observation is crucial for the construction of adequate reactor models as well as for optimal reactor operation and control.

In the following, a single pseudo-homogeneous CSTR model is used to represent fully mixed reactive conditions and to illustrate its implications on uniqueness, multiplicity and stability. Afterward, the single CSTR is extended to a series of CSTRs (cell model) in order to approach conditions as they prevail in real fixed-bed reactors. All investigations are exemplified for methanation under realistic reactive conditions.

RESULTS

As indicated by the previous section, back-mixing is an essential feature that determines multiplicity. In order to show how this applies to real reactors, the following derivations shall serve as a guideline for multiplicity analysis, exemplified for catalytic methanation. Beginning with the well-known limiting case of a fully mixed reactive volume illustrates the fundamental parameters that characterize the range and intensity of multiplicity.

CSTR Analogy

The technical relevance of this limiting case can be found, for instance, with Berty reactors, which are widely used for catalyst characterization. Although the relationships presented here are already state of knowledge, they are crucial for later excursions toward industrial-scale fixed-bed reactors. Further on, a CSTR model as described in **Supplementary Section S1** is used. The required mass and energy balances read accordingly:

$$\text{mass balance}: \; X_{\mathrm{CO_2}} = \frac{\tau}{\varepsilon} \frac{\mathrm{R_{meth}}\left(T, p, w_\alpha\right)}{c_{\mathrm{CO_2,in}}}, \tag{5}$$

$$\text{energy balance}: \; X_{\mathrm{CO_2}} = \frac{(1+\mathrm{St})}{\Delta T_{\mathrm{ad}}}\left(T - T_{\mathrm{op}}\right). \tag{6}$$

Consequently, steady-state operation of a single CSTR is governed by the equality of **Eqs. 5** and **6**. In order to evaluate unique and non-unique operating points, **Supplementary Table S1** provides a reference setting that corresponds to carbon dioxide methanation in a fixed-bed reactor including realistic parameter ranges.

The six key parameters in **Supplementary Table S1** are highlighted in bold and result in **Figure 4** for variations of the operating temperature and **Figure 5** for variations of the Stanton number. The operating temperature is given in **Supplementary Eq. S19** and reflects changes in coolant and inlet temperature, whereas the Stanton number mainly results from changes in the coolant heat transfer. The left side of both figures shows that under realistic conditions, multiple equilibrium (or operating) points are indeed attainable, similar to the theoretical discussions in **State-Space Multiplicity**. The right side in both figures illustrates how hysteresis emerges when the operating temperature varies within realistic ranges. Apart from variations in operating temperature and Stanton number, one might also consider variations of the residence time τ. Higher residence times correspond to higher Damköhler numbers and increase the curvature of the mass balance operating curve (**Eq. 5**) and, thus, increase the hysteresis.

These results explicitly show that under perfect back-mixing at most three operating points are attainable, whereas two are stable (OP 1 and OP 3) and one is unstable (OP 2). As seen in the upper right figures, the unstable operating points are always surrounded by stable ones and cover a significant part of the attainable conversion range. If these unstable states are ignored for reactor design and operation, a significant potential might get lost. This clearly demonstrates the close connection between multiplicity and stability. Here, the generalized criterion for stability of a CSTR at a certain operating point is known to result from mass and energy-based sensitivities according to

$$\left.\frac{\mathrm{d}X}{\mathrm{d}T}\right|_{\mathrm{OP}} = \frac{\tau}{\varepsilon\, c_{\mathrm{in}}} \left.\frac{\mathrm{dR}}{\mathrm{d}T}\right|_{\mathrm{OP}} < \frac{1+\mathrm{St}}{\Delta T_{\mathrm{ad}}}, \tag{7}$$

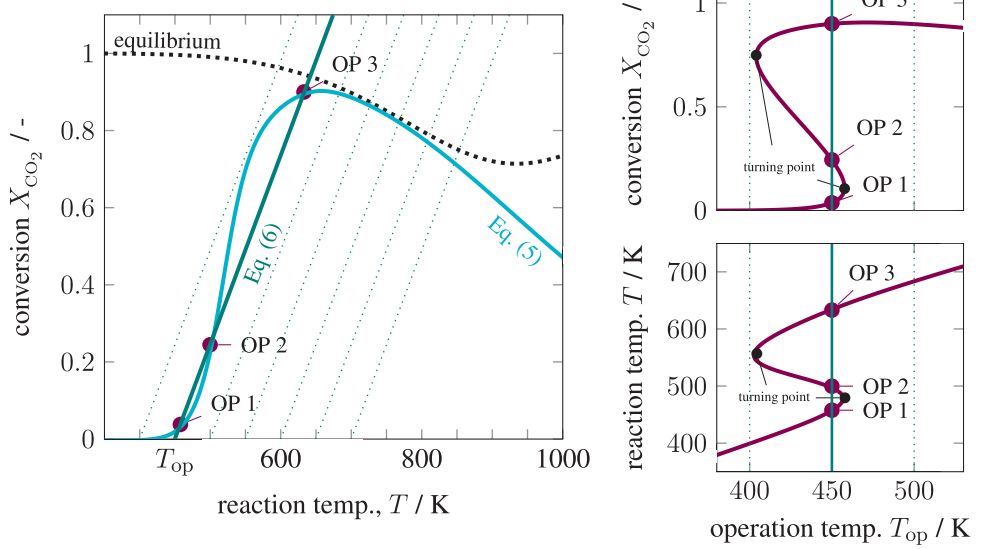

FIGURE 4 | State-space diagram for mass and energy balance **(left)** and for all equilibrium points **(right)** under variation of the operating temperature, reference setting taken from **Supplementary Table S1**.

which is equivalent to the criteria proposed by van Heerden (1953) and Gilles and Hofmann (1961). Note that sensitivities might also be considered with respect to other parameters than temperature. However, this work focuses primarily on thermo-kinetic multiplicities, for which temperature sensitivities are the most relevant. The mass-based sensitivity may be further evaluated by resolving the total differential at constant τ and c_{in}, such that

$$0 = \frac{\mathrm{d}X}{\mathrm{d}T} - \frac{\tau}{\varepsilon\, c_{in}} \frac{\mathrm{d}R}{\mathrm{d}T} = \frac{\mathrm{d}X}{\mathrm{d}T} - \frac{\tau}{\varepsilon\, c_{in}} \left(\frac{\partial R}{\partial T} + \frac{\partial R}{\partial X} \frac{\mathrm{d}X}{\mathrm{d}T} \right)$$

$$\Rightarrow \quad \frac{\mathrm{d}X}{\mathrm{d}T} = \frac{\dfrac{\tau}{\varepsilon\, c_{in}} \dfrac{\partial R}{\partial T}}{1 - \dfrac{\tau}{\varepsilon\, c_{in}} \dfrac{\partial R}{\partial X}}.$$

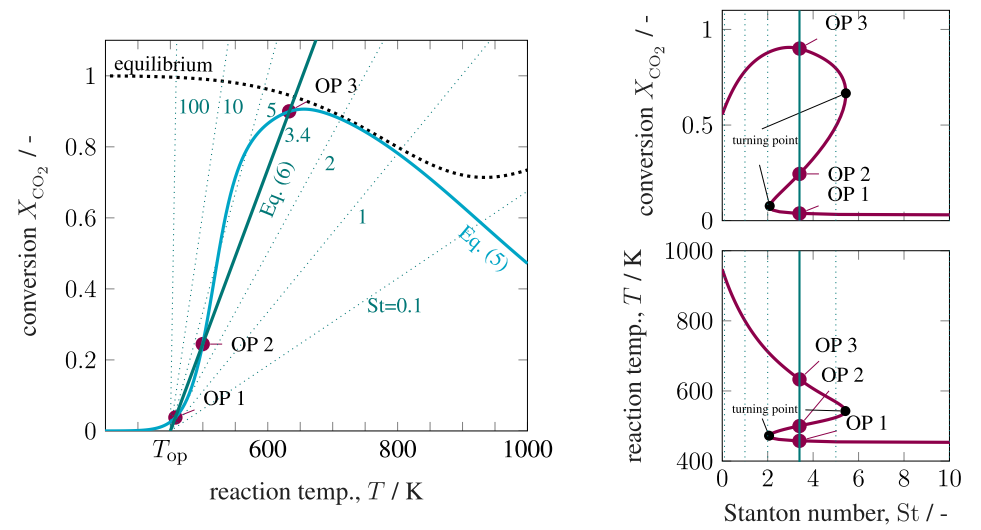

FIGURE 5 | State-space diagram for mass and energy balance **(left)** and for all equilibrium points **(right)** under variation of the Stanton number, reference setting taken from **Supplementary Table S1**.

Plugging this into **Eq. 7** leads to the rate-based CSTR stability criterion

$$\text{CSTR stability:} \quad \frac{\frac{\tau}{\varepsilon\, c_{\text{in}}}\frac{\partial \text{R}}{\partial T}}{1-\frac{\tau}{\varepsilon\, c_{\text{in}}}\frac{\partial \text{R}}{\partial X}} < \frac{1+\text{St}}{\Delta T_{\text{ad}}}. \tag{8}$$

In comparision, Szeifert et al. (2007) comprehensibly reviewed available criteria for reactor stability, runaway, and parametric sensitivity. Among those, the authors recommend using the Ljapunov stability criterion for a PFTR in space (or for a batch reactor in time), which is very similar to the upper CSTR stability criterion. In case of an equimolar reaction the PFTR stability criterion accordingly reads

$$\text{PFTR stability:} \quad \frac{\frac{\tau}{\varepsilon\, c_{\text{in}}}\frac{\partial \text{R}}{\partial T}}{\text{St}-\frac{\tau}{\varepsilon\, c_{\text{in}}}\frac{\partial \text{R}}{\partial X}} < \frac{1}{\Delta T_{\text{ad}}}.$$

Both criteria reveal that reactor stability is supported under intensive cooling conditions ($\text{St}\to\infty$) and suppressed under reduced cooling conditions ($\text{St}\to 0$). As explained in **State-Space Multiplicity** the PFTR is primarily considered to have a unique solution for fixed parameters. Hence, the features stability, runaway, and parametric sensitivity need to be separated from multiplicity, which was already highlighted by (Bilous and Amundson, 1956). Until today, this separation is often considered to be generally valid. However, in the CSTR case a strong coupling of these features is clearly given. From the above explanations, generalized criteria for uniqueness and multiplicity within the operating range $\mathscr{O}$ derive very similar to the stability criterion and read

$$\text{CSTR uniqueness:} \quad \max_{T\in\mathscr{O}} \frac{\text{d}X}{\text{d}T} = \left.\frac{\text{d}X}{\text{d}T}\right|_{T^*} \le \frac{1+\text{St}}{\Delta T_{\text{ad}}}, \tag{9}$$

$$\text{CSTR multiplicity:} \quad \max_{T\in\mathscr{O}} \frac{\text{d}X}{\text{d}T} = \left.\frac{\text{d}X}{\text{d}T}\right|_{T^*} > \frac{1+\text{St}}{\Delta T_{\text{ad}}}. \tag{10}$$

On the left side, the mass-based sensitivity corresponds to the steepest conversion gradient at the inflection point $T = T^*$ of **Eq. 5**. On the right side, the energy-based sensitivity corresponds to the constant conversion gradient of **Eq. 6**. Although the uniqueness criterion applies to all operating points in $\mathscr{O}$ (sufficient condition for uniqueness), the multiplicity criterion only indicates the existence of some operating points with multiple steady states in $\mathscr{O}$ (necessary condition for multiplicity). Thus, even if the multiplicity criterion holds, unique solutions in $\mathscr{O}$ might still exist. Furthermore, discontinuous jumps at the *turning points* from a stable extinguished to a stable ignited branch - and vice versa - is also solely induced by the existence of multiplicity. These jumps coincide with what is generally denoted as *parametric sensitivity* and *reactor runaway* (Morbidelli and Varma, 1982). Moreover, the equivalence strikingly demonstrates the close connection between stability, runaway, parametric sensitivity, and multiplicity when back-mixing is present. However, commonly accepted criteria for reactor runaway and stability do not consider back-mixing at all (Szeifert et al., 2007; Kummer and Varga, 2019). To close this gap, the next section applies the upper correlations for mass and energy to a series of CSTRs, where a finite number of stages corresponds to finite back-mixing.

CSTR Cascade Analogy

In order to approach a more realistic description of industrial-scale fixed-bed reactors, this section extends the previous relations to a CSTR cascade with multiple stages. Note that such cascades also mimic finite volume schemes, which are widely used to solve dispersion models numerically. **Supplementary Section S2** provides the entire cascade model notation, mass and energy balances, as well as the solution strategy. The resulting equations of each CSTR stage {i} are

$$\text{mass balance:} \quad X_{\text{CO}_2}^{\{i\}} = \frac{1}{n}\frac{\tau}{\varepsilon\, c_{\text{CO}_2,\text{in}}}\text{R}_{\text{meth}}^{\{i\}} = C_n \text{R}_{\text{meth}}^{\{i\}}, \tag{11}$$

$$\text{energy balance:} \quad X_{\text{CO}_2}^{\{i\}} = \frac{(1+\text{St}_n)}{\Delta T_{\text{ad}}^{\{i\}}}\left(T^{\{i\}} - T_{\text{op}}^{\{i\}}\right). \tag{12}$$

In order to separate different multiplicity sources, isothermal and non-isothermal cascades are discussed in the following.

Two Isothermal CSTRs

Under intensive cooling conditions ($\text{St}\to\infty$) or negligible heat effects ($\Delta T_{\text{ad}}^{\{i\}}\to 0$) the CSTR cascade becomes isothermal, meaning that $T_{\text{in}} = T_{\text{cool}} = T^{\{i\}}$. The corresponding implicit nonlinear equation system results from **Eq. 11** and reads

$$\begin{aligned} 0 &= X_{\text{CO}_2}^{\{1\}} - C_2 \text{R}_{\text{meth}}^{\{1\}}, \\ 0 &= X_{\text{CO}_2}^{\{2\}} - C_2 \text{R}_{\text{meth}}^{\{2\}}, \end{aligned} \tag{13}$$

which can be solved consecutively (stage-wise) or simultaneously for $X_{\text{CO}_2}^{\{1\}}$ and $X_{\text{CO}_2}^{\{2\}}$ by root-finding algorithms (e.g., Newton–Raphson method). The solution of **Eq. 13** is illustrated in **Figure 6**.

As seen on the left side of **Figure 6**, the operating point (depicted by bullets) of each CSTR lies on a straight line in the R-X diagram. The unique intersection at any temperature proves, that no purely kinetic multiplicity (C_2^{m} in **Figure 3**) exists for the rate expressions used in this work. Since intraparticle and interfacial transport resistances are neglected ($\eta_{\text{meth}} = 1$), the multiplicity sources C_1^{m} and C_1^{e} are also absent. This graphical analysis is also applicable to other reactions in order to check for these multiplicity sources. The right side of **Figure 6** depicts the stage operating range as well as the overall operating range for two CSTRs in series and compares it to scenarios with 1, 10, and 100 stages. The comparison shows the well-known tendency that the higher the stage number, the higher the conversion.

Two Non-Isothermal CSTRs

The operating points for a series of non-isothermal CSTRs are additionally determined by individual stage temperatures deviating from inlet and cooling temperature $T_{\text{in}} = T_{\text{cool}} \neq T^{\{i\}}$. Thus, the nonlinear equation **System 13** needs to be extended by the stage energy balances in **Eq. 12** such that

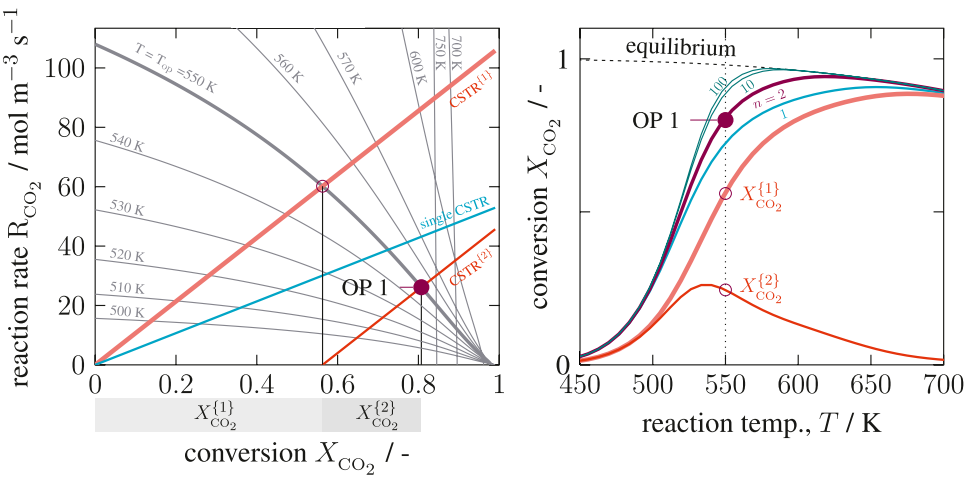

FIGURE 6 | State-space diagram for a cascade of two isothermal Continuous Stirred Tank Reactors (CSTRs) in the R–*X* **(left)** and *X*–*T* **(right)** plane, reference setting taken from **Supplementary Table S1** but T_{op} = 550 K.

$$
\begin{aligned}
0 &= X^{\{1\}}_{CO_2} - C_2 R^{\{1\}}_{meth},\\
0 &= X^{\{1\}}_{CO_2} \Delta T^{\{1\}}_{ad} + (1 + St_2)\left(T^{\{1\}}_{op} - T^{\{1\}}\right),\\
0 &= X^{\{2\}}_{CO_2} - C_2 R^{\{2\}}_{meth},\\
0 &= X^{\{2\}}_{CO_2} \Delta T^{\{2\}}_{ad} + (1 + St_2)\left(T^{\{2\}}_{op} - T^{\{2\}}\right).
\end{aligned}
\tag{14}
$$

This system can be solved again stage-wise or simultaneously for $X^{\{1\}}_{CO_2}$, $X^{\{2\}}_{CO_2}$, $T^{\{1\}}$, and $T^{\{2\}}$ by root-finding algorithms. The previous section showed that one single stage allows for up to three multiple solutions, which indicates that the CSTR cascade in **Eq. 14** also generates multiple steady states. In theory, if each stage exhibits up to three multiple steady states (OP 1, 2, and 3), a total number of 3^n state combinations arise for the entire cascade. Standard root-finding algorithms, however, converge only to one local solution of **System 14**. Thus, finding all solutions requires further efforts, which is part of the following discussions.

The graphical solution of **System 14** is shown in **Figure 7** considering three of nine possible combinations ([1–1], [2–1], [3–1]). This figure comprehensively shows how the first operating point influences its downstream stage. The more conversion is achieved within the first stage, the less remains within the next stage. Furthermore, the energy-based operating line (green) of the second stage becomes steeper due to the reduced ATR. Both effects simultaneously reduce the occurrence for multiplicities within the second stage, if the first stage operates at an ignited state (OP 2 or 3). Later, this will be an essential aspect to interpret solutions of multi-stage CSTRs. Enumerating all possible solutions within the relevant coolant temperature range leads to the results in **Figure 8**.

Compared to the single CSTR, the hysteresis is more pronounced, and intermediate solutions emerge. Although combinatorics allows nine multiple steady states, only seven remain significant after enumeration. The combinations [3–2]

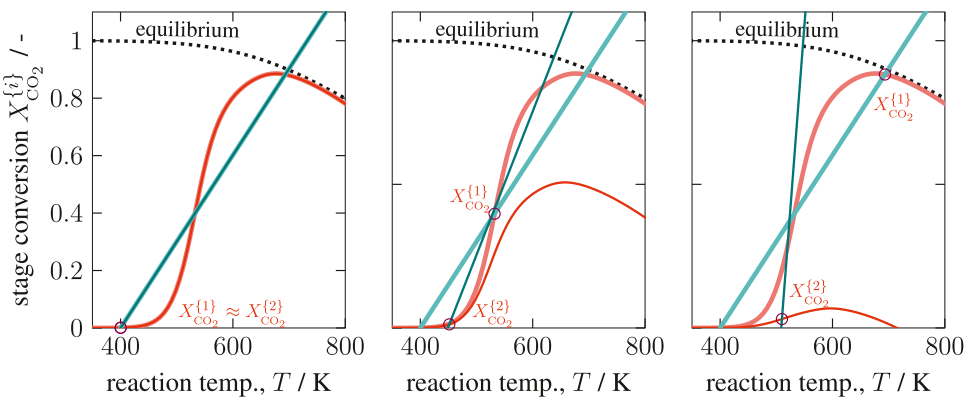

FIGURE 7 | Graphical solution of a two-stage CSTR series with state combination [1-1], [2–1], and [3–1], reference setting taken from **Supplementary Table S1** but $T^{\{1\}}_{op}$ = 400 K and $T_{in} = T_{cool}$.

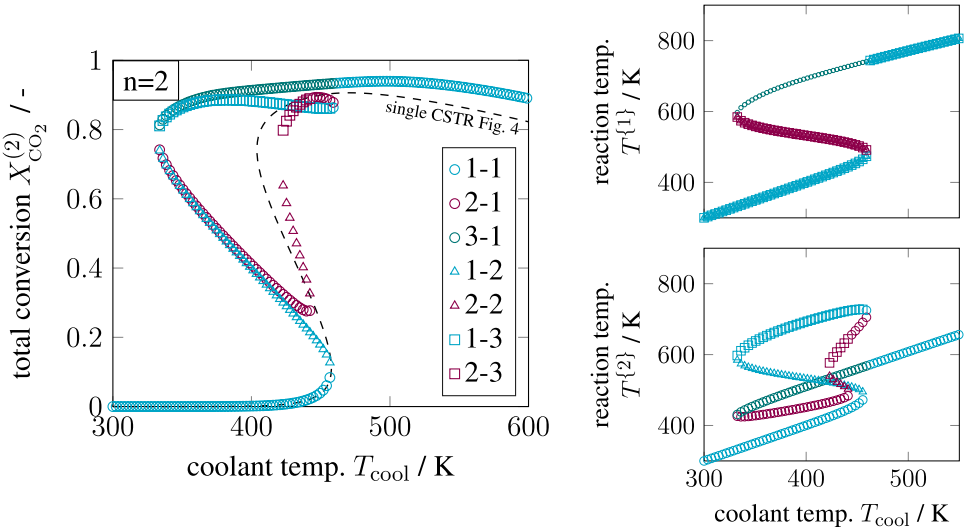

FIGURE 8 | Enumerative solution of significant operating points in a two-stage CSTR series, reference setting taken from **Supplementary Table S1** but $T_{in} = T_{cool}$. Note: T_{cool} is constant over the entire cascade, whereas T_{op} changes in each CSTR stage.

and [3–3] cancel out, due to the previous discussions on **Figure 7**. In addition, combinations [2–2] and [2–3] are rather seen as fragile because they exist in a very narrow operating range. In consequence, multiplicity driven by combinatorics is divided into significant and non-existing paths, as illustrated in **Figure 9**. These findings indicate that multiplicity in a CSTR cascade attributes only to a few stages. In order to confirm this hypothesis, a multi-stage cascade is analyzed in the following.

Multi-Stage CSTR Cascade

The enumeration effort of a multi-stage CSTR cascade increases exponentially with the number of stages if all possible combinations are taken into account. With six stages, there exist already 3^6 = 729 state combinations for all coolant temperature increments (here 300), leading to over 200'000 solver runs. Although a brute force enumeration would provide all solutions, many of them will be insignificant, due to missing physical constraints. Thus, a more elegant way is the use of bifurcation theory and numerical continuation techniques, which track solution branches according to slight parameter changes (e.g., coolant temperature) within a predefined range. During these changes, the eigenvalues of the linearized system equations may change such that the system becomes unstable. The shift to instability occurs if some eigenvalues cross the imaginary axis. At this point, bifurcation can take place from which new branches spread. However, this method also suffers from extensive computational efforts due to the eigenvalue calculation and possible inaccuracies of the systems Jacobian close to the bifurcation point. Furthermore, there is no guarantee that this method obtains all solutions. More details on bifurcation theory and numerical continuation techniques can be found in (Heinemann and Poore, 1981; Jensen and Ray, 1982; Kubíček and Marek, 1983; Wagialla and Elnashaie, 1995).

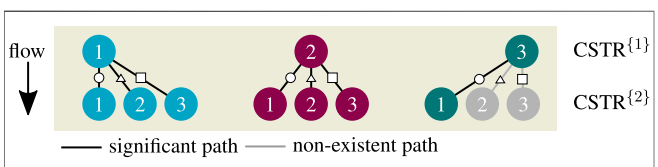

FIGURE 9 | Possible state combinations for a two-stage CSTR cascade.

In this work, the enumeration of all solutions was found to be the more convenient and illustrative approach. It will be shown that the non-existent solutions can be excluded already in advance. Together with efficient nonlinear computation techniques (here provided by CasADi; Andersson et al., 2018) the enumeration of all solutions with reasonable computational effort becomes feasible. Accordingly, the results for three to six CSTRs in series are illustrated in **Figure 10**.

Most importantly, the solutions in **Figure 10** aggregate in three main clusters forming - similar to a single CSTR - a stable ignition and extinction branch, as well as an unstable intermediate branch. The number of multiple steady states increases with increasing stage number *n*, but most solutions persistently converge to the three main clusters. Once again, each relevant solution has not more than two stages exhibiting multiplicity. Cascades with more stages as represented by **Figure 11** confirm that two stages are sufficient to map the dominating state clusters. These two stages are further on denoted as *key stages*, which may exist at any position within the cascade. The key stage solutions directly at the inlet are colored in **Figure 10**. Solutions with the same key stage combination but different locations along the cascade aggregate within the same cluster. For instance, the upper ignition branch is covered by *n* [···1–3–1···] combinations, the middle unstable branch is

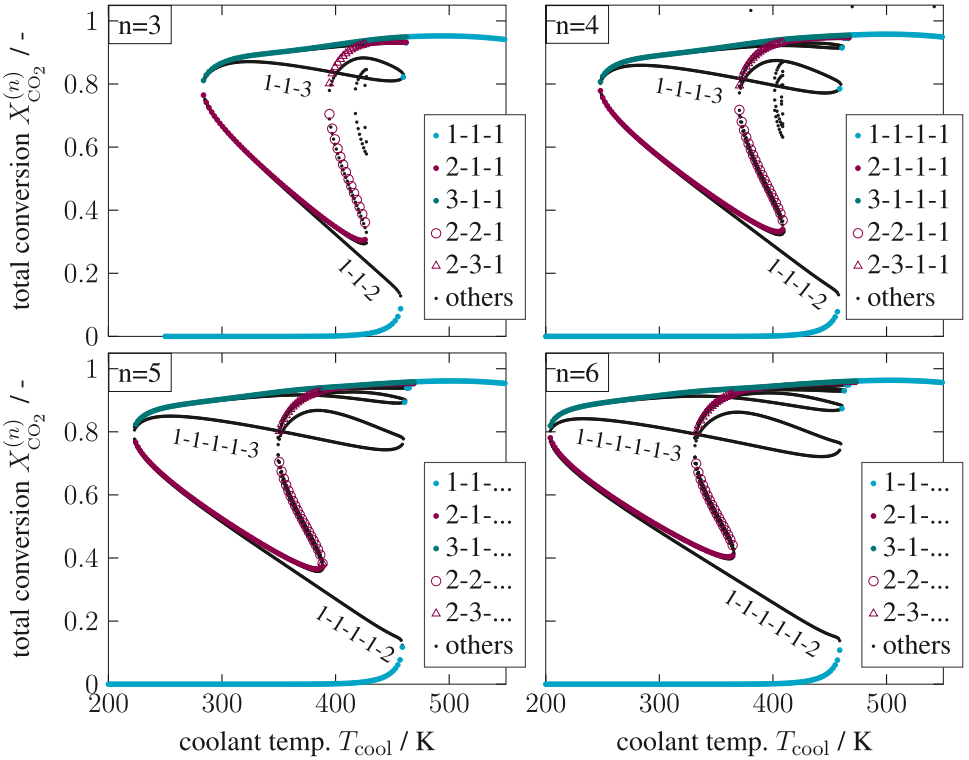

FIGURE 10 | Enumerative solution of operating points (OPs) in a multi-stage CSTR cascade, color—OPs of two key stages at the inlet, black—OPs of subordinate branches, reference setting taken from **Supplementary Table S1** but $T_{in} = T_{cool}$.

covered by n [⋯1–2–1⋯] combinations, and the lower extinction branch is covered by n [⋯1–1–1⋯] combinations. Again $n-1$ [⋯1–2–2–1⋯] and $n-1$ [⋯1–2–3–1⋯] fragile combinations exist but appear only in a narrow operating range. This clustering can be explained by the insignificance of previous stages at the extinguished state [⋯1⋯]. The insignificance partly eliminates if the inlet and coolant temperature of the cascade differ, which is, however, not considered here. Beyond that, subordinate branches (in black) develop from the last stage ([⋯1–2] [⋯1–3]). These observations are summarized in the pathway structure of **Figure 12**, showing the relevant state combinations of a multi-stage CSTR cascade.

As illustrated in **Figure 11**, the clustering of all key stage solutions still remains for higher stage numbers. It was found that the hysteresis loop widens significantly with increasing stage number. However, after reaching a certain stage number, the hysteresis loop degenerates again until it finally disappears. Furthermore, different shapes of the unstable intermediate branch emerge, depending on the parameter setting. The unstable branch evolves more or less pronounced, as indicated by variations of the residence time in **Figure 11**. This is in particular relevant if an operation at these unstable branches is aspired (Bremer and Sundmacher, 2019).

Technically, key stages are the analogy of narrow reaction fronts in real fixed-bed reactors. Those fronts often develop

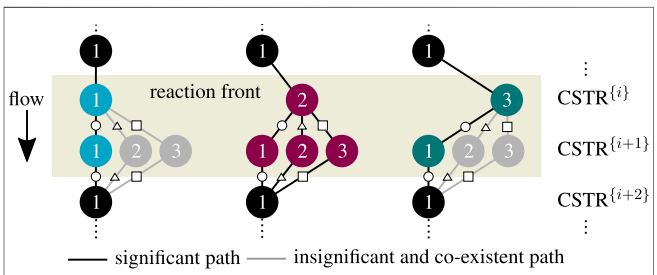

FIGURE 11 | Possible state combinations of a multi-stage CSTR cascade with two key stages.

within a very short reactor segment, preferably close to the reactor inlet. Considering this, the key stages become less likely if they are located further downstream, which curtails the relevance of the black subordinate branches associated with the last stage. In real reactors, the actual reaction front position is typically determined by second-order effects (e.g., preheating, dispersion, flow maldistribution, heat conduction within the reactor jacket).

From all this, the following three-level hierarchy of thermo-kinetic multiplicity in fixed-bed reactors can be drawn:

Assumption	Multiplicity in all stages		Two key stages (reaction front)		Cluster formation
Max #MSS	3^n	⇒	$4n-1$	⇒	3 to **5**

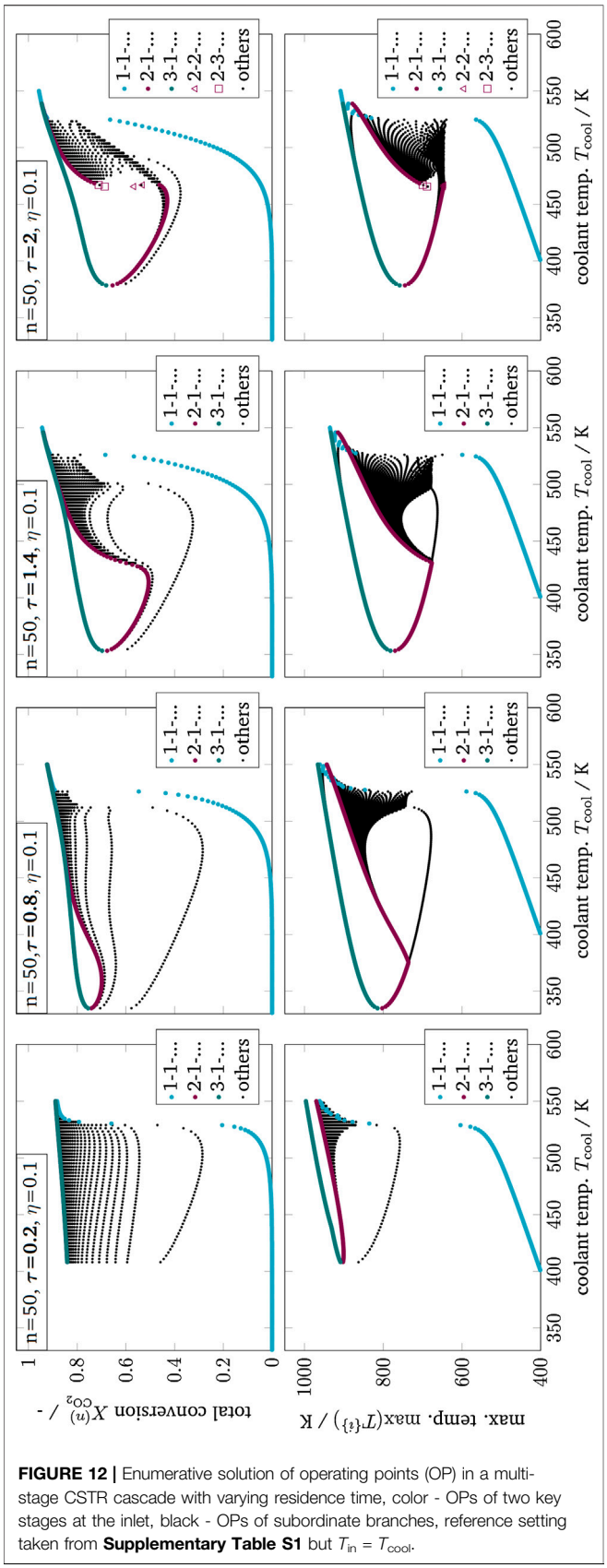

FIGURE 12 | Enumerative solution of operating points (OP) in a multi-stage CSTR cascade with varying residence time, color - OPs of two key stages at the inlet, black - OPs of subordinate branches, reference setting taken from **Supplementary Table S1** but $T_{in} = T_{cool}$.

Moving from left to right considers more physical details and approaches the situation in real fixed-bed reactors. This three-level hierarchy compromises many different and controversial opinions found in the literature (see **State-Space Multiplicity**). For instance, the findings of Eigenberger (1972a), and Eigenberger (1972b) reporting only three to five multiple steady states are mainly associated with cluster formation, whereas studies that report an infinite number of multiple steady states (for $n \to \infty$) neglect clustering and count each state separately.

So far, state clustering and its connection to reaction fronts and multiplicity in real reactors is rather disregarded in literature. One reason might be the missing availability for efficient numerical tools, which have only been accessible in recent years. Since the previous considerations mainly address multiplicity trends, it remains to be shown under which conditions uniqueness applies.

Until today, an exact uniqueness criterion for non-isothermal fixed-bed reactors largely remains an open question (Dochain, 2018). The axial dispersion model has been a favorite target for extensive mathematical analyses but often limited to first-order reactions under isothermal conditions (Schmitz, 1975; Varma, 1980; Arce and Ramkrishna, 1991). However, numerous studies provide qualitative trends pointing in similar directions. For instance, Jensen and Ray (1982) summarized, that the solution will be unique for sufficiently high Bodenstein numbers, large heat transfer coefficients, or small Damköhler numbers. The previous results are very much in line with these qualitative trends, but moreover, they reveal generalized criteria for stability, uniqueness, and multiplicity of non-isothermal fixed-bed reactors. These criteria are derived in the following.

Stability, Uniqueness, and Multiplicity Criteria for Real Non-Isothermal Reactors

The observations from above show that the thermo-kinetic multiplicity feature of the first stage is entirely capable of representing the three main state clusters. Consequently, if the first stage is free of multiplicity, then all following stages are also free of multiplicity. This key feature enables the criteria of the first CSTR stage (see **Eqs 8**-**10**) to be assigned to the entire CSTR cascade (cell model) according to

$$\text{stability (CM):} \quad \frac{\mathrm{d}X^{\{1\}}}{\mathrm{d}T} < \frac{1+\frac{\mathrm{St}}{\mathrm{n}}}{\Delta T_{\mathrm{ad}}^{\{1\}}},$$

$$\text{uniqueness (CM):} \quad \max_{T \in \mathscr{D}} \frac{\mathrm{d}X^{\{1\}}}{\mathrm{d}T} = \left.\frac{\mathrm{d}X^{\{1\}}}{\mathrm{d}T}\right|_{T=T^*} \leq \frac{1+\frac{\mathrm{St}}{\mathrm{n}}}{\Delta T_{\mathrm{ad}}^{\{1\}}},$$

$$\text{multiplicity (CM):} \quad \max_{T \in \mathscr{D}} \frac{\mathrm{d}X^{\{1\}}}{\mathrm{d}T} = \left.\frac{\mathrm{d}X^{\{1\}}}{\mathrm{d}T}\right|_{T=T^*} > \frac{1+\frac{\mathrm{St}}{\mathrm{n}}}{\Delta T_{\mathrm{ad}}^{\{1\}}},$$

with $T = T^*$ as inflection point of **Eq. 11** corresponding to the steepest conversion gradient. For simplicity, the index CO_2 is omitted here and in the following.

Consequently, in the absence of purely kinetic and isothermal multiplicity, uniqueness in non-isothermal CSTR cascades boils down to very few key parameters, lumped together as mass and energy-based thermal sensitivity. Both sensitivities are evaluated in **Figure 13** with respect to the methanation reference setting of **Supplementary Table S1**.

According to the reference setting in **Figure 13**, uniqueness can only be guaranteed for cascades with several thousand stages. This fact still applies to a wide range of heat transfer and catalyst activity, as indicated by variations of the Stanton number and effectiveness factor. Intensified heat transfer mainly affects cascades with higher back-mixing and leads to reduced multiplicity regions. In some scenarios, uniqueness is guaranteed for low and high back-mixing conditions, but not for the intermediates (e.g., for St = 100 and $\eta = 1$). In contrast, reducing the ATR (e.g., via product gas recycling) always leads to diminished multiplicity regions. At adiabatic conditions ($\mathrm{St} \to 0$), back-mixing does not influence the energy-based thermal sensitivity, and uniqueness becomes solely determined by the mass-based thermal sensitivity and the ATR. Not shown is the influence of the remaining key parameters, pressure, and residence time. However, both are indirectly incorporated into the Stanton number and effectiveness factor.

The equivalence of stage and Bodenstein number in **Eq. 3** at low back-mixing (Bo > 100) allows for the transition from cell to dispersion models.[a] Therefore, we introduce a *surrogate conversion* $\tilde{X}$ which allows for applying the first stage mass balance from **Eq. 11** to dispersion models according to

$$0 = \tilde{X} - \frac{2}{\mathrm{Bo}} \frac{\tau}{\varepsilon\, c_{\mathrm{in}}} \mathrm{R} = \tilde{X} - C_{\mathrm{Bo}} \mathrm{R}, \tag{15}$$

which is then used to calculate the mass-based thermal sensitivity of a fixed-bed reactor. Together with the adapted energy-based thermal sensitivity from **Eq. 12** at elevated Bodenstein numbers (Bo > 100) the previous criteria read as

$$\text{stability (DM)}: \quad \frac{\mathrm{d}\tilde{X}}{\mathrm{d}T} < \frac{1 + \dfrac{2\,\mathrm{St}}{\mathrm{Bo}}}{\Delta T_{\mathrm{ad,in}}}, \tag{16}$$

$$\text{uniqueness (DM)}: \quad \max_{T \in \mathscr{O}} \frac{\mathrm{d}\tilde{X}}{\mathrm{d}T} = \left.\frac{\mathrm{d}\tilde{X}}{\mathrm{d}T}\right|_{T=T^*} \leq \frac{1 + \dfrac{2\,\mathrm{St}}{\mathrm{Bo}}}{\Delta T_{\mathrm{ad,in}}}, \tag{17}$$

$$\text{multiplicity (DM)}: \quad \max_{T \in \mathscr{O}} \frac{\mathrm{d}\tilde{X}}{\mathrm{d}T} = \left.\frac{\mathrm{d}\tilde{X}}{\mathrm{d}T}\right|_{T=T^*} > \frac{1 + \dfrac{2\,\mathrm{St}}{\mathrm{Bo}}}{\Delta T_{\mathrm{ad,in}}}, \tag{18}$$

with $T = T^*$ as inflection point of **Eq. 11** corresponding to the steepest conversion gradient. The evaluation of the reference setting from **Supplementary Table S1** leads to the same results as in **Figure 13** with n = Bo/2.

The generalized **Criteria 16-18** have not been found in literature yet. They can be used as an a priori estimate for any exothermic reaction and reactors at any scale, only requiring apparent rate expression, coolant heat transfer coefficient, inlet condition, and back-mixing intensity. Note that no expensive computation of the entire dispersion model is required, which makes it easy to use for reactor design, operation, and safety analysis. The criteria, however, demand for a representative Bodenstein number either mass or energy-based. As illustrated in **State-Space Multiplicity**, the energy feedback is of major interest for thermo-kinetic multiplicity, which indicates that the three to ten times smaller energy-based Bodenstein number is the most reasonable choice. Furthermore, the here proposed criteria recommends considering axial dispersion even for high Bodenstein numbers beyond 400. This is contrary to commonly accepted criteria of Hlaváček and Marek (1966), Mears (1976), Young and Finlayson (1973), and Mederos et al. (2009), which did neither consider multiplicity nor reactor stability.

In order to access the mass-based sensitivity on the left, the total differential applied to the implicit **Eq. 15** may help:

$$0 = \frac{\mathrm{d}\tilde{X}}{\mathrm{d}T} - C_{\mathrm{Bo}} \frac{\mathrm{dR}}{\mathrm{d}T} = \frac{\mathrm{d}\tilde{X}}{\mathrm{d}T} - C_{\mathrm{Bo}} \left(\frac{\partial \mathrm{R}}{\partial T} + \frac{\partial \mathrm{R}}{\partial \tilde{X}} \frac{\mathrm{d}\tilde{X}}{\mathrm{d}T} \right).$$

Consequently, the sensitivity is represented by

$$\frac{\mathrm{d}\tilde{X}}{\mathrm{d}T} = \frac{C_{\mathrm{Bo}} \dfrac{\partial \mathrm{R}}{\partial T}}{1 - C_{\mathrm{Bo}} \dfrac{\partial \mathrm{R}}{\partial \tilde{X}}}. \tag{19}$$

Thus, the mass-based sensitivity only requires valid reaction rates, their partial derivatives and the main reactor parameters used in **Eq. 15**. For *first-order, equimolar reactions*, the first Damköhler number from **Supplementary Eq. S7** can be used to further simplify **Eq. 19** via

$$\tilde{X} = \frac{2}{\mathrm{Bo}} \mathrm{Da_I} \left(1 - \tilde{X}\right) = \frac{\dfrac{2}{\mathrm{Bo}} \mathrm{Da_I}}{1 + \dfrac{2}{\mathrm{Bo}} \mathrm{Da_I}},$$

$$\frac{\mathrm{d}\tilde{X}}{\mathrm{d}T} = \frac{\dfrac{2}{\mathrm{Bo}} \mathrm{Da_I}}{1 + \dfrac{2}{\mathrm{Bo}} \mathrm{Da_I}} \left(1 - \tilde{X}\right) \frac{E_{\mathrm{A}}}{\mathscr{R} T^2} = \frac{\dfrac{2}{\mathrm{Bo}} \mathrm{Da_I}}{\left(1 + \dfrac{2}{\mathrm{Bo}} \mathrm{Da_I}\right)^2} \frac{E_{\mathrm{A}}}{\mathscr{R} T^2}. \tag{20}$$

With **Eq. 20**, the mass-based sensitivity can be evaluated within the relevant temperature range to identify the maximum gradient at T^* and $\mathrm{Da_I^*}$. Thus, there is no further need to solve the implicit **Eq. 15**. Note that the here used Damköhler number remains as a function of temperature such that the above criteria condense to

[a]This equivalence is exploited when the finite volume upwind scheme is used to solve dispersion models numerically. In this case, the corresponding number of finite volumes in flow direction inherently contains a certain degree of back-mixing. If the number of finite volumes is too low, an artificial dispersion (so-called numerical diffusion) will superimpose other dispersion components included in the model.

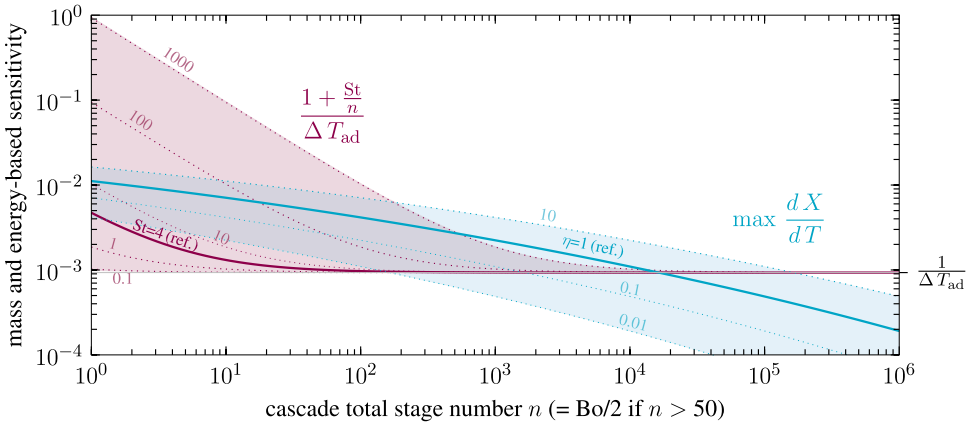

FIGURE 13 | First stage mass and energy-based sensitivity for non-isothermal CSTR cascades with various stage number, effectiveness factor and Stanton number, reference setting taken from **Supplementary Table S1**.

$$\text{stability}\left(1^{\text{st}}-\text{order, equimolar}\right):\quad \frac{\frac{2}{\mathrm{Bo}}\mathrm{Da_I}}{\left(1+\frac{2}{\mathrm{Bo}}\mathrm{Da_I}\right)^2}\frac{E_\mathrm{A}}{\mathscr{R}T^2}<\frac{1+\frac{2\,\mathrm{St}}{\mathrm{Bo}}}{\Delta T_{\mathrm{ad,in}}}, \tag{21}$$

$$\text{uniqueness}\left(1^{\text{st}}-\text{order, equimolar}\right):\quad \frac{\frac{2}{\mathrm{Bo}}\mathrm{Da_I^*}}{\left(1+\frac{2}{\mathrm{Bo}}\mathrm{Da_I^*}\right)^2}\frac{E_\mathrm{A}}{\mathscr{R}T^{*2}}\leq\frac{1+\frac{2\,\mathrm{St}}{\mathrm{Bo}}}{\Delta T_{\mathrm{ad,in}}}, \tag{22}$$

$$\text{multiplicity}\left(1^{\text{st}}-\text{order, equimolar}\right):\quad \frac{\frac{2}{\mathrm{Bo}}\mathrm{Da_I^*}}{\left(1+\frac{2}{\mathrm{Bo}}\mathrm{Da_I^*}\right)^2}\frac{E_\mathrm{A}}{\mathscr{R}T^{*2}}>\frac{1+\frac{2\,\mathrm{St}}{\mathrm{Bo}}}{\Delta T_{\mathrm{ad,in}}}, \tag{23}$$

with T^* and $\mathrm{Da_I^*}$ as arguments of the maximum gradient of **Eq. 20**. Although these simplified criteria are not adequately applicable for methanation due to the strong influence of the thermodynamic equilibrium, they comprehensively show how the key parameters affect multiplicity. At the beginning of this section, the current state in the literature was highlighted to be rather qualitative. The statement of Jensen and Ray (1982) saying that the solution will be unique for sufficiently high Bodenstein numbers ($\mathrm{Bo}\to\infty$), large heat transfer coefficients ($\mathrm{St}\to\infty$), or small Damköhler numbers ($\mathrm{Da}\to 0$) is perfectly represented by the **Criteria 22 and 23**. Furthermore, the limiting case of an adiabatic CSTR ($\mathrm{St}\to 0$, $\mathrm{Bo}/2\to 1$) applied to **Criteria 21** is equivalent to the stability criterion presented by Kimura and Levenspiel (1977).

In extension to the infinite back-mixing case in **CSTR Analogy**, it can be confirmed that stability and uniqueness are closely related under finite back-mixing conditions. However, the finite back-mixing case ($1<\mathrm{Bo}/2<\infty$) is typically not considered in the literature (Szeifert et al., 2007; Kummer and Varga, 2019), or was found to be insignificant (Balakotaiah et al., 1995) for stability analysis. In contrast, this work shows a distinct relevance of multiplicity for real reactors, so that back-mixing must also be highly relevant for stability, runaway, and parametric sensitivity. In this regard, the quantitative description of all features results in the here proposed **Criteria 17 and 22**.

DISCUSSIONS

In summary, uniqueness and multiplicity of real non-isothermal reactors have proven to be decisive characteristics. In addition to the qualitative descriptions prevailing in the literature, the criteria proposed here represent a novel quantitative measure applicable to any exothermic reaction and reactors at any scale. This work also shows that mass and energy back-mixing represents the essential link between uniqueness, multiplicity, stability, runaway, and parametric sensitivity, which are usually treated independently in the literature. The observation that back-mixing remains relevant for these characteristics even at high Bodenstein numbers implies that generally accepted back-mixing criteria of Hlaváček and Marek (1966), Mears (1976), Young and Finlayson (1973), and Mederos et al. (2009) are insufficient for real non-isothermal reactors.

In addition, the CSTR cascade model indicates that a narrow reaction front, not larger than two representative CSTR stages (key stages), mainly determines uniqueness and multiplicity in real non-isothermal fixed-bed reactors. The illustrated state-clustering of the cascade model accounts for the fact that this reaction front may occur at any position within the fixed-bed. From this, a three-level hierarchy is derived, which unifies controversial opinions that still exist in the literature.

In summary, the presented methodology, as well as the derived criteria, shall allow for easier accessibility of fundamental reactor characteristics. This is particularly useful for the future objective of operating chemical reactors more flexible and within larger operating ranges.

Therefore the derived criteria may be used for reactor design, control, and safety purposes. Ignoring uniqueness and multiplicity would disregard a broad operating range and thus a substantial reactor performance potential.

DATA AVAILABILITY STATEMENT

The raw data supporting the conclusions of this article will be made available by the authors, without undue reservation.

AUTHOR CONTRIBUTIONS

JB and KS contributed conception and design of the study. JB organized the content, ran the computational experiments, and derived the criteria. KS motivated the detailed bifurcation analysis and supervised the project. JB wrote the first draft of the manuscript. All authors contributed to manuscript revision, read and approved the submitted version.

FUNDING

This research work was partly supported by the DFG Priority Program SPP 2080 "Catalysts and reactors under dynamic conditions for energy storage and conversion", funded by the Deutsche Forschungsgemeinschaft (DFG, German Research Foundation) under Grant Number 406914011. The author Jens Bremer is also affiliated to the International Max Planck Research School (IMPRS) for Advanced Methods in Process and Systems Engineering, Magdeburg, Germany. Open Access funding provided by the Max Planck Society.

SUPPLEMENTARY MATERIAL

The Supplementary Material for this article can be found online at: https://www.frontiersin.org/articles/10.3389/fenrg.2020.549298/full#supplementary-material.

REFERENCES

Adaje, J., and Sheintuch, M. (1990). Comparison of multiplicity patterns of a single catalytic pellet and a fixed catalytic bed for ethylene oxidation. *Chem. Eng. Sci.* 45, 1331–1342. doi:10.1016/0009-2509(90)87125-C

Agrawal, R., West, D. H., and Balakotaiah, V. (2007). Modeling and analysis of local hot spot formation in down-flow adiabatic packed-bed reactors. *Chem. Eng. Sci.* 62, 4926–4943. doi:10.1016/j.ces.2006.11.057

Andersson, J. A. E., Gillis, J., Horn, G., Rawlings, J. B., and Diehl, M. (2018). CasADi—A software framework for nonlinear optimization and optimal control. *Math. Program. Comput.* 11(3), 1–36.

Arce, P., and Ramkrishna, D. (1991). Pattern formation in catalytic reactors: the role of fluid mixing. *AIChE J.* 37, 98–110. doi:10.1002/aic.690370109

Balakotaiah, V., Kodra, D., and Nguyen, D. (1995). Runaway limits for homogeneous and catalytic reactors. *Chem. Eng. Sci.* 50, 1149–1171. doi:10.1016/0009-2509(94)00463-2

Balakotaiah, V., and Luss, D. (1983). Multiplicity features of reacting systems. *Chem. Eng. Sci.* 38, 1709–1721. doi:10.1016/0009-2509(83)85028-3

Bilous, O., and Amundson, N. R. (1956). Chemical reactor stability and sensitivity: II. Effect of parameters on sensitivity of empty tubular reactors. *AIChE J.* 2, 117–126. doi:10.1002/aic.690020124

S. M. Biollaz and T. J. Schildhauer (Editors) (2016). *Synthetic natural gas from coal, dry biomass, and power-to-gas applications*. Hoboken, NJ: John Wiley & Sons, Inc.

Bostandzhiyan, S. A., and Shkadinskii, K. G. (2010). Multiple steady states and transitional regimes in a cylindrical fixed-bed catalytic reactor. *Theor. Found. Chem. Eng.* 44, 119–125. doi:10.1134/S0040579510020016

Bremer, J., and Sundmacher, K. (2019). Operation range extension via hot-spot control for catalytic CO_2 methanation reactors. *React. Chem. Eng.* 4, 1019. doi:10.1039/C9RE00147F

Dochain, D. (2018). Analysis of the multiplicity of steady-state profiles of two tubular reactor models. *Comput. Chem. Eng.* 114, 318–324. doi:10.1016/j.compchemeng.2017.10.028

Dommeti, S. M. S., Balakotaiah, V., and West, D. H. (1999). Analytical criteria for validity of pseudohomogeneous models of packed-bed catalytic reactors. *Ind. Eng. Chem. Res.* 38, 767–777. doi:10.1021/ie980365g

Dramé, A. K., Lobry, C., Harmand, J., Rapaport, A., and Mazenc, F. (2008). Multiple stable equilibrium profiles in tubular bioreactors. *Math. Comput. Model.* 48, 1840–1853. doi:10.1016/j.mcm.2008.05.008

Eigenberger, G. (1972a). On the dynamic behavior of the catalytic fixed-bed reactor in the region of multiple steady states-I. The influence of heat conduction in two phase models. *Chem. Eng. Sci.* 27, 1909–1915. doi:10.1016/0009-2509(72)87049-0

Eigenberger, G. (1972b). On the dynamic behavior of the catalytic fixed-bed reactor in the region of multiple steady states-II. The influence of the boundary conditions in the catalyst phase. *Chem. Eng. Sci.* 27, 1917–1924. doi:10.1016/0009-2509(72)87050-7

Eigenberger, G. (1983). Dynamik und stabilität verfahrenstechnischer prozesse. *Chem. Ing. Tech.* 55, 503–515. doi:10.1002/cite.330550702

Elnashaie, S., and Elshishini, S. S. (1993). "Modelling, simulation and optimization of industrial fixed bed catalytic reactors," in *Topics in chemical engineering*. Philadelphia, Pa: Gordon and Breach, Vol. 7.

Fache, A., Marias, F., and Chaudret, B. (2020). Catalytic reactors for highly exothermic reactions: steady-state stability enhancement by magnetic induction. *Chem. Eng. J.* 390, 124531. doi:10.1016/j.cej.2020.124531

Fischer, K. L., and Freund, H. (2020). On the optimal design of load flexible fixed bed reactors: integration of dynamics into the design problem. *Chem. Eng. J.* 393, 124722. doi:10.1016/j.cej.2020.124722

Gao, J., Wang, Y., Ping, Y., Hu, D., Xu, G., Gu, F., et al. (2012). A thermodynamic analysis of methanation reactions of carbon oxides for the production of synthetic natural gas. *RSC Adv.* 2, 2358–2368. doi:10.1039/c2ra00632d

Gilles, E. D. (1977). Dynamisches verhalten von Festbettreaktoren. *Chem. Ing. Tech.* 49, 142–149. doi:10.1002/cite.330490211

Gilles, E. D., and Hofmann, H. (1961). Bemerkung zu der Arbeit: "an analysis of chemical reactor stability and control". *Chem. Eng. Sci.* 15, 328–331. doi:10.1016/0009-2509(61)85038-0

Harold, M. P., and Luss, D. (1985). An experimental study of steady-state multiplicity features of two parallel catalytic reactions. *Chem. Eng. Sci.* 40, 39–52. doi:10.1016/0009-2509(85)85045-4

W. M. Haynes (Editor) (2017). *CRC handbook of chemistry and physics: a ready-reference book of chemical and physical data*. 97th Edn. Boca Raton, London and New York: CRC Press.

Heinemann, R. F., and Poore, A. B. (1981). Multiplicity, stability, and oscillatory dynamics of the tubular reactor. *Chem. Eng. Sci.* 36, 1411–1419. doi:10.1016/0009-2509(81)80175-3

Heinemann, R. F., and Poore, A. B. (1982). The effect of activation energy on tubular reactor multiplicity. *Chem. Eng. Sci.* 37, 128–131. doi:10.1016/0009-2509(82)80079-1

Hlaváček, V., and Marek, M. (1966). Axialer stoff- und Wärmetransport im adiabatischen Rohrreaktor—II. Numerische Untersuchung—ablauf einer

einfachen Reaktion bezw. einer Folgereaktion. *Chem. Eng. Sci.* 21, 501–513. doi:10.1016/0009-2509(66)85064-9

Jaree, A., Budman, H. M., Hudgins, R. R., Silveston, P. L., Yakhnin, V., and Menzinger, M. (2001). Temperature excursions in reactors packed with segregated layers of catalyst and inert solids. *Chem. Eng. Sci.* 56, 5719–5726. doi:10.1016/S0009-2509(01)00285-8

Jensen, K. F., and Ray, W. H. (1982). The bifurcation behavior of tubular reactors. *Chem. Eng. Sci.* 37, 199–222. doi:10.1016/0009-2509(82)80155-3

Kalthoff, O., and Vortmeyer, D. (1980). Ignition/extinction phenomena in a wall cooled fixed bed reactor. *Chem. Eng. Sci.* 35, 1637–1643. doi:10.1016/0009-2509(80)80056-X

Kiewidt, L. (2017). Solid sponges as support for heterogeneous catalysts in gas-phase reactions. PhD thesis. Bremen: University of Bremen.

Kiewidt, K., and Thöming, J. (2019). Pareto-optimal design and assessment of monolithic sponges as catalyst carriers for exothermic reactions. *Chem. Eng. J.*, 359, 496–504. doi:10.1016/j.cej.2018.11.109

Kimura, S., and Levenspiel, O. (1977). Temperature excursions in adiabatic packed bed reactors. *Ind. Eng. Chem. Proc. Des. Dev.* 16, 145–148. doi:10.1021/i260061a610

Kopyscinski, J., Schildhauer, T. J., and Biollaz, S. M. A. (2010). Production of synthetic natural gas (SNG) from coal and dry biomass—a technology review from 1950 to 2009. *Fuel* 89, 1763–1783. doi:10.1016/j.fuel.2010.01.027

Koschany, F., Schlereth, D., and Hinrichsen, O. (2016). On the kinetics of the methanation of carbon dioxide on coprecipitated NiAl(O). *Appl. Catal. B Environ.* 181, 504–516. doi:10.1016/j.apcatb.2015.07.026

Kreitz, B., Wehinger, G. D., and Turek, T. (2019). Dynamic simulation of the CO_2 methanation in a micro-structured fixed-bed reactor. *Chem. Eng. Sci.* 195, 541–552. doi:10.1016/j.ces.2018.09.053

Kubíček, M., and Marek, M. (1983). "Computational methods in bifurcation theory and dissipative structures," in *Springer series computational physics*. Berlin, Heidelberg and New York, NY: Springer. doi:10.1007/978-3-642-85957-1

Kummer, A., and Varga, T. (2019). Completion of thermal runaway criteria: two new criteria to define runaway limits. *Chem. Eng. Sci.* 196, 277–290. doi:10.1016/j.ces.2018.11.008

Lee, C. K., Morbidelli, M., and Varma, A. (1987). Steady state multiplicity behavior of an isothermal axial dispersion fixed-bed reactor with nonuniformly active catalyst. *Chem. Eng. Sci.* 42, 1595–1608. doi:10.1016/0009-2509(87)80164-1

Lemmon, E. W., McLinden, M. O., and Friend, D. G. (1998). "Thermophysical properties of fluid systems," in *NIST chemistry webbook, NIST standard reference database*. Editors P. J. Linstrom and W. G. Mallard (Gaithersburg, MD: National Institute of Standards and Technology), Vol. 69. doi:10.18434/T4D303

Levenspiel, O. (1999). *Chemical reaction engineering*. 3rd Edn. Hoboken, NJ: Wiley.

Liu, S.-L., and Amundson, N. R. (1962). Stability of adiabatic packed bed reactors. an elementary treatment. *Ind. Eng. Chem. Fund.* 1, 200–208. doi:10.1021/i160003a008

Liu, S.-L., and Amundson, N. R. (1963). Stability of adiabatic packed-bed reactors. effect of axial mixing. *Ind. Eng. Chem. Fund.* 2, 183–189. doi:10.1021/i160007a004

Marwaha, B., and Luss, D. (2003). Hot zones formation in packed bed reactors. *Chem. Eng. Sci.* 58, 733–738. doi:10.1016/S0009-2509(02)00602-4

Mears, D. E. (1976). On criteria for axial dispersion in nonisothermal packed-bed catalytic reactors. *Ind. Eng. Chem. Fund.* 15, 20–23. doi:10.1021/i160057a004

Mederos, F. S., Ancheyta, J., and Chen, J. (2009). Review on criteria to ensure ideal behaviors in trickle-bed reactors. *Appl. Catal. Gen.* 355, 1–19. doi:10.1016/j.apcata.2008.11.018

Mohl, K. D., Kienle, A., Sundmacher, K., and Gilles, E. D. (2001). A theoretical study of kinetic instabilities in catalytic distillation processes: influence of transport limitations inside the catalyst. *Chem. Eng. Sci.* 56, 5239–5254. doi:10.1016/S0009-2509(01)00243-3

Moioli, E., Gallandat, N., and Züttel, A. (2019). Parametric sensitivity in the Sabatier reaction over Ru/Al_2O_3—theoretical determination of the minimal requirements for reactor activation. *React. Chem. Eng.* 4, 100–111. doi:10.1039/C8RE00133B

Morbidelli, M., Servida, A., and Varma, A. (1986). Optimal catalyst activity profiles in pellets. 4. Analytical evaluation of the isothermal fixed-bed reactor. *Ind. Eng. Chem. Fund.* 25, 307–313. doi:10.1021/i100023a001

Morbidelli, M., and Varma, A. (1982). Parametric sensitivity and runaway in tubular reactors. *AIChE J.* 28, 705–713. doi:10.1002/aic.690280502

Nekhamkina, O., and Sheintuch, M. (2012). Are 3-D models necessary to simulate packed bed reactors? Analysis and 3-D simulations of adiabatic and cooled reactors. *AIChE J.* 58, 3494–3503. doi:10.1002/aic.13752

Nibbelke, R. H., Hoebink, J. H. B. J., and Marin, G. B. (1998). Kinetically induced multiplicity of steady states in integral catalytic reactors. *Chem. Eng. Sci.* 53, 2195–2210. doi:10.1016/S0009-2509(98)00055-4

Padberg, G., and Wicke, E. (1967). Stabiles und instabiles Verhalten eines adiabatischen Rohrreaktors am Beispiel der katalytischen CO-Oxydation. *Chem. Eng. Sci.* 22, 1035–1051. doi:10.1016/0009-2509(67)80167-2

Papadias, D., Edsberg, L., and Björnbom, P. (2001). Effect of eccentricity and interaction between kinetics and mass transfer on the behaviour of catalytic annular reactors: a comparison between lumped and distributed models. *Chem. Eng. Sci.* 56, 4863–4878. doi:10.1016/S0009-2509(01)00132-4

Pérez-Ramírez, J. (2000). The six-flow reactor technology: a review on fast catalyst screening and kinetic studies. *Catal. Today.* 60, 93–109. doi:10.1016/S0920-5861(00)00321-7

Pita, J., Balakotaiah, V., and Luss, D. (1989). Thermoflow multiplicity in a packed-bed reactor: conduction and cooling effects. *AIChE J.* 35, 373–384. doi:10.1002/aic.690350305

Puszyński, J., and Hlavacek, V. (1984). Experimental study of ignition and extinction waves and oscillatory behavior of a tubular nonadiabatic fixed bed reactor for the oxidation of carbon monoxide. *Chem. Eng. Sci.* 39, 681–692. doi:10.1016/0009-2509(84)80175-X

Puszyński, J., Šnita, D., Hlaváček, V., and Hofmann, H. (1981). A revision of multiplicity and parametric sensitivity concepts in nonisothermal nonadiabatic packed bed chemical reactors. *Chem. Eng. Sci.* 36, 1605–1609. doi:10.1016/0009-2509(81)80004-8

Schmitz, R. A. (1975). "Multiplicity, stability, and sensitivity of states in chemically reacting systems—a review," in *Chemical reaction engineering reviews*, Editor H. M. Hulburt (Washington, DC: American Chemical Society), Vol. 148, 156–211. doi:10.1021/ba-1975-0148.ch007

Schmitz, R. A., and Amundson, N. R. (1963). An analysis of chemical reactor stability and control-VII. *Chem. Eng. Sci.* 18, 447–456. doi:10.1016/0009-2509(63)80033-0

Sheintuch, M. (1987). The determination of global solutions from local ones in catalytic systems showing steady-state multiplicity. *Chem. Eng. Sci.* 42, 2103–2114. doi:10.1016/0009-2509(87)85031-5

Sheintuch, M. (1997). Dynamics of catalytic reactions and reactors. *Catal. Today.* 36, 461–476. doi:10.1016/S0920-5861(96)00237-4

Sinkule, J., Hlaváček, V., and Votruba, J. (1976a). Modeling of chemical reactors-XXXI. *Chem. Eng. Sci.* 31, 31–36. doi:10.1016/0009-2509(76)85005-1

Sinkule, J., Votruba, J., Hlaváček, V., and Hofmann, H. (1976b). Modeling of chemical reactors-XXX. *Chem. Eng. Sci.* 31, 23–29. doi:10.1016/0009-2509(76)85004-X

Szeifert, F., Chován, T., Nagy, L., Abonyi, J., and Árva, P. (2007). Runaway of chemical reactors: parametric sensitivity and stability. *Hungar. J. Ind. Chem.* 35. doi:10.1515/127

Theurich, S., Rönsch, S., and Güttel, R. (2019). Transient flow rate ramps for methanation of carbon dioxide in an adiabatic fixed-bed recycle reactor. *Energy Technol.* 8, 1901116. doi:10.1002/ente.201901116

Trinh, S., and Ramkrishna, D. (1996). Pattern formation in fixed bed catalytic reactors-I. *Chem. Eng. Sci.* 51, 4887–4901. doi:10.1016/0009-2509(96)00298-9

Trinh, S., and Ramkrishna, D. (1997). Pattern formation in fixed-bed catalytic reactors-II. *Chem. Eng. Sci.* 52, 3561–3578. doi:10.1016/S0009-2509(97)00148-6

van Heerden, C. (1953). Autothermic processes. *Ind. Eng. Chem.* 45, 1242–1247. doi:10.1021/ie50522a030

Varma, A. (1980). On the number and stability of steady states of a sequence of continuous-flow stirred tank reactors. *Ind. Eng. Chem. Fund.* 19, 316–319. doi:10.1021/i160075a016

Viswanathan, G. A., Sheintuch, M., and Luss, D. (2008). Transversal hot zones formation in catalytic packed-bed reactors. *Ind. Eng. Chem. Res.* 47, 7509–7523. doi:10.1021/ie8005726

Wagialla, K. M., and Elnashaie, S. S. E. H. (1995). Bifurcation and complex dynamics in fixed-bed catalytic reactors. *Chem. Eng. Sci.* 50, 2813–2832. doi:10.1016/0009-2509(95)00042-4

Wedel, S., and Luss, D. (1984). Steady-state multiplicity features of an adiabatic fixed-bed reactor with Langmuir-Hinshelwood kinetics; carbon monoxide or carbon dioxide methanation. *Ind. Eng. Chem. Fund.* 23, 280–288. doi:10.1021/i100015a003

Wenzel, M. (2018). Reverse water-gas shift chemical looping for syngas production from CO_2. PhD thesis. Magdeburg: Otto-von-Guericke-Universität Magdeburg. doi:10.25673/13421

Wood, D. A., Nwaoha, C., and Towler, B. F. (2012). Gas-to-liquids (gtl): a review of an industry offering several routes for monetizing natural gas. *J. Nat. Gas Sci. Eng.* 9, 196–208. doi:10.1016/j.jngse.2012.07.001

Xu, J., and Froment, G. F. (1989). Methane steam reforming, methanation and water-gas shift: I. Intrinsic kinetics. *AIChE J.* 35, 88–96. doi:10.1002/aic.690350109

Young, L. C., and Finlayson, B. A. (1973). Axial dispersion in nonisothermal packed bed chemical reactors. *Ind. Eng. Chem. Fund.* 12, 412–422. doi:10.1021/i160048a004

Zaldívar, J. M., Cano, J., Alós, M. A., Sempere, J., Nomen, R., Lister, D., et al. (2003). A general criterion to define runaway limits in chemical reactors. *J. Loss Prev. Process. Ind.* 16, 187–200. doi:10.1016/S0950-4230(03)00003-2

Zimmermann, R. T., Bremer, J., and Sundmacher, K. (2020). Optimal catalyst particle design for flexible fixed-bed CO2 methanation reactors. *Chem. Eng. J.* 387, 123704. doi:10.1016/j.cej.2019.123704

GLOSSARY

Latin

$\boldsymbol{A}$ surface (m^2)

Bo Bodenstein number

$\boldsymbol{c}$ concentration (mol/m^3)

c_p heat capacity (J/(kgK))

$\boldsymbol{C}$ constant (various)

$\mathbf{Da_I}$ first Damköhler number

$\mathscr{D}$ diffusion coefficient (m^2/s)

$E_\mathbf{A}$ activation energy (kJ/mol)

$\boldsymbol{F}$ specific gas flow ($NL/(hg_{cat})$)

k heat transport coefficient (W/(mK))

$\boldsymbol{k}$ reaction rate constant ($mol/(bar\,g_{cat}s)$)

$\boldsymbol{K}$ adsorption and equilibrium constant (various)

$\boldsymbol{L}$ reactor length (m)

$\dot{\boldsymbol{m}}$ mass flow (kg/s)

$\boldsymbol{M}$ molar mass (kg/mol)

$\boldsymbol{n}$ total stage number in CSTR cascade

Pe Péclet number

$\boldsymbol{p}$ pressure (bar)

r mass-based reaction rate ($mol/(g_{cat}s)$)

$\tilde{\mathbf{r}}$ molar reaction rate ($mol/(m^3_{cat}s)$)

$\boldsymbol{R}$ inner radius of tubular reactor (m)

R reactive source term ($mol/(m^3s)$)

$\mathscr{R}$ universal gas constant ($J/(mol\,K)$)

St Stanton number

$\boldsymbol{T}$ temperature (K)

$\boldsymbol{v}$ superficial velocity (m/s)

$\boldsymbol{V}$ reactor volume (m^3)

$\dot{\boldsymbol{V}}$ volume flow (m^3/s)

$\boldsymbol{w}$ mass fraction

$\boldsymbol{X}$ conversion

$\boldsymbol{x}$ molar fraction

Greek

ΔH adsorption enthalpy (J/mol)

$\Delta_R\tilde{G}^0$ Gibbs free energy of reaction (STP) (J/mol)

$\Delta_R\tilde{H}^0$ Reaction enthalpy (STP) (J/mol)

$\Delta T_\mathbf{ad}$ adiabatic temperature rise (K)

$\boldsymbol{\varepsilon}$ fixed-bed void fraction

$\boldsymbol{\eta}$ catalyst effectiveness factor

$\boldsymbol{\lambda}$ thermal conductivity (W/(mK))

$\boldsymbol{\nu}$ stoichiometric coefficient

$\boldsymbol{\rho}$ density (kg/m^3)

$\boldsymbol{\tau}$ residence time (s)

Subscripts

$_\alpha$ component {CH_4, CO_2, H_2O, H_2}

$_{\mathbf{Bo}}$ Bodenstein number

$_{\mathbf{cat}}$ catalyst phase

$_{\mathbf{cool}}$ cooling

$_{\mathbf{eq}}$ equilibrium

$_{\mathbf{gas}}$ gas phase

$_{\mathbf{in}}$ inlet

$_{\mathbf{meth}}$ methanation reaction

$_{\mathbf{mix}}$ mixture

$_{\mathbf{n}}$ total stage number

$_{\mathbf{op}}$ operation

$_{\mathbf{OP}}$ operation point

$_{\mathbf{out}}$ outlet

$_{\mathbf{ref}}$ reference

$_{\mathbf{p}}$ particle

$_{\mathbf{z}}$ axial

Superscripts

^{0} STP

$^{\mathbf{c}}$ catalyst

$^{\mathbf{e}}$ energy

$^{\mathbf{eff}}$ effective

$^{\mathbf{exp}}$ experimental

$^{\mathbf{g}}$ gas

$^{\mathbf{m}}$ mass

* arg max value

Abbreviations

ATR adiabatic temperature rise

CM cell model

DM dispersion model

DEN denominator

CSTR continuously stirred tank reactor

PFTR plug flow tubular reactor

RWGS reverse water-gas shift

STP standard temperature and pressure

Advantages of publishing in Frontiers

OPEN ACCESS
Articles are free to read for greatest visibility and readership

FAST PUBLICATION
Around 90 days from submission to decision

HIGH QUALITY PEER-REVIEW
Rigorous, collaborative, and constructive peer-review

TRANSPARENT PEER-REVIEW
Editors and reviewers acknowledged by name on published articles

Frontiers
Avenue du Tribunal-Fédéral 34
1005 Lausanne | Switzerland

Visit us: www.frontiersin.org
Contact us: frontiersin.org/about/contact

REPRODUCIBILITY OF RESEARCH
Support open data and methods to enhance research reproducibility

DIGITAL PUBLISHING
Articles designed for optimal readership across devices

FOLLOW US
@frontiersin

IMPACT METRICS
Advanced article metrics track visibility across digital media

EXTENSIVE PROMOTION
Marketing and promotion of impactful research

LOOP RESEARCH NETWORK
Our network increases your article's readership